Understanding and Exploiting Wind Tunnels with Porous Flexible Walls for Aerodynamic Measurement

Kenneth A. Brown

Dissertation submitted to the Faculty of the
Virginia Polytechnic Institute and State University
in partial fulfillment of the requirements for the degree of

Doctor of Philosophy
in
Mechanical Engineering

William Devenport, Chair
Aurelien Borgoltz
K. Todd Lowe
Mayuresh Patil
Ricardo Burdisso
Rakesh Kapania

July 21, 2016
Blacksburg, Virginia

Keywords: wind tunnel, Kevlar wall, wall interference, panel method, fabric mechanics

Understanding and Exploiting Wind Tunnels with Porous Flexible Walls for Aerodynamic Measurement

Kenneth A. Brown

(ABSTRACT)

The aerodynamic behavior of wind tunnels with porous, flexible walls formed from tensioned Kevlar has been characterized and new measurement techniques in such wind tunnels explored. The objective is to bring the aerodynamic capabilities of so-called Kevlar-wall test sections in-line with those of traditional solid-wall test sections. The primary facility used for this purpose is the 1.85-m by 1.85-m Stability Wind Tunnel at Virginia Tech, and supporting data is provided by the 2-m by 2-m Low Speed Wind Tunnel at the Japanese Aerospace Exploration Agency, both of which employ Kevlar-wall test sections that can be replaced by solid-wall test sections. The behavior of Kevlar fabric, both aerodynamically and mechanically, is first investigated to provide a foundation for calculations involving wall interference correction and determination of the boundary conditions at the Kevlar wall. Building upon previous advancements in wall interference corrections for Kevlar-wall test sections, panel method codes are then employed to simulate the wind tunnel flow in the presence of porous, flexible Kevlar walls. An existing two-dimensional panel method is refined by examining the dependency of correction performance on key test section modeling assumptions, and a novel three-dimensional method is presented. Validation of the interference corrections, and thus validation of the Kevlar-wall aerodynamic performance, is accomplished by comparing aerodynamic coefficients between back-to-back tests of models carried out in the solid- and Kevlar-wall test sections. Analysis of the test results identified the existence of three new mechanisms by which Kevlar walls cause wall-interference. Additionally, novel measurements of the boundary conditions are made during the Kevlar-wall tests to characterize the flow at the boundary. Specifically, digital image correlation is used to measure the global deformation of the Kevlar walls under wind loading. Such data, when used in conjunction with knowledge of the pre-tension in the Kevlar wall and the material properties of the Kevlar, yields the pressure loading experienced by the wall. The pressure loading problem constitutes an inverse problem, and significant effort is made towards overcoming the ill-posedness of the problem to yield accurate wall pressure distributions, as well as lift measurements from the walls. Taken as a whole, this document offers a comprehensive view of the aerodynamic performance of Kevlar-wall test sections.

The author received support primarily from the Virginia Tech Stability Wind Tunnel. Secondary funding was provided by the National Science Foundation under Grant No. OISE-1316985 and the Japan Society for the Promotion of Science under ID: SP13004.

Understanding and Exploiting Wind Tunnels with Porous Flexible Walls for Aerodynamic Measurement

Kenneth A. Brown

(GENERAL AUDIENCE ABSTRACT)

Traditional wind tunnels, which measure the aerodynamic behavior of vehicles and components relevant to the aerospace industry, enclose some test object with solid walls and accelerate flow around the object. A new configuration has been developed which uses instead flexible, porous walls which are formed from tensioned Kevlar fabric. The original advantage of this configuration lies in its ability to produce high fidelity measurements of the acoustic signature of a model in a stream of air. This new configuration also has been emerging as tool for making the traditional measurements of aerodynamic behavior noted above. However, special considerations have to be made for the so-called Kevlar-wall test section because of the flexibility and porosity of the walls. This study focuses on understanding and exploiting Kevlar-wall wind tunnels with the hope to bring the aerodynamic measurement capabilities of Kevlar-wall test sections in-line with those of traditional solid-wall test sections. The primary facility used for this purpose is the Stability Wind Tunnel at Virginia Tech, and supporting data is provided by the Low Speed Wind Tunnel at the Japanese Aerospace Exploration Agency, both of which employ Kevlar-wall test sections that can be replaced by solid-wall test sections. The behavior of Kevlar fabric, both aerodynamically and mechanically, is first investigated to provide a foundation for calculations of the effect of the Kevlar's porosity and flexibility on the flow around a model in the test section. Building upon previous advancements in this area, computer simulations are then employed to predict the wind tunnel flow in the presence of porous, flexible Kevlar walls. An existing two-dimensional simulation is refined by examining the dependency of the simulation on key modeling assumptions, and a novel three-dimensional method is presented. Validation of the simulations' effectiveness in providing accurate corrections for the Kevlar porosity and flexibility is accomplished by comparing measurements between back-to-back tests of models carried out in the solid- and Kevlar-wall test sections. Additionally, novel measurements of the deflection and pressure distributions over the Kevlar walls are made during the Kevlar-wall tests. Specifically, a three-dimensional camera imaging system is used to measure the deformation of the Kevlar walls under wind loading. Such data, when used in conjunction with knowledge of the pre-tension in the Kevlar wall, yields the pressure loading experienced by the wall. Taken as a whole, this document offers a comprehensive view of the aerodynamic performance of Kevlar-wall test sections.

Acknowledgments

I am very grateful to the professors who have taught me the last four years. Particularly, as my main adviser, Dr. Devenport has educated me in every aspect of work including technical knowledge, writing, presenting, scheduling, managing, logbooking, seeing the importance of small achievements, and understanding the place of my work in the larger scientific community. He always has an eye out for my long-term interests, as well as the short-term goals, and has given advice both professionally and personally. I could not have asked for a better adviser. Dr. Borgoltz has also contributed significant time to teaching me about wind tunnel testing which I appreciate very much. Additionally, I have had useful conversations with each of Dr. Lowe, Dr. Patil, Dr. Burdisso, and Dr. Kapania. Dr. Canfield was an excellent mentor on the structural side of membrane mechanics and finite element simulations.

The tests performed for this study would not have been made without the worthwhile work of Bill Otejens, Mike Morton, and Tim Meyers of the Stability Wind Tunnel. Liselle Joseph gave much needed help multiple times when we were running out of time in the wind tunnel. Dan Cadel was invaluable in his assistance with optics and image processing. Thank you to Nanya Intaratep for her help with trip fabrication and other testing issues. Matt Kuester offered important advice on wind tunnel instrumentation. Nathan Alexander has been a helpful colleague. Nick Molinaro, Manuj Awasthi, Ian Clark, Anthony Millican, and Henry Murray gave their time to help with the wind tunnel tests. Julio Estrella was my first undergraduate minion and did excellent work with porosity testing, tension meter development, and the glamorous job of installing new Kevlar windows. Stephanie Hoang was his very capable protégé who worked effectively on development and testing of the tension meter. Julian Brown played a huge role in the development of the camera system described in Chapter 7 and was always a fun work partner. Thank you to all of you.

The Aerospace and Ocean Engineering Shop has been integral to my work, and I want to say thank you to James Lambert, Scott Patrick, Andy Tawney, Cameron Hollandsworth, and Matt Mills. The staff of the Aerospace and Ocean Engineering Department has been ever helpful including Rita Caldwell, Shannon Bennett, Jon Couch, Amy Burchett, and Kelsey Spencer. Cathy Hill of the Mechanical Engineering Department is an all-star graduate adviser.

A special part of my graduate studies was spending a summer in Tokyo, Japan. I would like

to sincerely thank all the workers at the Japanese Aerospace Exploration Agency's Aircraft System Research Group and the Wind Tunnel Technology Center for their warm hospitality and assistance. Dr. Kazuomi Yamamoto offered me amazing hospitality and support as I worked for his group. Mr. Hiroki Ura and Mr. Hiroshi Uchida were also a huge help and good friends, as well as were all the wind tunnel engineers. Others who contributed much time and effort include Dr. Yasushi Ito, Dr. Mitsuhiro Murayama, Dr. Kazuhisa Amemiya, Mrs. Junko Mohri, Mr. Kentaro Tanaka, Mr. Tohru Hirai, and all the members of Dr. Naoko Tokugawa and Mr. Hiroaki Ishikaw's research group.

I would like to acknowledge those with whom I have shared office space for the last two years. I will truly miss my workout partners and friends Di Zhang, Haoting Wang, Wenjiang Xu, as well as my two favorite officemates, Fan He and Ning Liu. Tobias Ecker, Tamy Guimares-Bucalo, Kara Crosser, Marcie Stuber, and all the people mentioned three paragraphs ago are also awesome. To all the members of the Aerial Orb Experts intramural teams; we are truly champions, and no one can take that away from us.

I also want to commend my roommates of the last 6 years, including Andrew Skinner, Thomas Curley, Adam White, Sam Tabacchi, Joe Cline, Lucas Shoults, Scott Hopkins, Mark Bychowski, Eli White, Patrick Trail, and Taylor Terrill, for their never-ending efforts to try to draw me away from studying and working hard. Thank you to Daniel and Sarah Patino who have finally stopped taking advantage of my washer and dryer. Dietrich and Carlie Linde are punks, but I love them anyway. Darrell and Laura Cook are amazing friends.

Lastly, my mother, father, brother, sister-in-law, niece and nephew are ever close to my heart and supportive always. Thank you!

Contents

List of Figures

List of Tables

Chapter 1

The Kevlar-Wall Test Section

Since 2006, the Stability Wind Tunnel at Virginia Tech has pioneered a new type of test section for aeroacoustic and aerodynamic testing[1][2][3]. Applications for the Kevlar-wall anechoic test section, as it is called, are the collection of noise data from wind turbine blades[4] and wing models[5], research of the effects of surface discontinuities and surface roughness on pressure fluctuations in the boundary layer[6, 7], and the study of rotors embedded in a boundary layer[8], for example. The Kevlar-wall test section has the advantage in all these cases of providing detailed acoustic measurements without the need for an open-jet test section, thus making it the emerging standard for aeroacoustic testing. In less than a decade, the Kevlar-wall wind tunnel has matured for use in full-scale testing through improvements to both the aeroacoustic and aerodynamic measurement capabilities as reviewed in Devenport *et al.*[9]. Facilities other than Virginia Tech to adopt this technology include the Japanese Aerospace Exploration Agency (JAXA) and the Naval Sea Warfare Center Carderock Division as described in Glegg and Devenport[10].

The Kevlar-wall test section is novel in that the flow is contained within tensioned side walls made of Kevlar fabric while noise is allowed to pass outside the walls where it can be measured by acoustic instrumentation that is shielded from the flow. As shown by the layout of a generic Kevlar-wall test section in Figure 1.1, the Kevlar-wall configuration consists of a test section flanked by two anechoic chambers. Large rectangular openings in the side walls cover the full height of the test section and a large portion of the streamwise length of the test section to serve as acoustic windows. These openings are covered with tensioned sheets of plain woven Kevlar fabric which act to contain the freestream flow, thus shielding acoustic instrumentation inside the anechoic chambers from the flow. The ceiling and floor surfaces are rigid panels also covered with Kevlar that cover acoustically treated sections above and below the test section, respectively, except in the regions of the model mounting.

The advantages of such a Kevlar-wall test section from an aeroacoustic standpoint are fairly apparent. The test section acts acoustically as if it were an open-jet test section, yet does not produce the large shear layers characteristic of such test sections nor requires a jet-

catcher. Jaeger[11] describes initial developments that led to using Kevlar as a shielding device for microphone arrays, and Devenport *et al.*[9] highlights the acoustic advantages of the full Kevlar-wall configuration including the reduction of parasitic noise and opportunity for closer microphone mounting. Debrouwere[12] has shown Kevlar and its associated wall boundary layer to have favorable acoustic properties.

The advantages from an aerodynamic standpoint, compared to an open-jet section, are a dramatic reduction in lift interference for a much closer simulation of free-flight. Some of the hardships of measuring aerodynamic characteristics in open-jet test sections are illustrated in Moreau *et al.*[13], for instance, where strong streamline curvature effects produce effective angle of attack corrections typically in excess of 50%, as well as un-correctable distortions in the pressure distributions over the model. As the demands of high Reynolds number testing lead to larger ratios of chord to test section height, the aerodynamic interference problem in open-jet test sections is exacerbated.

The aerodynamic advantages of a Kevlar-wall test section, compared to a solid-wall test section, are that the Kevlar-wall test section exhibits a reduction in wall interference effects, at least for low to moderate loading conditions. This reduction is due to the boundary conditions of the porous, flexible Kevlar walls which tend to place the test section's aerodynamic performance between that of a solid-wall and an open-jet test section.

This study examines multiple aspects of the aerodynamic performance of Kevlar-wall test sections, seeking to propel forward the capability of aerodynamic measurements in such test sections to a level comparable to that of the aerodynamic industry-standard solid-wall test sections. Examined in this work are the characterization of Kevlar fabric itself and validation and refinement of techniques to correct aerodynamic data for the effects of wall interference. The configurations considered include two- and three-dimensional lifting models with the aim towards providing a generalized framework and methodology for performing high fidelity measurements of aerodynamic performance in Kevlar-wall test sections.

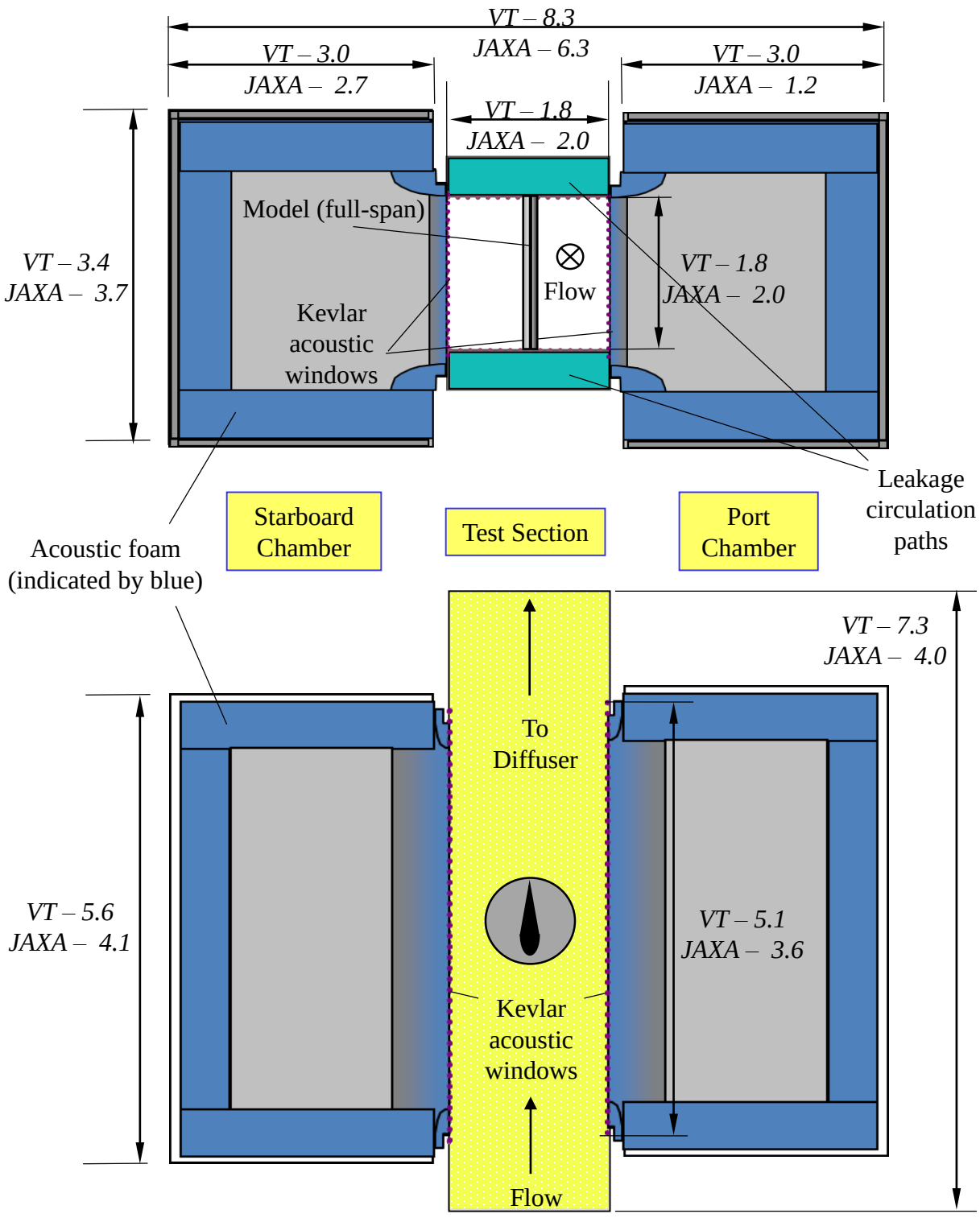

Figure 1.1: Schematic drawings of a Kevlar-wall test section showing the cross-sectional view (above) and the planform view (below). Dimensions in meters are given for the Kevlar-wall test sections of both Virginia Tech's (VT) Stability Wind Tunnel and the Japan Aerospace Exploration Agency's (JAXA) 2m-by-2m Low Speed Wind Tunnel.

Chapter 2

Literature Review

2.1 Overview of Solid-Wall Test Sections

As the foundation of aerodynamic ground testing is the solid-wall test section, the wall-interference mechanisms, wall-interference correction methods, and measurement techniques of such test sections will be reviewed below.

2.1.1 Wall Interference Mechanisms for Solid-Wall Test Sections

When considering aerodynamic corrections in wind tunnels, there are three freestream conditions experienced by a model that are affected by the presence of the wind tunnel walls which are the dynamic pressure, angle of attack, and Mach number[14].

Change to dynamic pressure around the model due to the presence of the walls is usually termed blockage. Blockage occurs when mass flow must accelerate or decelerate to maintain continuity while passing through restricted space such as a wind tunnel test section. For the case of closed, or solid-wall, test sections, blockage leads to an increase in dynamic pressure as the flow must accelerate past a model blocking its path. For the case of open-jet test sections, blockage effects generally lead to a decrease in the dynamic pressure as the flow expands and thus decelerates beyond the dimensions of the nozzle outlet. Blockage can be divided into two categories. First, solid blockage accounts for the change in dynamic pressure of the flow in the region around the model due to the change in test section area caused by the presence of the model. Second, wake blockage occurs by the same principal as solid blockage except that the model's wake, a viscous region of low momentum flow separate from the freestream flow, is the structure creating the change in test section area.

Change to the angle of attack experienced by the model due to the presence of the walls is usually termed lift interference. Lift interference, by definition, is any effect that alters the

circulation around the model[15]. Lift interference may be considered in a first-order sense as a change to the angle of attack, and higher-order representation must consider changes in the flow curvature, as well. Specifically, changes streamline curvature from the free-flight case produces an increase in angle of attack, lift, and quarter-chord pitching moment for solid-wall test sections and a decrease in these for open-jet test sections. Furthermore, in the case of semi-span wings, the presence of the wind tunnel test section affects the downwash normal to the freestream direction. For the solid-wall test section, a wing will have a smaller downwash and larger upwash relative to the same angle of attack in free-flight. This can be accounted for by calculating an effective angle of attack, slightly larger than the measured geometric angle of attack, which is equivalent to the free-flight angle of attack. The measured lift and drag must then be transformed to align with the effective angle of attack. The same process occurs for open-jet test sections, but the downwash and upwash changes are in the reverse directions.

Mach number is typically of lesser importance for low-speed wind tunnel testing, and it is corrections for dynamic pressure and angle of attack rather Mach number which will be the focus of this study.

2.1.2 Correction Methods for Solid-Wall Test Sections

This section presents a review of past work in wall interference corrections. The first three sections focus on well-established methods used among the wind tunnel community: classical corrections, panel method corrections, and measured variable corrections. Included throughout these will be discussion on the details of the blockage and lift interference corrections and their application to wind tunnel testing. Corrections to account for blockage and lift interference due to wind tunnel walls are typically first-order; they correct the freestream, or far-field, value but neglect changes in distribution of these values across the model.

2.1.2.1 Classical Correction Methods

Classical corrections are defined by four characteristics: the use potential flow theory, inclusion of wall effects as perturbations to the flow, assumption that model geometries small relative to the wind tunnel size and have straight, downstream trailing wakes, and assumption of wind tunnel walls that are straight, infinite, and require either constant pressure or zero normal velocity[15]. An analysis known as the method of images adheres to these characteristics and represents the model as a set of singularities that produce a flow field similar to that of the actual model. The singularities typically employed are doublets to model solid blockage, sources to model wake blockage, and vortices to model circulation. In addition to the singularity placed at the model location, appropriate placement of singularities outside the test section is then sought to exactly cancel the normal velocity produced by the internal singularity at the test section walls. This placement takes the form of images

located in the model's streamwise location but spaced apart in the normal direction by the test section height and extending to infinity. When the velocity induced by these images is summed over a sufficiently large number of images, the streamlines at the location of the wind tunnel walls become straight, and they thus simulate the actual wind tunnel wall if the boundary layer thickness is neglected. The result is that the singularities outside the test section describe the incremental interference for a given component of velocity due to the presence of the walls which allows for correction of the measured angle of attack and aerodynamic coefficient data. The incremental interference velocities are typically evaluated either at the model quarter-chord, the model half-chord, or by an average over the model.

Throughout this section, corrections are given as a function of Mach number which can be derived from different methods. Using the method of the Prandtl-Glauert transformation, for instance, the compressible flow solution can be derived from the incompressible solution by scaling the y- and z-axes by the Prandtl-Glauert factor, $\beta = \sqrt{1 - M_\infty}$, and scaling the pressure coefficients and longitudinal velocity by $1/\beta^2$[16].

2.1.2.1.1 Blockage Corrections

In contrast to free-flight where the flow is free to expand or contract in the direction normal to the freestream, mass flow through a test section must be conserved, so changes in flow area lead to changes in flow velocity. Both solid blockage and wake blockage are accounted for by a correction factor, ε, given by Equation 2.1

$$\varepsilon = \frac{u}{V_\infty} \tag{2.1}$$

where u is the incremental velocity in the streamwise direction induced by the walls at the quarter-chord location of the model and V_∞ is the uncorrected freestream velocity. The factor ε is used to produce the corrected dynamic pressure, q, by Equation 2.2

$$q_c = q(1 + 2\varepsilon + \varepsilon^2) \approx \frac{q}{1 - 2\varepsilon} \tag{2.2}$$

where q_c is the corrected value. Considering compressibility effects, the above equation becomes Equation 2.3[16]

$$q_c \approx \frac{q}{1 - (2 - M_\infty^2)\varepsilon}. \tag{2.3}$$

The corrected dynamic pressure is ultimately used to adjust lift, moment, and drag coefficients which are normalized on dynamic pressure.

Solid Blockage For two-dimensional flows over airfoils, Allen and Vincenti[17] recommend the solid blockage correction given by Equations 2.4, 2.5, and 2.6

$$\varepsilon_{sb} = \frac{1}{[1-M^2]^{1.5}}\Lambda\sigma \tag{2.4}$$

$$\Lambda = \frac{16}{\pi}\int_0^t \frac{y}{c}[[1-P(\frac{x}{c})](1+\frac{\partial y}{\partial x})]^{0.5}\,\mathrm{d}(\frac{x}{c}) \tag{2.5}$$

$$\sigma = \frac{\pi^2}{48}(\frac{c}{h})^2 \tag{2.6}$$

where M is the uncorrected Mach number, x and y are the abscissa and ordinate of the base profile of the airfoil, P is the measured pressure coefficient distribution at the given chordwise location, c is the airfoil chord, and h is the test section dimension in the thickness-wise direction. The derivation of this correction, described in part below, is given in full detail by Lock[18] and Glauert[19]. This correction is based upon a relation between the airfoil's thickness and chord and an equivalent upstream-pointing doublet of strength $\frac{\pi}{2}\Lambda t^2 U_\infty$ which produces a potential flow-field equivalent to that of a cylinder $t\sqrt{\Lambda}$ in diameter. Using an infinite series of images of the doublet above and below the test section, the increment to the freestream velocity in the streamwise direction is calculated ignoring higher order terms of t/h and c/h. In order to find the value of Λ, the experimentally measured pressure distribution around the airfoil is used to calculate the velocity along the airfoil surface by Bernoulli's equation which is then integrated and used to give the effective doublet strength.

For three-dimensional flow over wings, Herriot[16] recommend the solid blockage correction given by Equations 2.7 and 2.8

$$\varepsilon_{sb} = \frac{1}{[1-M^2]^{1.5}}\frac{K_2\tau_3 2cst}{C^{1.5}} \tag{2.7}$$

$$K_2 = \frac{\pi^{1.5}}{16}\frac{\Lambda}{t/c} \tag{2.8}$$

where τ_3 is a look-up factor depending primarily on the ratio of the wingspan to tunnel span and the tunnel aspect ratio, C is the tunnel cross-sectional area, and s is the wingspan. The derivation of this correction is the same as for the two-dimensional case above, except that the two-dimensional point doublet becomes a three-dimensional line doublet. Herriot notes that the effective thickness of a constant strength line doublet is greater at its center-span and diminishes at its tips, but a constant strength doublet is a suitable approximation.

Wake Blockage Similarly to solid blockage, wake blockage induces a change in the streamwise velocity felt at the model location due to the blockage of the wake behind the model. The wake has less dynamic pressure than the surrounding freestream fluid due to the viscous effects experienced by the flow which result in transfer of dynamic pressure to thermal energy[17]. Although the dynamic pressure, and thus the velocity, in the wake are reduced, the total mass flow through the test section must be maintained to satisfy mass continuity, so the inviscid flow outside the wake must accelerate to account for the loss of velocity in the wake.

To calculate the blockage effect of a wake in two-dimensions, a source whose strength is determined by the measured drag coefficient is placed at the airfoil location along with an infinite series of source images on either side of the test section. The flow created by this series of sources does not violate the boundary condition of the closed wind tunnel walls, but does induce both a velocity acting against the freestream velocity in the upstream and a velocity acting with the freestream in the downstream. An incremental addition to the freestream is then required to maintain the upstream freestream velocity at its measured value which is given by Equations 2.9 and 2.10

$$\varepsilon_{wb} = \frac{1 + 0.4M^2}{1 - M^2}\tau C_d \tag{2.9}$$

$$\tau = \frac{c}{4h} \tag{2.10}$$

where C_d is the uncorrected drag coefficient[17]. Herriot[16] derives the same formula for wake blockage in the case of three-dimensional wings using a three-dimensional point source to represent the wake.

2.1.2.1.2 Lift Interference Corrections

The presence of the wind tunnel walls alters the direction of streamlines as compared to their free-flight behavior. For two-dimensional flow, the wall-effect is to increase the curvature of the streamlines. For three-dimensional flow, increased curvature is augmented by reductions in the downwash felt over the model. In both cases, the effect for a solid-wall test section amounts to the effective free-flight angle of attack being more severe than the geometric wind tunnel angle of attack. Method of images approaches for both two- and three-dimensional models are presented below.

Two-Dimensional Lift Interference Allen and Vincenti[17] use a method of images analysis to correct for the streamline curvature in two-dimensional flow. The lift of the airfoil is represented by a vortex sheet spread over the chordline. The sum of images of the vortex sheet moving progressively away from the test section produce a zero transverse

velocity at the tunnel boundaries. Along the singularity location on the chordline, the result is that the streamwise component of velocity due to the vortex sheet images cancels while the velocity normal to the chord due to the images adds one to another. This additive velocity is the walls' interference on the flow. The analysis assumes that the model is small relative to the test section, the model is negligibly thin, and angles of attack are small, however, experience has shown the method to valid for airfoils of finite thickness and angles of attack up to flow separation. It is interesting to note that there is a streamwise component of induced velocity, also, as one moves away from the singularity location. This component is only significant for large models and is usually neglected. The upwash induced by the walls can be accounted for with a correction to the angle of attack, lift, and pitching moment as given in Equations 2.11, 2.12, and 2.13

$$\Delta\alpha_{sc} = \frac{1}{\sqrt{1-M^2}}\frac{57.3\sigma}{2\pi}[C_l + 4C_{m,\frac{1}{4}c}] \quad (in \quad degrees) \tag{2.11}$$

$$\Delta C_{l,sc} = -\frac{1}{1-M^2}\sigma C_l \tag{2.12}$$

$$\Delta C_{m,\frac{1}{4}c,sc} = \frac{1}{1-M^2}\frac{\sigma}{4}C_l \tag{2.13}$$

where C_l is the uncorrected lift coefficient and $C_{m,\frac{1}{4}c}$ is the uncorrected coefficient of moment about quarter-chord.

This preceding correction is accurate to the second order of $\frac{c}{h}$ meaning that only the first and second order terms of chord over tunnel height have been retained and the others assumed negligible. Ewald[15] warns that such a second order analysis is valid only for models with $\frac{c}{h} < 0.4$ for the incompressible case and with $\frac{c}{\beta h} < 0.4$ for the compressible case. For cases outside these envelopes, Ewald offers the corrections to the fourth order of $\frac{c}{h}$.

Three-Dimensional Lift Interference Three-dimensional wings must shed vorticity into the wake which results in so-called *downwash* both upstream and downstream of the model. Downwash acts to reduce the effective angle of attack seen by the model, and the transformation of the direction of the freestream velocity results in the appearance of a so-called *induced drag*. When wind tunnel walls are present around a model, the downwash is reduced; the effective angle of attack is larger than it would otherwise be in free-flight. In order to correct for such effects, the method of images approach presented by Barlow *et al.*[20] represents the model and its images by horseshoe vortices. The necessary increase in angle of attack to be applied to wind tunnel data is in Equation 2.14

$$\Delta\alpha_{dw} = \frac{180}{\pi}\frac{S}{C}C_L\delta \quad (in \quad degrees) \tag{2.14}$$

where S is the wing planform area, C is the tunnel cross-sectional area, C_L is the lift coefficient normalized on the wing planform area (rather than simply the chord as in the two-dimensional case), and δ is a look-up factor depending on the span load distribution, the ratio of model span to tunnel width, the shape of the test section, and whether or not the wing is on the tunnel centerline. The reduction in downwash caused by the tunnel walls increases in magnitude slightly moving from the model leading edge to trailing edge, and the quarter-chord location is selected as the point of evaluation. Unlike the correction for streamline curvature where the angle of attack is altered relative to a fixed freestream, the downwash effect of the wind tunnel walls alters the effective freestream direction experienced by the model. The correction for downwash therefore takes the form of a coordinate system rotation as in Equations 2.15 and 2.16

$$C_{L,dw} = C_L cos(\Delta\alpha_{dw}) - C_D sin(\Delta\alpha_{dw}) \approx C_L \tag{2.15}$$

$$C_{D,dw} = C_L sin(\Delta\alpha_{dw}) + C_D cos(\Delta\alpha_{dw}) \approx C_L \Delta\alpha_{dw} + C_D \tag{2.16}$$

where the approximations result because $cos(\Delta\alpha_{dw}) \approx 1$, C_D and $sin(\Delta\alpha_{dw})$ are both small values, and $sin(\Delta\alpha_{dw}) \approx \Delta\alpha_{dw}$. The downwash correction thus amounts to a change in the effective angle of attack and an increase in the induced drag felt by the model.

In addition to the downwash correction of Equation 2.14, a further streamline curvature correction accounts for the change in boundary-induced upwash along the chord. This correction takes the simplified form shown in Equation 2.17

$$\Delta\alpha_{sc} = \tau_2 \Delta\alpha_{dw} \quad (in \quad degrees) \tag{2.17}$$

where τ_2 is a look-up factor based on the tunnel dimensions and model chord length, a is the lift curve slope, the supscript sc indicates the additive correction owing to the upwash variation along the chord, and the supscript u indicates the uncorrected values. The magnitude of τ_2 is significantly less than unity for typical setups, and thus the effect of upwash variation along the chord is sometimes neglected.

2.1.2.1.3 Drag Corrections

Pressure gradients at the model location in a wind tunnel develop due to boundary layer growth on the wind tunnels walls along the length of the tunnel and the presence of the wake behind a model, both of which cause a decrease in total flow area and thus higher velocities and lower pressures downstream than upstream. In the presence of a pressure gradient in a wind tunnel, an additional correction required for the drag data is for horizontal buoyancy. There are two factors that contribute to horizontal buoyancy, both of which stem from the

pressure gradient present in wind tunnels of constant cross-section[19]. The first contribution to horizontal buoyancy comes directly from the streamwise pressure gradient, $\frac{\partial p}{\partial x}$, which when multiplied by the volume of the model yields a drag force on the model that would not exist in free-flight. The second contribution is a result of the squeezing of streamlines as the wall boundary layer grows which acts to accelerate the flow. The model and a virtual mass around the model can be thought of as accelerating relative to the flow, and this causes an additional drag force on the model. For an open test section, on the other hand, this effect produces a thrust force instead as the flow expands and decelerates. The total buoyancy drag force, D_B, including both contributions for a two-dimensional flow is in Equation 2.18

$$D_B = \frac{6h^2}{\pi}\Lambda\frac{\partial p}{\partial x} \tag{2.18}$$

where h is the height of the test section, Λ and σ are as defined in the blockage section ,and $\frac{\partial p}{\partial x}$ is the streamwise pressure gradient[17]. A method of images calculation yields the pressure gradient due to the presence of the wake as Equation 2.19

$$\frac{\partial p}{\partial x} = -\frac{1+0.4M^2}{[1-M^2]^{1.5}}\frac{\pi C_d q c}{6h^2} \tag{2.19}$$

where q is the uncorrected dynamic pressure. Combining Equations 2.18 and 2.19, the drag due to the pressure gradient caused by a two-dimensional wake is given in Equation 2.20

$$\Delta C_{d,b} = \frac{1+0.4M^2}{[1-M^2]^{1.5}}\Lambda\sigma C_d \tag{2.20}$$

where the subscript b indicates it is the buoyancy component of the drag correction only. For the three-dimensional case, Herriot[16] calculates Equation 2.21

$$\Delta C_{D,b} = \frac{1+0.4M^2}{[1-M^2]^{1.5}}\frac{K_1\tau_3 V_w}{C^{1.5}}C_D. \tag{2.21}$$

where K_1 depends on the base profile shape of the wing and V_w is the volume of the wing. This correction to drag is in addition to the corrections for solid and wake blockage as described above. Barlow *et al.*[20] state that the buoyancy effect caused by the growing boundary layer on the wind tunnel walls is usually insignificant for wings, only becoming significant for longer models such as full airplane or torpedo models.

2.1.2.1.4 Combined Corrections

The blockage, lift interference, and drag corrections of the previous sections are here combined to produce several useful formulas to compute all the aerodynamic corrections of a

solid-wall test section. Note that blockage parameter, ε, is related to the global coefficients through Equation 2.3 which relates the dynamic pressure to ε. All corrections assume $\gamma = 1.4$.

Two-Dimensional Corrections The combined corrections for two-dimensional flow are given below in Equations 2.22, 2.23, 2.24, and 2.25

$$\Delta\alpha = \frac{1}{\sqrt{1-M^2}}\frac{57.3\sigma}{2\pi}(C_l + 4C_{m,\frac{1}{4}c}) \quad (in \quad degrees) \tag{2.22}$$

$$C_{l,c} = C_l[1 - \frac{1}{1-M^2}\sigma - \frac{2-M^2}{[1-M^2]^{1.5}}\Lambda\sigma - \frac{(2-M^2)(1+0.4M^2)}{1-M^2}\tau C_d] \tag{2.23}$$

$$C_{m,\frac{1}{4}c} = C_{m,\frac{1}{4}}[1 - \frac{2-M^2}{[1-M^2]^{1.5}}\Lambda\sigma - \frac{(2-M^2)(1+0.4M^2)}{1-M^2}\tau C_d] + C_l\frac{1}{1-M^2}\frac{\sigma}{4} \tag{2.24}$$

$$C_{d,c} = C_d[1 - \frac{2-M^2}{[1-M^2]^{1.5}}\Lambda\sigma - \frac{(2-M^2)(1+0.4M^2)}{1-M^2}\tau C_d] \tag{2.25}$$

There is no term for buoyancy drag correction in Equaiton 2.25 because drag data taken with a wake rake do not detect the presence of any streamwise pressure gradient and therefore do not measure buoyancy drag. For models that do not have significant streamwise extent such as airfoils this is not believed to introduce significant error to the drag measurement as noted above.

Three-Dimensional Corrections The combined corrections for three-dimensional flow are given below in Equations 2.26, 2.27, 2.28, and 2.29

$$\Delta\alpha = (1+\tau_2)[57.3\frac{S}{C}C_L\delta] \quad (in \quad degrees) \tag{2.26}$$

$$C_{L,c} = C_L[1 - \frac{2-M^2}{[1-M^2]^{1.5}}\frac{K_2\tau_3 2cst}{C^{1.5}} - \frac{(2-M^2)(1+0.4M^2)}{1-M^2}\tau C_D] \tag{2.27}$$

$$C_{M,\frac{1}{4}c} = C_{M,\frac{1}{4}}[1 - \frac{2-M^2}{[1-M^2]^{1.5}}\frac{K_2\tau_3 2cst}{C^{1.5}} + \frac{(2-M^2)(1+0.4M^2)}{1-M^2}\tau C_D] \tag{2.28}$$

$$C_{D,c} = C_D[1 - \frac{2-M^2}{[1-M^2]^{1.5}}\frac{K_2\tau_3 2cst}{C^{1.5}} - \frac{(2-M^2)(1+0.4M^2)}{1-M^2}\tau C_D] + \frac{S}{C}C_{L,u}^2\delta \tag{2.29}$$

Note that again the buoyancy correction to drag is not included in Equation 2.29.

It is noted that for testing with reflection plane models, it is accurate to treat the corrections as if both halves of the model were present in a tunnel with doubled span[20]. Some vorticity is shed into the wake from the root boundary layer from reflection plan models, so the lift curve slope is sometimes lower and the induced drag higher than in the case of a full model.

2.1.2.2 Panel Method Correction Methods

Another approach to corrections are through panel methods which fall under the category of conventional corrections as specified by Ewald[15] as they are less restrictive than classical corrections, the only assumption remaining from the classical assumptions being that wall effects can be treated as perturbations to the flow. Panel methods may be used for corrections either standalone or in combination with static wall pressure measurements. First, several examples of standalone approaches will be examined followed by the static wall pressure approaches in the following section. All the examples presented are three-dimensional panel method codes unless otherwise noted.

Ulbrich[21] describe the panel method code ANTARES used at the NASA Ames 11-ft. Transonic Wind Tunnel. The model is represented with both a point doublet to simulate blockage and a line doublet to simulate lift interference. The walls are represented by a paneling of linearly varying source panels. Per standard practice with panel methods, the coefficient matrix describing the effect of each panel's source strength on the velocity components at the control point of every other panel is calculated from potential flow theory. The resultant matrix is found by summing the freestream velocity and porous velocity of each panel. Inverting the coefficient matrix using a double-precision solver and multiplying it by the resultant matrix yields the strengths of all the panels. The blockage, $\frac{u}{U_\infty}$, and lift interference, $\Delta\alpha$, are then given by the sum of the influence of each wall panel at the model location as given by Equations 2.30 and 2.31

$$\frac{u}{U_\infty} = \frac{1}{U_\infty}\sum_{n=1}^{N}[C_n]_1\mu_n \tag{2.30}$$

$$\Delta\alpha = tan^{-1}[\frac{v_m}{U_\infty}] = tan^{-1}[\frac{1}{U_\infty}\sum_{n=1}^{N}[C_n]_2\mu_n] \tag{2.31}$$

where N is the total number of wall panels, the n subscript indicates the index of the wall panels, C is the vector of influence coefficients of each of the wall panels on the model location, the subscripts 1 and 2 indicate either the u or v components of the induced velocity, respectively, and μ_n is the strength of each wall panel. For clarity later on, the above equations are cast in the form of influence coefficients rather than the velocity potential form

of Ulbrich[21]. Also note that for small angles, the tangent operator is not necessary. The above corrections might be classified as first order because they only consider the effect of the tunnel walls on the velocity perturbations and not on the distribution of those perturbations.

Joppa[22] used a vortex-filament panel method to produce corrections to wind tunnel data of high lift wings in closed test sections. The lift produced by the wing is represented by a vortex at the quarter-chord location, and the walls by a set of vortex panels, or a vortex lattice. Joppa's work is innovative in that it uses an iterative procedure to calculate the wake trajectory behind the airfoil rather than assume a linear deflection or no deflection at all. Unlike the method of Ulbrich which considers the wall's contribution to velocity at the model, the angle of attack correction of Joppa is found by directly differencing the flow solution around the model within the wind tunnel and that without the wind tunnel. Once the flow solution for both of these is calculated, the correction angle of attack is given by Equation 2.32

$$\Delta\alpha = tan^{-1}(\frac{V_y}{V_x})_T - tan^{-1}(\frac{V_y}{V_x})_{FS} \tag{2.32}$$

where V_x and V_y are the horizontal and vertical velocity components, respectively, at some sample point on or about the model. This approach is again considered something of a first-order approach.

A two-dimensional approach, the panel method of Bowcutt[23] takes a slightly different perspective. Less attention is given to the wake as in Joppa, however, Bowcutt models several other viscous phenomenon with great detail. An airfoil model is paneled with constant strength source panels on the outer airfoil profile to create solid blockage and constant strength vortex panels on the camber line to create lift. Four different viscous flow phenomena are accounted in Bowcutt's code including boundary layer growth on the wind tunnel walls, the separation bubble, if applicable, behind a stalled wing, the free-shear layer, if applicable, between the freestream and separation bubble, and the viscous wake downstream. These phenomena lead to corrections for horizontal buoyancy, solid blockage, wake blockage, and streamline curvature. Bowcutt's approach to the correction parameters follows the same method as Joppa in that it takes the difference in tunnel and free-flight solutions and applies that same difference to the measured wind tunnel data. Rather than angle of attack, however, Bowcutt differences the coefficients of lift, moment, and drag from the two solutions. The author notes that methods such as these that compare the wind tunnel and free-flight solutions leverage the fact that the same errors present in the wind tunnel solution due to the invicid modeling should also be present in the free-fight solution and should roughly cancel.

Mokhtar and Britcher[24] use an approach that is especially interesting because the boundary shape changes in an iterative fashion. Their panel method uses a horseshoe vortex to create lift on a simulated airfoil. The study was done for open-jet test sections and included a two-step iteration procedure to arrive at the final boundary conditions. First, the wind tunnel walls are formed from solid, straight panels which impose non-penetration through the walls.

Second, the slopes of the wall panels are adjusted according to the velocity distribution and the flow solution resolved using a constant pressure boundary condition. The second step involves iterations and was facilitated with the one-step method, leading to convergence usually within 4 iterations.

While the above studies generally apply first-order corrections to dynamic pressure and angle of attack, panel methods can account for higher-order streamline curvature corrections. Extending the work of Allen and Vincenti[17] as derived in Appendix A, corrections to angle of attack and the global aerodynamic coefficients are accomplished with knowledge of the derivatives of the flow vector at the model location as shown in Equations 2.33, 2.34, 2.35, and 2.36 for two-dimensional flow ,

$$\alpha_c = \alpha_g + (v/V_\infty)\frac{180}{\pi} + 57.3\sqrt{1-M^2}c(\frac{1}{4} + \frac{C_m}{C_l})\frac{\partial(v/V_\infty)}{\partial x} \quad (degrees) \tag{2.33}$$

$$C_{l,c} = C_l\frac{1}{(1+u/V_\infty)^2} - \frac{1}{\sqrt{1-M^2}}\frac{\pi}{2}c\frac{\partial(v/V_\infty)}{\partial x} \tag{2.34}$$

$$C_{m,c} = C_m\frac{1}{(1+u/V_\infty)^2} + \frac{1}{\sqrt{1-M^2}}\frac{\pi}{8}c\frac{\partial(v/V_\infty)}{\partial x} \tag{2.35}$$

$$C_{d,c} = C_d\frac{1}{(1+u/V_\infty)^2} \tag{2.36}$$

where u and v are the stream-wise and stream-normal components of wall-induced velocity, respectively.

In some of the preceding panel method examples, a set of inviscid singularities is used to represent the wind tunnel flow, the accuracy of which may understandably be called into question. Of course, the internal singularities used to represent the airfoil in the test section are not an exact replication of the actual flow field in the wind tunnel. However, wind tunnel corrections are far-field effects[22, 23], and these effects on singularities are the same as those on the actual model. The far-field effects of the tunnel walls are generally small in and of themselves, so small errors in interference solution will have an even smaller effect on the corrected global quantities[23]. Thus, errors in the interference modeling and solution can be considered to have a second-order effect on the final corrected quantities. Furthermore, Iyer and Everhart[25] state that the exact placement of singularities is not important due to the far-field nature of wind tunnel corrections.

Relations between measured aerodynamic coefficients and equivalent singularity representations are given by Allen and Vincenti[17] and Herriot[16]. Wake blockage is modeled by a source whose strength, q_0, is scaled on the measured drag coefficient as shown in Equation 2.37

$$q_0 = \frac{1}{2} c C_d U_\infty. \tag{2.37}$$

Solid blockage is modeled by an upstream pointing doublet whose strength, μ_0, is scaled according to Equation 2.38

$$\mu_0 = \frac{1}{8} \pi \Lambda c^2 U_\infty \tag{2.38}$$

where Λ is defined by Equation 2.5. The circulation in a two-dimensional flow situations is modeled by a vortex whose strength, γ_0, is scaled according to the measured drag coefficient as in Equation 2.39

$$\gamma_0 = \frac{1}{2} c C_l U_\infty. \tag{2.39}$$

For three-dimensional flow situations, the circulation can be modeled by a horseshoe vortex centered on the model and trailing downstream.

2.1.2.3 Boundary Measurement Correction Methods

The last category of correction methods are measured variable methods which are inherently not a priori. They are useful when linear theory used by the classical corrections is not valid[15]. Measured variable methods consist of the one-variable and the two-variable methods.

2.1.2.3.1 One-Variable Method

The one-variable, or wall pressure signature, method uses streamwise rows of static wall pressure taps to infer wall interference. It is termed as such because it traditionally dealt with only one component of the interference velocity, the u-component velocity, although it was later adapted to include the v-component, as well. The one-variable method makes use of panel methods in conjunction with measured wall pressure data. The presence of the airfoil is represented as before with a set of singularities, in the case of Mokry[26] with a discrete distribution of horseshoe vortices to represent lift, with distributed sources to represent wake blockage, and with distributed doublets to represent solid blockage. From the measured wall pressure data is subtracted the pressure induced by the model singularities and the empty test section wall pressure data, thus yielding the component of wall interference acting on the lift and blockage, respectively. Placing a source or sink at each wall pressure port, a least-squares regression provides a best fit of the source and sink strengths that matches the wall interference signature. From these singularity strengths, the wall interference at

any point in the test section can be calculated in a panel method solution. The number of measurement points required for an accurate correction is surprisingly low, with only around 10 points total required for a test section with model chord to test section width equal to 0.2[15].

Ulbrich and Steinle[27] use a slightly extended version of the one-variable method. The procedure uses the measured pressures to set the influence coefficients in a three-dimensional panel method solution. The matching condition between the panel method and measured wall pressures is the velocity at the walls which is computed from measured static pressures with the energy equation. Once the panel method solution is found, the freestream panel method solution is subtracted from that with the wind tunnel walls.

Moses[28] employs a closed wall, three-dimensional panel method correction approach that also uses measured wall static pressures to calculate interference corrections. The test section is represented by 140 rectangular panels with the constant strength doublet panels on either end of the test section extending far upstream and downstream, respectively. The panels are extended in either direction to prevent toroidal flow around the test section in the case of the upstream panels and to provide tunnel panels to interact with the wake panels in the case of the downstream panels. The author takes the approach of holding the measured pressure distribution on the airfoil constant as the effect of the walls are iteratively removed from the panel method calculation. This is done with an inner and outer flow solution which are synced with each other using a cylindrical surface that acts as an interface. The outer solver calculates the perturbation velocity along the interface starting from measured wall static pressures and passes this velocity to the inner solver. The inner solver then calculates the perturbation pressure on the interface due to such a change in perturbation velocity and returns the result to the outer solver. This iteration continues as the non-penetration boundary condition of the tunnel walls iteratively is removed. The result is that the angle of attack, twist, camber, and other geometric values are varied along the span to keep the pressure distribution the same throughout the change in boundary condition.

2.1.2.3.2 Two-Variable Method

The two-variable method of Ashill is founded in the use of perturbation potential theory where the perturbation potential of the walls can be found by taking the difference of the wind tunnel perturbation potential and the free-flight perturbation potential[15]. A Green's function, $G = 1/r$, is used to analyze this difference, and the result is that two-variables need to be measured at the wind tunnel boundary such as streamwise velocity and transverse velocity. The streamwise velocity can be determined as with one-variable method from static wall pressures. For solid-wall tunnels, the transverse velocity is everywhere zero. For porous-walled tunnels it is more difficult to determine the transverse velocity. A major advantage of the two-variable method is that no mathematical model is necessary. Ashill notes that while one-variable methods are suited best for attached flows because the model can be represented

relatively easily by a set or singularities, for high-lift situations or for models with detached and complex flow, the two-variable method offers the better solution. A trade-off between the methods is in the number of pressure measurements required, with the two-variable method requiring significantly more boundary pressure measurements and a means to determine the transverse velocity in porous- or slotted-walled tunnels. The two-variable method also can handle walls of arbitrary shape such as is the case with the focus of this paper on Kevlar-wall test sections.

2.1.3 Measurements in Solid-Wall Test Sections

The wall-interference corrections reviewed above rely on the accurate measurement of global aerodynamic coefficients. Steady aerodynamics in solid-wall test sections are traditionally measured via a force balance or by mean pressure measurements. The former is often employed in three-dimensional flow situations, and the latter in two-dimensional flow situations. As the majority of the work in this study is directed toward two-dimensional flow, a brief review will be given below on mean pressure measurements in solid-wall test sections. Mean pressure measurements may be performed in three places: on the model, in the wake, or at the test section boundaries. Each of these measurements has a purpose as detailed below. There are many examples in the literature of each of the three types of pressure measurements. The reader is directed towards Barlow *et al.*[20] for a more thorough review.

Pressure measurements on an airfoil are made through pressure taps which are typically less than 1-mm in diameter and drilled into the outer surface of the model. The pressures are sampled near the midspan to avoid vorticity being shed from the tips. Beneath the surface, these taps are connected to plastic tubing which leads to a pressure scanner. The pressure readings around the airfoil profile are integrated to produce both the lift and the pitching moment of the model. The pressure distributions may also be integrated to give the pressure drag, but pressure drag ignores the important skin friction contribution.

Pressure measurements in the model's wake yield the total drag and are performed with a so-called *wake rake*. The wake rake measures the stagnation and static pressures at intervals across the test section. By a control volume analysis, it can be shown that the drag produced by the model is equivalent to lost momentum in the wake[29].

Pressure measurements at the test section boundaries allow comparison with numerical predictions, as well as provide an alternate means to measure the lift of a model. Since the lift produced by the model must impose an equal and opposite reaction on the wind tunnel walls, the wall pressure distribution can be integrated to yield the lift. A small correction is usually applied since a fraction of the transverse momentum produced by the lifting model will be carried out of the test section and remain unmeasured by the wall pressure taps. Pitching moment and drag values calculated from wall pressures are not of high accuracy.

2.2 Kevlar-Wall Test Sections

This section discusses the state-of-the-art in Kevlar-wall wind tunnel testing. First will be discussed the wall interference mechanisms for Kevlar-wall test sections, followed by a review the previous work in the field of Kevlar-wall corrections both for two- and three-dimensional lifting configurations. Finally, some opportunities for the future in Kevlar-wall test sections are presented.

2.2.1 Wall Interference Mechanisms Kevlar-Wall Test Sections

Devenport *et al.*[9] outlines the non-traditional sources of wall-interference in Kevlar-wall test sections that extend beyond those of solid-wall test sections, at least for two-dimensional models. These sources are attributable to two factors: wall porosity and wall flexibility. Devenport *et al.* give three main mechanisms by which the wall porosity and flexibility produce behavior different from that observed in solid-wall test sections, these three mechanisms working to modify the lift interference and blockage characteristics of the test section with respect to the conventional solid-wall test section. These three mechanisms are given in Figure 2.1(a)-(c).

First, the wall porosity offers a reduction in blockage in the case of a model at low lift because the model pressure field causes a fraction of flow in the upstream to be diverted out of the test section, later to return to the test section at a downstream location. Since mass must be conserved in the anechoic chambers and the chamber sealing is relatively tight compared to the mass of air coming through the Kevlar windows, the flow re-enters the test section around the airfoil where the static pressure is lower. This re-entering flow creates blockage which is similar in many respects to the wake blockage behind an airfoil.

Second, the wall porosity reduces the effective angle of attack compared to the solid-wall case which which serves to reduce or change the sign of the overall lift interference correction. This occurs because the pressure difference between the tunnel- and chamber-sides of the Kevlar imposed by the model causes normal velocity into and out of the test section on the suction- and pressure-walls, respectively, which reduces the far-field effective angle of attack experienced by the airfoil.

Third, the wall deflection into and out of the test section imposed by the model's pressure field on the suction- and pressure-sides, respectively, results in a smaller effective test section width and thus increased blockage. To explain, the streamlines near the wall that define the effective width of the test section are those that trail straight downstream. For a solid-wall test section, these streamlines exist directly at the wall if one ignores boundary layer effects, while for Kevlar-wall test sections, the curved flow surfaces of the walls push these streamlines inboard.

In summary, the current state of knowledge is that Kevlar-wall test sections have two non-

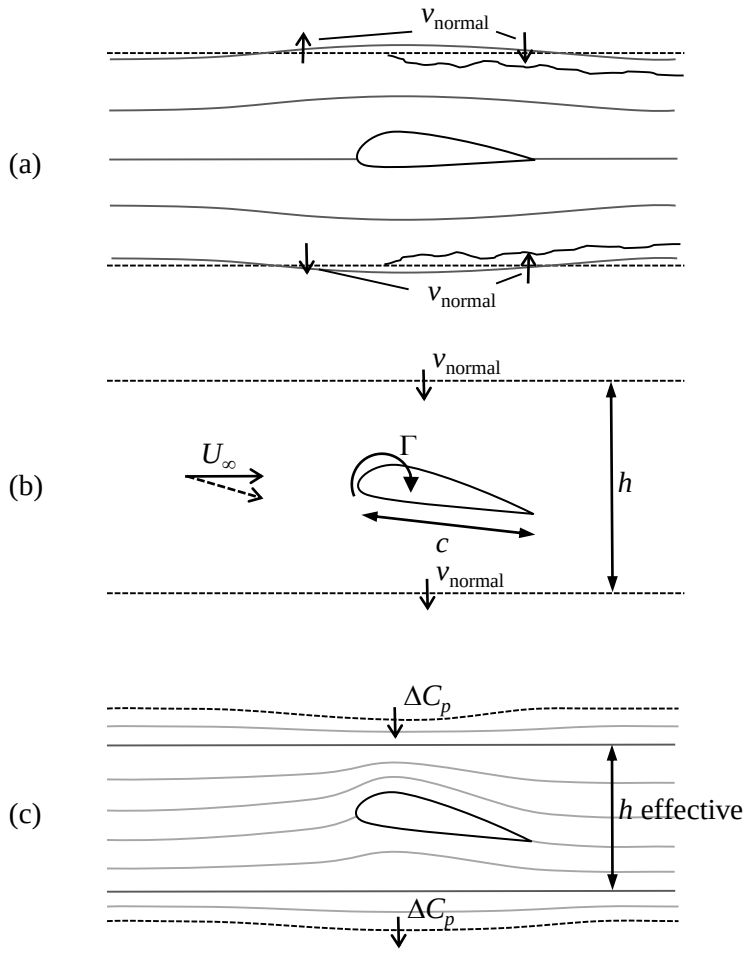

Figure 2.1: Schematic of Kevlar-related wall-interference mechanisms present in Kevlar-wall test sections. (a) Reduction in blockage at low loading due to diversion of flow through the porous walls. (b) Far-field angle of attack reduction induced by wall porosity. (c) Increase in blockage due to narrowing of the effective test section height. Figure adapted from Devenport *et al.*[9].

traditional corrections due to the wall porosity and one non-traditional corrections due to the wall deflection. The flexibility and porosity of the Kevlar wall are unique and critical boundary conditions which have implications for the aerodynamic performance in Kevlar-wall test sections.

2.2.2 Correction Methods for Kevlar-Wall Test Sections

Given the non-traditional boundary conditions presented above, the first section below details some unique wind tunnel configurations designed to minimized wall interference that have similar boundary conditions to Kevlar-wall tunnels. The second section reviews the fundamentals and progress of methods made in the Kevlar-wall wind tunnel community.

2.2.2.1 Minimum-Correction Test Sections

Minimum-correction test sections are here given as those that are neither fully open nor fully closed. A review of the types of hybrid test sections and their use is presented to give background to the developments of the hybrid Kevlar-wall test section as they share some commonalities. Several types of minimum-correction test sections for low-speed wind tunnel testing are in existence. Each attempts to reduce wall interference corrections by replicating the far-field free-flight conditions experienced by a model. These test sections are categorized as adaptive wall, active wall, and ventilated[20].

Adaptive wall test sections attempt to replicate the shape of the streamlines that would be present in free-flight in the far-field of a given model. The shape is iteratively adjusted until the static pressure distribution along the walls matches as close as possible that computed by potential flow theory for the model in free-flight.

The active wall tunnel as demonstrated by Bernstein and Joppa[30] uses suction and blowing in an attempt to match the free-flight flow at the wind tunnel floor and ceiling. The conditions to be matched are the mass and momentum flow normal to the control surface. As it is not practical to have a continuously variable distribution of suction or blowing along the streamwise direction, a series of 12 plenums above and below the tunnel floor and ceiling provide the suction or blowing over a full-span model. The use of porous walls leads to choice of matching either the integrated mass flow or integrated momentum flow over the corresponding free-flight control surface but not both. Matching mass flow leads to overcorrecting the lift data to be below the free-flight lift value. The reverse is true for matching momentum flow. The experimental study was performed at Reynolds number equal to 0.4 million and with wall open-area ratios of 5 and 31%, the higher porosity producing lift results closer to the correct value. The authors note there is still uncertainty as to whether the injection of flow into the test section is consistent with the potential flow representation of the model.

Ventilated test sections such as those with slotted or perforated walls are often used in

transonic testing with the slots used to dissipate shocks at high Mach numbers. The main barrier in this work is determining the velocity and character of the flow into the test section at the suction-side wall[20] which has particular relevance for the Kevlar-wall test section. Towards these ends, the work of several authors is reviewed below.

The fundamental relationship under consideration is how the normal velocity at the wall affects the normal velocity at the edge of the boundary layer, the latter being required to make far-field corrections. According to the continuity equation,

$$\frac{v_e}{u_e} = \frac{1}{\rho_e u_e}\frac{d}{dx}(\rho_e u_e \delta^*) + \frac{\rho_w v_w}{\rho_e u_e} \tag{2.40}$$

where u is the tangential, or streamwise, velocity component, v is the normal velocity component with positive values indicating flow into the test section, δ^* is the displacement thickness of the boundary layer, and the subscripts w and e refer to the wall and the edge of outer edge of the boundary layer, respectively. The equation is here given in compressible form since the authors under consideration tested in the transonic regime. In each study, the goal was to find v_e which is the necessary input for inviscid flow solvers used in wall-interference correction. It is necessary first to measure or model the two terms on the right-hand side of Equation 2.40.

Ivanov[31] studied primarily flows for which $v_w > 0$ on plates with open-area ratios from 2 to 24%. The relationship between v_w and ΔC_p, the pressure difference between the wall and plenum normalized on the freestream conditions, was independent of the direction of v_w, as well as linear for $\Delta C_p < 0.06$ but became non-linear for higher ΔC_p's. The constant of proportionality between v_w and ΔC_p decreases strongly with Reynolds number. All experiments were done with a relatively thick boundary layer: $\delta^*/d > 1$. Changing the thickness of the boundary layer had no effect on the above findings. It was found that the thickness of equalization layer, the layer within which the discrete nature of the perforations is visible, is 5 to 7% of boundary layer thickness. A transverse pressure gradient in the boundary layer was measured. Measuring boundary layer profiles yielded $d\delta^*/dx$, and since v_w was already known from the flow rate of the plenum, v_e is calculated from Equation 2.40 assuming the pressure gradient in the streamwise direction is known. Setting now v_e as a function of ΔC_p, it was found a linear relationship with the coefficient of proportionality varying by a factor of 2.5-2.6 between flow entering and leaving the test section with the larger values for the entering case.

Glazkov *et al.*[32] made similar measurements to Ivanov although the wall-side static pressures were measured just outside the boundary layer instead of at the wall. They found that the constant of proportionality between v_w and ΔC_p was affected by the surrounding boundary layer parameters. Based on measurements, v_e is given as a cubic function of v_w which has higher slope in the inflow region than the outflow region. Initially, it was believed that there is an inherent directional dependence of the velocity relationship. However, later it was inferred that it is the boundary layer thickness which governs the velocity relationship.

The boundary layer of the suction-side is always thicker than that of the pressure-side, so the suction-side velocities are higher.

Chan[33] measured the pressure-velocity relationship to have varying degrees of non-linearity, depending on the ratio of boundary layer displacement thickness to perforation diameter, δ^*/d. As with Ivanov, for $\delta^*/d > 0.25$, the inflow relationship is purely linear and is given as Equation 2.41

$$\frac{\rho_w v_w}{\rho_e u_e} = -0.316[\Delta C_p - \frac{(\Delta C_p \delta^*/d)_0}{\delta^*/d}] + [\frac{\rho_w v_w}{\rho_e u_e}\frac{d}{\delta^*}]_0 \tag{2.41}$$

where the subscript 0 refers to the values at $\delta^*/d = 0.25$. Equation 2.41 demonstrates an interesting point that was found by multiple authors which is that $v_w \neq 0$ when $\Delta C_p = 0$. Assuming an equilibrium boundary layer, the authors also give a correlation between v_w and v_e as in Equation 2.42

$$\frac{v_e}{u_e} = 2.125\frac{\rho_w v_w}{\rho_e u_e} + [1.2656(\frac{\rho_w v_w}{\rho_e u_e})^2 + 2.25x10^{-6}]^{\frac{1}{2}}. \tag{2.42}$$

This correlation is bounded such that v_e is between 1 and 3.25 times larger than v_w, the larger constant of proportionality being applicable for large inflow velocities. This result appears to be a common finding among the literature on perforated wind tunnels. Given Equations 2.40, 2.41, and 2.42, the value $d\delta^*/dx$ can be calculated which, along with a wall pressure distribution, defines the boundary layer effect on the model. Boundary layer measurements with Chan's configuration indicated that the pressure-side boundary layer is virtually non-existent because it is blown out of the tunnel.

Crites and Rueger[34] provided insightful flow visualization measurements of the flow in perforated wall which indicates different mechanisms for the cases of $v_w < 0$ and $v_w > 0$. For the former, the flow entering the perforations has streamwise momentum that creates an impact pressure on the downstream side of the holes. This impact pressure forces some flow through the perforation and also creates a fountain on the upstream side. The impact pressure explains the non-zero v_w measured by all authors at $\Delta C_p = 0$. For the case of $v_w > 0$, there is no impact pressure. To collapse the data, they give functions relating v_w and ΔC_p which are between linear and quadratic. The quadratic dependence is much more prominent for the case of $v_w > 0$. They also found that the data reduction was better when a ΔC_p was taken as $\Delta C_p\sqrt{\delta^*/d}$.

In summary of the work on perforated wind tunnels, for relatively thick boundary layers, the relationship between v_w versus ΔC_p is linear for the range of ΔC_p's encountered in most transonic tests. However, the relationship appears to tend toward nonlinear for the larger ΔC_p's which would be characteristic of the Kevlar walls. On the suction wall, the momentum from the incoming flow mixes out within 5-7% of the boundary layer thickness. The value v_e is between 1 to 3.25 larger than v_w on the suction-side wall, but the value is around 1 for

the pressure-side wall. At least part of this difference appears to be due to less resistance met on the suction-side where the boundary layer is thicker.

2.2.2.2 Kevlar-Wall Test Section Correction Methods

Continuing on now to the test section of interest in this study, the wall-interference methods for Kevlar-wall test sections are here divided in those for two-dimensional flow and three-dimensional flow.

2.2.2.2.1 Corrections for Two-Dimensional Flow

Given an understanding of the interference mechanisms at-play in Kevlar-wall test sections, we now look to the methods available for correcting such interference effects. Kevlar-wall aerodynamics have been a subject of research at Virginia Tech's Stability Wind Tunnel ever since this configuration was first developed[1, 2, 3, 9]. A brief review on the current progress is given below.

Pressure data measured from airfoils were originally corrected with a modified and extended version of the traditional solid-wall corrections as documented in Devenport *et al.*[3]and Devenport *et al.*[9] and given here as Equations 2.43 and 2.44

$$\frac{u'_{pw}}{U_\infty} = \Omega \frac{u'_{sw}}{U_\infty} \tag{2.43}$$

$$|\Delta\alpha| \sim |C_l \frac{c}{h}| \tag{2.44}$$

where the subscript pw indicates porous, or Kevlar-wall values, the subscript sw indicates solid, or solid-walled, values, Ω is a dimensionless value between 0 and 1, c is the chord of the airfoil, and h is the height of the test section. Equation 2.43 represents the blockage correction where Ω acts to scale the blockage effects of hard walls to a smaller value for use with flexible, porous walls which was first derived from the work in Ewald[15]. In Devenport *et al.*[3], an empirically determined scaling constant of 0.42 was used. For the lift interference correction, they derive Equation 2.44 which accounts for the porosity effect of the Kevlar on the angle of attack which scales with the lift, and so circulation, felt at the Kevlar-wall. Equation 2.44 was used in addition to the streamline curvature correction of Equation 2.11.

Investigation towards a fundamental consideration of the flow physics in Kevlar-wall test sections culminated with the development, by Devenport *et al.*[9], of corrections based entirely on first principles and the independently measured or known physical characteristics of the system. The method developed accounts for the transpiration of air through the

Kevlar walls, the deflection of those walls under aerodynamic load, and the leakage of air between chambers. These characteristics are incorporated into a two-dimensional panel method model of the flow over the airfoil between the test section walls, which is then used to infer the influence of the walls upon the model flow, and thus the equivalent free flight conditions. The model involves no adjustable constants.

The method described by Devenport *et al.* employs a linear vortex/source panel method that places a paneled model of a test airfoil between two rows of panels representing the test section walls, including the flexible, porous areas associated with the Kevlar acoustic windows. The paneling of the test section walls includes power-law spacing in the streamwise direction to provide higher density paneling near the model location. The airfoil is typically modeled using 200 variable-length panels. The Kutta condition is enforced by the placement of two vortex panels on the finite-thickness trailing edge. One panel bridges the trailing edge from the pressure-side to the chordline and the other from the chordline to the suction-side. The strengths of these panels are determined by requiring that the flow pass smoothly over the trailing edge; in other words, that there is zero vorticity at the corners of the trailing edge. A source panel parallel to these vortex panels and spanning the full trailing edge thickness is used to represent the wake.

The panel method code is unique from other wind tunnel panel methods because of its treatment of the boundary conditions at the port and starboard walls with both the deflection and pressure generated by aerodynamic load varying across the Kevlar portions of the walls. To model these effects the panel method uses two nested iterative loops. The inner loop solves the two-dimensional inviscid flow problem to find the pressure distribution along the airfoil and walls for a given wall deflection by characterizing the transverse velocity through the Kevlar via an experimentally determined relationship as in Equation 2.45

$$v_{normal} = k_c \Delta p^{0.5} (\frac{\Delta p}{\Delta p + k_p})^{0.073} \tag{2.45}$$

where Δp is the pressure difference across the Kevlar wall and k_c and k_p, constants obtained from independent tests of the Kevlar cloth, are 0.0625-$m/s/\sqrt{Pa}$ and 50-Pa[9]. The inner loop iteratively adjusts the pressure inside the test section and chambers until the mass balance entering and leaving each chamber is satisfied. The pressures of the suction- and pressure-side anechoic chambers, $p_{suction}$ and $p_{pressure}$, respectively, are related by Bernoulli's equation as in Equation 2.46

$$p_{suction} = p_{pressure} - \frac{\rho}{2} sgn(\dot{m}_p)(\frac{\dot{m}_p}{A_{leak}}) \tag{2.46}$$

where ρ is the air density, $\dot{m}_p$ is the mass exchange from the pressure to suction chambers, and A_{leak} is the effective free-flow leakage area between chambers. A_{leak} describes the area of an opening from a given anechoic chamber that for the same pressure difference would

pass a mass flow equal to the summed mass flow seeping through the distributed leakage areas throughout the chamber.

The outer loop adjusts the wall deflections so that the tension in each wall produces static equilibrium with the pressure load acting on it through a finite difference solution of the simplified thin membrane equation under tension as in Equation 2.47

$$\frac{\partial^2 w}{\partial x^2} + \frac{\partial^2 w}{\partial y^2} = \frac{\Delta p}{T} \tag{2.47}$$

where T is the Kevlar tension per unit lateral length, Δp is again the pressure difference across the Kevlar, and w is the out-of-plane deflection. Here, an isotropic tension has been assumed and the shear term neglected which represents a first-cut approach to modeling the wall deflections. By taking the second derivatives of deflection and inputting the tension of the wall, the pressure difference across the wall is determined. Convergence of the whole nested loop calculation takes a few seconds on a laptop computer.

With a flow solution in-hand, interference corrections can be obtained multiple ways. Devenport *et al.*[9] calculates a free-flight solution for the same airfoil, and then the pressure distributions over the airfoils in the wind tunnel and free flight are compared. In this case, the wind tunnel solution is corrected for blockage and lift interference, as in Allen and Vincenti[17], except that the blockage and lift interference parameters are fed into an optimization problem between the wind tunnel and free flight pressure distributions. The pressure distributions over the airfoil from the tunnel solution and free-flight solution are optimized by adjusting the free-flight angle of attack and the wind tunnel blockage factor, producing a porosity-adjusted angle of attack, α_e, and a blockage scaling variable, Ω. Both α_e and Ω are then used in conjunction with Equations 2.8, 2.17, 2.18, and 2.19 to calculate the corrected angle of attack, lift, moment, and drag coefficients, respectively. Therefore, the solid-wall correction of Allen and Vincenti is adapted for use in test sections with wall porosity and deflection which is justified since the changes in angle of attack and blockage induced by the Kevlar walls are predominantly far-field effects that can still be modeled by classical wind tunnel analyses.

The α_e in the preceding paragraph is an intermediate angle of attack which gives the far-field angle of attack, corrected for the presence of the Kevlar porosity and deflection, but not corrected for streamline curvature. This is the angle of attack at which the model would be positioned in an equally dimensioned solid-wall test section to replicate as close as possible the flow experienced in the Kevlar-wall test section. The relationship between the corrected angle of attack, α_c, the effective angle of attack, α_e, the streamline correction, $\Delta\alpha_{sc}$, and the Kevlar influence on far-field angle of attack, $(v/V_\infty)\frac{180}{\pi}$, is given in Equation 2.48. This last quantity invokes the small angle approximation and is given as the slope of the vector of wall-induced velocity at the model location. Traditionally, it has been believed that v/V_∞ is due to the porosity of the walls rather than the deflection.

Table 2.1: Inputs to the panel method simulation of Devenport *et al.*[9].

Input Parameter	Value
Kevlar Pre-Tension, T_0	1500 N/m
Effective Kevlar Modulus, E	2643841 N/m
Kevlar Strain Multiplier, a_ε	2.7283
Inflow Multiplier, a_{inflow}	2
Effective Leakage Area, A_{leak}	0.15 m^2
C_p Convergence Tolerance, $C_{p,tol}$	1e-4
T Convergence Tolerance, T_{tol}	1e-5

$$\alpha_c = \alpha_e + \Delta\alpha_{sc} = \alpha_g + \Delta\alpha_{sc} + (v/V_\infty)\frac{180}{\pi} \quad (degrees). \tag{2.48}$$

There are seven inputs to the panel method as shown in Table 2.1. Kevlar pre-tension, T_0, is the uniform, initial unloaded tension assumed for both Kevlar walls which is typically set at the listed 1500-N/m in the Stability Wind Tunnel per Devenport *et al.*[3]. Kevlar modulus, E, is the effective modulus of elasticity of the woven Kevlar fibers calculated from the modulus of Kevlar 49 fibers[35] and the cross-sectional density of those fibers in plain woven 120-style weave. The Kevlar strain multiplier, a_ε, is used to simulate the increase in pore size of Kevlar with stretching by augmenting the porosity coefficient, k_c, of Equation 2.45 as in Equation 2.49

$$dk_c = \frac{\overline{\varepsilon_{port}} + \overline{\varepsilon_{starboard}}}{2\sqrt{\rho}} a_\varepsilon \tag{2.49}$$

where $\overline{\varepsilon}$ is the average strain over the specified wall and ρ is the air density. This relationship is theoretically derived from the narrowing of the Kevlar fibers during straining due to the Poisson effect. The inflow multiplier, a_{inflow}, scales the velocity of the flow re-entering the test section from the anechoic chambers to model the blockage created in the actual tunnel by flow re-entering the test section with zero streamwise momentum. Effective leakage area, A_{leak}, is the means to lump the distributed leakage areas throughout the chamber into a single effective free-flow area as given in Equation 2.46. The convergence values for C_p and T, $C_{p,tol}$ and T_{tol}, respectively, set the tolerance required to break the iteration loops. Their values have been determined by studying the convergence of the panel method solution during the iteration loops and are conservatively small to assure convergence in both iteration loops is reached if at all possible.

An alternate way than outlined in Devenport *et al.*[9] to infer the interference corrections is through a purely far-field approach which relies on the principle that the wall interference can be captured by the effect of the walls on the flow velocity and its derivatives at the

airfoil location as described in Section 2.1.2.2. In this approach, the model is represented simply by a set of singularities: a doublet, vortex, and source. This simplifies and quickens the panel method solution without noticeable loss of accuracy since the walls are in the aerodynamic far-field of the model. Furthermore, as the singularity strengths are dictated in part according to the lift and drag measured on the model, the singularity representation of the model has applicability even after stall which is not the case for a paneled model which will not stall. Thus, the latest unpublished work on corrections for two-dimensional flow in Kevlar-wall test sections uses the singularity representation of the model with the correction formula derived in Appendix A.

The panel method technique described above effectively corrects aerodynamic data from Kevlar-wall test sections, at least for two-dimensional flow situations[9, 36, 37]. For instance, side-by-side tests of the same model in the different test sections have shown corrected lift coefficients to be typically within the error of the measurement for the attached flow regime. For the tests of Brown[36], differences in $C_{l,max}$ between test sections averaged 2.9%. Comparisons of drag and pitching moment between test sections show good agreement in shape, at least, if not some residual scaling differences.

2.2.2.2.2 Corrections for Three-Dimensional Flow

Somewhat less attention has been paid to three-dimensional configurations than the above two-dimensional configurations. Work by Ito *et al.*[5] at the Japanese Aerospace Exploration Agency found that the corrected solid-wall drag and uncorrected Kevlar-wall drag were nearly identical, suggesting that the Kevlar-wall flow was already nearly identical to that of free-flight. However, the uncorrected Kevlar-wall lift proved too high, so they proposed, based on empirical observations, that the lift coefficient, C_L, be corrected simply by the difference in C_p between the two chambers as in Equation 2.50

$$\Delta C_L = C_{p,starboard} - C_{p,port} \tag{2.50}$$

where a capital L is now used to denote the lift coefficient in the three-dimensional case. This equation is physically intuitive since both the difference in chamber C_p's and the correction magnitude of Kevlar-wall data both appear to scale with C_L. No rigorous derivation was presented, but nonetheless the method gives an approximate correction. The method was found to adequately correct lift data for the high-lift model studied by Ito *et al.*, and no correction method was specified for the pitching moment.

Most recently, a preliminary study by the author adapted the panel method approach of the previous section to the three-dimensional case and applied the result to data from the Japanese Aerospace Exploration Agency's 2-m by 2-m Low Speed Wind Tunnel[38]. The performance of the Kevlar-wall test section at the Japanese Aerospace Exploration Agency was surprisingly close to that of the solid-wall test section there even before correction.

The Kevlar-wall test section featured a substantial reduction in lift interference from the solid-wall case.

2.2.3 Measurement Opportunities in Kevlar-Wall Test Sections

As demonstrated by Devenport *et al.*[9] and Ito *et al.*[5], Kevlar-wall test sections are capable of producing accurate data from airfoil pressure taps, wake rakes, and force-balances. One area that remains to be developed is the measurement of wall pressures. A preliminary approach has been used by Brown[36, 38, 39] which is to install small pressure taps on the chamber side of the Kevlar walls. These pressure taps open to the flow-side of the test-section to provide pressure readings of the test section flow. The taps are not permanent and become dislodged when the Kevlar is placed under high loading.

An intriguing possibility is to instead employ the Kevlar itself as a sensing surface, in much the same way that a strain gauge measures a load. Utilizing the Kevlar as a sensing surface might afford measurement of the full global pressure field rather than discrete readings from pressure taps. Such a concept is to be pursued in this work.

2.3 Tensile Behavior of Plain-Woven Fabric

In order to understand the flexible nature of Kevlar walls, the tensile behavior of Kevlar fabric is here investigated. Modeling of fabrics can be performed both on the meso-scale looking at fiber-to-fiber interactions and on the macro-scale looking at the continuum behavior. In this section, first will be presented introductory knowledge on the fiber-to-fiber interactions with the goal of informing the later discussion on the continuum representation, constitutive properties, and membrane mechanics.

2.3.1 Fiber-to-Fiber Interaction

The fabric under consideration is assumed to be plain-woven in accordance with the Kevlar fabric used in this study. Plain-woven fabrics have fibers running in perpendicular directions, alternatively running above and below transverse fibers in what is known as the warp and weft directions. Because of manufacturing processes, warp yarns are typically wavier, or have more crimp, than weft yarns, at least in the untensioned state[41]. A *balanced* plain-woven fabric, is one where the physical and geometrical properties are the same in the warp and weft fiber directions[42], although the effective properties in these directions are not necessarily equivalent due to differences in crimp.

Several fiber-to-fiber mechanisms play a role in fabric deformation, including crimp exchange, yarn stretching, yarn flattening, yarn twist, yarn compaction, yarn slip, and trellising[43, 40].

Most relevant to the current discussion are the first two which will be discussed below: crimp exchange and yarn stretching.

Crimp exchange occurs when fibers in one direction are strained, causing them to straighten and causing those in the perpendicular direction to become more crimped to accommodate the displacement imposed on them. Deformation from crimp exchange depends on the ratio of stresses between the warp and weft directions rather than on the absolute magnitude of these stresses[40].

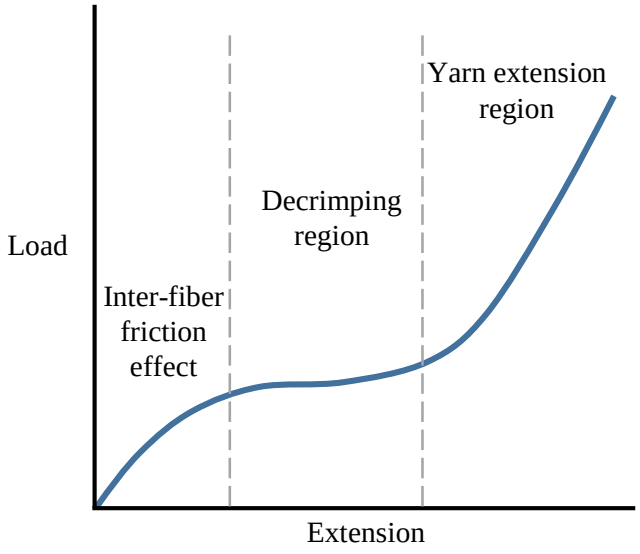

Figure 2.2: Load-extension curve for a woven fabric. Figure reproduced from Hearle *et al.*[40].

Yarn stretching becomes the important mechanism after a certain degree of strain in one fiber direction causes a fabric to become uncrimped. Yarn stretching is governed by the stress-strain relation of the fibers themselves which may or may not be linear. The stiffness of the fabric, at least for the case of woven Kevlar, increases once it is uncrimped and the yarns begin to stretch[41].

The effect of crimp exchange and yarn stretching is illustrated by Figure 2.2 which shows a load-extension curve for a fabric under a state of tensile stress, either uni-axial or bi-axial. In general, the stress-strain relationship of fabric has a third region, inter-fiber friction region. Raftenberg and Mulkern[44], however, hypothesizing that the inter-fiber friction effect may be negligible due to Kevlar's strength, show the stress-displacement data for uni-axial stress of Kevlar with just the latter two regions: an initial, nonlinear, positive-curvature region during which the fibers are uncrimping and a latter linear region corresponding to the stretching of the yarns.

2.3.2 Continuum Representation

Rather than mesoscale modeling of the fibers themselves, Hearle *et al.*[45] discuss macroscopic modeling using continuum models to represent fabric deformation. While the strain field of a fabric cannot be considered continuous if the region of interest is only several unit cells in length, the continuum assumption is valid if the nonuniformity of the deformation is small on the scales of the fiber unit cells. This is the case for a fabric such as the plain-woven

Kevlar employed in this study because there are 13 unit cells per centimeter contained within a fabric which has a characteristic length of over 1.85-m.

The orthotropic elastic lamina model has been proposed as a suitable continuum model for fabrics[46]. The orthotropic designation refers to the fact that the two directions of the fibers correspond to two perpendicular planes of elastic symmetry. The elastic designation can be employed for fabrics when strains are small enough to permit Hookean approximations to the nonlinear constitutive properties. The lamina designation refers to the small thickness of the material under consideration. Because of their small thickness, lamina are modeled as experiencing plane stress which assumes that the out-of-plane stresses are negligible.

The relations between stress and strain for an orthotropic elastic lamina, including only membrane forces and excluding the effects of bending/twisting, are given in Equation 2.51

$$\begin{bmatrix} \sigma_1 \\ \sigma_2 \\ \tau_{12} \end{bmatrix} = \begin{bmatrix} \frac{E_1}{(1-\nu_1\nu_2)} & \frac{\nu_2 E_1}{(1-\nu_1\nu_2)} & 0 \\ \frac{\nu_1 E_2}{(1-\nu_1\nu_2)} & \frac{E_2}{(1-\nu_1\nu_2)} & 0 \\ 0 & 0 & G \end{bmatrix} \times \begin{bmatrix} \varepsilon_1 \\ \varepsilon_2 \\ \gamma_{12} \end{bmatrix} \tag{2.51}$$

where σ is normal stress, τ is shear stress, ε is normal strain, γ is shear strain, E is the elastic moduli, ν is Poisson's ratio, G is the shear modulus, and the subscripts on the stresses and strains indicate one of the two orthotropic components[45]. Note that the subscripts on the Poisson's ratios indicate the direction from which the strain is being applied. As symmetry dictates that $E_1\nu_2 = E_2\nu_1$, there are only four unknown constitutive parameters: E_1, E_2, ν_1, and G. Unlike for the case of isotropic plates, $G \neq \frac{E}{2(1+\nu)}$. Instead, G is an independent constitutive constant. It is noted that Equation 2.51 assumes negligible bending/twisting stress and, of course, therefore no elastic coupling between the bending/twisting strains and membrane strains. For such a lamina, a more appropriate designation is *membrane*. In the case of pre-tensioned Kevlar walls, the flexural rigidity of the Kevlar sheet is on the order of 0.007-N/m, and the length/thickness ratio is over 10,000 which is characteristic of a membrane. Thus, the modeling strategy in this work is one of a thin membrane as represented by Equation 2.51.

On the topic of the assumption of elastic behavior of fabrics as asserted above, some measurements have shown that even for small tensile stress, there is hysteresis between the loading and unloading of the stress-strain curve. The hysteresis originates from non-conservative forces between fibers although the measurements were performed on fabrics of significantly different strength and chemical makeup than Kevlar [47, 48]. Clulow and Taylor[49] tested plain-woven cotton fabric and found that mechanical pre-conditioning reduced hysteresis between loading/loading cycles though it did not eliminate it. They also observed that the cotton fabric's bi-axial tensile behavior stabilized after eight cycles, presumably because the yarns became extended and flattened. Beccarelli[50] states that fabrics tend towards elastic character after several cycles of loading and unloading. For the purposes of this study, it is assumed that non-elastic effects are minimized by mechanical pre-conditioning of the fabric

from multiple loading/unloading cycles. This assumption seems furthermore valid given the smooth nature of the Kevlar fibers which would suggest that non-conservative forces acting between fibers are minimal.

2.3.3 Constitutive Properties

Using the continuum model of Equation 2.51, the constitutive behavior of the Kevlar fabric is reduced to four parameters. It is now desired to know the functional form of these parameters since they may not be constants as suggested by Figure 2.2. While a number of models are available to estimate such parameters, experimental measurements have greater importance versus theoretical predictions because of the difficulty in modeling fabric behavior[52].

Three classic tests used to characterize the constitutive properties of a material are planar shear tension tests, uni-axial tension tests, and equibi-axial tension tests which, taken together, sweep through the full range of possible stress states in the strain invariant space[53]. States of bi-axial tension are the predominant internal stress states experienced by a deforming membrane such as a Kevlar wall. While some maintain that uni-axial tests are not an adequate substitute for bi-axial tests[54], the greater experimental resources required for bi-axial tests have led to relatively fewer bi-axial than uni-axial experiments.

In general, it is not completely clear how the presence of bi-axial versus uni-axial tension changes the elastic constants of a fabric. Zheng *et al.*[55] relate experimental values between uni-axial and bi-axial tension tests with varied success for three plain-woven fabrics. They show that uni-axial stress-strain curves can be scaled by $1-\nu_1\nu_2$ to approximate bi-axial stress-strain curves, at least for a load ratio of one. Similarly, Buet-Gautier and Boisse[56] and Xue

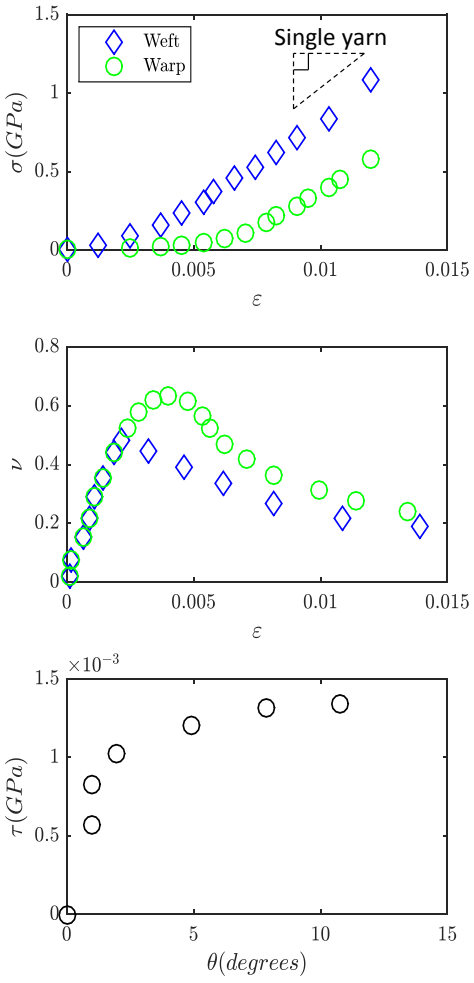

Figure 2.3: Data reproduced from experiments by Zhu *et al.*[51] on 328-style woven Kevlar for (a) uni-axial extension results, (b) biaxial extension results, and (c) shear test results.

et al.[42] show that values of E and ν determined from an unequal bi-axial test produce acceptable agreement with experimental results for corresponding uni-axial and equal bi-axial tests, suggesting that there are not significant higher-order differences between uni-axial and bi-axial tests other than the simple scaling mentioned above. For the purposes of this study, the bi-axial load ratio is similarly assumed not to affect the value of the elastic moduli. In accordance with Zheng *et al.* and Xue *et al.*, Poisson ratio's will be treated as a constant. Information on methods where the elastic moduli *are* treated as functions of the bi-axial load ratio can be found Birchall *et al.*[54] and Galliot and Luchsinger[57].

Much of the experimental information on woven Kevlar's tensile behavior stems from research on ballistics protection such as bullet-proof vests or containment of fan blades. Such studies include Dong *et al.*[41], Raftenberg and Mulkern[44], Naik *et al.*[58], and Zhu *et al.*[51]. All of these authors abide by the guidelines that the elastic modulus should be measured from a sample of fabric rather than estimated from the strength of individually-tested fibers because of the crimp exchange phenomenon[46]. An example of the results of these authors is shown in Figure 2.3 and will be referred to in the following subsections.

2.3.3.1 Elastic Modulus

Dong *et al.*[41] performed uni-axial tensile tests on five Kevlar fabrics of various specifications. The most similar fabric to the Kevlar used in the current study may be the K779-style fabric though it has twice the yarn count. The K310-style has roughly the same yarn count but twice the denier of Kevlar used in the current study. Dong *et al.*'s uni-axial tests found there was bi-linear behavior of the stress-strain curves which corresponds to the decrimping region and yarn stretching region in Figure 2.2. For the K779 in the warp direction, the lower slope region extends from 0 to 0.08 strain after which the transverse fibers are completely uncrimped and the tensile extension of the yarns becomes dominant which increases the slope. For the K779 in the weft direction, the initial linear region is small or non-existent while the second linear region extends to 0.03 strain before the yarns fail. In general, across all the scrims, the weft direction is stiffer for a given strain than the warp direction which appears to be a result of a shortened initial linear region for the weft direction as well as a steeper slope in both linear regions. Such a shortened initial linear region is consistent with the knowledge that weft yarns have less initial crimp than warp yarns due to manufacturing processes. The authors note that it seems to be characteristic of fabrics with high yarn counts such as K779 and K310 that the initial linear region of the weft direction is short because the fine weave causes the warp yarns to become uncrimped at low strains.

Raftenberg and Mulkern[44] performed uni-axial tensile tests on the plain-woven 706-style Kevlar with the same number of threads per inch as this study's 120-style though with 600-denier. The fabric is composed of Kevlar KM2 fibers which have roughly half the modulus of Kevlar 49 fibers but are tougher. Fitting their tensile data to a bi-linear model, they showed

that the weft direction is stiffer in both the initial de-crimping region and the yarn-stretching region and has a shorter de-crimping region than the warp direction, all of which agree with Dong *et al.*'s[41] observations. Curve-fits were also made to exponential and quartic models, and the quartic model best captured the shape of the stress-displacement curves.

Naik *et al.*[58] performed uni-axial tensile tests on the plain-woven 328-style Kevlar with half the number of threads per inch as this study's 120-style and with 1420-denier. Both the warp and weft directions show a small de-crimping region followed by the yarn extension region. As seen previously, the stiffness in the weft direction is larger than in the warp direction. Poisson's ratio was observed to be highly non-linear with a high initial Poisson's ratio that dropped off sharply as the fabric became de-crimped. After reaching the yarn-stretching region, Poisson's ratio continued to drop though at a much slower rate. For the extension tests in the warp direction and after leaving the de-crimping region, Poisson's ratio falls from about 0.7 to 0.6. For the weft direction, the corresponding values are 0.2 and 0.09.

Zhu *et al.*[51] observed from uni-axial tests on 328-style the two regions of tensile behavior corresponding to de-crimping and yarn stretching. These data are reproduced in Figure 2.3(a). The fabric experiences de-crimping only up to strains of 0.01, at the most, before entering into the yarn extension region where the modulus resembles that for a single Kevlar yarn. In contrast to the other authors reviewed above, Zhu *et al.*'s linear curve fits of the yarn stretching region showed no significant difference between that the elastic moduli of the warp and weft directions. However, they do note that the length of the de-crimping region is roughly 2.6 times greater for the warp direction than weft which agrees with previous authors.

An overview of the uni-axial tensile test results are presented in Table 2.2. In the table, ε_{cross} is the approximate strain at which the tensile behavior transitions, or crosses-over, from the de-crimping region to the yarn-stretching region. E_{crimp} and $E_{ext.}$ are the values of linear curve-fits to the de-crimping region and yarn-stretching region, respectively. Several clear trends emerge from the comparison in Table 2.2. The crimp region always extends to a greater ε_{cross} for the warp direction than the weft which is a result of manufacturing processes that create greater waviness in the warp than weft direction. The fraction $E_{crimp}/E_{ext.}$ is always greater for weft direction than the warp and much less than one, ranging from 0.04 to 0.13 for the warp direction and from 0.14 to 0.31 for the weft direction. In three out of the four cases where $E_{ext.}$ is reported, $E_{ext.}$ is greater for the weft direction than for the warp with the difference between the two being up to 35%. Thus, there are clearly differences between the warp and weft directions that should be properly modeled.

Of those considered in Table 2.2, the most significance to the present study are likely the last two by Zhu *et al.* and Naik *et al.* because they use the same Kevlar 49 yarns as in the Kevlar-wall wind tunnels under consideration. It is useful to note that these authors report ε_{cross} to be between 0.0025 and 0.010. For reference, the initial pre-strain expected in wind tunnel applications assuming an isotropic pre-tension of 1,500-N/m is between 0.001 and 0.004, the variation being a result of the as of yet unknown modulus in the de-crimping

region of the Kevlar. As the Kevlar walls deform, the strain will increase from these pre-strain values. Thus, the Kevlar behavior in wind tunnel applications may, at times, operate in both the de-crimping region and yarn extension region.

Table 2.2: Mechanical properties of plain-woven, balanced Kevlar fabric from various authors.

Author	Yarn Properties			Warp			Weft		
	Type	Count (yarns/in.)	Size (denier)	ε_{cross}	$E_{crimp}/E_{ext.}$	$E_{ext.}$ (GPa)	ε_{cross}	$E_{crimp}/E_{ext.}$	$E_{ext.}$ (GPa)
Dong *et al.*[41]	159	70x70	200	0.093	0.04	17	0.005	0.31	23
Dong *et al.*[41]	Comfort	35.5x35.5	400	0.028	0.04	20	0.003	0.26	24
R and M[44]	KM2	34x34	600		0.13∗			0.14∗	
Naik *et al.*[58]	49	17x17	1420	0.010†		93	0.005†		105
Zhu *et al.*[51]	49	17x17	1490	0.0065	<=0.06	117-132	0.0025	<=0.20	117-120

∗ Values are derived from the division of stress-displacement moduli rather than stress-strain moduli
† Values have been roughly estimated from graphics

2.3.3.2 Apparent Poisson's Ratio

The Poisson's ratio of a woven fabric, termed the effective or apparent Poisson's ratio, comes about because an extension of fibers in one principle direction tends to crimp and thus contract the fibers in the opposite direction. For uni-axial tension cases, the apparent Poisson's ratio is only significant in the initial nonlinear region of the strain-displacement curve, after which the transverse fibers are completely crimped and show no further contraction[41, 58]. The apparent Poisson's ratio then decreases with strain in a nonlinear fashion. For bi-axial cases, on the other hand, Poisson's ratio may take a more prominent effect as the loaded transverse fibers cannot be un-crimped so easily as in the uni-axial case. Zhu *et al.*[51] performed bi-axial tests on Kevlar by pre-straining cruciform specimens in one of the fiber directions and then gradually increasing the strain in the other direction as shown in Figure 2.3(b). Unlike the uni-axial results of Dong *et al.*[41] where the Poisson's ratio appeared negligible, the apparent Poisson's ratio initially increases from a value of zero to a maximum of 0.48-0.75 during which the uncrimping process is in full operation. Subsequently, the Poisson's ratio drops and levels to a value of roughly 0.15 at fabric failure. The higher pre-strain cases had higher maximum Poisson's ratios. This result is consistent with the concept that the fibers in the test direction have to overcome greater crimping due to larger pre-strains in the transverse direction. For each case, the maximum Poisson's ratio occurs at a strain of roughly 0.0025. As referenced earlier in this section, Xue *et al.*[42] reduced the form of Poisson's ratio to a constant which appeared acceptable for their results, and the same will be done in this study.

2.3.3.3 Shear Modulus

Shear rigidity in fabrics originates from the resistance to deformation of the crimped fibers, from the friction between two yarns at the center of rotation, from the flexure of the yarns in the plane of the fabric, and from the compression of yarns for the case of tightly-spaced yarns[46]. The former three have to do with rotation of yarns about one another while the last is due to shear-locking. Shear-locking is the phenomenon when sheared fibers have rotated so far that there is no longer any space between fibers. This situation increases the shear modulus substantially but implies large yarn rotations that are not experienced in testing with Kevlar-wall wind tunnels. For the pre-locking regime, the shear modulus is usually much less than the tensile modulus for fabrics[46]. Dong *et al.*'s[41] tests, for instance, showed the shear modulus for the K706-style fabric was 0.4-MPa as compared to the tensile moduli of 1.5 to 1.8-GPa which amounts to over three orders of magnitude difference. Zhu *et al.*[51] report a shear stress of no more than 1.5E-3 GPa for shear angles below 15 degrees as shown in Figure 2.3(c). Studies have shown that the shear stress increases in the presence of bi-axial tension due to higher normal forces between yarns. Even assuming increases in shear force by a factor of 5 to 10 as reported for a plain-woven carbon fiber fabric[59], the magnitude of the shear force in Kevlar would still be dwarfed by the tensile forces. In light of the small magnitude of the shear modulus compared to the tensile modulus, a value of zero will be assumed for this study.

2.3.4 Membrane Mechanics

As noted in the previous section, woven fabric can be modeled as an orthotropic elastic membrane. The geometry and coordinate system of a differential membrane element are given in Figure 2.4. The figure includes tension forces per unit length T_x, T_y, and T_{xy}, normal-acting pressure p, and thickness h. The boundary conditions have yet to be specified for the membrane.

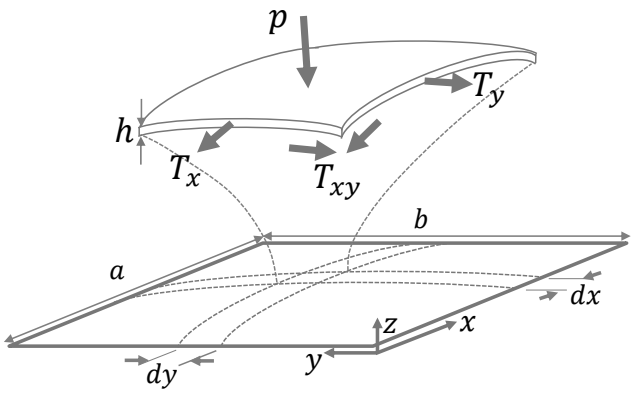

Figure 2.4: Differential membrane element.

Below are reviewed both the in-plane and out-of-plane problems of static membrane mechanics. The state of stress in the pre-tensioned Kevlar walls before deformation corresponds to an in-plane problem. The deformation of the Kevlar under wind loading additionally requires consideration of the out-of-plane problem.

2.3.4.1 In-Plane Problem

Following Timoshenko and Woinowky-Krieger [60] the governing equations of the static membrane problem are presented below. First, the in-plane equilibrium relations for a membrane element such as shown in Figure 2.4 are given by Equations 2.52 and 2.53 under the assumption of no body forces

$$\frac{\partial T_x(x,y)}{\partial x} + \frac{\partial T_{xy}(x,y)}{\partial y} = 0 \tag{2.52}$$

$$\frac{\partial T_y(x,y)}{\partial y} + \frac{\partial T_{xy}(x,y)}{\partial x} = 0 \tag{2.53}$$

where T is the internal stress per unit length experienced by the membrane in the direction indicated by the subscripts with x and y referring to in-plane normal stresses and xy referring to in-plane shear stress. There are three unknowns in the above equations but only two equations. A third equation can be found by manipulating the strain-displacement relations of Equations 2.54, 2.55, and 2.56

$$\varepsilon_x = \frac{\partial u}{\partial x} + \frac{1}{2}(\frac{\partial w}{\partial x})^2 \tag{2.54}$$

$$\varepsilon_y = \frac{\partial v}{\partial y} + \frac{1}{2}(\frac{\partial w}{\partial y})^2 \tag{2.55}$$

$$\gamma_{xy} = \frac{\partial u}{\partial x} + \frac{\partial v}{\partial y} + \frac{1}{2}\frac{\partial w}{\partial x}\frac{\partial w}{\partial y} \tag{2.56}$$

where ε_x, ε_y, and γ_{xy} are strains in the direction indicated by their subscripts, and u, v, and w are the displacements in the $x-$, $y-$, and $z-$directions, respectively. In Equations 2.54, 2.55, and 2.56, the second-order terms other than the out-of-plane term have been neglected as these are typically small. Differentiating these equations twice and substituting 2.54 and 2.55 into 2.56 yields Equation 2.57

$$\frac{\partial^2 \varepsilon_x}{\partial y^2} + \frac{\partial^2 \varepsilon_y}{\partial x^2} + \frac{\partial^2 \gamma_{xy}}{\partial x \partial y} = (\frac{\partial^2 w}{\partial x \partial y})^2 - \frac{\partial^2 w}{\partial x^2}\frac{\partial^2 w}{\partial y^2} \tag{2.57}$$

which is often termed the compatibility equation due to its restriction of the strain values to those compatible with the displacements. In order to write Equation 2.57 in terms of stresses, we first re-write the stress-strain relations of Equation 2.51 as Equations 2.58, 2.59, and 2.60

$$\varepsilon_x = \frac{1}{hE_x}(T_x(x,y) - \nu_{xy}T_y(x,y)) \tag{2.58}$$

$$\varepsilon_y = \frac{1}{hE_y}(T_y(x,y) - \nu_{yx}T_x(x,y)) \tag{2.59}$$

$$\gamma_{xy} = \frac{1}{hG}T_{xy}(x,y) \tag{2.60}$$

where E is the tensile modulus, ν is Poisson's ration, G is the shear modulus, h is the membrane thickness, and the subscripts denote the two orthogonal axes. Substituting Equations 2.58, 2.59, and 2.60 into Equation 2.57 results in Equation 2.61

$$\frac{1}{hE_x}\frac{\partial^2 T_x(x,y)}{\partial y^2} + (\frac{1}{G} - \frac{2\nu_{xy}}{E_x})\frac{\partial^2 T_{xy}(x,y)}{\partial x \partial y} + \frac{1}{hE_y}\frac{\partial^2 T_y(x,y)}{\partial x^2} = (\frac{\partial^2 w}{\partial x \partial y})^2 - \frac{\partial^2 w}{\partial x^2}\frac{\partial^2 w}{\partial y^2} \tag{2.61}$$

which expresses the in-plane stresses in relation to the out-of-plane displacement, w. For the in-plane membrane problem, the right-hand side of Equation 2.61 goes to zero which yields, along with Equations 2.52 and 2.53, three equations and three unknowns.

Use of the so-called Airy stress functions[61] offers a solution to the in-plane problem. The approach recasts the internal stresses, $T's$, as shown Equations 2.62, 2.63, and 2.64

$$T_x(x,y) = h\frac{\partial^2 F}{\partial y^2} \tag{2.62}$$

$$T_y(x,y) = h\frac{\partial^2 F}{\partial x^2} \tag{2.63}$$

$$T_{xy}(x,y) = -h\frac{\partial^2 F}{\partial x \partial x} \tag{2.64}$$

where F is the Airy stress function, its form yet to be specified. Writing the internal stresses in this form is seen to automatically satisfy Equations 2.52 and 2.53. Substituting Equations 2.62, 2.63, and 2.64 into Equation 2.61 and again considering only the in-plane problem (so the right-hand side of 2.61 is zero) yields Equation 2.65

$$\frac{1}{E_x}\frac{\partial^4 F(x,y)}{\partial y^4} + (\frac{1}{G} - \frac{2\nu_{xy}}{E_x})\frac{\partial^4 F(x,y)}{\partial x^2 \partial y^2} + \frac{1}{E_y}\frac{\partial^4 F(x,y)}{\partial x^4} = 0 \tag{2.65}$$

which is known as the orthotropic biharmonic equation[62]: a fourth-order, linear differential equation. The traditional biharmonic equation for the isotropic case can be found by inserting the relation $G = \frac{E}{2(1+\nu)}$, however, the orthotropic equation is the appropriate one for this analysis as discussed in Section 2.3.2. Timoshenko and Goodier[61] demonstrate using polynomials for the functional form of F. An example of a fourth-degree polynomial representation is shown in Equation 2.66

$$F = \frac{a}{4*3}x^4 + \frac{b}{3*2}x^3y + \frac{c}{2}x^2y^2 + \frac{d}{3*2}xy^3 + \frac{e}{4*3}y^4 \tag{2.66}$$

where the letters $a - e$ are constants which can be adjusted to change the nature of the loading. Traditionally, the constants are specified to satisfy the boundary conditions for a particular problem. As Equation 2.66 is a fourth-degree polynomial, taking the fourth-derivative and substituting into Equation 2.65 yields that $e = -(2c + a)$. Therefore, the constants $a - e$ can be adjusted to any values and still satisfy the compatibility equation as long as $e = -(2c+a)$. For lower-order representations of the Airy stress function, there are no such requirements. For higher-order representations, the number of requirements increase. Since Equation 2.65 is linear, any combination of Airy stress functions of polynomials of different orders can be superposed to give a desired solution.

2.3.4.2 Out-of-Plane Problem

When transverse stresses and deflections are present, the membrane problem must be analyzed with the out-of-plane equilibrium equation as in Equation 2.67

$$p + T_x(x,y)\frac{\partial^2 w}{\partial x^2} + T_y(x,y)\frac{\partial^2 w}{\partial y^2} + 2N_{xy}(x,y)\frac{\partial^2 w}{\partial x \partial y} = 0 \tag{2.67}$$

where p is the pressure load acting on the differential element. Equations 2.61 and 2.67 form what is known as the Foppl equations which, along with the definitions of Equations 2.62, 2.63, and 2.64, represent a system of non-linear differential equations in two equations and two unknowns which are F and w. Such a problem is difficult to analyze, and various levels of simplification can be afforded as described below.

Three levels of analysis are available: (1) linear theory, (2) geometric non-linear theory, and (3) geometric and material non-linear theory[63]. In linear theory, the membrane only resists out-of-plane motion due to the change in angle of the in-plane forces towards the angle of the out-of-plane stretching as the membrane deforms. Mathematically, this corresponds to the assumptions that Equations 2.54, 2.55, and 2.56 are equal to zero which is termed the small strain assumption. This results in the decoupling of Equation 2.67 from Equation 2.61, and the linear theory thus needs only a single degree of freedom in the out-of-plane direction. Additionally, linear theory assumes that the change in the direction of p in Equation 2.67

with deformation is negligible which is termed the small deflection assumption. Linear theory is valid only for pre-tensioned membranes, and for a given pre-tension, the theory loses applicability as the out-of-plane deformation increases. The geometric non-linear theory has degrees of freedom in all three directions. It accounts for large strains and large deflections. Geometric nonlinear theory is valid for all membrane deflection before stresses get so large that material non-linearity is a factor. The material non-linear theory assumes some form of the constituive relations such that E, G, and ν of Equations 2.58, 2.59, and 2.60 are no longer constants.

Practically, solution approaches to the linear and non-linear problems require certain functional form to be assumed for the unknown membrane displacements. Some insight into which functional forms are appropriate can be found from Table 2.3. It can be seen that exact analytic representations of the deflection solution do not exist for geometrically non-linear deformation of thin structures. Thus, a combination of basis functions are used for a series solution technique where the accuracy of the solution depends on the number of terms kept in the basis function series.

Table 2.3: Review of solutions for uniformly loaded strings and membranes.

		String	Circular membrane	Rectangular membrane
Linear	Gov. Eqn.	$T\frac{d^2w}{dx^2} = -p$	$\sigma_r \frac{\partial^2 w}{\partial r^2} = -\frac{p}{h}$	$\sigma_x \frac{\partial^2 w}{\partial x^2} + \sigma_y \frac{\partial^2 w}{\partial y^2} = -\frac{p}{h}$
	Exact Soln.	Yes	Yes	No
	Approach	$w = ax^2 + bx + c$ [64]	$w = \frac{a}{4}\frac{pa}{\sigma_0 h}(1 - \frac{r^2}{a^2})$[65, 66]	Modified cosine series[61]
Nonlinear∗	Gov. Eqn.	$\frac{dw}{dx}\|1 + \frac{dw}{dx}^2\|^{-1.5} = -\frac{p}{T}$	$\sigma_r \frac{\partial^2 w}{\partial r^2} + \frac{\partial \sigma_r}{\partial r}\frac{\partial w}{\partial r} = -\frac{p}{h}, \sigma_\theta = \frac{\partial}{\partial r}(r\sigma_r)$	Equations 2.61 and 2.67 #
	Exact Soln.	No	No	No
	Approach	Assume no out-of-plane strain[64]	Power series[67, 68]	Double sine series[69]

∗ Nonlinear solutions account for geometric nonlinearity only

Governing equations in reference [69] are given for the isotropic case rather than the orthotropic case shown in Equation 2.61

† Solution is for pressure loading represented by a double-Fourier series rather than a uniform load

2.4 Porosity of Plain-Woven Fabric

In order to understand the transpiration through the Kevlar walls under wind loading, the pressure-velocity relationship through porous materials is here investigated. It is considered the work of Hoerner[70] who gave a background of the aerodynamics of screens and fabrics. Hoerner proposed a model for the pressure-velocity relationship across fabrics that serves as a useful starting point for the current work.

First, Hoerner postulates a drag coefficient for porous materials as a function of the solidity, φ, which is defined as unity minus the open-area ratio. Drag coefficients, C_D, are usually based on the wetted area of a body which Hoerner assumes to be approximately proportional to φ so that C_D can be formulated as in Equation 2.68

$$C_D = \frac{D}{q_x S_{proj.}} = \frac{\Delta p}{q_x \varphi} = \frac{\Delta p}{q} \frac{(1-\varphi)^2}{\varphi} \tag{2.68}$$

where D is the drag force, $S_{proj.}$ is the projected area of the fabric yarns, Δp is the pressure drop across the fabric, q_x is the average dynamic pressure through the narrowest area of the fabric pores. On the far right-hand side, q_x has been replaced by the relation $q_x = \frac{q}{(1-\varphi)^2}$ where q is the velocity upstream of the fabric. The relation $D = \frac{S_{proj.} \Delta p}{\varphi}$, which can be found by summing the forces in a control volume around the fabric, has been used in the sequence of equations, also.

There are, in fact, two different contributors to C_D. The pressure drop experienced by fluid flow through a fabric is due to both viscous forces and dynamic forces which correspond to the same phenomena which produce drag on a cylinder in a freestream: skin friction and separation-induced pressure drag, respectively. For the viscous contribution, Hoerner gives Equation 2.69

$$C_{D,viscous} = \frac{40}{Re_x^{0.75}} \tag{2.69}$$

where Re_x is the Reynolds number which is based on the velocity through the narrowest area of the fabric pores, as well as the diameter of the fabric yarns. The constants have been empirically determined from a collection of pressure-velocity data through fabrics and screens. With use of Equation 2.68, it can be shown that Equation 2.69 has the form $q_x \sim \Delta p^{0.8}$. The exponent on the pressure term is thus close to the value of unity observed very low Reynolds number flows. The second contributor to C_D is the difference in dynamic pressure between the front and back sides of the fabric which is due to losses from pressure-induced separation over the back-side of the yarns. The solidity of the fabric dictates the area over which the dynamic forces act, so Hoerner gives Equation 2.70

$$C_{D,dynamic} = \varphi. \tag{2.70}$$

Therefore, in this limiting case of only dynamic forces acting on the fabric, the pressure drop is proportional to the *square* of velocity which follows from the Bernoulli equation. Such a relationship was shown to hold for wire meshes when $\varphi > 0.5$, at least for $Re_x > 10^3$.

Finally, by substituting Equations 2.69 and 2.70 into Equation 2.68 and solving for the pressure difference, we have Equation 2.71

$$\Delta p = \frac{1}{2} \rho u^2 [C(\frac{ud}{\nu(1-\varphi)})^{-0.75} + \varphi] \frac{\varphi}{(1-\varphi)^2}. \tag{2.71}$$

where the constant C was found empirically to be 40.

Equation 2.71 provides a semi-empirical means to determine the pressure-velocity relationship through a fabric. Equation 2.45 of Devenport *et al.*[9] bears resemblance to Equation 2.71 in that it contains a dynamic pressure term and a viscous correction term. This form is the model for the work to be done in the present study.

One aspect of particular concern to the current work is the dependence of the porosity relationship on the tension of the fabric. The only previous work to the author's knowledge in the area of tension dependence is by Natarajan[71]. He provides both pressure-velocity data and optical data demonstrating that woven fabric porosity increases with uni-axial strain because the interstices between adjacent yarns become larger. In several limited instances, the porosity initially dropped with increasing strain before rising again because the fabric was initially wrinkled. For these cases, low strain levels straightened the fabric which reduced the number of interstices exposed to the flow without expanding the interstices' size, and thus the porosity initially decreased with strain.

2.5 Justification, Objectives, and Approach

This chapter has thus far introduced the solid-wall test section as the industry standard for aerodynamic measurements, as well as the Kevlar-wall test section and the relevant physics of its unique boundary condition. The overarching goal of this work is to achieve the same level of understanding and validation of the aerodynamic performance of Kevlar-wall test sections as is already available in conventional solid-wall test sections.

While the state-of-the-art in Kevlar-wall corrections already is well-developed in terms of the two-dimensional panel method described above, there is still room for improvement. Corrected pressure distributions between test sections show good agreement except for some cases of a slight offset of the Kevlar-wall data relative to the solid-wall data. Devenport *et al.*[9] cites a possible over-prediction of blockage when the Kevlar is highly loaded based on analysis of pressure distributions. Brown[36] also references slightly exaggerated blockage, both at high and low loading situations. The drag measured in the Kevlar-wall test section may be slightly offset below that of the solid-wall test section which may again be attributable to over-prediction of the apparent dynamic pressure, and a similar argument might be applied to some of the pitching moment data. In terms of three-dimensional flow situations, the panel method approach is unverified for Kevlar-wall test sections. Therefore, there exists a need for further development of wall-interference corrections including higher fidelity inputs and modeling strategies for the panel method approach. Efforts towards such are grouped below as Thrust 1.

The unique boundary conditions of the Kevlar-wall test section also pose a difficulty from an instrumentation point-of-view. While conventional pressure measurements around the airfoil surface and in its wake are regularly achieved in Kevlar-wall test sections, there is no robust method by which to measure the wall pressure distributions which are routinely measured in

solid-wall test sections. The preliminary technique of wall-mounted taps as described above has had limited success and is not practical as a long-term installation. Rather, it is desired to have a full-field, non-contact measurement of the loading at the boundary condition which is the final goal of the objectives of Thrust 2.

Thrust 1:

- Directly measure the fundamental sources of wall interference unique to flexible, porous-wall wind tunnels
- Employ such measurements to generate engineering models for correcting aerodynamic data from wall interference effects in porous, flexible-wall wind tunnels
- Assess the relevance of models of varying fidelity for performing wall-interference corrections in flexible, porous-wall wind tunnels
- Identify potential sources of residual error in the wall interference corrections scheme

Thrust 2:

- Determine appropriate functional forms to represent the geometrically nonlinear deflection field of membranes in the context of flexible-wall deflection in wind tunnels
- Select appropriate methods for de-noising full-field deflection measurements of membranes under pressure loading
- Demonstrate the measurement of a membrane's pre-tension field from its deflection behavior under hydrostatic loading
- Determine full-field deflection of a membrane by non-contact measurements from without the wind tunnel test section
- Use the above methods to test the hypothesis that full-field method deflection measurements of flexible-wall wind tunnels can produce non-contact measurement of loading at the boundary conditions

The above are accomplished in several steps. Chapter 3 introduces the wind tunnel facilities and instrumentation used during this study. Chapter 4 details preliminary out-of-tunnel experiments on samples of Kevlar fabric that yielded information about the mechanical and aerodynamic properties of the fabric to be used throughout the remainder of the chapters. Chapter 5 implements a modified panel method to correct Kevlar-wall data from two dimensional models, building upon the achievements of previous literature to increase the fidelity of the corrections modeling. Validation of the corrections modeling is performed versus solid-wall data measured with the same model at the same facility. Chapter 6 presents a

three-dimensional version of the same panel code as in the previous chapter, which is then verified against the two-dimensional version and validated with comparisons between corrected data from three-dimensional models in Kevlar- and solid-wall test sections. Chapter 7 introduces a stereo camera system for non-contact measurements of the Kevlar deflection which provide structural information at the Kevlar boundary that is employed to produce the pressure distribution over the wall, as well as the lift produced by a model.

Chapter 3

Wind Tunnel Facilities and Instrumentation

Described first in this chapter is the Stability Wind Tunnel at Virginia Tech. The Stability Wind Tunnel contributed to both Thrusts 1 and 2 and it is by default the facility under consideration unless otherwise noted. The Low Speed Wind Tunnel at the Japanese Aerospace Exploration Agency is used in a supporting role for Thrust 1 and is described second in this chapter.

3.1 Primary Facility: 1.85-m by 1.85-m Stability Wind Tunnel

The Stability Wind Tunnel was fabricated at the NACA Langley Research Center in the 1930's before being relocated to Virginia Tech in the late 1950's. The tunnel's test section and sealed control room sit outside Randolph Hall on the Virginia Tech campus as shown in Figure 3.1(a).

The schematic of the single-return circuit can be seen in Figure 3.1(b). The drive and fan send the wind tunnel flow first into an air exchange tower where air from the atmosphere is mixed with tunnel air to stabilize the tunnel flow temperature. From the tower, the air turns two corners with the aid of guide vanes and passes into the 5.5-m by 5.5-m square settling chamber which is coated on all 4 walls with 50-mm thick urethane foam liner do dampen fan and motor noise. The flow next passes through 7 turbulence-reducing screens with open-area ratio of 60% before accelerating through the 9:1 contraction. The removable test section has a constant 1.85-m by 1.85-m (6-ft. by 6-ft.) cross section and is 7.3-m (24-ft.) long. Vortex generators at the rear of the test section add vorticity to the flow to promote mixing and prevent boundary layer separation as it enters the 3-degree slanted diffuser which is lined

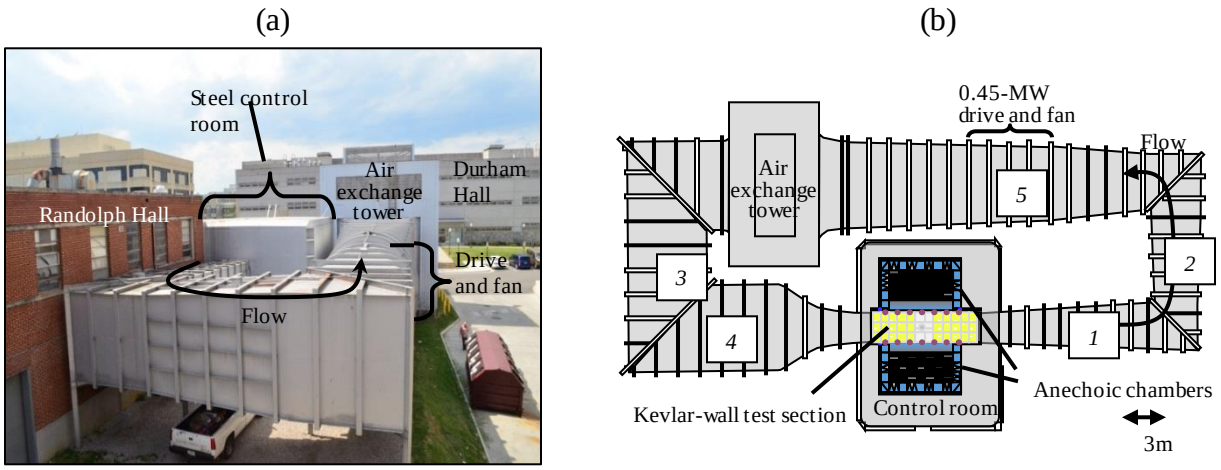

Figure 3.1: (a) Photograph and (b) plan-view schematic of the closed-circuit Stability Wind Tunnel at Virginia Tech. The steel control room is sealed from inside Randolph Hall by an airlock. The tunnel is in anechoic configuration as depicted in (b) with the Kevlar-wall test section flanked on either side by anechoic chambers. (Illustration credit: William J. Devenport.)

with 50-mm thick melamine foam to again reduce noise contamination of the test section from the fan and motor. Finally, the flow turns 180-degrees again and returns to the fan. Pressure equalization of the tunnel flow with the control room pressure occurs at the rear of the test section where slots for a rake traverse are located.

The tunnel is powered by a 0.45-MW, variable speed, DC drive turning a 4.3-m diameter, 8-bladed fan. The fan produces flow velocities in the test section up to 80-m/s with no blockage for a maximum Reynolds per meter up to 5 million. Turbulence intensities levels are as low as 0.016% and no more than 0.031%, the higher levels occurring at higher freestream velocities as shown in Table 3.1.

The Stability Wind Tunnel features two exchangeable test sections, the solid-wall and Kevlar-

Table 3.1: Freestream turbulence levels.

Freestream Velocity	RMS Streamwise Fluctuations
U_∞ (m/s)	u'/U_∞
12	0.016%
21	0.021%
30	0.024%
48	0.029%
57	0.031%

wall test sections which are each installed and removed by overhead lifts. When installed, a test section rests on support elements so that its leading and trailing edges adjoin with the contraction and diffuser, respectively. Strips of aluminum and expanding foam are used to cover the several centimeters clearance openings at the leading and trailing edges.

3.1.1 Solid-Wall Test Section

The solid-wall test section can be seen from its upstream end with a vertically-mounted airfoil in Figure 3.2. The floor and ceiling are aluminum plates, 0.61-m (2-ft.) on a side, and there are 12 streamwise rows and 3 width-wise rows. The plates are fixed to the tunnel at each corner with bolts countersunk into the aluminum to yield a smooth flow surface. At the joints where plates meet each other, foil tape is used if necessary to smooth any steps in the flow surface which may be on the order of 1 to 2-mm. Where the floor and ceiling plates meet the walls, there is a streamwise gap up to 2-cm which is sealed with aluminum foil tape.

The port and starboard wall flow surfaces are formed from 12.7-mm (0.5-in.) thick panels and their supporting steel frame. Each panel runs 0.76-m (30-in.) streamwise and 1.70-m (67-in.) spanwise, nearly the full span height of the tunnel. Each panel is bolted to the steel frame along all 4 edges and if necessary any steps in the flow surface at the meeting of the panels and frame are smoothed with foil tape. The panels, either Lexan or aluminum, were in Lexan configuration for the tests in this study. The dimensions of the test section vary little from the nominal dimensions. The width at the floor is between 1.850-m to 1.856-m (72.8-in. to 73.1-in.) measured from the fore to aft of the test section. Using a Pro 360 digital protractor with a +/-0.2 degree maximum error, the angularity of each of the 4 walls was found to be everywhere within 0.8-degrees of the nominal value and everywhere within 0.4-degrees of the nominal value at the model location.

A common testing configuration at the Stability Wind Tunnel is two-dimensional flow over airfoil sections. Full-span models with tubular quarter-chord spars on either end are rotated through angles of attack by a bearing and turntable system whose axis of rotation is midway between the test section walls and 3.56-m from the leading edge of the test section. The bearing and its mounting plate are located below the test model, providing support for the airfoil and allowing rotation about the airfoil quarter-chord axis. The spar of the airfoil, typically 8.9-cm (3.5-in.) outer diameter, slides into a collar mounted to the bearing. The turntable is located above the test section and again has a collar to receive the airfoil spar as seen in the cross-section A-A of Figure 3.2. The spar is fixed to a collar with pins so that the turntable governs the rotation of the airfoil. The turntable is a Kinematics model ZE14C slew drive powered by a BK Precision 9123A variable DC power supply and capable of applying torques up to 1000 N-m. Disk elements attached to the collar of either the turntable or bearing rotate with the airfoil while the surrounding plates remain stationary. Mylar strips cover any spanwise gap between the model and the floor/ceiling. Aluminum

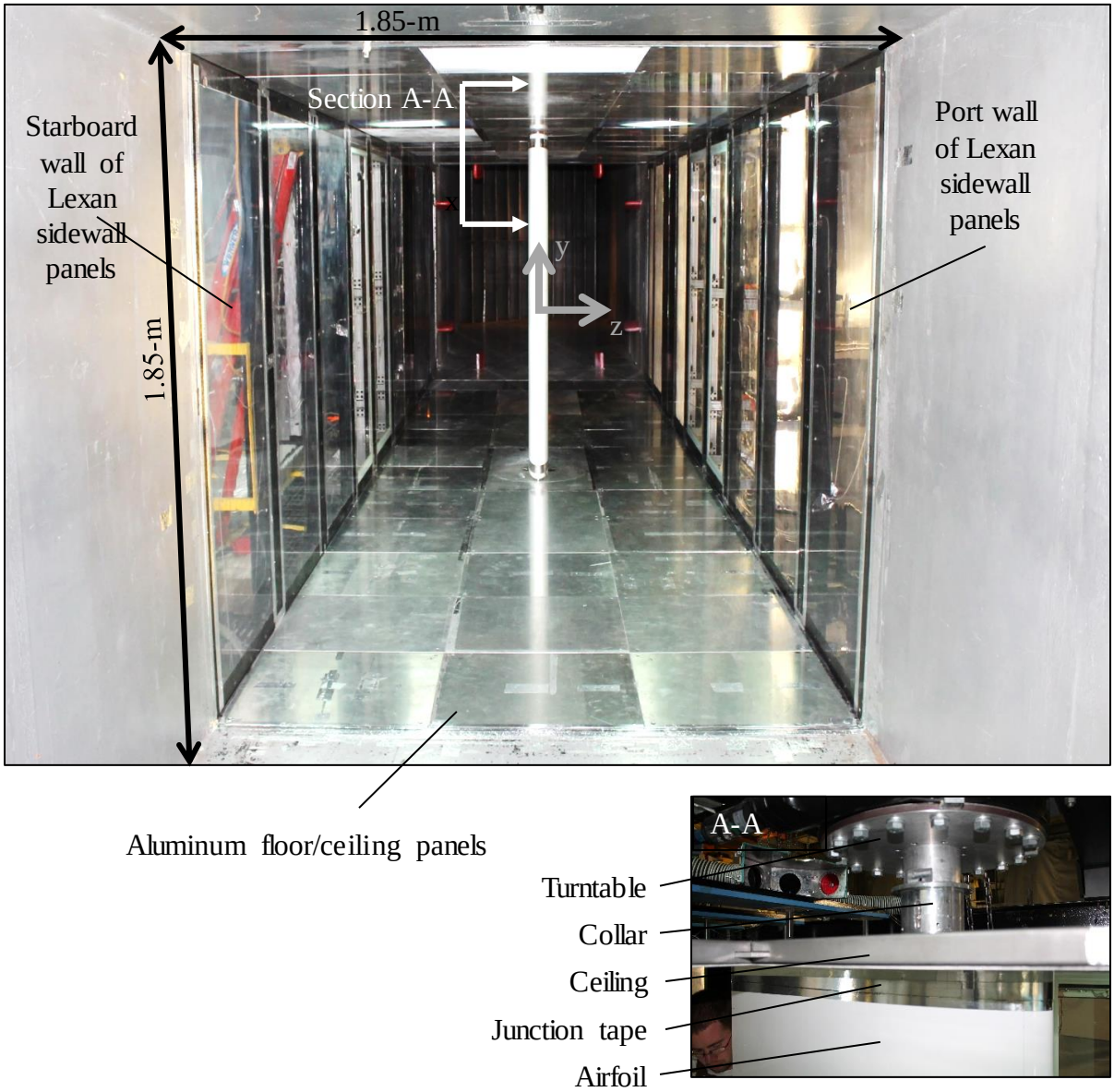

Figure 3.2: Downstream-looking view of the ceiling of the 1.85-m by 1.85-m solid-wall test section with a full-span airfoil model installed. The end of the contraction and the start of the constant-area test section is given by the location $x = 0$. The section view of A-A shows the workings of the turntable and mounting system.

foil tape is used to seal the Mylar, at least in the region where the airfoil profile overlaps the disk elements.

Zero angle of attack location is set for each airfoil by aligning the chordline at the trailing edge to the tunnel centerline as given by the joints in the floor panels. Alignment is typically within 1-mm at the trailing edge of each airfoil, which produces uncertainties of ± 0.08 degrees in the zero-angle setting for a 0.91-m chord airfoil which rotates about its quarter-chord. Additional uncertainty in the absolute angle of attack may be present due to any misalignment of the test section with the freestream flow direction. The above uncertainty represents a bias which is constant for any given run across all angles of attack. On the other hand, the relative uncertainty within any given angle of attack sweep is around 0.1 degrees based on the accumulated experience of wind tunnel engineers. As the magnetic encoder used to measure rotation has a resolution of 0.003 degrees, this relative angle of attack uncertainty is not due to the instrumentation but rather to slight rotation of the model originating in the pin joint between the airfoil shaft and the turntable sleeve. This uncertainty is a static value for any given angle of attack but exists nonetheless.

The angle of attack is also measured by a second, independent system which consists of one or more Acuity AR700-32 laser displacement sensors directed at the airfoil. The system provides a more direct means of measuring angle of attack which is useful given concerns about load-induced deformation in the model and mounting system[72]. When the laser measurement is located at least 0.6-m from the airfoil center of rotation, the angle of attack is read to within ± 0.1 degrees. Although the use of multiple lasers is now the preferred practice for measuring angle of attack at the Stability Wind Tunnel, the laser system in this study employed only one laser. Since the laser angle was only measured during some tests used in this study, the measurements from such tests will be used for diagnostic purposes to bound the error in the encoder angle of attack.

The laser system was calibrated against the magnetic encoder which was performed with the flow off when there was no possible deformation of either the model or mounting system. With the flow on, back-to-back tests with the laser and encoder systems revealed some discrepancies during tests of the NACA0012. Figure 3.3(a) shows the difference between the laser and encoder readings, $\alpha_{laser} - \alpha_{encoder}$, plotted versus $\alpha_{encoder}$ from 18 back-to-back polar sweeps. Offsets were applied to each polar in Figure 3.3 to force them through the origin due to a seeming temperature-dependent drift in the laser system reading. The value $\alpha_{laser} - \alpha_{encoder}$ is clearly a strong function of angle of attack as shown by the consistent negative slopes of the data from different polars. Upon closer examination, it is seen that three groupings of polars corresponding to the three nominal freestream dynamic pressures exist. The correlation between data was found to collapse when $\alpha_{laser} - \alpha_{encoder}$ is plotted versus the dimensional lift value as shown in Figure 3.3(b). Such information suggests one of three possibilities: (1) the model and mounting system are translating in the test section under lift loading, (2) the model is flexing under the lift loading, or (3) the model is rotating under lift loading. With only one laser reading in this case, there is no way to be sure whether it is primarily (1), (2), or (3). Measurements made outside the tunnel on similar

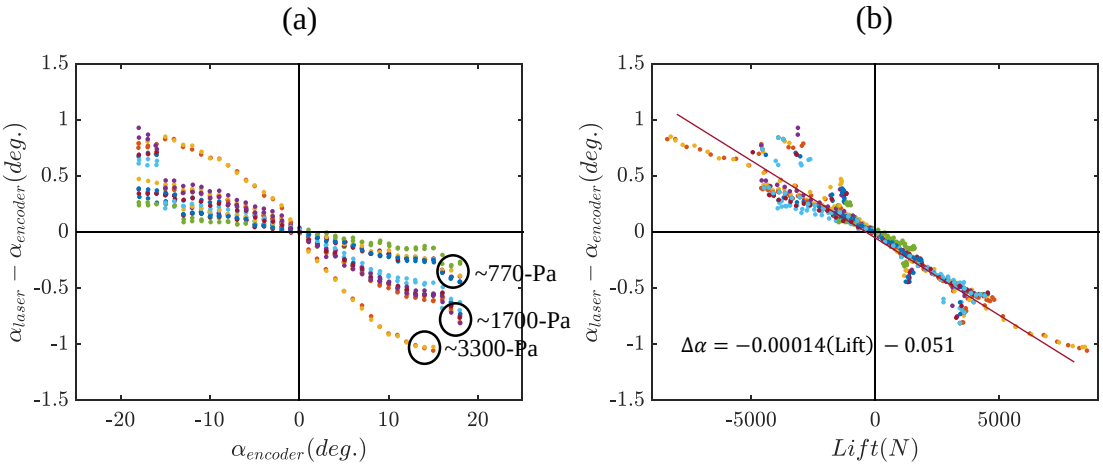

Figure 3.3: Difference in angle reading between laser and encoder systems plotted against (a) encoder angle and (b) lift force. Data are shown from 18 polar sweeps performed back-to-back on the NACA0012 airfoil used in this study. The groupings in (a) represent tests performed under the nominal freestream dynamic pressures as noted. Removed from the data above are offsets between α_{laser} and $\alpha_{encoder}$ which were seemingly due to a dependence of the laser reading on flow temperature.

airfoils suggest that (3) is dominant due to deformation of the pin connecting the airfoil spar to the collar mount. While the deformation mechanism is not fully understood, there is clearly a strong dependence on lift. This dependence is captured by the best-fit line to the data in Figure 3.3(b), and the error in the encoder reading is up to 1 degree for the highest loading situation on the model.

Since the error in the encoder reading is repeatable, it will not be removed from the data in the remainder of this study. All results to be reported below are encoder angles of attack. The relative angle of attack uncertainty thus remains at 0.1 degrees as noted above for the encoder. In the following chapters when data from different wind tunnel test campaigns are compared, the nominal freestream dynamic pressures of the data are matched as best as possible. Small angle of attack errors will be present in the comparisons due to differences in the achieved dynamic pressure between campaigns, but these have been found to be small compared to the differences in the data otherwise.

The freestream dynamic and static pressure in the test section are derived from measurements with four static pressure ports: two in the contraction and two in the settling chamber. The redundancy allows for calculating an average of two pressures at each location. The freestream dynamic pressure is inferred from these static pressures through calibration constants which are set based on independent velocity measurements by a Pitot-static probe. Example calculations using the constants are shown in Appendix D. For the solid-wall test section these constants are 0.9874 and 0.4135 for the settling chamber and contraction, re-

spectively. For reference, the Kevlar-wall test section uses values of 0.9871 and 0.4074 which are slightly different due to a small difference in flow resistance through the test section.

Assuming the calibration of the wind tunnel contraction and settling chamber ports to have negligible uncertainty, the sources of uncertainty in the measurement of the freestream velocity are the contraction pressure measurement, the settling chamber pressure measurement, the barometric pressure measurement, and the freestream temperature measurement. The contraction and settling chamber pressures are measured with the Esterline scanner with range of ± 2.5-psi and accuracy of 9-Pa. The barometric pressure is measured with a Validyne DB-99 Digital Barometer with resolution of 0.01-in. of mercury and the freestream temperature is measured with an Omega Thermistor type 44004 with accuracy ± 0.2 degrees C. An analysis of the propagation of error as outlined in Appendix D was used to relate the uncertainties in the primary measurements described above to the uncertainties in the calculated freestream velocity and dynamic pressure. The uncertainty of the freestream velocity is ± 0.5-m/s at 35-m/s and 0.3-m/s at 70-m/s. The uncertainty decreases with increasing freestream velocity since the uncertainties of the pressures used to infer the freestream velocity become smaller relative to the nominal pressures as the velocity increases. On the other hand, the freestream dynamic pressure uncertainty does not vary with freestream velocity and is 21-Pa for the current setup. The range in uncertainty of the freestream dynamic pressure thus varies between 0.6% and 3%. While the uncertainties presented on the plots in this study employ this uncertainty, it is suspected that the freestream uncertainty is in reality lower than that calculated from the analysis of the propagation of error. The quoted accuracy of the Esterline pressure scanners used for the freestream velocity measurement includes not only uncertainty due to hysteresis and non-linearity but also due to non-repeatability, the effect of which should be minimized by the internal averaging procedure of the pressure scanners, a procedure which is additional to an external averaging procedure to be described shortly. An analysis of the stagnation C_p's measured by the wake rake indicate that the accuracy of the freestream velocity is considerably better than that predicted by quoted uncertainty of the scanners. For these reasons, it is suspected that the uncertainties derived from the analysis of the propagation of error are exaggerated although they will be used in the remainder of this study.

The freestream velocity and static pressure values calculated correspond to the front of the test section. In the solid-wall test section, the freestream velocity is increased slightly moving in the streamwise direction due to the reduction in flow area caused by the boundary layer growth along the walls. The increase in freestream velocity is accompanied by a decrease in freestream pressure. Equation 3.1 is used to correct C_p data measured over models for the drop in freestream static pressure between the upstream measurement location and the model location

$$C_p' = \frac{C_p - C_{p,r\infty}}{1 - C_{p,r\infty}}, \quad C_{p,r\infty} = -0.00025083U_\infty + 0.0178625. \tag{3.1}$$

These relations are derived from measurements of the floor pressures in the solid-wall test section made along the length of the test section with no model in-place. There is a slight dependence on freestream velocity such that the static pressure drop is less severe at higher velocities which follows since the boundary layer thickness decreases with velocity. Unless otherwise noted, all data from the Stability Wind Tunnel's solid-wall test section are corrected with Equation 3.1 before any other corrections are applied. Unlike in the solid-wall test section, the boundary layer in the Kevlar-wall test section develops differently due to the Kevlar porosity, and this development is intended to be captured implicitly by the panel method simulation described in Chapter 5.

3.1.2 Kevlar-Wall Test Section

The Kevlar-wall test section, shown from the upstream view in Figure 3.4(a), uses the same turntable system for airfoils and has the identical 1.85m-by-1.85m cross section and 7.3-m length as the solid-wall test section, however, the port and starboard walls are made from tensioned Kevlar fabric and the ceiling and floor surfaces from perforated plates that are also covered with Kevlar fabric.

The Kevlar windows are the test section's most unique feature, extending 4.2-m of the total 7.3-m test section length and spanning from the floor to the ceiling as shown previously in the schematic representations of Figures 3.5 and 3.6. The windows have varying constructions, sometimes being formed from separate pieces of Kevlar fabric sewn and glued together and sometimes being formed from a single piece of Kevlar fabric. The latter is now standard practice at the Stability Wind Tunnel, however, the measurements which will later be designated Campaign 2 were taken with the older configuration. This configuration consists of three pieces of Kevlar fabric with two sewn and glued seams approximately 40-mm wide that run the length of the test section at locations around 30-cm above and below the floor and ceiling, respectively. The Kevlar is tensioned in both the horizontal and vertical directions with a tensioning frame to a target tension of 1500-N/m as measured by a Newman ST-Meter 2E tension meter. For both the newer and older configuration of Kevlar walls, tension is produced by applying torque to rollers on the perimeter of the tension frame, and the Kevlar is held in the rollers by an interference fit between locker rod and grooves in the rollers. The tensioning frame has dimensions of 5.37-m by 2.51-m and is held clamped to the test section frame by corner L-brackets along the perimeter. The clamping location is offset from the wall opening so that the Kevlar is stretched over the opening. Magnets spaced roughly 5-cm apart run the perimeter of the opening to keep the Kevlar pressed as firmly as possible against the test section under loading conditions.

The floor and ceiling surfaces are again made from aluminum plates, 0.61-m (24-in.) on a side, as in the solid-wall test section. However, the plates are this time perforated to allow transmission of sound to volumes of space above and below the test section designed to absorb sound. Kevlar is stretched over the top of the aluminum plates to provide a

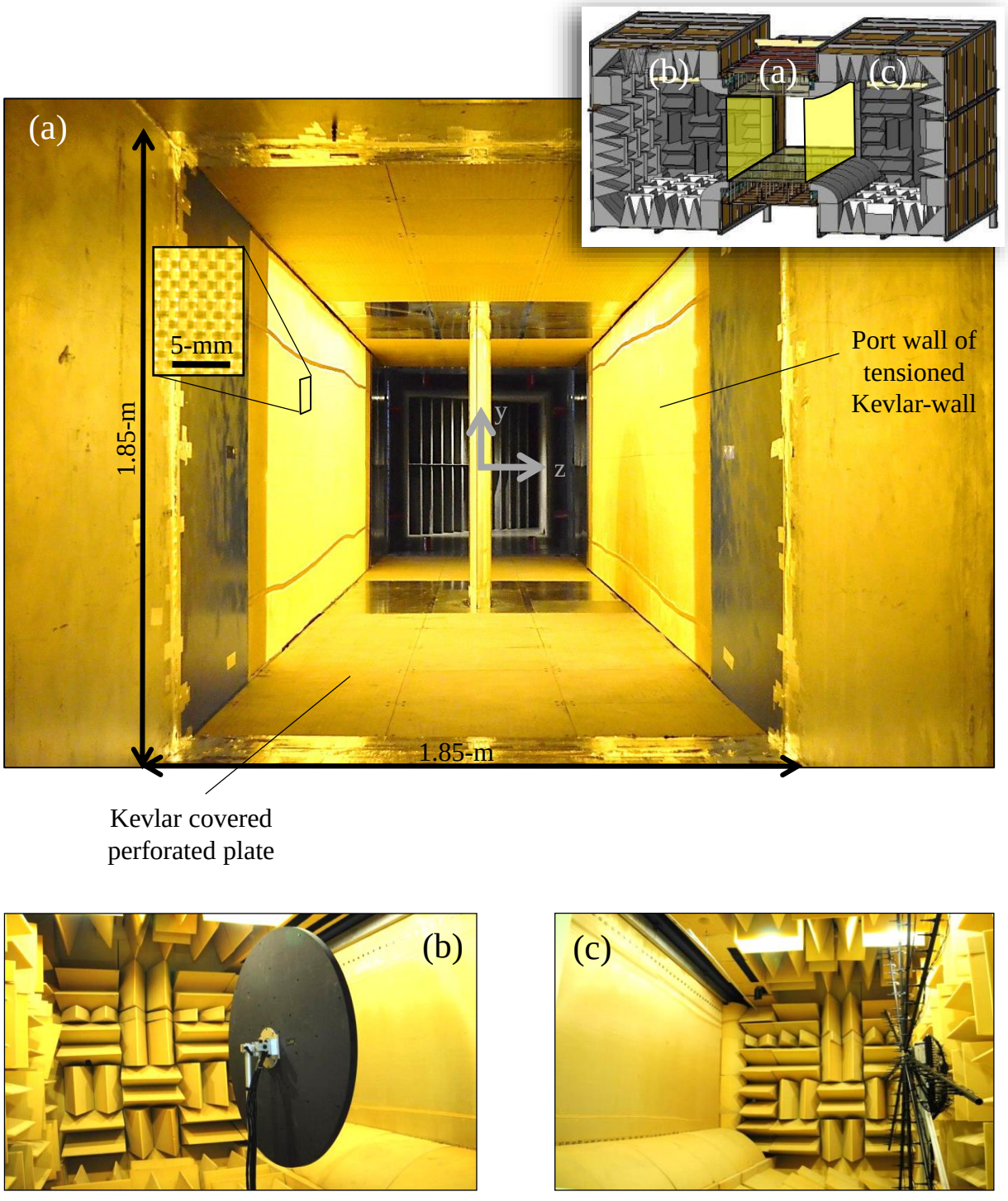

Figure 3.4: (a) Downstream-looking view of the 1.85-m by 1.85-m Kevlar-wall test section with a full-span airfoil model installed. The (b) starboard and (c) port anechoic chambers are shown with microphone arrays in-place. The end of the contraction and the start of the constant-area test section is given by the location $x = 0$.

smooth, uninterrupted flow surface. For the measurements of this study, there were two different configurations used for the ceiling and floor panels. In both cases, there were three rows of aluminum panels surrounding the model on both the floor and ceiling as shown in Figure 3.4(a). For the tests which will later be designated as Campaign 2, the outer streamwise rows of Kevlar-covered panels on the floor were replaced with standard aluminum panels to allow for pressure instrumentation on the floor.

As acoustic waves pass through the low-attenuating Kevlar they enter the anechoic chambers on either side of the test section to be measured by acoustic instrumentation such as seen in Figure 3.4(b)-(c). As seen in Figures 3.5 and 3.6, the chambers each run 5.6-m long in the streamwise direction, thus they are longer than the streamwise length of the Kevlar walls but not as long as the whole 7.3-m length of the test section. The chambers are each 3.0-m wide and 3.4-m high, as measured from the outer walls which are fashioned from square steel beams that support 19-mm thick medium-density fiberboard (MDF). Panels of MDF are joined with 1.3-cm by 5.7-cm (0.5-in. by 2.25-in.) strips of wood that overlap and screw into the panel on either side. The joints are covered in paint although in some areas the seal provided by the paint has cracked over time. Lining the inside of the MDF walls, floor, and ceiling are foam wedges that absorb frequencies of sound above 140-Hz. The wedges are 0.61-m tall and vary in width depending on their location. Around the Kevlar windows, quarter-elliptical foam pieces mate up to the Kevlar at the floor and ceiling leaving just open the 1.85-m test section height. At the upstream and downstream ends of the walls, the closest row of wedges are pressed against the Kevlar thus covering roughly 30 streamwise centimeters of fabric.

Behind the quarter-elliptical foam pieces are areas of Kevlar fabric both above and below the test section that account for the 0.68-m difference in heights of the inner test section and Kevlar tensioning frame. These sections of fabric are exposed to the volumes of space above and below the test section floor and ceiling which are typically filled with foam wedges to again absorb acoustic waves and prevent reflection back into the test section. The volumes of space above and below the test section are designed to be sealed from the control room, thus ideally yielding the test section and chambers an isolated system permitting no mass exchange with the control room.

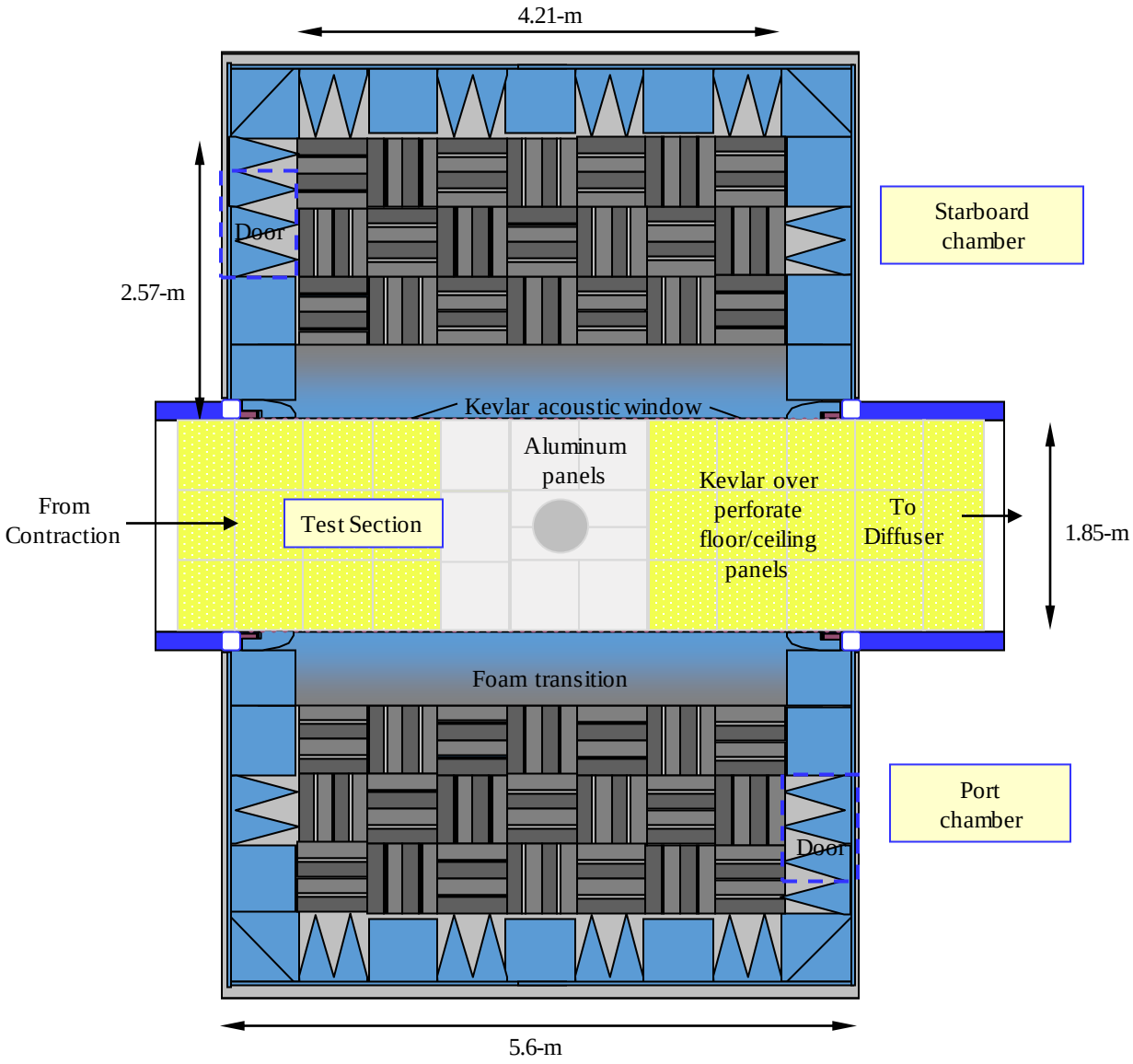

Figure 3.5: Plan view cross-section of the Kevlar-wall test section (center) between the two anechoic chambers. (Illustration credit: William J. Devenport.)

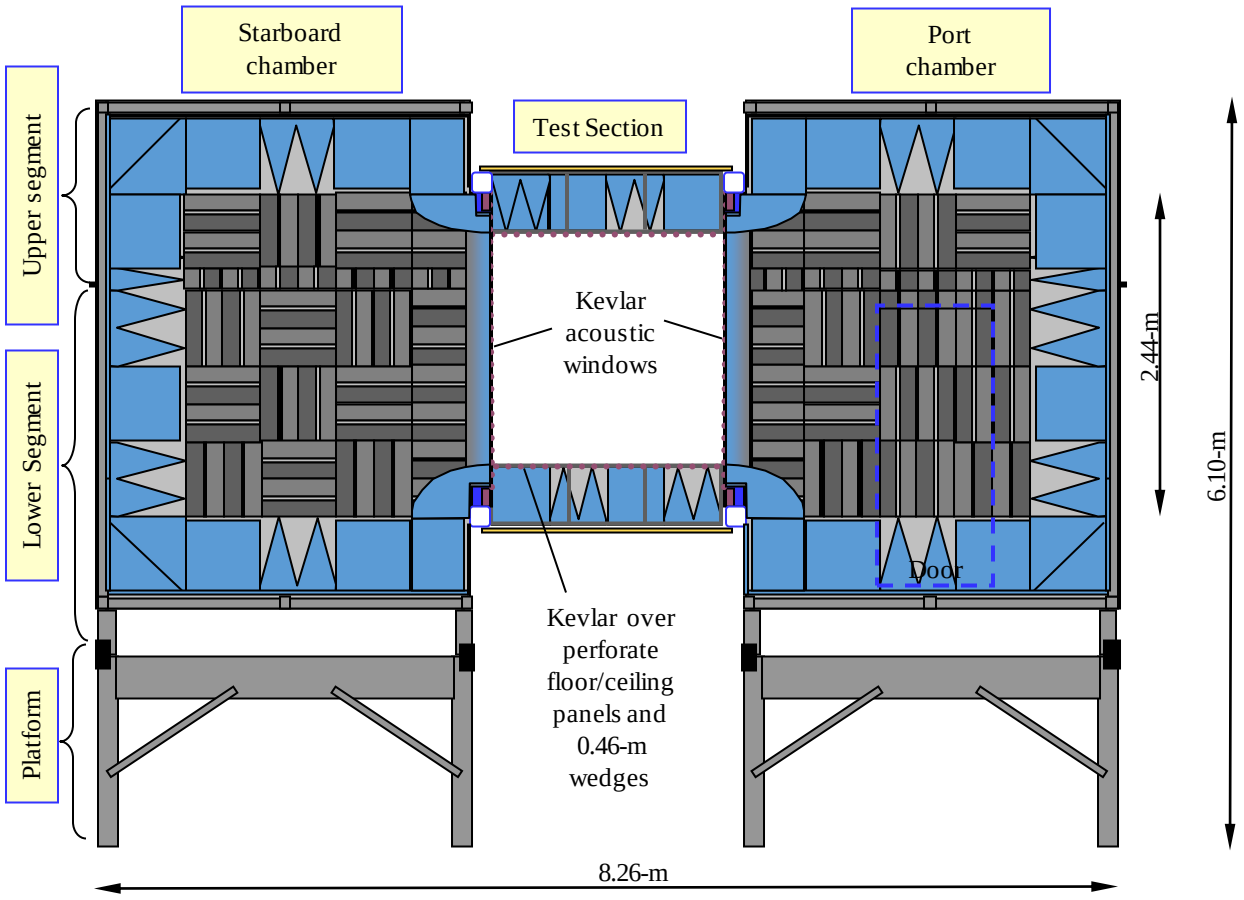

Figure 3.6: Cross-section of the Kevlar-wall test section (center) between the two anechoic chambers looking downstream. (Illustration credit: William J. Devenport.)

3.1.3 Airfoil Model

The main aim of this study is to directly compare the aerodynamics of the solid-wall and Kevlar-wall test sections by observing pressure data measured on airfoils in both test sections. Brown[36] took measurements on three airfoils including a 0.914-m chord and a 0.203-m chord NACA0012, and a 0.610-m chord DU00-W-212. For the present work, the 0.914-m chord NACA0012 has been selected for focused testing.

The 0.914-m (36-in.) NACA0012 as shown in Figure 3.7 is constructed of a composite fiberglass exterior enclosing a core of steel ribs and polyurethane foam. The airfoil profile and port locations were measured by a FaroArm Coordinate Measurement Machine as described in Devenport et al. (2010a). The FaroArm has a rated accuracy of ± 0.025-mm, however, experiences by engineers at the Stability Wind Tunnel dictate that this accuracy is around ± 0.5-mm. Comparing 300 measured profile y-coordinates near the midspan of the airfoil with the theoretical y-coordinates for the measured x-coordinates, the measured profile differs slightly in its thickness from the theoretical profile. The mean increase in the thickness direction of the measurement relative to the theoretical shape is 0.10% and 0.08% chord, or 0.93-mm and 0.74-mm, for the upper and lower sides of the airfoil, respectively. The added thickness of the airfoil originates from the base profile as well as the presence of a hatch located across midspan on one side of the airfoil which provides access to the pressure instrumentation inside the model. The hatch is on the suction-side at positive angles of attack, and tape is used to smooth over the transition to the hatch around all four

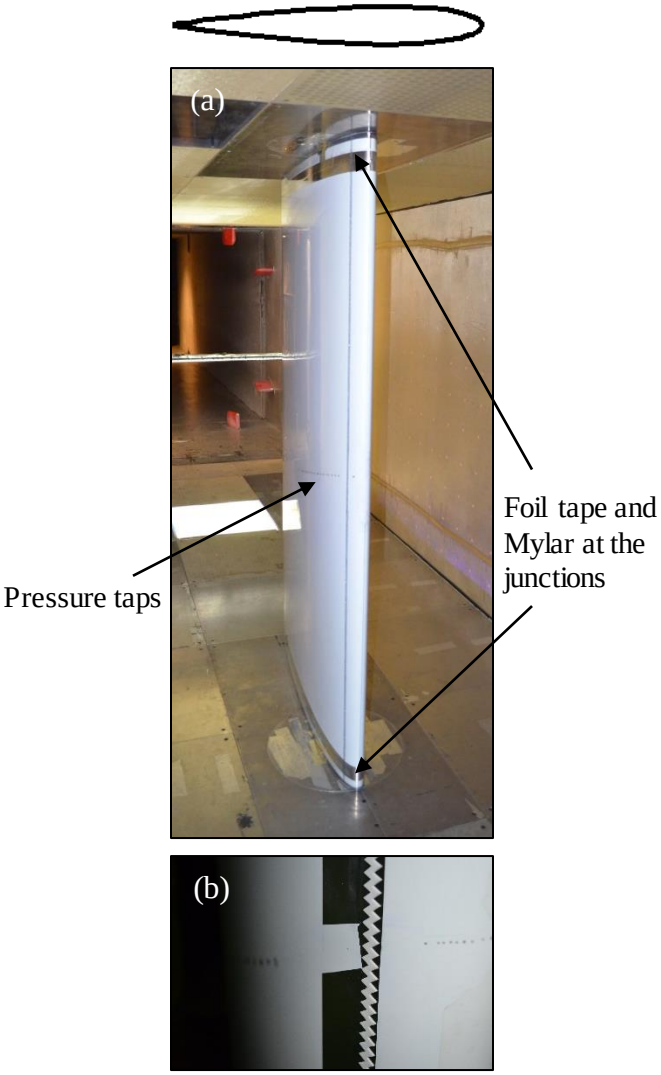

Figure 3.7: (a) Full-tunnel view and (b) close-up view of the 0.91-m NACA0012. In (b), the leading edge of the trip is installed at 5% chord and is mounted on foil tape.

edges. Trials of the theoretical and measured profiles in a panel method solver showed the deviation of the airfoil profile from the theoretical to be of small aerodynamic consequence, and processing of airfoil pressure data used the theoretical rather than the measured profile.

The 0.914-m (36-in.) NACA0012 has 81 pressure taps of 0.5-mm diameter near the midspan region that are spaced apart in the spanwise direction in an attempt to avoid contamination of the downstream ports by the upstream ports. The ports are spaced apart by 1- to 3-mm spanwise in the leading edge region and by up to 12-mm spanwise over the rest of the airfoil. The spanwise offsets create rows of taps that are angled roughly 13-degrees from the chordwise direction. The rows double back after the midchord location so that the ports do not go further than a distance of 7% chord from the midspan location. After checking the pressure-holding capability of each port, 72 of the 81 ports were deemed usable. The port locations for this model are given in Appendix H.

For the runs in the tripped condition, the airfoil was fitted with serrated trip tape of the type Turbulator from the Glasflgel Company as seen in Figure 3.7(b). The tape is 0.425-mm high, and the leading edge of the tape was aligned to the 5% chord location on both the pressure and suction sides. The tape was adhered to foil mounting tape that is 0.1-mm high and extended from 5-11% chord. Thus, the total height of the serrated trip tape above the airfoil surface was 0.525-mm.

3.1.4 Airfoil Pressure Measurements

Standard measurement techniques were used to gather the airfoil pressures. Pressure taps in the airfoil models are connected to 1.6-mm Tygon tubing which lead to an Esterline 9816/98RK pressure scanner with a range of ± 2.5-psi, accuracy of ± 0.05% full scale (which accounts for hysteresis, nonlinearity, and non-repeatability), or ± 9-Pa, and resolution of ± 0.003% full scale, or ± 0.5-Pa. Pressure measurements are averaged over at least 25 readings, each individual reading consisting of an internal average of hundreds pressure measurements. The pressures are then integrated along the chordwise direction to yield lift and pitching moment. Periodically during a test day, scanners are re-zeroed to reduce drift effects on the measurements. The operating temperature range of 0 to 50 degrees Celsius was never exceeded in the indoor control room during testing.

The pressure-holding capability of each tap in the model was checked with a hand-held Fluke 7181G Pressure Calibrator by covering the tap hole on the model with tubing from the calibrator, applying a pressure on the order of 5-in. of water from the calibrator, and cross-checking the pressure reading of the calibrator with the Esterline scanner. Pressure ports that were clogged or leaking were removed from the data acquisition software.

Uncertainties in the aerodynamic coefficients are estimated based on the uncertainty analysis presented in Appendix D.1. The primary measurements included in the error propagation calculations are the model pressures, model pressure tap locations, model chord length,

contraction pressure, settling chamber pressure, barometric pressure, and temperature. The 20:1 odds uncertainties at $C_{l,max}$ are 0.039, 0.020, and 0.011 for the 0.91-m NACA0012 at dynamic pressures of 770-Pa, 1700-Pa, and 3300-Pa, respectively, which corresponds to 2.4%, 1.3%, and 0.7% of the measurement.

Some uncertainties that are not accounted for in the error analysis but believed to be small are uncertainties due to the calibration constants used in calculation of the freestream velocity, the unsteadiness of the freestream flow, the freestream pressure drop through the test section as given by Equation 3.1, the correlation time of structures in the boundary layer passing of the airfoil pressure transducers, and the two-dimensionality of the flow. The calibration constants are trusted with a degree of confidence at the Stability Wind Tunnel since C_p values on leading edge pressure ports of airfoils can read nearly exactly unity for certain angles of attack meaning that the calibration constants are faithfully calculating the stagnation pressure. The RMS fluctuation in velocity has been measured only as high as 0.031% as shown in Table 3.1 which is negligible compared to the uncertainty in the freestream velocity measurement already presented. The pressure data are an average of 25 points taken at a sampling rate of 100 measurements per channel per second. These samples are not guaranteed to be independent of each other if the correlation time of the boundary layer is large. However, given that multiple pressure scanners are used to measure airfoil pressures in most tests, the sampling time of the pressure data are longer than 1 second which allows for the passing of many correlation times. The two dimensionality of the flow at the pressure tap locations can be verified with wake rake cross-sections downstream of the airfoil which was performed for some of the tests in this study though not reported here.

3.1.5 Wake Pressure Measurements

A wake rake consisting of 120 Pitot probes was used to measure drag and wake cross-sections downstream of the model as seen in Figures 3.8. All but 7 of the 120 probes are made of 1.6-mm diameter stainless steel tubing and used to measure the stagnation pressure over the width of the tunnel. The remaining 7 probes are 3-mm diameter Pitot-static probes of type Dwyer model 167 which are spaced more sparsely along the span of the wake rake to measure static pressure, in addition to stagnation pressure. The probes are connected to one of the four 16TC/Digital Temperature Compensated (DTC) Gen 2 pressure scanners that can be seen spaced over the top side of the rake in Figures 3.8(a). The rake is formed by a streamlined strut of chord 16.5-cm (6.5-in.) and thickness 2.5-cm (1-in.) from which extend support rods and the probes. The probes extend ahead of the streamlined body by 0.31-m (12.25-in.) measured from the probe tip to the center of the strut. The Pitot-tubes are spaced apart by 25-mm (1-in.) in the outer regions and 6-mm (0.25-in.) in the center region which equates to spacing of 15 and 40 tube diameters, respectively. The wake rake is located either 1.75-m or 2.78-m downstream of the model quarter-chord location for the solid-wall and Kevlar-wall test sections, respectively. The instrumentation wiring from the rake exited the tunnel through the starboard-side rake slot machined into the tunnel walls,

and excess length of wires were taped to the tunnel wall to avoid flapping in the tunnel flow. For drag measurement, the rake was positioned midway between the test section floor and ceiling. For verification of the two-dimensionality of the flow over the airfoil, the rake can be traversed from 5- to 178-cm (2- to 70-in.) above the tunnel floor, typically in increments of 10-cm (4-in.) with increments of 2.5-cm (1-in.) near the floor and ceiling.

The 16TC/Digital Temperature Compensated (DTC) Gen 2 pressure scanner noted above is produced by Pressure Systems, Inc. Each of these scanners have 32 ports and one reference port with a range of ± 2.5-psi and a rated accuracy of ± 0.03% full scale, or ± 5-Pa. Each scanner is temperature compensated by an internal temperature sensor and internally stored temperature calibration data. This compensation capability makes the DTC scanners ideal for in-tunnel mounting. Measurement averaging and re-zeroing procedures were the same for the DTC scanners as for the Esterline scanners.

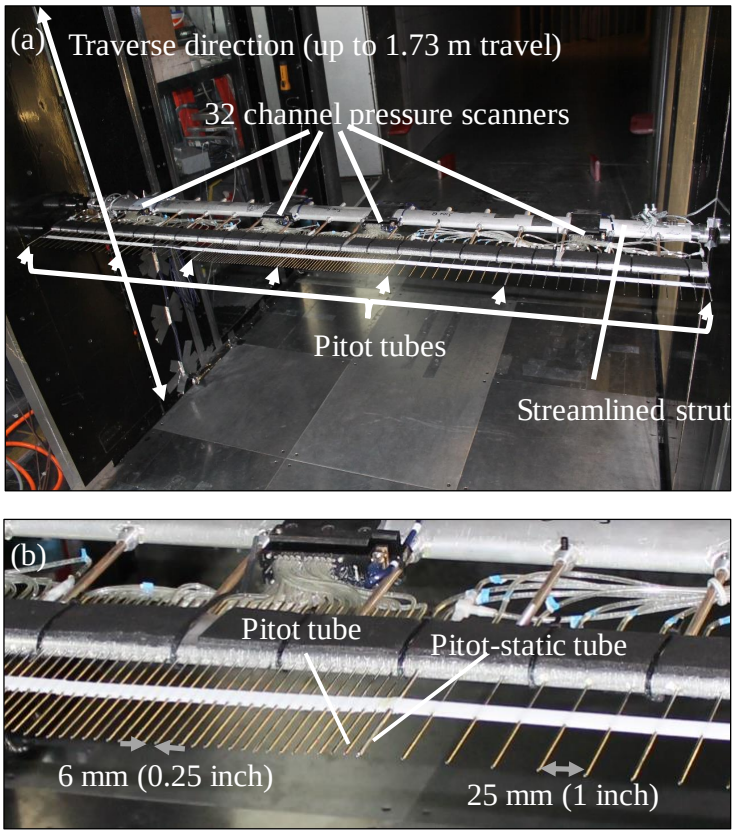

Figure 3.8: (a) Wake rake mounted in the rear of the test section as seen from the port-side of the test section and looking downstream and (b) a detail view of the Pitot and static probes. Static probes in (a) are indicated by the arrow heads.

Rake data is post-processed to calibrate out bias which originates from uncertainty in the pressure transducers, possible misalignment of the Pitot probes with the freestream direction, and interference on the static pressure measurement due to the blockage effects of the probe tubes and strut. The highest C_p value recorded by given a Pitot probe over the course of an angle of attack sweep occurs when the probe is experiencing the full dynamic pressure of the tunnel flow. However, the measured value may deviate slightly from unity due to the possible biases noted above. A calibration is thus performed by taking the difference between the highest C_p value recorded and unity. This difference is then added to all subsequent read-

ings made by the given probe. The difference between the stagnation pressure measured by each of the Pitot probes and the static pressure measured by the 7 static pressure ports yields the dynamic pressure at the given location. The rake wake was used only for tests with Reynolds number less than or equal to 2.25 million due to unsustainable flow-induced vibration at higher Reynolds that caused the rake to oscillate in the spanwise direction such as a vibrating, simply-supported beam.

The quoted uncertainty in drag is not calculated with an error analysis but rather based on two measurements of an identical setup before and after a complete uninstallation and reinstallation of the model at the Stability Wind Tunnel. The drag uncertainty was thus found to be 5% of the measured drag value.

3.1.6 Wall Pressure Measurements

In addition to the conventional pressure measurements described in the previous section, pressure taps were installed in the Kevlar walls to measure the midspan pressure distribution over the walls. The pressure ports are made by sanding off one side of a polypropylene connector designed to accept 1.59 mm (1/16 in.) inner diameter tubing as shown in Figure 3.9a. The connector and its attached Tygon tubing are then hot-glued to the chamber-side of the Kevlar wall as in Figure 3.9b. The tubing then runs down the wall and to a pressure scanner.

Figure 3.10 illustrates the step-by-step process by which the pressure ports are installed. First, the woven Kevlar fibers in the vicinity of the pressure port are stretched and pushed aside to open a passageway through the wall using thin electrical wire, the result being seen in Figure 3.10a. The polypropylene connector is then threaded with a thin electrical wire (b), dabbed with high temperature hot-glue (c), and bonded to the chamber-side of the Kevlar wall (d) and (e). The wire acts to plug the opening of the connector during gluing, as well as locate it on the wall. After drying, the wires are pulled out from the tunnel-side (f) and reamed out with either the wire or a 0.508-mm (0.020-in.) drill bit and handheld chuck to remove excess glue (g). Finally, remaining debris is blown out from the port by use of compressed air (h).

An important aspect of this design is that the finished pressure tap does not penetrate through the Kevlar, and therefore does not add any protrusions to the tunnel-side Kevlar flow surface. During the installation process above, excess glue may seep through the Kevlar and harden on the tunnel-side surface. These surfaces are smoothed by rubbing a finger over the port opening until the glue crumbles away. As with solid-wall test sections, a technique to minimize any residual imperfections in the flow-side facing quality of the pressure taps is to take reference data with no model in the test section. The runs with no model in the test section are taken at increments of 5-m/s over the full range of velocities in the test matrix, and the data are interpolated to match the exact velocities of each measurement in the test matrix. The difference of the with-model pressures and without-model pressures then reveals explicitly the effects of the model on the walls. It may be noted that the leading edge of

the rake probes are positioned just 52-cm downstream of the last wall ports. Therefore, the furthest downstream wall measurements may experience some blockage effects from the wake rake although the influence is not expected to be large and is not taken into account.

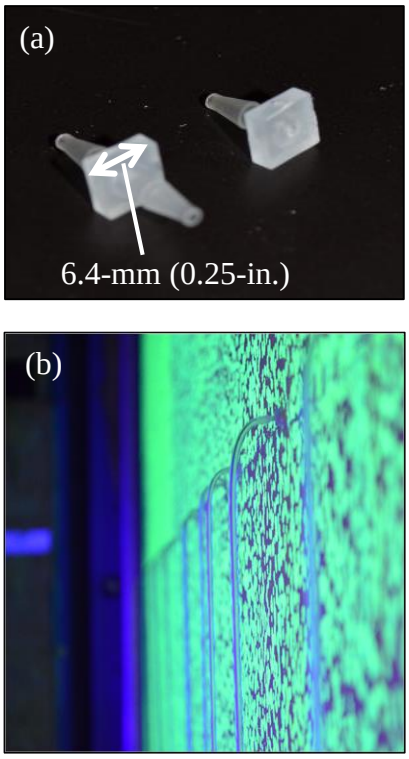

Figure 3.9: (a) Polypropylene connector (left) before and (right) after flattening of the Kevlar-side face. (b) Image of chamber side of Kevlar showing the midspan row of wall-mounted pressure ports and Tygon tubing.

The arrangement of the ports for two different test campaigns to be studied later are shown in Figure 3.11. For Campaign 2, the spacing between ports at midspan is 30.5-cm (12-in.) for a total of 16 ports per wall. The spanwise rows of ports were not considered for this study. For Campaign 3, the spacing away from the airfoil is 20.3-cm (8-in.), and the spacing near the airfoil is 10.2-cm (4-in.) for a total of 30 ports per wall.

Wall pressure measurements were made using the DTC Gen 2 pressure scanners with range of ±2.5-psi for Campaign 2 and the Esterline scanner with range of ±10 inches of water for Campaign 3. The pressure-holding capability of each port was checked with a hand-held Fluke 7181G Pressure Calibrator in a similar way to the model pressure-checks described above. The ports leaked air faster than typically seen in other pressure checks, presumably because of the difficulty of making a good seal of the pressure calibrator tubing over the woven Kevlar surface. However, as this should not be an indication of leakage of the pressure line itself, the majority of the ports were passed in the pressure checks. The static pressure in the anechoic chambers is sensibly constant and is measured with open-ended Tygon tubing leading directly to the Esterline scanner with range of ±10 inches of water.

Uncertainties in the lift coefficient derived from the wall pressure measurements are estimated based on the uncertainty analysis presented in Appendix D.2. The primary measurements included in the error propagation calculations are the wall pressures, wall pressure tap locations, model chord length, contraction pressure, settling chamber pressure, barometric pressure, and temperature. The 20:1 odds uncertainties at $C_{l,max}$ are 0.039, 0.020, and 0.012 for the 0.91-m NACA0012 at dynamic pressures of 770-Pa, 1700-Pa, and 3300-Pa, respectively, which corresponds to 2.4%, 1.3%, and 0.8% of the measurement.

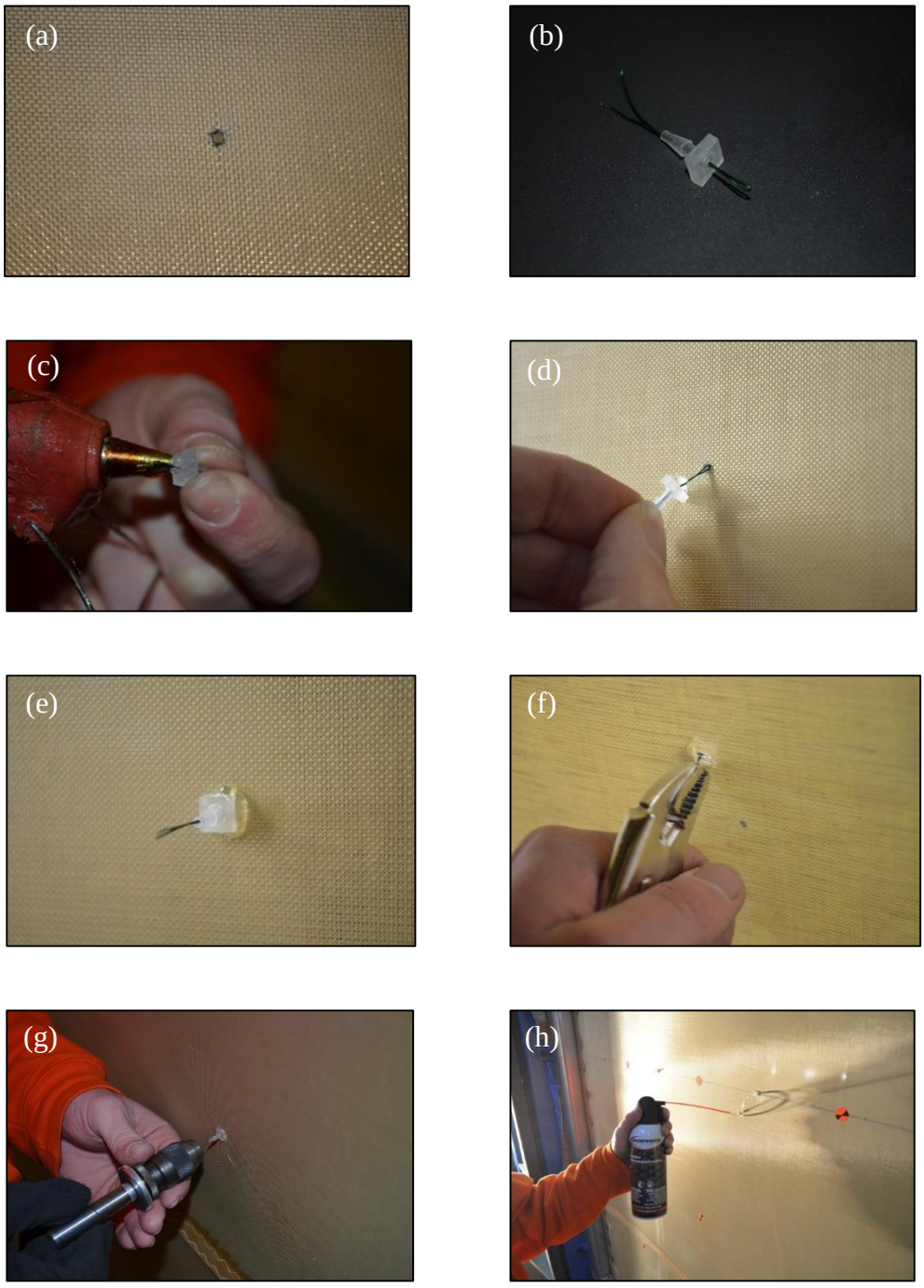

Figure 3.10: Step-by-step installation procedure for the pressure taps mounted on the Kevlar wall.

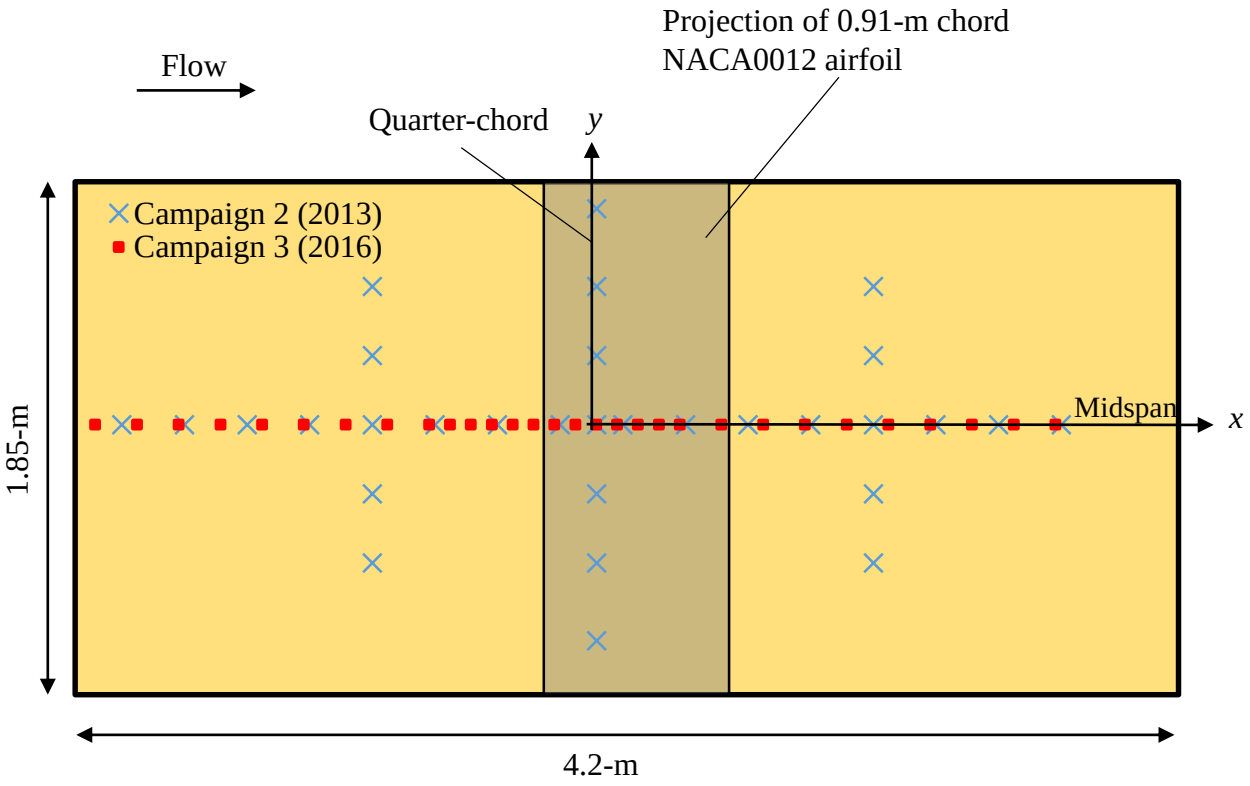

Figure 3.11: Arrangement of the pressure taps mounted on the Kevlar walls. The layout is the same for the port and starboard walls.

3.1.7 Wall Deformation Measurements

As part of the characterization of the boundary conditions of the Kevlar-wall test section, wall deformations have been measured. Previously, such measurements have been made on a Kevlar-wall test section with infrared sensors on a traverse rig developed at the Japan Aerospace Exploration Agency[5]. However, the current measurement system rather employs three-dimensional digital image correlation (3D-DIC) techniques to measure the full-field deformation of the Kevlar walls in the Stability Wind Tunnel under wind loading.

The 3D-DIC system used for the present measurements consists of cameras mounted in each anechoic chamber and focused on the Kevlar walls. The walls are marked with a high contrast, randomized pattern consistent with DIC convention. As the Kevlar walls deflect under wind loading, images are taken and processed to calculate the displacement, strain, and ultimately pressure loading of the Kevlar walls. During airfoil testing, the calibrated camera system captures the deformation of the Kevlar walls for each angle of attack in the test matrix.

The first subsection addresses the setup of the walls and camera system, followed by discussions of camera calibration, feature-matching calculations, and uncertainty. The DIC calibrations and processing performed in this study are done through the software DaVis 8.2.3 from LaVision GmbH, and reference is made throughout this section to specific selections to be made in this software.

3.1.7.1 Experimental Setup

DIC requires a pattern of high optical contrast on the surface of interest in order to correlate the same point in space between two camera views[73]. The pattern must also be random since a repeating pattern would not produce a unique match in the correlation algorithm. The random pattern, or speckle pattern, employed in this study is made of circular specks that are randomized in both location and size on the Kevlar walls. There are on average 3.5 speckles per cm^2 with a mean diameter of 3.4-mm and standard deviation of 0.5-mm which produces 31% coverage of the Kevlar. The pattern is produced with the tools shown in Figure 3.12. A linoleum screen printing block is patterned with raised speckles by engraving away background material with a laser-engraver. Fluorescent water-based block printing ink is rolled onto the speckle pattern, and the pattern is pressed against a mounted and pre-tensioned Kevlar sheet. In order to increase the ink transfer, pressure is applied to the back side of Kevlar with a rubber squeegee while the pattern is held in-place. The speckles, which are designed to be barely visible under ordinary lighting, are illuminated with UV-light during measurements as shown in Figure 3.13(b).

The Stability Wind Tunnel's 3D-DIC system uses Canon Rebel T3 cameras which are digital single-lens reflex (DSLR) cameras. The cameras have 4272- by 2848-pixel sensors which are complimentary metal-oxide sensors (CMOS) with 5.2-μm square pixels. The lenses are EF-S

18-55mm 1:3.5-5.6 IS II lenses from Canon. Each camera is mounted to a Manfrotto 808RC4 camera mount which is then bolted to an 80/20 aluminum support. The aluminum support is fixed to two L-brackets, each of which is bolted in two places to the steel beams which form the super-structure of the anechoic chamber. Sufficient torque was applied to all connections to eliminate slip during the duration of the testing.

In each chamber, four cameras are stationed according to Figure 3.14. The logic for the camera placement hinges on the aim to capture half of the Kevlar wall in each camera's field-of-view (FOV) so as to have two stereo-paired cameras viewing the upstream half and two stereo-paired cameras viewing the downstream half of each wall. It should be stated that while camera systems composed of more than two cameras viewing the same scene have inherently higher accuracy than traditional binocular systems[74], such an arrangement is not leveraged here because the DaVis 8.2.3 software uses only two cameras to perform triangulation even if there are more cameras available. In order for each camera to view at least half the Kevlar wall, the cameras are placed at the maximum z=2.4-m in depth from the Kevlar and at the largest possible baseline separation of B=2.3-m as shown in Figure 3.14. The two stereo pairs are separated by a distance of 2.2-m so that they are centered on their respective FOV's.

Figure 3.12: Tools used for speckling the Kevlar sheet: linoleum screen printing block, screen printing ink, and soft rubber brayer.

Given the camera locations, the FOV's required to capture the full extent of the Kevlar wall in the horizontal and vertical directions are ∼47 degrees and ∼31 degrees, respectively. The focal length, f, required for such FOV's is calculated according to Equation 3.2

$$f = \frac{n_p \Delta d}{2tan(\frac{1}{2}FOV)} \tag{3.2}$$

where n_p is the number of pixels in the image sensor in the direction under consideration, Δd is the width of each pixel, and FOV is the field-of-view in radians. The largest allowable f calculates to 25-mm and 26-mm for the horizontal and vertical directions, respectively. In practice, focal lengths of 21-mm to 24-mm were used to allow for some overlap of the FOV between the upstream and downstream stereo pairs of cameras.

Another consideration in the design of camera systems is the depth-of-field (DOF). Although camera apertures are sometimes modeled as pinholes, real cameras have finite-sized apertures which can only truly focus at one depth along the optical axis. At other points in the scene

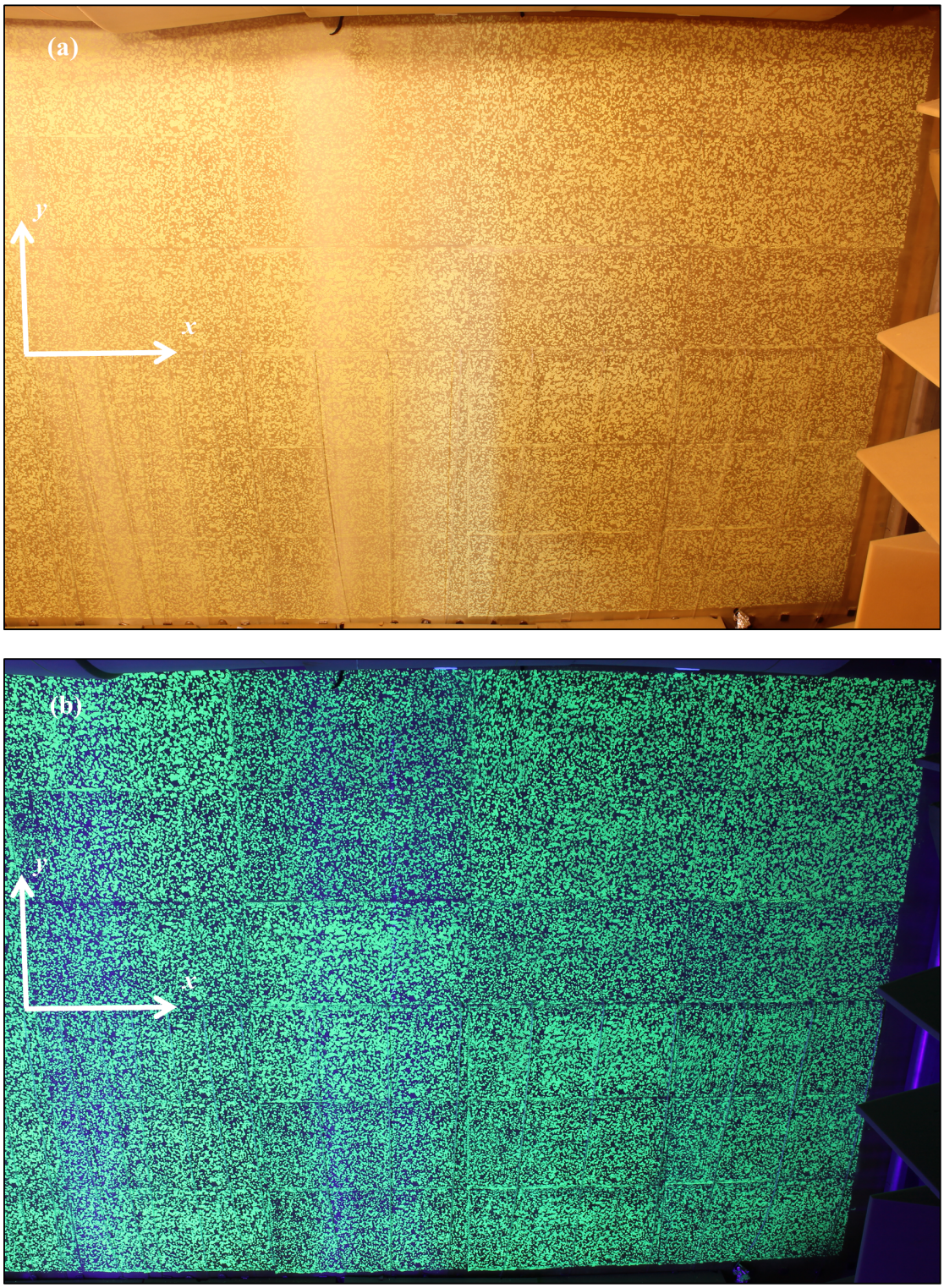

Figure 3.13: Kevlar wall with speckle pattern and wall pressure ports shown in (a) ordinary lighting and (b) under fluorescent lighting.

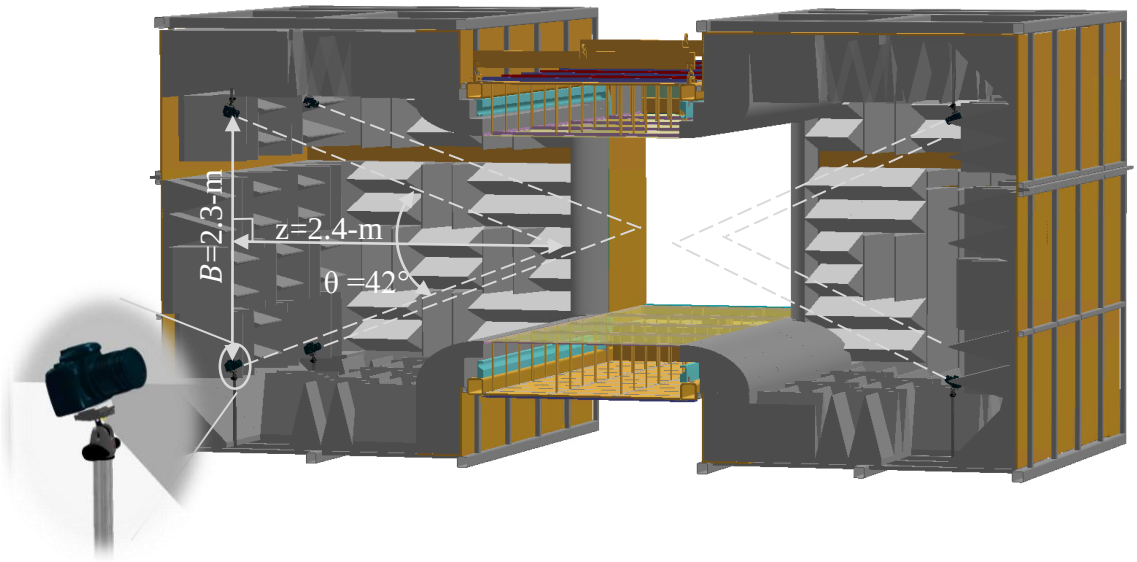

Figure 3.14: Rendering of the Stability Wind Tunnel in anechoic configuration with cameras installed in the anechoic chambers. Note the Kevlar walls are not pictured.

not on this axis, a circle of confusion exists which becomes significant after it passes a certain threshold[75]. The hyperfocal length, H, of a camera is the minimum depth at which the camera can be focused and still maintain focus within a given circle of confusion to an infinite depth as given by Equation 3.3

$$H \approx \frac{f^2}{Nc} \tag{3.3}$$

where f is again the focal length, N is the f-number describing the aperture size, and c is the admissible circle of confusion with typical values being $\frac{f}{1000}$[74, 76]. If the camera is focused to a point at a distance H or larger, then the camera achieves the maximum DOF possible for the given f, N, and c which is $\frac{H}{2}$ to ∞. Given the above camera configuration and using an f-stop of $f/18$, the value of H=1.2-m. According to the 2.4-m depth of the cameras from the Kevlar wall, the camera will be focused well beyond this hyperfocal length, and the whole Kevlar wall will therefore remain within the DOF even as it deflects in and out of the tunnel.

A final consideration in the design of the camera system is the exposure parameters. An ideal image capture would entail small aperture to increase DOF, fast exposure time to minimize blur, and low ISO number to reduce noise in the image sensor. Trade-offs must be made, however, since it is not often possible to achieve all of these at once. A typical strategy in DIC measurements might consist of taking simultaneous images from stereo-paired cameras

which ensures that measurements will be accurate even if the object in consideration has motion. As the Kevlar walls are sometimes subject to vibration at high loading, simultaneous capture is desired. However, the image acquisition software used here does not have true simultaneous capability, so an alternative strategy was pursued. Leveraging the fluctuating nature of the motion of the Kevlar under high loading, it was proposed to use a long image capture time to gather a sort of average signature of the Kevlar location. Such an approach is not known to be verified in the literature and thus has a high uncertainty associated with it. Granted, motion of the Kevlar walls is not a concern over the majority of an angle of attack sweep, and a long capture time does not present significant uncertainty in these cases. A welcome side-effect of a long exposure time is that the lighting requirements are reduced. This allowed for illumination via UV lights that lit high contrast fluorescent patterns painted on the Kevlar. The long exposure time also necessitated the use of a low ISO number which is favorable from an intensity noise point-of-view. Some authors average multiple images from a static scene to reduce intensity noise [77], however, using the low ISO number works towards the same purpose though the long exposure time may increase noise. In total, the cameras were operated at an aperture of f/18, an exposure of 8 seconds, and an ISO of 100.

Remote capture of pictures is accomplished by connecting the cameras to a central computer with a USB hub and with the software DSLR Remote Pro Multi-Camera by Breeze Systems. Images are converted from 14-bit raw format to bitmap format which is lossless before being imported to the DaVis software. Pre-processing in the DaVis software includes transforming the coordinate system to be centered on the quarter-chord and midspan location of the wall as shown by the coordinate systems in Figure 3.13. For each stereo pair of cameras, the xy-plane is defined as the best-fit plane to the undeformed wall, and the origin is manually selected by clicking. The same point on the Kevlar, as indicated by a pressure port, is used to define both the coordinate systems of both the upstream and downstream stereo-pairs of cameras.

3.1.7.2 Camera Calibration

Most camera calibrations techniques, including the one used in this work, utilize the pinhole model which assumes that any measured point in space, the optical center of the camera, and the point's projection onto the image plane are all co-linear[78]. Camera calibration then requires estimating intrinsic parameters of the camera including the focal length, scale factors in the x- and y-axes, and skew between the axes, among other possibilities, as well as estimating six extrinsic parameters of the camera's location in relation to a world coordinate system as described by three translational and three rotational degrees of freedom[76, 78]. Once correspondence between pixel coordinates and world coordinates has been obtained for a number of calibration points, most calibration methods consist of solving an initial linear problem to estimate the transformation matrix between pixel and world coordinates, followed by a non-linear optimization to minimize the differences between the calibration marker locations and their predicted positions by varying the intrinsic and extrinsic param-

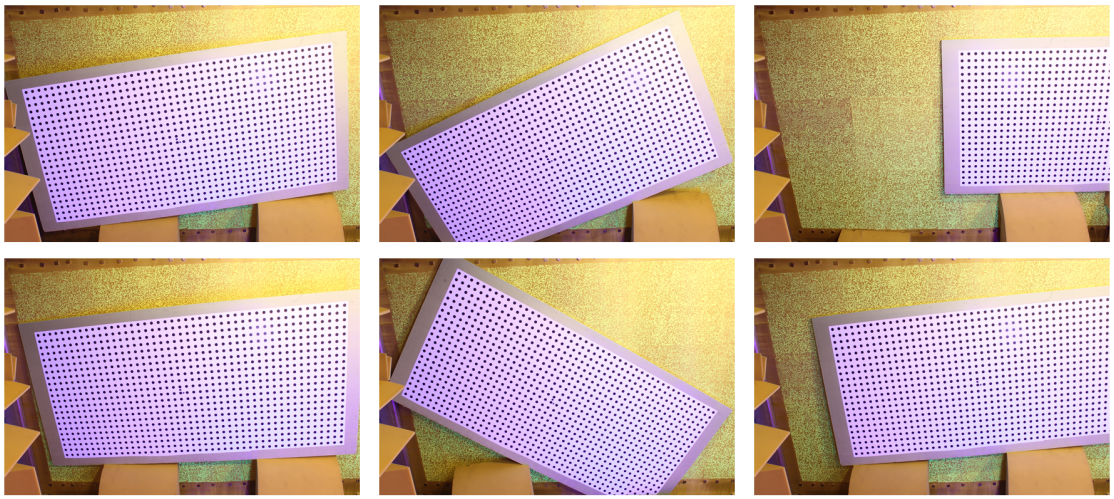

Figure 3.15: Six orientations of the calibration plate used to calibrate one of the stereo-pairs of cameras of the Stability Wind Tunnel's 3D-DIC system.

eter estimations[78]. Varying the intrinsic and extrinsic parameters as such is termed *bundle adjustment*. Several types of distortion which violate the pinhole assumption are modeled and corrected by adding intrinsic parameter terms to the bundle adjustment process. Decentering distortion caused by a misaligned assembly is handled by allowing the origin, or principal point, in the x- and y-directions on the image sensor to vary during the bundle adjustment. Radial distortion caused by imperfect lens shape is modeled and corrected by polynomials that are functions of distance from the image center, and the polynomial coefficients are varied during bundle adjustment.

Calibrations can be performed with several methods including the following: three-dimensional reference object (or two-dimensional reference object with known linear translation in the out-of-plane direction), two-dimensional reference objects at scattered orientations, one-dimensional line calibration, or self-calibration[78]. The highest accuracy is achieved with a three-dimensional reference object or precisely translated two-dimensional object which has been the conventional approach for camera calibration and might associated with the world-reference technique of Tsai[78]. A newer technique which is often associated with the planar auto-calibration technique of Zhang[78] forgoes three-dimensional reference objects for two-dimensional ones because of the lower cost, ease of use, and still acceptable accuracy of the two-dimensional method[79].

The setup of the Stability Wind Tunnel suggests either of the world-reference method or the planar auto-calibration method are possible scenarios by which a camera system might be calibrated. First, a calibration following the world-reference method is possible given a calibration pattern is projected onto the Kevlar wall and some additional surface perpen-

dicular to the wall. Second, a calibration following the planar auto-calibration method is possible given a two-dimensional calibration plate that is moved around the Kevlar with various orientations in all six degrees of freedom. The benefits of the first appear to be the potential for higher accuracy and better out-of-plane coverage given a well-engineered setup with a calibrated projector. The benefits of the second appear to be a simpler setup with still comparable accuracy. A direct comparison of the accuracy of the two methods is considered in Sun and Cooperstock[79]. While the world-reference method using a projected pattern produced higher accuracy, it was noted that the calibration objects used for the planar auto-calibration method are significantly simpler than those used for the world-reference method and can be made to a high accuracy. For instance, a laser-printed checkerboard pattern might have a standard deviation of noise less than 0.5-mm which would require considerable cost to achieve with the world-reference method. Considering the availability of calibration plates and the current lack of hardware in the Stability Wind Tunnel to execute an accurate world-reference based approach, the planar auto-calibration is pursued in this work.

Some details are here given related to the best-practices for the planar auto-calibration technique. Zhang[80] varied the number of calibration images from 2 to 16, finding a significant decrease in calibration error moving from 2 to 3 images and a leveling of the error by 16 images. The orientation of the calibration plate in the images seems to be optimal at an angle of around 45-degrees to the image plane although it was noted that this may decrease marker-finding accuracy due to foreshortening. In addition to collecting a significant number of such tilted orientations to aid the out-of-plane resolution, there should be some orientations that are perpendicular to the optical axes of the cameras to generate good in-plane resolution[76].

The primary calibration plate used in this study is shown in Figure 3.15. It consists of a grid of 46 by 22 dots of diameter 22-mm with 49-mm center-to-center spacing for a total size of 2.3- by 1.1-m. The grid pattern is printed on a plotter and spray-glued to a foam board. The flatness of the foam board was a mild concern, however, the accuracy of the calibrations was sufficient. An alternate calibration plate was used for one of the four stereo-pairings and consisted of a grid of 41 by 23 dots of diameter 19-mm with 19-mm spacing for a total size of 0.8- by 0.4-m. A total of 5 or 6 images were used to calibrate each stereo pair of cameras, and the different orientations of the plate were in general agreement with the guidelines of Zhang noted above. For each stereo pair, the orientations of the calibration plate were varied from perpendicular to the optical axis of one of the cameras to $\sim$20 degrees off-axis. The plate was translated across the FOV over the sequence of 5 to 6 images.

DaVis 8.2.3 software from LaVision is used to perform a bundle adjustment calibration of the type planar auto-calibration using the pinhole fitting model. Some details of the results are here presented as averages over the eight camera calibrations. For de-centering distortion, the mean deviation of the principal point from nominal was 2-pixels in the direction of the longer sensor side and 14-pixels in the direction of the shorter sensor side. Pixel aspect ratio was optimized but was unity to within 4 significant digits. Radial distortion terms up to the second-order were included in the optimization with an average first-order value of 2.2-pixels

and an average second-order value of 0.3-pixels. A metric for the accuracy of a particular calibration is the average deviations of the de-warped pixel positions which should be less than 2-pixels and ideally lower than 0.3-pixels for an excellent calibration[81]. The values achieved in the current study averaged 1.2-pixels.

3.1.7.3 Feature-Matching

Feature-matching in DIC involves dividing a reference image into a number of windows, representing the transformation between the reference and deformed images by a shape function, and optimizing the shape function parameters until the correlation coefficient is minimized between the original and deformed images[82]. After completing the first optimization, the window is displaced by a step size of a specified number of pixels in the reference image, and the process is repeated again and again. The final result is a grid of displacement and strain data where each data point is an average of the displacement/strain components within its window. To give a ballpark indication of the sub-pixel accuracy available from feature-matching, Reu[83] calculates a matching error of ± 0.03-pixels and the software producer LaVision[81] estimates ± 0.05-pixels. As will be discussed throughout this section, the sub-pixel accuracy of feature-matching, and thus the accuracy of the final displacement and strain data to be discussed in the following section, is affected by the window size, image resolution, speckle size, shape function, interpolation function for sub-pixel correlation, optimization algorithm, and definition of the correlation coefficient[82]. This section includes comments on the selection of the first five of the above parameters for the present study, the last two being internal to the DaVis software. It is noted that the discussion in this section centers around feature-matching which is a technique that is equally applicable to both 2D- and 3D-DIC. The difference for 3D-DIC, as used in this study, is that the images to be correlated come from different cameras. After the correlation, the calculation proceeds by triangulating the three component location of each matched window for a sequence of deformation images from which displacement and strain are then available[73].

Bornert *et al.*[82] identify two error regimes related to feature-matching. The first is the *mismatch* error regime which is due to the inability of a low-order shape function to match the actual displacement field in high gradient situations. If window size is decreased, strains are reduced, or higher-order shape functions are used, the second error regime appears which is the *ultimate* error regime. In the ultimate error regime, where appropriate interpolation functions are critical, error decreases with larger window size due to a larger sample size of speckles available to use in the correlation process and thus corresponding increase in statistical accuracy. For 3D-DIC, it is recommended to use higher-order (such as second-order) shape functions along with large windows to handle perspective differences in views of the same window from different angles, and so the ultimate error regime becomes the primary concern for 3D-DIC. In this study, shape functions are taken to be second-order polynomials rather than first-order which, though increasing computational cost by two to three times, yields a 10% accuracy gain[81]. As recommended, the window size selected,

61-pixels by 61-pixels, is relatively large and leans towards higher accuracy at the cost of spatial resolution.

The ultimate error regime is also dependent on the sub-pixel interpolation functions. Sutton *et al.*[76] detail the means of obtaining sub-pixel accuracy in matching algorithms via interpolating gray values of images to a finer grid than the original pixel grid. In order to keep the error in the differentiated strain values reasonable, appropriate interpolation functions are necessary to minimize bias in these sub-pixel correlations, a bias that results from phase error of the interpolation functions as well as intensity noise. The phase error, which originates from representing a complex pixel signal by a polynomial interpolation function, is non-zero everywhere except at the pixel locations and halfway in-between those locations which generates a characteristic S-shaped bias curve[73]. Among typically used functions, the cubic B-splines are recommended over cubic polynomials[76] while other authors recommend the quintic B-spline[82]. For the present experiments, the interpolation functions are selected as sixth-order splines, the higher accuracy option of the two offered in the DaVis software. It should be noted that bias is also introduced from the interpolation functions when intensity noise is present since the interpolation functions act as low-pass filters for the noise. As intensity noise is always present in photogrammetry and especially with cameras using CMOS sensors, efforts should be made to reduce intensity noise as discussed in Section 3.1.7.1.

Sutton *et al.* also give a detailed statistical analysis of the bias due to both the above mentioned phase error and the intensity noise, as well as the derivation of variance introduced by the intensity noise. Both the bias terms and the variance term are inversely proportional to the sum of the squares of the gradients in the image pattern. This leads to optimum speckle patterns of high contrast and small correlation length though not too small to prevent aliasing[73, 76]. Grediac and Hild[73] recommend a speckle diameter of 4- to 10-pixels, and Sutton *et al.*[76] states that speckles should occupy at least 3- by 3-pixels on the sensor with each window nominally containing a block of 3- by 3-speckles. In the present experiments, the smallest speckles in the FOV occupy approximately 3- by 3-pixels on the sensor, as suggested. The window size of 61-pixels by 61-pixels contains over 100 speckles, a large number which increases accuracy at the cost of spatial resolution. In addition to the speckle requirements, using cameras with relatively large dynamic range such as 10-bit or higher quantization (and utilizing this dynamic range via proper illumination) increases the image contrast which again reduces both bias and variance of the feature-matching process[76]. The cameras used presently have 14-bit dynamic range.

Not mentioned in the previous paragraph is another user-controlled parameter which is the step size, or the pixel distance between one reference window to the next. In terms of strain calculations, larger step sizes do, in fact, result in higher precision because of an effectively larger gauge length which comes at the cost of lower spatial resolution[73, 81]. However, in this study strains are calculated from the derivatives of displacement data that have been projected onto basis functions with large length scales, thus reducing local fluctuation of strain values in a similar way as a large gauge length might do. Unlike the strain field,

it is important to note that the balance between accuracy and spatial resolution of the displacement field is *not* affected by the step size but only by the window size[73].

3.1.7.4 Displacement Uncertainty

The previous two sections have described the steps necessary to reduce calibration error and feature-matching error. Of course, errors will never be completely eliminated, and we now turn our attention to evaluate the uncertainty in the final measured displacements from the 3D-DIC system. Error in the final measurement due to the camera calibrations, though not quantified here, was controlled by following the above-mentioned guidelines. Feature-matching error, approximated here by ± 0.05-pixels as noted in the previous section, will propagate into error in the three-dimensional displacement components via so-called *quantization error*[83]. Quantization error can be predicted to some degree with models and will be discussed below.

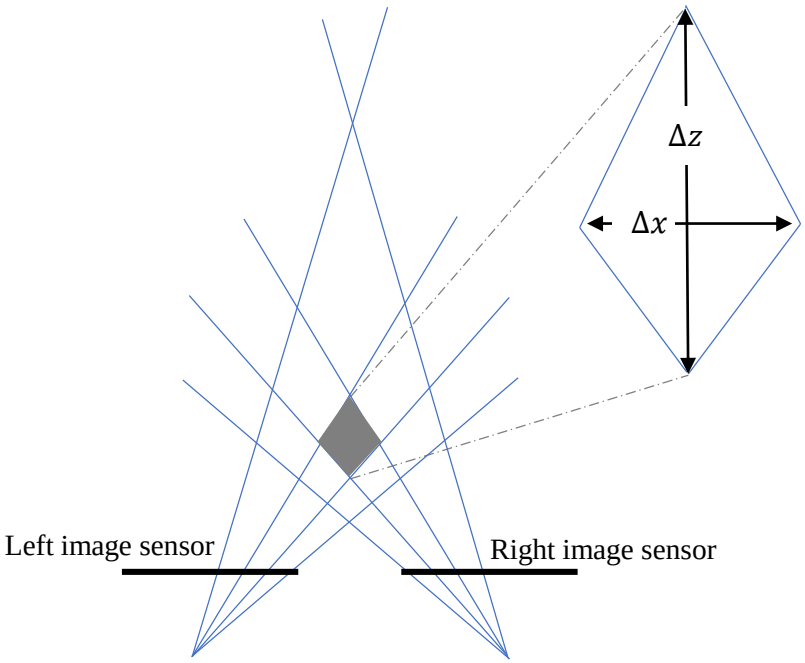

Figure 3.16: Two-dimensional depiction of quantization uncertainty in stereo camera systems. Δx is the in-plane uncertainty and Δz is the out-of-plane uncertainty. Figured reproduced from Matthies and Shafer[84].

The cause for quantization error fundamentally is that the image sensor is composed of discrete pixels which, as shown in two-dimensions in Figure 3.16, limits the accuracy with which the three-dimensional coordinates of a point in space can be known. In practice, the discretization is significantly finer than the pixel width due to the sub-pixel feature-matching accuracy of well executed DIC measurements. Each of the quadrilaterals formed by the intersecting lines in Figure 3.16 indicates the uncertainty in the triangulation calculation at the given location due to the uncertainty in the true position of the feature of interest on the camera sensors. The shape of the quadrilateral uncertainty bounds are square-like at locations close to

the cameras but become skewed as the distance from the cameras increases.

Mathematically, the situation in Figure 3.16 is illustrated by Equation 3.4

$$\Delta z = \frac{z^2}{fB + z\Delta d}\Delta d \approx \frac{z^2}{fB}\Delta d \tag{3.4}$$

where Δz is the depth resolution, z is the depth to the measurement plane, B is the baseline separation of the optical axes, f is the focal length of the cameras, Δd is the size of one pixel element on the image sensor (or the sub-pixel size achievable by the matching algorithm), and the approximation is made due to the typically small magnitude of $z\Delta d$ compared to fB[74]. Note that the values z, B, and f are illustrated in Figure 3.14. Stochastic versions of Equation 3.4 are available, as well[74, 84]. Design of the stereoscopic systems are made in light of Equation 3.4, as a tradeoff exists between the variables z, B, f, and the correlated field of view of the two cameras. Spacing the cameras close to the measurement plane (small z), at high magnification (large f), and far apart from one another (large B) all lower Δz in as given in Equation 3.4 and Figure 3.16. Similar relationships as Equation 3.4 can be developed for the in-plane resolutions, and these are generally smaller than the out-of-plane resolutions[74]. This situation can be observed in Figure 3.16 where Δz is greater than Δx. The relative magnitude of the in-plane and out-of-plane resolutions will be compared further below.

Equation 3.4 is strictly valid for so-called *canonical* camera systems where the optical axes of the two cameras are parallel. A *convergent* system with non-parallel optical axes was adopted for the present work. For convergent systems, the accuracy is further affected by the pan, or stereo, angle between the optical axes of the two cameras. As the stereo angle increases, the shape of the quadrilaterals in Figure 3.16 become less skewed towards the out-of-plane direction. In most 3D-DIC applications, it is desirable to keep the quadrilaterals somewhat skewed because in-plane strain measurements are much more strongly affected by noise than out-of-plane strain measurements[76]. Thus,

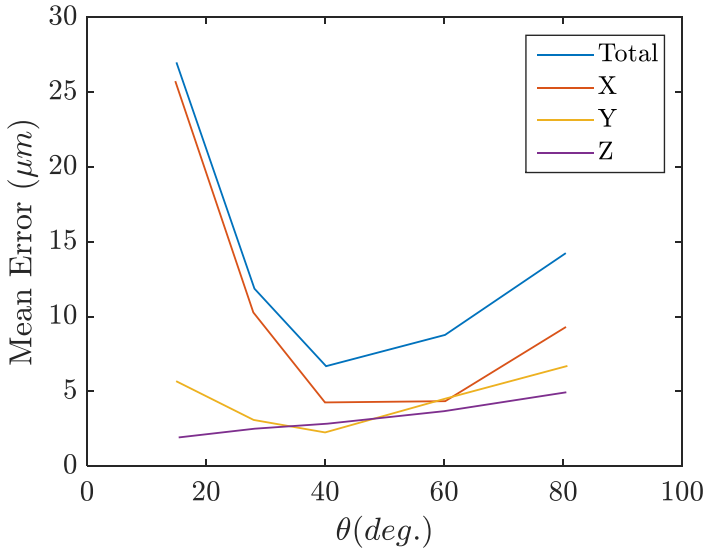

Figure 3.17: Effect of stereo angle, θ, on accuracy of displacement data according to experiments by Luo *et al.*[77]. Tilt and swing angles were near zero.

Sutton *et al.*[76] recommend a stereo angle of 10- to 30-degrees to balance in-plane and out-of-plane sensitivity, as well as to prevent large perspective differences between images which hinders feature-matching. However, the authors also note that when the $\frac{1}{2}(\frac{\partial w}{\partial x})^2$ and $\frac{1}{2}(\frac{\partial w}{\partial y})^2$ terms of Equations 2.54 and 2.55 become significant as is the case with Kevlar-wall deflection, it is acceptable to increase the stereo angle up to 60-degrees even though it reduces the accuracy of the in-plane measurements. Such a claim is substantiated by the experimental findings of Luo *et al.*[77] as reproduced in Figure 3.17. Here, the out-of-plane error, as well as total error, are minimized between a stereo angle of 40- to 60-degrees. The divergence of the out-of-plane error at low stereo angles is an artifact of the experimental design but has some application to the present measurements. As Luo *et al.* decreased the stereo angle, the baseline separation was decreased while the depth increased, these changes being made to keep the object in the FOV and to improve camera focus. The increase in depth causes the mean error to diverge since z is raised to the second power in Equation 3.4. In practice, for a given FOV, the optimal configuration is usually a convergent one with stereo angles between 40- and 60-degrees appearing ideal for applications with high out-of-plane strain. Such information explains in part the experimental setup shown in Figure 3.14 which has a stereo angle of 42 degrees.

Using the experimental setup shown in Figure 3.14, $\Delta z = 28\text{-}\mu m$ according to Equation 3.4 for a feature-matching accuracy of ± 0.05-pixels. As noted, this equation is not strictly valid in light of a non-zero stereo angle and, in practice, the uncertainties were slightly larger. Uncertainty estimates were derived from measurements of a rigid speckle pattern affixed to a translation stage with 10-μm resolution. The measurements were performed concurrently to the wind tunnel tests using the setup as defined by Figure 3.14. The in-plane uncertainty was estimated at $\pm 40\text{-}\mu m$ for 20:1 odds, and the out-of-plane uncertainty to be $\pm 60\text{-}\mu m$. The variance of the uncertainty is much larger than the bias as is typical in DIC applications[73]. Each new deformation image during an angle of attack sweep was calculated relative to the undeformed state, an option that was utilized in the DaVis software so that errors would not stack up across sequential angle of attack measurements[81].

Through the best-practice techniques discussed, the displacement uncertainty is minimized to as great an extent as possible. An additional source of uncertainty that was not accounted for in the uncertainty estimates just described is due to deformation of the pressurized anechoic chambers during testing. This uncertainty turned out to be significant for some cases, especially those tests involving high dynamic pressures. Further remarks on this error will be made in Chapter 7.

3.1.8 Experimental Campaigns

To provide the foundation for the developments of this study, data from the 0.91-m NACA0012 model presented in Section 3.1.3 were measured during three test campaigns including two in the Kevlar-wall test section and one in the solid-wall test section at the Stability Wind Tun-

nel. While the model and experimental setup remained generally unchanged between test campaigns, some differences such as Kevlar type, nominal Kevlar pre-tension, and leakage area between the anechoic chambers are present. The test conditions for each test campaign with the NACA0012 are given in Table 3.2. The table lists different fabric types which refer to the designations given in Section 4.1. The nominal Kevlar pre-tension, T_0, is reported which derives from measurements with a hand-held tension meter where the reported tensions represent an average value for each wall. The leakage area, A_{leak}, represents the effective size of the opening between anechoic chambers that would exist if all the leakage openings were aggregated. This measurement was performed by first sealing the Kevlar walls and chamber so that only leakage through the volumes of space above and below the test section could occur. Applying a pressure difference to the chamber with a blower and measuring the volumetric flow rate through the blower then yields the effective leakage area. The A_{leak} values reported are the average of the individual tests on both anechoic chambers.

Specific to each test campaign, Table 3.3 catalogs each of the runs with the NACA0012. Each of the rows in Table 3.3 corresponds to an angle of attack sweep. Typical angle of attack sweeps range from -18 degrees to 18 degrees. For the data in Runs 3-1 to 3-6, the angle of attack sweep was performed in reverse from 18 degrees back down to -18 degrees. This detail is noted because the data is reported such that the hatch in the model as described in Section 3.1.3 was always on the suction side at positive angles of attack. For Run 3-3, only angles up to $\pm$ 12 degrees were attained. In Table 3.3, the condition of the model is reported as either untripped or tripped, the latter corresponding to using the trip tape from Section 3.1.3 at 5% chord on both the pressure and suction sides. The flow conditions in the table are indicated by the freestream dynamic pressure, Q_∞, the Reynolds number, Re, and the Mach number, Ma. The airfoil C_p column indicates if pressure data from the model's midspan pressure taps were recorded. The wake C_p column indicates if the wake rake described in Section 3.1.5 was used to collect pressures downstream of the model. The wall C_p column indicates if wall pressure taps such as described in Section 3.1.6 were used to collect pressure data. The wall displacement column indicates if the camera system described in Section 3.1.7 was used to collect wall deformation data. For all measurements in Campaigns 2 and 3, the pressures in the anechoic chambers were measured throughout the angle of attack sweeps. Raw data from each angle of attack sweep listed in Table 3.3 are presented in Appendix C including global aerodynamic coefficients, airfoil pressure coefficients, wall pressure coefficients, and wall deformations, if applicable. Chapter 5 will include comparisons of data between Campaigns 1, 2, and 3, and Chapter 7 will additionally employ Campaign 3's data.

Table 3.2: Test conditions for different experimental campaigns on the NACA0012.

Campaign	Test Section	Year	Kevlar	T_0 (N/m)	A_{leak} (m^2)
1	Solid-wall	2013	N/A	N/A	N/A
2	Kevlar-wall	2013	Fabric A	1500∗	0.15
3	Kevlar-wall	2016	Fabric B, speckled	1600 (port), 2100 (star)	0.18

∗ value represents a target value from the tensioning process that occurred when the Kevlar was first installed

Table 3.3: Test conditions for reference NACA0012 data.

Campaign-Run	Condition	Q_∞ (Pa)	Re	Ma	Airfoil C_p	Wake C_p	Wall C_p	Wall Disp.
1-1	Untripped	6.61E2	2.0E6	1.0E-1	Yes	Yes	No	N/A
1-2	Tripped	6.55E2	2.0E6	1.0E-1	Yes	Yes	No	N/A
1-3	Untripped	2.79E3	3.9E6	2.1E-1	Yes	No	No	N/A
1-4	Tripped	2.77E3	3.9E6	2.1E-1	Yes	No	No	N/A
2-1	Untripped	6.23E2	2.0E6	9.6E-2	Yes	Yes	Yes	No
2-2	Tripped	6.08E2	2.0E6	9.5E-2	Yes	Yes	Yes	Prelim.∗
2-3	Untripped	2.45E3	3.9E6	1.9E-1	Yes	No	Yes	Prelim.∗
2-4	Tripped	2.40E3	3.9E6	1.9E-1	Yes	No	Yes	No
3-1	Untripped	7.43E2	2.0E6	1.1E-1	Yes	No	Yes	Yes
3-2	Tripped	6.59E2	2.0E6	1.0E-1	Yes	No	Yes	Yes
3-3	Untripped	3.11E3	3.8E6	2.3E-1	Yes	No	Yes	Yes
3-4 †								
3-5 ‡	Untripped	1.63E3	3.0E6	1.6E-1	Yes	No	Yes	Yes
3-6 ‡	Tripped	1.54E3	3.0E6	1.5E-1	Yes	No	Yes	Yes

∗ wall displacements measured with a preliminary version of the setup and processing described in Section 3.1.7 which had lower spatial resolution than the final arrangement
† there was no data taken in Campaign 3 to correspond to Runs 1-4 and 2-4
‡ there was no data taken in Campaigns 1 or 2 to correspond to Runs 3-5 and 3-6

3.2 Supporting Facility: 2.0-m by 2.0-m Low Speed Wind Tunnel

The current study also utilizes measurements taken at the the Japanese Aerospace Exploration Agency's 2m-by-2m Low Speed Wind Tunnel shown in Figure 3.19. This facility is a continuous, single return, subsonic wind tunnel with 4-m long removable rectangular test section of square cross section 2-m on edge. The maximum flow speed in the test section is about 67-m/s with a Reynolds number per meter up to roughly 4.25 million. The tunnel forms a closed loop with no air exchange tower, the only openings being in the vicinity of the test section as described below. The Low Speed Wind Tunnel has exchangeable solid-wall, Kevlar-wall, open-jet, and gust sections, the first two of which are used in the current study.

3.2.1 Solid-Wall Test Section

The solid-wall test section, shown from the inside in Figure 3.20(a), is 4-m long, 2-m wide and 2-m high at the upstream end and 2.04-m on edge at the downstream end. The area expansion is designed to compensate for boundary layer growth along the walls and eliminate any streamwise pressure gradient and associated buoyancy drag. The only opening of the tunnel circuit to the atmosphere is at the downstream end of the test section where there is a 3- to 6-cm wide gap. All other doors and potential openings around the circuit are sealed.

In the vicinity of the model, a circular turntable system in the floor sits flush with both the floor and the ceiling as shown in Figure 3.20. This 1.5-m diameter turntable provides structural support for semi-span models mounted vertically at the center of the test section. When mounted, the quarter chord position of the model is centered within $\pm$1-cm of the side walls of the tunnel and 2.0-m from the upstream end of the test section. This is the same position of the model mount in the Kevlar-wall test section. The accuracy of the zero degree angle of attack position is within 0.1 degree based on geometric reasoning after laser sheet alignment of the pressure transducers on the wing tip. The turntable system has a resolution of significantly better than 0.1 degrees, so the accuracy of the angle of attack reading is roughly 0.1 degrees relative to the zero angle of attack position.

3.2.2 Kevlar-Wall Test Section

The Kevlar-wall anechoic test section, shown in Figure 3.20, has the same dimensions as the solid-wall section. The Kevlar acoustic windows extend 3.6-m in the streamwise direction. The test section ceiling and floor also include acoustically treated panels. The floor includes a turntable system similar to that of the solid-wall test section. The tunnel circuit again vents to atmosphere through a 3- to 6-cm wide gap at the downstream end of the test section. Additionally, with the Kevlar-wall test section, two sets of symmetrically placed breather

windows on the diffuser sidewalls are opened. These were found to be necessary to eliminate a 5-Hz resonance generated in the circuit due to the added volume of the anechoic chambers.

The anechoic chambers on either side of the test section are constructed from an external cladding of sheet metal and an interior lining of acoustic foam wedges of height 0.25-m, depicted as a gray layer in Figure 3.19. The door of each chamber has rubber lining around the perimeter and heavy-duty latches to create a tight seal. Where the chamber meets the test section, a 6.5-cm foam strip runs along the chamber perimeter and 38 latch clamps are used to ensure a tight fit with the test section.

3.2.3 Wing Models

Two wings were used at the Japanese Aerospace Exploration Agency's facility: a NACA0012 and a high lift model. As described in Imamura et al. (2005), the first of these is a rectangular wing having NACA0012 profile as shown in Figure 3.21(a). The size of the model is 0.4-m in chord and 1.0-m in span, and it is made of aluminum alloy and painted glossy black. The NACA0012 profile is maintained all the way from the flat-cut tip to the root which is raised several millimeters off the tunnel floor. There is instrumentation for both static pressure taps and flush-mounted pressure transducers although these are not used in the present study.

The second model, shown in Figure 3.21(b), is a simplified high-lift wing model named OTOMO that was previously used in high-lift device noise studies at the Japanese Aerospace Exploration Agency and at Virginia Tech[5]. The model is rectangular with a nominal 0.6-m chord and 1.35-m span, equipped with a full span slat at the leading edge and a 70% span single-slotted flap at the trailing edge. The slat and flap chords are 15% and 30% of the stowed wing chords, respectively, with deflection angles of 25 degrees for the slat and 35 degrees for the flap when fully deployed in three-element landing configuration as for the current study. The total chord in landing configuration is 0.73-m which is 22% larger than the nominal chord, although the nominal chord is conventionally used when calculating normalized coefficients. A body-pod at the root has geometry of 1.65-m length and 0.4-m width formed by an elliptical cross-section. To avoid the growing boundary layer on the tunnel wall, several millimeters is left below the body-pod and above the wind tunnel floor.

3.2.4 Force Balance Measurements

Lift, drag, and pitching moment were measured with a four-component pyramid type balance located below the test section. The balance measures lift, drag, pitching moment, and rolling moment with respective ranges of the balance being +/-7000N, +/-1400N, +/-1000N-m, and +/-6500N-m. It has a rated accuracy of +/-0.2% full scale.

3.2.5 Wall Pressure Measurements

The pressure on the tunnel-side of the Kevlar walls was measured with a system similar to that described in Section 3.1.6. The pressure ports are made of custom 3D-printed rectangular prisms, 6-mm on a side and 3-mm in height and made from hard vinyl chloride plastic. A 1.6-mm diameter bore is drilled into the face to accommodate plastic tubing of the same outer diameter. A finer, 1-mm diameter hole is then drilled in the center of the larger bore and through the other side of the plastic to create a static tap. The installation process is the same as described previously by Figure 3.10. Pressures were sensed using a solid state scanner with a range of ±20 inches of water and a resolution of ±10 Pa, which corresponds to a C_p resolution of roughly ±0.005 at a freestream flow speed of 60-m/s. The 61 ports on each Kevlar wall were spaced in both the streamwise and spanwise directions with higher density in the region near the wing as shown by Figure 3.18. After pressure-testing the ports, an empty-tunnel calibration was run for all flow speeds on the test matrix. Post-processing of the wall pressure measurements subtracted the empty test section readings at the appropriate flow speed from each test case as also described in Section 3.1.6. Pressures in the sub and main anechoic chambers were measured with five tubes spaced around each chamber, but placement of the tubes had no measurable effect on the readings.

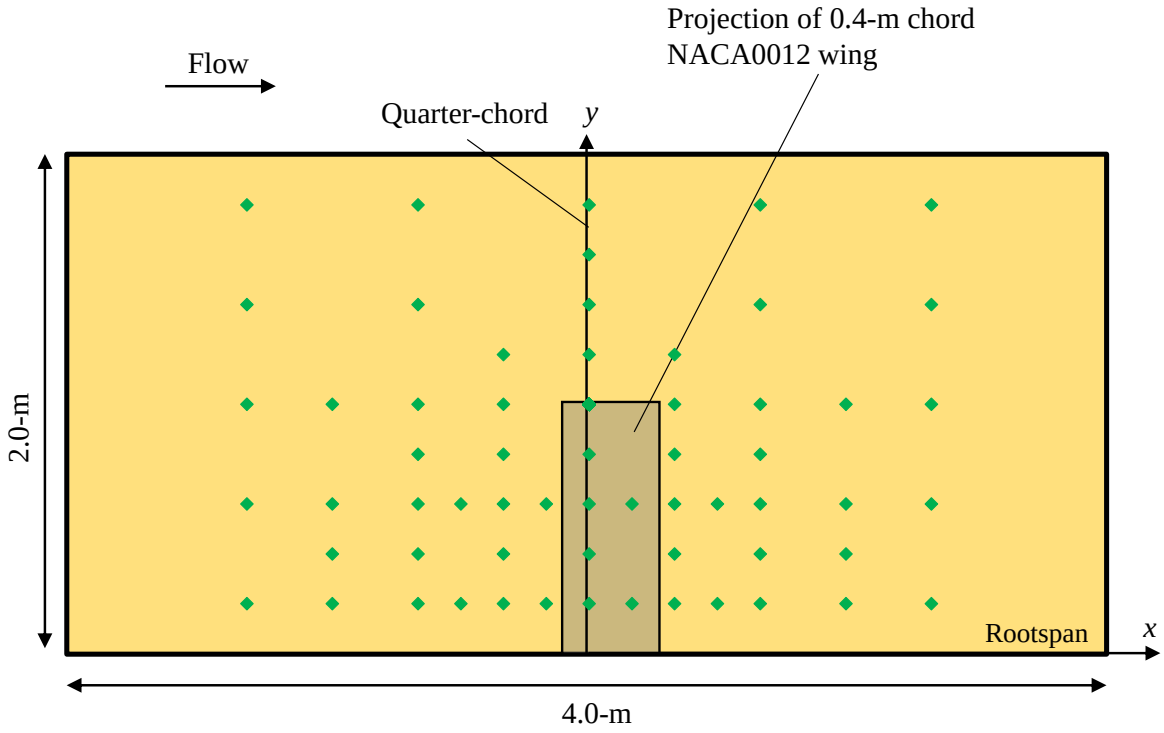

Figure 3.18: Arrangement of the pressure taps mounted on the Kevlar walls. The layout is the same for the port and starboard walls.

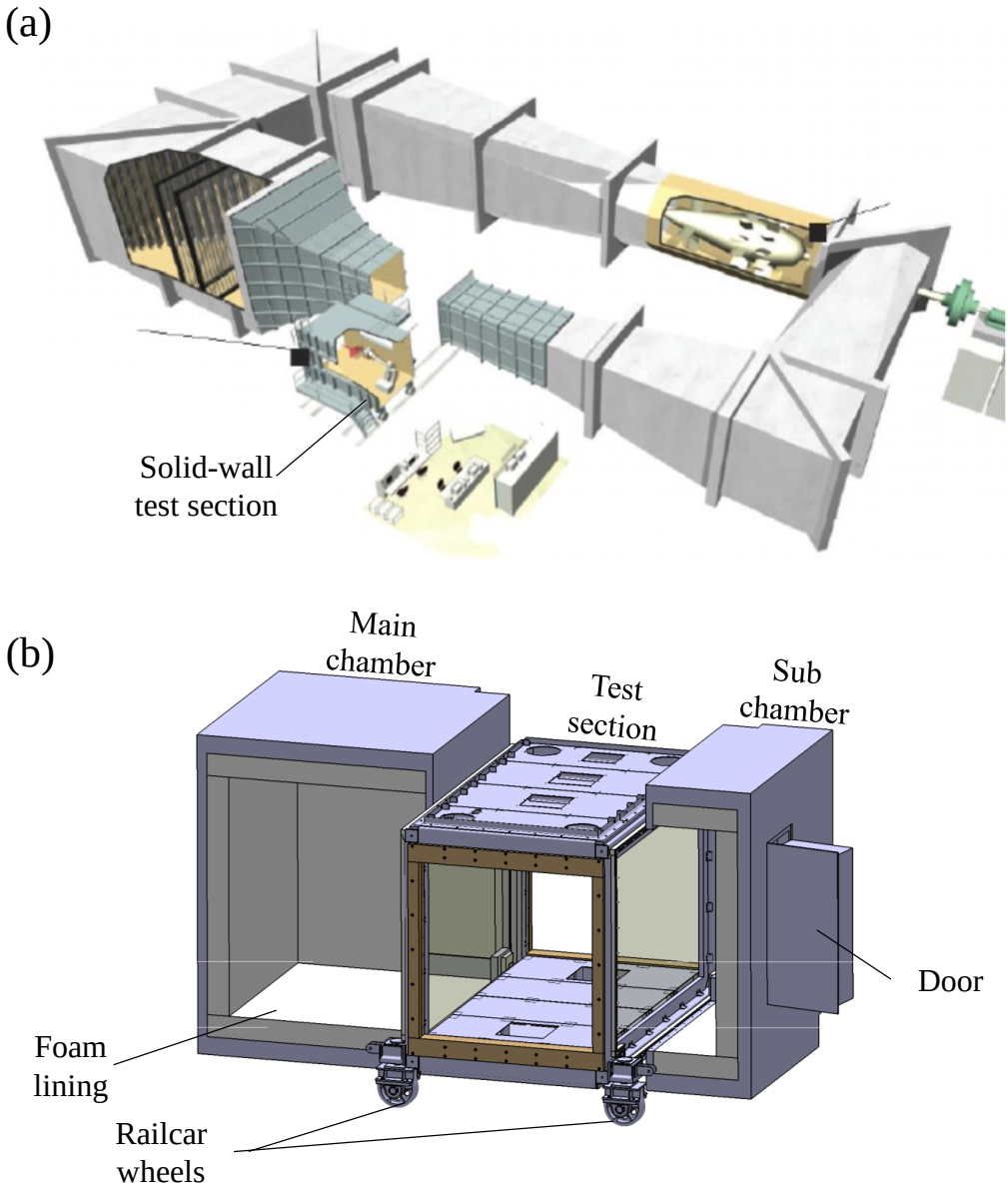

Figure 3.19: The Japan Aerospace Exploration Agency's (JAXA) 2-m by 2-m Low Speed Wind Tunnel (a) circuit shown with the solid-wall test section removed from the circuit and (b) removable Kevlar-wall test section in cross-sectional view.

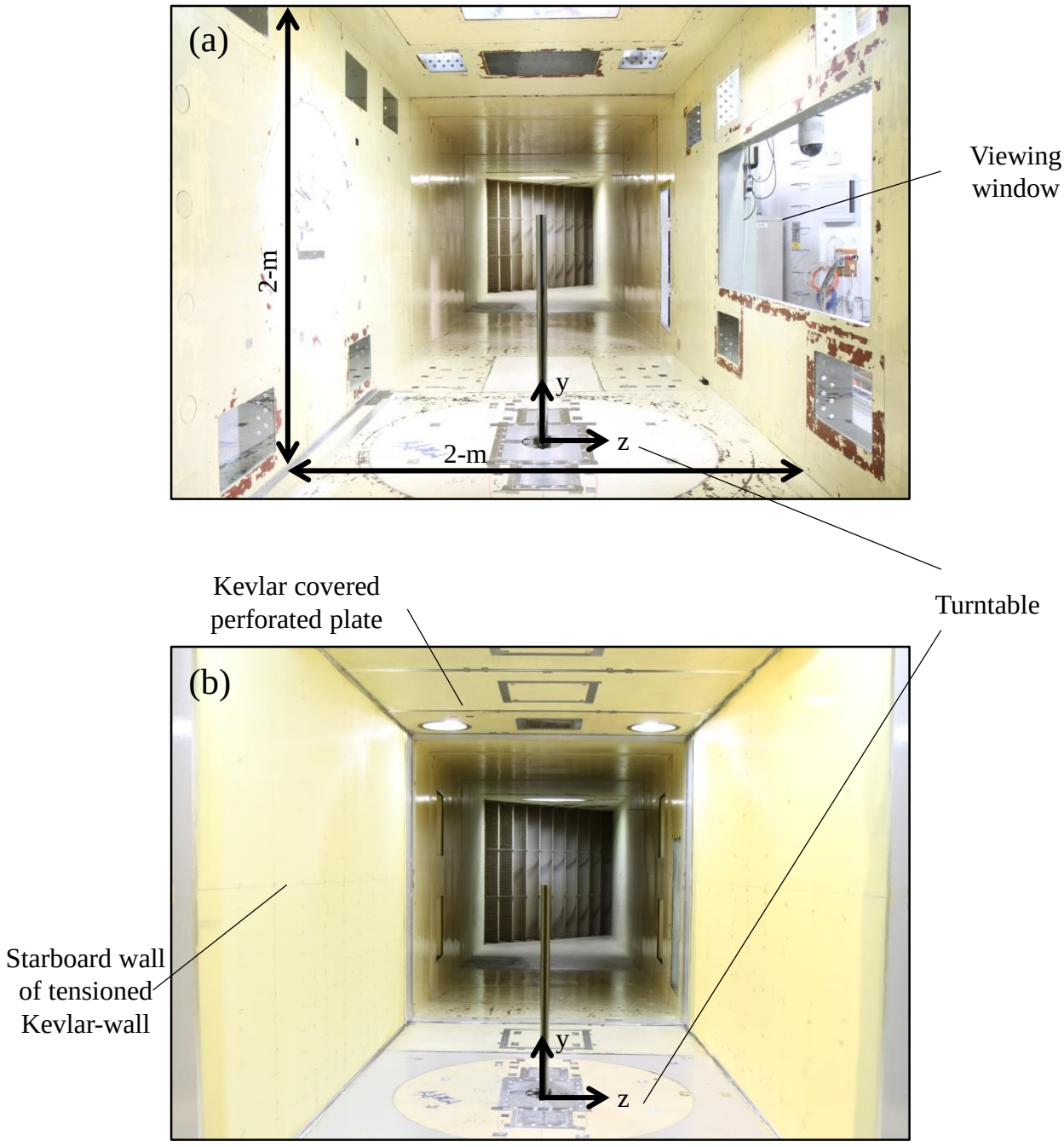

Figure 3.20: Downstream-looking view in the (a) solid-wall and (b) Kevlar-wall test sections with the semi-span NACA0012 wing installed.

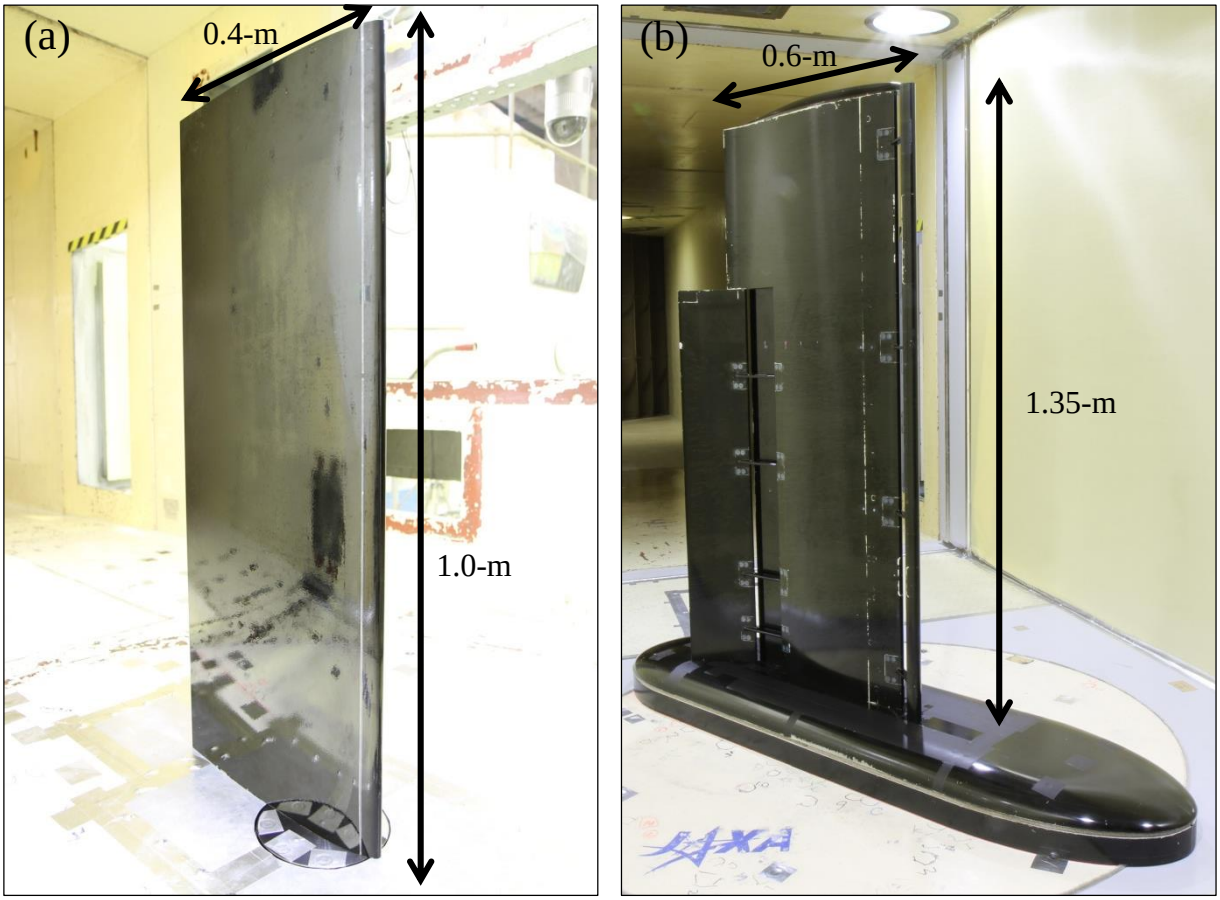

Figure 3.21: Wings tested for this study include (a) the NACA0012 and (b) the three-element OTOMO high-lift model, shown here with slat and flaps deployed for landing configuration.

Chapter 4

Mechanical and Aerodynamic Properties of Kevlar Fabric

The Kevlar fabric used on the wind tunnel walls is a point of intense focus in this study. This chapter sets the stage for the following chapters by presenting detailed characterization of the Kevlar fabric both mechanically and aerodynamically which is in fulfillment of the first objective of Thrust 1 in Chapter 2: to directly measure the fundamental sources of wall interference unique to flexible, porous-wall wind tunnels. Specifically, the wall interference associated with the flexibility of the walls is dependent on the material properties of the Kevlar which will be measured in Section 4.2, and the interference associated with the porosity is dependent on the fabric's resistance to normal flow which is described in Section 4.3.

4.1 Manufacturer-Based Variations

The plain-woven fabric is composed of military grade Kevlar 49 fibers and was selected for its characteristic of transmitting acoustic waves with relatively low attenuation[3]. Specifically, the fabric is style 120, the volume equivalent to 120 fiberglass, which is used in applications where minimum thickness and a smooth surface are critical[85]. Style 120 Kevlar consists of nominally 13.4 fibers per cm (34.0 per $in.$) at a thickness of 0.08-mm and with a dry weight of 58-g/m^2. While all the fabrics in this study have the nominal characteristics listed above, significant variation in porosity has been observed in Kevlar from different manufacturers, owing apparently to differences in the pre-treating of the Kevlar fibers.

Three of the fabrics considered in this study are displayed in Figure 4.1 where the black regions correspond to the openings which give the Kevlar its porosity. Close inspection reveals differences between the fabrics, most noticeably, that the openings between fibers are smaller in Fabric B than Fabric A. This observation has been verified quantitatively

Table 4.1: Comparison of optically measured properties of Kevlar 120 fabric from different manufacturers.

Fabric	Measured OAR	Measured yarns/cm	Vendor
A	5.9%	14	Hexcel
B	1.8%	14	EAS Fiberglass Co., LTD
B, speckled	$\sim$ 1.2%	14	EAS Fiberglass Co., LTD
C	$\sim$ 3.9%	-	-

through a simple image processing technique that discriminates the dark, porous regions of the image. Using a much larger sample size than presented here and drawing fabric from multiple locations along the manufacturer's roll, it was found that the open-area ratio (OAR) of Fabric A is 5.9% and that of Fabric B is 1.8% as shown in Table 4.1. Counting the number of yarns per centimeter reveals that this difference in porosity is due to yarn shape rather than yarn spacing, as both fabrics have approximately the same number of yarns per inch. Presumably, the Fabric B has a flatter cross-section than Fabric A though this has not been verified with measurements. Given that all Kevlar 120 is presumably controlled to have a linear mass density of 195 denier, and since Fabrics A and B have roughly equivalent yarn spacing, it is suggested that the cross-sectional area of Kevlar filaments in all Kevlar 120 weaves will be comparable, regardless of the shape of those filaments. Thus, it is assumed in this study that the material properties such as elastic modulus and Poisson's ratio of each fabric are the same.

In some of the experiments in this study, Fabric B was painted with a random speckle pattern for use with a deformation-sensing camera system to be described later. While the open-area ratio of the speckled fabric was not measured with the image processing technique, the 31% nominal coverage fraction of the speckles suggests that the open-area ratio of the speckled Fabric B will be $\sim$1.2%.

Another variation of Kevlar fabric, Fabric C, was used in tests performed at the Japanese Aerospace Exploration Agency which will be described in Chapter 6. There were fewer measurements made on this fabric, however, the image processing technique described above provided a rough estimate of the open-area ratio as shown in Table 4.1.

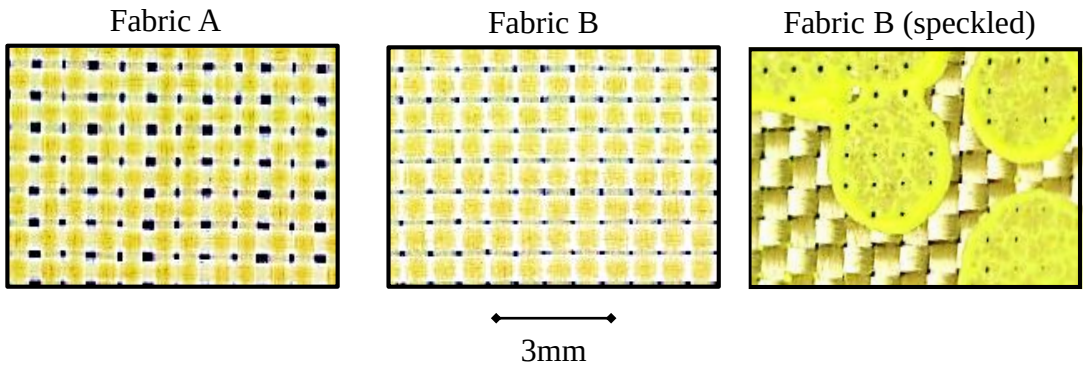

Figure 4.1: Different variations of Kevlar fabric used in this study.

4.2 Identification of Material Properties

Implied in the analysis of the remainder of this study is the knowledge of the constitutive properties of Kevlar fabric. Following on the theory of mechanical behavior of woven fabrics in Section 2.3, this section will describe the exact constitutive relations to be used. First, a review of so-called *identification methods* will be presented, followed by description of of the implementation of such a method on a Kevlar sample inflated under a uniform pressure.

4.2.1 Review of Identification Methods

Material identification is the process of inferring a small set of constitutive properties of a material based on measurements of its deformation under a known load. As the material identification problem cannot be completed by solving forward problems, it is defined as an inverse problem[73], much as the load-inferencing techniques of Chapter 7.

As discussed in Section 2.3.3, any dependence of Kevlar's constitutive properties on the bi-axial load ratio will not be explicitly delineated in this study but averaged into a single value of the elastic modulus for each orthogonal direction. In any event, it appears preferable to obtain constitutive property data from bi-axial tests rather than uni-axial tests. Static bi-axial tests can be performed several ways including: tubular inflation tests, planar bi-axial tension tests, and bulge (or inflation) tests[50]. The pre-existing structure of the Kevlar walls lends itself to testing via bulge methods, and this is the technique pursued in this study. A brief overview of the work on identification methods is given here with a tilt towards understanding the behavior of bulging membranes as a function of elastic modulus and Poisson's ratio.

Since the 1950's, the bulge test has been used to measure the constitutive properties of

thin-film membrane materials. The method for such measurements centers around analytic approximations of stress and strain at the pole of a circular bulging membrane which are functions of two measured values: the applied pressure difference across the membrane and the maximum out-of-plane deflection of the bulged membrane.

Assuming the deflection of a membrane clamped at its boundaries to have the curvature of a hemispherical cap and averaging the strain over the cap, Beams[86] gives the approximate relation between pressure difference, p, and maximum deflection, D, as in Equation 4.1

$$p = C_1 \frac{hD}{a^2}\sigma_0 + C_2 \frac{E}{1-\nu}\frac{hD^3}{a^4} \tag{4.1}$$

where C_1 and C_2 are analytically calculated constants, E is the elastic modulus, ν is Poisson's ratio, a is either the radius of a circular membrane or half-side length of a square membrane, h is the thickness of the membrane, D is the deflection of the pole, and σ_0 is a uniform pre-tension in the membrane. The cubic Equation 4.1, under certain assumptions, can be curve-fit to bulge data to yield the pre-stress, σ_0, and the bi-axial modulus, $E/(1-\nu)$ at the membrane centerpoint. Later authors have removed some of the assumptions of Beams' analysis and re-calculated Equation 4.1[87, 88, 89]. Lin[88], for instance, found that C_2 is not constant but is actually a weak function of Poisson's ratio such that $C_2 = \frac{1}{3}(7-\nu)$. Using finite elements and fitting the data to the form of Equation 4.1, it was found that C_2 is equal to $2.67(0.957 - 0.208\nu)$, $1.37(1.446 - 0.427\nu)$, and $1.33(1+\nu)^{-1}$ for circular, square, and rectangular membranes, respectively. Lin found by varying several parameters that the effect of elastic modulus, Poisson's ratio, residual stress, and thickness, at least in the case of circular membranes, is predominantly to scale the deflection profiles rather than change their shape.

The bulge test methods described previously utilize analytic knowledge of the state of stress at the membrane centerpoint in conjunction with the measured deflection at the centerpoint to arrive at an estimate for the constitutive properties. With the emergence of full-field measurement techniques for deformation, authors have been able to perform bulge test experiments where the strain field itself is measured [90, 53, 91], however, these are typically limited to the case of circular membranes due to the simplified boundary condition.

On the other hand, Kyriacou *et al.*[92], uses the technique of inverse finite element model updating[73] which is nearly identical to the technique of non-linear iterative regularization described in Section 7.1.1.2. The only difference between this technique and that described in Section 7.1.1.2 is that the unknown quantities of interest are now the constitutive properties rather than the loading. Kyriacou *et al.*, for instance, uses a Levenberg-Marquardt algorithm with multiple finite element runs to find the constitutive properties that minimize the least-squares difference between membrane displacements from the experiment and finite element simulation.

In the case of square or rectangular membranes where there are no analytic descriptions

available of the stress given full-field strain measurements, the inverse finite element model updating is the only option. Stanford *et al.*[93] use such an approach to calculate values for the elastic modulus and Poisson's ratio of a pre-tensioned rectangular membrane made of latex. A finite element analysis of the membrane wing contains inputs for the elastic modulus and Poisson's ratio. These inputs are varied until an optimal combination are found so that the deflections of the finite element model match the measured deflections. Such an approach is adopted in the present work.

4.2.2 Bulge Test Setup

In order to perform bulge test measurements without the time constraints of testing in the Stability Wind Tunnel, a reduced-scale Kevlar frame and plenum were constructed and used. The sealed plenum is of wooden construction as rendered in Figure 4.2a where the Kevlar fabric has been removed. The reduced-scale Kevlar frame is manufactured with the same internal structure as the full-scale versions used with the wind tunnel test section described in Section 3.1.2. Namely, the Kevlar is held tight into a groove by locker rods on each of the four sides. The grooves are located in rollers that can then be tightened to create pre-tension in the Kevlar. Wooden beams brace the frame along its longer dimension to reduce bowing which violates the fixed boundary condition use in the finite element solver. During testing only the three right-most beams shown in Figure 4.2a were in-place. Figure 4.2b shows the actual construction including an installed Kevlar sheet with a random speckle pattern, produced according to the description in Section 3.1.7.1.

A pressure difference across the Kevlar is produced by a Cincinnati HP-4C17 centrifugal blower which is connected to a flange mounted on the plenum by corrugated tubing of diameter 15-cm (6-in) as shown on the right of Figure 4.2b. As pressure is applied, the Kevlar sheet bulges outwards. Sealing of the fabric region is accomplished with 1- to 2-mm thick, impermeable plastic sheeting which blankets the Kevlar from inside the plenum and clings to the fabric when the system is pressurized. Pressures inside the plenum are measured from pressure taps with Tygon tubing that leads to the Esterline scanner unit described in Section 3.1.4 with a range of ± 10 inches of water.

Pre-tension measurements at 77 locations spread over the Kevlar surface were performed prior to testing with a Newman ST-Meter 2E tension meter. These measurements indicated mean pre-tensions of 1,523-N/m and 1,349-N/m in the x- and y-directions, respectively. However, the Kevlar lost significant tension either before or during the test which could be attributed to slippage of the Kevlar from the locking grooves. The loss of tension invalidated the tension meter measurements, and while no further measurements were made, the tension was estimated to be close to 500-N/m after the test. The implications of this approximation will be noted in the next section.

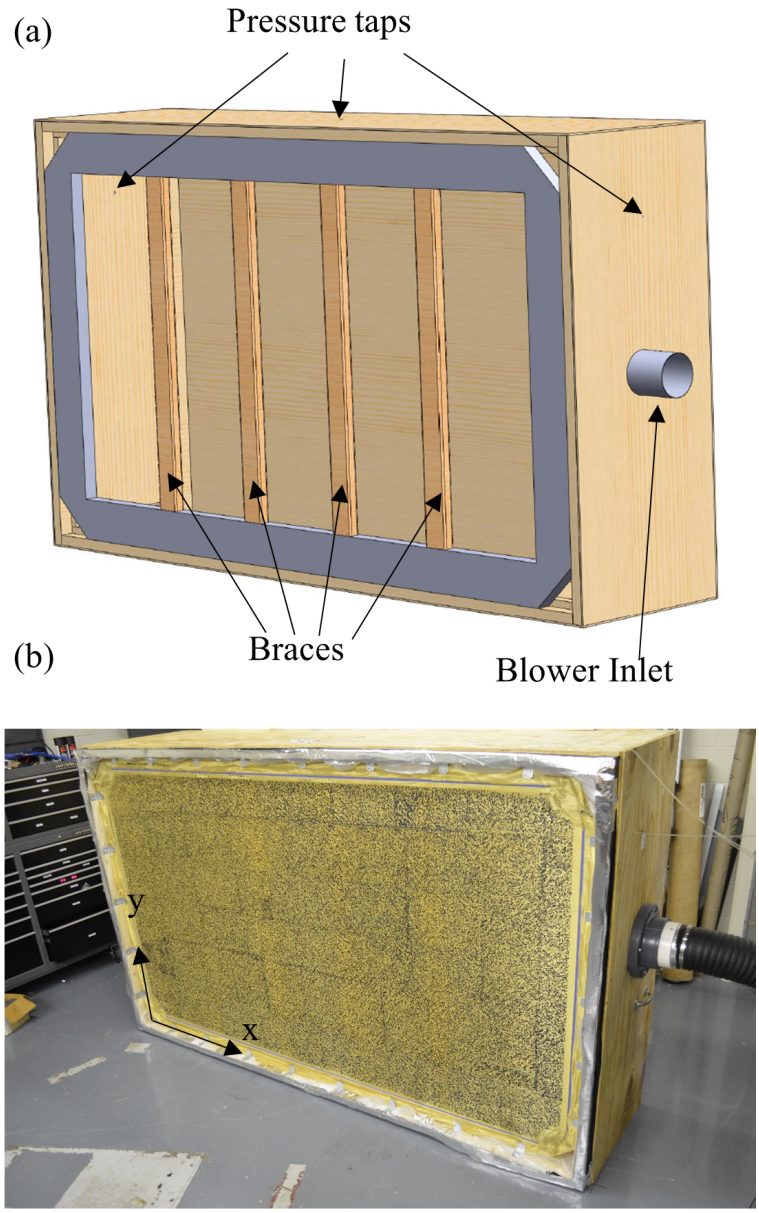

Figure 4.2: Reduced-scale plenum and Kevlar frame for preliminary bulge tests including (a) a rendering without a Kevlar sheet and (b) a photograph of the actual construction with a speckled Kevlar sheet.

4.2.3 Bulge Test Measurements

Following the previously described work of authors such as Kyriacou *et al.*[92] and Stanford *et al.*[93], a finite element simulation is used in conjunction with an experimental bulge test to infer the constitutive properties of the Kevlar in bi-axial tension. The Kevlar used for the bulge test measurements is the Fabric B described in Section 4.1. Although the open-area ratio of Fabric A and B are different, the nominal fiber counts per yarn are identical, so it is believed that the mechanical properties of the two fabrics should be comparable.

Appendix E contains descriptions of the finite element formulation, convergence studies, and verification. As discussed in the appendix, temperature loading is used to impose pre-tension on the membrane such that a uniform 500-N/m of pre-tension is generated in both orthogonal directions according to the post-test estimate of pre-tension. Of the four independent constitutive constants laid out in Section 2.3.2, E_x, E_y, ν_{xy}, and G, all but the shear modulus are included in the finite element updating process (G is usually three orders of magnitude smaller than the elastic moduli as described in Section 2.3.3 and is set to 0.50E6-Pa for all simulations). As seen in the equations of Section 2.3.4, the moduli terms in membrane mechanics are multiplied by the membrane thickness. For fabrics, where the thickness is often ambiguous, it is practical to quote the thickness used along with the material properties. For reference, the effective thickness used in the finite element simulations is 0.0210-mm which is calculated by dividing the bulk density by the linear density of a Kevlar 49 yarn and multiplying by the number of threads per meter[51].

The update strategy was to set E_x and E_y in order that the profile *shapes* agreed between the simulation and experiment after normalizing on the value of maximum deflection. In accordance with the observations in the previous section, the Poisson's ratio has a relatively small effect on the solution and acts primarily to scale the membrane profiles rather than change their shape. Once the correct profile shapes are obtained by adjusting E_x and E_y, Poisson's ratio allows a small degree of flexibility to scale the finite element simulation to match the experimental results.

Experimental results were measured using three-dimensional digital image correlation. The setup, processing, and accuracy specifications largely mirror those described in Section 3.1.7. Two cameras were positioned 1.7-m from the plenum wall so that the field-of-view included the entire wall. Black speckling was applied to the Kevlar with a printing block similar to the one in Figure 3.12. The wall was imaged throughout the pressure sweep from zero pressure difference to 1,359-Pa and back to zero.

Results of the reduced-scale bulge test and corresponding finite element comparison are shown in Figures 4.3 and 4.4 for the case of the maximum pressure loading of 1,359-Pa. The constitutive properties used to obtain this result are: E_x = 1.33E10-Pa, E_y = 3.12E10-Pa, and ν_{xy} = 0.40 where the subscripts correspond to the coordinate system of Figure 4.2b. Calculating ν_{yx} from the above values yields 0.93. Averaging these results across the two orthogonal directions yields E_{avg} = 2.23E10-Pa and ν_{avg} = 0.67. In comparison, the biaxial

modulus calculated with the analytic method of Lin[88] is 9.21E10-Pa which equates to E_{avg} = 3.09E10-Pa using $\nu = 0.67$.

As expected, the modulus in the x-direction is smaller than that in the y-direction since the x-direction corresponds to the warp direction. As reported in Table 2.2, the warp direction of fabrics typically have lower modulus in the low-strain regime than the weft direction. In earlier tests which did not include bracing of the frame, the opposite trend was observed which was due to deformation of the tensioning frame under loading; bowing of the frame caused exaggerated out-of-plane displacements compared to the displacements simulated with a completely fixed boundary condition. The bowing in earlier tests was predominantly in the y-direction, originating from the two longer sides of the tension frame since the deflection of a doubly-cantilevered beam goes in proportion to its length to the fourth power. The optimal finite element solution was therefore biased towards a lower y-direction modulus to compensate for the bowing. With the addition of braces, the bowing along the longer dimension of the frame was minimized, however, there is still the possibility that slippage of the Kevlar from the locking grooves may have caused the same effect, especially since the pre-tension was observed to fall during the course of the experiment. Therefore, the moduli reported above may be slightly understated for the given pressure difference, if anything.

Regarding the non-linear nature of the Kevlar material properties as described in Section 2.3.3, the finite element simulation was run again with a reduced pressure loading of 473-Pa but using the same constitutive properties derived from the higher loading case. The result indicates a 5% smaller out-of-plane deformation at the Kevlar center-point for the simulation than the experiment. This is attributed to the reduction of the moduli in the actual Kevlar as strain decreases according to Figure 2.2. While a full characterization of the Kevlar modulus with strain level is ultimately desired, the approximation from the larger loading case will be used in this study. For this larger loading case, the tension at the center-point of the Kevlar under pressure loading was simulated to be 2,900- and 5,500-N/m in the x- and y-directions, respectively, which is comparable to simulated tensions in the Stability Wind Tunnel under airfoil loading. It is noted that with tensions as large as these, nonlinear tensile forces are dominating over pre-tension forces which should minimize the error incurred in the constitutive property estimates due to approximating the pre-tension as 500-N/m in the finite element simulation.

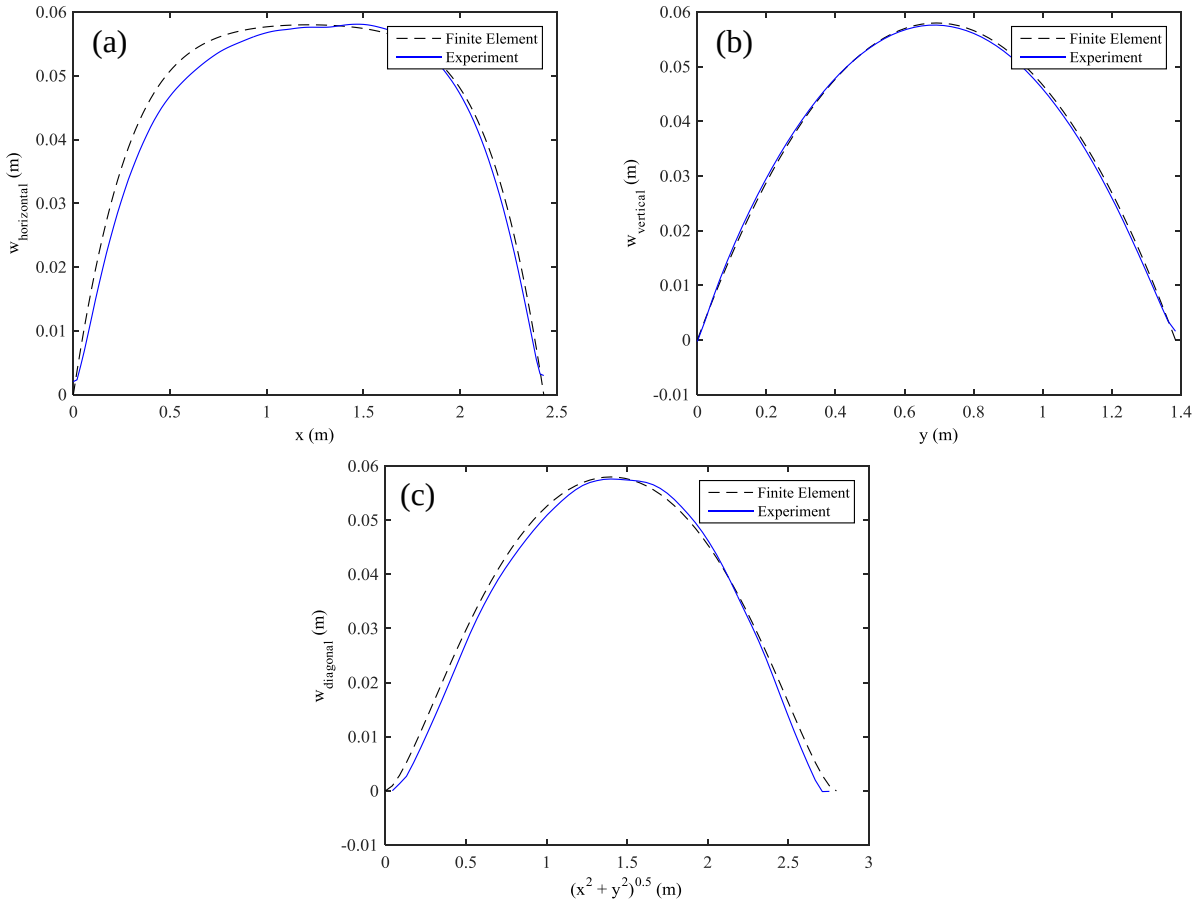

Figure 4.3: Comparison of deflection profiles between finite element simulation and experiment on a reduced-scale Kevlar wall for a pressure difference across the Kevlar of 1,359-Pa.

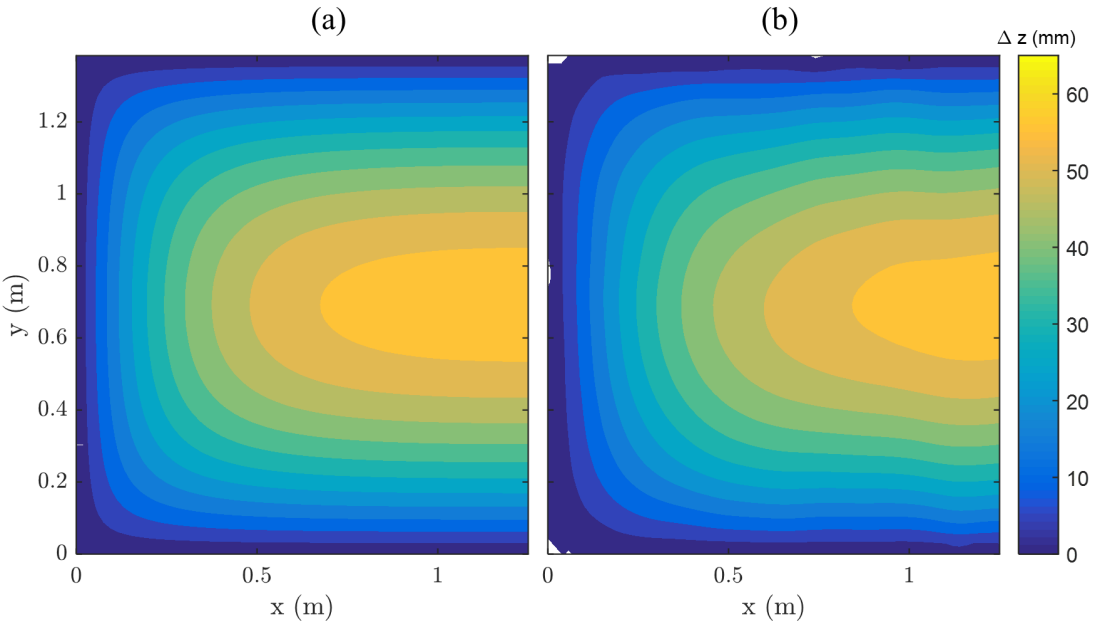

Figure 4.4: Comparison of deflection contours between (a) finite element simulation and (b) experiment on a reduced-scale Kevlar wall for a pressure difference across the Kevlar of 1,359-Pa. Wall deformations on the opposite plane of symmetry are similar to those shown here.

4.3 Characterization of Porosity

Kevlar fabric has porosity that allows for transverse flow in the presence of a pressure gradient from one side of the Kevlar to the other. This pressure-velocity relationship was presented in Devenport *et al.*[9]. Here, this relationship will be cast in a more general form.

First, it might be considered if the porosity relationship can be directly related to the optically measured porosities of Table 4.1 Indeed, the normal velocity through the Kevlar can be thought of as a function of the measured open-area ratio (OAR) assuming an inviscid-type flow through the pores. Equation 4.2 below gives this relationship and is derived from using the continuity and Bernoulli equations between a point upstream of the fabric and a point at the streamwise location of the fabric

$$v_{normal} = \sqrt{\frac{\Delta p}{\frac{1}{2}\rho(\frac{1}{(V_c OAR)^2} - 1)}} \approx \frac{V_c OAR}{\sqrt{\frac{1}{2}\rho}}\sqrt{\Delta p} \tag{4.2}$$

where V_c is the vena contracta ratio for flow through a nozzle, taken to be 0.64. The continuity equation used to derive Equation 4.2 reduces to $v_{pore} = v_{bulk}/(V_c OAR)$ where v_{bulk} is the mean velocity in the duct well upstream and downstream of the fabric. The value of k_c geometrically implied by the optically measured OAR's assuming Bernoulli behavior flow through the pores is thus

$$k_{c,inviscid} \approx \frac{V_c OAR}{\sqrt{\frac{1}{2}\rho}}. \tag{4.3}$$

Equation 4.3 predicts the k_c value given by Devenport *et al.*, for instance, as 0.0505 which is within 20% of the reported value of 0.0625. The prediction comes out too small, apparently due to uncertainty in the optical measurement of OAR, as well as uncertainty in the exact value of V_c for flow through a Kevlar fabric. Detailed flow measurements and analysis in the rest of this section will offer an accurate characterization of k_c and several other relevant porosity parameters, as well as consider the effect of tension on the porosity.

4.3.1 Normalization of Porosity Data

To put forth a general porosity relationship that is applicable under various test conditions, it is practical and necessary to normalize the porosity data on the relevant fluid properties, as noted in ASTM-D737, for instance. A related scientific goal is to find the correct similarity parameters to wholly describe the problem of flow through plain-woven fabric which will be pursued below.

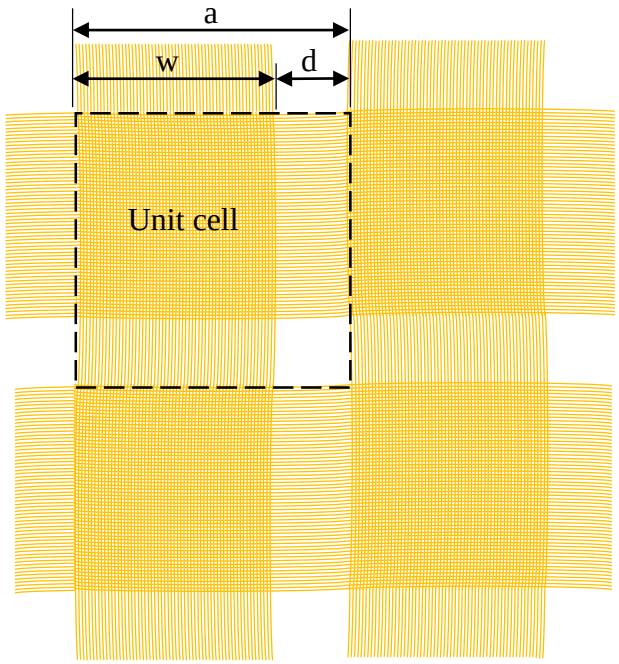

Figure 4.5: Plain-woven fabric with unit cell outlined.

Not yet considering the mechanical properties of the fabric, at least seven parameters affect the flow problem through plain-woven fabric: the local normal velocity through fabric pores, v_{pore}; the pressure drop across the fabric, Δp; the unloaded pore width of the fabric, d_0; the unloaded pore spacing of the fabric, a_0; the unloaded thickness of the fabric, h_0; the fluid density, ρ; the fluid dynamic viscosity, ν, and likely other parameters including terms to describe the cross-sectional shape and degree of crimping of the fibers. As before, $v_{pore} = v_{bulk}/(V_c OAR)$ where v_{bulk} is the mean velocity in the duct well upstream and downstream of the fabric, $V_c = 0.64$ and OAR is the optically measured open-area ratio. For the case where the fabric is covered with a speckle pattern having its own open-area ratio of $OAR_s = 0.69$, the continuity equation becomes $v_{pore} = v_{bulk}/(V_c OAR_s OAR)$. Considering a square unit cell of the fabric as will be shown later in Figure 4.5, a_0 and d_0 are related by $d_0 = a_0\sqrt{OAR}$ which is the same regardless of speckles. To reduce the number of variables, the properties of the Kevlar 120 weave are here considered to be a well controlled. Therefore, it is assumed that h is the sensibly equal between different Kevlar 120 weaves. The yarn spacing specification of 13.4 yarns/cm (34.0 yarns/in.) also suggests that x_0 will be the same among all Kevlar 120 weaves which has been verified according to the data in Table 4.1. The result is a set of five parameters of interest: v_{bulk}, Δp, d_0, ρ, ν.

There is only one choice for the non-dimensionalization of these variables, and it yields two Π-terms according to Equation 4.4

$$\Pi_1 = \frac{v_{pore} d_0}{\nu}, \quad \Pi_2 = \frac{\Delta p d_0^2}{\frac{1}{2}\rho\nu^2}. \tag{4.4}$$

The first of these terms is a Reynolds number based on the pore width and pore velocity. Hoerner[70] utilizes a similar Reynolds number based on the yarn width rather than pore width, but this was found to be not as favorable for the present case. The second term was used in Devenport *et al.*[3] where they labeled the quantity ν/d_0 as the viscous scaling velocity.

To distinguish them from the dimensional values, the porosity coefficients for the non-dimensional case will be designated by a capital K rather than a lower-case k.

4.3.2 Porosity Testing Apparatus

Industries associated with textile fabric and gas filtration perform porosity tests routinely, and as such have developed a set of standardized testing methods. The porosity testing in this study conforms in many respects to the relevant ASTM standards which are ASTM-D737 (*Standard Test Method for Air Permeability of Textile Fabrics*)[94] and ASTM- (*Standard Methods for Gas Flow Resistance Testing of Filtration Media*)[95]. In this section, the standards are referenced in comparison with the setup of the porosity test apparatus used in this study.

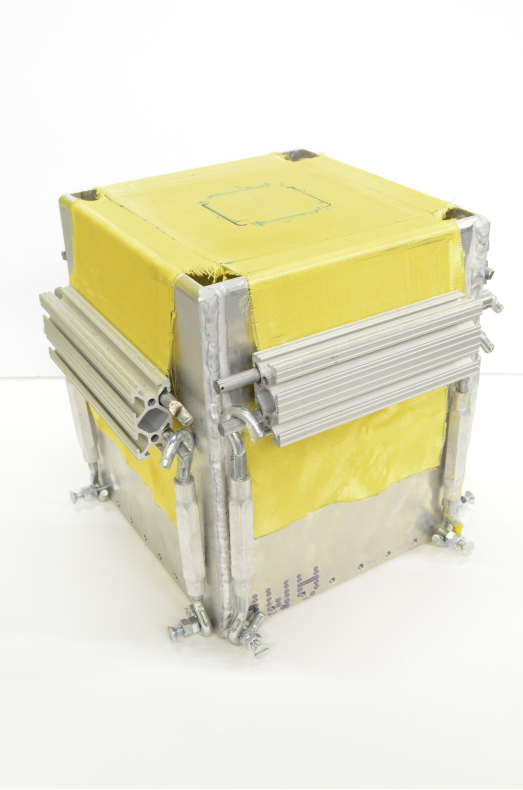

Figure 4.6: Tensioning frame for Kevlar sample.

A sample of Kevlar is stretched over a square opening, 19-cm (7.5-inches) per side, as shown in Figure 4.6. The opening has 6.4-mm (0.25-inch) fillets on the outer edges so that the Kevlar passes smoothly over the 90-degree turn and down towards the tensioning mechanism which consists of aluminum rods/slots to lock the Kevlar in place and turnbuckles to enforce tension on the Kevlar in the measurement region. The tensioning frame is mounted on top of the inlet duct of the nozzle apparatus described by Figure 4.7.

Flow normal to the Kevlar is provided by a Cincinnati HP-4C17 centrifugal blower which is used in suction configuration for the present tests and connected to the outlet end of the nozzle apparatus shown in Figure 4.8. The flow first enters a 14-cm (5.5-inch) inner diameter, aluminum inlet and travels for 17-cm (6.5-inches) before reaching the Kevlar face. Although the boundary layer development over such a small distance does not significantly diminish the static pressure from that of atmospheric, the upstream pressure at the Kevlar is still measured by one to three pressure taps 1.9-cm (3/4-inch) upstream of the Kevlar. On the downstream side of the Kevlar, the flow encounters aluminum ducting of the same internal diameter as upstream. Four pressure taps spaced 6.4-cm (2.5-inches) downstream of the Kevlar face are used to measure the pressure drop across the Kevlar. The flow then passes through a section of honeycomb into a plenum and finally through a nozzle which opens to a corrugated tube

leading to the centrifugal suction fan. The flow velocity is known based on the contraction ratio of the nozzle and pressures measured both in the plenum which is upstream of the nozzle and at the nozzle outlet. Whenever there are more than one pressure tap at a given flow station, the taps are spaced 90-degrees from each other around the circumference according to ASTM-F778 and an average reading is used in the data reduction. All pressure measurements are made with Esterline 9816-98RK pressure scanner with a range of ± 10-inches of water and accuracy of ± 0.05% full scale (which accounts for hysteresis, nonlinearity, and non-repeatability), or ± 1-Pa. Flow temperature measurements are made with an Acurite thermometer with a resolution of 0.1-degrees Fahrenheit.

The internal flow path through the porosity apparatus is described in summary by Figure 4.8 with reference to a recommended configuration of ASTM-F778. The layouts of the two apparatuses are in agreement. It is emphasized in the ASTM standard that edge leakage, defined as "air flow that passes into or bypasses the test specimen in geometric planes other than those intended for resistance measurement," must be minimized. Towards these ends, the fabric is sandwiched between two 3.2-mm (1/8-inch) thick Neoprene gaskets running the outer perimeter of the duct as recommended by ASTM-D737. The gaskets have a diameter roughly 1.6-mm (1/16-inch) greater than that of the ducting to which they are mated, and compression is supplied to the Neoprene gaskets by four threaded rods. The durometer of top gasket is A60 (medium-hard) and that of the bottom is A75 (hard). Although the durometer is harder than specified in the standard, examination of the gaskets after testing revealed the pattern of the Kevlar weave which suggests good sealing was achieved.

Figure 4.7: Construction of the in-house porosity testing apparatus.

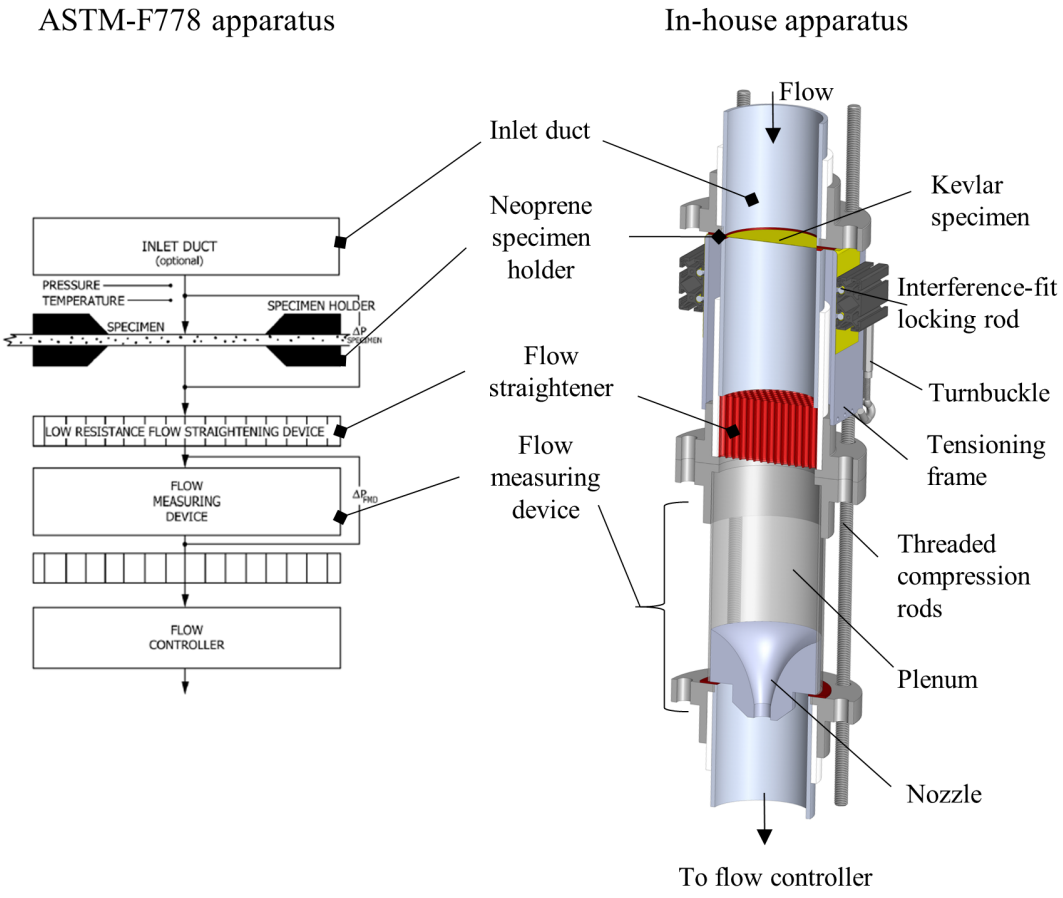

Figure 4.8: Comparison of porosity testing apparatuses from ASTM-F778[95] and the in-house design. Image reproduced with the permission of ASTM International.

4.3.3 Porosity Measurements

Using the apparatus described in Section 4.3.2, the relationship between Π_1 and Π_2 has been measured for three different variations of Kevlar fabric. These measurements were designed to replicate the findings of Devenport *et al.*[9] regarding the pressure-velocity relationship of flow through Kevlar, as well as test the robustness of the pressure-velocity relationship to fabrics with varying open-area ratios and pre-tensions. The data for each Kevlar sample is generated by sweeping the flow velocity through the porosity apparatus from low to high and then back down to low. No significant hysteresis is detectable in the tests as variations between the up- and down-sweeps are typically on the order of the uncertainty of the measurement which is ±3.7-Pa for the pressure difference. Corrections were applied to the velocity measurements to account for the pressure in the nozzle deviating from that of the ambient during a calibration run, and those corrections were in all cases less than 0.1% of the measured velocity.

Raw data and curve fits for Fabric A, Fabric B, and Fabric B with speckling at a nominal tension of 6,000-N/m are shown in Figure 4.9. Comparing the three fabrics measured in the current study, the non-dimensionalization collapses the data with a good amount of success, given its simplicity. In dimensional terms for a given pressure, the velocity of Fabrics B and B with speckles are $\approx 75\%$ and 83%, respectively, less than that of Fabric A. These differences fall to under 10% with the scaling applied. The fabric used to derive the results of Devenport *et al.* corresponds to Fabric A in the present study, and the non-dimensionalization for Devenport *et al.*'s data has been performed using the air density from the source data. The non-dimensionalized version of the relationship in Devenport *et al.* (Equation 2.45) shows $\approx 12\%$ higher K_c than found in this study. It is theorized that tighter sealing around the edges of the fabric in the present experiment minimized the edge leakage, a factor which was not strongly controlled in the original experiments of Devenport *et al.*. Additionally, the pressure range of measured data in the current study is four times greater for Fabric A than that of the source data of Devenport *et al.*. The largest absolute pressure difference for Fabric A achieved in this study was 1000-Pa. This pressure difference covers the full pressure range experienced by the Kevlar walls of the Stability Wind Tunnel for a typical model at a chord Reynolds number of 2-million. At a chord Reynolds number of 4-million, the largest pressure differences on the wall may reach up to $\approx$ 1750-Pa.

The behavior of the fabrics in Figure 4.9 can be approximated by Devenport *et al.*'s Equation 2.45; however, some updates to the equation are helpful, especially to include the non-dimensional representations of velocity and pressure difference described in Section 4.3.1. The curve fits shown in Figure 4.9 are made according to Equation 4.5

$$\Pi_1 = K_c(\Pi_2)^{K_n}\left(\frac{\Pi_1^4}{\Pi_1^4 + K_p}\right)^{1-K_n} \tag{4.5}$$

where K_c, K_n, and K_p are non-dimensional values specific to each fabric. The value K_c,

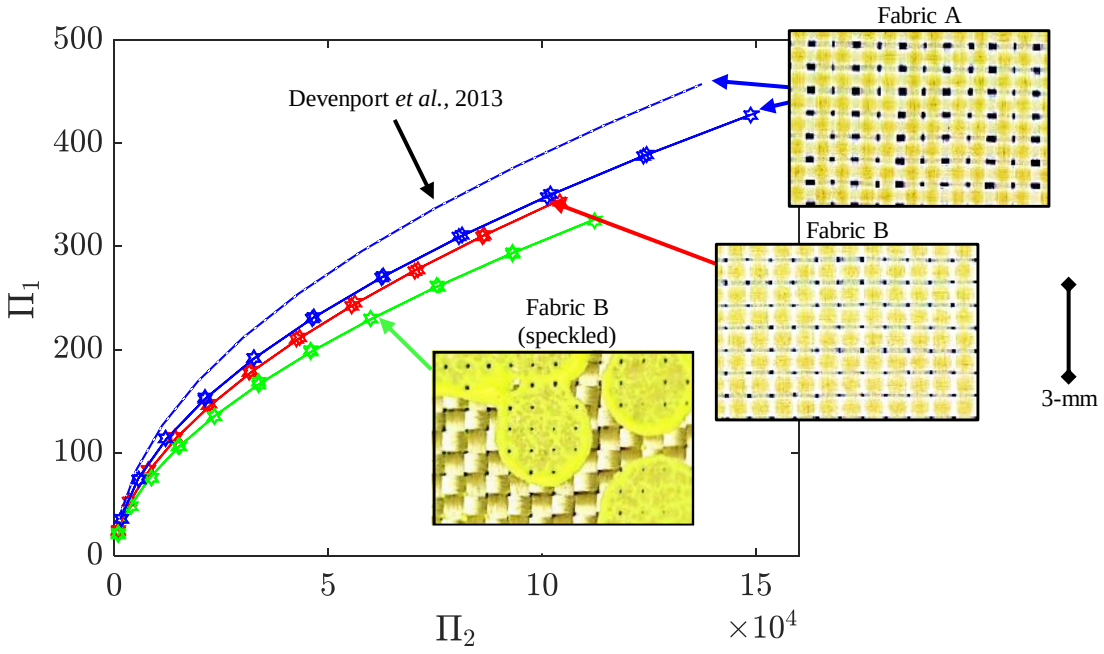

Figure 4.9: Π_1 vs. Π_2 for various fabrics, including raw data and curve fits to Equation 4.5. These data are taken with nominal pre-tensions of 6000-N/m. Both the upwards and downwards velocity sweeps are overlaid.

the constant of proportionality between Π_1 and $\Pi_2^{K_n}$, is the non-dimensional version of k_c in Equation 2.45. The value K_n takes the place of the 0.5 exponent in Equation 2.45 so that the porosity relation now contains flexibility to use power-law behavior other than strictly 0.5 over the full extent of the porosity curve. Such behavior might be expected given the viscous nature of flow through small pores. As with Equation 2.45, the formulation of Equation 4.5 lends itself to varying the power-law exponent additionally at low flow rates via the viscous multiplier term, $(\frac{\Pi_1^4}{\Pi_1^4+K_p})^{1-K_n}$. The value K_p plays the same role as k_p in Equation 2.45 which is to specify the location in the porosity curve where the initial region of higher viscous effects fade.

Other than the differences in the terms and constants note above, there are three more subtle differences between Equation 2.45 and Equation 4.5. First, the new viscous multiplier term of Equation 4.5 is governed by the magnitude of the pore Reynolds number, Π_1, rather than the pressure difference or non-dimensionalized version thereof. This change was made because it is intuitive that the transition from a region of higher viscous flow effects to lower viscous flow effects should be denoted by a Reynolds number term rather than a pressure difference term. Second, to make the expression more general, the exponent of the viscous multiplier term has been increased to a value of one as seen for pure Stokes flow. Third, the Π_1 terms in the viscous multiplier term are now raised to the fourth power which gives a sharper transition according to measured data.

The motivation behind some of the modifications included in Equation 4.5 are illustrated in Figure 4.10. This figure plots the ratio of $\Pi_1/\Pi_2^{k_n}$ versus Π_1, and shows a range of pre-tension values which will be discussed in the next section. The K_n values used to scale each fabric are selected in accordance that $\Pi_1/\Pi_2^{K_n}$ remains constant moving into the higher Reynolds number range which could be understood as the threshold where the vena contracta is stabilizing to constant geometry, for instance. The best-fit values of K_n for each fabric, as shown in Table 4.2, are greater than 0.5 due to viscous effects. At lower Reynolds numbers, the ratio $\Pi_1/\Pi_2^{K_n}$ generally falls off except for three cases of Fabric B. Most likely, there are actually two phenomena at play here. Besides the transitioning Reynolds number effect, the fabric is also experiencing different levels of un-crimping which cause the pore openings to expand. Since the degree of uncrimping is predominantly affected by the pre-tension value rather than the small amount of added tension due to flow-induced strain, the drop in $\Pi_1/\Pi_2^{K_n}$ at low Π_1 values appears to be mostly due to a Reynolds number effect rather than an un-crimping effect, with the possible exception of the unspeckled Fabric B. Therefore, at Π_1 values less than roughly 100, K_n must increase if any attempt to better fit the data is made. As noted before, this increase is handled by the viscous multiplier term in Equation 4.5.

Table 4.2: Comparison of Kevlar porosity parameters.

Fabric	K_n	K_c	K_p
A	0.53	0.772	2E5
B	0.56	0.533	4E4
B, speckled	0.56	0.485	4E4

Best-fit values of K_c, K_n, and K_p are cataloged in Table 4.2. Despite the success of the non-dimensional scaling, there are still non-negligible differences in the best-fit values between each fabric which indicates that the problem is not fully characterized by two Π terms. Considering the comparison of Fabrics A and B, the latter has lower K_c and higher K_n, both of which are consistent with smaller pores as also verified by visual inspection of the pore sizes in Figure 4.9. Note that tests of the speckled Fabric B were only performed at a single pre-tension of 6,000-N/m and have a degree of uncertainty associated with imperfections in the speckling application, both to the wind tunnel walls and to the testing sample. The assumption that only the number of open pores and not the pore size is affected by the speckling process was partially validated by the fact that K_n and K_p are the same for Fabric B regardless of speckling. However, there is a remaining 10% difference in K_c which could be due to either uncertainty in the optical measurement of OAR or differences between the nominal and achieved OAR_s, both of which are used in the scaling for the speckled data. For the latter, as shown by close-ups in Figure 4.1 taken after the porosity test, some pores that were covered with speckle still found a way to open up again during testing. Openings on the speckles of the actual Kevlar walls were also apparent in places.

Two practical notes regarding the application of the non-dimensional porosity relation are here made. Setting aside the viscous multiplier term, conversion of the k_c constant in the dimensional porosity relation of Equation 2.45 to K_c of the new non-dimensional version in Equation 4.5 can be done with Equation 4.6

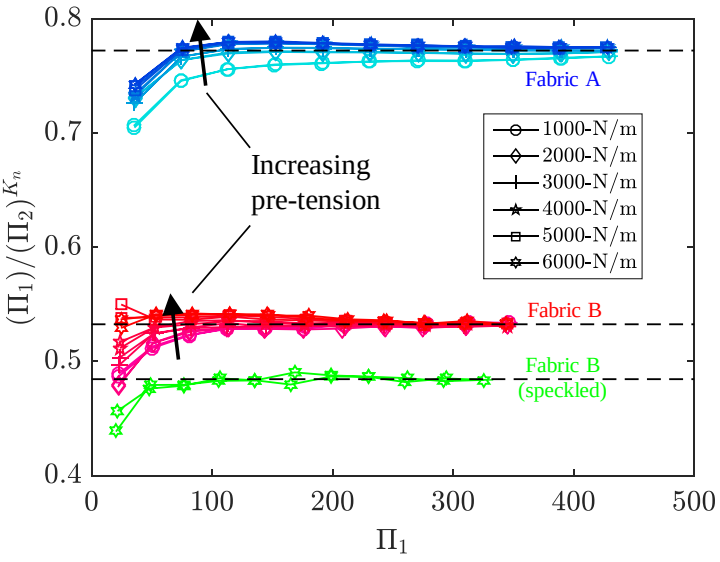

Figure 4.10: Power-law behavior of different fabrics over a range of pre-tension values.

$$K_c = \frac{k_c}{V_c OAR}\frac{d_0}{\nu}\left(\frac{d_0^2}{\frac{1}{2}\rho\nu^2}\right)^{-K_n} \Rightarrow \frac{k_c}{V_c OAR}\sqrt{\frac{1}{2}\rho} \tag{4.6}$$

where the arrow symbol indicates the further simplification of setting $K_n = 0.5$. It is also noted that Equation 4.5 is an implicit function for the velocity through the Kevlar. Without loss of more than 10% accuracy at a Π_2 value of 25, the viscous multiplier term, $(\Pi_1^4/\Pi_1^4 + K_p)^{1-K_n}$, can be dropped if simplicity is desired. This loss of accuracy shortly drops to less than 0.4% at a Π_2 value of 50.

4.3.4 Strain Effect on Porosity

Figure 4.10 shows the effect of pre-tension on the ratio $\Pi_1/\Pi_2^{K_n}$; higher pre-tension increases the ratio. Similar to that of Natarajan (2003), this finding is interpreted as the pores opening up under pre-tension which may be due to the yarns lengthening in the axial direction, contracting in the transverse direction, and un-crimping. While the effect of tension on the porosity of Kevlar fabric might be aptly described by one or two more Π terms in Equation 4.4, there is the possibility of retaining the original simplicity of the non-dimensional flow analysis by inserting a functional relationship for the effect of strain on open-area ratio. Such a means is pursued here using the same framework that led to the strain multiplier given by Equation 2.49.

The relationship between Π_1 and Π_2 has been seen to approximately follow a power-law

behavior such as given by the simplified version of Equation 4.5 which is Equation 4.7

$$\Pi_1 = K_c(\Pi_2)^{K_n}. \tag{4.7}$$

Replacing each of the Π terms by their dimensional components from Equation 4.4 and simplifying yields Equation 4.8

$$v_{normal} = K_c \frac{V_c OAR}{(\frac{1}{2}\rho)^{K_n}} \nu^{1-2K_n} w_0^{2K_n-1} \Delta p^{K_n}. \tag{4.8}$$

With the assumption of inviscid flow, $K_n = 0.5$, and the ν and w_0 terms fall out which yields Equation 4.9

$$v_{normal} = K_{c,inviscid} \frac{V_c OAR}{\sqrt{\frac{1}{2}\rho}} \sqrt{\Delta p}. \tag{4.9}$$

This is the non-dimensional corollary of Equation 4.2. Comparing the two and using the relationship $OAR = OAR_0 + \Delta OAR$, it is seen that $K_{c,inviscid}$ reduces to the two terms shown in Equation 4.10

$$K_{c,inviscid} = 1 + \frac{\Delta OAR}{OAR_0}. \tag{4.10}$$

The first term on the right-hand side of Equation 4.10 indicates that for an unloaded fabric under the assumption of inviscid flow, the non-dimensionalized porosity coefficient is simply unity. While $K_c = 1$ is an over-prediction according to the findings in the previous section, we are aware that this first term is approximate due to the inviscid flow assumption, and as such, it will be discarded and instead measured directly. The second term is also approximate by the same logic, but as its magnitude is less than 5% that of the first term, the second term could be retained as a useful correction to the measured value of the first term. In other words, the measured value of K_c will be simply scaled by the factor $(1 + \Delta OAR/OAR_0)$ to account for the strain effect.

Thus, we look to find the effect of straining of the Kevlar fibers on the OAR. The unstrained open-area ratio, OAR_0, according to the dimensioning of Figure 4.5 is simply given by Equation 4.11

$$OAR_0 = \frac{(a_0 - w_0)^2}{(a_0)^2} \tag{4.11}$$

where w_0 is the unstrained width of an individual Kevlar yarn and a_0 is the unstrained side length of the square fabric unit cell. Under a strain given by ε, a_0 will increase by the factor

$(1+\varepsilon)$ and w_0 will decrease by the factor $(1-\varepsilon\nu)$ where ν is Poisson's ratio of an individual Kevlar yarn. Therefore, the increase in open-area ratio due to strain, ΔOAR is given by Equation 4.12

$$\Delta OAR = \frac{(a_0(1+\varepsilon) - w_0(1-\varepsilon\nu))^2}{(a_0(1+\varepsilon))^2} - OAR_0. \tag{4.12}$$

It is now desired to compare this analytically derived strain effect on porosity with experiments. It is noted that increasing the strain of the fabric causes some pores to be excluded from the measurement region. However, the factor $(1+\varepsilon)$ in the denominator of the first term of Equation 4.12 accounts for this exclusion effect. In the wind tunnel, no pores are ever excluded from the flow area, but as the denominator of the first term of Equation 4.12 increases with strain, so does the area of the bulging Kevlar, so the equation is valid within and without the wind tunnel.

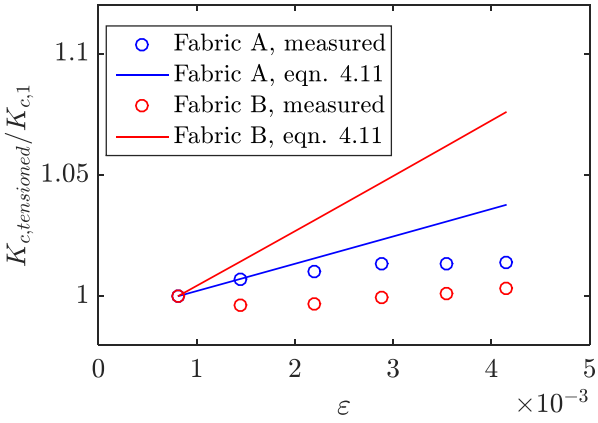

Figure 4.11: Variation in porosity coefficient K_c with increasing pre-strain, ε. The data from each fabric are normalized on the K_c value of each respective fabric's lowest tension case.

It should also be stated that the strain in the Kevlar mounted in the testing apparatus necessarily increases with increasing dynamic pressure from the suction flow. Yet in the limit of high pre-tension, the increment in tension due to the flow diminishes. Calculations based on the theory given by Equation 4.1 indicate that the tension increment will indeed be an order of magnitude smaller than the imposed pre-tension variations, this ratio being even smaller for the high pre-tension cases.

Using the tensioning frame described previously, tensions from as low as 1000-N/m to as high as 6000-N/m were achieved. Whereas the curve-fit values presented in Table 4.2 were averaged for each fabric across different pre-tension values, separate curve-fits are presently applied to each case of pre-tension. The change in the value of K_c relative to the lowest tension case for two fabric variants is shown in Figure 4.11. In general, there is a small increase in measured K_c with ε, however, the gains undervalue the predictions by a factor ranging from 2.5 to 25. It appears that the simple strain model of a fabric unit cell does not do justice to all the physics experienced by the Kevlar yarns. Specifically, it seems that there must be a *flattening* of yarns with strain which is all but negating the opening of the pores due to axial lengthening and any Poisson contraction of the yarns. Since the magnitude of

the largest measured increase in K_c is only 1.4%, and since the maximum strain represented in Figure 4.11 is already on the order of the maximum strains experienced by the Kevlar walls of the Stability Wind Tunnel, for instance, the strain effect on the fabric is deemed negligible for the fabrics in this study. As such, no correction term will be applied to the measured porosity coefficients to account for the strain effect.

Chapter 5

Interference Corrections for Two-Dimensional Models

This chapter pertains to the second through fourth objectives of Thrust 1 in Chapter 2: to employ measurements of the fundamental sources of wall interference to generate engineering models for correcting aerodynamic data, to assess the relevance of models of varying fidelity for performing wall-interference corrections in flexible, porous-wall wind tunnels, and to identify potential sources of residual error in the wall interference corrections scheme.

5.1 Survey of Raw Data Across Campaigns

The three experimental campaigns described by Tables 3.2 will be referenced throughout this chapter. The specific runs performed during these campaigns are presented in Table 3.3, and the selection of several reference data sets to be compared in this chapter was made with the following logic. Data on tripped models is preferred over data on untripped models since the former are less sensitive to small variations in the surface preparation of the model which may be accumulated during model installation or removal. Since the model was removed and re-installed between each campaign, this is an important consideration. However, among the runs listed in Table 3.3, there are unfortunately no tripped runs from Campaign 3 at the highest freestream dynamic pressure. Neither are there any solid-wall data at the middle dynamic pressure case. Therefore, tripped data from the lowest dynamic pressure case will be compared which is Runs 1-2, 2-2, and 3-2 for Campaigns 1, 2, and 3, respectively. It is also desired to compare high freestream dynamic pressure data since the effect of the Kevlar on the test section aerodynamics is more prominent when high loading is placed on the walls. Towards these ends, the case of the untripped model at the highest dynamic pressure will also be compared which is Runs 1-3, 2-3, and 3-3 for Campaigns 1, 2, and 3, respectively. Data for runs at other conditions may be found in Appendix C. Below is a comparison of

the raw data measured across all three campaigns for the two reference run conditions noted above.

The airfoil C_p distributions are shown in Figure 5.1 for the two reference run conditions during all three campaigns. As a whole, the flow character over the airfoil is similar for all three campaigns at both test conditions. Differences between the campaigns are evident on the suction-side of the model, particularly for Campaign 2. The Campaign 2 data has suction-side C_p's that are more positive than the data from other campaigns in every subfigure of Figure 5.1. At low loading such as in Figure 5.1(a) and (d), such behavior indicates that the blockage experienced by the model is lower during Campaign 2. At higher loading situations such as in Figure 5.1(b-c) and (e-f), the implication is that the airfoil may be experiencing less lift interference, as well as lower blockage during Campaign 2. The corresponding data of Figure 5.1 at negative angles of attack show the same trends as the positive angles of attack as can be verified in Appendix C.2.

The global aerodynamic coefficients at various angles of attack are shown in Figures 5.2 and 5.3 for the two reference run conditions during all three campaigns. The symmetry of the NACA0012 profile and well-behaved nature of the flow is evident within the linear region from roughly -12 to 12 degrees. Nearing stall, there are some asymmetries such as a delayed positive stall angle for Campaign 2, for instance, which might be a result of slightly different surface preparation of the airfoil for this campaign. Comparing between campaigns, there are differences larger than the error bars, especially for the reference run condition of higher dynamic pressure as in Figure 5.3. These differences center around the Campaign 2 data which again stands apart as was also the case in the airfoil C_p comparisons. For the C_m comparison, on the other hand, the two Kevlar-wall results are grouped together, and the solid-wall data of Campaign 1 stands somewhat apart. Only the lower dynamic pressure run condition has C_d data available and only for Campaigns 1 and 2. Here we see that the C_d is lower for Campaign 2, possibly indicating lower blockage in the test section for this campaign.

The midspan wall C_p distributions at various angles as measured by the physical taps described in Section 3.1.6 are shown in Figures 5.4 and 5.5 for the two reference run conditions during the Kevlar-wall Campaigns 2 and 3, respectively. For all the cases shown, the suction side experiences the strongest C_p magnitudes and has its apex slightly downstream of the pressure-side apex. For the data in Figure 5.4, there is general agreement between campaigns given slightly greater suction-side C_p magnitudes in Campaign 3 due the greater achieved freestream dynamic pressure as tabulated in Table 3.3. Moving to the run condition with higher dynamic pressure in Figure 5.5, there are three major differences between campaigns. The first is again the larger C_p magnitudes on the suction side for Campaign 3 which is suspected to be a result of the difference in freestream dynamic pressure between campaigns. The second is the augmented concave down region on the suction side for Campaign 2. The third and most compelling is that there is a noticeable pressure drop through the test section for the case of Campaign 2 which does not exist in Campaign 3. The wall C_p at the exit of the test section varies by more than 0.1 between campaigns at 12 degrees angles of attack

as seen in Figure 5.4(c) and (e).

The explanation for the difference in pressure gradient between campaigns may be found in the larger open-area ratio of the Kevlar fabric in Campaign 2. The more porous fabric results in larger v_{normal} through the walls and a less severe pressure difference across the fabric's thickness. The static C_p's in each of the chambers are therefore able to take on values closer to their respective flow-side C_p's as generated by the flow over a model in the test section. Since mass must be conserved in the chambers, the combined result is that relatively high volumes of air leak from the pressure-side chamber to the suction-side chamber for the case of Campaign 2. This situation implies high amounts of re-entrant flow from the anechoic chamber to the test section, particularly on the suction-side wall. As the flow re-enters with no streamwise momentum, it causes a degree of blocking to occur which accelerates the flow as it moves through the test section. A similar concept is the effect of wake blockage; the total mass flow in the test section remains constant but the viscous deceleration of a certain flow region accelerates the inviscid flow in the regions around it. Thus, at least for the range of porosities tested, Kevlar-wall test sections with semi-sealed anechoic chambers experience a porosity-induced pressure gradient in the streamwise direction. It is seen that higher pressure gradients correlate with higher Kevlar porosities.

The static C_p's measured in the anechoic chambers throughout angle of attack sweeps are shown in Figure 5.6 for the two reference run conditions during the Kevlar-wall Campaigns 2 and 3. The so-called chamber C_p is dependent on the loading placed on the chamber by the model, as well as the sealing of the chamber from the control room and from the opposite anechoic chamber. As the angle of attack and loading on the walls increase, the chamber C_p's tend towards the C_p's experienced on the flow sides of each wall. As a result, the chamber C_p curves somewhat resemble C_l curves, except that after stall the high blockage in the test section causes a strong drop in C_p in both chambers. The comparison between Campaigns 2 and 3 indicates that the chambers experienced less pressurization in Campaign 3 than in Campaign 2. This fact, which has implications for the porous flow through the Kevlar, is a believed result of the lower porosity of the Kevlar in Campaign 3 which allowed the fabric to sustain greater pressure differences across its thickness.

The wall deformation contours from one side of the test section as measured with the optical system of Section 3.1.7 are next compared for the two reference run conditions during the Kevlar-wall Campaigns 2 and 3. Specifically, Figures 5.7, 5.8, 5.9, and 5.10 show data from Runs 2-2, 2-3, 3-2, and 3-3, respectively. These figures show only the out-of-plane deflection component which is typically two orders of magnitude greater than the in-plane components. Some common characteristics among the data are that there are everywhere smoothly varying contours, as well as symmetry about the midspan line, $y = 0$. The maximum deflection of the Kevlar during an angle of attack sweep occurs just before stall on the suction-side wall. For the data in Figures 5.7, 5.8, 5.9, and 5.10, the maximum values are 37-mm, 85-mm, 55-mm, 115-mm, respectively. Referencing Table 3.3 for the dynamic pressures of each run, the larger deflection magnitudes of Campaign 3 are seen to be a result of larger dynamic pressure. The magnitude of the deflections increases with dynamic pressure, though the

increase is not linear due to the non-linear strain stiffening of the Kevlar. Other than the difference in deflection magnitudes, another notable difference between the data from Campaign 2 and Campaign 3 is the streamwise distribution of deflection. For Campaign 2, there is a noticeable bulge out of the test section on the upstream suction wall as shown in Figure 5.7(a-b) and Figure 5.8(a-b). This outwards bulge corresponds to the large concave-down region noted in the midspan wall C_p's for Campaign 2 and is believed a function of the lower porosity of the Kevlar used during Campaign 2.

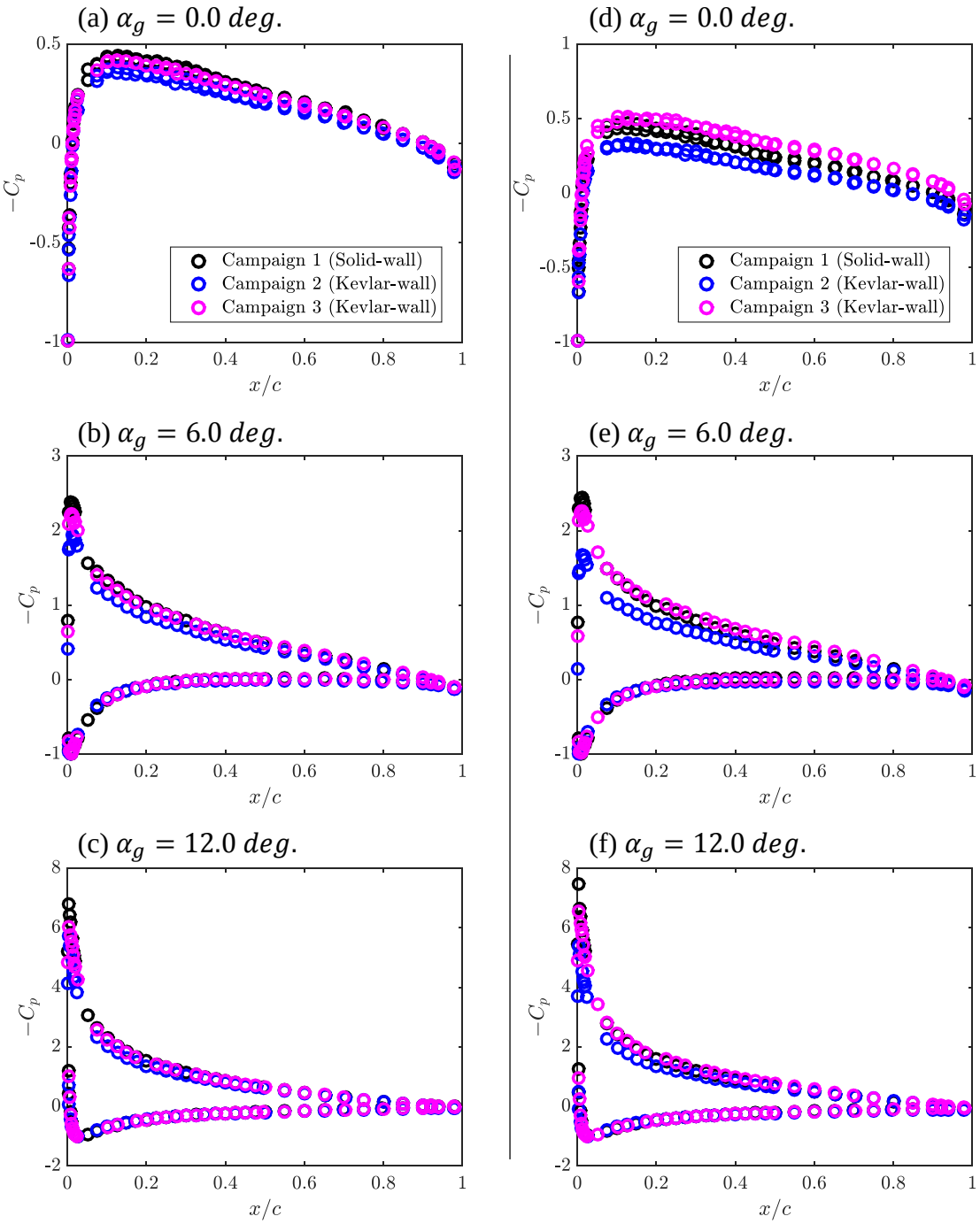

Figure 5.1: Uncorrected pressure coefficient, C_p, versus chordwise position, x/c, for the NACA0012. In descending order of the legend, the runs in (a)-(c) are Run 1-2, Run 2-2, and Run 3-2 which correspond to a tripped model at 2.0E6 Reynolds number. The runs in (d)-(f) are Run 1-3, Run 2-3, and Run 3-3 which correspond to an untripped model at 3.9E6 Reynolds number. Small angle of attack offsets have been applied as noted in Appendix C.1, and the geometric angles have been interpolated to the reported nominal values.

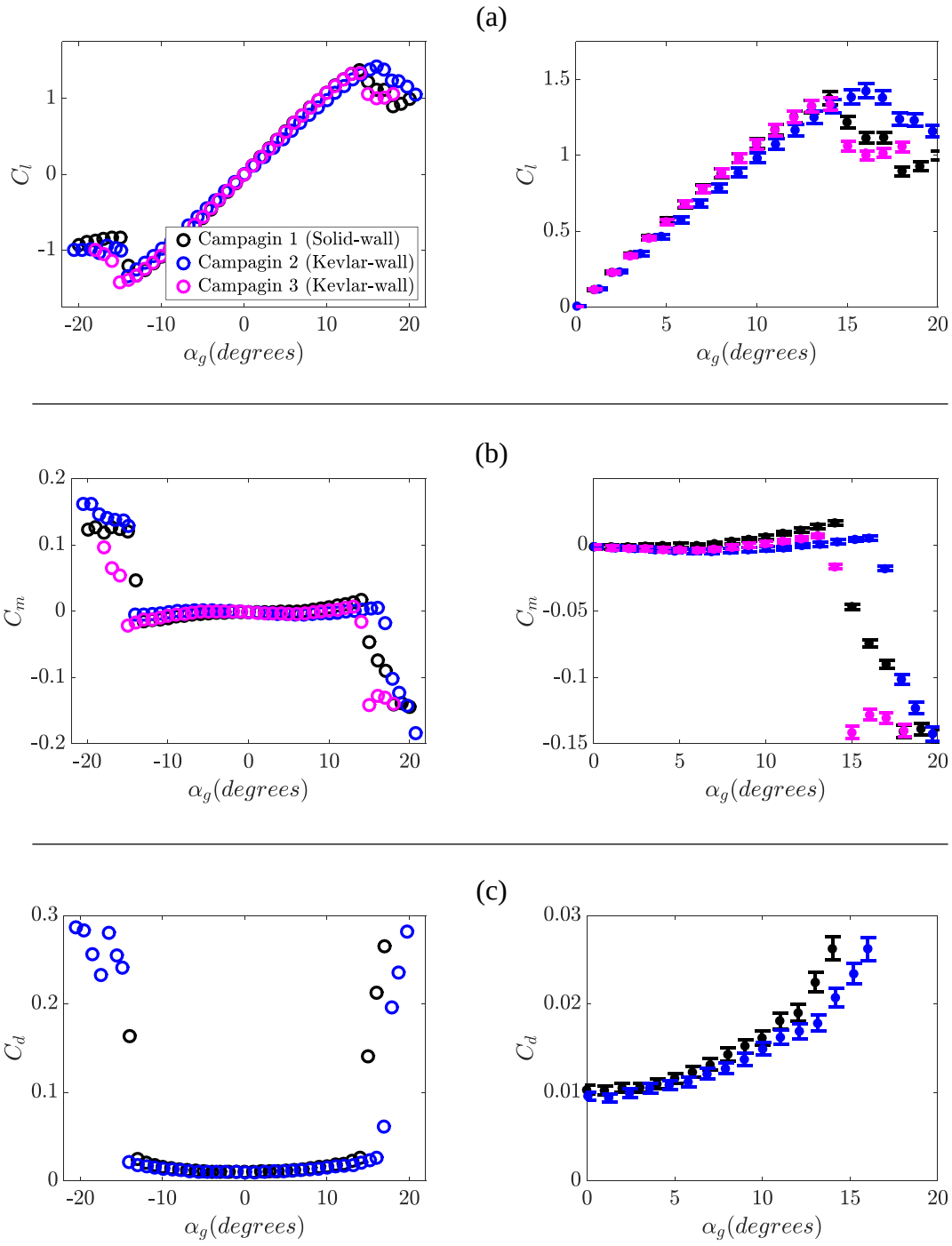

Figure 5.2: Uncorrected global aerodynamic coefficients versus angle of attack, α_g, for the NACA0012. In descending order of the legend, the runs in each plot are Run 1-2, Run 2-2, and Run 3-2 which correspond to a tripped model at the reference run condition with lower dynamic pressure. Small angle of attack offsets have been applied as noted in Appendix C.1. Data on the left- and right-hand side are the same data but shown at different scales.

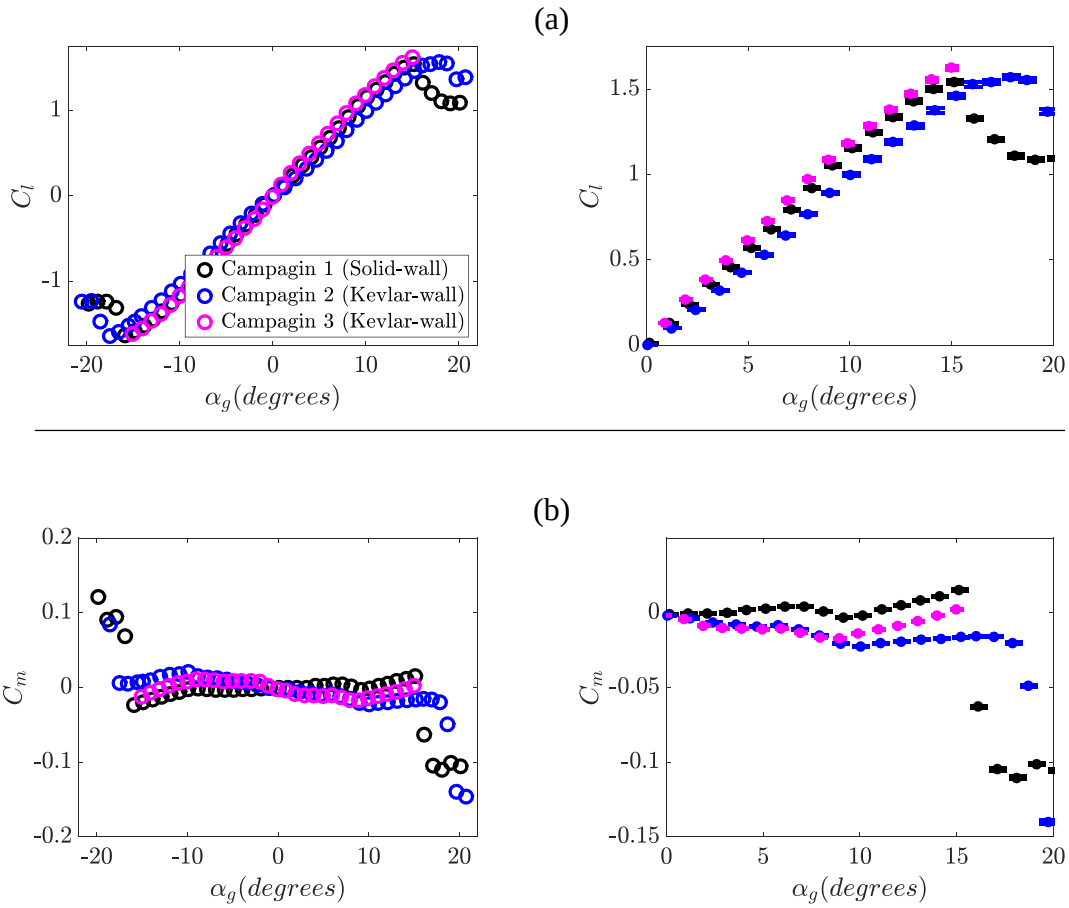

Figure 5.3: Uncorrected global aerodynamic coefficients versus angle of attack, α_g, for the NACA0012. In descending order of the legend, the runs in each plot are Run 1-3, Run 2-3, and Run 3-3 which correspond to an untripped model at the reference run condition with higher dynamic pressure. Small angle of attack offsets have been applied as noted in Appendix C.1. Data on the left- and right-hand side are the same data but shown at different scales.

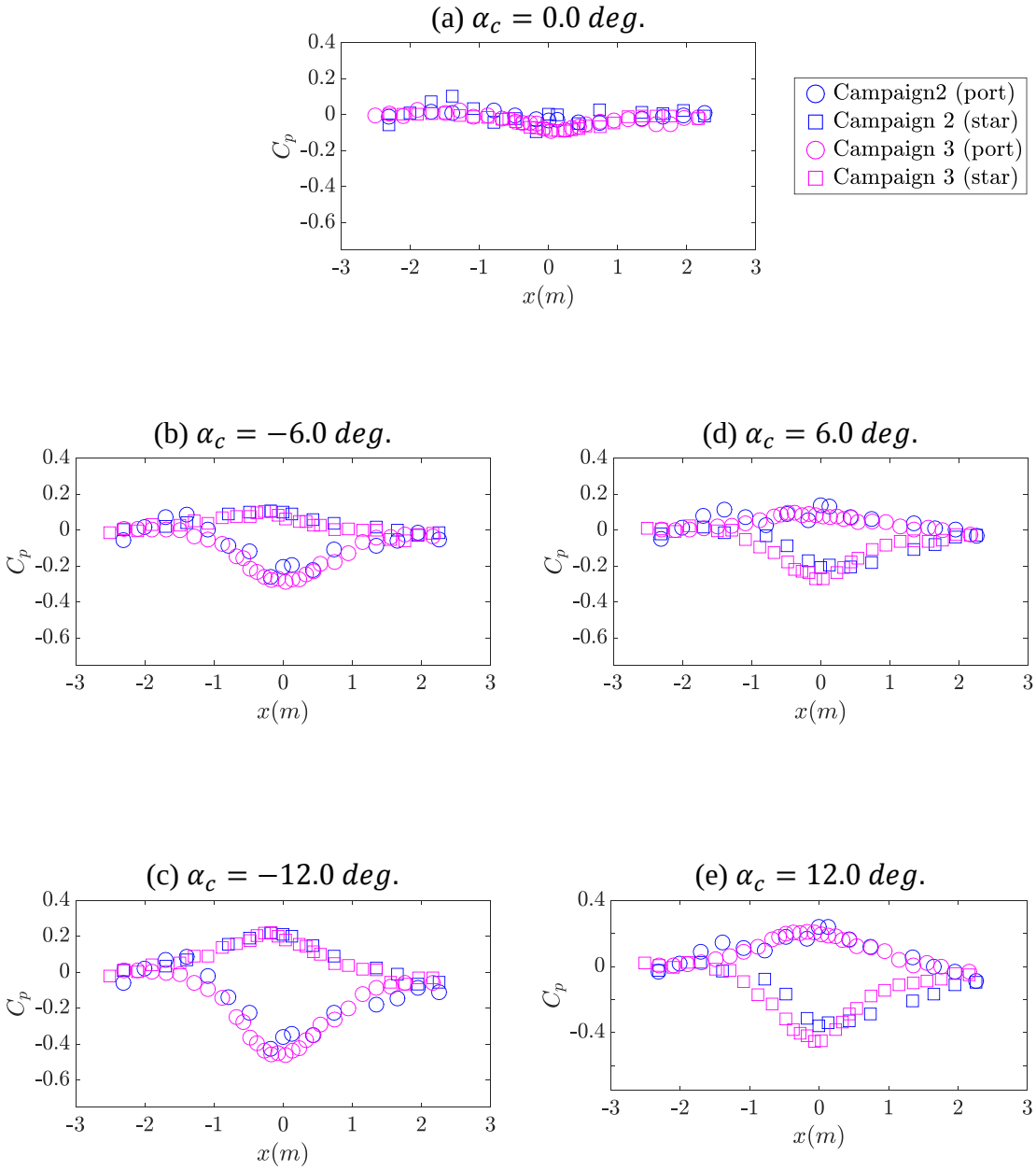

Figure 5.4: Wall C_p at midspan vs. streamwise location, x, for Runs 2-2 and 3-2 as measured by the physical taps described in Section 3.1.6. Data have been interpolated to the nominal angles reported. The data shown have had the empty test section results subtracted from them.

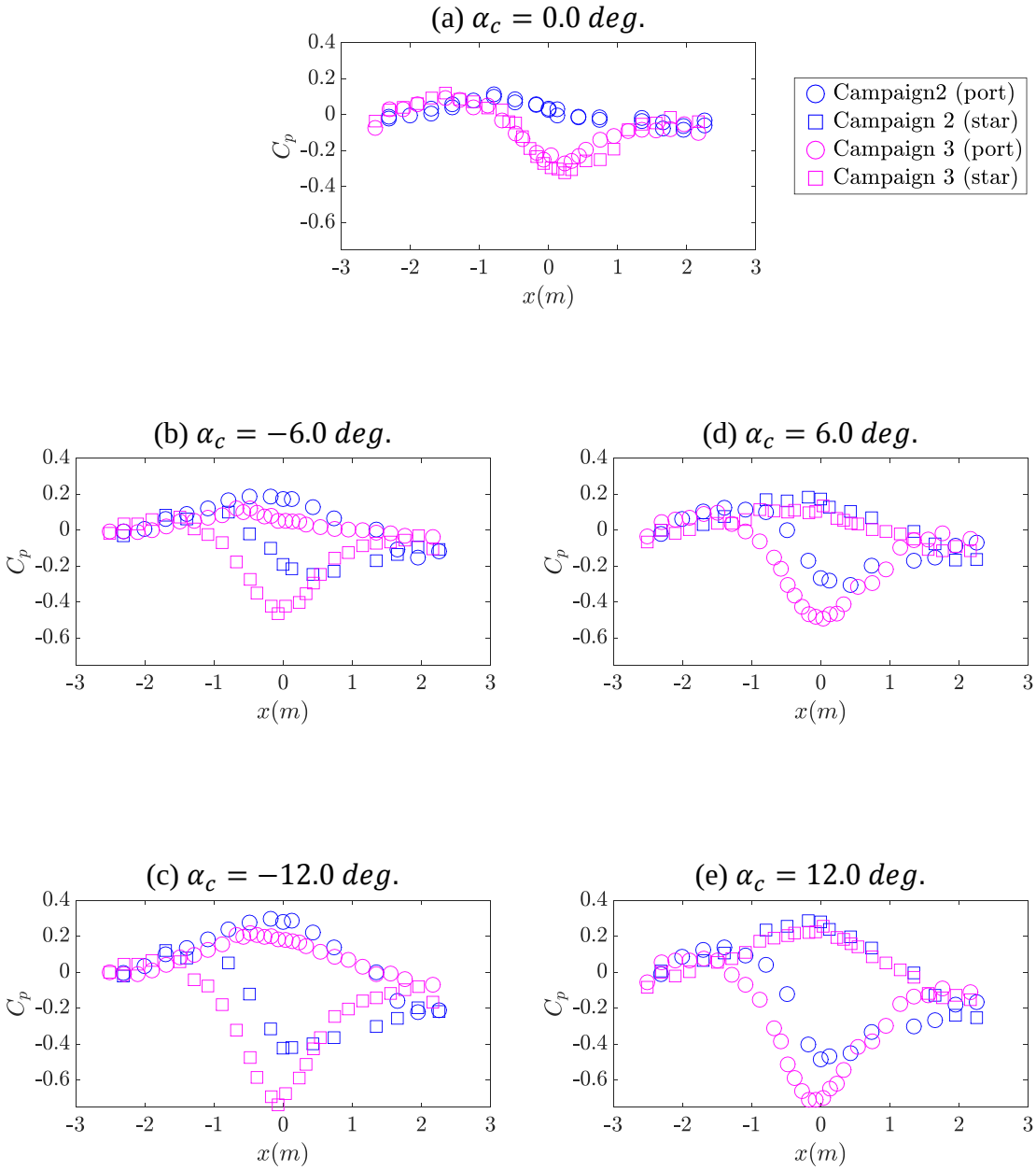

Figure 5.5: Wall C_p at midspan vs. streamwise location, x, for Runs 2-3 and 3-3 as measured by the physical taps described in Section 3.1.6. Data have been interpolated to the nominal angles reported. The data shown have had the empty test section results subtracted from them.

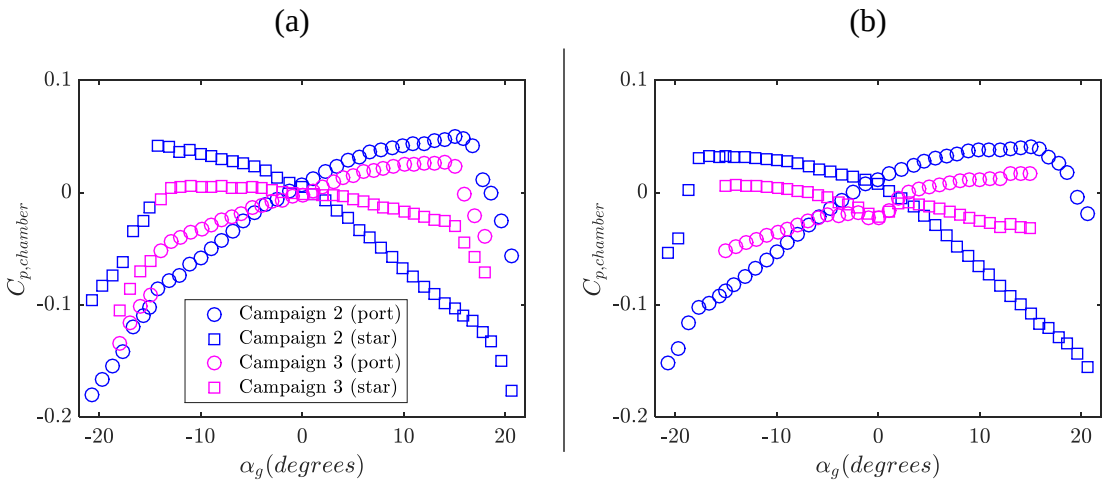

Figure 5.6: Chamber pressure coefficient, $C_{p,chamber}$, vs. angle of attack, α_g, for (a) Runs 2-2 and 3-2 and (b) Runs 2-3 and 3-3.

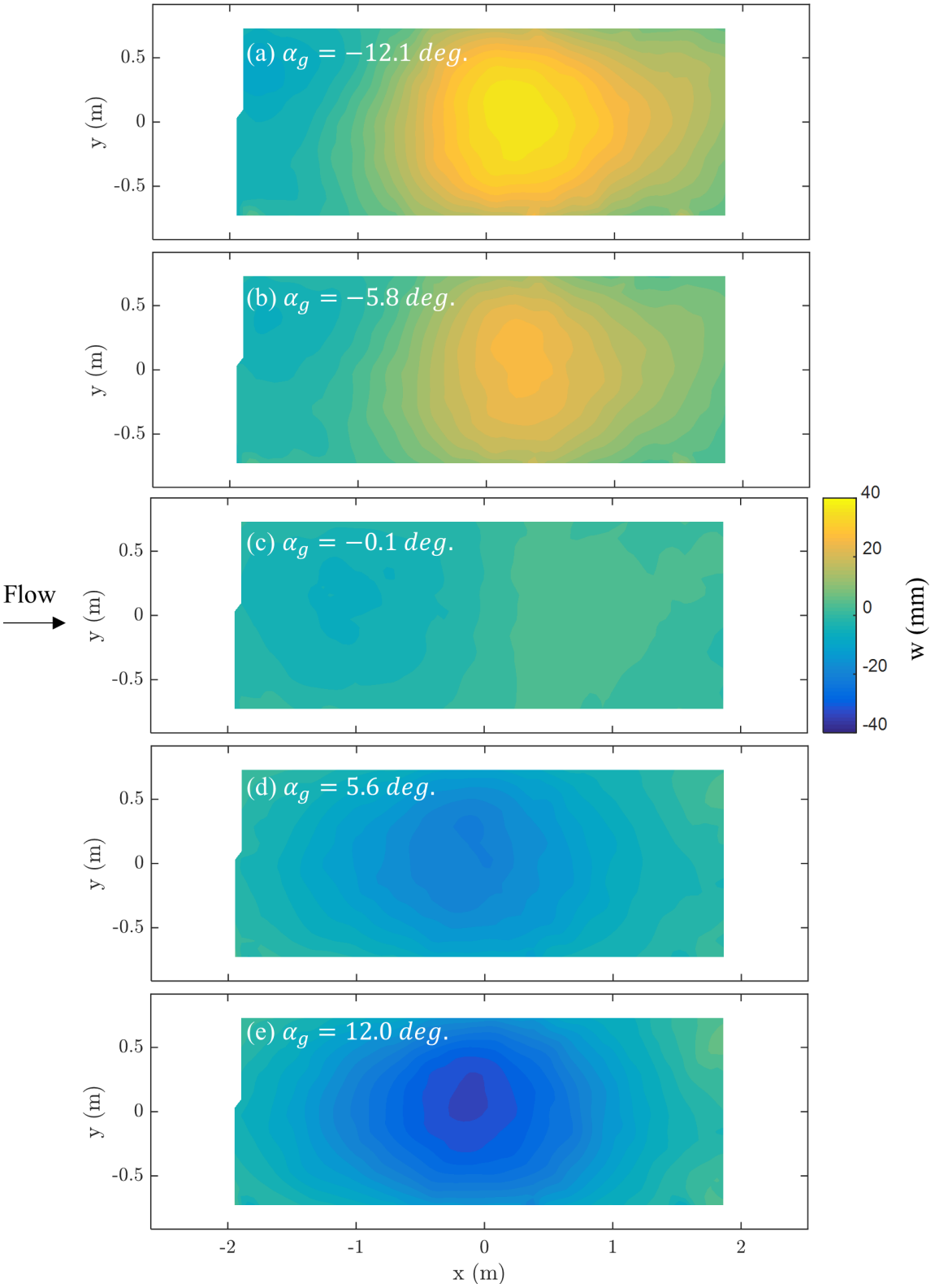

Figure 5.7: Measured wall deformation in the w-component vs. location over the starboard wall for Run 2-2. Positive values of w indicate deflection *into* the flow.

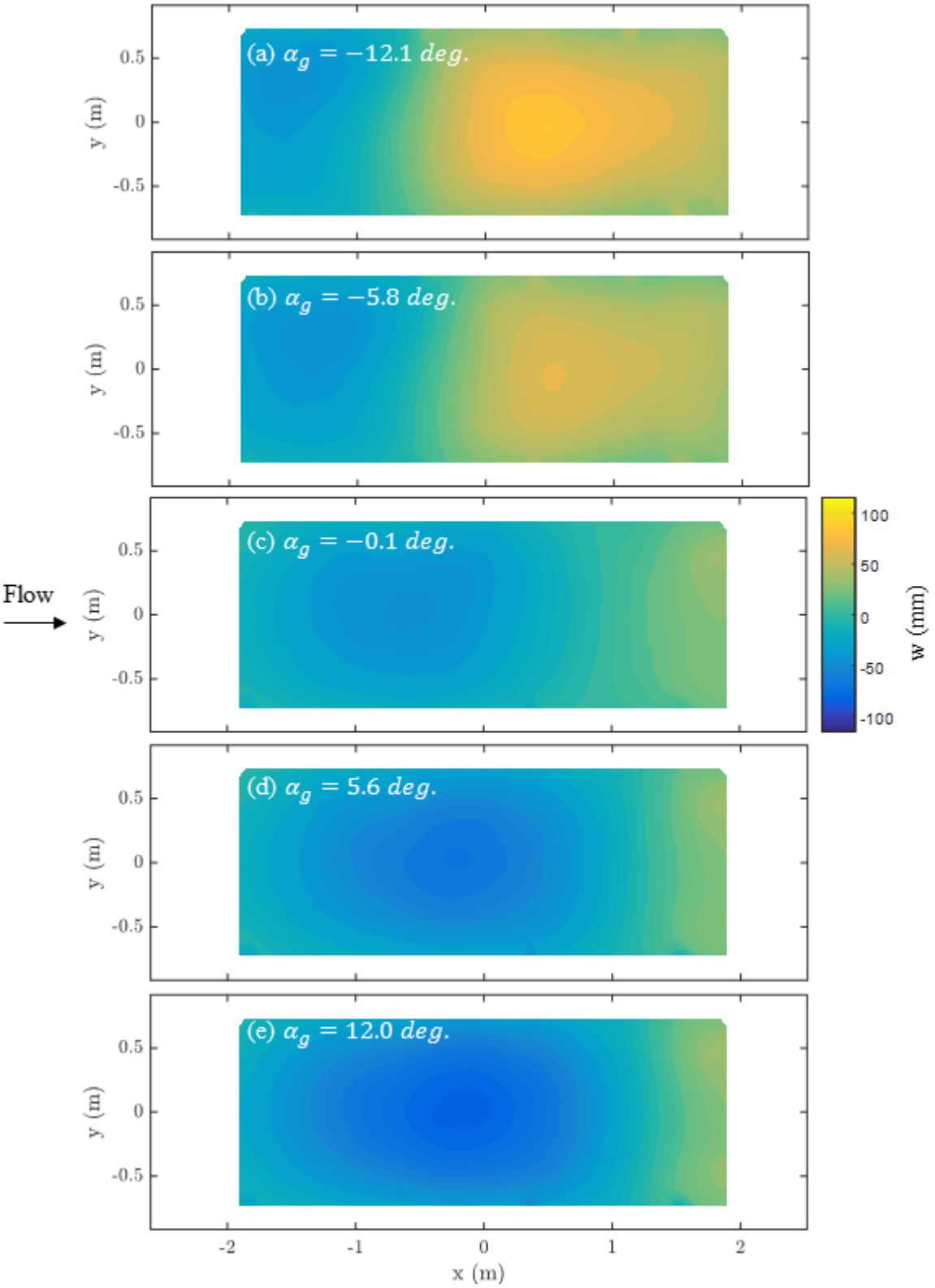

Figure 5.8: Measured wall deformation in the w-component vs. location over the starboard wall for Run 2-3. Positive values of w indicate deflection *into* the flow.

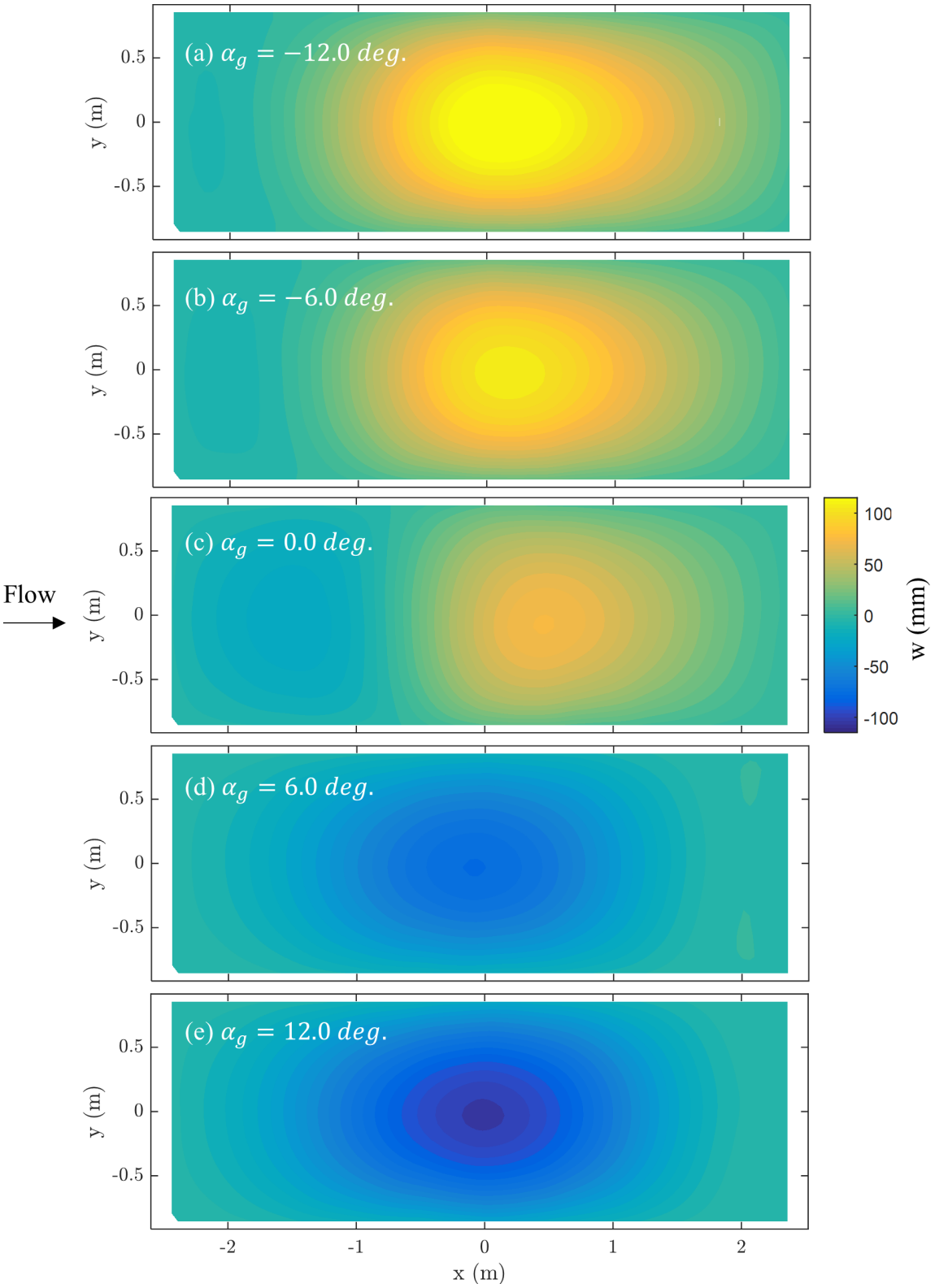

Figure 5.9: Measured wall deformation in the w-component vs. location over the port wall for Run 3-2. Positive values of w indicate deflection *into* the flow.

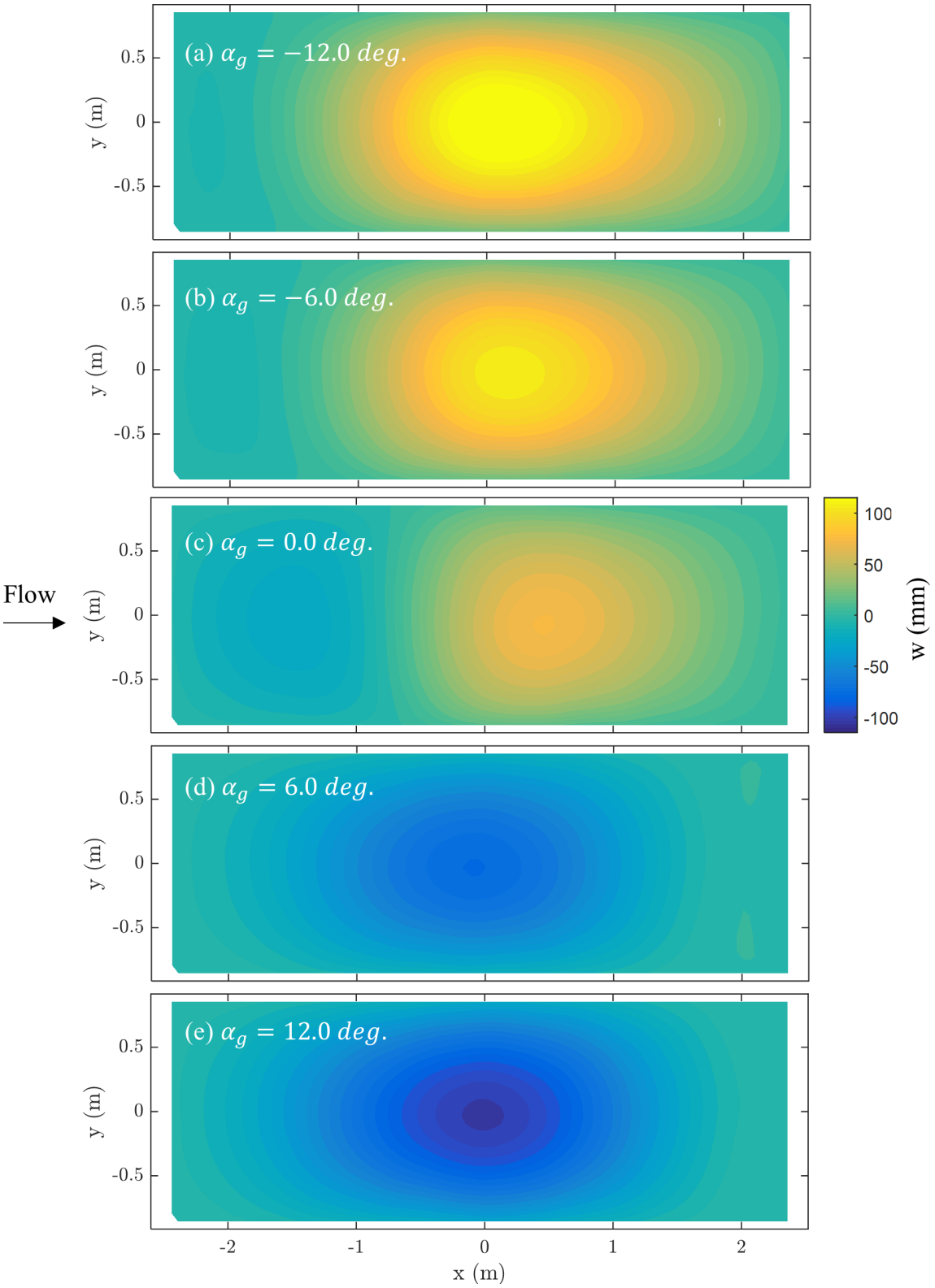

Figure 5.10: Measured wall deformation in the w-component vs. location over the port wall for Run 3-3. Positive values of w indicate deflection *into* the flow.

5.2 Baseline Performance of Panel Method Correction

Proceeding from the raw data in the previous section, we now consider the correction of the data for wall-interference effects. Unless otherwise noted, corrections applied to the data in the rest of this chapter are performed with a two-dimensional panel method simulation using the singularity representation of the airfoil along with Equations 2.33, 2.34, 2.35, and 2.36. For the Kevlar-wall cases, the panel method abides by that of Devenport *et al.* as introduced in Section 2.2.2.2.1 except that the singularity representation of the model is used rather than a full paneled airfoil. Devenport *et al.* did not report a porosity relation for Fabric B or the speckled version thereof that was used in Campaign 3, so the results of Section 4.3.3 were curve-fit to Equation 2.45 to yield $k_c = 0.01081\ m/(s\sqrt{Pa})$ assuming $k_p = 50\text{-}Pa$. Additionally, the values of pre-tension and leakage area for Campaign 3 are updated from the original values of Devenport *et al.* according to the new measurements as listed in Table 3.2. As not all of the runs under consideration have corresponding drag data available, the source strength of Equation 2.37 for data from every campaign is calculated with the drag measured during Run 2-1 of Table 3.3.

Lift polars will be used as means to assess the accuracy of various wall-interference correction methods with the solid-wall results from Campaign 1 acting as the standard for comparison. Figure 5.11 shows the uncorrected lift polars presented in the previous section plotted alongside the corrected data using the method of Devenport *et al.* for all three test campaigns. It is apparent that the Kevlar-wall data from Campaign 2, which uses the more porous Fabric A, hardly needs correcting at all to match the corrected solid-wall data. The Kevlar-wall data from Campaign 3, which uses the less porous Fabric B, behaves more like a solid-wall test section.

For the data from the reference run condition of lower dynamic pressure as in Figure 5.11(a), the Kevlar-wall correction slightly overshoots the solid-wall curve for Campaign 2 and slightly undershoots it for Campaign 3. However, disagreement with the solid-wall is never greater than a $C_{l,c}$ of 0.025 among the unstalled angles of attack for both campaigns. For the higher dynamic pressure run condition as in Figure 5.11(b), the Kevlar-wall correction for Campaign 2 again matches the solid-wall correction to within a $C_{l,c}$ of 0.025 among the unstalled angles of attack. However, $C_{l,c}$ for Campaign 3 is larger than that of Campaign 1 by as much as 0.08. The predominant reason for this divergence is due to the strain correction to porosity included in the Devenport *et al.* model. It has already been shown in Section 4.3 that this correction is non-physical, or at least is significantly smaller than that predicted by Equation 2.49. The Kevlar used in Campaign 3 represents an ∼80% reduction in open-area ratio from that used in Campaign 2. For Campaign 3 in highly strained cases, the artificial correction overwhelms the porosity calculation, sometimes doubling or tripling the original open-area ratio.

The corresponding airfoil $C_{p,c}$ distributions for Figure 5.11 are shown in Figure 5.12 and shed understanding on the previous lift polar comparisons. Figure 5.12 plots corrected

pressure coefficients interpolated to a common α_c. The correction is performed as described in Appendix A. For the Campaign 2 data in Figure 5.12, the Devenport *et al.* model is slightly overestimating blockage across the board as seen by comparing the $C_{p,c}$'s between the Kevlar-wall and solid-wall tests. Consistent with the reported findings from Devenport *et al.*, the overestimation is most noticeable at the higher dynamic pressure case in (d)-(f) where the Campaign 2 data has less negative $C_{p,c}$'s on the suction side. At the mid-range angles of attack in (b) and (e), the Campaign 2 data additionally shows signs that the magnitude of v/V_∞ is too large as seen by Campaign 2's more positive $C_{p,c}$'s on the pressure side. For the Campaign 3 data, while the estimation of blockage is more accurate, the angle of attack correction is not strong enough. As evidence, it can be seen that the C_p distribution on both the suction and pressure sides has greater absolute value for Campaign 3 than for Campaign 1. It is suspected that the reason for this error is that v/V_∞ is too negative which stems from the ballooning of the strain multiplier correction described in the previous paragraph.

The midspan wall C_p's are next examined for Runs 2-3 and 3-3 in Figure 5.13 by comparing the simulated wall C_p's of the Devenport *et al.* method to measurements made using the Kevlar-wall pressure taps described in Section 3.1.6. Despite the larger scatter in the data due to surface imperfections around the pressure taps, the measured C_p's are shown here before subtraction of the empty test section C_p's to provide a one-to-one comparison with the panel method simulation. For the Campaign 2 result, Run 2-3, as in Figure 5.13(a)-(c), the data implies that the simulation is overestimating blockage upstream of the model as shown by the more negative C_p's of the simulated results there. Downstream of the model, the opposite is true. The simulation's error in predicting blockage is a result of failing to capture the pressure gradient through the test section. As noted in Section 5.1, the substantial pressure gradient measured through the test section for Campaign 2 is believed due to the higher porosity of the fabric in this campaign. Even though the simulation correctly uses a larger porosity in Campaign 2 than Campaign 3, it is likely that the large pressure gradient is not predicted either because the blocking effect of the re-entrant flow or the leakage paths between anechoic chambers are not modeled correctly. For the Campaign 3 result, Run 3-3, as in Figure 5.13(d)-(f), the data implies that the simulation is slightly underestimating blockage in the vicinity around the model. Campaign 3 uses the lower porosity Kevlar, so the pressure gradient through the test section is much smaller which results in more favorable comparison of the measured and simulated results.

The simulated chamber C_p's are compared to the measured data for Runs 2-3 and 3-3 in Figure 5.14(a)-(b), respectively. For Campaign 2 in Figure 5.14(a), there is general agreement between the simulation and measurement, granted small differences at high loading and an overall C_p offset of 0.016. The offset, which implies that the actual freestream flow is slower than simulated, may be a result of small volumes of freestream flow bypassing the airfoil via un-modeled leakage paths. The data from Campaign 3 in Figure 5.14(b) have a much smaller range than that of Campaign 2 which is understood in light of the porosity argument of the previous paragraph. As well, the Campaign 3 data has more significant errors in the simulation than were found for Campaign 2. For instance, the

simulation is predicting too negative a C_p on the suction side by roughly a factor of two which suggests that the transpiration velocities from the suction chamber will be under-predicted. The difference between the prediction accuracy of the chamber C_p's between campaigns is not apparently due to differences in the resistance to leakage flow between chambers. The leakage area between chambers was measured in 2013 to be 0.14- and 0.16-m^2 for the port and starboard sides, respectively, according to the measurement method described in Section 3.1.8. Remeasured in 2016, the values were 0.15- and 0.20-m^2 which are sufficiently similar to the previous measurements to have confidence that the internal leakage paths in the volumes above and below the test section were not appreciably altered between campaigns. It is possible that other flow paths not included in the leakage measurement, such as flow through the ceiling and floor panels, are significantly affecting the chamber C_p's.

The midspan deformation distributions for several angles of attack during Runs 2-3 and 3-3 are given in Figure 5.15(a)-(b), respectively. The simulation is under-predicting the maximum deformation on both the pressure and suction sides by around a factor of two as was previously reported by Brown[36]. This result is expected since the findings of Section 4.2 indicate that the Kevlar modulus of elasticity used in the Devenport *et al.* model is a great exaggeration of the true value.

Though the Kevlar-wall correction method of Devenport *et al.* is in some cases quite effective, it is clear that there are some remaining discrepancies when comparing corrected results with solid-wall results, as well as comparing measured boundary conditions with those simulated. There still exists room for improvements to the correction accuracy by higher fidelity modeling of certain physics.

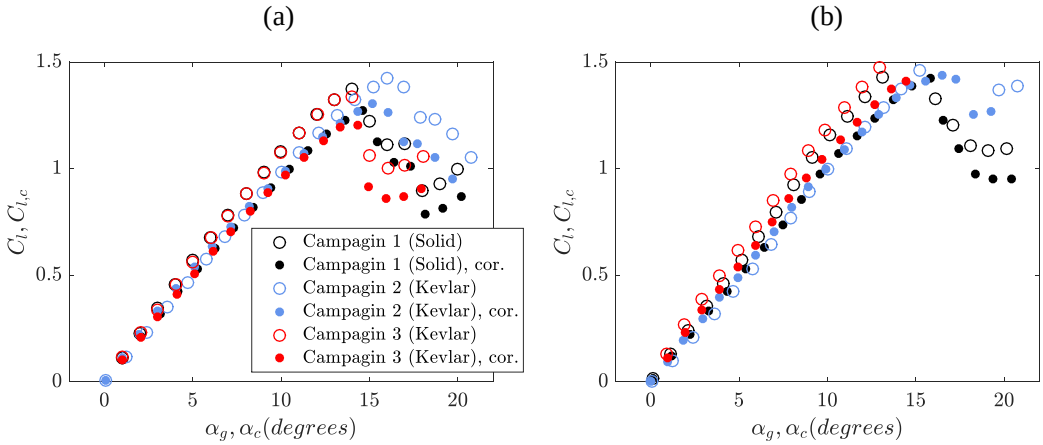

Figure 5.11: Coefficients of uncorrected and corrected lift, C_l and $C_{l,c}$, versus uncorrected and corrected angle of attack, α_g and α_c, for the NACA0012 using the Devenport *et al.* model. In descending order of the legend, the runs in (a) are Run 1-2, Run 2-2, and Run 3-2. The runs in (b) are Run 1-3, Run 2-3, and Run 3-3. Small angle of attack offsets have been applied as noted in Appendix C.1.

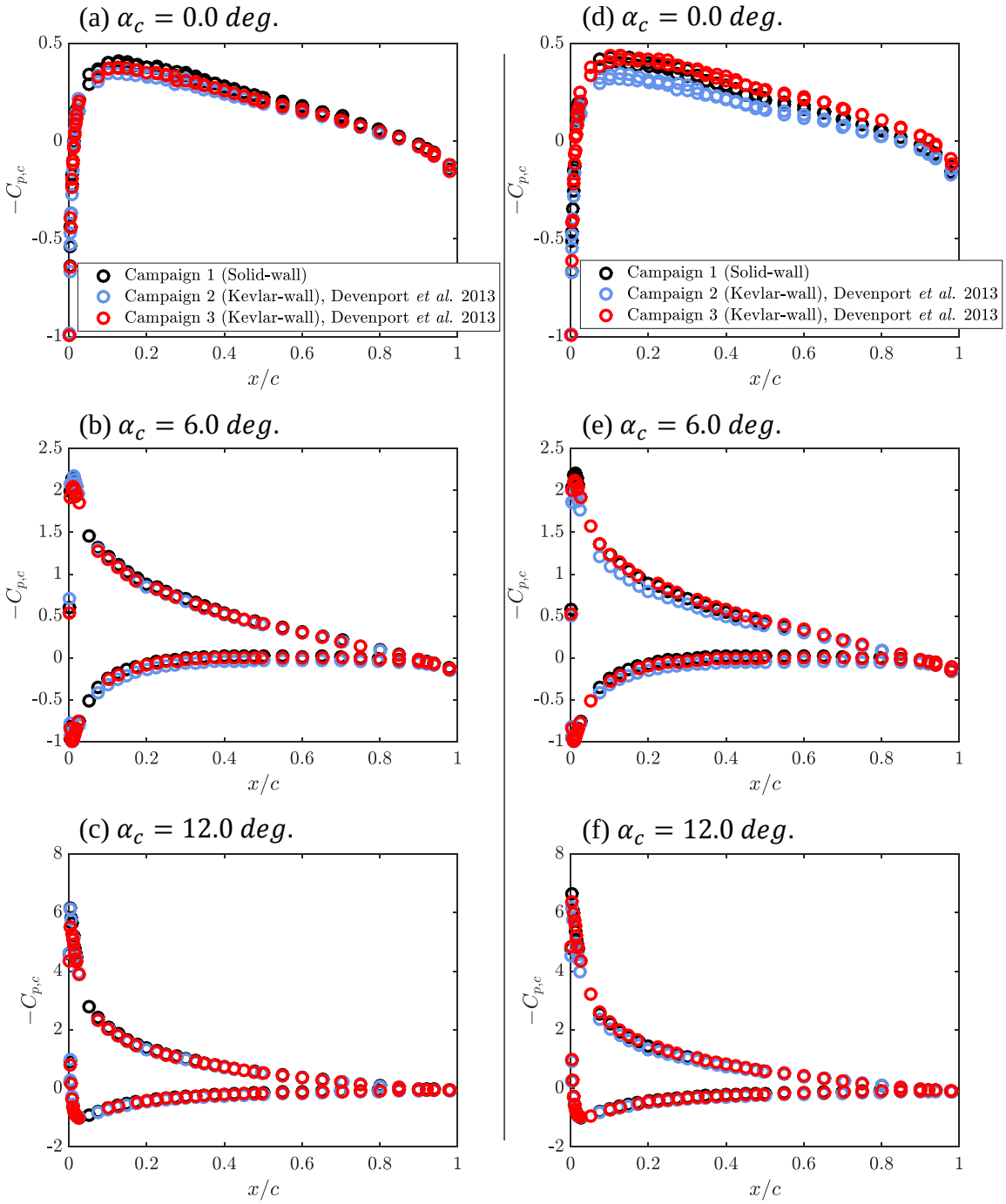

Figure 5.12: Corrected pressure coefficient, $C_{p,c}$, versus chordwise position, x/c, for the NACA0012 using the Devenport *et al.* model. In descending order of the legend, the runs in (a)-(c) are Run 1-2, Run 2-2, and Run 3-2. The runs in (d)-(f) are Run 1-3, Run 2-3, and Run 3-3. Small angle of attack offsets have been applied as noted in Appendix C.1, and the corrected angles have been interpolated to the reported nominal values. Corrections applied according to Appendix A.

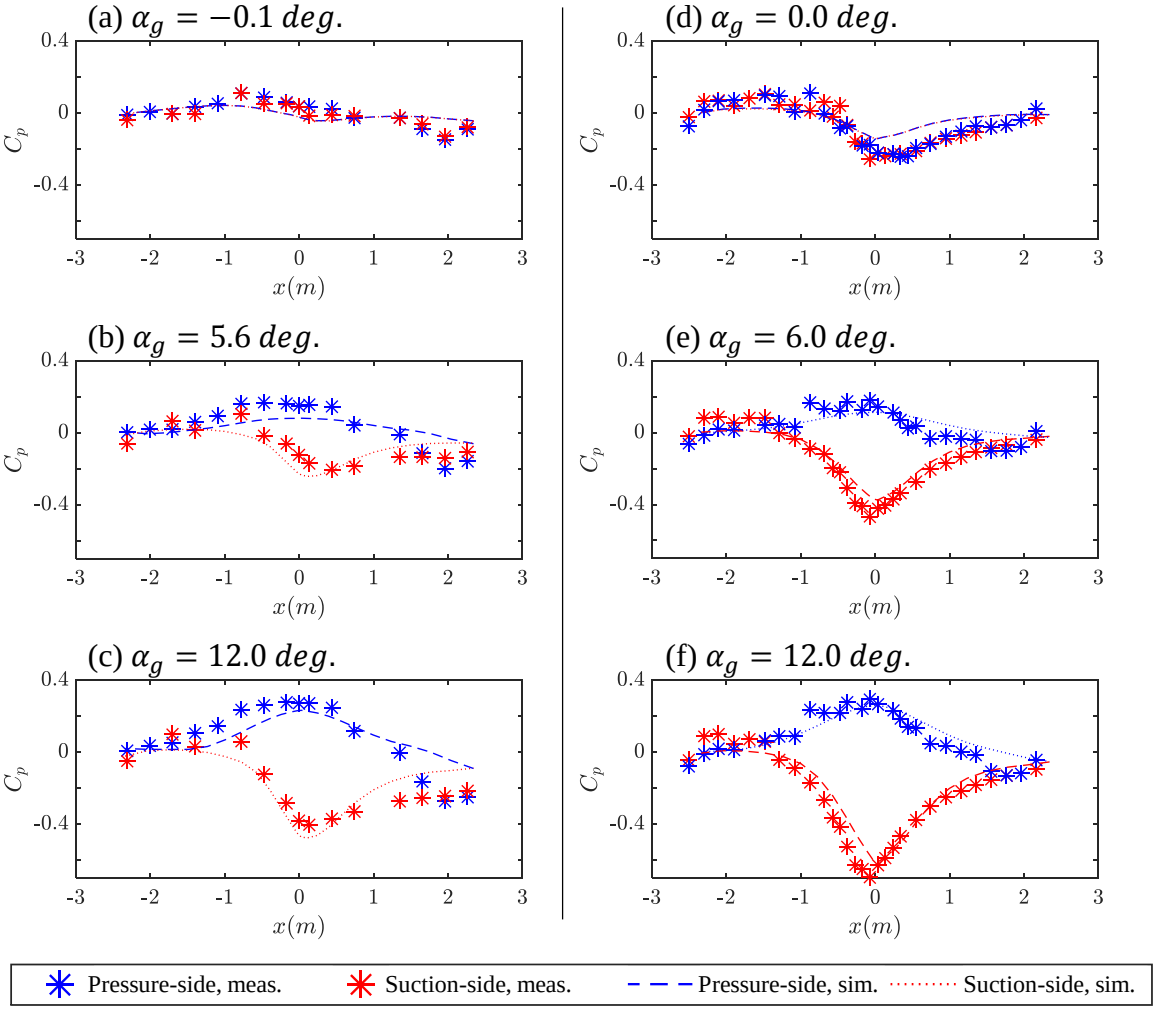

Figure 5.13: Wall pressure coefficient, C_p, vs. streamwise location, x, for (a)-(c) Run 2-3 and (d)-(f) Run 3-3. Simulations are according to Devenport *et al.*

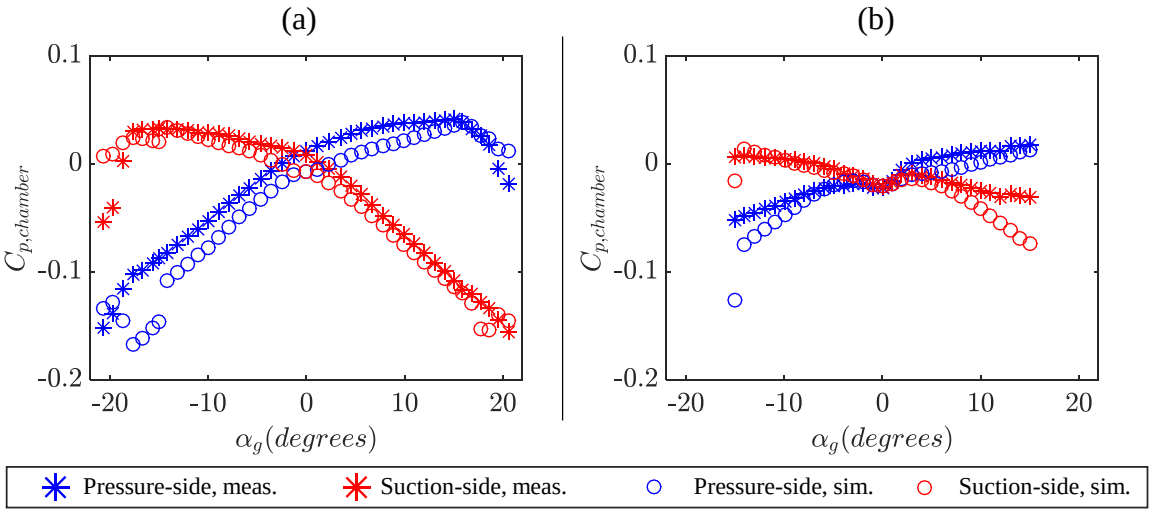

Figure 5.14: Chamber pressure coefficient, $C_{p,chamber}$, vs. angle of attack, α_g, for (a) Run 2-3 and (b) Run 3-3. Simulations are according to Devenport *et al.*

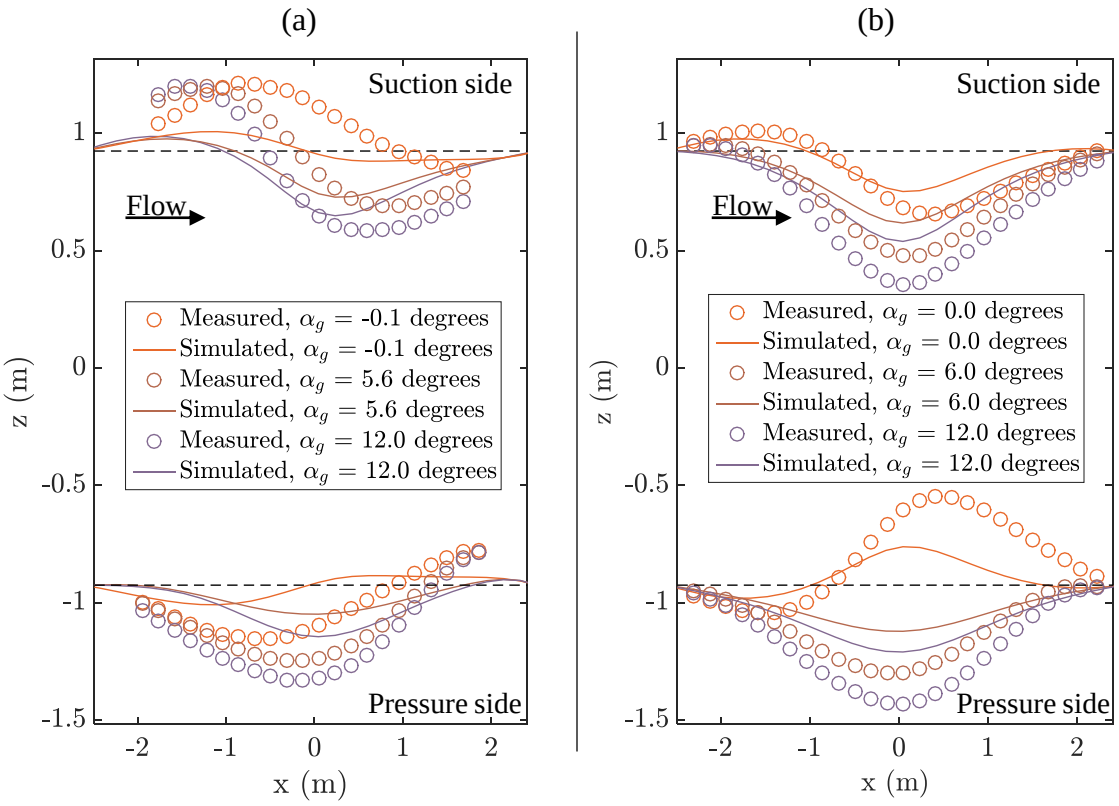

Figure 5.15: Midspan wall profile, z, versus streamwise location, x, for three different angles of attack for (a) Run 2-3 and (b) Run 3-3. Deflections are magnified by a factor of 5 for clarity. Simulations are according to Devenport *et al.*

5.3 Modified Performance of Panel Method Correction with Improved Modeling Strategies

To address the residual differences between corrected data from solid-wall and Kevlar-wall test sections, an investigation has been carried out of key test section modeling assumptions. It has been reasoned that the most relevant of these assumptions are associated with the pressure-velocity relationship through the Kevlar, the boundary layer growth along the test section walls, the deformation modeling of the Kevlar, the pressure difference modeling across the Kevlar, and the representation of the flow field as two-dimensional. The first four of these, having been identified as having a high impact and strong possibility of offering improvement to the wall interference modeling fidelity, are pursued specifically below. The last is addressed indirectly in the following chapter during verification of a three-dimensional panel method.

As before the investigation proceeds using the reference data sets of Runs 1-2, 2-2, and 3-2 and Runs 1-3, 2-3, and 3-3 introduced in Section 5.1. The panel method simulation of Devenport *et al.* is again applied just as in the previous section. One-by-one, changes reflecting higher fidelity modeling of the wall boundary conditions are applied to the panel method, and the resulting effect on the test section flow and corrections performance are evaluated. In each case, the nominal values of Devenport *et al.* are used except for that of the parameter under consideration. After assessing the impact of each change to the panel method, the change is undone before moving on to the next item. To provide a quantitative view of the changes in modeling strategies on the correction performance, the correction parameters queried from the panel method simulations are shown in Figures 5.16, 5.17, and 5.18. The relevant parameters are u/V_∞, v/V_∞, and $\partial(v/V_\infty)/\partial x$, respectively, which may be found in Equations 2.33-2.36 and 2.48. Finally, the $C_{l,c}$ data are compared in Figures 5.19. Note that in Figure 5.19, the solid-wall data from Campaign 1 are subtracted out of the Campaign 2 and 3 data in order to highlight small differences in $C_{l,c}$ between the campaigns.

The effect of each of the four high-impact developments noted above are detailed in the subsections below with reference throughout to Figures 5.16-5.19. Plotted alongside the four studies in these figures is the effect of all the new inputs combined which will be termed the *combined inputs model* and discussed after the initial four studies.

Also included throughout the following subsections as supporting evidence for the effect of the modified modeling strategies on the test section flow are comparisons of simulated distributions of either v_{normal} or wall C_p before and after each modification to the panel method. Of the two reference run conditions introduced in Section 5.1, the higher dynamic pressure case is chosen for these comparisons which is Runs 2-3 and 3-3 of Table 3.3. Comparisons are made at an angle of attack of 12 degrees, though the trends generally hold at other angles, as well as other dynamic pressures.

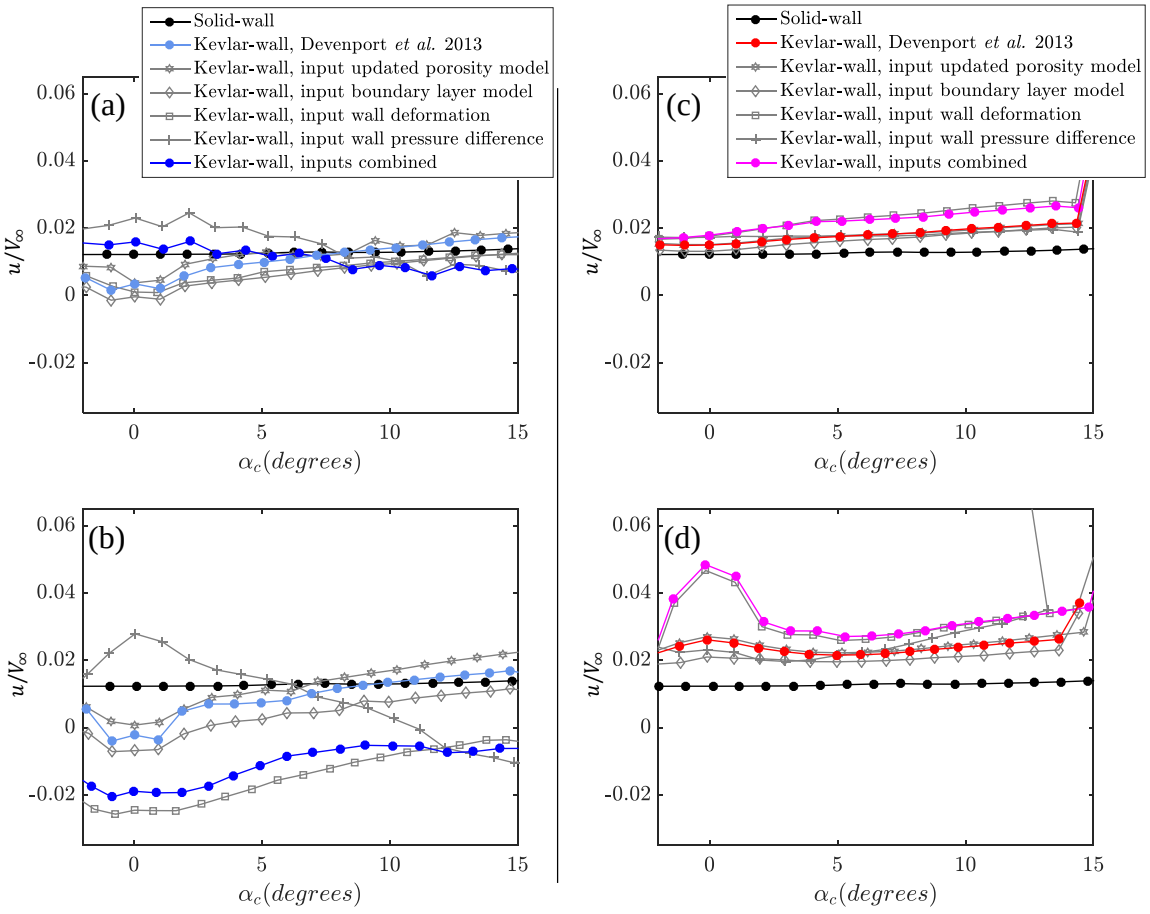

Figure 5.16: Blockage fraction, u/V_∞, vs. corrected angle of attack, α_c, for (a) Run 2-2 (tripped, 2.0E6 *Re* number), (b) Run 2-3 (untripped, 3.9E6 *Re* number), (c) Run 3-2 (tripped, 2.0E6 *Re* number), and (d)Run 3-3 (untripped, 3.9E6 *Re* number).

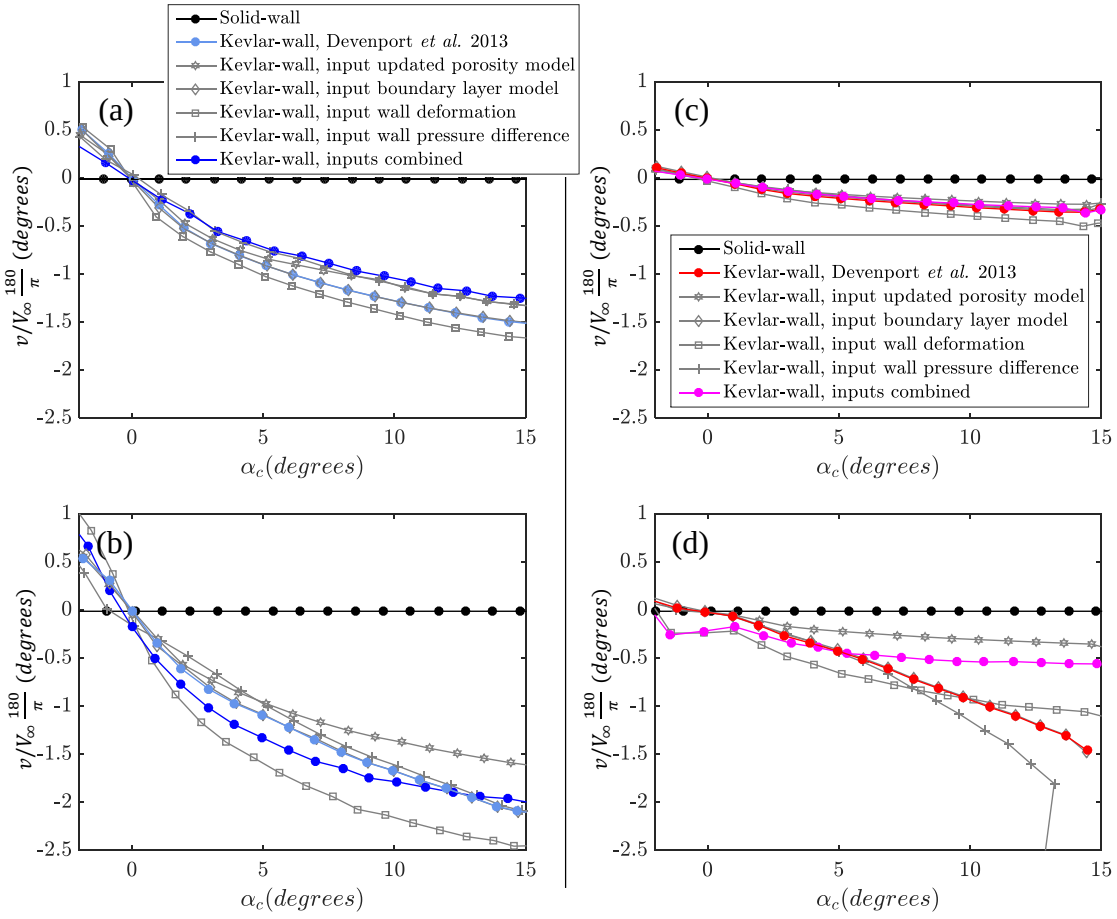

Figure 5.17: Kevlar-induced angle of attack change, $(v/V_\infty)\frac{180}{\pi}$, vs. corrected angle of attack, α_c, for (a) Run 2-2 (tripped, 2.0E6 *Re* number), (b) Run 2-3 (untripped, 3.9E6 *Re* number), (c) Run 3-2 (tripped, 2.0E6 *Re* number), and (d)Run 3-3 (untripped, 3.9E6 *Re* number).

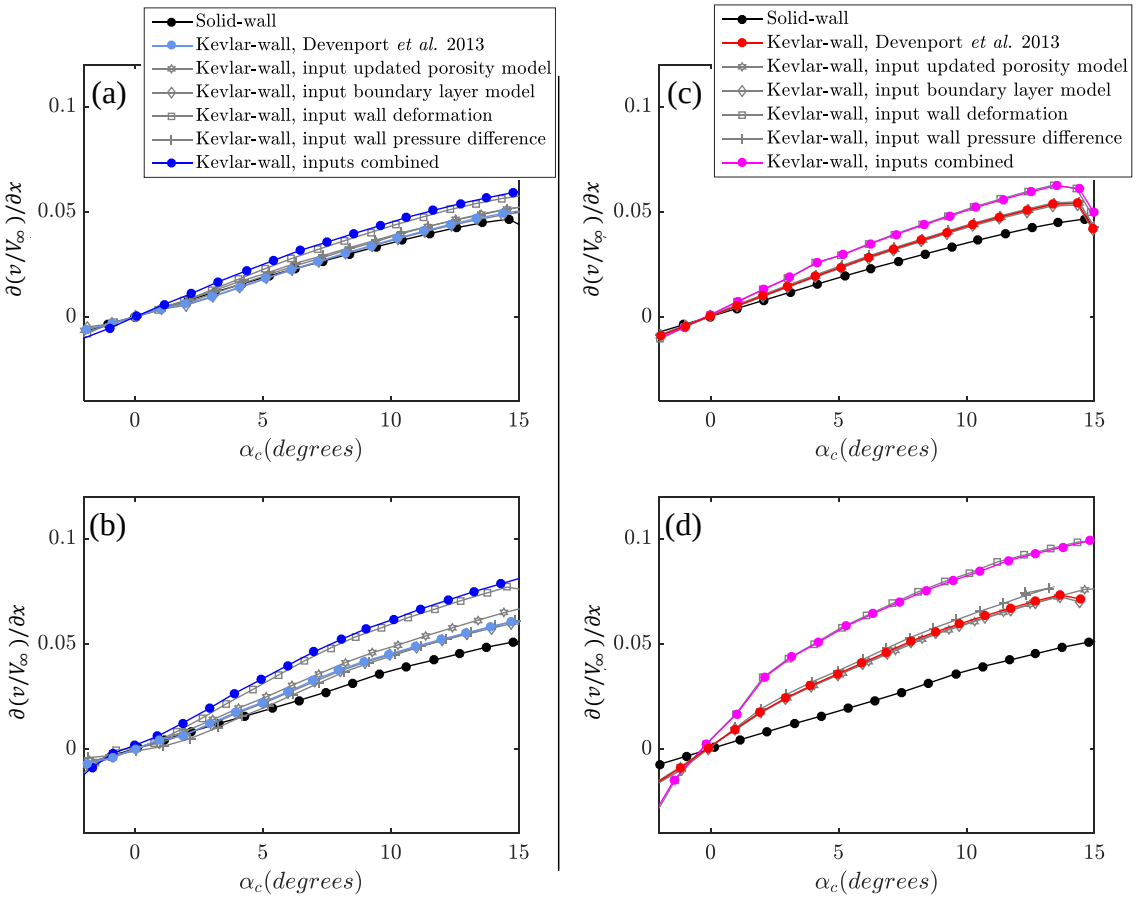

Figure 5.18: Derivative of vertical interference velocity, $\partial(v/V_\infty)/\partial x$, vs. corrected angle of attack, α_c, for (a) Run 2-2 (tripped, 2.0E6 *Re* number), (b) Run 2-3 (untripped, 3.9E6 *Re* number), (c) Run 3-2 (tripped, 2.0E6 *Re* number), and (d)Run 3-3 (untripped, 3.9E6 *Re* number).

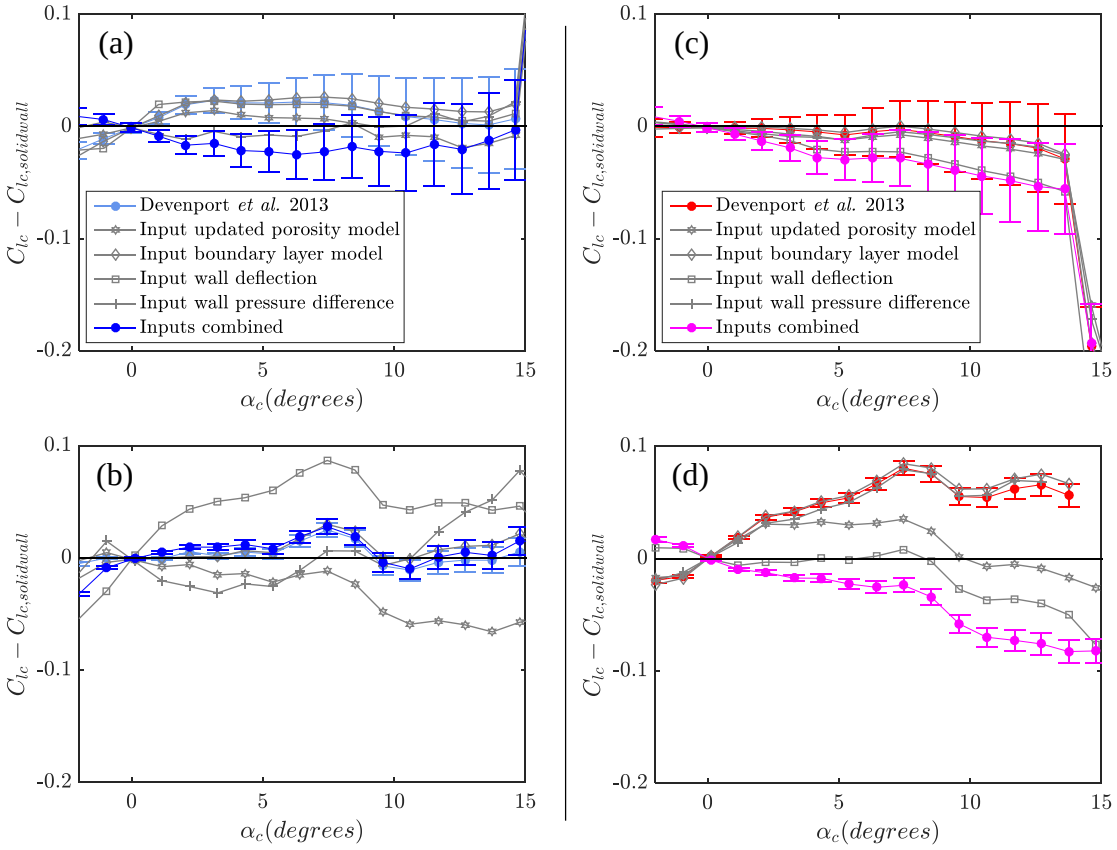

Figure 5.19: Deviation in corrected lift, C_{lc}, between test sections vs. corrected angle of attack, α_c, for (a) Run 2-2 (tripped, 2.0E6 *Re* number), (b) Run 2-3 (untripped, 3.9E6 *Re* number), (c) Run 3-2 (tripped, 2.0E6 *Re* number), and (d)Run 3-3 (untripped, 3.9E6 *Re* number). The magnitude of the error bars is calculated in Appendix D.1.

5.3.1 Wall Porosity

Detailed and accurate measurements of the Kevlar porosity were already presented in Section 4.3, and now the effect of those measurements in the context of wall interference will be examined. The original porosity relation is that given by Equation 2.45 using $k_c = 0.0625\text{-}m/s/\sqrt{Pa}$ and $k_p = 50\text{-}Pa$ for Fabric A and $k_c = 0.01081\text{-}m/s/\sqrt{Pa}$ and $k_p = 50\text{-}Pa$ for Fabric B with speckles. The updated relation is that given by Equation 4.5 using the constants in Table 4.2 for the appropriate fabric. All the details of the new porosity relation's development may be found in Section 4.3.

Applying the new porosity to the panel method simulation, the results show small effects on u/V_∞ and $\partial(v/V_\infty)/\partial x$, however, $(v/V_\infty)\frac{180}{\pi}$ is lowered by up to 0.5 degrees as in Figure 5.17(b) at $C_{l,max}$. This result is a direct consequence of a lower magnitude of v_{normal} through the Kevlar which mitigates the far-field angle of attack reduction described by the flow mechanism in Figure 2.1(b). The lower v_{normal} values may be observed in Figure 5.20 which compares simulated v_{normal} values for Runs 2-3 and 3-3 at 12 degrees angle of attack using both the original and updated porosity relations.

For the Campaign 2 result, Run 2-3, as in Figure 5.20(a), using the updated porosity relation reduces v_{normal} by 20-25% at each streamwise location along the test section. The removal of the artificial strain effect on porosity accounts for a 17% reduction, improvements to the porosity test apparatus such as to reduce edge leakage account for another 13% reduction, and the non-dimensionalization of the relation actually increases the porosity to make up the remainder. Unlike the removal of the strain effect and the update of the test apparatus, the non-dimensionalization of the porosity relationship described in Section 4.3 has only a minor effect on the final corrected data. For instance, considering a difference of 10% between the air density in the porosity characterization tests and the tunnel tests, the simulated v_{normal} will only be in error by 5% according to the non-dimensionalization. Changes in v_{normal} already have only a second-order effect on the final corrected quantities, so the effect of using the non-dimensionalized relationship is small.

For the Campaign 3 result, Run 3-3, as in Figure 5.20(b), using the updated porosity relation reduces v_{normal} by a substantial 65-70%. This time, the reduction is overwhelmingly dominated by the removal of the artificial strain effect. The reason for the heightened sensitivity to the strain effect in the case of Campaign 3 is that the effect, given by Equation 2.49, does not scale with the porosity of the fabric. Therefore, when the Kevlar porosity drops by more than a factor of three from Campaign 2 to Campaign 3, the strain correction balloons into a nonphysical value of the same order as the nominal porosity itself.

In terms of the lift performance, the reduction in v_{normal} due to the new porosity relation and associated change in v/V_∞ translate to a decrease in the $C_{l,c}$ slope in all four subfigures of Figure 5.19. At the highest measured angle of attack for Figure 5.19(d), removing the error due to the strain correction lowers $C_{l,c}$ by over 0.07.

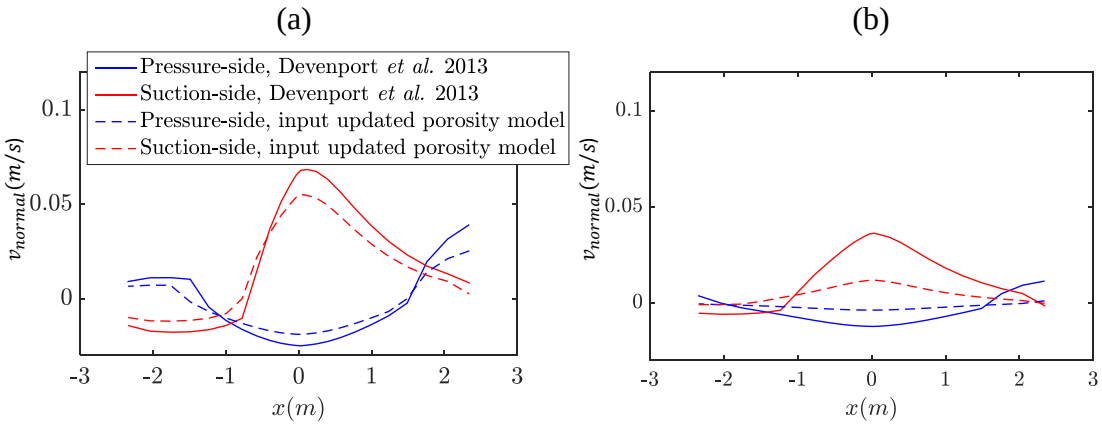

Figure 5.20: Simulated normal velocity through the Kevlar walls, v_{normal}, vs. distance along the test section, x, for (a) Run 2-3 and (b) Run 3-3 at 12 degrees geometric angle of attack. Results are shown with the porosity relation of Devenport *et al.* and with that of the present study. Positive values of v_{normal} indicate transpiration *into* the test section.

5.3.2 Wall Boundary Layer

The growth of the boundary layer along each of the four test section walls is not yet included in the panel method correction of Devenport *et al.* which leads to an under-prediction of the pressure drop through the test section. The development of the boundary layer segment of the panel method code is detailed in Appendix B. As described in the appendix, the boundary layer segment meshes with the deflection iteration loop so that no additional nested loops are added to the panel method.

Applying the boundary layer model to the panel method simulation, the trend on the correction performance is small but consistent. In every case of Figure 5.16, inclusion of the boundary layer decreases u/V_∞ while having no sensible effect in Figures 5.17 or 5.18 on v/V_∞ or $\partial(v/V_\infty)/\partial x$, respectively. The physical explanation is that the boundary layer creates a pressure gradient through the test section. This change induces some flow to divert out of the test section and bypass the model as demonstrated by the flow mechanism in Figure 2.1(a).

To illustrate this process, Figure 5.21(a)-(b) compares simulated wall C_p distributions with and without the boundary layer model in the Kevlar-wall test section. As before, the comparison is made for Runs 2-3 and 3-3 at 12 degrees angle of attack. Over the length of the test section, the presence of the boundary layer causes an additional 0.025 drop in C_p. This pressure gradient is created by the growing wall boundary layer which constricts the test section area and accelerates the inviscid flow as it moves through the test section. The pressure gradient created by the boundary layer then alters the distribution of v_{normal} as plotted in Figure 5.21(c)-(d). Note that the v_{normal} values plotted correspond only to the porous flow through the Kevlar and do not include the added transpiration velocity of the boundary

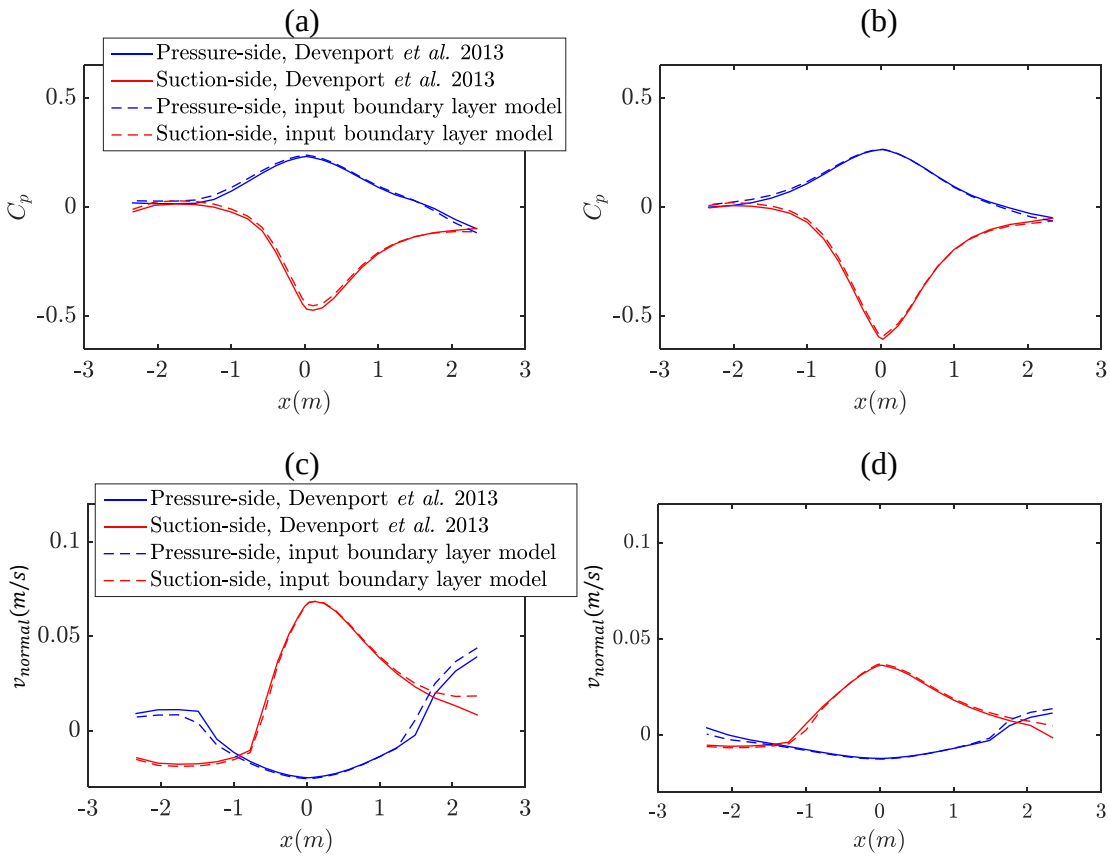

Figure 5.21: Simulated midspan wall C_p and v_{normal} through the Kevlar walls vs. distance along the test section, x, for (a,c) Run 2-3 and (b,d) Run 3-3 at 12 degrees geometric angle of attack. Results are shown with and without the wall boundary layer model present. Positive values of v_{normal} indicate transpiration *into* the test section.

layer model. Plotted in such a way, it can be seen that the presence of the boundary layer's pressure gradient increases the mass flow leaving the test section upstream of the model as is visible on both tunnel walls at $x < -1\text{-}m$. The extra mass flow then re-enters the test section downstream of the model as seen at $x > 1\text{-}m$. The net effect of this flow diversion mechanism is a reduction in mass flow and thus u/V_∞ at the model location. As shown in Figure 5.19, the reduction in u/V_∞ translates to an increase in $C_{l,c}$ at every positive angle of attack with a maximum increase of 0.012.

5.3.3 Wall Deflection

In Section 5.2, it was noted that the deformation magnitudes of the panel method simulation according to Devenport *et al.* are generally half of their measured values. One solution to this inconsistency is to bypass the low-fidelity finite difference solution of membrane

deflection used in the Devenport *et al.* approach by directly inputting measured deformation profiles into the panel method simulation. The deformation profiles were measured with the camera system described in Section 3.1.7, and introductory results were presented in Section 5.1. Deformation contours of all the runs introduced by Table 3.3 are also presented in Appendix C.4, for reference. The contours, which are mostly symmetric about the midspan plane, are averaged in the spanwise direction before being used in the two-dimensional panel method. With measured deflections being input to the code, the panel method solution no longer uses the deflection iteration loop described in Section 2.2.2.2.1.

The dependence of the simulated test section flow on the source of the wall deformation information is sizable, although general trends are hard to define. Upon inputting the measured wall deflections into the simulation, it was expected that $C_{l,c}$ would decrease relative to the solid-wall value since the measured wall deflections have greater magnitude than the simulated ones. The larger magnitude would thus narrow the effective test section height and reduce $C_{l,c}$ via the mechanism described by Figure 2.1(c). This was indeed the case for Campaign 3. However, the $C_{l,c}$ for Campaign 2 rises for Run 2-3 upon the input of the measured wall deflections as shown by Figure 5.19.

The unexpected rise in $C_{l,c}$ upon the input of the measured deflections into the simulation is firstly traced to a larger magnitude of v/V_∞ which can be verified in Figure 5.17(b). Typically, it has been believed that the only Kevlar-related mechanism to alter the effective angle of attack is the porosity as demonstrated in Figure 2.1(b). On the contrary, Figure 5.17(b) indicates that the Kevlar walls' deflection is having a measurable impact on the angle of attack experienced by the model. The physical reasoning is that the walls on both the suction and pressure sides deflect in the direction opposite the lift and thus channel the flow in that direction. If the apex of the deflections of both walls are not centered on the model's quarter-chord, then the flow will still be angled in the direction opposite the lift when it reaches quarter-chord. In such a scenario, wall deflection contributes to v/V_∞. The reason for the more negative v/V_∞'s in Campaign 2 over Campaign 3 is seemingly the asymmetry with respect to the quarter-chord location present in the suction-side deflection distribution for Campaign 2 as shown in Figure 5.15(a).

The unexpected rise in $C_{l,c}$ upon the input of the measured wall deflections into the simulation is also traceable to a lower u/V_∞ which can be verified in Figure 5.16(b). It is reasonable to question whether the Kevlar deflection may have reduced u/V_∞ simply because the cross-sectional flow area through the test section increased due to the deflection. Figure 5.22 confirms this hypothesis at a local level by comparing simulated C_p's along the wall with both simulated and measured wall deflection profiles. As before, the comparison is made for Runs 2-3 and 3-3 at 12 degrees angle of attack. For Run 2-3 in Figure 5.22(a), the pressure-side C_p near the quarter-chord rises upon the input of the measured wall deflections relative to the simulated ones. The reason is that the measured profiles in Figure 5.15(a) on the pressure side are more exaggerated than the simulated ones and allow for greater flow expansion and thus deceleration in the vicinity of the wall. Looking instead at a different installation of the Kevlar from Campaign 3 as in Figure 5.22(b), the increase in deflection

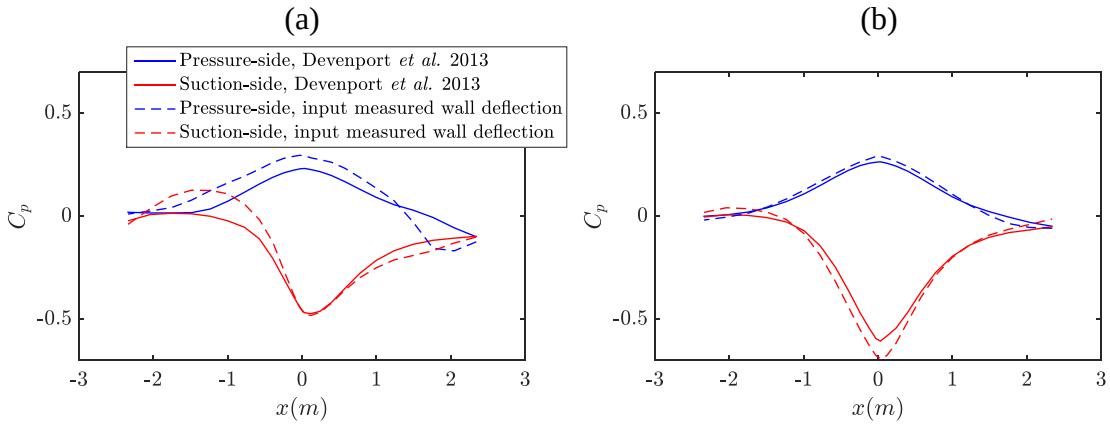

Figure 5.22: Simulated wall C_p at the midspan of the Kevlar walls vs. distance along the test section, x, for (a) Run 2-3 and (b) Run 3-3 at 12 degrees geometric angle of attack. Results are compared between simulated and measured wall deflections being input into the simulation.

and thus C_p magnitude on the suction side this time dominates and acts to reduce the overall flow area of the test section. In this case, the blockage at the model location is increased.

Finally, it is apparent from Figure 5.15 that streamline curvature is also being affected by the wall deflection, and this effect is captured by the $\partial(v/V_\infty)/\partial x$ term in Equations 2.33, 2.34, and 2.35. Indeed, inputting the measured wall deflections into the Devenport *et al.* model produces a noticeable increase in $\partial(v/V_\infty)/\partial x$ as shown by Figure 5.18. This third new mechanism of Kevlar-wall interference increases $\partial(v/V_\infty)/\partial x$ at the model location and works to lower $C_{l,c}$.

In spite of the increase in $\partial(v/V_\infty)/\partial x$ upon inputting the measured wall deformations, the data from Campaign 2 see an overall rise in $C_{l,c}$ due to reduced u/V_∞ and more negative v/V_∞. The maximum increase in $C_{l,c}$ is 0.062 as in Figure 5.19(b). For Campaign 3, the increase in $\partial(v/V_\infty)/\partial x$ is aided by an increase in u/V_∞ which together act to lower $C_{l,c}$ by as much as 0.106 as in Figure 5.19(d).

An interesting consequence of inputting the measured wall deformations is the spike in u/V_∞ at low angles of attack for Campaign 3. This spike occurs because the less porous fabric of Campaign 3 is able to sustain higher pressure differences across its thickness by nature. It therefore experiences little pressure relief from the suction field imposed on it by the model's blockage at low-lift. The result is that the fabric gets pulled into the test section, increasing u/V_∞. This suction effect is manifest as a pronounced drop in C_p in both the wall pressures of Figure 5.13(d) and the chamber pressures around zero-lift of Figure 5.14(b).

5.3.4 Wall Pressure Difference

Both the flow-side and chamber-side C_p's are critical boundary conditions of the Kevlar-wall test section, in part, because together they govern the mass flow into and out of the test section via porous flow through the walls. In Section 5.2, it was noted that there were inconsistencies between the panel method simulation and experimental results both in terms of the flow-side wall C_p's, as well as the chamber-side C_p's. The former was most obvious in the lack of simulated pressure gradient through the test section. In the latter, there were errors especially in the suction-side simulations of the chamber C_p which is believed to be due to un-modeled leakage paths between the chambers. In an attempt to side-step these inconsistencies, it is possible to directly input the measured wall pressure differences into the simulation. To the accuracy of the porosity relation, this is equivalent to inputting measured wall porosities into the simulation. With measured porosities being input to the code, the panel method solution thus no longer uses the porosity iteration loop described in Section 2.2.2.2.1.

Direct input of the measured wall pressure differences has been implemented in the panel method simulation, and the most apparent effect on the correction parameters is on u/V_∞ as in Figure 5.16. For three out of the four subfigures of Figure 5.16, u/V_∞ increases slightly at low angles of attack compared to the Devenport *et al.* result, and the opposite happens at high angles of attack. Little weight is given to the increase in u/V_∞ at low angles of attack since the scatter in the measured wall C_p's becomes relatively large at low angles of attack. At high angles of attack, the reason for the reduced u/V_∞ is illustrated by Figure 5.23 for Runs 2-3 and 3-3 at 12 degrees angle of attack. Comparing Figure 5.23(a) with Figure 5.21(c), it is apparent that using the measured wall pressure differences for Campaign 2 has the same effect on the v_{normal} distributions as does adding the boundary layer model: to increase the flow diversion mechanism around the model. In both cases, the driving force behind the diversion is the presence of a pressure drop through the test section. Figures 5.23(a) and 5.21(c) indicate that the pressure gradient and flow diversion imposed by using the measured wall pressure differences in the simulation is larger than that implied simply by the wall boundary layer effect. The extra strength of pressure gradient is due to the blocking effect of the re-entrant flow from the suction-side wall. The resulting rise in $C_{l,c}$ using the measured wall pressure differences for Campaign 2 is as large as 0.072 for Run 2-3 as seen in Figure 5.19(b). For the Campaign 3 results, Run 3-3, as in Figure 5.23(b), using the measured wall pressure differences increases the porous flow into the test section on the suction side due to the lower absolute value of the measured chamber C_p with regards to the simulated one. The pressure gradient through the test section is smaller due to the lower porosity of the Kevlar, and so the effect of using the measured wall pressure differences is more muted than in Campaign 2. The resulting changes in $C_{l,c}$ using the measured wall pressure differences for Campaign 3 are always less than 0.008 as seen in Figure 5.19(b) and (d).

A strange feature of the measured chamber C_p's is an outlier that is present in the subfigure

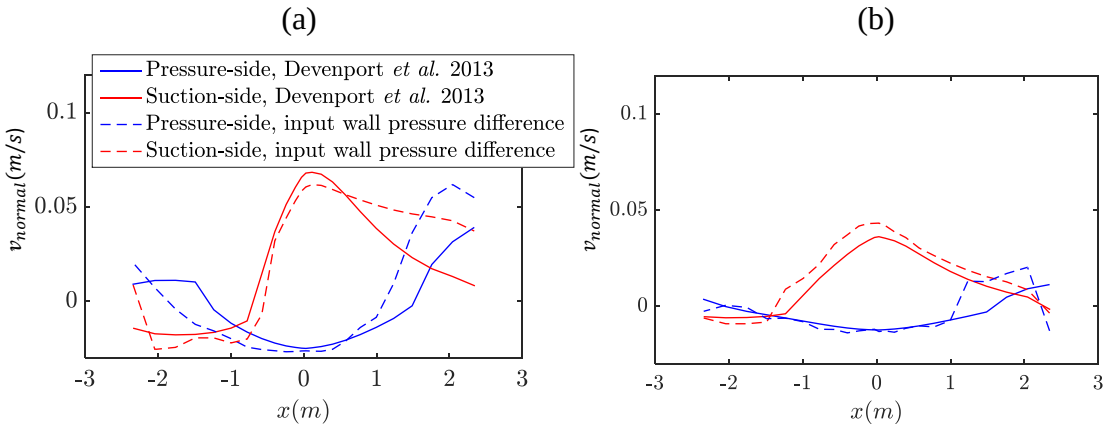

Figure 5.23: Simulated normal velocity through the Kevlar walls, v_{normal}, vs. distance along the test section, x, for (a) Run 2-3 and (b) Run 3-3 at 12 degrees geometric angle of attack. Results are shown with wall porosities being calculated both from simulated and measured pressure differences across the wall. Positive values of v_{normal} indicate transpiration *into* the test section.

(d) of each of Figures 5.16 5.17, 5.18, and 5.19. The outlier is particularly obvious in Figure 5.16(d). This data point was the first in the polar sweep sequence, and it is believed that there was insufficient time for the chambers to become fully pressurized before the data acquisition began. Consideration of pressurization time for the anechoic chambers have not been evaluated previously.

5.3.5 Combined Inputs

Plotted alongside the perturbation studies is the effect of all the new inputs combined which is termed the *combined inputs model*. Note that for this model, the panel method simulation has direct input of the wall deformation and wall pressure difference, so no iterating is necessary for those purposes. Iterations do still take place, however, to update the reference velocity in panel method which scales the transpiration velocities, boundary layer growth, and model singularity strengths. Convergence is reached when the change in the reference velocity is less that 0.0001% which typically occurs after 4-5 iterations.

For the Campaign 2 data in Figure 5.19(a)-(b), the $C_{l,c}$ of the Devenport *et al.* model and the combined inputs model are in reasonable agreement. For the reference run condition at the lower dynamic pressure as in Figure 5.19(a), using the combined inputs model results in a maximum $C_{l,c}$ drop of ∼0.04, locating the Kevlar-wall data just below the solid-wall value. The higher dynamic pressure case in Figure 5.19(b) illustrates quite nicely the presence of compensating errors in the Devenport *et al.* model. For example, Figures 5.16(b) and 5.17(b) show that inputting the measured deflections to the Devenport *et al.* model reduces u/V_∞

and v/V_∞, both of which effects increase $C_{l,c}$ for a given corrected angle of attack. Conversely, inputting the updated porosity relation reduces $C_{l,c}$ which is a direct response to a decrease in the magnitude of v/V_∞. Combining the inputs together along with the boundary layer input, we see virtually no change in $C_{l,c}$ between the Devenport *et al.* model and the combined inputs model. Thus, the overestimation of u/V_∞ noted by Devenport *et al.* was compensated for by errors in the porosity relation.

The comparisons for the Campaign 3 data again demonstrate the concept of compensating errors, however, now it is quite apparent that there are still hidden errors even in the combined inputs model of this study. The combined effect of the inputs is to lower the $C_{l,c}$ relative to that of the Devenport *et al.* model as shown in Figure 5.19(c)-(d). The main contributors to the lowered $C_{l,c}$ are the updated porosity relation input and the measured wall deflection input. For the porosity input at the higher dynamic pressure case, the non-physical correction to porosity based on strain from the Devenport *et al.* model had been playing a large role on the highly strained walls. Removal of this non-physical correction raises $C_{l,c}$. For the deflection input, inputting the measured deflections imposes more severe deflections on the walls which increases u/V_∞ in all cases due to the narrowing of the effective test section width.

5.4 Sources of Residual Error in Modified Correction Method

Given the advances in the knowledge-base for Kevlar-wall test sections noted above, it is also clear that some test section aerodynamics are still not fully understood. This can be reasoned since the overall result of the combined inputs model does not always produce exact comparison with the solid-wall test section results. Particularly, the correction to lift is too strong in three out of the four cases of Figure 5.19. To identify the root cause of the residual errors, the airfoil $C_{p,c}$'s and wall C_p's derived from the combined inputs model are considered next.

Figure 5.24 shows the airfoil $C_{p,c}$ distributions between campaigns after correction with the combined inputs model. These results can be compared with those of Figure 5.12 which show the same data except corrected by the method of Devenport *et al.* For Campaign 2, the combined inputs model still slightly over-predicts blockage, though now the over-prediction occurs predominantly when there is low rather than high loading on the walls as was the case in Figure 5.12 . For Campaign 3, the large error due to the ballooning of the strain correction to porosity is now eliminated though there are still some deviations from the solid-wall data, especially on the suction side of the airfoil.

Figure 5.25 compares the wall C_p distributions between the measurement and the simulation using the combined inputs model. The comparison is notably more favorable than for the

original Devenport *et al.* model shown in Figure 5.13. Specifically, the porosity-induced pressure drop through the test section described in Section 5.1 is now captured in all cases which is a result, even more so than of the boundary layer model, of the input of measured wall deflections and wall pressure differences. As with the airfoil C_p distributions, the wall C_p distributions from Campaign 2 also indicate that the simulation is over-predicting blockage around the model location. An explanation is that there is unaccounted for diversion and re-circulation of flow from the test section via the floor and ceiling panels.

While the over-prediction of blockage for the case of Campaign 2 may explain the lift curve misalignment in Figure 5.19, the wall C_p distributions for Campaign 3 offer no evidence that the blockage prediction is wrong. Rather, based on the lift results of Figure 5.19, it is reasonable to suggest that the flow velocity coming from the suction-side wall could be under-predicted in the panel method simulation of Campaign 3. Even with the detailed measurements of Section 4.3, there should be further work in characterizing the porous nature of the Kevlar. First, it should be stated that the in-tunnel pressure differences experienced by the Kevlar require extrapolation of the porosity measurements by almost half an order of magnitude in terms of pressure difference. As well, the application of the speckles onto the fabric used in Campaign 3 was not perfectly uniform, neither on the wind tunnel walls nor on the sample which generated the porosity coefficients. Potentially even more relevant, however, is that the porosity results should be measured in the presence of a passing boundary layer. In-tunnel measurements are therefore suggested as performed in transonic studies of perforated wind tunnel walls[31, 32, 33, 34]. The predictions given indicate a boundary layer thickness effect on porosity that has not been considered in Kevlar-wall testing up until this point.

Another potential error source is flow paths for leakage other than directly between the two anechoic chambers. Some evidence exists for such paths based on the combined inputs model presented above. In the combined inputs model, the velocities into and out of the test section are specified by measured pressure differences and should be trustworthy. Summing the mass flows from each chamber leads in some cases to large volumes of unaccounted leakage flow as shown in Figure 5.26. For Run 2-3 in Figure 5.26(a), this leakage flow is significant; roughly 50% of the total flow into the test section at $C_{l,max}$ comes from another source other than the opposite chamber. It is hypothesized that flow is seeping out of the test section from the floor and ceiling panels upstream of the model which also explains the underestimated blockage in Figure 5.25(b)-(c). Consideration of floor and ceiling flow should therefore be a consideration of future efforts.

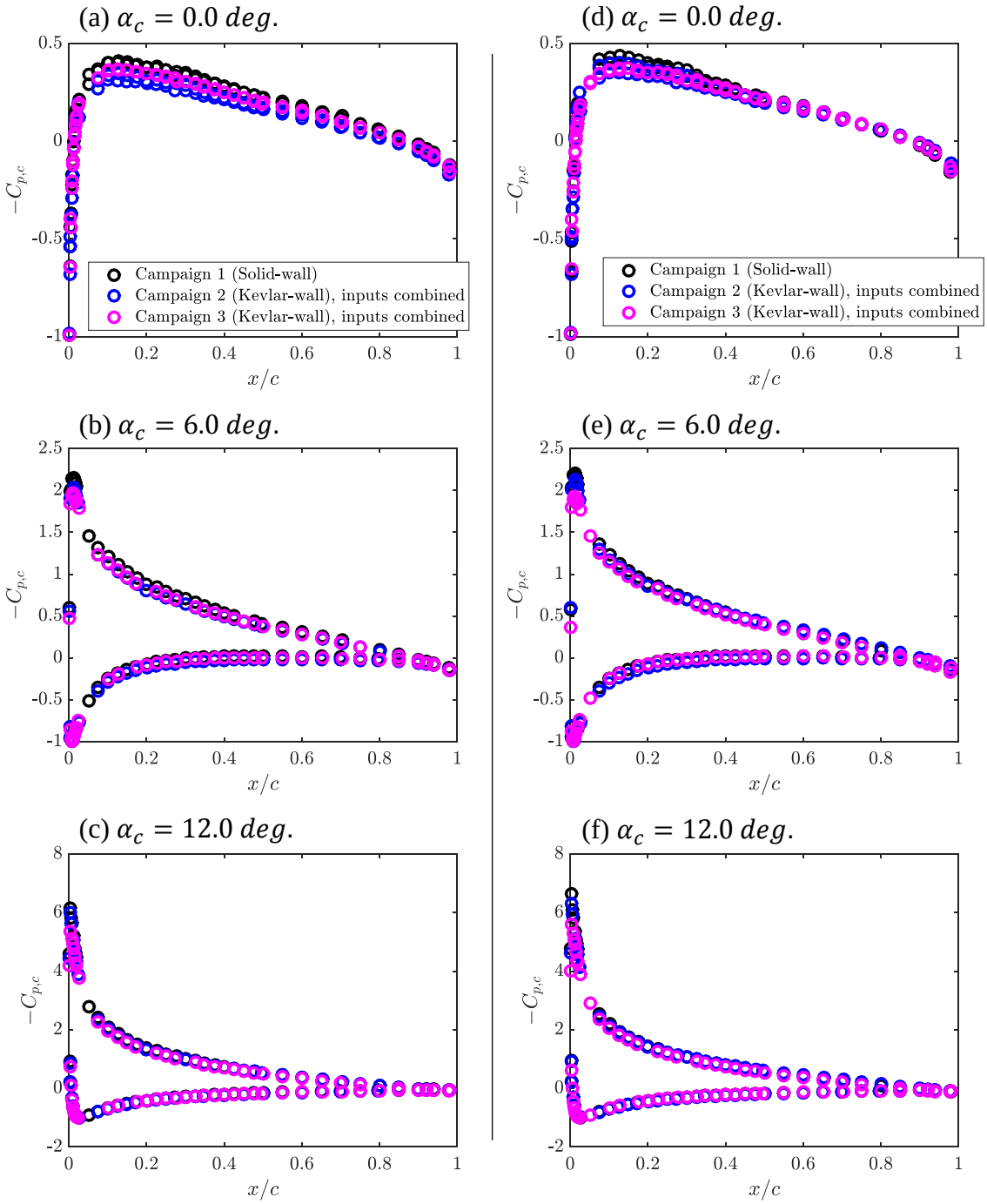

Figure 5.24: Corrected pressure coefficient, $C_{p,c}$, versus chordwise position, x/c, for the NACA0012 using the combined inputs model. In descending order of the legend, the runs in (a)-(c) are Run 1-2, Run 2-2, and Run 3-2. The runs in (d)-(f) are Run 1-3, Run 2-3, and Run 3-3. Small angle of attack offsets have been applied as noted in Appendix C.1, and the corrected angles have been interpolated to the reported nominal values. Corrections applied according to Appendix A.

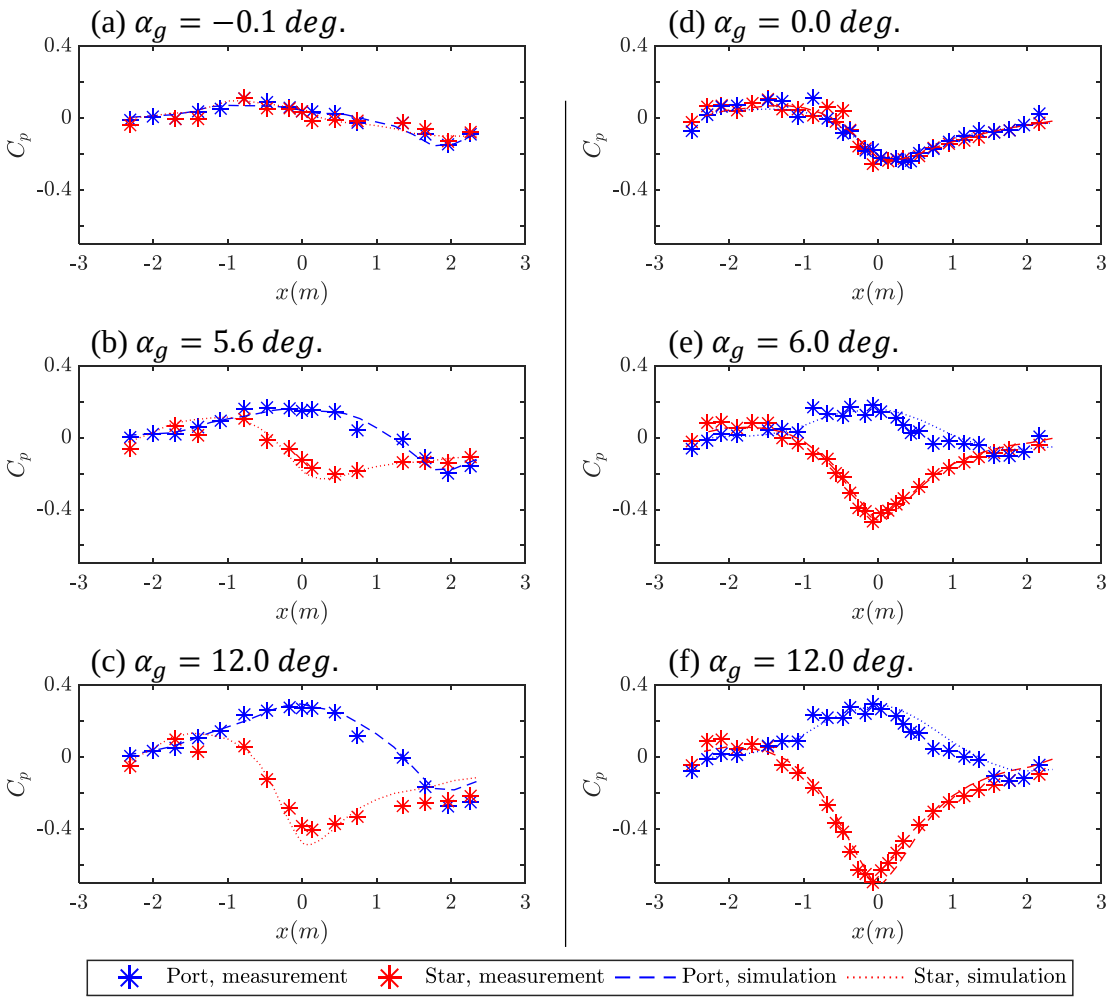

Figure 5.25: Wall pressure coefficient, C_p, vs. streamwise location, x, for (a)-(c) Run 2-3 and (d)-(f) Run 3-3. The simulations are performed using the combined inputs model.

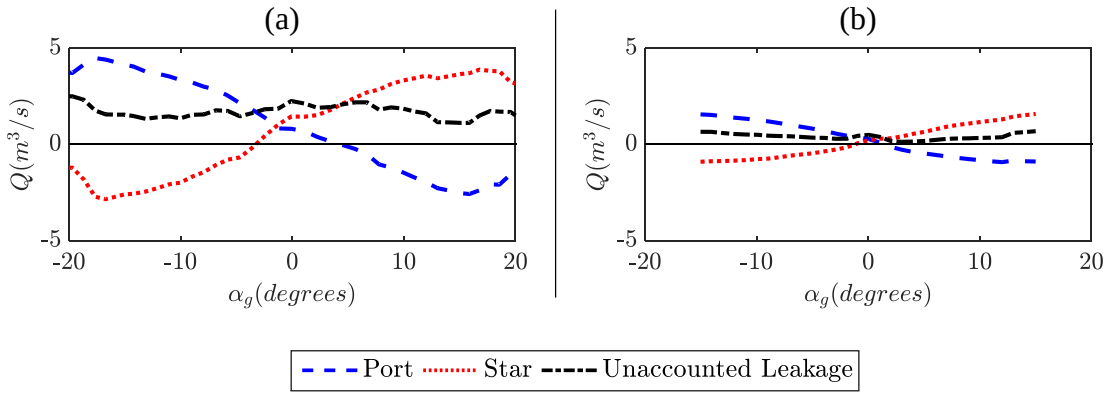

Figure 5.26: Volumetric transpiration flow, Q, vs. angle of attack, α_g, for (a) Run 2-3 and (b) Run 3-3. Positive values of Q indicate transpiration *into* the test section.

5.5 Sensitivity of Wall-Interference to Key Test Section Parameters

Given the residual errors in the correction technique as described in the previous section, it is here considered the sensitivity of the wall-interference to key parameters in the Kevlar-wall test section modeling and design. In this section, first will be performed a parameter study on the key modeling inputs to the panel method simulation, followed by discussion of the optimal test section design for minimum wall-interference.

5.5.1 Parameter Study of Key Modeling Inputs

A parameter study was performed using the panel method simulation to assess the sensitivity of the simulation to key inputs. The motivation for such a study is dual-purposed: (1) to determine which inputs should be examined most rigorously during the continued development of wall-interference corrections schemes for Kevlar-wall test sections, and (2) to lay the framework for the discussion on the optimum configuration for Kevlar-wall test sections to be made in the following section. The inputs to be studied related to the porosity of the Kevlar are: OAR, A_{leak}, a_{inflow}, K_c, K_n, and K_p. Based on the unspeckled version of Fabric B, the baseline values for each of these parameters are $OAR = 0.018$, $A_{leak} = 0.15\text{-}m^2$ $a_{inflow} = 2$, $K_c = 0.485$, $K_n = 0.56$, and $K_p = 4E4$. The baseline values related to the Kevlar flexibility are $T_0 = 1500\text{-}N/m$ and $E = 1.26E11\text{-}Pa$ assuming $h = 0.021\text{-}mm$. A parameter study is performed by varying each of these parameters individually over an appropriate range of values. The parameter study is performed using the 0.91-m chord NACA0012 data from Runs 3-1, 3-3, and 3-5 as tabulated in Table 3.3. These runs range in dynamic pressure from 770- to 3300-Pa, and comparisons are shown at nominal angles of attack of 6 and 12 degrees.

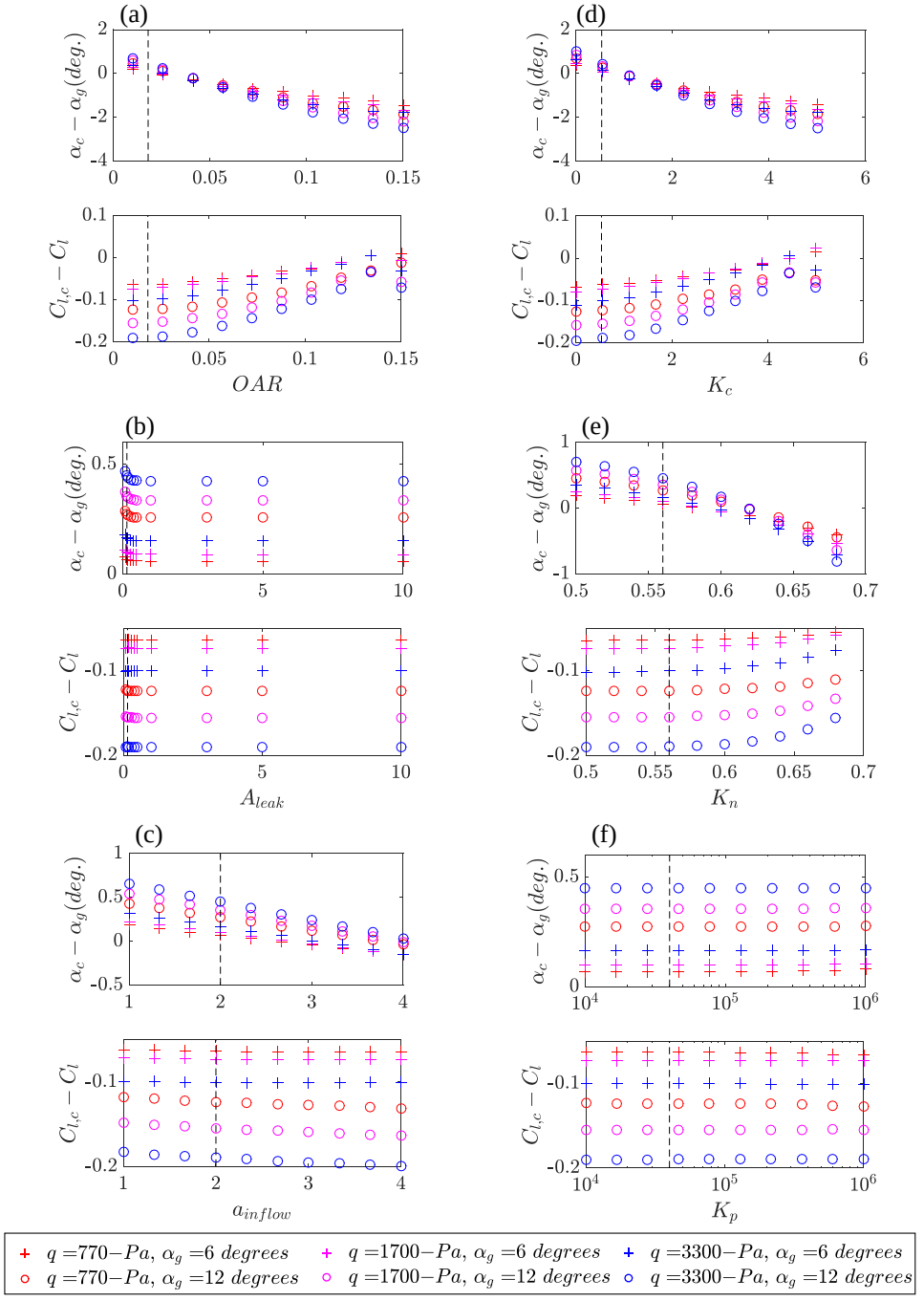

Figure 5.27: Effect of six key panel method inputs related to the porosity of the Kevlar walls on the resulting angle of attack correction, $\alpha_c - \alpha_g$, and lift coefficient correction, $C_{l,c} - C_l$, in the Kevlar-wall test section. The baseline values of each parameter are indicated by the vertical dashed lines.

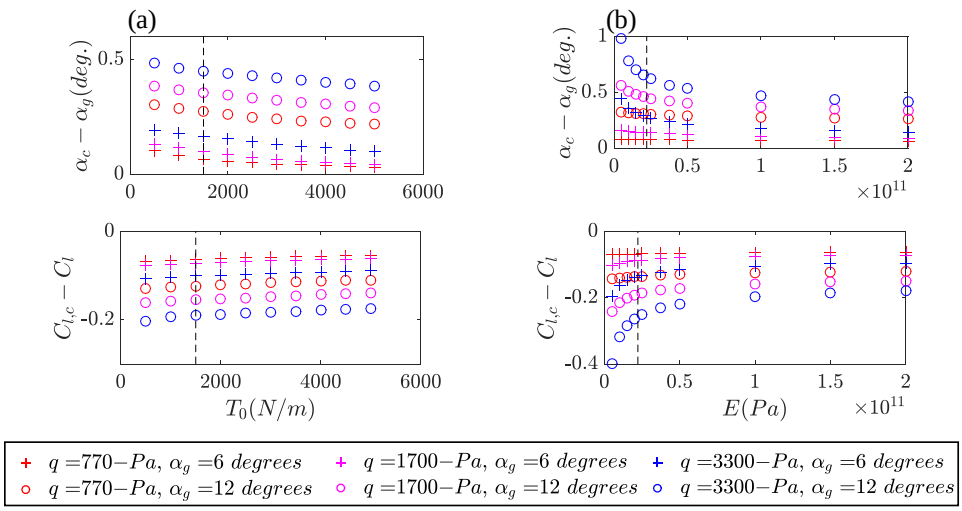

Figure 5.28: Effect of two key panel method inputs related to the flexibility of the Kevlar walls on the resulting angle of attack correction, $\alpha_c - \alpha_g$, and lift coefficient correction, $C_{l,c} - C_l$, in the Kevlar-wall test section. The baseline values of each parameter are indicated by the vertical dashed lines.

The effect of the parameter variations on both the total angle of attack correction and the lift coefficient correction in the Kevlar-wall test section are shown in Figures 5.27 and 5.28 for the porosity and flexibility parameters, respectively.

Figure 5.27(a) examines the wall interference over a range of values for the fabric's open-area ratio, OAR. This parameter is relevant for study because the effect of the Kevlar porosity on the test section aerodynamics is a function of the dimensional relationship between v_{normal} through the Kevlar and Δp across the Kevlar which has direct dependence on OAR according to Equation 4.6. Increasing OAR allows more porous flow through the Kevlar and moves the total angle of attack correction from positive, such as with a solid-wall test section, to negative, such as with an open-jet test section, due to the far-field reduction in effective angle of attack provided by wall porosity. Interestingly, for low angles of attack, the dependence of α_c on OAR fades away as OAR increases. The angle of attack reduction apparently is reducing the lift produced by the model to the extent that further opening of the Kevlar pores is self-regulated by lower loading and pressure difference across the Kevlar walls. The minimum correction for $C_{l,c}$ occurs as the porosity is maximized which is consistent with the concept of flow diversion out of the test section which reduces the blockage at the model location.

Figure 5.27(b) examines the wall interference over a range of values for A_{leak} which represents the effective leakage area between the two anechoic chambers as described in Section 2.2.2.2.1. Assuming a leakage area more than 0.1-m^2, there is relatively low sensitivity of the Kevlar-wall aerodynamics to A_{leak} within the range of values simulated. As A_{leak} increases towards

the limit of completely unsealed anechoic chambers, the pressure differences and thus transpiration across the Kevlar will be exaggerated resulting in $\alpha_c - \alpha_g$ falling closer to zero and $C_{l,c} - C_l$ becoming more negative.

Figure 5.27(c) examines the wall interference over a range of values for a_{inflow}. As introduced in Section 2.2.2.2.1, a_{inflow} scales the velocity of the flow re-entering the test section from the anechoic chambers to model the blockage created in the actual tunnel by flow re-entering the test section with zero streamwise momentum. The nominal a_{inflow} is based on the physical insight that the re-entrant flow decelerates a portion of the test section flow of equal volume which, according to continuity, causes expansion to twice its original volume. Finally, it may be concluded that the total blockage created by the re-entrant flow is two times the volume of the re-entrant flow itself. This value has not been verified experimentally, and as suggested by studies of perforated wind tunnel walls in the transonic community, there is reason to believe a_{inflow} should be greater than two depending on how the wall boundary layer develops. The parameter study shows a relatively strong effect of a_{inflow} on the angle of attack correction and a more moderate one on the lift coefficient correction.

Figure 5.27(d) examines the wall interference over a range of values for K_c which specifies the constant of proportionality between Π_1 and Π_2 of Equation 4.5. Figure 5.27(d) is nearly identical to that of OAR in Figure 5.27(a) since it is the factor $K_c OAR$ which governs the effect of the Δp across the Kevlar on the v_{normal} through the Kevlar as seen in Equation 4.6. Just as with OAR, increasing K_c allows more porous flow through the Kevlar and moves the total angle of attack correction from positive to negative due to the far-field reduction in effective angle of attack provided by wall porosity. The minimum correction for the lift coefficient occurs as the porosity is maximized which is consistent with the concept of flow diversion out of the test section.

Figure 5.27(e) examines the wall interference over a range of values for K_n which specifies the power-law relationship between Π_1 and Π_2 of Equation 4.5. While the lift coefficient correction is relatively insensitive to the coefficient, the angle of attack correction decreases from positive to negative values with increasing exponent for the same reason as cited above for K_c.

Figure 5.27(f) examines the wall interference over a range of values for K_p which represents the value of $(\Pi_1)^4$ where the transition takes place between the lower and higher Reynolds number regions of the porosity curve. Wall-interference correction is not significantly affected by K_p over the entire parameter range; the total variation within any given test condition is less than 0.02 degrees for the angle of attack correction and within 0.003 for the lift coefficient correction. Therefore, it can be concluded that the low Reynolds number range of the pore flow as discussed in Section 4.3.3 does not have a significant influence on test section aerodynamics.

Figure 5.28(a) examines the wall interference over a range of values for T_0 which represents the pre-tension in the Kevlar walls. Increasing T_0 reduces the magnitude of the wall deflections which decreases the magnitude of $C_{l,c} - C_l$ due to a larger effective test section width.

Similarly, the larger effective test section height reduces the streamline curvature correction so that $\alpha_c - \alpha_g$ tends towards more negative values as T_0 increases.

Figure 5.28(b) examines the wall interference over a range of values for E which represents the effective modulus of elasticity of the woven Kevlar fabric. The observed results are explained by the same phenomena of the previous paragraph because higher E decreases the deflection magnitudes. It is interesting to note that the value of E is actually irrelevant for the low dynamic pressure cases and angles of attack because at these conditions the membrane deflection is linearly behaved. At higher loadings, geometrically non-linear membrane deflection becomes dominant, so E comes into play and has a strong influence on the correction magnitudes.

Considering the relative uncertainty of each parameter over the range of values studied, the inputs that have the most noteworthy effects on the test section aerodynamics are the product of K_cOAR, as well as a_{inflow}, T_0, and E. All of these have been characterized by the measurements of Chapter 4 although some areas for improvement exist. Notably, the value of a_{inflow} in the presence of a crossing boundary layer should be studied in further work.

5.5.2 Test Section Design

The data of the previous section lend itself to considering the optimum configuration for Kevlar-wall test sections. Before discussing the specifics of the test section design, a note is given about the philosophy of reducing wall-interference in Kevlar-wall test sections.

The hope of reducing wall-interference via appropriately tuned Kevlar-wall test sections must be handled with care. Initially, the porosity of a Kevlar wall appears to be quite favorable from an interference standpoint because it reduces the far-field effective angle of attack. This reduction counters the increase in angle of attack due to streamline curvature. However, the far-field reduction has not fundamentally reduced the uncertainty of the measurement in the same way that it would using a wider tunnel, for instance. In the case of the wider tunnel, the correction magnitudes become smaller, so errors in the correction model will have diminishing effect on the corrected quantities. In the case of the far-field reduction in angle of attack, the overall correction magnitude is smaller than if the far-field reduction were not present, but the correction model has become more complicated. We now have two additive corrections that are both of the same order of magnitude. The probability distribution for the sum of two random variables is equal to the root-sum-square of the two random variables. Thus, the uncertainty in the corrected angle of attack may even be larger with the far-field reduction than without it.

The same philosophy may not, however, apply in full to blockage corrections since these are multiplied into the corrections equations. Reducing blockage via the use of a specific configuration of a Kevlar-wall test section over a solid-wall test section does, in fact, reduce the uncertainty of the final corrected quantities. This last conclusion only holds true, how-

ever, if the prediction of the blockage reduction maintains a certain level of precision. As such, reducing blockage via Kevlar walls is not as effective as using a wider solid-wall test section, for instance. For the latter, the accuracy of the correction has not changed, and the magnitude has still decreased.

With the above philosophy of wall interference correction in mind, the optimal configuration of Kevlar-wall test sections for minimum wall-interference is now considered. Once the test section dimensions have been chosen, there are three further design decisions that affect the wall-interference characteristics: Kevlar stiffness, Kevlar porosity, and sealing of the anechoic chambers.

For the Kevlar stiffness, it is recommended to increase the pre-tension of the Kevlar to as large a value as possible so that the sheet does not tear from the boundaries when placed under full loading. Larger pre-tensions lead to smaller deflections under loading which mitigates the blockage increase of Kevlar-wall test sections due to the wall deflection and effective narrowing of the test section width. Smaller deflections also imply less contribution of the Kevlar deflection to the far-field angle of attack change. If the option exists to also increase the modulus of the Kevlar by using a different fabric type, this option seems best since the Kevlar would then be stiffer. A stiffer fabric means that less pre-tension is required in order to maintain similar levels of deflection under wind loading.

For the Kevlar porosity, it is recommended to keep this as low as possible. This guideline follows from the discussion about the increased uncertainty due to the far-field angle of attack correction. While it is true that the blockage in the test section is inversely proportional to the porosity, it is believed that it is most imperative to reduce the uncertainty introduced into the correction problem due to the far-field angle of attack correction. Maintaining a lower porosity also maintains the pressure drop felt through the tunnel down to levels similar to those in a solid-wall test section. This is favorable from the point-of-view of reducing buoyancy drag.

For the sealing of the anechoic chambers, it appears that complete sealing is preferable though not required. As indicated by Figure 5.27(e), the leakage area has little effect on blockage but a strong effect on the angle of attack correction. As the leakage approaches zero, the far-field angle of attack correction diminishes since there are no longer any large pressure differences between chambers to drive the wall transpiration process. Thus, the completely unsealed test section appears less favorable, but the far-field correction magnitude is still manageable as shown in Figure 5.27(e).

5.6 Novel Kevlar-Related Interference Mechanisms

The data presented in this chapter have brought to light new information regarding the wall-interference mechanisms in Kevlar-wall test sections. The data in Figures 5.16, 5.17,

and 5.18, for instance, make it clear that there are some Kevlar-specific wall-interference mechanisms which are not encompassed in the three original mechanisms of Devenport *et al.* as reproduced in Figure 2.1.

Given the new understanding, Figure 5.29 is here proposed as a more systematic approach to identifying relevant mechanisms. A total of six separate mechanisms are shown which are generated from identifying an individual mechanism for both wall porosity and wall deflection as related to each of the three interference parameters in Figures 5.16, 5.17, and 5.18. It is logical that each of the six mechanisms will have some effect on the correction of aerodynamic data in Kevlar-wall test sections. To test this hypothesis, an explicit study of each mechanism has been carried out using the same runs as shown in Figures 5.16, 5.17, and 5.18. The validity of the proposed wall-interference mechanisms and their relative importance to the interference correction process will be judged under controlled conditions where the porosity and deflection are varied individually.

To validate the proposed mechanisms of Figure 5.29, Figures 5.30 and 5.31 show results from four different simulations of Runs 2-3 and 3-3, respectively. One simulation is run with both the porosity and deflection segments turned off. In another, porosity is included using the updated porosity relation given by Equation 4.5 using the constants in Table 4.2 for the appropriate fabric. The porosities are solved for using iteration as described in Section 2.2.2.2.1. In another simulation, the porosity segment is disabled and the deflection segment enabled. The deflections used are those measured experimentally as was done in Section 5.3.3. Finally, the simulation is run with the porosity segment and the deflection segment both enabled. The correction parameters u/V_∞, v/V_∞, and $\partial(v/V_\infty)/\partial x$ are queried from the simulation for each angle of attack.

Figure 5.29 (a) illustrates the effect of wall porosity on the blockage in the test section. The mechanism at work was originally detailed in Devenport *et al.* and is one of flow diversion which is most prevalent when there is a pressure gradient through the test section. This mechanism was demonstrated in Section 5.3.2 where higher static pressures upstream of the model caused flow to enter the anechoic chambers. The flow bypassed the model and returned to the test section downstream of the model. Such a course reduced the total mass flow around the model and thus the blockage in the test section. Figures 5.30(a) and 5.31(a) confirm that a drop in u/V_∞ occurs between the solid-wall simulation and the porosity-only simulation. The magnitude of the drop is steady at a u/V_∞ value of 0.03 for Figures 5.30(a) and 0.002 for Figures 5.31(a). The latter has much smaller magnitude because it corresponds to Campaign 3 which used the Kevlar with significantly lower porosity. In Devenport *et al.* the flow diversion mechanism was predominantly thought to operate when there is low loading on the walls, but here we see it steadily in effect over the full range of angles of attack.

Figure 5.29 (b) illustrates the effect of wall porosity on the effective far-field angle of attack experienced by the model. The mechanism works just as described in Devenport *et al.*; the loading on the walls induces porous flow through them which causes a net velocity in

the stream-normal direction. The loading direction is such that the effective far-field angle of attack is always reduced from the solid-wall case as seen in the porosity-only data of Figures 5.30(b) and 5.31(b). Again the magnitude of the reduction is much smaller for the case of Campaign 3 which used the lower porosity fabric.

Figure 5.29 (c) illustrates the effect of wall porosity on the upwash distribution experienced by the model. This effect is present because the porous flow through the Kevlar walls is not uniformly distributed. Previously, it was assumed that the change in stream-normal flow due to wall porosity could be simply summed up in the far-field correction discussed in the previous paragraph. There is, however, a small change in $\partial(v/V_\infty)/\partial x$ due to the adding of porosity to the solid-wall simulation as shown in Figures 5.30(c) and 5.31(c). The difference amounts to a drop in $\partial(v/V_\infty)/\partial x$ of 0.004, or 9%, for the Campaign 2 data in Figure 5.30(c) and a drop of 0.0013, or 3%, for the Campaign 2 data in Figure 5.31(c). These changes are relatively small and will have a near negligible effect on the final corrected quantities.

Figure 5.29 (d) illustrates the effect of wall deflection on the blockage in the test section. The mechanism at work was detailed in Devenport *et al.*, however, it only accounted for increases in blockage due to wall deflection. As Figure 5.30(a) shows, adding wall deflection to the solid-wall simulation can also produce a decrease in u/V_∞ at the model location. As demonstrated in Section 5.3.3, the physical reason for the change in u/V_∞ is the change in flow area through the test section caused by the deflecting walls. If the deflection distribution widens the flow area at the model location, then u/V_∞ will decrease as in Figure 5.30(a). On the other hand, if the deflection distribution narrows the flow area at the model location, then u/V_∞ will increase as in Figure 5.31(a). This finding is in contrast to the mechanism proposed by Devenport *et al.* as illustrated by Figure 2.1(c) which held that blockage increases with wall deflection irregardless of the direction of the deflection.

Figure 5.29 (e) illustrates the effect of wall deflection on the effective far-field angle of attack experienced by the model. As discussed in Section 5.3.3, the physical reasoning is that the walls on both the suction and pressure sides deflect in the direction opposite the lift and thus channel the flow in that direction. If the apex of the deflections of both walls are not centered on the model's quarter-chord, then the flow will still be angled in the direction opposite the lift when it reaches quarter-chord. This novel mechanism is explicitly confirmed in Figures 5.30(b) and 5.31(b). For the deflection-only data in these respective figures, the wall deflections lower $(v/V_\infty)\frac{180}{\pi}$ by up to 0.76 and 0.20 degrees which represent 37% and 37%, respectively, of the total v/V_∞. The effect of wall deflection on the far-field angle of attack represents an addition to the body of knowledge on Kevlar-wall test sections.

Figure 5.29 (f) illustrates the effect of wall deflection on the upwash distribution experienced by the model. This effect is present because the wall deflection is not uniformly distributed. As can be pictured from Figure 5.29 (f), the wall deflection impinges on the streamlines around the model and increases their curvature. This mechanism consistently increases $\partial(v/V_\infty)/\partial x$ by around a factor of two as shown in Figures 5.30(c) and 5.31(c). The effect of wall deflection on upwash represents an addition to the body of knowledge on Kevlar-wall

test sections.

At least five of the six mechanisms described above play a noticeable roll in wall-interference corrections for Kevlar-wall test sections with the exception being the change in upwash due to wall porosity. These six mechanisms serve as an update to the original three proposed by Devenport *et al.*

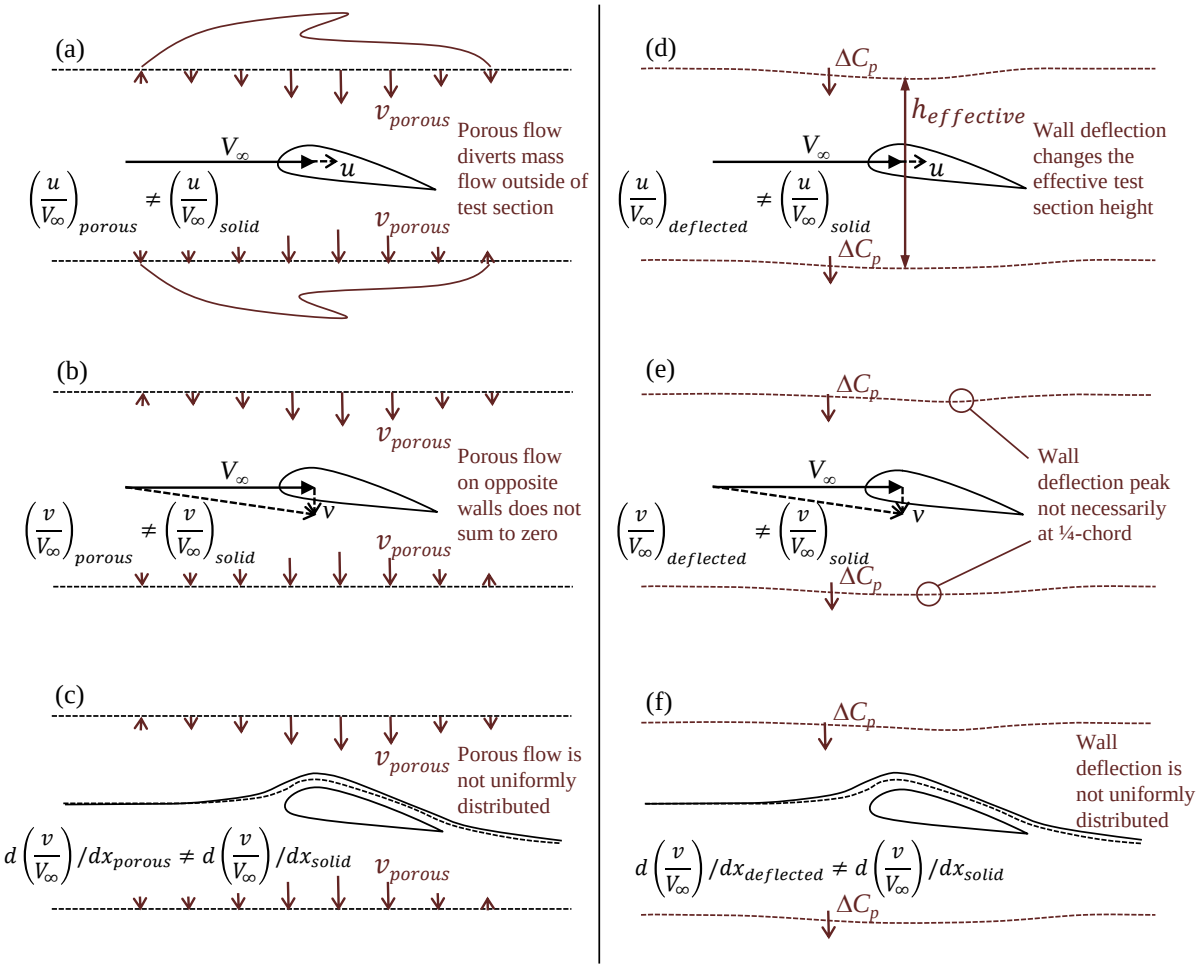

Figure 5.29: Updated schematic of Kevlar-related wall-interference mechanisms present in Kevlar-wall test sections. The left column shows the effects of wall porosity and the right column the effects of wall deflection. (a) and (d) pertains to blockage, u/V_∞, (b) and (e) pertain to angle of attack, α, and (c) and (f) pertain to upwash along the chord, $\partial(v/V_\infty)/\partial x$.

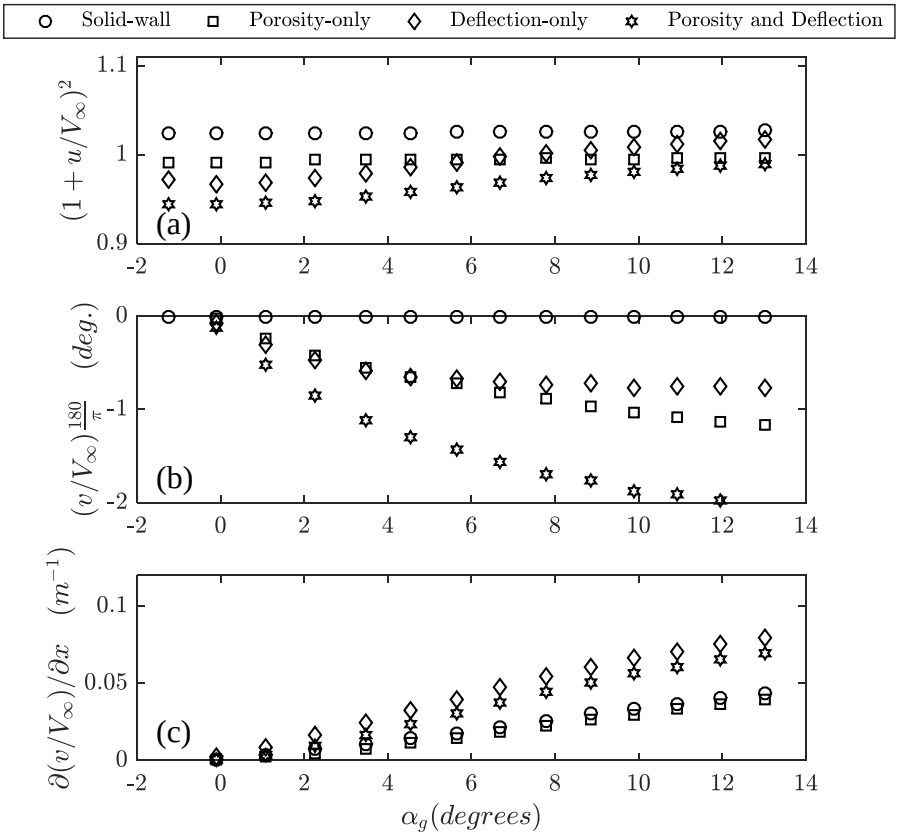

Figure 5.30: Correction parameters queried from the panel method simulation vs. angle of attack for Run 2-3 of Table 3.3. The panel method simulation is run in four different modes as shown in the legend.

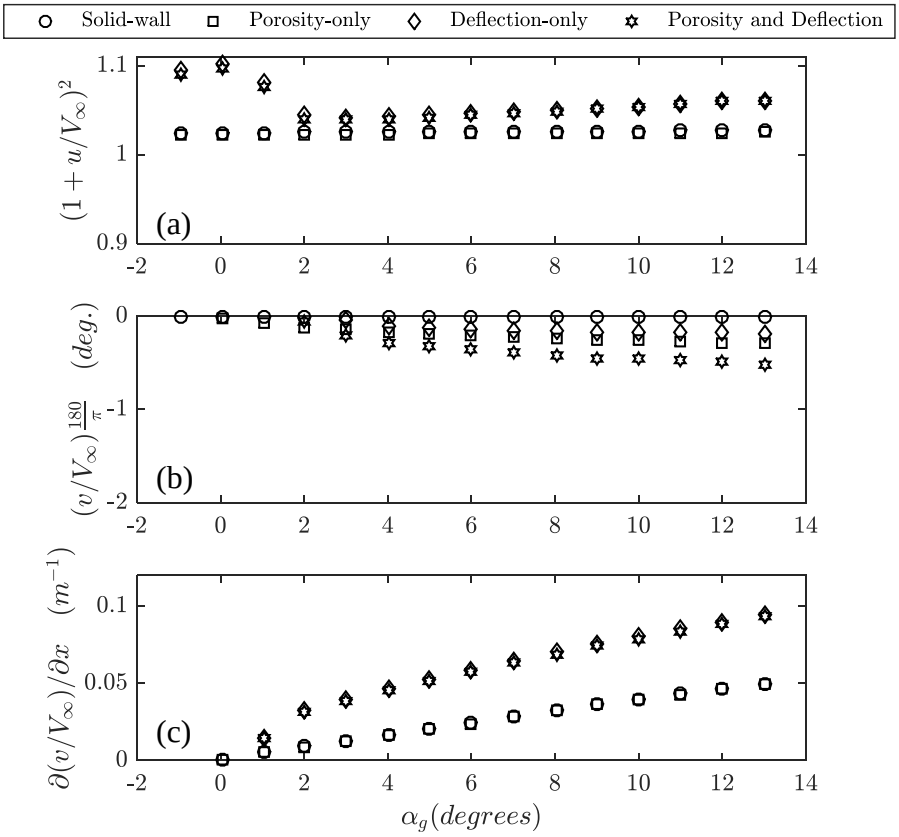

Figure 5.31: Correction parameters queried from the panel method simulation vs. angle of attack for Run 3-3 of Table 3.3. The panel method simulation is run in four different modes as shown in the legend.

Chapter 6

Interference Corrections for Three-Dimensional Models

As with the previous chapter, this chapter pertains to the second through fourth objectives of Thrust 1 in Chapter 2. Extension is here made, however, to a more general three-dimensional correction method which is valid for wings, as well as airfoils.

As noted in Section 2.2, there is some existing work in the literature comparing aerodynamic performance of the solid-wall and Kevlar-wall test sections for three-dimensional models[5, 38]. Here, the author seeks to develop and validate a three-dimensional version of the interference correction model presented by Devenport *et al.*[9]. This model was presented in preliminary form in [38] and is studied in full detail below.

6.1 Description of Three-Dimensional Panel Code

The three-dimensional method used in this study is built from panels of vortex rings of four straight vortex elements which are mathematically equivalent to panels of constant strength doublets[96]. The influence matrix is formed by evaluation of the Biot-Savart law between each vortex ring and the control point of each panel in the solution. The method proceeds by solving the set of linear equations that satisfies a Neumann boundary condition at each control point. This method is quite similar to the vortex lattice method although the vortex elements are made of rings rather than horseshoe vortices.

The four walls consist of vortex ring panels that are sized to match the cross-sectional dimensions of the wind tunnel of interest. The paneled length of the walls runs 16-m, or more than 8 tunnel widths, in the streamwise direction which matches the length-to-width ratio of Ulbrich [21] and exceeds that of Joppa [22] by a factor of 2. As in the two-dimensional panel code described in Chapter5, the panels in the streamwise direction are spaced more

densely near the model location according to 1.5-power law scaling. The reference velocity in the test section is queried on the tunnel centerline at a location 6-m upstream of the quarter-chord location.

6.2 Verification of Panel Code

Verification of the panel method code is performed first against theoretical solutions for the case of the solid-wall test section and then against the two-dimensional panel method of Chapter 5.

6.2.1 Solid-Wall Test Section

A convergence study yielded the appropriate values for the number of panels per wall in the streamwise and circumferential directions. The calculations compare the blockage and lift interference corrections for discrete singularities placed near the test section centerline with results produced by the method of images solution in Ulbrich[21]. First, an upstream-facing point doublet is used to simulate the effects of blockage in the test section. The diameter of the sphere produced by this point doublet was 1-m which imposes an extreme blockage ratio of 23% in a test section with the Stability Wind Tunnel's dimensions or 20% in a test section with the Low Speed Wind Tunnel's dimensions. Second, a semi-infinite line doublet which starts at the model location and trails downstream is used to simulate the effects of lift in the test section. Such a line doublet is only truly a good simulation of lift for a model that has small size with respect to the test section area, however, such an approximation is accepted for the current verification purposes. The strength of the line doublet is specified with a lift coefficient, model span, and model chord which took values of 1.5, 1.85-m, and 0.9-m, respectively. The potential flow equations for the point and line doublets, as well as the method of images solutions that were used for reference are found in Ulbrich. The method of images solutions employ 200 images above and below the test section as recommended by Ulbrich.

To simulate the wall interference in the panel method code, the boundary panel strengths are solved to satisfy the no-penetration boundary condition under the influence of the singularities and the freestream, and the interference factors calculated from the induced velocity of the walls at the model location. Plots of two convergence studies are shown in Figure 6.1. The quantities plotted, $\Delta u/U_\infty$ and $\Delta v/U_\infty$, express the perturbation to each velocity component induced by the test section walls. For the panel method data, the terms Δu and Δv are the result of the induced velocity component plus the difference of the realized freestream velocity with the specified freestream velocity for each velocity component. This addition was found necessary to match the method of images results for the $\Delta u/U_\infty$ case. As the number of panels in the streamwise direction in Figure 6.1a increases, the blockage and lift

interference produced by the point and line doublet, respectively, form asymptotes. Figure 6.1b similarly shows convergence as the number of circumferential panels per wall are increased. In both subfigures, the blockage results show larger deviations from the exact solution than the lift interference results. It was selected to use 90 streamwise panels and 16 circumferential panels per wall as this produces only 1.6% error and 0.0003% error for the blockage and lift interference, respectively, as compared to the method of images solution. Such paneling produces a total of 5760 wall panels as shown in Figure 6.2. Given the power law spacing in the streamwise direction, there are panels as short as 2.7-cm at the model location and as long as 26.5-cm near the test section entrance and exit. All the panels are a uniform 11.6-cm wide in the circumferential direction.

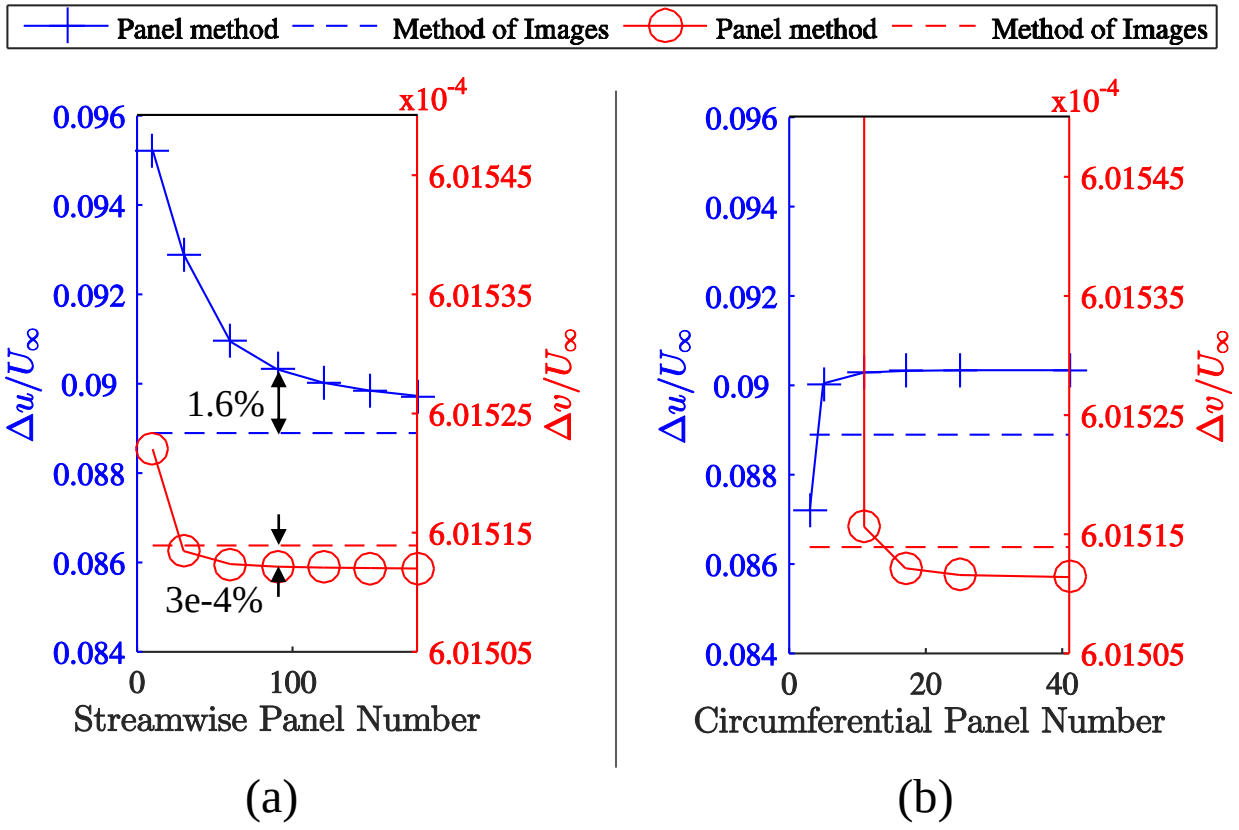

Figure 6.1: Convergence study on number of (a) streamwise panels per wall and (b) circumferential panels per wall. The blockage results are queried at the longitudinal center of the test section midway between the walls, and the lift interference results are queried at the longitudinal center and at a 0.1-m offset from the cross-sectional center in both the y- and z-directions. Results in (a) are performed with 16 circumferential panels and those in (b) are performed with 90 streamwise panels.

The above paneling parameters were furthermore verified by querying the interference values

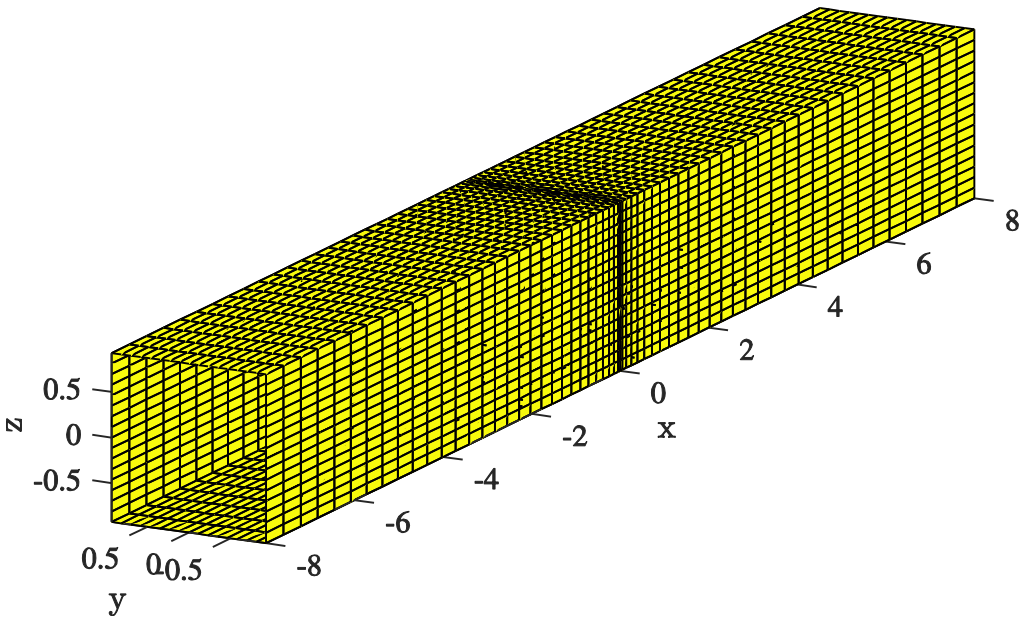

Figure 6.2: Wind tunnel paneling for three-dimensional panel method using the cross-sectional dimensions of the Stability Wind Tunnel. All dimensions are in meters.

at different streamwise and spanwise locations using the same point and line doublets described previously as shown in Figure 6.3. Here, the wall interference is evaluated at intervals along the tunnel centerline as in (a) and (c) and at intervals along the tunnel span as in (b) and (d). The disagreement near the extreme ends of the test section in (a) and (c) are end effects. In (a), the rise in centerline u-velocity near the test section ends is reasonably believed to be due to non-uniform inflow and outflow cross-sections resulting from the transition in local boundary conditions. In (c), the drop-off in the predicted v-velocity near the end of the test section is due to the fact that the line doublet is semi-infinite while the test section length is finite. The end effects in (a) and (c) should not influence the flow in the region of the model. Similarly, the outlier points in (b)and (d) correspond to the querying of velocity immediately at the test section wall which will no longer be in the far-field of the vortex rings that make up the wall.

As a final check on the performance of the three-dimensional panel method in solid-wall configuration and as a reference for the following section, comparisons are here made of the three-dimensional panel method code with the two-dimensional code of Chapter 5. The three-dimensional wall paneling is here coupled with two-dimensional singularity elements applied at the model location, in accordance with the two-dimensional panel method approach presented earlier. Specifically, the wake blockage, solid blockage, and lifting effects

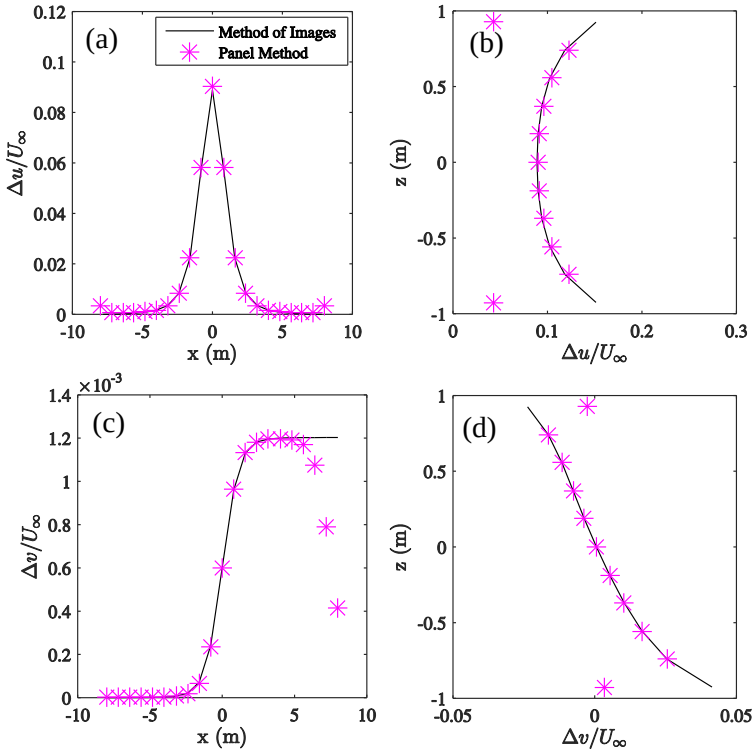

Figure 6.3: Comparison of the three-dimensional panel method to the method of images including blockage results in (a) and (b) and lift interference results in (c) and (d).

are represented by Equations 2.37, 2.38, and 2.39, respectively. As previously, the work in this subsection leverages the far-field nature of wind tunnel corrections where the model is represented by a set of singularities that are not part of the coefficient matrix as described in Section 2.2.2.2.1. The freestream conditions and aerodynamic coefficients needed to calculate the model's singularity strengths are taken from Run 2-1 on the NACA0012 as described in Table 3.3. Both the two- and three-dimensional panel method are here run with the porosity and deflection iteration loops turned off.

Figure 6.4 shows the comparison of the wall pressures between the two- and three-dimensional methods at 7.76 degrees geometric angle of attack. As expected, the three-dimensional results do not differ significantly along the span, and the agreement between the two- and three-dimensional results is good. The only differences between the two at the scale presented is near the suction peak where the three-dimensional result appears jagged, possibly due to coarse paneling relative to the two-dimensional method.

Similarly, Figure 6.5 shows little variation between the two- and three-dimensional results for three wall interference correction parameters. The total variation in blockage ratios plotted in Figure 6.5(a) is consistently 0.1% across angles of attack and the largest deviation in $\partial(v/V_\infty)/\partial x$ evaluated at the origin in Figure 6.5(b) is 4.2% which occurs at the 10-degree

angle of attack case. Any such differences between the two- and three-dimensional results would likely go away as the paneling densities of the methods increase, but this is not practical due to long run-times for the three-dimensional method. The values of v/V_∞ as in Figure 6.5(c) are numerically zero for both the two- and three-dimensional results.

Inserting the values plotted in Figure 6.5 into Equations 2.33, 2.34, 2.35, and 2.36, the result is the corrected angle of attack, as well as the corrected lift, moment, and drag coefficients, respectively. The corrected data are plotted in Figure 6.6 with excellent agreement between the two- and three-dimensional codes. The 4.2% difference in $\partial(v/V_\infty)/\partial x$ noted above does not appreciably affect the final corrected quantities. The maximum differences between two- and three-dimensional coefficients at 10-degrees angle of attack for Figure 6.6(a-c), respectively, are 3E-3, 1E-5, and 5E-4 which are at least half an order of magnitude smaller than the experimental uncertainties for the Stability Wind Tunnel quoted in Brown[36].

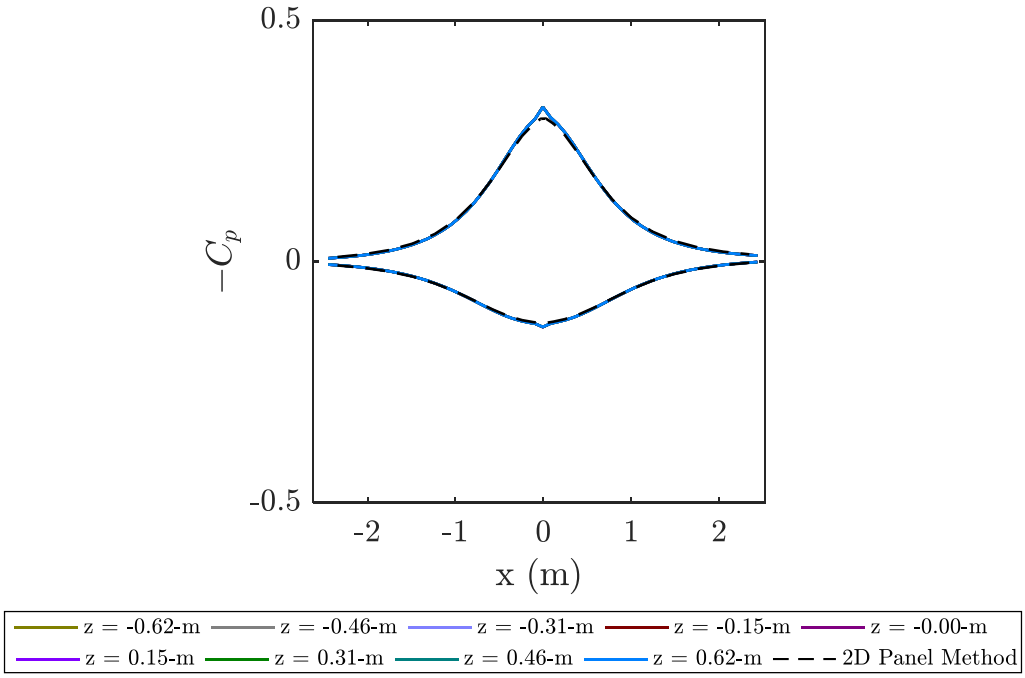

Figure 6.4: Comparison of wall pressure coefficient, $-C_p$, versus streamwise location along the test section, x, between the two- and three-dimensional results for the case of the solid-wall test section at 7.76 degrees geometric angle of attack. The data from the three-dimensional results are sampled at various spanwise locations as indicated in the legend.

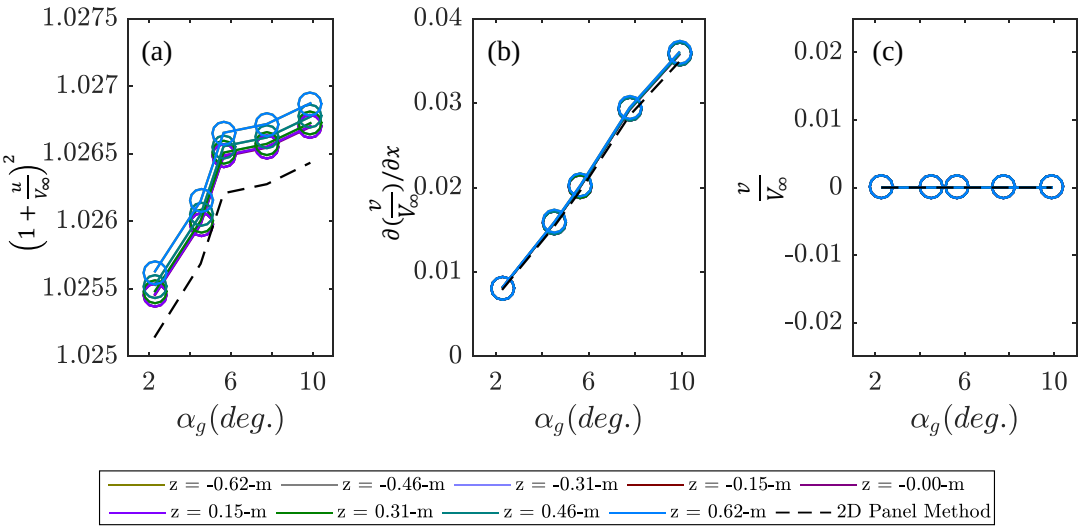

Figure 6.5: Comparison of wall interference correction parameters between the two- and three-dimensional results for the case of the solid-wall test section. The plots show polar variations in quarter-chord values of (a) blockage in terms of dynamic pressure ratio, (b) horizontal gradient of v-velocity, and (c) slope of the velocity vector. The data from the three-dimensional results are sampled at various spanwise locations as indicated in the legend.

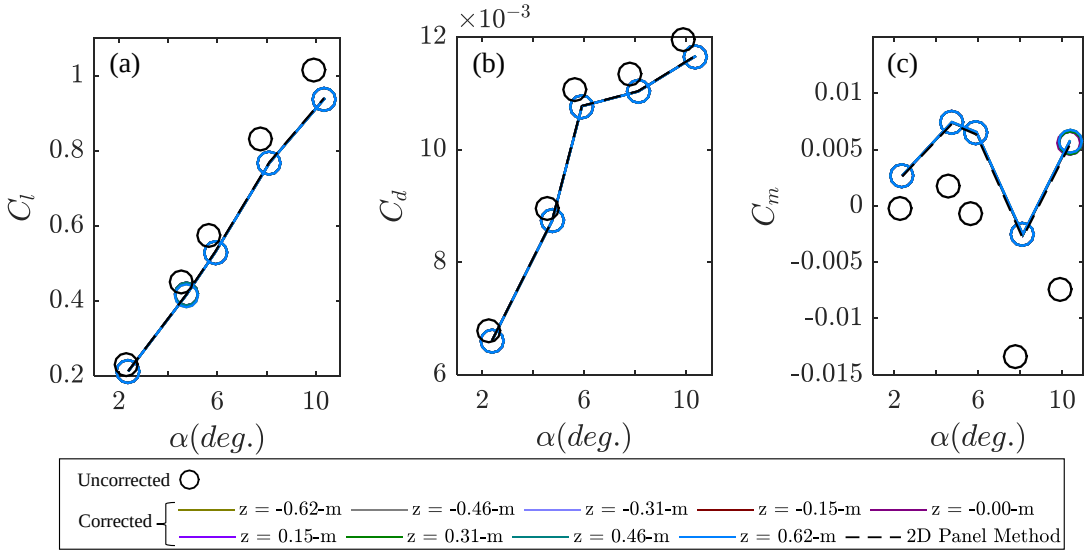

Figure 6.6: Comparison of corrected global coefficients between the two- and three-dimensional results for the case of the solid-wall test section. The plots show polar variations of corrected (a) C_l, (b) C_d, and (c) C_m. The corrections from the three-dimensional results are applied using the values of the correction parameters sampled at various spanwise locations as indicated in the legend. Uncorrected data are shown for reference.

6.2.2 Kevlar-Wall Test Section

The three-dimensional panel method in Kevlar-wall configuration uses the same paneling described in the previous section for the solid-wall configuration, however, it also embodies all the wall porosity and wall flexibility features of the two-dimensional method described in Section 2.2.2.2.1. The porous, flexible region of each wall consists of 510 panels which adhere to Equations 2.45 and 2.47 to solve for wall transpiration and deflection, respectively, as well as to Equation 2.46 to simulate the pressure in the anechoic chambers. The same nested iteration scheme as described in Section 2.2.2.2.1 is employed here for the three-dimensional version of the code.

For verification purposes in this section, all the panel method inputs listed in Table 2.1 including the Kevlar pre-tension, Kevlar modulus, strain multiplier, in-flow multiplier, and leakage area are maintained at the original values of Devenport *et al.*[9]. Additionally, the test section dimensions in this section are taken to be the values from the Stability Wind Tunnel's Kevlar-wall test section. The Kevlar porosity relation is that of Fabric A using the original formula from Devenport *et al.*

As in Section 6.2.1, a check on the performance of the three-dimensional panel method is made by comparing the three-dimensional code with the two-dimensional version of Chapter 5. The freestream conditions and aerodynamic coefficients needed to calculate the model's singularity strengths are taken from Run 2-1 on the NACA0012 as described in Table 3.3. Both the two- and three-dimensional panel method are here run with the porosity and deflection iteration loops turned on. Figure 6.7 shows the character of the pressure distribution is well-matched between the two- and three-dimensional results. For the three-dimensional results, it is possible to distinguish spanwise variation due to the wall deflection. On the suction wall, for instance, the $-C_p$ is least at the extreme span locations and increases at mid-span due to the the reduced flow area caused by the bulging Kevlar. Differences between the two- and three-dimensional results can be found in a slight downstream shift of the three-dimensional pressures, as well as a change in concavity near $x = -2$-m on the pressure side for the three-dimensional results that is likely due to non-convergence of the three-dimensional solution's inner pressure loop. Convergence of pressures near zero may be hampered by the form of Equation 2.45 which has an infinite slope at zero. Figure 6.8 shows comparisons of additional wall boundary conditions including transverse velocity through the Kevlar and wall deflection of the Kevlar. Some of the same characteristics as in Figure 6.7 are seen here: non-convergence issue near the zero pressure region in (a) and a slight offset in the deflection profiles in (b). It is noted that the deflection magnitude of the two- and three-dimensional results generally coincide for a span location of z=$\pm$ 0.62-m which is reasonable given that the two-dimensional code averages the deflection across the whole span. It should be borne in mind when interpreting these comparisons that the two codes are, in fact, simulating different flows, and thus differences between them are permissible.

Three of the key wall interference parameters plotted in Figure 6.9 indicate that the three-

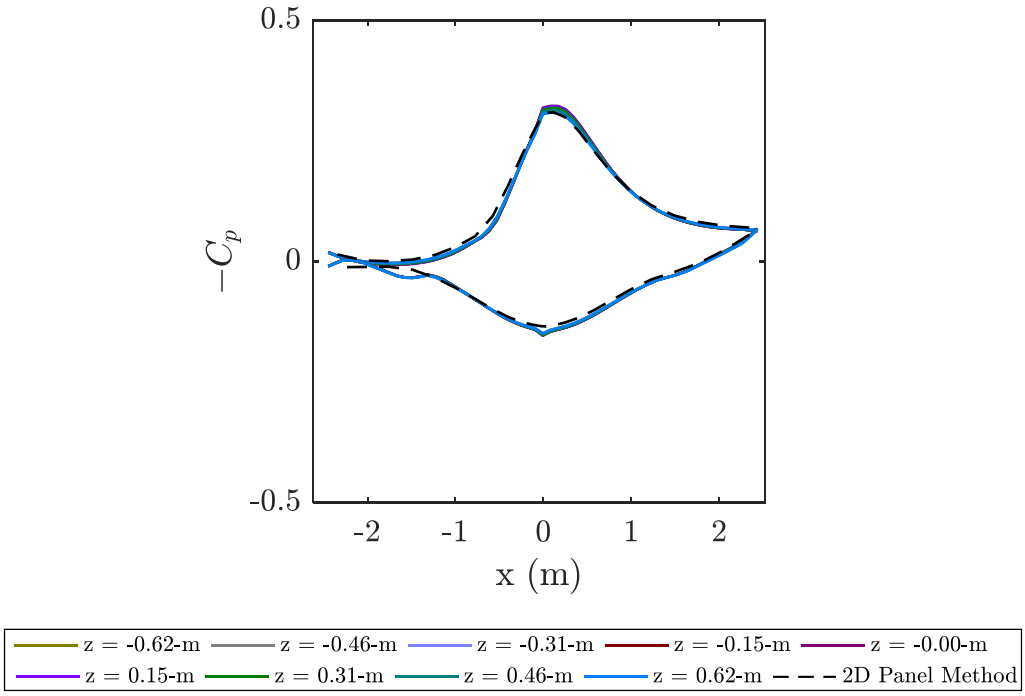

Figure 6.7: Comparison of wall pressure coefficient, $-C_p$, versus streamwise location along the test section, x, between the two- and three-dimensional results for the case of the Kevlar-wall test section at 7.76 degrees geometric angle of attack. The data from the three-dimensional results are sampled at various spanwise locations as indicated in the legend.

dimensional results maintain the same general character as the two-dimensional results and show some degree of variation in the magnitude of the correction parameters versus the two-dimensional results. The largest discrepancy in blockage is 0.5% which occurs at 10-degrees angle of attack in Figure 6.9(a). It should be noted that the blockage results suffer particularly from a lack of complete convergence in the inner pressure loop of the three-dimensional code and sometimes the two-dimensional code. The results of Figure 6.9(b) and (c) show, at most, differences of 3% and 7%, respectively.

Inserting the values plotted in Figure 6.9 into Equations 2.33, 2.34, 2.35, and 2.36, the corrected angle of attack, lift, drag, and moment coefficients, respectively, are computed and then plotted in Figure 6.10. The maximum differences between two- and three-dimensional coefficients at 10-degrees angle of attack for Figure 6.6(a-c), respectively, are 7E-3, 7E-5, and 3E-4 which are again smaller than the experimental uncertainties for the Stability Wind Tunnel quoted in Brown[36].

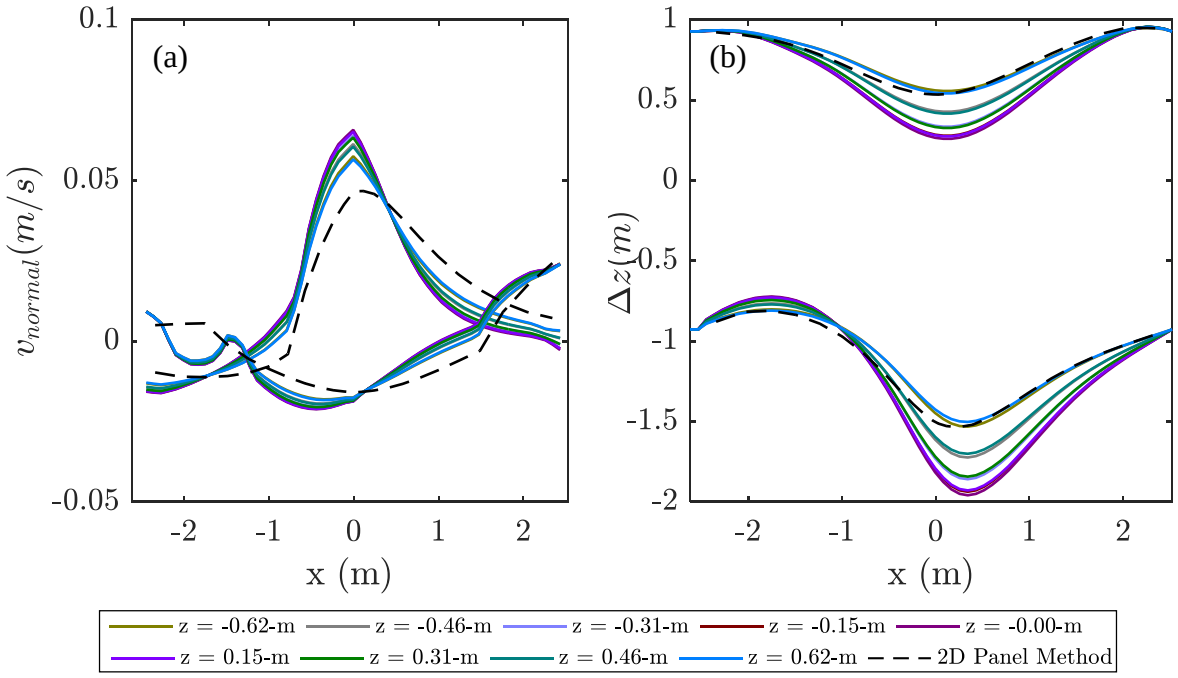

Figure 6.8: Comparison of wall boundary conditions between the two- and three-dimensional results for the case of the Kevlar-wall test section. The plots are at a geometric angle of attack of 7.76 degrees and show (a) normal velocity through Kevlar versus streamwise location along the test section, x, and (b) normal deflection of Kevlar versus x. The data from the three-dimensional results are sampled at various spanwise locations as indicated in the legend. The deflections in (b) are scaled up by a factor of 15 for clarity.

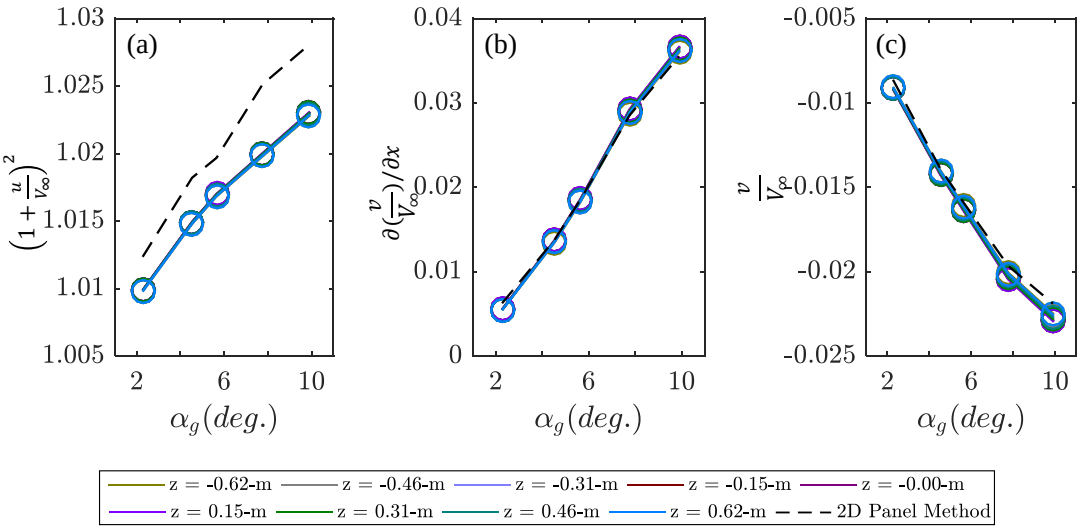

Figure 6.9: Comparison of wall interference correction parameters between the two- and three-dimensional results for the case of the Kevlar-wall test section. The plots show polar variations in quarter-chord values of (a) blockage in terms of dynamic pressure ratio, (b) horizontal gradient of v-velocity, and (c) slope of the velocity vector. The data from the three-dimensional results are sampled at various spanwise locations as indicated in the legend.

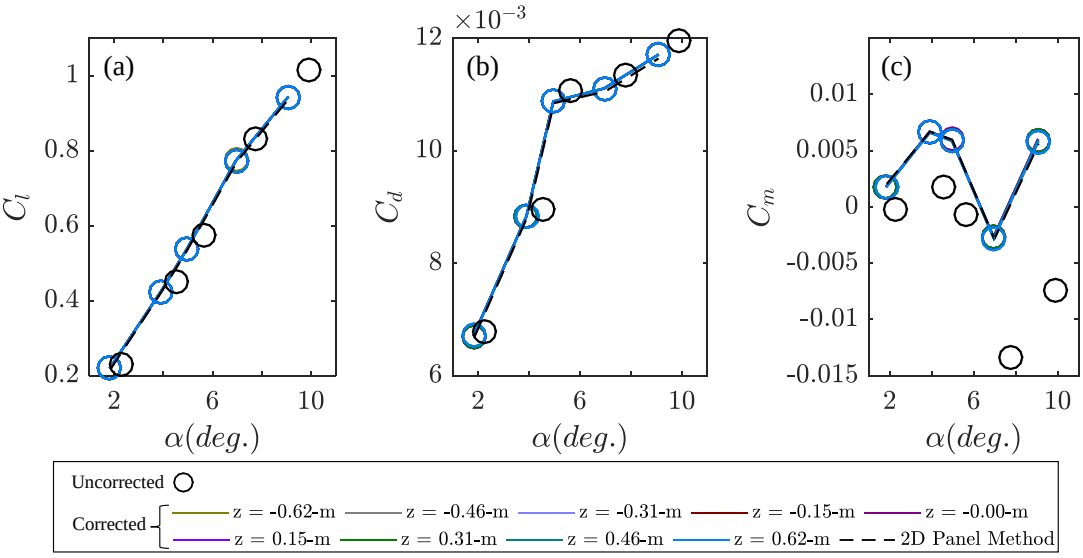

Figure 6.10: Comparison of corrected global coefficients between the two- and three-dimensional results for the case of the Kevlar-wall test section. The plots show polar variations of corrected data for (a) C_l, (b) C_d, and (c) C_m. The corrections from the three-dimensional results are applied using the values of the correction parameters sampled at various spanwise locations as indicated in the legend. Uncorrected data are shown for reference.

6.3 Validation of Panel Code

Having been verified against theoretical solutions and a two-dimensional panel method code, the three-dimensional code is now utilized to simulate a wing model. This section presents the results of tests with the wing models in the Japanese Aerospace Exploration Agency's 2m-by-2m Low Speed Wind Tunnel, both with the solid-wall and Kevlar-walled test sections, and compares the global aerodynamic coefficients, wall pressures, and chamber pressures between the measurement and simulation.

Departing from the approach of Chapter 5, the model is here represented by a paneled wing. Such a paneling is convenient since a high-lift model is to be simulated, of which there is less published literature relating to the singularity representation. The 0.4-m chord NACA0012 wing described in Section 3.2.3 is paneled along its span with 14 panels and around its airfoil profile with 30 panels for a total of over 400 panels. The 0.6-m chord OTOMO high-lift wing contains three separate pieces, each of which have more than 700 panels. The slat and main body are paneled the full 1.35-m span of the model, while the flap is paneled 0.945-m according to the model geometry. Wake downwash is created by a series of horseshoe vortices trailing 50 chord lengths straight downstream from the trailing edge whose strengths are specified to enforce the Kutta condition. Wake blockage is not currently accounted for in the panel method. To avoid paneling difficulties around the root of the wing, the test section and wing are mirrored across the root plane. This doubles the size of the test section and the wingspan but is still physically appropriate since the symmetry of the mirrored image will produce streamlines along the root plane, thus simulating a solid-wall there. The test section reference velocity is taken at the center of the mirrored test section which corresponds to the centerline of the root plane. A body pod was sometimes present for tests in the wind tunnel but was not modeled in the panel method meaning that the blockage predicted may be slightly lower than actual.

The inputs to the panel method used in this chapter are given by Table 6.1. The pre-tension is derived from measurements with a tension meter at the center of each Kevlar wall. The effective Kevlar modulus is taken from the findings of Section 4.2.3, the strain multiplier is set to zero in accordance with Section 4.3.4, and the inflow multiplier is taken at 2 according to the two-dimensional panel method. The leakage area is based on estimates by engineers, and this area was doubled before being input to the simulation to account for the mirroring of the test section across the root plane. Based on the construction of the Kevlar-wall test section at the Low Speed Wind Tunnel facility, it is believed that there is little to no cross-flow directly between chambers, so the chamber leakage model was modified so that the chambers exchange mass with only the control room which is taken to be at zero static pressure.

The porosity of the Kevlar at the Low Speed Wind Tunnel, Fabric C in Table 4.1, has not been measured with the same rigor as the other fabrics considered in this study, and as such there is high uncertainty associated with the porosity of Kevlar C. The porosity values are

Table 6.1: Inputs to the panel method simulation for this chapter.

Input Parameter	Value
Kevlar Pre-Tension, T_0	4000 N/m
Effective Kevlar Modulus, E	467823 N/m
Kevlar Strain Multiplier, a_ε	0
Inflow Multiplier, a_{inflow}	2
Effective Leakage Area, A_{leak}	0.01 m^2
C_p Convergence Tolerance, $C_{p,tol}$	1e-4
T Convergence Tolerance, T_{tol}	1e-4

not available for publication but most closely resemble those of Fabric B.

6.3.1 Global Aerodynamic Coefficients

Below, the panel method correction is applied to the Kevlar-wall results and validated against solid-wall data. For both the solid- and Kevlar-wall cases, the blockage and lift interference values are calculated by summing the influence of the wall panels at the model quarter-chord location as in Equations 2.30 and 2.31. According to the equations, the interference velocities are scaled to account for differences in the specified and realized freestream velocities in the tunnel which arise due to the effect of singularities acting at the freestream reference point. The realized freestream velocity is measured 6-m upstream of the model quarter-chord and always fell within 1% of the specified velocity for the cases considered in this paper. As before, the terms Δu and Δv are the result of the induced velocity component plus the difference of the realized freestream velocity with the specified freestream velocity for each velocity component. No wake blockage was simulated in the panel method simulation, however, the method of images correction as given by Equation 2.9 was applied to all data. It should be kept in mind that this equation is not strictly valid for the Kevlar-wall case.

Note that the solution of the paneled wing is generated in the free-flight case and its influence on the wall panels subsequently calculated. Such a technique introduces error into the correction since the model will be operating at too low an effective angle of attack and producing to little lift compared to the actual model in the wind tunnel.

It should be mentioned that spanwise variation in wall-interference is not negligible for semi-span models. The lift-inteference is greatest at the root plane while the blockage is minimum at this location. In this section such variation will not be considered, and all the wall-interference results are reported at the root plane, or at $z = 0$.

6.3.1.1 NACA0012 Model

Figure 6.11 shows the uncorrected and corrected lift data for the 0.4-m NACA0012 wing in the tripped condition in both test sections at a Reynolds number of 1.4E6. Note that a 0.4-degree offset in the measurements made in the Kevlar-wall test section has been subtracted from these data before interpolating the aerodynamic coefficients back to integer values of geometric angle of attack to match the solid-wall data. The source of this error, which is considerably more than the ± 0.1 degree uncertainty of the laser sheet alignment procedure, remains under investigation. Looking first at the uncorrected results in Figure 6.11(a), the Kevlar-wall data shows a lift-curve slope that is rotated slightly clockwise relative to the solid-wall data. The lift curve slope in the solid-wall section, measured between 0 and 10 degrees, is 3.89 rad-1 as compared to 3.76 rad-1 for the Kevlar section a difference of 3.2%. Similarly, the maximum lift coefficient measured with the Kevlar walls is 2.5% less than that for the solid walls. The angles of maximum lift appear to be the same at 16 degrees, although exact comparison is difficult due to the 0.4-degree offset in the Kevlar-wall data. Overall the difference between Kevlar and solid-wall test section results is less than seen in airfoil tests in the Virginia Tech wind tunnel as given in Chapter 5. This is mostly a function of smaller model size relative to the test section and the lower overall interference effects expected with three-dimensional configurations although the different porosity, pre-tension, and leakage levels in the the Japanese Aerospace Exploration Agency facility may also play a role.

Solid-wall measurements were corrected both using the method of Barlow *et al.*[20] via Equations 2.26-2.29 and the panel method via Equations 2.30 and 2.31. Streamline curvature was not corrected, but this correction has a small magnitude relative to the downwash correction. Data corrected with the two methods appears closely consistent in Figure 6.11(b). Figure 6.11(b) also includes the panel method corrected Kevlar-wall data. Wall interference corrections for both test sections are small and lower the lift-curve slope by 4.9% for the solid-wall test section and by 4.3% for the Kevlar-wall test section. These small corrections, almost completely a result of lift interference as opposed to blockage, are assumed to be a result of the size of the test section dimensions being over four times the length of the chord.

Comparing the corrected data between test sections, the effectiveness of the panel method correction can be simplistically evaluated based on the agreement of the lift curve slopes, here measured between 0 and 10 degrees. After the 4.9% and 4.3% corrections above, the Kevlar-wall data with a slope of 3.60 rad^{-1} is again rotated slightly clockwise of the solid-wall data at 3.69 rad^{-1} for a difference of 2.4%. It is expected that the slopes of the data between test sections will be in better agreement after correction which is the case as 3.2% becomes 2.4%. In order to bring the corrected slopes into complete agreement, either the blockage or lift interference correction predicted by the panel method would need to be reduced for the Kevlar-wall case. Note that the angle of attack corrections for the Kevlar-wall test section are seen to result in an effective angle of attack that is greater than the geometric value as is the case in solid-wall test sections. This characteristic was also observed in Chapter 5 for

Kevlar walls made from lower porosity fabric.

Figure 6.12 shows a comparison of blockage and lift interference versus angle of attack as computed with Equations 2.30 and 2.31. In figure 6.12(a), the blockage in the solid-wall test section remains relatively flat with angle of attack while that of the Kevlar-wall test section varies, the two crossing each other around 2 degrees angle of attack. As with the results of Chapter 5, increased blockage with increased loading on the Kevlar walls is presumed to be due to the increased deflection of the walls which narrows the effective test section width. At low loading, the decrease in the Kevlar-wall blockage relative to the solid-walled is believed to be due to the upstream diversion of flow out of the test section into the anechoic chambers, the flow then returning to the test section downstream at the model location where the static pressure is lower. It is noted that neither wake blockage nor a verified Kevlar porosity value are yet included in the panel method and will have a substantial impact on the blockage.

The lift interference comparison in Figure 6.12(b) shows the Kevlar-wall test section producing 10-50% less interference than the solid-wall with the smaller reductions coming at higher loading. This result is expected since the porosity of the Kevlar walls, combined with the pressure difference between the pressure- and suction-side walls and their respective chambers, produces transpiration velocity through the Kevlar. The transpiration enters the test section at the suction-side wall and exits the test section at the pressure-side wall, acting to reduce the effective angle of attack and cancel part of the increase in angle of attack due to the downwash correction.

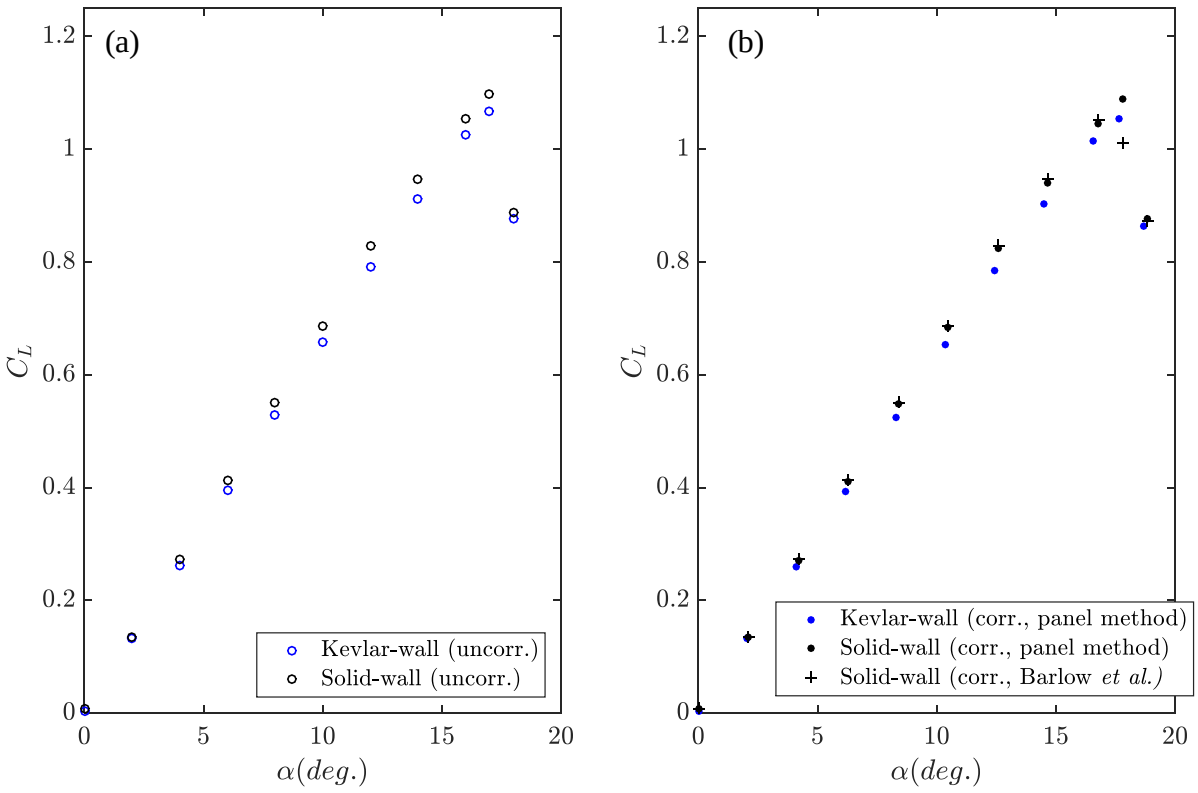

Figure 6.11: Lift coefficient versus angle of attack of (a) uncorrected and (b) corrected data from the NACA0012 in both the solid-wall and Kevlar-wall test sections at a Reynolds number of 1.4E6 and in the tripped condition.

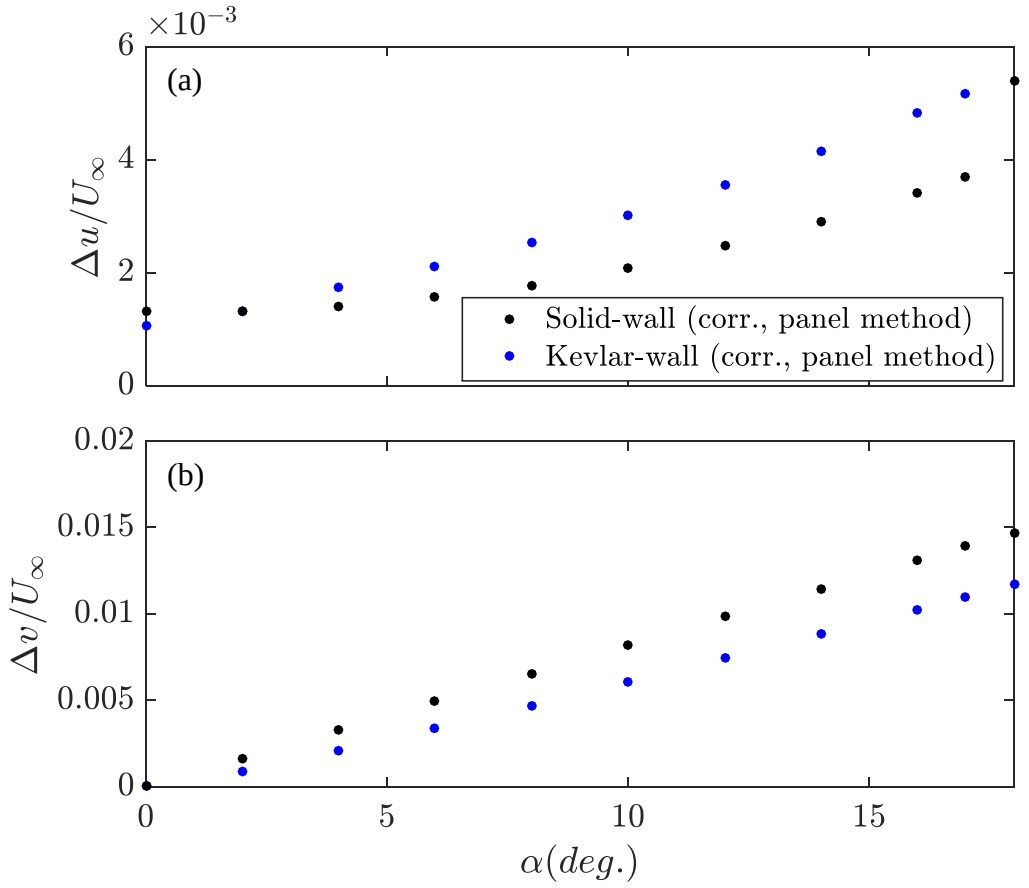

Figure 6.12: Comparison of (a) blockage and (b) lift interference corrections versus angle of attack between test sections for the NACA0012.

6.3.1.2 OTOMO High-Lift Model

Figure 6.13 shows the uncorrected and corrected lift data for the 0.6-m OTOMO high-lift model in landing configuration in the untripped condition in both test sections. The solid-wall data is at a Reynolds number of 2.0E6 and the Kevlar-wall data is at 1.8E6. As before, 0.4 degrees is subtracted from the angles measured in the Kevlar-wall test section. The classical correction is not given in this case since Barlow *et al.* does not provide corrections for high-lift models. It should be noted that the OTOMO has both a 50% larger chord than the NACA0012 and substantial camber, so it requires much larger correction magnitudes.

Before correction, the data measured in the two test sections is quite similar with just a 1.8% difference in slope. After the correction this value actually increases to 3.5%, however, given the ∼13% magnitude of the correction to the slope, agreement to the solid-wall results within 4% is encouraging. We suspect that a significant proportion of this 4% discrepancy derives from uncertainty in the porosity relation.

The stall characteristics in the two test sections are not identical for the OTOMO model. In the solid-wall test section, the beginnings of flow separation appear around 12-degrees angle of attack, but a second semi-linear region is then seen extending to about 23-degrees. In the Kevlar-wall test section the same behavior is seen except that the lift begins to drop off around 16 degrees. Unfortunately, measurements in this test section were not performed beyond 20-degrees angle of attack. Figure 6.14(a) reveals that the blockage component of the correction for the Kevlar-wall test section is now everywhere larger and increasing at a larger rate than in the solid-wall test section, likely due to the high loading and thus high deflection experienced by the Kevlar walls which narrows the effective test section width. Figure 6.14(b) shows that the lift interference comparison is qualitatively the same as for the NACA0012 with the Kevlar-wall test section producing now 7-14% less interference than the solid-wall.

The larger magnitude of the corrections with the OTOMO model make for interesting comparisons of some of the other aerodynamic properties. Figures 6.15 and 6.16 compare pitching moment about quarter-chord and drag, respectively, showing again both uncorrected and corrected data. The pitching moment correction moves the data of both test sections upwards yielding better agreement between test sections after correction. Similarly for the drag coefficient, the correction brings the data from the two test sections into slightly better qualitative agreement, but the final result is still in some disagreement. The corrected drag in the Kevlar-wall test section is greater than that in the solid-wall test section even as the correction term $C_{L,u}\Delta\alpha_{dw}$ of Equation 2.16 is larger for the solid-wall than Kevlar-wall test section. Note that the effective freestream direction used to calculate $\Delta\alpha_{dw}$ includes the 0.4 degree offset in the Kevlar-wall test section so that the correction to induced drag is accurate. Consideration of the wake pressure gradient correction which is not accounted for in the panel method may yield better drag results.

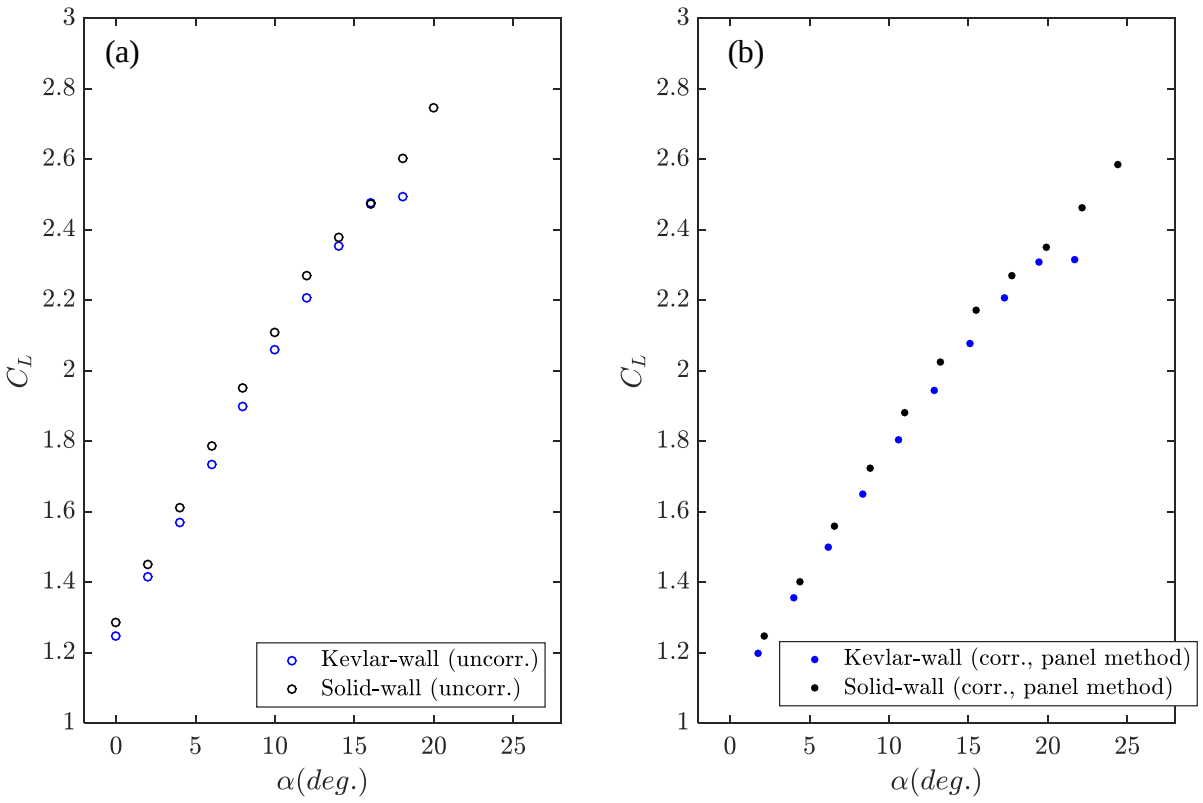

Figure 6.13: Lift coefficient versus angle of attack of (a) uncorrected and (b) corrected data from the OTOMO high-lift model in landing configuration in both the solid-wall and Kevlar-wall test sections at a Reynolds number of 1.8-2.0E6 and in the untripped condition.

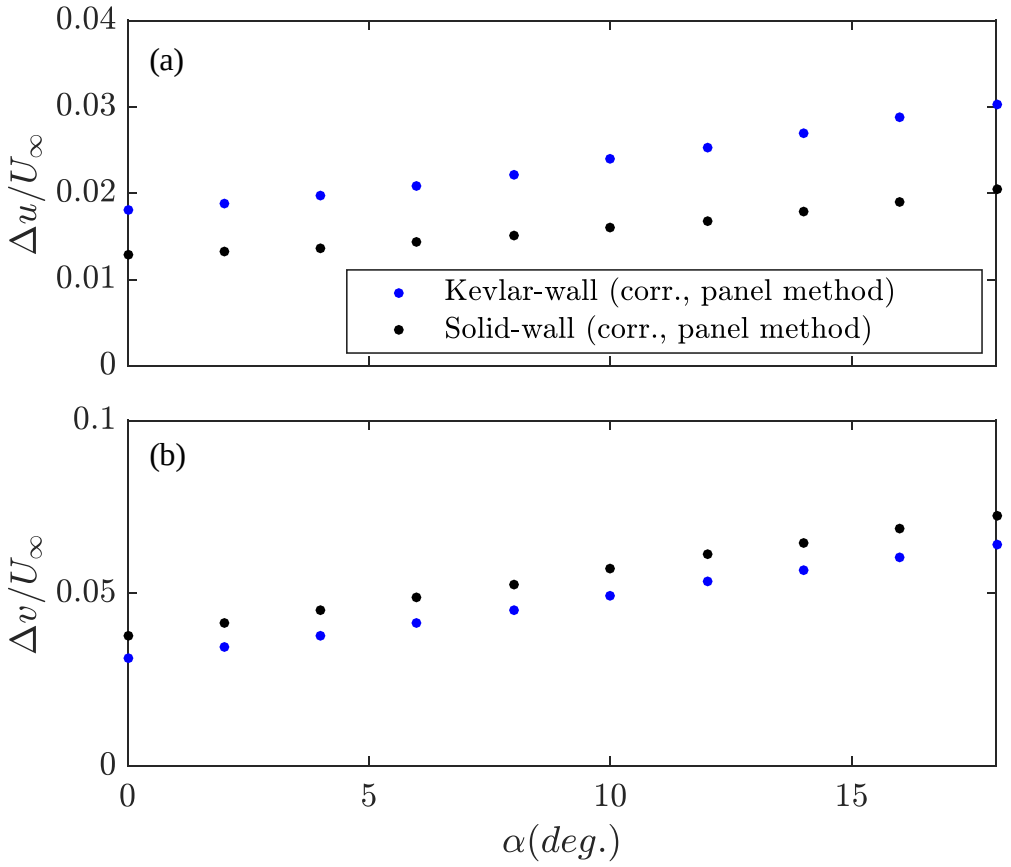

Figure 6.14: Comparison of (a) blockage and (b) lift interference corrections versus angle of attack between test sections for the OTOMO high-lift model.

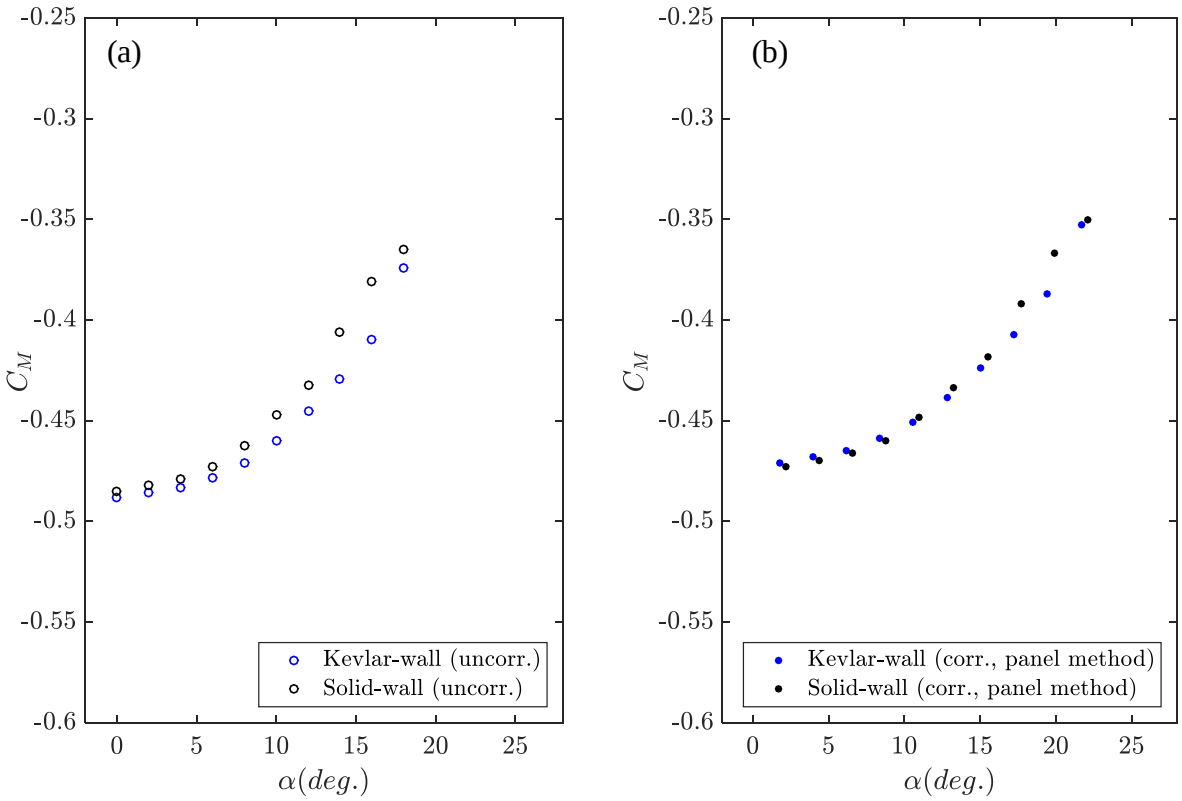

Figure 6.15: Pitching moment coefficient about quarter-chord versus angle of attack of (a) uncorrected and (b) corrected data from the OTOMO high-lift model in landing configuration in both the solid-wall and Kevlar-wall test sections at a Reynolds number of 1.8-2.0E6 and in the untripped condition.

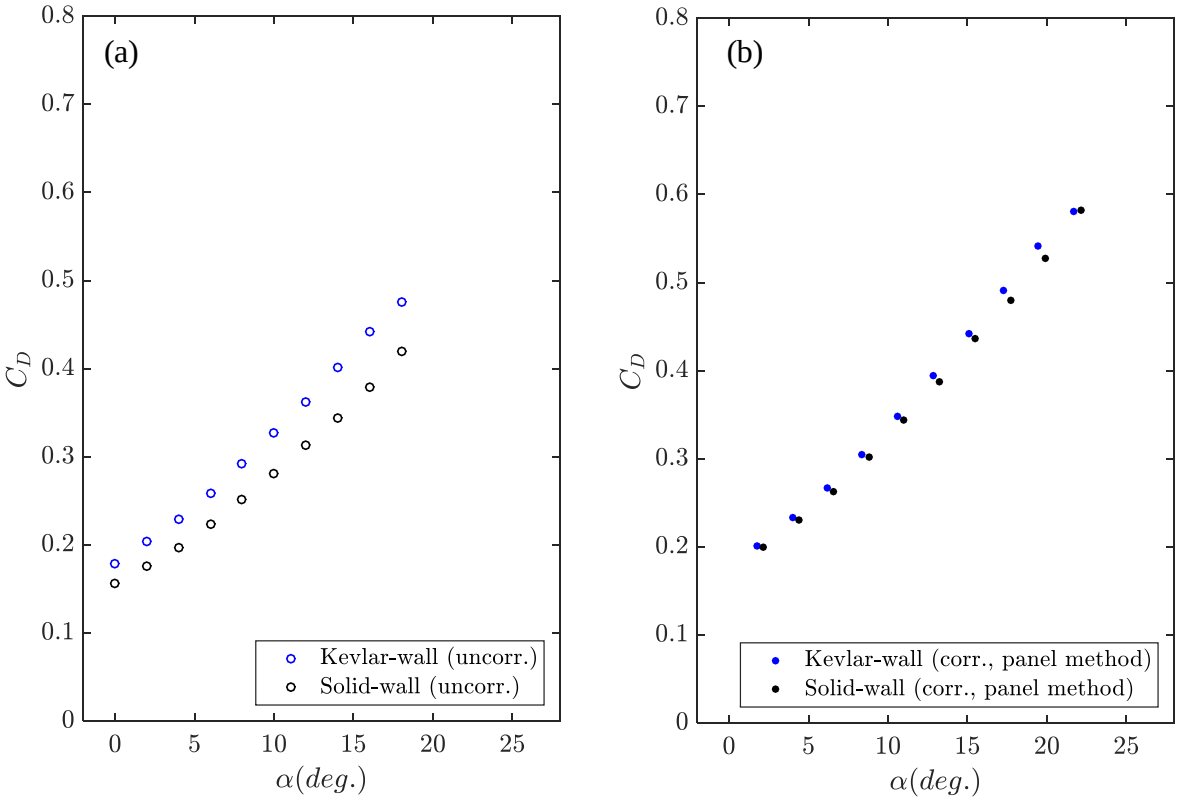

Figure 6.16: Drag coefficient versus angle of attack of (a) uncorrected and (b) corrected data from the OTOMO high-lift model in landing configuration in both the solid-wall and Kevlar-wall test sections at a Reynolds number of 1.8-2.0E6 and in the untripped condition.

6.3.2 Wall Pressure

Figures 6.17 shows the measured Kevlar-wall C_p distributions for the NACA0012 compared with the panel method predictions for an angle of attack of 15 degrees. Smoothing of the measured data is accomplished with a locally weighted linear regression algorithm which solves a two-dimensional, weighted linear regression problem at every data point, the weights of neighboring points falling off with distance from the point. Overall, the shape of the distributions is as expected with the maximum C_p just around the root of the wing. From observation of the spanwise gradients at the wing location, the simulation appears to capture the loading distribution of the wing well, especially on the pressure side. The C_p magnitudes are comparable between the simulation and measurement with the simulation yielding pressure- and suction-side C_p extremes of 0.09 and -0.11, respectively, and the measurement yielding 0.09 and -0.07. Thus, there may be an over-prediction of blockage on the suction side of the model.

The simulation does not capture the small low pressure bubble starting downstream of the wing on the pressure side which could be due to improper modeling of the blockage effect of the flow re-entering the test section from the chambers. Alternatively, the wake's trajectory in the test section brings it closer to the pressure-side wall and likely lowers the pressure there which is not accounted for in the simulation. Another difference between the simulation and measurement is related to what might be described as an approximate axis of symmetry of the pressure distributions located at $x = 0$. While the simulation does show a slight incline towards downstream, the suction-side measurement shows a pronounced turn into the direction of the flow that is not captured in the simulation. This incline could again be related to the vortical wake, specifically the wing tip vortices.

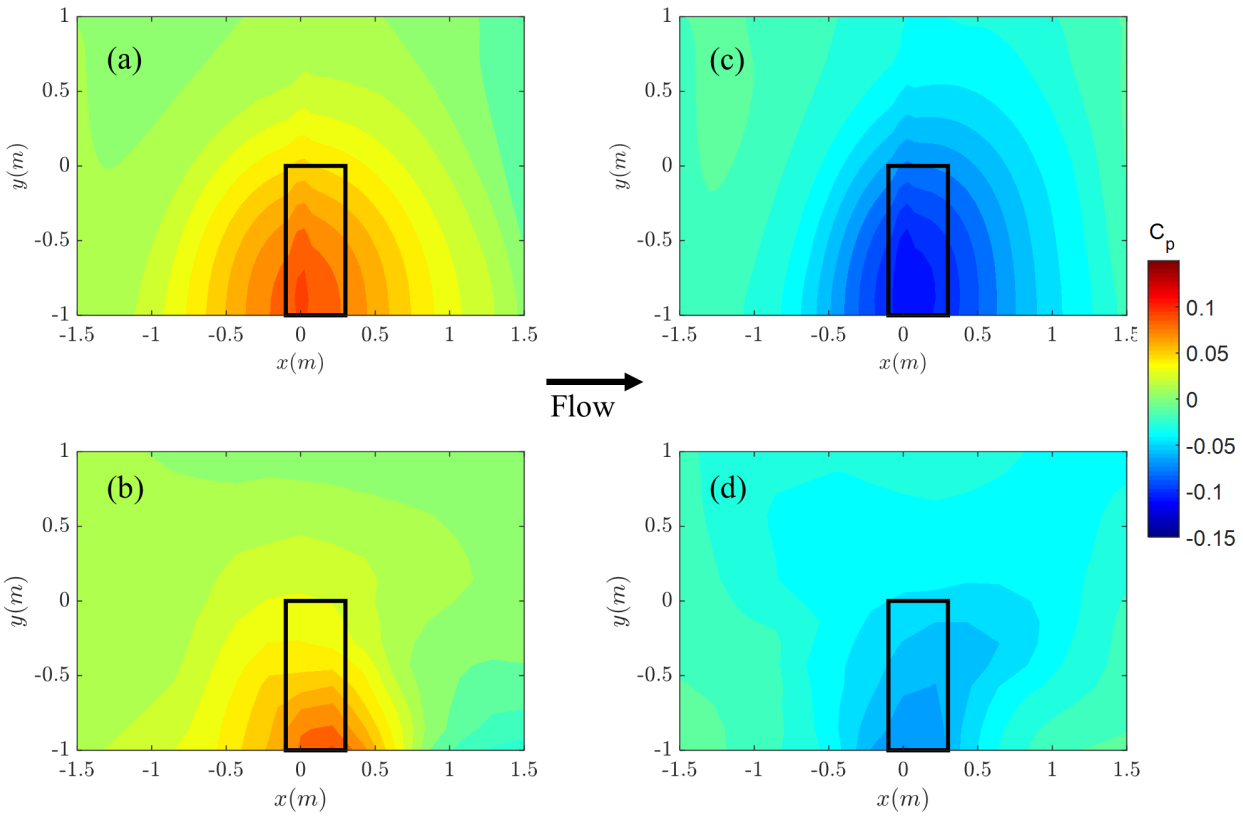

Figure 6.17: Comparison of simulated and measured Kevlar-wall C_p distributions for the NACA0012. The semi-span wing is shown by the black outlines, and quarter-chord is at x = 0.

6.3.3 Chamber Pressure

Figures 6.18 compares the simulated and measured chamber pressures for the tests of the two wings above. For the NACA0012 experimental data in Figures 6.17(a), there is an asymmetry in the chamber pressures as the main chamber does not appear to hold pressure or suction as well as the sub chamber. However, the overall agreement between experimental and simulated data is quite good for the NACA0012 especially on the main chamber side. The OTOMO model imposes an extreme loading case on the Kevlar walls and thus the chamber pressures, and it is seen in Figures 6.17(b) that the agreement in this case is only fair. The main chamber again does not appear to hold pressure as well as the sub chamber. In both chambers and especially the main chamber, the simulation leakage area input, set at 0.01-m^2 for each chamber based on engineers' estimates, may be too small since the actual chambers appear to have more pressure relief than the simulated chambers.

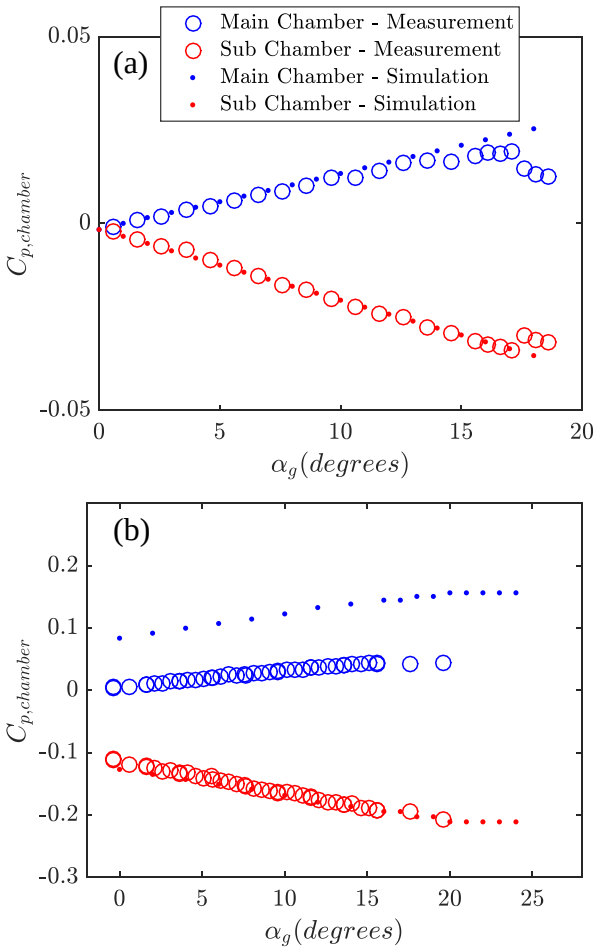

Figure 6.18: Comparison of simulated and measured chamber pressures versus angle of attack for (a) the NACA0012 and (b) the OTOMO high-lift model in landing configuration.

Chapter 7

Inferring Kevlar Boundary Conditions from Global Wall Deflection Measurements

This chapter is dedicated to the development and validation of a new measurement system at the Stability Wind Tunnel to infer the pressure boundary condition from wall deflection. First, background on the inverse problem in static aeroelasticity will be presented, followed by details of the pre-tension measurements performed on the Kevlar walls, a description of wall displacement measurements, calculation of the wall pressure distributions, and experimental validation of the measurements.

7.1 Review of Inverse Methods in Static Mechanics

This section deals with the inverse loading problem in static mechanics. For clarity, it is noted that the inverse loading problem is distinct from the often-referenced inverse design problem which is usually concerned with determining the topology of a wing, for instance, to produce a desired aerodynamic performance.

7.1.1 Theory of Inverse Problems

Below is first presented the theory of linear inverse problems which serves as a background and aid to the discussion on non-linear inverse problems that follows.

7.1.1.1 Linear Inverse Problems

In the case of the forward problem in structural mechanics, the loading, boundary conditions, and constitutive properties are known and used as inputs to solve for the response of the system in terms of its displacement and internal stress fields[73]. On the other hand, the inverse problem typically substitutes knowledge of the loading for knowledge of the displacement with the goal of inferring the loading and internal stress fields. The inverse problem is separate from the identification problem which has to do with the determination of several constitutive properties of a material rather than the full loading distribution. Throughout the following discussion on the inverse problem, the constitutive properties are assumed to be known.

Stevens[97] notes that the simplest inverse problems in structural mechanics are those with single inputs and single outputs, such as in the case of a simple strain gage. The force felt at the strain gage's location is a function of the deflection within the gage, this function being either calculated analytically or characterized through calibration. The difficulty in inversion comes when the number of unknowns increases so that neither analytic solutions nor calibration are capable of characterizing the system.

Unlike the forward problem, the inverse problem is not well-posed according to Hadamard in that the solution is not guaranteed to exist, the solution is not guaranteed to be unique, and the solution does not necessarily depend continuously on the input data [98]. Specifically, the last of these manifests itself in high sensitivity of the inverse solution to small errors in the input data. This state of events follows naturally from the setup of the governing equilibrium equations in structural mechanics which involve derivatives of the displacement field on the left-hand side that are equated to loads on the right-hand side[93]. The process of differentiation amplifies errors in a data set, so small errors in the input displacement field results in larger errors in the final solution of loading[97].

A more formal explanation of the ill-posedness of inverse problems can be found in Tikhonov and Arsenin[99] who use the example of the Fredholm integral equation of the first kind as in Equation 7.1

$$d = Kf \equiv \int_a^b k(x,s)f(s)ds \tag{7.1}$$

where d and k are known, f is unknown and contained in the interval $[a,b]$, and K is an operator on f as shown. It is shown that for a function d that is known to within some degree of accuracy, the inaccuracy of the resulting f can be arbitrarily large.

Equation 7.1 is an expression of a continuous problem which, for the convenience of working with finite-dimensional measurements and/or finite-dimensional modeling techniques, can be projected onto a finite-dimensional space by first approximating f as a linear superposition of basis functions, f_n, as defined in Equation 7.2

$$\mathbf{f}_n = \sum_{j=1}^{n} \xi_j \Phi_{nj} \tag{7.2}$$

where ξ are weighting factors of the basis functions Φ [100]. Then, Equation 7.1 becomes Equation 7.3

$$d(x_i) = \sum_{j=1}^{n} \{ \int_a^b k(x_i, s) \Phi_{nj}(s) ds \} \xi_j, \qquad i = 1, ..., m \tag{7.3}$$

which, in matrix form, is $d_m = [K_{mn}] f_n$. Or, explicitly accounting for the approximate nature of the input data d, the matrix form can be written as in Equation 7.4

$$\mathbf{d} = K\mathbf{f} + \boldsymbol{\eta} \tag{7.4}$$

where $\mathbf{d}$ and $\mathbf{f}$ are now boldface to indicate they are vectors, and $\boldsymbol{\eta}$ is a vector of the errors contained in d. The above process of discretization that leads to Equation 7.4 is a projection method[100]. The unknown weighting factors, ξ_j, are solved to yield least-squares minimization of Equation 7.5

$$\mathbf{f_{lsq}} = arg \min_{\mathbf{f}} ||K_{mn}\mathbf{f_n} - \mathbf{d_m}||^2 \tag{7.5}$$

where $\mathbf{f_{lsq}}$ is the minimizer in a least-squares sense (the $|| \cdot ||$ operator represents the L^2 norm). As long as the problem is determined or over-determined, then there is a unique $\mathbf{f_{lsq}}$. For the case of under-determined problems, further regularization such as by singular value decomposition is required to arrive at a unique solution.

For the continuous representation in Equation 7.1, it was stated based on Tikhonov and Arsenin's[99] work that the inaccuracy of the resulting f can be arbitrarily large for a given d that is known to within some degree of accuracy. The corollary of this statement for the discrete system in Equation 7.4 is that the global matrix K is ill-conditioned which can be the case in structural problems where the stiffness matrix K derived from finite element methods is sparse. Inversion of an ill-conditioned global matrix causes small measurement errors in $\mathbf{d}$ to balloon into large errors in the calculated loading $\mathbf{f}$[101]. Since the projected solution $\mathbf{d}$ is thus unstable, it must desired to find a related stable solution which will satisfy Equation 7.4, at least approximately.

Methods by which to arrive at a related, stable solution are known as regularization methods. It should be mentioned that the projection method described above has an inherent regularizing effect. When the noise in measurements is relatively low and a finite-dimensional space of small size is selected (i.e. - when the problem is strongly over-determined), projecting

the measurements onto a finite-dimensional space can sometimes be enough to reduce the noise propagation and ill-posedness of the problem[98]. However, regularization by projection typically requires that the dimension of the space being projected onto must be low so that spurious noise is damped out, and such a low-order projection does not lend itself to useful solutions [100].

Therefore, along with the projection of noisy data onto a finite-dimensional space, other regularization techniques, as they are called, are sometimes necessary. An article by Vogel[102], used as a guide below, gives a review of regularization methods for discrete, linear problems including filtering methods, variational methods, and iterative methods.

Filtering methods can be used on the matrix K to reduce its ill-conditioning. When K is symmetric and positive definite, then singular value decomposition produces Equation 7.6

$$K = Udiag(s_i)U^T \tag{7.6}$$

where the singular values s_i are the eigenvalues of K, and U are a collection of orthogonal, normalized eigenvectors. Substituting Equation 7.6 into Equation 7.4 and multiplying both sides of by K^{-1} results in Equation 7.7

$$K^{-1}\mathbf{d} = Udiag(s_i^{-1})U^T\mathbf{d} = \mathbf{f} + \sum_{i=1}^{n} s_i^{-1}(\mathbf{u}_i^T\boldsymbol{\eta})\mathbf{u}_i \tag{7.7}$$

where u_i are the column vectors of U. As expected from the previous discussion above on the ill-conditioned nature of K, the inversion of K is unstable because of the small singular values in the denominator of the right-hand term of Equation 7.7. All ill-conditioned K matrices will produce a cluster of singular values near zero[101]. The severity of ill-posedness can be roughly quantified by the decay rate of the singular values[102]. Mildly ill-posed problems have a decay rate $s_i = \mathcal{O}(i^{-\beta})$ (for some $\beta > 1$), and severely ill-posed problems have a decay rate $s_i = \mathcal{O}(e^{-i})$[98]. In order to deal with these small singular values, one can multiply the right-hand term of Equation 7.7 by a regularizing filter, $\omega_\alpha(s^2)$. If this multiplier is set to unity, then the solution for $\mathbf{f}$ is just the least-squares solution to Equation 7.5 which is not desirable due to noise amplification[101]. One specific filtering method, truncated singular value decomposition (TSVD), uses for $\omega_\alpha(s^2)$ a piecewise function that is unity for all values of s^2 greater than some regularization parameter, α, and is 0 for all other values of s^2. Another filtering method is Tikhonov-Phillips regularization which uses $\frac{s^2}{s^2+\alpha}$ for the multiplier $\omega_\alpha(s^2)$. Several other filter factors are presented in Hansen and O'Leary[101]. In both TSVD and Tikhonov-Phillips regularization, the value of α should be selected so as to filter out unwanted noise but keep the essential information in the signal. Sometimes, the convergence to the exact solution and the rate of convergence as the experimental error, δ, goes to zero can be proven *a priori* which aids in the selection of an appropriate α. Other times, the selection of α is made *a posteriori* which will be discussed further below.

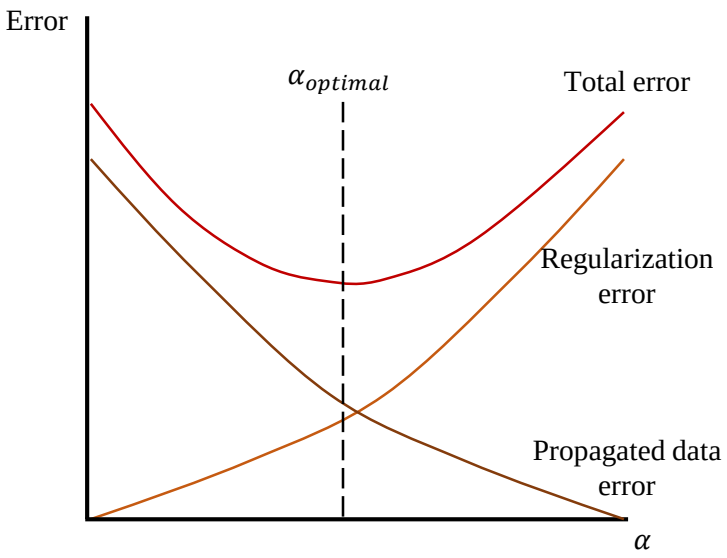

Figure 7.1: Error behavior as a function of regularization parameter, α. Figure adapted from Engl and Kugler[98].

Variational regularization, often referred to simply as Tikhonov regularization, also seeks to minimize Equation 7.5 but with a penalty term added to it so that the regularized solution, $\mathbf{f}_\alpha$, is the $\mathbf{f}$ which satisfies Equation 7.8

$$\mathbf{f}_\alpha = arg\ \min_{\mathbf{f}}[||K\mathbf{f} - \mathbf{d}||^2 + \alpha||\mathbf{f}||^2] \tag{7.8}$$

where α is again the regularization parameter[98]. The use of $||\mathbf{f}||$ in the right-hand term in Equation 7.8 is the conventional formulation for Tikhonov regularization. Beck and Woodbury[103] term such a formulation as a zeroth-order regularization. First- or second-order terms such as $||\mathbf{f}'||$ or $||\mathbf{f}''||$ could also be used where the order corresponds to the order of differentiation of $||\mathbf{f}||$. Zeroth-order terms reduce large magnitude fluctuations but bias towards zero whereas first-order terms bias towards a constant while still reducing fluctuations, and second-order terms penalize high curvatures in the solution. Another formulation of Equation 7.8 is to replace $||\mathbf{f}||^2$ by $||\mathbf{f} - \mathbf{f_0}||^2$ where f_0 is an estimate of the final solution based on any *a priori* information available [104].

Another method of regularization is through iterative methods which also seek to minimize the term $||K\mathbf{f} - \mathbf{d}||^2$ in Equation 7.5. Initially, $\mathbf{f}$ is set to a vector of zeroes, and a gradient method is used to iteratively converge to the exact solution for $\mathbf{f}$. The exact solution could be calculated more simply by matrix inversion of K, but iterative methods are different in that the iteration stops after a specified number of iterations. Therefore, the regularization parameter, α, is defined simply as the number of iterations allowed for the gradient solver before termination. Contrary to the previous discussions of α, for the case of iterative

regularization, larger values of α indicate less regularization whereas smaller values of α indicate more regularization. It can be seen that by allowing fewer iterations, the solution will be relatively smooth because it has not moved very far from the initial zero solution.

For each of the methods (filtering, variational, and iterative), there is some choice of regularization parameter that must be made with the goal of balancing the attenuation of noise propagation with the loss of information due to the additional constraints of the regularization method. A graphical illustration of this balance is given by Figure 7.1.

In cases where there is no mathematical proof related to convergence, *a posteriori* selection of the regularization parameter is required. The discrepancy rule provides such a selection by specifying that α, starting at a high value, should be decreased until Equation 7.9 is just satisfied

$$||K\mathbf{f}_\alpha - \mathbf{d}|| = \delta \tag{7.9}$$

where $\mathbf{f}_\alpha$ is the regularized solution. Hansen and O'Leary[101] note that the discrepancy principle is generally known to oversmooth the solution - i.e. remove more information than just noise. They note one alternative which is generalized cross-validation (GCV), however, this method is not good in the face of correlated noise. Rather, the L-curve method plots the left term of Equation 7.8 versus its right term for different values of α. The plot has an L-shaped corner where the solution changes from being dominated by overfitting of noise to oversmoothing, and this is the location at which the appropriate α is found.

Another nuance of regularization techniques as noted by Beck and Woodbury[103] is the formulation of the operator in the first term of Equation 7.8, for instance. If errors have zero mean, constant variance, are uncorrelated, and have a Gaussian distribution, then they are additive and a least-squares (L^2-norm) operator is appropriate. If the variances are not constant, a weighted least-squares is appropriate where the weighting is the the reciprocal of the variance. Another type of error is multiplicative errors which occur when variance is proportional to the magnitude of the measurement. The operator should then be normalized on the measurement magnitude.

7.1.1.2 Non-Linear Inverse Problems

This section follows the guide of Engl and Kugler[98]. Non-linear problems have the same form as Equation 7.1 except that the matrix K is now dependent on d. Non-linear inverse problems have the same ill-posedness as linear inverse problems, however, not all the techniques available for the linear case are applicable to the non-linear case. Specifically, regularization via filtering methods related to singular value decomposition is not applicable anymore.

Variational regularization such as Tikhonov regularization can be performed, as before, by

adding a penalty term to the minimization problem, however, the solution must be reached through iterative techniques rather than through closed-form matrix inversion techniques. Equation 7.8, unlike in the linear case, is usually non-convex, and it is common for gradient-based methods to get stuck in local minimum which are not global minimum[98][105].

As before, iterative regularization specifies the number of iterations to be performed towards minimizing Equation 7.5 without adding an explicit regularization term. Iterative techniques are based on Equation 7.10

$$f_{k+1} = f_k = G_k(f_k, d) \tag{7.10}$$

where k specifies the iteration number and G_k can have different forms depending on what type of iteration method is used. Descent methods and Newton methods are two choices[104]. Nonlinear Landweber iteration is used often as a descent method. Newton's method requires the calculation of an inverse of the gradient of the K matrix and will be unstable, but regularized versions of Newton's method that are stable are the Levenberg-Marquardt method and iteratively regularized Gauss-Newton method. As in the linear case, the iterations must be stopped at the appropriate time in order to provide the regularizing effect. The discrepancy principle can again be used to determine when to stop. Iterative methods have been proven successful for mildly non-linear problems but not yet for strongly non-linear problems[105].

7.1.2 Literature Review

Below is a review of past work on inverse problems in structural mechanics. This includes several regularization methods and relates to static problems unless otherwise noted. In the interest of the present work, highlight will be made of several non-linear inverse examples in addition to the more numerous examples of linear inverse problems. Not included below are methods based on neural networks which require a large amount of up-front data to train the neural network to inversely identify loading from structural measurements as in Sofyan and Trivailo [106], for instance.

The most direct approach to inferring loading from displacement data involves what is referred to as the direct approach by Stanford *et al.*[93] which involves straightforward matrix multiplication of measured deflections with the inverted stiffness matrix from a finite element representation of the structure. As noted, this approach can be very sensitive to noise in the input displacements and is not generally found in published studies in the mechanical sciences. Alternatively, one can use the regularized approach to stabilize the solution as described in the previous section. Such is the case for all the literature reviewed below. First is presented authors who used regularization via least-squares projection methods only, and following is those who used some sort of additional regularization such as filtering, variational, or iterative regularization. In each subsection, the literature are generally presented in chronological order.

7.1.2.1 Regularization by Projection

By way of summary, projection methods project the measured data onto a finite-dimensional model and solve for the input vector, or loading vector, that produces least-squares minimization with some observed data. In the case of over-determined linear problems, the result is a minimization problem to find the optimal loading vector. In the case of nonlinear problems, the loading must be arrived at iteratively. It is noted that as the number of basis functions in the finite-dimensional model reaches the number of degrees of freedom of the model, the regularized approach asymptotes to the direct approach described above[93]. The number of basis functions must therefore be kept relatively low in order for the projection method to provide a regularizing effect.

Shkarayev *et al.*[107] approaches the inverse problem seeking to reconstruct loads, stresses, and displacements from surface strain data such as on a wing of an aircraft. A number of unknown loading distributions, F_i, are first formulated in parametric form as Equation 7.11

$$F_i(x) = \sum_{j=1}^{l} a_{ij} R_{ij}(x) \tag{7.11}$$

where R_{ij} are specified basis functions which are taken to be Chebyshev polynomials, a_{ij} are unknown weighting factors, i's are the load case index, and j's indicate different terms of the spatial distribution function. Loading distributions for each load case are used to determine the nodal forces for a linear finite element model as a function of the weighting constants, a_{ij}. Similar to Equation 7.5 but using strains rather than displacement, a least-squares minimization function, S_i, for each load case i based on the measured and computed strains is constructed as a function of the unknown a_{ij}'s as in Equation 7.12

$$S_i = \{\sum_{j=1}^{m} a_{ij}\varepsilon_{ij} - \varepsilon_i^*\}^T \{\sum_{j=1}^{m} a_{ij}\varepsilon_{ij} - \varepsilon_i^*\} \tag{7.12}$$

where the superscript * indicates the experimental strains. As there are exactly the same number of measured strain locations as modeled strain locations, the minimization has a unique solution and is achieved by differentiating the function with respect to each a_{ij} and solving the linear system of equations. Different loading cases can be specified by different number of terms in the Chebyshev series, and the best may be chosen through a specified quality function. As no explicit regularization is employed, the method relies on the appropriateness of the form of R_{ij} and the number of terms retained during the projection of the measured strains onto the finite-element model. The authors demonstrate the inverse method through two numerical examples on a plate and a wing box which were able to reproduce loading distributions from strain data. In these two examples, the functional form of the loading distribution was known exactly and no simulation of experimental noise in

the strain data was present.

Coates *et al.* [108] continue on the same path as Shkarayev *et al.* except they express the loading function in Equation 7.11 not as Chebyshev polynomials but as a Fourier series. Furthermore, in Coates and Thamburaj [109], the pressure loading representation is extended to a double Fourier series of the form in Equation 7.13

$$p(x,y) = a_{00} + \sum_{m=1}^{\infty} a_{0m} cos(\frac{m\pi y}{K}) + \sum_{n=1}^{\infty} a_{n0} cos(\frac{m\pi x}{L}) + \sum_{m=1}^{\infty}\sum_{n=1}^{\infty} a_{nm} cos(\frac{m\pi y}{K}) cos(\frac{m\pi x}{L}) \tag{7.13}$$

where a's are coefficients to be determined, K is the width of the simulated wing, and L is the length of the simulated wing. The cosine series was selected because of its ability to handle the asymmetry inherent in a semi-span wing, and in practice, only a finite number of terms in the series are maintained. The overall rationale for using a Fourier series is that they are able to represent with a single set of coefficients several different functions that occur in intervals one-after-another unlike other functions that would require a piecewise arrangement, as well as the fact that there are existing databases of Fourier coefficients for different wing loadings although these were not used in the current study. Instead, a brief database of loading cases and associated strains was collected by first running direct simulations with a linear, thin plate finite element method of load cases with simple functional forms such as polynomial and exponential. The inverse technique was then used to compute the weighting coefficients for a Fourier series of specified number of terms for each of the previously mentioned polynomial loading cases. These coefficients and their associated nominal loading distributions embody the database of loading cases which might in a future implementation be defined from tables of Fourier coefficients for various wing loadings. Next, an unknown loading case is simulated directly using finite elements, and the inverse technique finds the weighting coefficients of the Fourier series which minimize the difference between the unknown loading strains and the inverse-calculated strains via least-squares as in Shkarayev *et al.*. Finally, the computed coefficients are compared to the database of coefficients to determine which polynomial loading distribution is most similar in the least-squares sense to the unknown distribution. The authors report that the inverse method selected the correct functions from the database even with 10% noise added to the input function although the selection of the correct form did not preclude error in the calculated coefficients of the given functions.

Tessler and Spangler [110] performed the inverse problem as related to plates and shells. Similar to previous authors, Tessler and Spangler use a least-squares projection method except that there are three least-squares minimizations corresponding to three deformation modes: membrane-stretching, bending, and transverse shear, the former of these being decoupled from the latter two. First, measured strains are fitted to a continuous approximation using a technique called *smoothing element analysis* based on a finite element approximation. Such a continuous approximation helps filter noise and allows the least-squares minimization function to be written in integral form. Using a displacement formulation of plate finite elements

with first-order shear-deformation theory, the three minimization functionals are constructed and differentiated with respect to each kinematic displacement which yields five Euler equations, two for the membrane stretching and three for the bending and shear deformation. The Euler equations, which equate experimental strains to finite element displacements, are then solved for the displacements after a functional form for the displacement field which satisfies the essential boundary conditions has been specified. In the example presented, the inverse method returns the exact displacement field calculated by the direct solution of the problem. However, the functional form of the loading distribution was known exactly and no simulation of experimental noise in the strain data was present.

Stanford *et al.* [93] measured the deformation of a membrane wing and solved the inverse pressure problem using least-squares projection as with previous authors except they use a linear, membrane formulation of finite elements. A set of polynomial functions ranging from 3rd- to 6th-order are employed as the basis functions to describe the pressure loading. A feature incorporated into the minimization algorithm is the use of factors to weight the relative importance of the residual at different nodes between experiment and simulation based on the confidence in the error-level of each individual node. The confidence level may be based on the perceived degree of modeling error, the standard deviation of experimental measurements, or the residual between experimental and modeling results for a simple hydrostatic pressure measurement. Finding the adjusted coefficient of determination not useful for judging the quality of the selected polynomial basis functions, the performance of polynomial series of different order was judged based on the agreement of the integrated wing lift with that measured from the sting balance. The integrated lift of the different polynomial series projections showed some scatter relative to the sting balance measurements. Some of the inversely calculated pressure distributions had non-intuitive features that are presumably the result of overfitting of experimental data with too many degrees of freedom.

Carpenter and Albertini [111] make use of full-field deformation data from digital image correlation measurements to infer pressure distributions on a geometrically non-linear membrane wing using least-squares projection. The authors take a simpler approach than the other articles in this section in that no finite element model is used. Instead, a regularization effect is achieved by projecting the full-field out-of-plane strain data onto a polynomial basis function which satisfies the essential boundary conditions. To prepare for the projection, the concept of the virtual strain sensor is used to extract strain data in both orthogonal directions at discrete locations by integrating the full-field strain over a local region. The polynomial basis function is posed as the out-of-plane displacement function and then differentiated and inserted into Equations 2.54 and 2.55 which must be used since the geometric non-linearity of the membrane cannot be neglected for this problem. However, the calculation of Equations 2.54 and 2.55 requires knowledge of the in-plane displacement, as well as the out-of-plane displacement. Thus, in order to close the problem, the authors use an empirical approximation for the in-plane strain components, u and v, as in Equation 7.14

$$u(x,y) = x - a\frac{S_x(x,y)}{S_x(a,y)}, \qquad v(x,y) = y - b\frac{S_y(x,y)}{S_y(x,b)} \tag{7.14}$$

where a and b are the lengths of the undeformed membrane in the x- and y-directions, respectively, and S is the arc-length of the membrane relative to the origin with the coordinate direction of the calculation given by the subscript. The arc-length calculation and thus the strain interpolation now involve only the out-of-plane displacement. Finally, the weighting coefficients of the basis functions are adjusted to minimize the difference between the measured and computed strains in both the orthogonal directions. The result is a polynomial representation of both strain and displacement that are used to directly evaluate Equation 2.51, as well as Equation 2.67, and produce a continuous pressure field. Two test cases were a hydro-static pressure test and a wind tunnel test. For the hydro-static test, the inverse technique produced a pressure distribution that was not quite flat and slightly biased towards higher pressure. As a comparison, the hydrostatic pressure field was reconstructed via direct calculation from the raw, full-field strain data measured by the digital image correlation system, and the results from this unregularized technique are centered around the correct mean value of pressure but understandably noisy. For wind tunnel tests of the membrane wing, differences in the measurement of lift coefficient between the sting balance and the integrated pressures of the inverse technique range from 0.05-0.2.

With the exception of the last example, all the articles in this section employed linear finite elements to perform the inverse problem. Similar methods could be employed with nonlinear finite elements, the only difference being that the solution would be arrived at with an appropriate iteration scheme rather through a closed form least-squares calculation.

7.1.2.2 Regularization by Other Methods

Maniatty *et al.* [112] use variational regularization for their inverse calculations on a linear, two-dimensional finite element model. The problem is formulated to minimize the difference between the approximate displacement measurements at selected points (which is given in this case by a reference finite element solution with noise added to the displacements) and inverse finite-element displacement data by varying the boundary loading, or tractions, in an iterative process. Added to an objective function similar to Equation 7.5 were regularization functionals to limit the absolute value of the tractions and rate of change between iterations of the tractions. Only the second of these was found to be effective, and it is given by Ω in Equation 7.15 as

$$\Omega = (\boldsymbol{\tau}^r - \boldsymbol{\tau}^{r-1})^T[F](\boldsymbol{\tau}^r - \boldsymbol{\tau}^{r-1}) \tag{7.15}$$

where $\boldsymbol{\tau}$ is the vector of tractions, F is an unweighted diagonal matrix, and r is the iteration number. The scaling of F can be chosen rather arbitrarily without effect on the converged

solution. Because Equation 7.15 contains terms related to the loading history, the minimization of the objective function produces a formula for the update of the traction vector. The updated traction vector can be used to calculate updated nodal displacements, and the process repeats until convergence. Two example problems are presented that solve for the tractions given input approximations of either displacement or strain at certain internal points. The error in the final tractions calculated by the inversion method was linearly related to the magnitude of noise added to the displacement data of the reference solution. The method of these authors could be used to predict the number, location, and accuracy of experimental displacement inputs required to achieve a certain accuracy in the inverse-calculated tractions although it was found that the number of inputs has only a weak effect on the solution as long as there are as many inputs as unknown tractions.

Schnur and Zabaras [113] follow on the work of Maniatty *et al.*, however, they present two variational regularization schemes that have more physical significance and offer the possibility of performing inversion with fewer input displacements than desired output tractions. The first scheme, termed *spatial regularization*, is an implementation of the standard Tikhonov regularization and uses a smoothing functional, Ω, which adds a penalty to Equation 7.5 which is shown in Equation 7.16 for one dimension as

$$\Omega = \frac{1}{2}\alpha_0 \int (\tau)^2 ds + \alpha_1 \int (\frac{\partial \tau}{\partial s})^2 ds + \alpha_2 \int (\frac{\partial^2 \tau}{\partial s^2})^2 ds \tag{7.16}$$

where τ's are the unknown tractions along the boundary s, and α's are the scaling terms for either the zeroth-, first-, or second-order regularization terms as indicated by the subscripts. Using as an input to the inversion problem a reference finite element solution of a square plate with noise added to the displacements, first-order terms were found most useful to reproduce accurate tractions and allowed the number of input displacements to be fewer than the output tractions to be calculated. The scaling of the first-order term can be determined by starting very small and increasing until a smooth solution is obtained, and the scaling must not increase too much or it will have a significant effect on the solution. The second scheme, termed the *keynode method*, leverages problem-specific knowledge of the distribution of the tractions, representing the tractions as a polynomial generally of third degree or less. Though requiring *a priori* knowledge of the traction distribution, this method, can reduce the number of unknown tractions to just several unknown keynodes which also stabilizes the solution. As expected, increasing the number of keynodes too high produces spurious results because the solution begins to fit to the noise in the data rather than the underlying traction distribution.

Maniatty and Zabaras [114] apply the Bayesian statistical approach to the spatial regularization technique of Schnur and Zabaras in order to provide an estimate of the uncertainties associated with inverse calculations. The statistics predicted with the Bayesian approach are compared with those calculated from Monte-Carlo simulations. The predicted statistics were conservative meaning they had larger error bounds than were found by the Monte-

Carlo simulations which is likely a result of the assumption of Gaussian noise in the data when, in reality, the noise was uniformly distributed. The paper provides an interpretation of the the α's in Equation 7.16 as the variance of the uncertainty due to both the error in the experimental displacements and the physical inaccuracies inherent in the finite-element simulation. Additionally, quantitative results are described on the balance between keeping the relative magnitude of the spatial regularization terms small in order to just stabilize the solution without significantly affecting it while keeping them large in order to minimize the uncertainty in the calculated solutions. The desired magnitude can be found by trial and error, and the final solution should be insensitive to the scaling of the regularization terms over one or two orders of magnitude. First-order regularization was used for most analyses of the example problems, this order apparently emerging as the best for the problems examined.

Ring[115] applies variational regularization techniques to find the pressure load and bending moment along a bending beam subject to breaking from measurements of its inclination. One method explored was to solve a regularized least-squares minimization problem using as constraints the equilibrium equation and assumptions about the boundary conditions. However, the piece-wise non-linearity in the constitutive relations of the problem was problematic for sequential quadratic programming algorithms. Instead, a two step procedure is used. First, the location of the breaks in the beam are determined by an inverse problem for the second derivative of deflection which uses a total variation regularization where the functional added to the least-squares minimization Equation 7.5 is given in Equation 7.17 as

$$\Omega = \int |f'|. \tag{7.17}$$

The total variation functional is a Tikhonov-like regularization term, similar to a first-order regularization term as described previously. Once the location of the breaks are determined, the loading distributions are inferred using an implementation of zeroth-order Tikhonov regularization.

Chock and Kapania [116, 117] use one- and two-dimensional, linear finite-element models combined with filtering regularization to infer loading from noisy structural measurements. The method is implemented with a T-stiffener beam and a plate where the inverse method is validated using reference data from a forward solution of the finite element code. Without noise added to the reference data, the bi-conjugate gradient method or SVD were needed to solve the least-squares minimization problem because ill-conditioning of the stiffness matrix was troublesome for descent methods. With the proper choice of the number of eigenvalues to maintain, SVD regularization also makes the solution process robust enough to handle noise in the experimental data.

Li and Kapania [118] present an extension of the work of Chock and Kapania and give several parameter studies for the inputs of an inverse finite element technique using both linear and nonlinear beam elements. As also recommended by Beck and Woodbury[103], the authors

find that it is preferable to calculate the least-squares residuals between measurement and simulated displacements as unity minus the ratio of the two rather than a simple difference so that smaller displacements have equal weighting as larger displacements. When determining element size, smaller finite elements do not necessarily produce more accurate results, and the minimum number of nodes that still gives an acceptable resolution should be used. Similarly, keeping the problem overdetermined such that there are more measurements than unknown nodal loadings in the model is desirable to prevent oscillating loads. One intelligible way to keep the problem overdetermined is to maintain as low of an order load representation as possible, as well as add regularization terms to the error matrix which decreases the degrees of freedom of the model. The variational regularization methods suggested all involve adding penalty terms to the least-squares minimization including a Tikhonov regularization term, a smoothing term representing the average deviation of the load from a linear distribution over each element, and a discontinuity term which represents the average load discontinuity between adjacent elements. Convergence is reached with a quasi-Newton method.

Xu *et al.*[119], with an interest in dynamic as well as static problems, use an extended Kalman filter to iteratively update finite element pressure loading to match measured displacements. The calculation of the sensitivity of the stiffness matrix to changes in pressure is computationally expensive since the stiffness matrix is assumed nonlinear, and thus the calculation is replaced by an estimation based on the secant modulus of previously calculated stiffness matrices. For the quasi-static case, the inverse problem is a scalar one as a single location is selected to monitor pressure and displacement. Initial values are selected for the pressure and variance of pressure, displacement, and strain, the extended Kalman filter is used to move towards a solution and convergence is met when tolerances for the difference between measurement and inverse finite element model in terms of either strain or out-of-plane displacement at a selected location are met. The results are validated with an experiment using a strain gage and the difference between identified load and experiment are usually under 1%.

Nakamura *et al.*[120] use strains sampled across a wing to determine the pressure load using a linear finite element analysis with shell elements and regularization by filtering and variational techniques. The first part of their work demonstrates regularization by projection as presented in Section 7.1.2.1. The terms of the least-squares objective function are normalized on strain magnitude, producing a similar effect as using the ratio of measured to simulated results in the least-squares formulation of Li and Kapania. For the case with noise added to the sampled strains, it was necessary to use truncated singular value decomposition to obtain reasonable results. For instance, the rank of the inverted matrix was reduced from 153 to 27 in the case of the best results for 1% measurement noise. The second and most unique part of their work centered around a prescribed loading that was derived from thin-airfoil theory. Added to the least-squares minimization function was a penalty parameter which described the variation of the load from the thin-airfoil calculation. A quasi-Newton method was used to update the pressure load and a parametric study of the effect of the scaling of the penalty parameter was performed. For the case with no measurement noise, it was found

that the useful range of the penalty parameter that produced more accurate results than simply applying least-squares to the minimization function was over 10 orders of magnitude wide. For the case with measurement noise, the penalty parameter produced better results than the truncated singular value decomposition method over 4 or 5 orders of magnitude of penalty parameter scaling. Of course, such positive results are not unexpected since the penalty parameter leverages the same form as the prescribed loading. However, Nakamura *et al.* present an intuitive means of regularization which utilizes aerodynamic knowledge to arrive at appropriate pressure distributions.

Dickinson and Singler [121], rather than pre-specify the functional form of the pressure loading, first solve the linear inverse problem at the PDE level. This method allows the exact functional form of the load to be determined, and discretization is only performed at the very end of the process. The downside is the high computational resources required to solve the weak form of the membrane equilibrium equation at every measurement location. Initial inverse solutions were run with no added noise to the reference finite element results. It was studied the effect of the number of measurement points on the solution accuracy, and the authors note that there is a point at which adding measurement points has no further effect on the solution accuracy. Some cases of loading are nonconforming in that they have nonzero Dirichlet boundary conditions or unsmooth distributions. One suggestion for handling such cases is to use a total variation regularization scheme. Other inverse solutions were run with noise added to the reference finite element data. Tikhonov regularization (zeroth-order) was used, and it was considered the effect of the regularization parameter α on the solution. Specifically, the value of α can be chosen so as to make the norm of the residual close to the noise estimate δ which is the discrepancy principle. It is noted that this method is formulated for linear problems and that the nonlinear problem would not be closed-form.

Alioli [122] is, to the author's knowledge, the first and only use of a nonlinear membrane formulation with the inverse finite element approach. Full-field strain and displacement data are first resampled onto a suitable grid using moving least squares. The minimization problem differences the measured and simulated strains using Equation 7.18

$$\Phi_e = \frac{1}{2}\int_A \mathbf{e}^{\mathbf{T}}\mathbf{D}\mathbf{e}dA \tag{7.18}$$

where A is the area of the membrane, e is the vector of differences between measured and computed strains, and D is the constitutive matrix of the membrane which acts as a weighting factor that makes the error have the same form as strain energy. Equation 7.18 is the same as the standard form of the least-squares minimization function seen by other authors except that the error is weighted by the constitutive matrix. A variational regularization term is also added to the error function to promote stability since membrane strains appear identical when deflected in opposite directions, and thus the inverse solution is not unique. The regularization term is given by Ω_u as in Equation 7.19

$$\Omega_u = \frac{T_x}{2}\int_A (\frac{\partial w}{\partial x} - \frac{\partial w_{ref}}{\partial x})^2 dA + \frac{T_y}{2}\int_A (\frac{\partial w}{\partial y} - \frac{\partial w_{ref}}{\partial y})^2 dA + T_{xy}\int_A (\frac{\partial w}{\partial x} - \frac{\partial w_{ref}}{\partial x})(\frac{\partial w}{\partial y} - \frac{\partial w_{ref}}{\partial y}) dA \tag{7.19}$$

where A's are the area of the membrane, T's are the tension components in the coordinate direction indicated by the subscript (xy subscript indicates shear), w are the out-of-plane displacements, and w_{ref} are the out-of-plane displacements of a reference solution. The reference solution is initially selected as a guess of the final membrane shape and is updated after each iteration until it goes to zero at convergence like a damped-least squares approach. The update formula for w_{ref} is given in Equation 7.20

$$w_{ref}^{i+1} = (1-\alpha) w_{ref}^{i} + \alpha(w_{ref}^{i} + \Delta w_{ref}^{i}) \tag{7.20}$$

where α is a relaxation parameter, and $\alpha = 1$ means no relaxation. The solution process requires nested loop iteration: an inner loop to solve the nonlinear finite element problem and an outerloop to converge on the regularized solution. Finally, after a displacement field has been calculated, a test function is used to calculate the pressure field over the membrane although it is inaccurate near the boundaries where it is forced to go to zero. The inverse analysis technique is used in a hydro-static pressure experiment and the inverse-calculated loading compared with the actual pressure loading and the loading calculated directly from the full strain field. There was qualitative agreement of the inverse-calculated pressure distribution with the actual hydrostatic pressure, and the error in the resultant force is 20%.

7.1.3 Present Approach

The inverse pressure calculations in this chapter are based on the out-of-plane equilibrium equation for a membrane, Equation 2.67. Using regularization by projection, the measured displacement data are fit to appropriately chosen basis functions and differentiated. The differentiated results are then input into Equations 2.54, 2.55, and 2.56 which account for geometrically non-linear deformations. Note that the present measurements do not use an empirical approach such as Carpenter and Albertani [111] to gather the in-plane components of deformation but rather measure them directly, despite their small magnitude. The strains from Equations 2.54, 2.55, and 2.56 are then substituted into Equation 2.51, and the resulting stresses are substituted into Equation 2.67. Therefore, we are able to directly compute the wall pressure, p, at each location along the Kevlar without being limited by compatibility, Equation 2.61, since all terms in the equilibrium equation are measured. The combination of the above equations results in the calculation for the wall pressure, p_{wall},

$$p_{wall} = p_{chamber} - [T_{x,0} + \frac{hE_x(\frac{\partial u}{\partial x} + \frac{1}{2}(\frac{\partial w}{\partial x})^2 + \nu_{xy}(\frac{\partial v}{\partial y} + \frac{1}{2}(\frac{\partial w}{\partial y})^2))}{1 - \nu_{xy}^2}]\frac{\partial^2 w}{\partial x^2} - [T_{y,0} + \frac{hE_y(\frac{\partial v}{\partial y} + \frac{1}{2}(\frac{\partial w}{\partial y})^2 + \nu_{yx}(\frac{\partial u}{\partial x} + \frac{1}{2}(\frac{\partial w}{\partial x})^2))}{1 - \nu_{yx}^2}]\frac{\partial^2 w}{\partial y^2}. \quad (7.21)$$

where $p_{chamber}$ is the pressure on the back side of the wall in the anechoic chamber and the shear terms have been neglected due to the small magnitude of the shear modulus as discussed in Section 2.3.3.3. Three types of terms exist on the right-hand side of Equation 7.21 which are pre-tension terms, material properties terms, and deflection terms. The pre-tension terms derive from the measurements to be described in Section 7.2, the material properties terms originate from the data presented in Section 4.2, and the displacements come from the tests to be described in Section 7.3.

7.2 Pre-Tension Measurements

Before proceeding with the inverse load calculations, it is required to know the initial tension distribution of the Kevlar walls which might be gained from one of two methods: (1) by applying a constant pressure across the Kevlar walls, measuring the displacements, and solving Equation 2.67 for T_x and T_y, or (2) by using an external device to make measurements spread around the Kevlar walls. Both will be examined below. The tension measurements to be described took place during Campaign 3, before any of the runs listed in Table 3.3 were completed. The fabric type was therefore Fabric B with speckles.

7.2.1 Full-Scale Bulge Test

The concept of the bulge test was introduced in Section 4.2. The full-scale implementation of the bulge test is now performed in the Stability Wind Tunnel with the tunnel flow off. The anechoic chambers that mate up against their respective Kevlar wall act as sealed plenums. This is a natural use for the chambers which are designed to be sealed to the outside except at the Kevlar wall itself where mass exchange with the test section occurs. In the region of the Kevlar wall, the chamber is sealed from the test section using impermeable plastic sheeting which eliminates any direct mass flow between the chamber and the test section. The sheeting creates a seal around the Kevlar wall with the help of aluminum foil tape, and special care is taken around the corners of the Kevlar wall to maintain the seal. Suction is applied to the chamber by a centrifugal blower with a maximum volumetric flowrate of 6,000-CFM. The blower, typically employed in the tunnel flow-control system, is connected

to either of the chambers with a 30-cm (12-in.) diameter hose that is mounted to a flange which is, in turn, bolted to the outside of the anechoic chamber.

As the calculation of pre-tension in the Kevlar requires the pressure difference across the wall, the pressure inside the test section was measured using pressure lines in the test section, and the pressure inside the anechoic chamber was measured with a pressure line that entered the chamber through a cutout for cable and tubing access. Both pressures were measured with the Esterline scanner unit described in Section 3.1.4 with range of ± 10 inches of water.

To take the measurements, the blower power was incrementally increased from 0-100% capacity with measurements taken every 10%. As suction was turned on, the impermeable sheet pulled flat against the tunnel-side of the Kevlar wall. By the feeling of a hand from inside the test section, it was clear that some flow leaked from the test section above and below the test section ceiling and floor, respectively, but this flow is unlikely to have introduced any significant non-uniformity in the pressure loading across the wall.

The deformation of the Kevlar under the pressure load was captured with the 3D-DIC system of Section 3.1.7. Only the out-of-plane components of deflection were retained since the Kevlar will asymptote to linear membrane behavior as it un-bulges. The uncertainty of the raw w-deformations are 60-μm as quoted previously for the DIC system. However, the uncertainty in the final calculation of pre-tension is difficult to quantify since this uncertainty will be mostly incurred by approximations in the governing equations as will be discussed.

The measured w-deformations were interpolated to a rectangular grid as shown in the half-wall contours of Figure 7.2. The maximum w for each pressure level is also plotted in Figure 7.2, and it is clear that Δp and w are proportional. The decidedly linear behavior of the Kevlar is a result of relatively high pre-tension compared to the applied pressure. Under wind loading from a model, the pressures reach over an order of magnitude greater values, and non-linear behavior is observed. Figure 7.2 also shows that the deformation profiles are smoothly varying, and there is little to no hysteresis in the deformation of the Kevlar.

Proceeding now to the calculation of the pre-tension distribution, Equation 2.67 is solved for T assuming $T_x = T_y = T$ and $T_{xy} = 0$. Calculating T at each bulge level and extrapolating to zero pressure yields the distribution of pre-tension, or T_0. Note that this pre-tension calculation does not adhere strictly to the compatibility restrictions of Equation 2.61. A convenient aspect of this bulge procedure is that no material properties have to be assumed. The material properties are non-consequential in the limit of linear membrane behavior.

The result of extrapolating T at zero pressure difference is shown in Figure 7.3. The variation in T_0 as calculated is almost exclusively in the x-direction. It is known from experience that because of the mounting method of the Kevlar, the gradients $\partial T_{x,0}/\partial x$ and $\partial T_{y,0}/\partial y$ are both small. Thus, the observed T_0 distribution closely resembles that of a $T_{y,0}$ distribution. This result follows since the length of the Kevlar wall is over three times its height. Therefore, $\partial^2 w/\partial y^2 >> \partial^2 w/\partial x^2$, and the $\partial^2 w/\partial y^2$ term dominates in Equation 2.67 and makes T_0 very close to $T_{y,0}$.

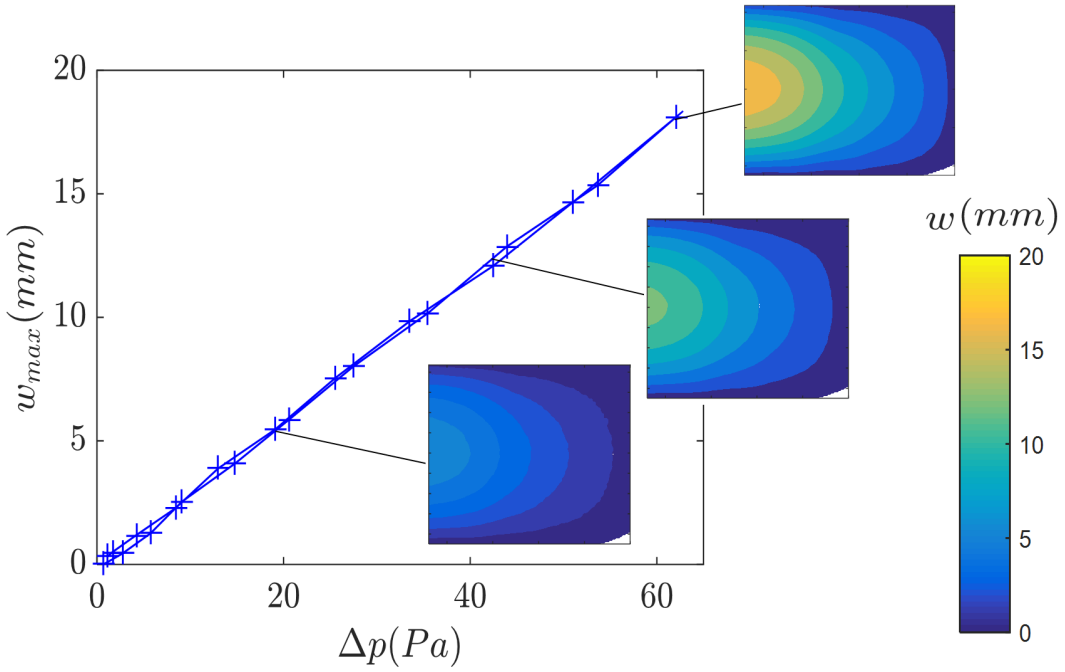

Figure 7.2: Out-of-plane deformation, w, versus pressure difference, Δp, across the Kevlar for the bulge test on the starboard wall. The plot shows the maximum w measured over the wall during the up- and down-sweeps of pressure. The contours show the bulge shape over the upstream half of the Kevlar wall for selected measurement points.

To improve upon this preliminary calculation, it is suggested that separate $T_{x,0}$ and $T_{y,0}$ values be extracted from the full-scale bulge test, such as with the use of Airy stress functions consisting of up to sixth degree polynomials. The stress function of Seide[69] may also prove useful.

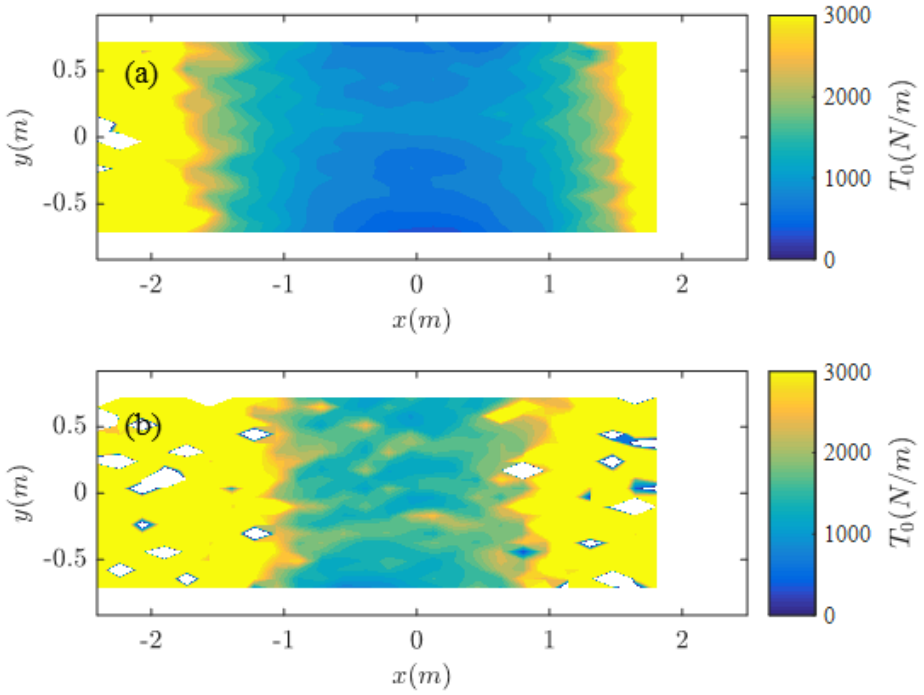

Figure 7.3: Tension distribution inferred from bulge tests on the Kevlar walls for (a) the port wall and (b) the starboard wall. The white space indicates the borders of the Kevlar that were not measured.

7.2.2 Tension Meter Test

Alternatively, the hand-held tension meter described in Appendix G was used to the measure the pre-tension distribution. These measurements occurred during the same day as the full-scale bulge test measurements without any other runs in-between. The values of $T_{x,0}$ and $T_{y,0}$ were measured at 35 grid points spread over each Kevlar wall. The positions for the measurements were located with a measuring tape and marked on the Kevlar with permanent marker. The plastic sheeting used for the bulge test was in-place when the tension meter measurements were taken, but there was slack in the sheeting and the flexural rigidity of this sheeting should be negligible compared to the measurement magnitude. The reported values of $T_{x,0}$ and $T_{y,0}$ are the result of an average of three individual measurements for each tension component at each measurement point. $T_{xy,0}$ was not measured for these measurements, having been found to be negligible from earlier measurements, as expected.

The tension distributions, which this time do not assume isotropy but contain separate $T_{x,0}$ and $T_{y,0}$ components, are shown in Figure 7.4. The distributions are physically intuitive as the tension becomes very large in the corners where the boundary conditions enforce no-deflection constraints from two directions at once. The high corner tension, as well as the high tension on the short side of the frame, are both predicted by Seide's[69] theoretical calculations. There are clear similarities between the $T_{y,0}$ distributions and the T_0 distributions of Figure 7.3, the reason for which was described above. Because they provide distinct values of both the $T_{x,0}$ and $T_{y,0}$ components of tension, the tension meter measurements are selected for continuing use the analysis below. In the future, the T_0 data gathered from bulge tests may still prove useful since this T_0 is essentially the $T_{y,0}$ component, and this component is the more impactful of the two tension components on the inverse pressure calculation.

Sample tension meter measurements were made throughout the course of Campaign 3 to monitor the tension. There was no apparent dependence of the Kevlar tension on room temperature, and the tension did not show strong variation throughout the duration of the campaign. However, after completion of the final run, Run 3-3, the tension showed a drop of $\sim$20% in some locations along the walls. As described in Table 3.3, this final run had the highest freestream dynamic pressure of any of the Kevlar-wall runs, and the increased loading on the walls evidently incurred some slippage of the Kevlar from its tensioning frame. This fact should be borne in mind when interpretting the inverse pressure calculation results for Run 3-3 to be presented later.

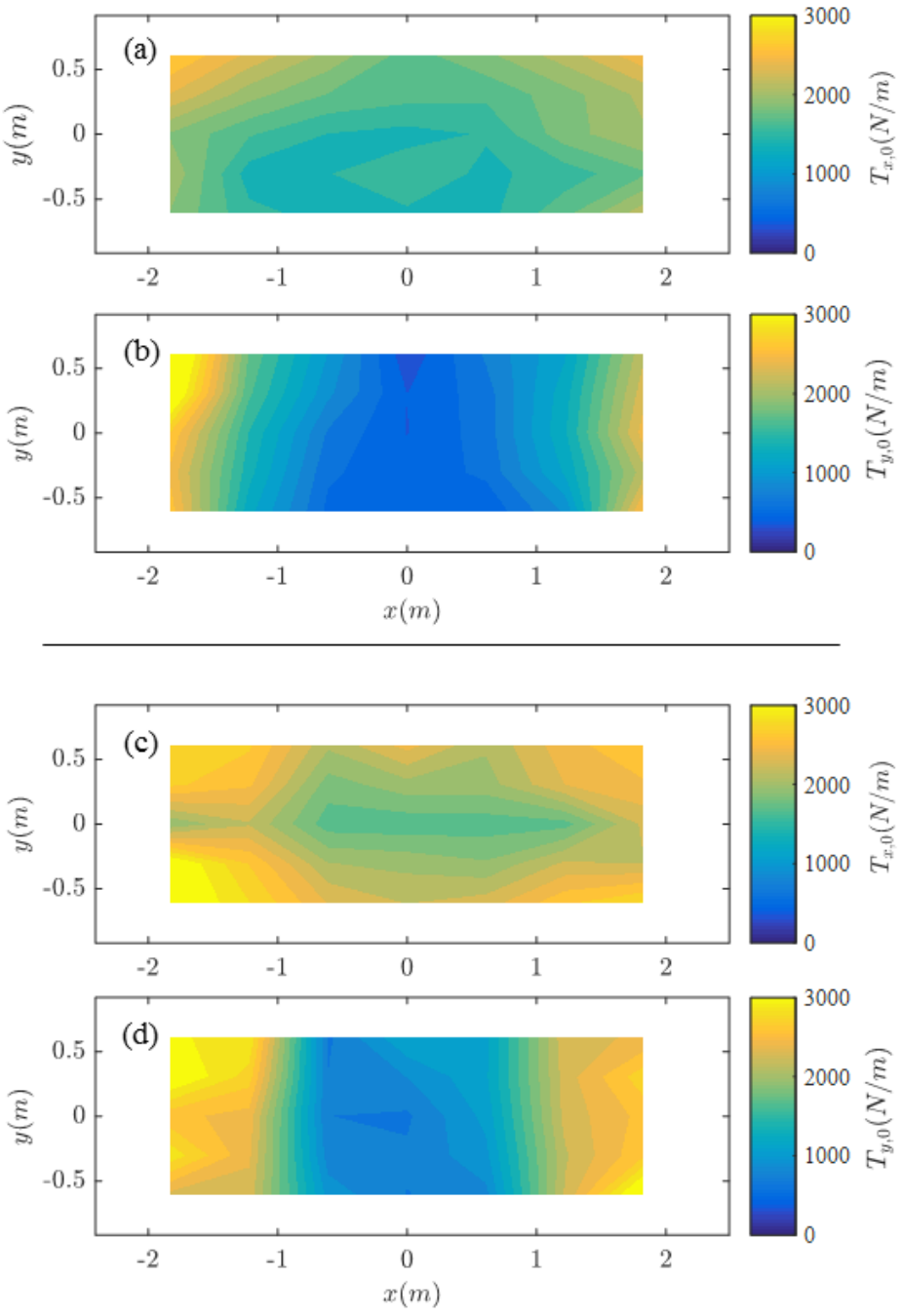

Figure 7.4: Pre-tension distribution measured in both the x- and y-directions with the hand-held tension meter for (a)-(b) the port wall and (c)-(d) the starboard wall. The measurement grid was 7 in the x-direction and 5 in the y-direction, and the white space indicates the borders of the Kevlar that were not measured.

7.3 Measurement of Wall Displacement

All the results in this chapter hinge on the accurate measurement of the global displacement field of the Kevlar walls during wind loading measurements. This section presents the displacement and displacement derivatives that are the necessary inputs into the inverse pressure problem. The data presented here are taken at the Stability Wind Tunnel during Campaign 3 using the DIC system described in Section 3.1.7.1.

The displacement data over a single Kevlar wall are captured from two separate pairs of stereo cameras. It was discovered after the testing that there was slight movement of the cameras upon pressurization of the anechoic chambers to which the cameras were mounted. Such movement is corroborated by the fact that tunnel engineers are aware of creaking as the chambers pressurize and un-pressurize. The force acting on the ceiling of the anechoic chamber, for instance, running at maximum dynamic pressure can reach 3000-N (680-lbs.).

Without knowledge of the direction or magnitude of the camera movements, it was not attempted to account for the bias created by movement *within* stereo camera pairs. However, it was noticed that differences *between* stereo pairs were dominated by translations rather than rotations and could be corrected by simple sub-millimeter translations. Therefore, the data from the downstream pair of stereo cameras was aligned in a least-squares fashion to that from the upstream pair over the 800-cm^2 of overlap area near the center of each Kevlar wall. A trend but not a rule is that the translation magnitudes, as well as the residual alignment error in overlap region, increase with increasing dynamic pressure. The above correction procedure adds a rigid-body translation uncertainty of roughly 0.5-mm to the absolute displacements, as well as uncertainty due to rigid-body rotation between pairs of cameras which was small but likely significant. In total, the achieved displacement uncertainty is significantly larger than the $\pm$40-μm and $\pm$60-μm uncertainties quoted in Section 3.1.7.1 for the in-plane and out-of-plane displacements, respectively. The uncertainty is best at low dynamic pressures which will be the focus of this section.

Deformed wall contours have been measured under the loading of the NACA0012 model during Campaign 3 of Table 3.3. The full catalog of data may be found in Appendix C.4. In this chapter, data will be shown for Runs 3-1, 3-3, and 3-5 of Table 3.3 which correspond to the untripped condition at dynamic pressures from 770-Pa to 3,300-Pa, or Reynolds numbers from 2- to 4-million. Additionally, all data presented in this section are at a geometric angle of attack of 7.78 degrees which is chosen to demonstrate the concepts of the data processing and membrane mechanics. Other angles of attack will be examined in the following section.

Contours of each of the three displacement components for both walls of the test section are shown in raw form in Figure 7.5. While the shapes of the w-displacement data are well-defined and generally symmetric, the in-plane $u-$ and v-displacements, which are notably two orders of magnitude less than the w-displacements, have varying features. Keeping in mind the 0.5-mm rigid body uncertainty noted above, the v-displacements show that the

fabric is displacing away from the midspan of the wall which is a result of the direction of the pressure vector tilting towards the outer edges. Near extreme y-values as seen especially in subfigure (e), the direction of the v-displacement reverses because the horizontal sides of the roller frame are bowing inwards under the tension of the fabric, and this deformation begins to dominate the v-displacement field. There is also banding occurring in the v-displacement data which would seem to be a result of the Kevlar tensioning process. For the u-displacements, there appears to be some contamination of the displacements by the w-displacements on the port side in subfigure (a) which would be a result of slight rotation of the Kevlar wall from the time the coordinate system was calibrated to the time of the measurement images. In general, however, the u-displacements indicate that the fabric is pulling inwards in the x-direction from its nominally fixed boundary condition which suggests that the vertical sides of the roller frame are are also bowing slightly under the tension of the fabric. The effect of the change in direction of the pressure vector is not significant in the case of the u-displacements for two reasons as it was for the v-displacements. First, the inclination angle of the Kevlar is more moderate in the x-direction than it was in the y-direction. Second, moving away from the origin in the x-direction, the pressure magnitude drops which was not the case along the y-axis.

The displacements from the DaVis software shown in Figure 7.5 have a spatial resolution of roughly 1.6-cm for a total of over 34,000 data points for each component of each wall. The processing of such data to mitigate the effect of measurement noise involved two steps. First, to reduce the run-time of the processing code in the second step, the displacements are projected onto a coarser grid consisting of 120 points in the x-direction and 46 points in the y-direction. The projection is accomplished by marching through the measurement space and simply averaging the data within each 4-cm by 4-cm interpolation window. Second, the data are regularized by least-squares projecting the 120-by-46 grid onto basis functions, either global or local. Several basis functions were compared including global polynomials, global Fourier series, and a locally weighted linear regression. The global polynomials were selected for primary use in this study as shown in Equation 7.22

$$u = \sum_{i=0}^{a}\sum_{j=0}^{b} l_{ij}x^i y^j \quad v = \sum_{i=0}^{c}\sum_{j=0}^{d} m_{ij}x^i y^j \quad w = \sum_{i=0}^{e}\sum_{j=0}^{f} n_{ij}x^i y^j \tag{7.22}$$

where x and y have their origin at the center-point of the Kevlar wall and coefficients l_{ij}, m_{ij}, and n_{ij} are determined by least-squares regression. The polynomials are here unrestrained at the boundary of the Kevlar, this arrangement being found to generally produce better results. Polynomials are preferred over a double Fourier series because the Fourier series forces the second derivative of w to zero at the boundary of the domain. This situation then requires that the pressure must return to zero at the boundaries which is not the case in the wind tunnel. One downside of the present formulation of the polynomials is that they are not orthogonal, however, this does not seem to be a fundamental problem if the values order of the polynomials do not get too high.

The selected values for the number of terms in the in-plane polynomials are $a = 14$, $b = 8$, $c = 18$, $d = 5$. These values were chosen by trial-and-error to minimize the adjusted coefficient of determination, R^2_{adj}, of the fit. Typical R^2_{adj} values were 0.95 and 0.80 for the u- and v-displacement components, respectively. Neither of the R^2_{adj} values are relatively close to unity which is due mostly to residual misalignment of the stereo cameras as a result of the unintended motion of the cameras. It should also be stated that the number of degrees in the in-plane components was such that the condition number of the inverted matrix in the least-squares fitting algorithm was greater than the reciprocal of the machine precision. However, this ill-conditioning was not apparently enough to introduce significant errors into the fitting calculation. The order of the polynomial selected for the w-displacement component is a subject of the following section. For the present, we use $e = 9$ and $f = 6$ which is close to the optimal values predicted in Appendix F.

The final result of the two-step regularization process is shown in Figure 7.6. Comparing Figures 7.5 and 7.6, it is seen that the regularized data retains the character of the raw data but smooths out fluctuations. Further consideration on the regularization strategy will be made in Section 7.5.

Taking analytic derivatives of the regularized deformation results, Figure 7.7 compares the midspan traces of the two types of deformation-induced strain terms found in Equations 2.54 and 2.55: first derivatives of the in-plane displacement and the square of first derivatives of out-of-plane displacement. These are the terms that can contribute to changes in T_x, T_y, and T_{xy} with deformation and that when large enough, cause Equation 7.21 to be non-linear. In the x-direction in Figure 7.7(a), there is very little overall induced-strain since the in-plane and out-of-plane terms work against each other. In the y-direction, on the other hand, there is negligible induced strain due to the out-of-plane motion; the out-of-plane displacement is symmetric about the midspan and therefore has zero slope at the midspan. Unlike in the x-direction, the in-plane strain in the y-direction is positive due to the stretching by the pressure vector, and the overall magnitude of induced-strain in the y-direction is significant.

The emerging picture of strain on the Kevlar walls is that the v-component strain has a significantly greater influence on the non-linear aspect of the inverse problem than the u-component strain. This conclusion is reiterated by the plots in Figure 7.8 where the magnitude of the deformation-induced stress is consistently twice as large in the y-direction as the x-direction. Furthermore, the pre-tension as described previously was found to already be significantly lower in the y-direction than the x-direction, so the y-direction deformation will be dominated by non-linear strain whereas the x-direction deformation will be dominated by linear pre-tension.

A note here is made about the negligence of the shear stress in the calculation of the Equation 7.21. Without a shear stress, there is an inherent incongruity in the in-plane equilibrium relations of Equations 2.52 and 2.53. The in-plane forces are not constant over the Kevlar wall, so there must be some mechanism to vary these forces. The magnitude of this effective shear term can be estimated by plotting just the $\partial T_x(x, y)/\partial x$ term, for instance, of

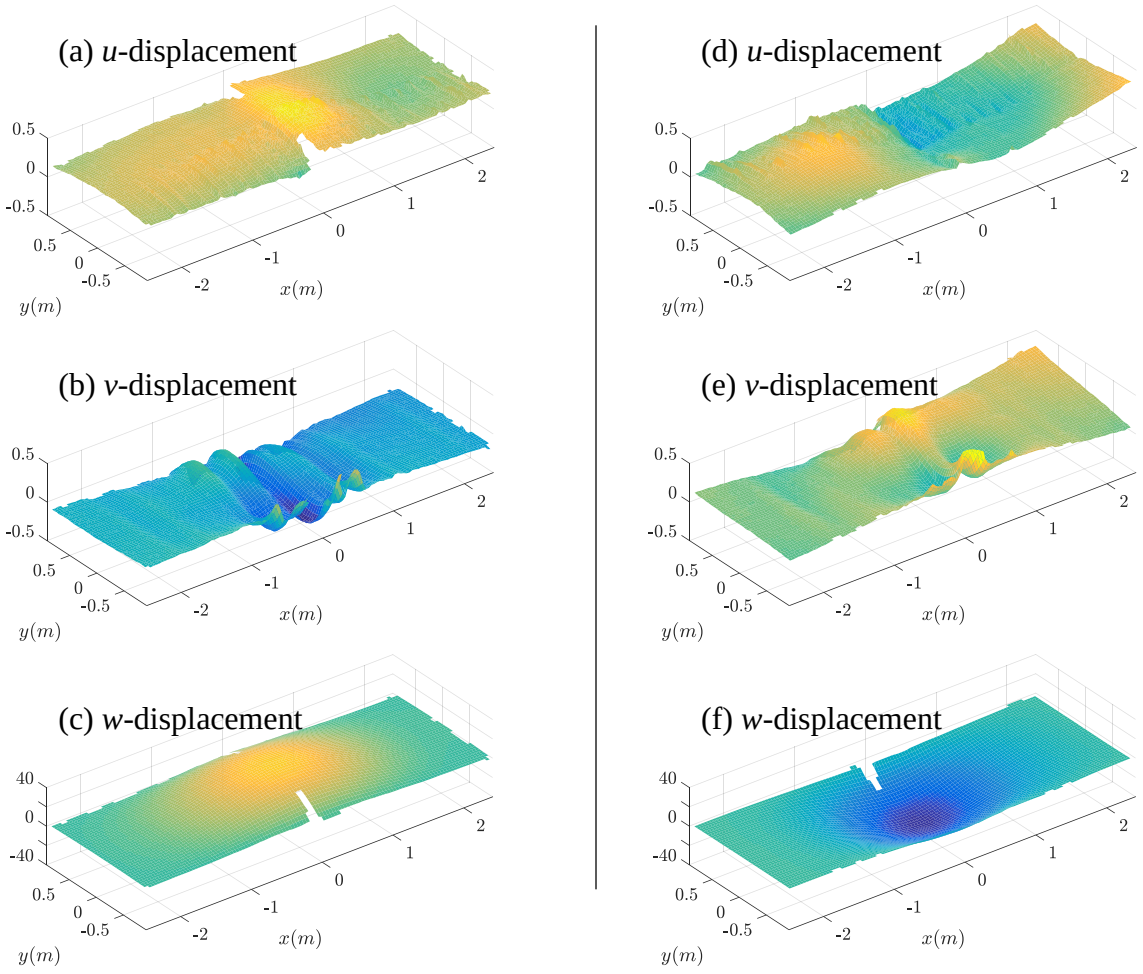

Figure 7.5: Raw displacement contours for the Kevlar on the (a-c) port side and (d)-(f) starboard side of the test section at a geometric angle of attack of 7.78 degrees and dynamic pressure of 770-Pa.

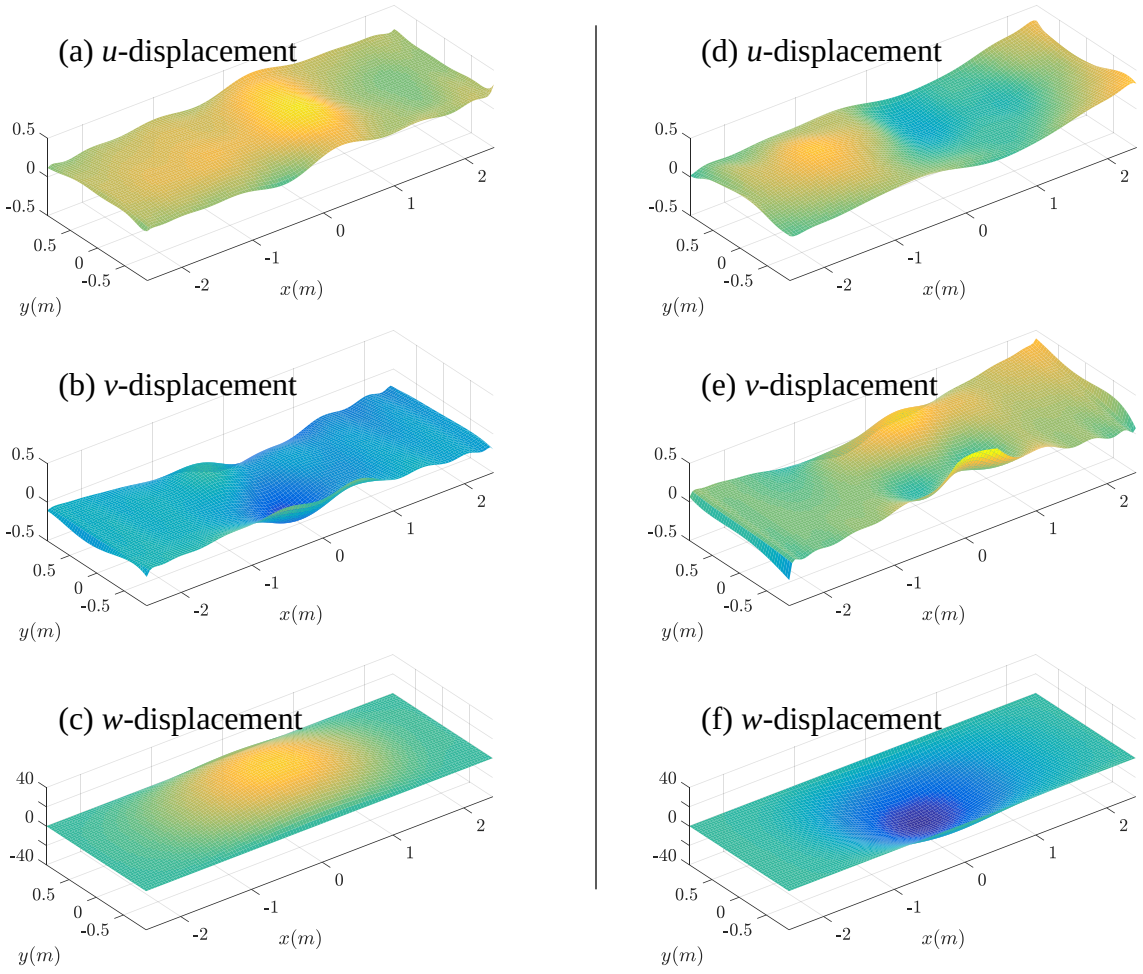

Figure 7.6: Polynomial-fitted displacement contours for the Kevlar on the (a)-(c) port side and (d)-(f) starboard side of the test section at a geometric angle of attack of 7.78 degrees and dynamic pressure of 770-Pa.

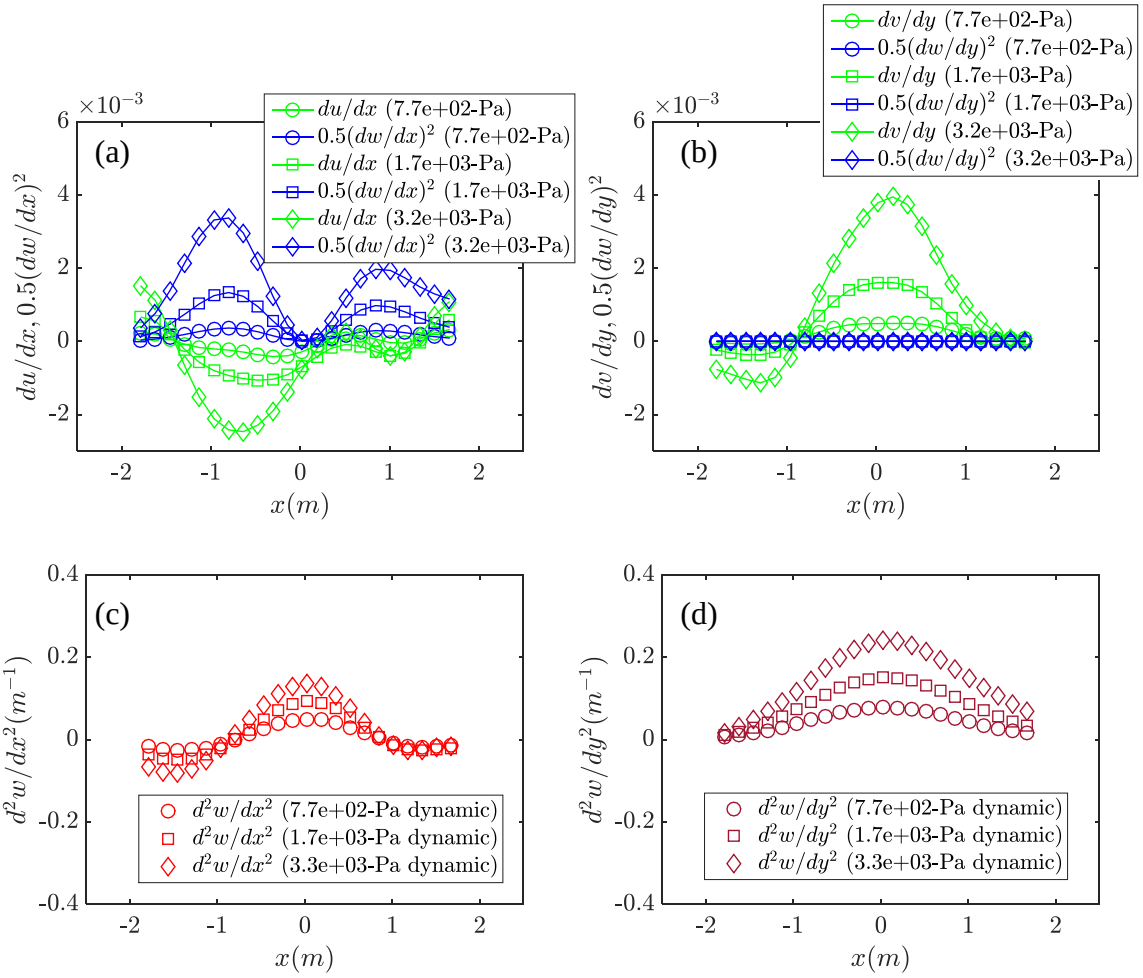

Figure 7.7: Comparison of the magnitude of deformation-induced strain terms for the (a) x-direction and (b) y-direction at a geometric angle of attack of 7.78 degrees and varying dynamic pressures. Results shown are for the suction side.

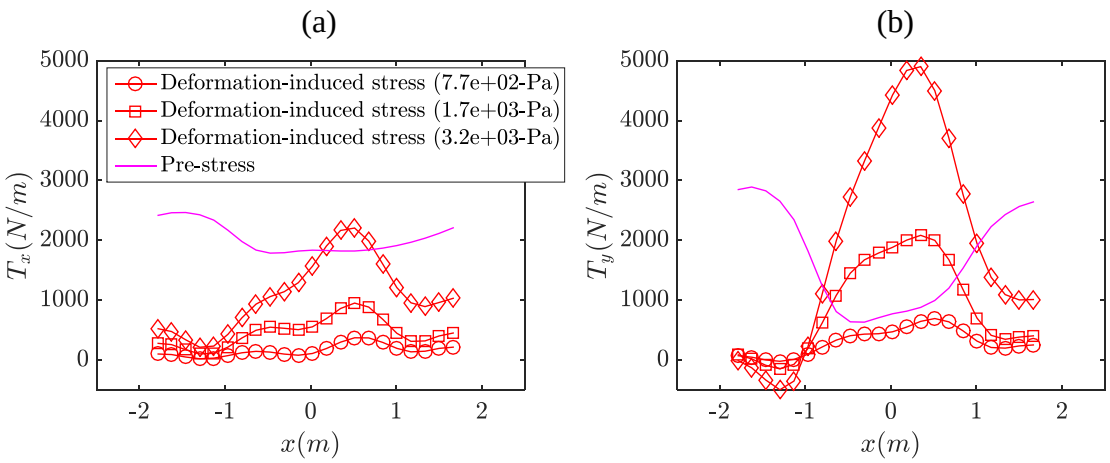

Figure 7.8: Comparison of the magnitude of deformation-induced stress and pre-stress for the (a) x-direction and (b) y-direction at a geometric angle of attack of 7.78 degrees and varying dynamic pressures. Results shown are for the suction side.

Equation 2.52, or just the $\partial T_y(x,y)/\partial y$ term of Equation 2.53. A sample of these plots are shown for the port wall of Run 3-1 in Figures 7.9 and 7.10, respectively. There do not seem to be strong trends between corresponding subfigures of Figures 7.9 and 7.10 which might be expected since the change in one component of in-plane tensile force is to be balanced by that in the other component according to Equations 2.52 and 2.53. Examining the magnitude of the $\partial T_x(x,y)/\partial x$ and $\partial T_y(x,y)/\partial y$ terms, the maximum change in in-plane tension over one meter of fabric is equivalent to $\sim 30-50\%$ of the maximum in-plane tension. Such magnitudes do not seem negligible, yet the final result of the equilibrium calculation does not appear to contain such high error as will be shown in the following section. It can only be concluded that further research needs to be pursued to quantify the validity of the assumption of neglecting shear stress in the out-of-plane equilibrium equation for the Kevlar fabric.

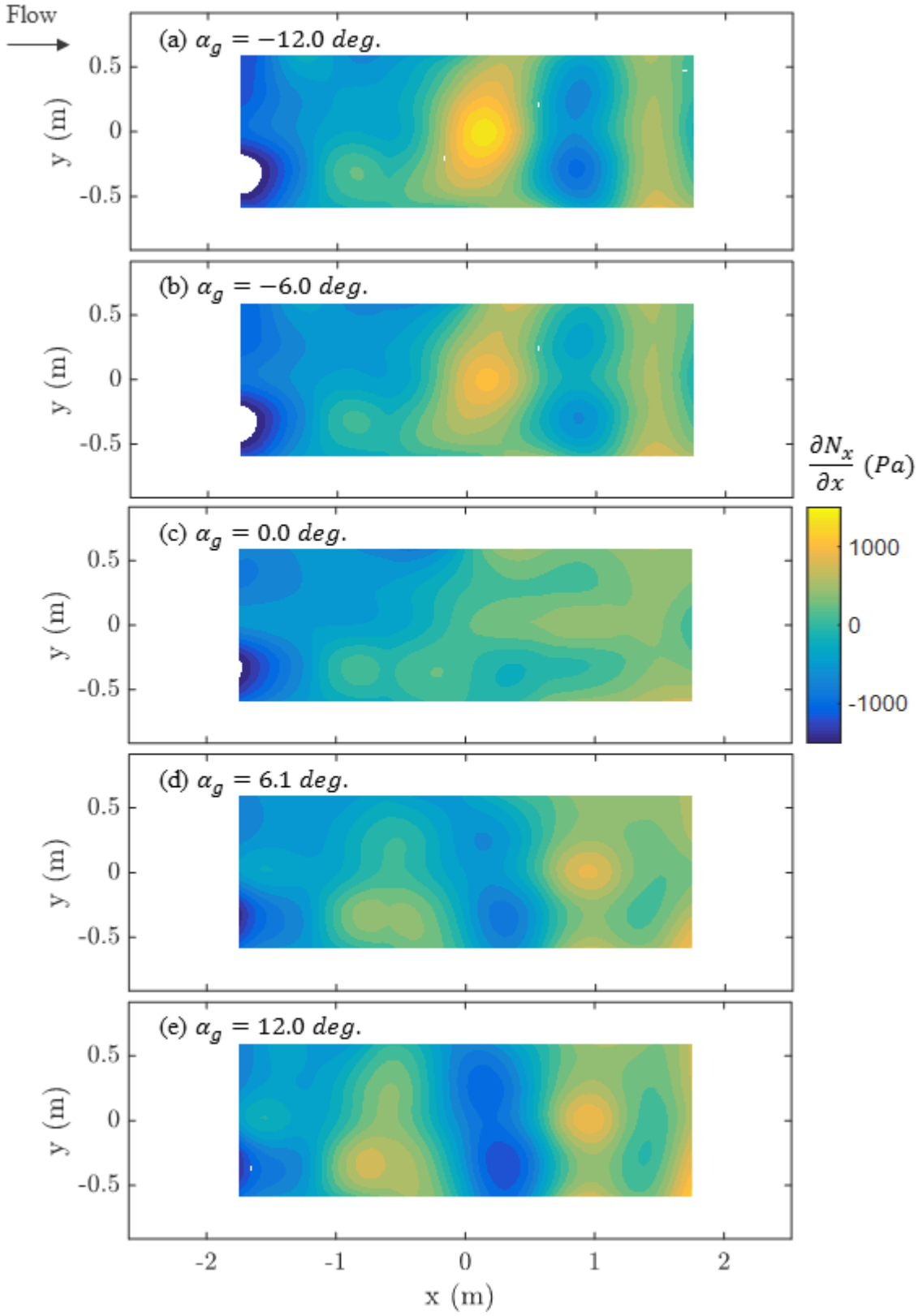

Figure 7.9: $\partial T_x(x,y)/\partial x$ term of Equation 2.52 for the port wall at the conditions of 770-Pa dynamic pressure (Run 3-1) using global polynomial basis functions.

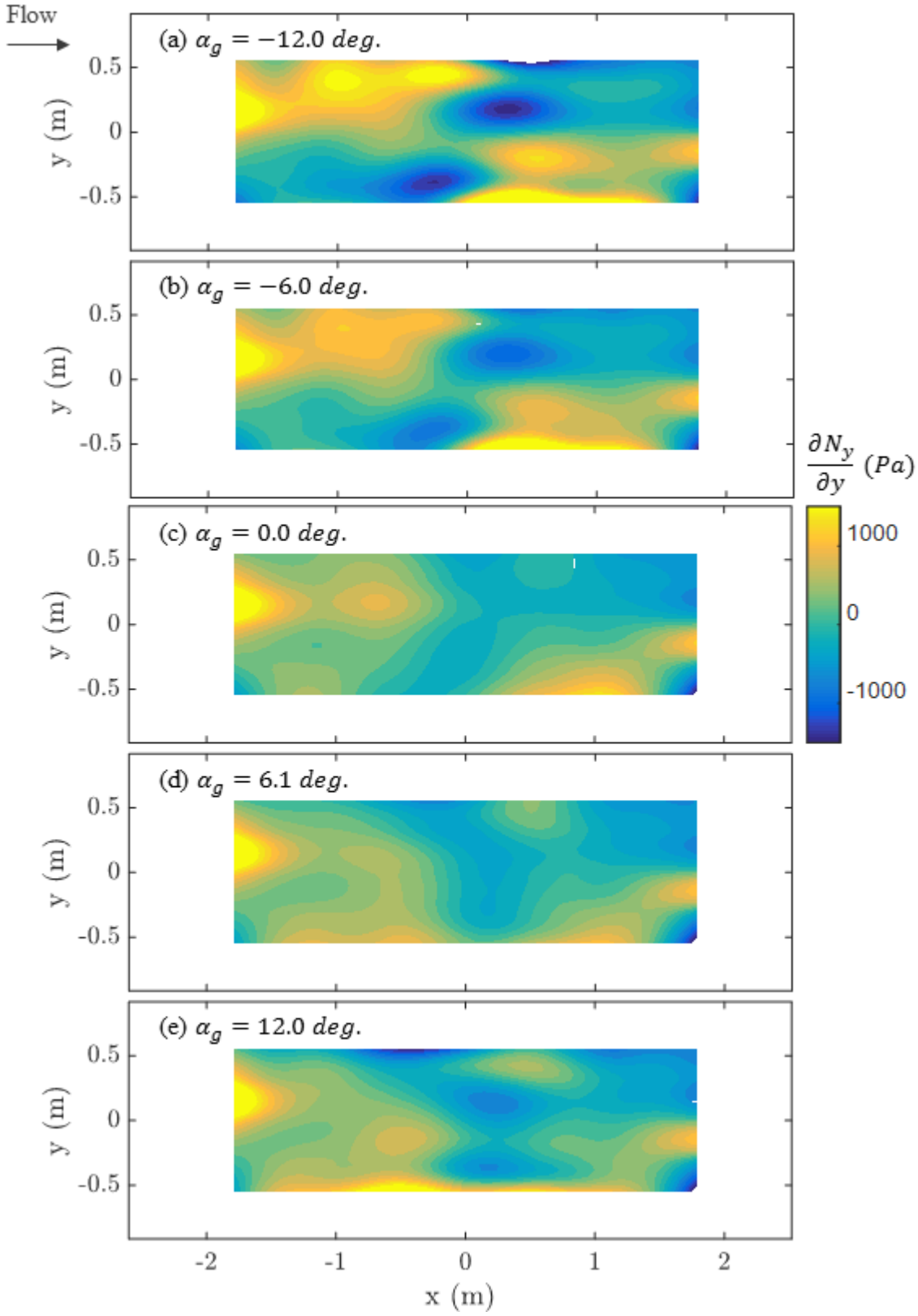

Figure 7.10: $\partial T_y(x,y)/\partial y$ term of Equation 2.53 for the port wall at the conditions of 770-Pa dynamic pressure (Run 3-1) using global polynomial basis functions.

7.4 Calculation of Wall Pressure Distribution

With the deformation data fitted to basis functions and analytic derivatives taken to yield the strain components, these components are inserted into Equation 7.21 which, along with the pre-tension data and material properties data, form the whole of the pressure calculation. The pre-tension maps come from the tension meter measurements of Figure 7.4. The material properties derive from the technique outlined in Section 4.2.3 (E_x = 1.33E10-Pa, E_y = 3.12E10-Pa, and $\nu_{xy} = 0.40$ with h = 0.021-mm).

Thus, the full-field wall C_p distributions are calculated as shown in Figures 7.11-7.16. The contours are smoothly varying and have greater absolute value C_p's on the suction surface than the pressure surface for equivalent angles of attack. It is clear that there is spanwise non-uniformity present in nearly all the measurements. The magnitude of the non-uniformity is suspected too large to be physically present in the flow, but rather it is believed that the definition of the material properties is in error. There are peaks of high C_p magnitude centered around $x \approx 0$ and $y \approx \pm 0.4$-m on both the pressure an suction sides. These peaks are correlated with peaks in the quantity $\partial^2 w/\partial y$ and may actually be representative of the true pressure acting along the span of the wall. If the assumed elastic modulus acting in the y-direction were increased, then the in-plane strain component would be felt more strongly around $y = 0$ and might level out the spanwise non-uniformity.

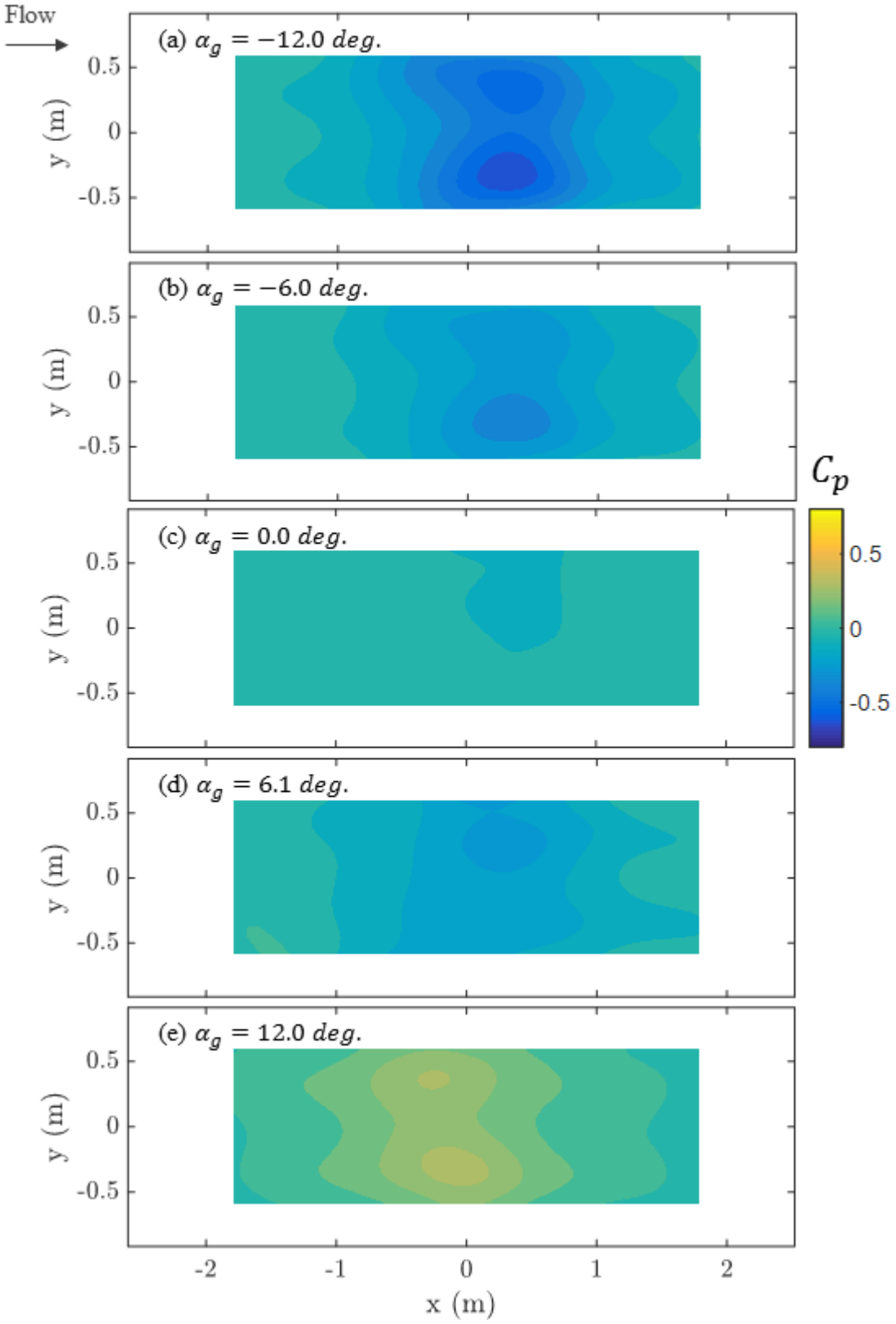

Figure 7.11: Optically inferred wall C_p distribution for the port wall at the conditions of 770-Pa dynamic pressure (Run 3-1) using global polynomial basis functions.

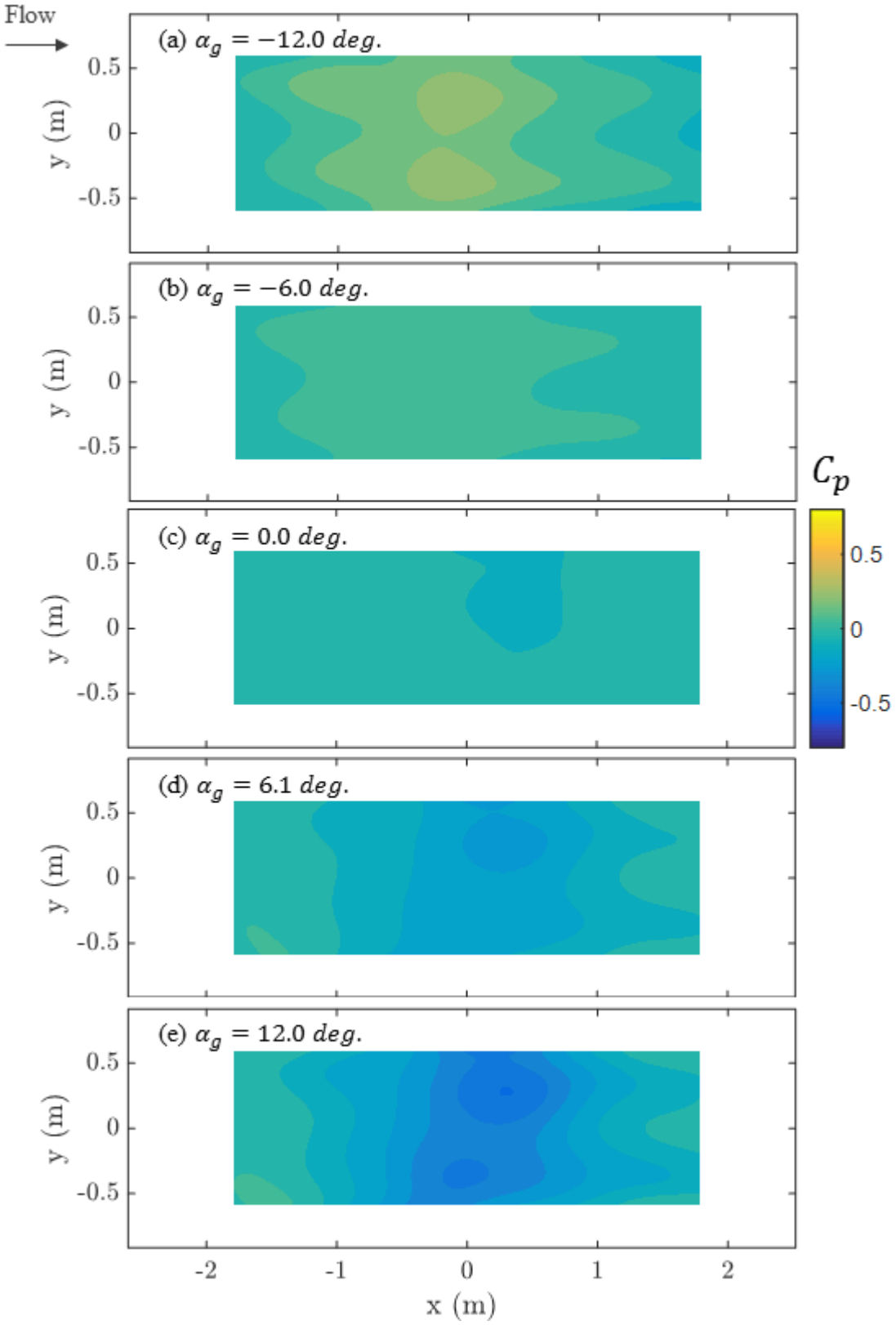

Figure 7.12: Optically inferred wall C_p distribution for the starboard wall at the conditions of 770-Pa dynamic pressure (Run 3-1) using global polynomial basis functions.

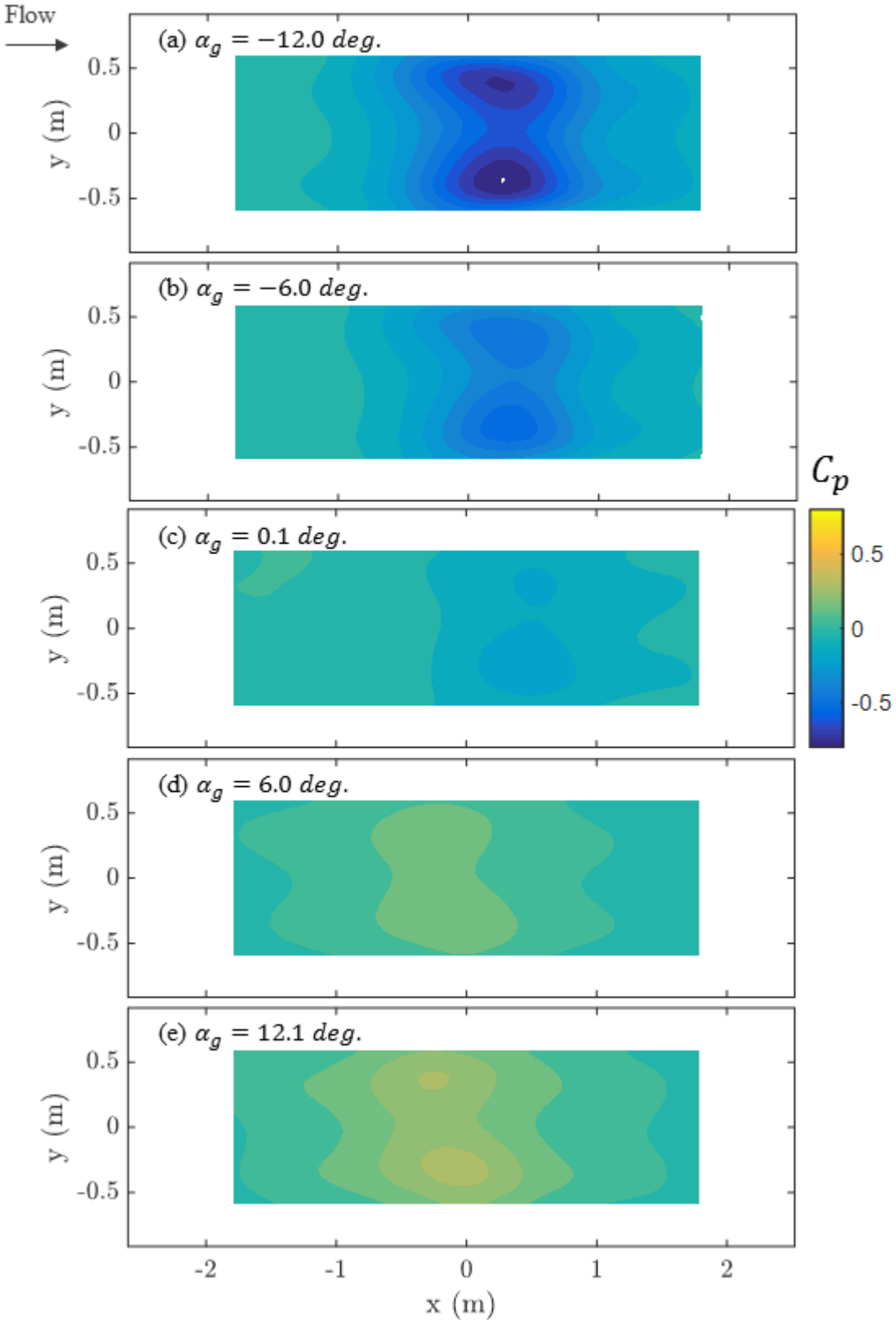

Figure 7.13: Optically inferred wall C_p distribution for the port wall at the conditions of 1770-Pa dynamic pressure (Run 3-5) using global polynomial basis functions.

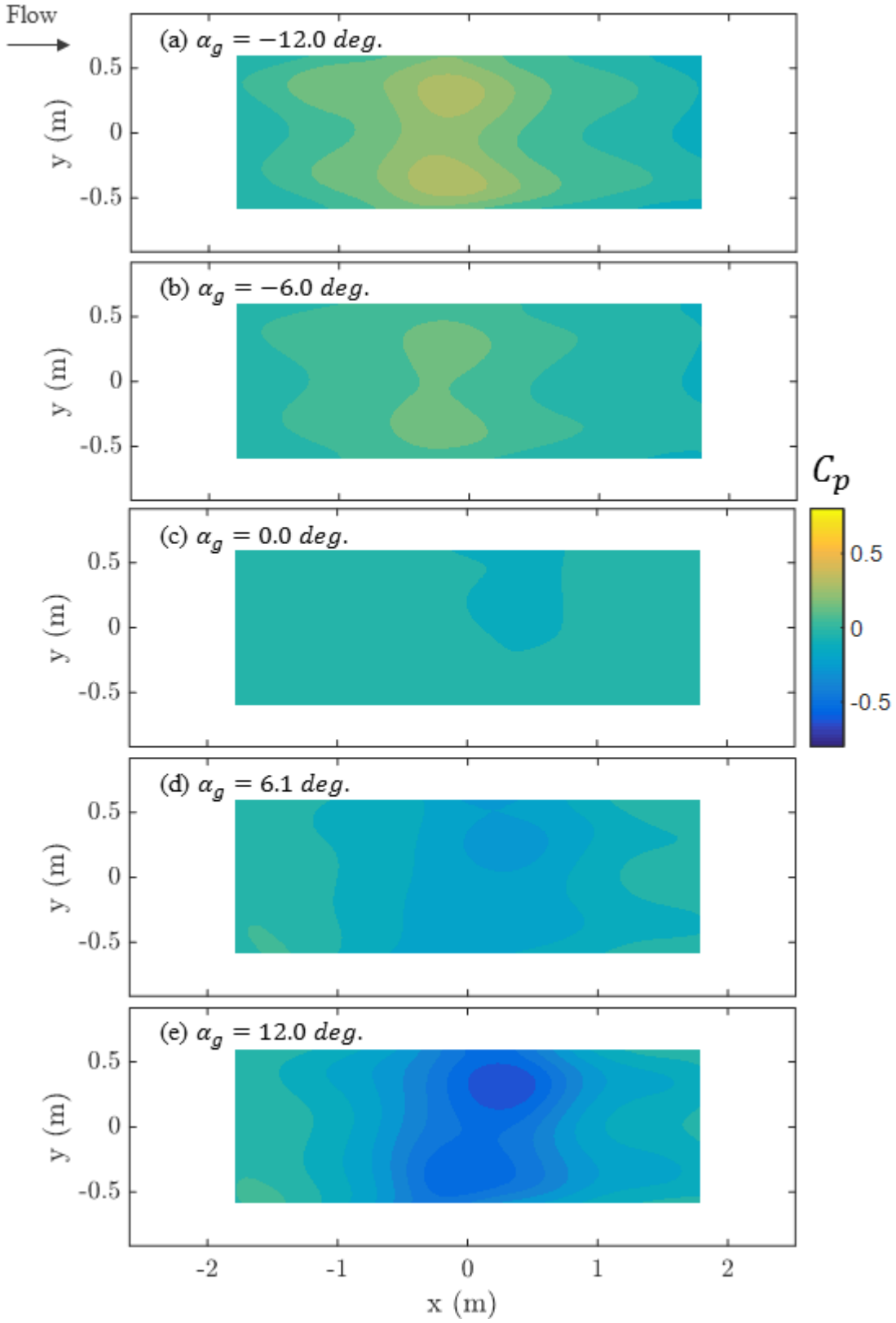

Figure 7.14: Optically inferred wall C_p distribution for the starboard wall at the conditions of 1770-Pa dynamic pressure (Run 3-5) using global polynomial basis functions.

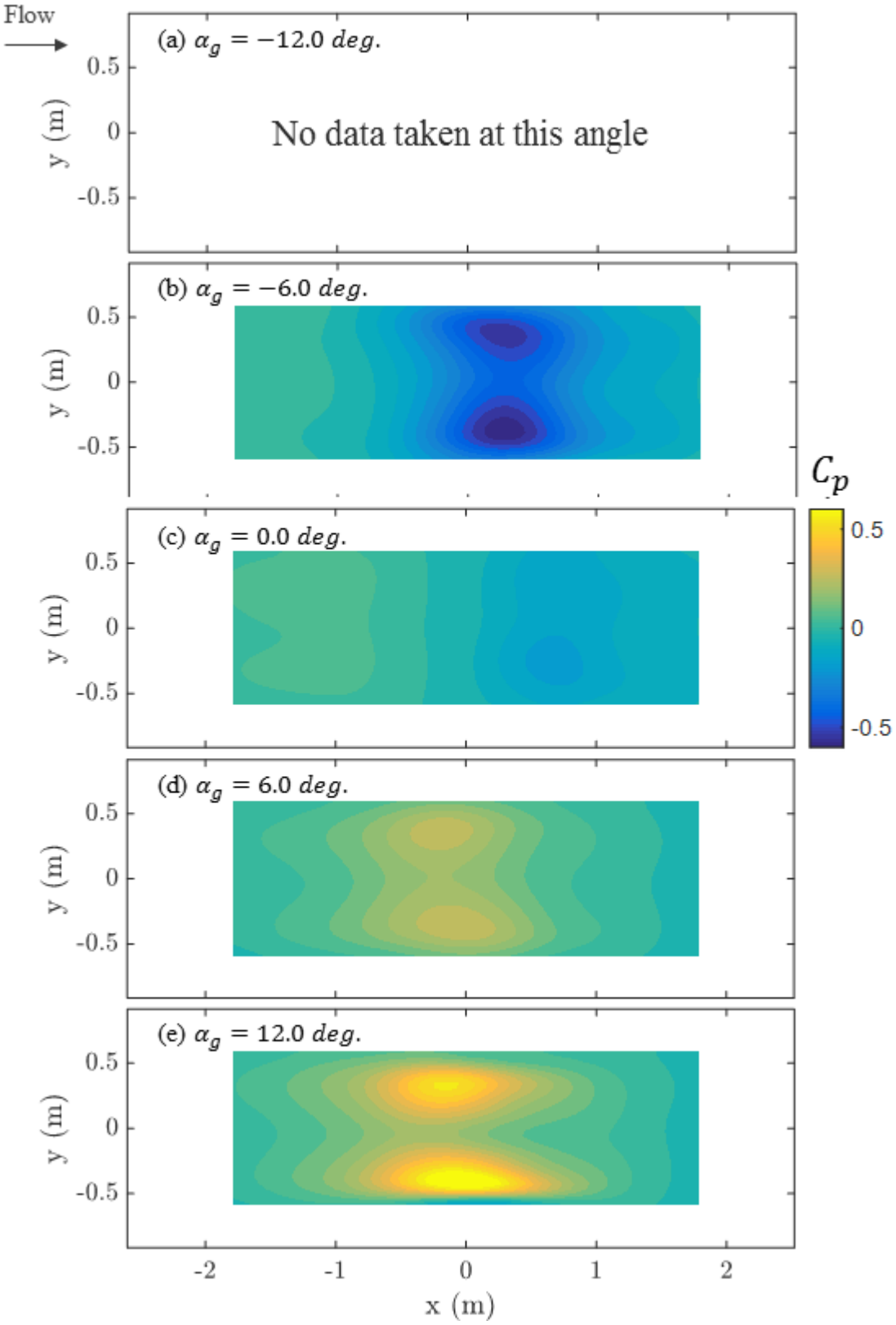

Figure 7.15: Optically inferred wall C_p distribution for the port wall at the conditions of 3300-Pa dynamic pressure (Run 3-3) using global polynomial basis functions.

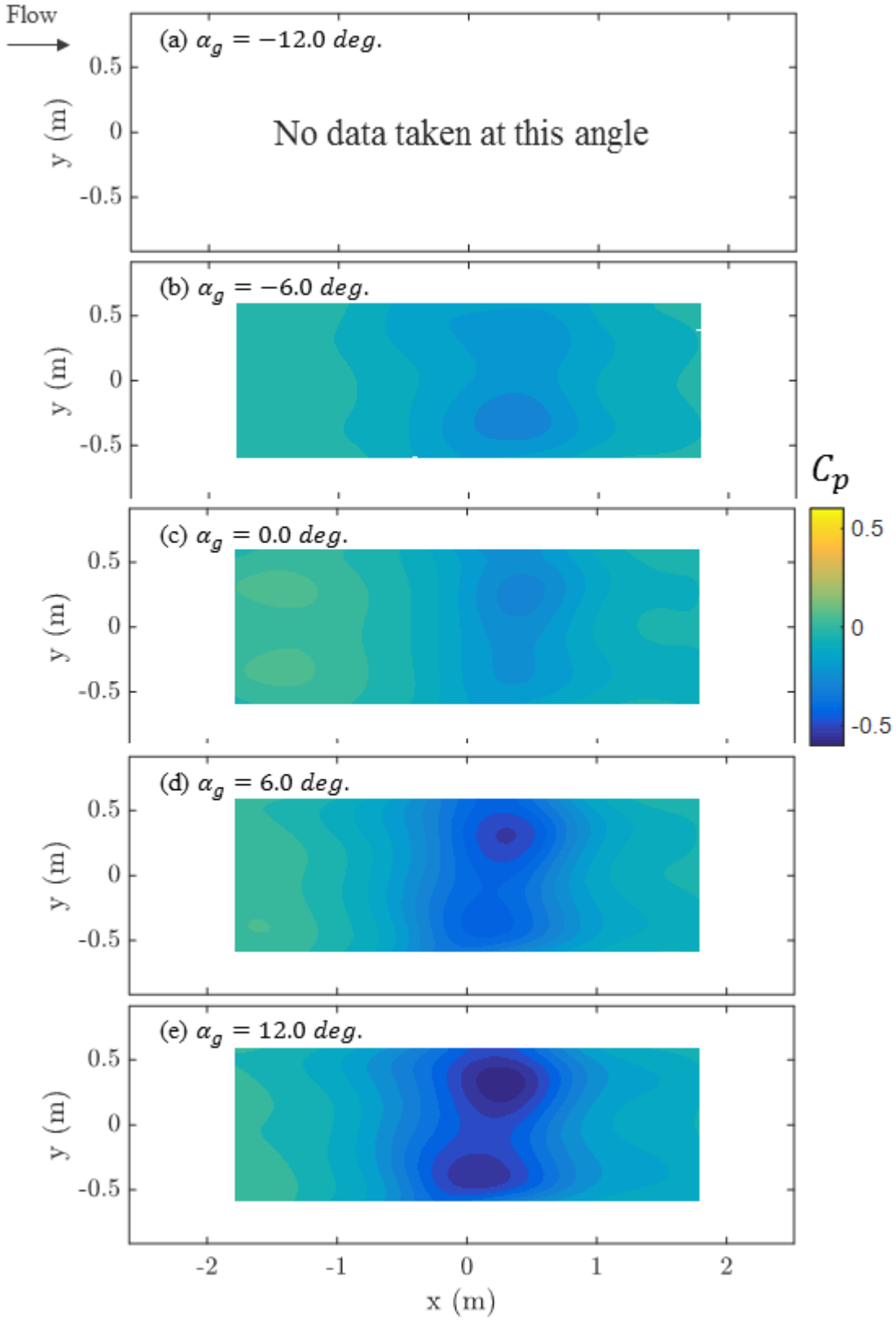

Figure 7.16: Optically inferred wall C_p distribution for the starboard wall at the conditions of 3300-Pa dynamic pressure (Run 3-3) using global polynomial basis functions.

7.5 Validation of Wall Pressure Distributions and Resultant Lift Force

While the spanwise non-uniformity of the results needs to be addressed with further study, we now consider just the data in the midspan region as is conventional for two-dimensional airfoil testing. The midspan pressure is taken as the average of the pressures within ±0.3-m of midspan. Returning again to the topic of the underlying basis functions of the displacement data, Figure 7.17 shows the midspan pressure data as calculated using three different displacement basis functions: global polynomials in subplot (a), global Fourier series in subplot (b), and locally-weighted polynomials in subplot (c). For (a) and (b), the order of the basis functions according to Equation 7.22 are $a = 14$, $b = 8$, $c = 18$, $d = 5$, $e = 10$, and $f = 8$. For (c), the basis function is a locally weighted regression algorithm developed by Matlab, termed the *loess* fit. The regression is performed with second-degree polynomials, and the window of the weighting function is set so as to use 6% of the total data points for each local surface fit. It is noted that with well-chosen basis functions, the shape of the optically measured pressure distribution is relatively independent of the basis functions. We will continue on with results from the global polynomials in the remainder of this chapter.

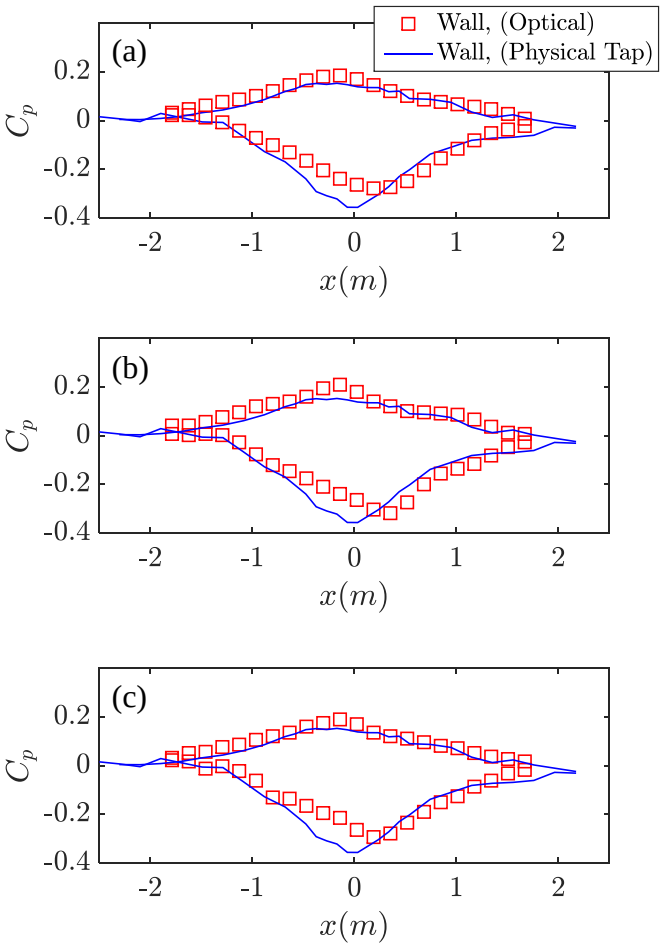

Figure 7.17: Comparison of C_p measured along the midspan of the wall with optical method and physical tap method using basis functions of (a) global polynomial series, (b) global Fourier series, and (c) locally-weighted polynomial surfaces. These data are for Run 3-1 at 7.78 degrees angle of attack.

Also plotted in Figure 7.17 are midspan pressure data measured with a second, independent measurement of the Kevlar-wall pressure distribution. This second measurement consists of physical pressure taps located at midspan which, as described in Sec-

tion 3.1.4, are temporary in nature. These measurements were made concurrently to the tests with the optical system described in Section 7.3 in order to validate the optical pressure measurement. Figure 7.17 affords a comparison between the optical pressure measurement and the physical tap measurement. A quantitative perspective on this comparison is next examined.

According to the discussion in Section 7.1.1.1, the optimal number of regularization parameters, or equivalently the optimum number of terms in the basis functions, should strike the appropriate balance between attenuating measurement noise and still capturing the essential information. Such a study was performed by parametrically varying the order of the global polynomials in both the x- and y- directions and calculating the RMS deviation between the optical and physical tap pressure measurements as shown in Figure 7.18. The selection of a 10-by-8 grid above is thus justified given the low RMS difference of 0.0013 C_p at this location.

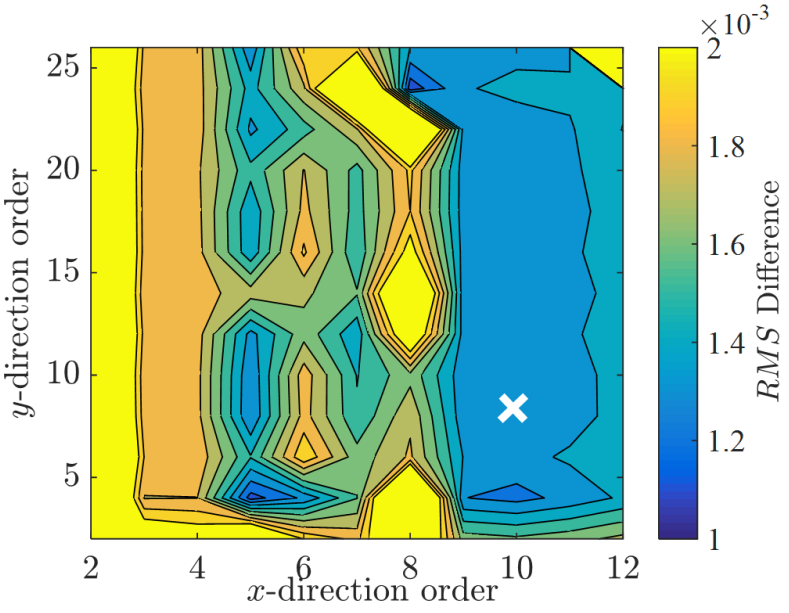

Figure 7.18: RMS deviation of optical and physical tap C_p measurements averaged for the port side over angles of attack from -18 to 18 degrees of Run 3-1. The RMS values are plotted as a function of the number of the order of polynomial basis function.

Considering now the optical pressure measurement at various angles of attack, Figure 7.19 shows the wall C_p distributions for three angles of attack sampled from the polar sweep of Run 3-1 shown in the bottom of the figure. Again, the midspan C_p is taken as the average of the C_p's within ±0.3-m of midspan. Note that the C_p's from the physical wall have had the empty-test section C_p's subtracted, but no corresponding process has been applied for the optical data. Both pressure measurement techniques yield the same overall distribution shape, yet with some finer differences apparent. The optical method is consistently undervaluing the suction peak by a C_p of around 0.05. Additionally, the suction peak for the optical data is offset downstream from the peak of the physical taps. One is tempted to blame an error in the coordinate system definition of the optical data, however, the same error appears on the suction peak at negative angles of attack. Therefore, the offset appears to be real. One

plausible explanation is that the offset is a result of residual misalignment due to unintended camera motion especially in the v-direction where the R^2_{adj} values of the surface fit are low. Alternatively, it is noted that the $x = 0$ location is a transition point in terms of the magnitude of terms in the membrane equilibrium equation, Equation 7.21. At $x = 0$, each of the terms Figure 7.7(b)-(d) reach a peak, however, the $\partial u/\partial x$ and $\frac{1}{2}(\partial w/\partial x)^2$ terms in Figure 7.7(a) reach a minimum. If the modulus of the Kevlar is under-valued, then the $\partial u/\partial x$ and $\frac{1}{2}(\partial w/\partial x)^2$ may not affect the C_p calculation strongly enough at the $x = 0$ location, and the observed offset is possible. The same logic holds when considering the $y-$direction deformation. It is quite believable that the linearized modulus from Section 4.2 could be under-predicted at this $x = 0$ location since the strain is high and non-linear stiffening may be occurring.

Integrating the wall C_p distributions along the streamwise direction, C_l is calculated and displayed in Figure 7.19 for Run 3-1, plotted along with the C_l integrated from the physical wall taps and the airfoil taps. The lift trends are replicated well by the optical measurement, including the disjointedness of the linear region at roughly positive and negative 7 degrees. Both types of wall measurements capture a less severe stall than the airfoil measurements which is characteristic for cases where stall originates from the midspan of the airfoil. The maximum difference in C_l between the airfoil and optical method is 0.07, or 5%, which occurs at $C_{l,max}$. This difference is within the error bars which are calculated according to Appendix D.

Figures 7.20 and 7.21 show the comparisons for dynamic pressures of 1700- and 3300-Pa, respectively, which correspond to Runs 3-5 and 3-3. For the 1700-Pa case, the offset of the suction peak is again present, however, now there is also an exaggeration of the pressure peak by the optical method. The result is that the optical method C_l is over-predicted along the majority of the lift curve. For the 3300-Pa case, the agreement between the physical tap and airfoil measurements starts to weaken which may be correlated to the fact that multiple wall pressure taps fell from their positions under the high stretching imposed on the Kevlar. For both dynamic pressures, the unrealistic increase in the optical C_l's may be attributed again to residual misalignment due to camera motion, or it might be a result of unaccounted for non-linearities in the material properties of the woven Kevlar. The measurement uncertainty in the optical method increases as the frestream dynamic pressure increases due to the stretching of the Kevlar. As the geometric non-linearity increases, the uncertainty in the material properties estimates contribute more strongly to the overall uncertainty.

The C_l data discussed above should not be taken without consideration of the momentum transfer between the flow immediately around the airfoil and the Kevlar walls. To do such, we take a three-dimensional control volume around the test section as shown in Figure 7.22 and apply a momentum balance in the z-direction. For the momentum balance, it is assumed steady-state, incompressible flow, and the contribution of skin friction is ignored. Taking the only body force to be that due to the lift loading, L, of the model, the integral momentum equation in the z-direction is

$$L = \rho \int_{c.s.} (\overrightarrow{V} \cdot \hat{k})(\overrightarrow{V} \cdot \hat{n}) dA + \rho \int_{c.s.} p(\hat{k} \cdot \hat{n}) dA \tag{7.23}$$

where ρ is the air density, $\overrightarrow{V}$, is the flow velocity vector at the control surface of interest, p is the pressure acting on the control surface, dA is the differential control surface area, $\hat{n}$ is the normal vector directed outwards from the control surface, and $\hat{k}$ is the unit vector in the z-direction. Ignoring the effects of any seepage through the floor and ceiling panels, only the four control surfaces shown in Figure 7.22 will be considered. For control surfaces 1 and 2, the rate at which transverse velocity is entering or exiting the test section is integrated over the area of the surfaces which is

$$\rho \int_{c.s.} (\overrightarrow{V} \cdot \hat{k})(\overrightarrow{V} \cdot \hat{n}) dA = \rho \int_{y_1}^{y_2} \int_{z_1}^{z_2} [-w_1 u_1 + w_2 u_2] dy dz$$

where u, v, and w are the components of $\overrightarrow{V}$ in the $x-$, $y-$, and $z-$directions, respectively, at the control surface indicated by their subscripts. Note that here the z-direction corresponds to that perpendicular to the airfoil span rather than parallel to it as in some sections of this document. Since control surfaces 1 and 2 are perpendicular to z, there is no contribution from surface pressures to the momentum balance. For control surfaces 3 and 4, the momentum exchange via porous flow through the walls which is given by

$$\rho \int_{c.s.} (\overrightarrow{V} \cdot \hat{k})(\overrightarrow{V} \cdot \hat{n}) dA = \int_{x_1}^{x_2} \int_{y_1}^{y_2} [w_{3,normal}^2 cos\theta_3 cos\varphi_3 - w_{4,normal}^2 cos\theta_4 cos\varphi_4] dx dy$$

where θ and φ are the angles of deflection of the Kevlar as defined in Figure 7.22. In order to be consistent with the calculation of porosity provided by Equations 2.45 and Equations 4.4, the normal velocity through the porous walls is given as $w_{normal,3}$ and $w_{normal,4}$ rather than w_3 and w_4. The relation between the two is found by $w_{normal,3} = w_3/cos\theta_3 cos\varphi_3$ and $w_{normal,4} = w_4/cos\theta_4 cos\varphi_4$. Note that for the specific case of Equation 2.45, the equation uses the bulk velocity through the fabric, but the present momentum analysis requires using the actual velocity through the individual pores. According to continuity, the pore velocity is larger than the bulk velocity by the factor $V_c OAR$ where V_c is the vena-contracta ratio in the pore and OAR is the open-area ratio of the fabric. In the momentum integral, the flow area must also be the pore area which is $V_c OAR$ times the total surface area. Next, we include the effect of the surface forces on control surfaces 3 and 4 as

$$\rho \int_{c.s.} p(\hat{k} \cdot \hat{n}) dA = \int_{x_1}^{x_2} \int_{y_1}^{y_2} [p_3 cos\theta_3 cos\varphi_3 - p_4 cos\theta_4 cos\varphi_4] dx dy$$

The C_l is finally calculated as in Equation 7.24

$$
\begin{aligned}
C_l = \; & \frac{L}{\frac{1}{2}\rho V_\infty^2 c} = \\
& \frac{1}{c}\int_{x_1}^{x_2}\int_{y_1}^{y_2}[C_{p_3}cos\theta_3 cos\varphi_3 - C_{p_4}cos\theta_4 cos\varphi_4]dxdy \\
& + \frac{2}{c}\int_{y_1}^{y_2}\int_{z_1}^{z_2}[\frac{-w_1u_1 + w_2u_2}{V_\infty^2}]dydz \\
& + \frac{2}{c}\int_{x_1}^{x_2}\int_{y_1}^{y_2}[\frac{w_{normal,3}^2 cos\theta_3 cos\varphi_3 - w_{normal,4}^2 cos\theta_4 cos\varphi_4}{V_\infty^2}]dxdy
\end{aligned}
\tag{7.24}
$$

where V_∞ is the freestream velocity and c is the model chord. The first term is by far the dominant term in the equation and relies on the measured wall C_p's. The data presented in Figures 7.19-7.21 are calculated from only the first term and under the assumption that the vector change in pressure due to Kevlar deformation is insignificant which is the same as setting $cos\theta cos\varphi = 1$. At the midspan location where the lift is typically calculated for two-dimensional airfoil testing, $cos\varphi$ is already quite near unity due to the symmetry of the wall deformation. Assuming furthermore that $cos\theta$ is equal to unity affects C_l by less than 0.2%, even for the case of the largest wall deflections as in Figure 7.21. The second term accounts for transverse momentum entering and exiting the control volume through the test section entrance and exit, respectively. The magnitude of this term depends on the streamwise extent of the pressure measurements. For a configuration like the Stability Wind Tunnel, this correction is typically on the order of 3% of C_l. Applying such a correction to lift data presented in Figures 7.19-7.21 would raise the C_l value, bringing the optical results of Figure 7.19 into better agreement with the physical tap results. The third term accounts for the transverse momentum entering or exiting the control volume through the Kevlar walls and is less than 0.5% of C_l even for the highest freestream dynamic pressure case considered in this study.

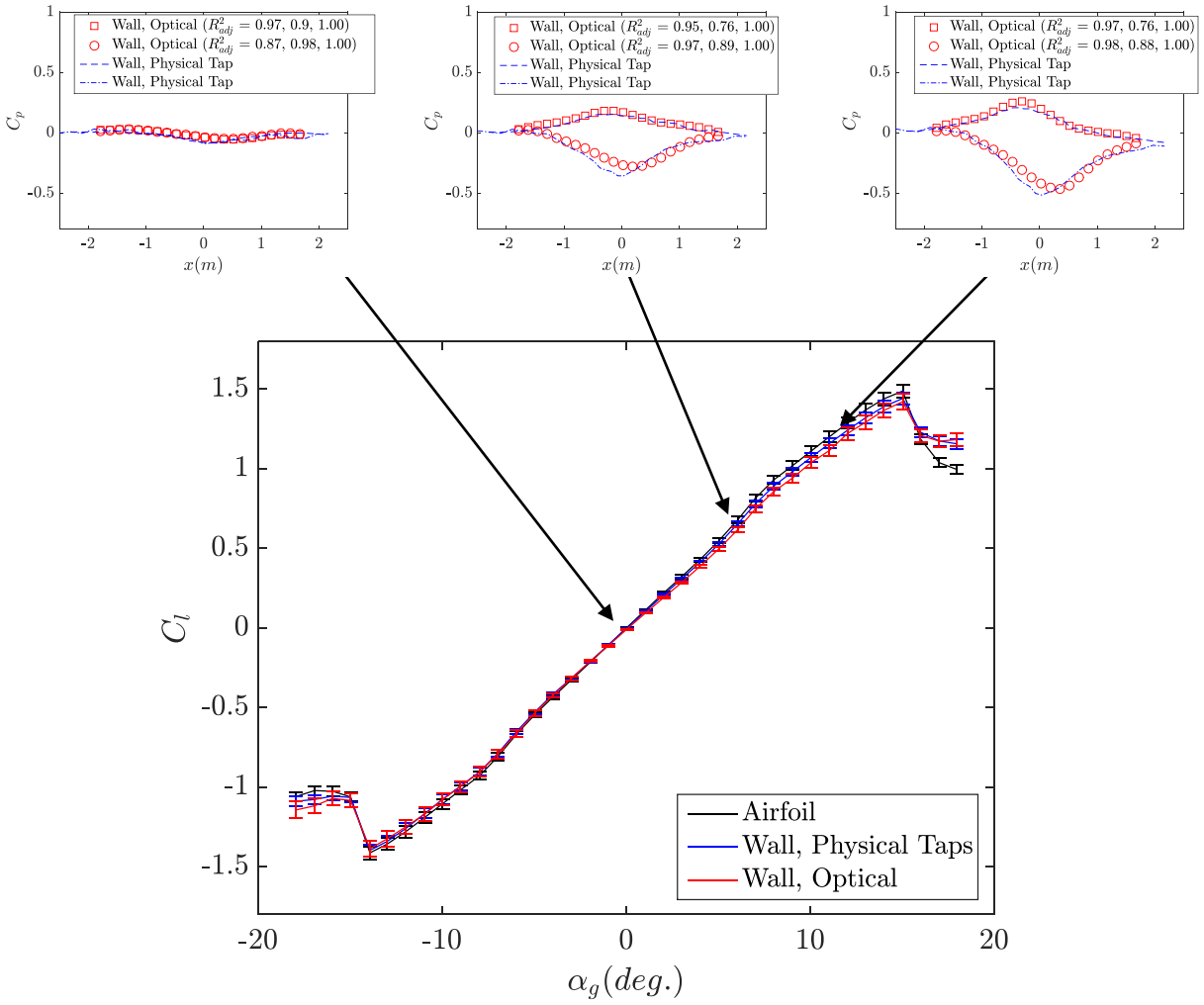

Figure 7.19: Optically inferred wall C_p and C_l for the case of 770-Pa dynamic pressure (Run 3-1) using global polynomial basis functions. The R^2_{adj} values correspond to the fit strength of the polynomials in the u-, v-, and w-directions, respectively.

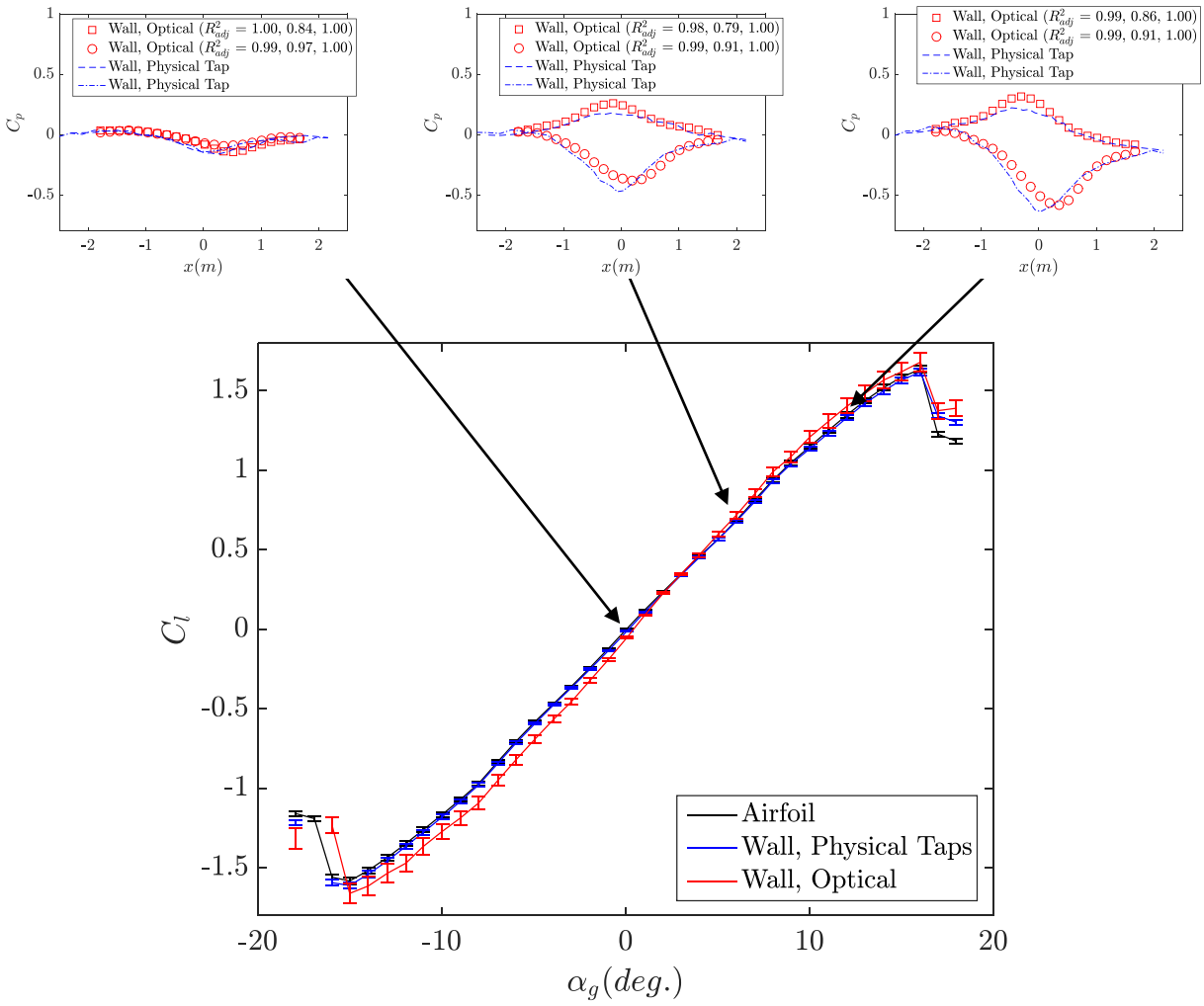

Figure 7.20: Optically inferred wall C_p and C_l for the case of 1700-Pa dynamic pressure (Run 3-5) using global polynomial basis functions. The R^2_{adj} values correspond to the fit strength of the polynomials in the u-, v-, and w-directions, respectively.

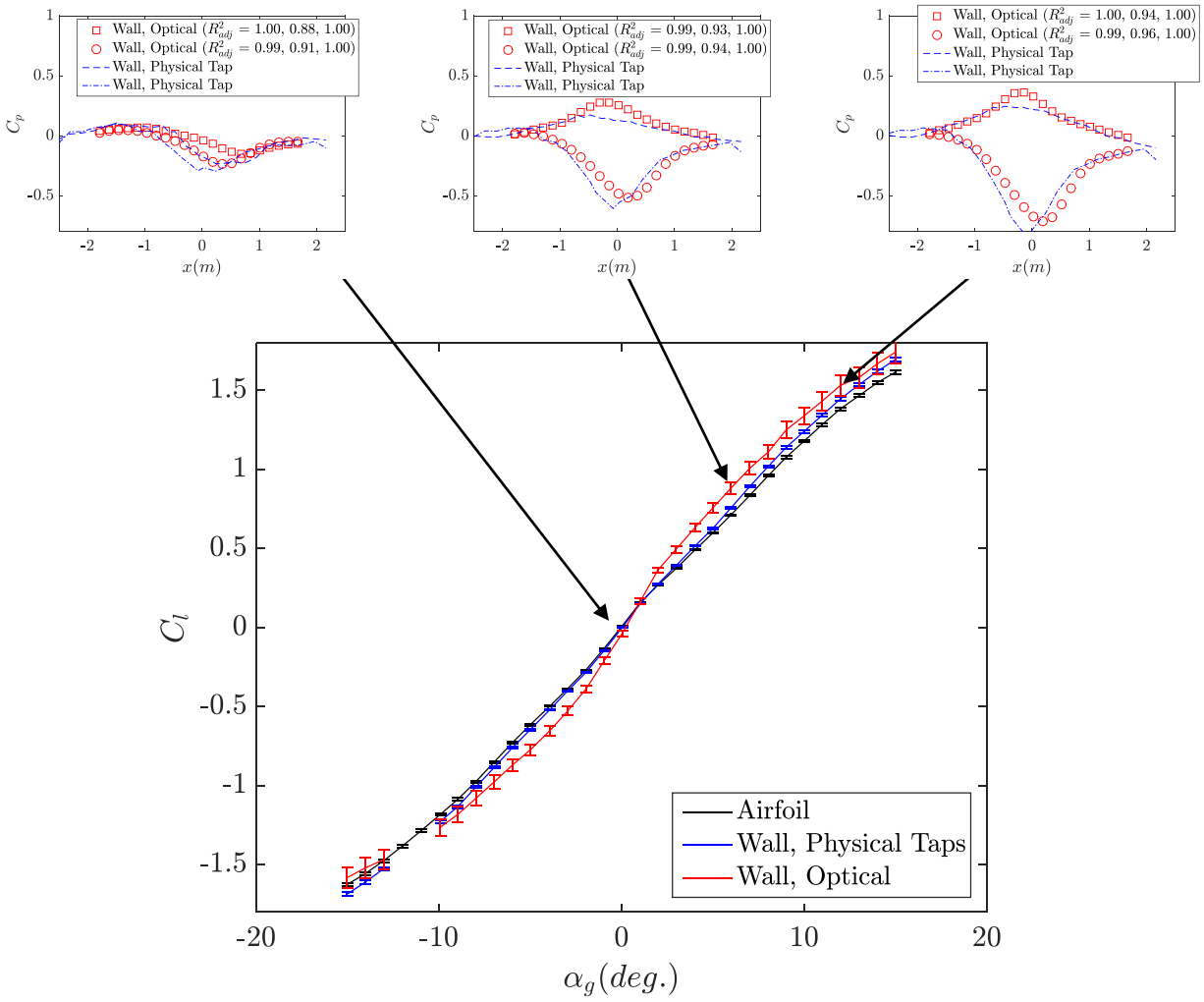

Figure 7.21: Optically inferred wall C_p and C_l for the case of 3300-Pa dynamic pressure (Run 3-3) using global polynomial basis functions. The R^2_{adj} values correspond to the fit strength of the polynomials in the u-, v-, and w-directions, respectively.

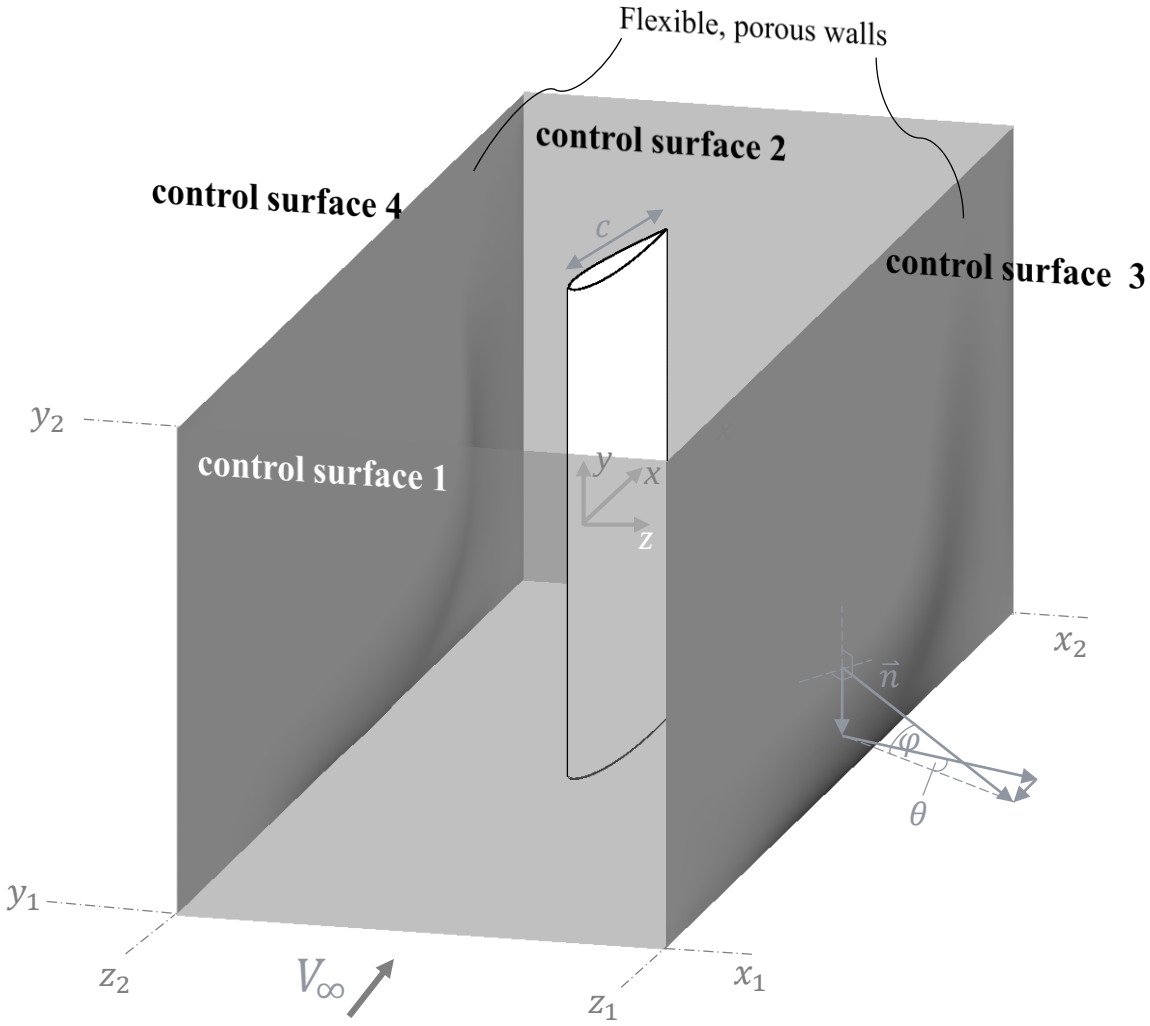

Figure 7.22: Control volume of a Kevlar-wall test section.

Chapter 8

Conclusion

The objective of this work has been to provide the framework for testing in Kevlar-wall test sections which will yield the same confidence level in aerodynamic measurements taken in Kevlar-wall test sections as those taken in solid-wall sections. As such, a comprehensive view of aerodynamics in Kevlar-wall test sections has been presented.

First, detailed characterization of the mechanical and aerodynamic properties of Kevlar fabric were presented. Measurements on a bulging Kevlar sample provided updated values of the material property constants. Porosity measurements through swatches of Kevlar fabric yielded a new non-dimensional form of the pressure-velocity relationship across the fabric, as well as the important knowledge that the strain level of the Kevlar fabric has little to no effect on its porosity.

It was then investigated the accuracy of wall interference correction methods of varying fidelity. Using a NACA0012 airfoil tested in both the solid-wall and Kevlar-wall test sections at the Stability Wind Tunnel at Virginia Tech, the effects of the porosity of the Kevlar walls, of the wall boundary layer, of the wall deflection, and of the pressure difference across the wall on test section aerodynamics in the two-dimensional case were quantified. Some deficiencies in the state-of-the-art Devenport *et al.*[9] panel method model were fixed in the updated panel method of the present work, including eliminating the strain correction to porosity and correctly modeling the pressure drop through the test section. The updated method still over-predicts the correction of the lift data in some instances. In order to eliminate the residual errors in the correction method, it is suggested that in-tunnel tests be made to gauge the effect of the boundary layer on the Kevlar porosity relation as has been done by experimenters using porous-wall wind tunnels in the transonic regime. Furthermore, consideration should be made of alternate leakage paths between the test section and anechoic chambers such as through the porous floor and ceiling panels. It is also recommended that to reduce the error in the wall-interference correction process, Kevlar-wall test sections should ideally be designed with low porosity, highly tensioned Kevlar, and the anechoic chambers should ideally be sealed from one another. Overall, the study of the Kevlar test section revealed

a set of six Kevlar-related wall interference mechanisms which represent an extension from the three original ones reported in Devenport *et al.*.

A three-dimensional panel method code was next verified and validated in the case of three-dimensional flow around semi-span wings. Validation was performed via experiments at the Low Speed Wind Tunnel at the Japanese Aerospace Exploration Agency which has both a solid-wall and Kevlar-wall test section. The three-dimensional panel method corrects Kevlar-wall lift data to within 4% slope of the corresponding solid-wall data. Perhaps because better definition of the porosity of the Kevlar is needed. The application of a three-dimensional version of the panel code to a Kevlar-wall test section is a first-of-its-kind development.

The final thrust of this work centered on the development and validation of a novel instrumentation technique for Kevlar-wall test sections. The pressure distributions over the Kevlar walls were inferred based on the global deformation of the walls under wind loading as measured by stereo digital image correlation. The inputs to the problem include the Kevlar material properties, the pre-tension in the walls, and the gradients of deformation under wind loading. Given the inverse nature of the problem, considerations were made to mitigate the effect of measurement noise on the computed loading. The main error sources, however, are suspected to be due to still poor definition of the Kevlar fabric's material properties, as well as unexpected shifting of the camera system as the wind tunnel flow began. Even so, the so-called optical method of wall pressure can be used to calculate lift to within a C_l of 0.07. Improvements to the measurement should include a high fidelity characterization of the Kevlar fabric's material properties, and the experimental setup should be modified to include rigid mounting between stereo-pairs of cameras, as well as fiduciary markings to identify any unintended camera movements.

Bibliography

[1] Smith, B. S., Camargo, H. E., Burdisso, R. A., and Devenport, W. J., "Development and Testing of a Novel Acoustic Wind Tunnel Concept," *11th AIAA/CEAS Aeroacoustics Conference (AIAA 2005-3053)*, 2005, DOI: 10.2514/6.2005-3053 .

[2] Remillieux, M. C., Crede, E. D., Camargo, H. E., Burdisso, R. A., Devenport, W. J., Rasnick, M., Van Seeters, P., and Chou, A., "Calibration and demonstration of the new Virginia Tech anechoic wind tunnel," *14th AIAA/CEAS Aeroacoustics Conference (AIAA 2008-2911)*, 2008, DOI: 10.2514/6.2008-2911.

[3] Devenport, W. J., Burdisso, R. A., Borgoltz, A., Ravetta, P., and Barone, M. F., "Aerodynamic and acoustic corrections for a Kevlar-walled anechoic wind tunnel," *16th AIAA/CEAS Aeroacoustics Conference (AIAA 2010-3749)*, 2010, DOI: 10.2514/6.2010-3749 .

[4] Devenport, W., Burdisso, R., Camargo, H., Crede, E., Remillieux, M., Rasnick, M., and Van Seeters, P., "Aeroacoustic testing of wind turbine airfoils," Tech. rep., 2010, Subcontract Report NREL/SR-500-43471.

[5] Ito, T., Ura, H., Nakakita, K., Yokokawa, Y., Ng, W., Burdisso, R., Iwasaki, A., Fujita, T., Ando, N., Shimada, N., et al., "Aerodynamic/aeroacoustic testing in anechoic closed test sections of low-speed wind tunnels," *16th AIAA/CEAS Aeroacoustics Conference (AIAA 2010-3750)*, 2010, DOI: 10.2514/6.2010-3750 .

[6] Awasthi, M., Devenport, W. J., Glegg, S. A., and Forest, J. B., "Pressure fluctuations produced by forward steps immersed in a turbulent boundary layer," *Journal of Fluid Mechanics*, Vol. 756, 2014, pp. 384–421, DOI: 10.1017/jfm.2014.405.

[7] Meyers, T., Forest, J. B., and Devenport, W. J., "The wall-pressure spectrum of high-Reynolds-number turbulent boundary-layer flows over rough surfaces," *Journal of Fluid Mechanics*, Vol. 768, 2015, pp. 261–293, DOI: 10.1017/jfm.2014.743.

[8] Alexander, N., Devenport, W., Morton, M. A., and Glegg, S. A., "Noise from a rotor ingesting a planar turbulent boundary layer," *Proc. of 19th AIAA/CEAS Aeroacoustics Conference (AIAA 2013-2285)*, 2013, DOI: 10.2514/6.2013-2285 .

[9] Devenport, W. J., Burdisso, R. A., Borgoltz, A., Ravetta, P. A., Barone, M. F., Brown, K. A., and Morton, M. A., "The Kevlar-walled anechoic wind tunnel," *Journal of Sound and Vibration*, Vol. 332, No. 17, 2013, pp. 3971–3991, DOI: 10.1016/j.jsv.2013.02.043 .

[10] Glegg, S. and Devenport, W., *The Aero and Hydroacoustics of Low Mach Number Flows: Fundamentals, Analysis and Measurements*, Elsevier, in press.

[11] Jaeger, S. M., Horne, W. C., and Allen, C. S., "Effect of surface treatment on array microphone self-noise," *AIAA Paper*, Vol. 1937, No. 6, 2000, DOI: 10.2514/6.2000-1937.

[12] Debrouwere, M., *An Assessment of Acoustically Transparent Wind Tunnel Walls*, Master's thesis, Delft University of Technology, 2013, http://www.lr.tudelft.nl/...

[13] Moreau, S., Henner, M., Iaccarino, G., Wang, M., and Roger, M., "Analysis of flow conditions in freejet experiments for studying airfoil self-noise," *AIAA journal*, Vol. 41, No. 10, 2003, pp. 1895–1905, DOI: 10.2514/2.1905 .

[14] Ulbrich, N., "Wind Tunnel Wall Interference Corrections (A Brief Overview)," Jacobs Technology Inc., Moffett Field, California, June 2009.

[15] Ewald, B., editor, *Wind Tunnel Wall Corrections (la Correction des effets de paroi en soufflerie)*. Advisory Group for Aerospace Research & Development (AGARD), NATO, 1998, AG-336.

[16] Herriot, J. G., "Blockage Corrections for Three-Dimensional-Flow Closed-Throat Wind Tunnels, With Consideration of the Effect of Compressibility," 1947, NACA-RM-A7B28.

[17] Allen, H. J. and Vincenti, W. G., "Wall interference in a two-dimensional-flow wind tunnel, with consideration of the effect of compressibility," Tech. rep., 1944, NACA-TR-782.

[18] Lock, C., "The Interference of a Wind Tunnel on a Symmetrical Body. R. & M. No. 1275," Tech. rep., H.M. Stationery Office, 1929.

[19] Glauert, H., *Wind tunnel interference on wings, bodies and airscrews*, Aeronautical research committee reports and memoranda, H.M. Stationery Office, 1933.

[20] Rae, W. H. and Pope, A., *Low-speed wind tunnel testing*, John Wiley, 1984.

[21] Ulbrich, N., "Description of panel method code ANTARES," Tech. rep., 2000, NASA CR-2000-209592.

[22] Joppa, R. G., "Wind tunnel interference factors for high-lift wings in closed wind tunnels," Tech. rep., 1973, NASA CR-2191.

[23] Bowcutt, K., "The use of panel methods for the development of low-subsonic wall interference and blockage corrections," *23rd AIAA Aerospace Sciences Meeting (AIAA 1985-0159)*, Vol. 14, 1985, DOI: 10.2514/6.1985-159.

[24] Mokhtar, W. A. and Britcher, C. P., "Boundary interference assessment and correction for open test section wind tunnels using panel methods," *42nd AIAA Aerospace Sciences Meeting (AIAA-2004-609)*, 2004, DOI: 10.2514/6.2004-609 .

[25] Iyer, V. and Everhart, J. L., "Application of pressure-based wall correction methods to two NASA Langley wind tunnels," *19th AIAA Applied Aerodynamics Conference (AIAA 2001-2472)*, 2001, DOI: 10.2514/6.2001-2472 .

[26] Mokry, M., "Subsonic Wall Interference Corrections for Half-Model Tests Using Sparse Wall Pressure Data (Corrections Subsoniques des Effets de Parois pour des Essais de Demi-Maquettes a L'Aide de Donnees Dispersees de Pression sur les Parois)," Tech. rep., National Aeronautical Establishment of Ottawa (Ontario), 1985, DTIC ADA162883.

[27] Ulbrich, N. and Steinle, F., "Semispan model wall interference prediction based on the wall signature method," *33rd AIAA Aerospace Sciences Meeting and Exhibit (AIAA 1995-0793)*, 1995, DOI: 10.2514/6.1995-793 .

[28] Moses, D., "Wind tunnel wall corrections deduced by iterating from measured wall static pressure," *AIAA journal*, Vol. 21, No. 12, 1983, pp. 1667–1673, DOI: 10.2514/3.60167.

[29] Goett, H. J., "Experimental Investigation of the Momentum Method for Determining Profile Drag," Tech. rep., 1939, NACA-TR-660.

[30] Bernstein, S. and Joppa, R. G., "Development of Minimum-Correction Wind Tunnels," *Journal of Aircraft*, Vol. 13, No. 4, 1976, pp. 243–247, DOI: 10.2514/3.58653.

[31] Ivanov, A., "An experimental study of gas flow near the perforated walls of a transonic wind tunnel," *Fluid Mechanics-Soviet Research*, Vol. 17, No. 4, 1988.

[32] Glazkov, S., Gorbushin, A., Ivanov, A., and Semenov, A., "Recent experience in improving the accuracy of wall interference corrections in TsAGI T-128 wind tunnel," *Progress in Aerospace Sciences*, Vol. 37, No. 3, 2001, pp. 263–298, DOI: 10.1016/S0376-0421(01)00007-0.

[33] Chan, Y., "Wall boundary-layer effects in transonic wind tunnels," *AGARD Conference Proceedings No. 335*, NATO, 1982, AGARD-CP-335.

[34] Crites, R. and Rueger, M., "Modeling the ventillated wind tunnel wall," *30th AIAA Aerospace Sciences Meeting and Exhibit (AIAA 1992-0035)*, 1992, DOI: 10.2514/6.1992-35 .

[35] DuPont, "Kevlar Technical Guide," 5401 Jefferson Davis Highway, Richmond, VA 23234.

[36] Brown, K. A., *A Study of Aerodynamics in Kevlar-Wall Test Sections*, Master's thesis, Virginia Tech, 2014, http://hdl.handle.net/10919/49383.

[37] Trail, P., Abaye, O., Thomason, W. E., Thompson, T. L., Gueye, F., Diedhiou, I., Diatta, M. B., and Faye, A., "Evaluating Intercropping (Living Cover) and Mulching (Desiccated Cover) Practices for Increasing Millet Yields in Senegal," *Agronomy Journal*, 2016, DOI: 10.2134/agronj2015.0422 .

[38] Brown, K., Devenport, W., Borgoltz, A., Ura, H., and Yamamoto, K., "Towards Interference Corrections for Three-Dimensional Models in Kevlar-Walled Anechoic Test Sections." 52nd AIAA Aerospace Sciences Meeting (AIAA 2014-0618), 2014, DOI: 10.2514/6.2014-0618 .

[39] Brown, K., Devenport, W., and Borgoltz, A., "Exploiting the characteristics of Kevlar-wall wind tunnels for conventional aerodynamic measurements," 30th AIAA Aerodynamic Measurement Technology and Ground Testing Conference (AIAA 2014-2110), 2014, DOI: 10.2514/6.2014-2110 .

[40] Hearle, J. W., Grosberg, P., and Backer, S., *Structural mechanics of fibers, yarns, and fabrics*, Wiley-Interscience, 1969.

[41] Dong, Z., Manimala, J., and Sun, C., "Mechanical behavior of silica nanoparticle-impregnated Kevlar fabrics," *Journal of Mechanics of Materials and Structures*, Vol. 5, No. 4, 2010, pp. 529–548, DOI: 10.2140/jomms.2010.5.529.

[42] Xue, P., Peng, X., and Cao, J., "A non-orthogonal constitutive model for characterizing woven composites," *Composites part A: Applied Science and manufacturing*, Vol. 34, No. 2, 2003, pp. 183–193, DOI: 10.1016/S1359-835X(02)00052-0.

[43] King, M. J., *A continuum constitutive model for the mechanical behavior of woven fabrics including slip and failure*, Ph.D. thesis, Massachusetts Institute of Technology, 2006, http://hdl.handle.net/1721.1/36192.

[44] Raftenberg, M. N. and Mulkern, T. J., "Quasi-Static uniaxial tension characteristics of plain-woven Kevlar KM2 fabric," Tech. rep., Weapons and Materials Research Directorate, Air Force Research Lab, 2002, ARL-TR-2891.

[45] Hearle, J., Thwaites, J., and Amirbayat, J., *Mechanics of flexible fiber assemblies*, NATO ASI Series, The Netherlands, 1980.

[46] Kilby, W., "2-Planar Stress–Strain Relationships in Woven Fabrics," *Journal of the Textile Institute Transactions*, Vol. 54, No. 1, 1963, pp. T9–T27, DOI: 10.1080/19447026308659910O.

[47] Hu, J., *Structure and mechanics of woven fabrics*, Elsevier, 2004.

[48] Williams, R. W., "Measuring and modeling the anisotropic, nonlinear and hysteretic behavior of woven fabrics," 2010, http://ir.uiowa.edu/etd/907/.

[49] Clulow, E. E. and Taylor, H., "An Experimental and Theoretical Investigation of Biaxial Stress–Strain Relations in a Plain-Weave Cloth," *Journal of the Textile Institute Transactions*, Vol. 54, No. 8, 1963, pp. T323–T347, DOI: 10.1080/19447026308660186.

[50] Beccarelli, P., *Biaxial Testing for Fabrics and Foils: Optimizing Devices and Procedures*, Springer, 2015, DOI: 10.1007/978-3-319-02228-4.

[51] Zhu, D., Mobasher, B., Vaidya, A., and Rajan, S. D., "Mechanical behaviors of Kevlar 49 fabric subjected to uniaxial, biaxial tension and in-plane large shear deformation," *Composites Science and Technology*, Vol. 74, 2013, pp. 121–130, DOI: 10.1016/j.compscitech.2012.10.012 .

[52] Bassett, R. J., Postle, R., and Pan, N., "Experimental methods for measuring fabric mechanical properties: A review and analysis," *Textile research journal*, Vol. 69, No. 11, 1999, pp. 866–875, DOI: 10.1177/004051759906901111.

[53] Machado, G., Favier, D., and Chagnon, G., "Membrane curvatures and stress-strain full fields of axisymmetric bulge tests from 3D-DIC measurements. Theory and validation on virtual and experimental results," *Experimental Mechanics*, Vol. 52, No. 7, 2012, pp. 865–880, DOI: 10.1007/s11340-011-9571-3.

[54] Birchall, M., Bridgens, B., and Gosling, P., "Membrane material behaviour: concepts, practice and developments," *Structural Engineer*, Vol. 82, No. 14, 2004, pp. 28–33.

[55] Zheng, J., Komatsu, T., Takatera, M., Inui, S., Bao, L., and Shimizu, Y., "Relationship between uniaxial and strip biaxial tensile properties of fabrics," *Textile Research Journal*, Vol. 78, No. 3, 2008, pp. 224–231, DOI: 10.1177/0040517507083439.

[56] Buet-Gautier, K. and Boisse, P., "Experimental analysis and modeling of biaxial mechanical behavior of woven composite reinforcements," *Experimental mechanics*, Vol. 41, No. 3, 2001, pp. 260–269, DOI: 10.1007/BF02323143.

[57] Galliot, C. and Luchsinger, R., "A simple model describing the non-linear biaxial tensile behaviour of PVC-coated polyester fabrics for use in finite element analysis," *Composite Structures*, Vol. 90, No. 4, 2009, pp. 438–447, DOI: 10.1016/j.compstruct.2009.04.016.

[58] Naik, D., Sankaran, S., Mobasher, B., Rajan, S., and Pereira, J., "Development of reliable modeling methodologies for fan blade out containment analysis–Part I: Experimental studies," *International Journal of Impact Engineering*, Vol. 36, No. 1, 2009, pp. 1–11, DOI: 10.1016/j.ijimpeng.2008.03.007.

[59] Nosrat-Nezami, F., Gereke, T., Eberdt, C., and Cherif, C., "Characterisation of the shear–tension coupling of carbon-fibre fabric under controlled membrane tensions for precise simulative predictions of industrial preforming processes," *Composites Part A: Applied Science and Manufacturing*, Vol. 67, 2014, pp. 131–139, DOI: 10.1016/j.compositesa.2014.08.030 .

[60] Timoshenko, S. and Woinowsky-Krieger, S., *Theory of plates and shells*, McGraw-Hill New York, 1959.

[61] Timoshenko, S. and Goodier, J., *Theory of Elasticity*, McGraw-Hill, New York, NY, 1970.

[62] Erb, D. A., *An exact plane-stress solution for a class of problems in orthotropic elasticity*, Master's thesis, Virginia Tech, 1981, http://scholar.lib.vt.edu/theses/available/etd-08152009-040212/.

[63] Stanford, B. and Ifju, P., "The validity range of low fidelity structural membrane models," *Experimental mechanics*, Vol. 48, No. 6, 2008, pp. 697–711, DOI: 10.1007/s11340-008-9152-2.

[64] de Costa Campos, L. M. B., *Generalized calculus with applications to matter and forces*, CRC Press, 2014.

[65] Campbell, J., "On the theory of initially tensioned circular membranes subjected to uniform pressure," *The Quarterly Journal of Mechanics and Applied Mathematics*, Vol. 9, No. 1, 1956, pp. 84–93, DOI: 10.1093/qjmam/9.1.84.

[66] Zhao, F., "Nonlinear solutions for circular membranes and thin plates," *The 15th International Symposium on: Smart Structures and Materials & Nondestructive Evaluation and Health Monitoring*, International Society for Optics and Photonics, 2008, pp. 69260W–69260W, DOI: 10.1117/12.775511.

[67] Hencky, H., "On the stress state in circular plates with vanishing bending stiffness," *Z. Math. Phys*, Vol. 63, 1915, pp. 311–317.

[68] Fichter, W., "Some solutions for the large deflections of uniformly loaded circular membranes," 1997, NASA-TP-3658.

[69] Seide, P., "Large deflections of rectangular membranes under uniform pressure," *International Journal of Non-Linear Mechanics*, Vol. 12, No. 6, 1977, pp. 397–406, DOI: 10.1016/0020-7462(77)90040-3.

[70] Hoerner, S. F., "Aerodynamic properties of screens and fabrics," *Textile Research Journal*, Vol. 22, No. 4, 1952, pp. 274–280, DOI: 10.1177/004051755202200405.

[71] Natarajan, K., *Air permeability of elastomeric fabrics as a function of uniaxial tensile strain*, Master's thesis, North Carolina State University, 2003, http://repository.lib.ncsu.edu/ir/handle/1840.16/1251.

[72] Kuester, M. S., Brown, K., Meyers, T., Intaratep, N., Borgoltz, A., and Devenport, W. J., "Wind Tunnel Testing of Airfoils for Wind Turbine Applications," *Wind Engineering*, Vol. 39, No. 6, 2015, pp. 651–660, DOI: 10.1260/0309-524X.39.6.651.

[73] Grédiac, M. and Hild, F., *Full-field measurements and identification in solid mechanics*, John Wiley & Sons, 2012.

[74] Grewe, L. L. and Kak, A. C., "Stereo vision," *Handbook of pattern recognition and image processing (vol. 2)*, Academic Press, Inc., 1994, pp. 239 – 317.

[75] Blostein, S. D. and Huang, T. S., "Error analysis in stereo determination of 3-D point positions," *Pattern Analysis and Machine Intelligence, IEEE Transactions on*, , No. 6, 1987, pp. 752–765, DOI: 10.1109/TPAMI.1987.4767982.

[76] Sutton, M. A., Orteu, J. J., and Schreier, H., *Image correlation for shape, motion and deformation measurements: basic concepts, theory and applications*, Springer Science & Business Media, 2009.

[77] Luo, P., Chao, Y., Sutton, M., and Peters Iii, W., "Accurate measurement of three-dimensional deformations in deformable and rigid bodies using computer vision," *Experimental Mechanics*, Vol. 33, No. 2, 1993, pp. 123–132, DOI: 10.1007/BF02322488.

[78] Zhang, Z., "Camera Calibration," *Emerging topics in computer vision*, edited by G. Medioni and S. B. Kang, chap. 1, Prentice Hall PTR, 2004, pp. 4–43.

[79] Sun, W. and Cooperstock, J. R., "An empirical evaluation of factors influencing camera calibration accuracy using three publicly available techniques," *Machine Vision and Applications*, Vol. 17, No. 1, 2006, pp. 51–67, DOI: 10.1007/s00138-006-0014-6.

[80] Zhang, Z., "Flexible camera calibration by viewing a plane from unknown orientations," *Computer Vision, 1999. The Proceedings of the Seventh IEEE International Conference on*, Vol. 1, IEEE, 1999, pp. 666–673, DOI: 10.1109/ICCV.1999.791289.

[81] LaVision GmbH, Gottingen, Germany, *StrainMaster Product-Manual*, August 2011.

[82] Bornert, M., Brémand, F., Doumalin, P., Dupré, J.-C., Fazzini, M., Grédiac, M., Hild, F., Mistou, S., Molimard, J., Orteu, J.-J., et al., "Assessment of digital image correlation measurement errors: methodology and results," *Experimental mechanics*, Vol. 49, No. 3, 2009, pp. 353–370, DOI: 10.1007/s11340-008-9204-7.

[83] Reu, P., "Uncertainty Quantification for 3D Digital Image Correlation," *Imaging Methods for Novel Materials and Challenging Applications, Volume 3*, edited by H. Jin, C. Sciammarella, C. Furlong, and S. Yoshida, chap. 43, Springer, 2013, DOI: 10.1007/978-1-4614-4235-6_43.

[84] Matthies, L., Shafer, S., et al., "Error modeling in stereo navigation," *Robotics and Automation, IEEE Journal of*, Vol. 3, No. 3, 1987, pp. 239–248, DOI: 10.1109/JRA.1987.1087097.

[85] Yang, H., *Kevlar aramid fiber*, Vol. 1, John Wiley & Sons Ltd., 1993.

[86] Beams, J., "Mechanical properties of thin films of gold and silver," *Structure and properties of thin films*, 1959, pp. 183–192.

[87] Tsakalakos, T., "The bulge test: a comparison of the theory and experiment for isotropic and anisotropic films," *Thin solid films*, Vol. 75, No. 3, 1981, pp. 293–305, DOI: 10.1016/0040-6090(81)90407-7.

[88] Lin, P., *The in-situ measurement of mechanical properties of multi-layer coatings*, Ph.D. thesis, Massachusetts Institute of Technology, 1990, http://hdl.handle.net/1721.1/14102.

[89] Vlassak, J. and Nix, W., "A new bulge test technique for the determination of Young's modulus and Poisson's ratio of thin films," *Journal of Materials Research*, Vol. 7, No. 12, 1992, pp. 3242–3249, DOI: 10.1557/JMR.1992.3242.

[90] Hsu, F., Schwab, C., Rigamonti, D., and Humphrey, J., "Identification of response functions from axisymmetric membrane inflation tests: implications for biomechanics," *International Journal of Solids and Structures*, Vol. 31, No. 24, 1994, pp. 3375–3386, DOI: 10.1016/0020-7683(94)90021-3.

[91] Neggers, J., Hoefnagels, J., Hild, F., Roux, S., and Geers, M., "Direct stress-strain measurements from bulged membranes using topography image correlation," *Experimental Mechanics*, Vol. 54, No. 5, 2014, pp. 717–727, DOI: 10.1007/s11340-013-9832-4.

[92] Kyriacou, S., Shah, A., and Humphrey, J., "Inverse finite element characterization of nonlinear hyperelastic membranes," *Journal of Applied Mechanics*, Vol. 64, No. 2, 1997, pp. 257–262, DOI: 10.1115/1.2787301.

[93] Stanford, B., Albertani, R., and Ifju, P., "Inverse methods to determine the aerodynamic forces on a membrane wing," 48th AIAA/ASME/AHS/ASC Structures, Structural Dynamics, and Materials Conference Conference (AIAA 2007-1984), 2007, DOI: 10.2514/6.2007-1984 .

[94] ASTM, "Standard Test Method for Air Permeability of Textile Fabrics," 2012, ASTM Standard D737–04.

[95] ASTM, "Standard Methods for Gas Flow Resistance Testing of Filtration Media," 2014, ASTM Standard F778–88.

[96] Katz, J. and Plotkin, A., *Low-speed aerodynamics*, Vol. 13, Cambridge University Press, 2001, Chpt. 14.

[97] Stevens, K. K., "Force identification problemsan overview," *Proceedings of the 1987 SEM Spring Conference on Experimental Mechanics*, 1987, pp. 14–19.

[98] Engl, H. and Kugler, P., "Nonlinear Inverse Problems: Theoretical Aspects and Some Industrial Applications," *Multidisciplinary methods for analysis optimization and control complex systems*, edited by V. Capasso and J. Périaux, Springer, Berlin., 2005.

[99] Tikhonov, A. N. and Arsenin, V. I., *Solutions of ill-posed problems*, V.H. Winston and Sons, 1977.

[100] Doicu, A., Trautmann, T., and Schreier, F., *Numerical regularization for atmospheric inverse problems*, Springer Science & Business Media, 2010.

[101] Hansen, P. C. and O'Leary, D. P., "The use of the L-curve in the regularization of discrete ill-posed problems," *SIAM Journal on Scientific Computing*, Vol. 14, No. 6, 1993, pp. 1487–1503, DOI: 10.1137/0914086 .

[102] Vogel, C. R., *Computational methods for inverse problems*, Vol. 23, Siam, 2002.

[103] Beck, J. V. and Woodbury, K. A., "Inverse problems and parameter estimation: integration of measurements and analysis," *Measurement Science and Technology*, Vol. 9, 1998, pp. 839–847, DOI: 10.1088/0957-0233/9/6/001.

[104] Kaltenbacher, B., Neubauer, A., and Scherzer, O., *Iterative regularization methods for nonlinear ill-posed problems*, Vol. 6, Walter de Gruyter, 2008.

[105] Mueller, J. L. and Siltanen, S., *Linear and nonlinear inverse problems with practical applications*, Vol. 10, Siam, 2012, DOI: 10.1137/1.9781611972344.

[106] Sofyan, E. and Trivailo, P., "Solving Aerodynamic Load Inverse Problems Using a Hybrid FEM–Artificial Intelligence," *3rd Australasian Matlab Users Conference [organised by CEANET and MATHWORKS]*, 2000, pp. 1–19.

[107] Shkarayev, S., Krashanitsa, R., and Tessler, A., "An inverse interpolation method utilizing in-flight strain measurements for determining loads and structural response of aerospace vehicles," Tech. rep., Association for Computing Machinery, 2001.

[108] Coates, C. W., Thamburaj, P., and Kim, C. J., "An inverse method for selection of Fourier coefficients for flight load identification," *46th AIAA/ASME/ASCE/AHS/ASC Structures, Structural Dynamics and Materials Conference (AIAA 2005-2183)*, 2005, DOI: 10.2514/6.2005-2183 .

[109] Coates, C. W. and Thamburaj, P., "Inverse method using finite strain measurements to determine flight load distribution functions," *Journal of Aircraft*, Vol. 45, No. 2, 2008, pp. 366–370, DOI: 10.2514/1.21905 .

[110] Tessler, A. and Spangler, J. L., "A least-squares variational method for full-field reconstruction of elastic deformations in shear-deformable plates and shells," *Computer Methods in Applied Mechanics and Engineering*, Vol. 194, No. 2, 2005, pp. 327–339, DOI: 10.1016/j.cma.2004.03.015 .

[111] Carpenter, T. J. and Albertani, R., "Aerodynamic load estimation: Pressure distribution from virtual strain sensors for a pliant membrane wing," 54th AIAA/ASME/ASCE/AHS/ASC Structures, Structural Dynamics, and Materials Conference (AIAA 2013-1917), 2013, DOI: 10.2514/6.2013-1917 .

[112] Maniatty, A., Zabaras, N., and Stelson, K., "Finite element analysis of some inverse elasticity problems," *Journal of Engineering Mechanics*, Vol. 115, No. 6, 1989, pp. 1303–1317, DOI: 10.1061/(ASCE)0733-9399(1989)115:6(1303).

[113] Schnur, D. and Zabaras, N., "Finite element solution of two-dimensional inverse elastic problems using spatial smoothing," *International Journal for Numerical Methods in Engineering*, Vol. 30, No. 1, 1990, pp. 57–75, DOI: 10.1002/nme.1620300105.

[114] Maniatty, A. M. and Zabaras, N. J., "Investigation of regularization parameters and error estimating in inverse elasticity problems," *International Journal for Numerical Methods in Rngineering*, Vol. 37, No. 6, 1994, pp. 1039–1052, DOI: 10.1002/nme.1620370610 .

[115] Ring, W., "Identification of the load of a partially breaking beam from inclination measurements," *Inverse problems*, Vol. 15, No. 4, 1999, pp. 1003–1020, DOI: 10.1088/0266-5611/15/4/311.

[116] Chock, J. M. K. and Kapania, R. K., "Load updating for finite element models," *AIAA journal*, Vol. 41, No. 9, 2003, pp. 1667–1673, DOI: 10.2514/2.7312 .

[117] Chock, J. and Kapania, R., "Finite element load updating for plates," 45th AIAA/ASME/ASCE/AHS/ASC Structures, Structural Dynamics and Materials Conference (AIAA 2004-2004), 2004, DOI: 10.2514/6.2004-2004.

[118] Li, J. and Kapania, R. K., "Load updating for nonlinear finite element models," *AIAA journal*, Vol. 45, No. 7, 2007, pp. 1444–1458, DOI: 10.2514/1.19073 .

[119] Xu, S., Deng, X., Tiwari, V., Sutton, M. A., Fourney, W. L., and Bretall, D., "An inverse approach for pressure load identification," *International Journal of Impact Engineering*, Vol. 37, No. 7, 2010, pp. 865–877, DOI: 10.1016/j.ijimpeng.2009.10.007.

[120] Nakamura, T., Igawa, H., and Kanda, A., "Inverse identification of continuously distributed loads using strain data," *Aerospace Science and Technology*, Vol. 23, No. 1, 2012, pp. 75–84, DOI: 10.1016/j.ast.2011.06.012.

[121] Dickinson, B. T. and Singler, J. R., "Distributed load estimation from noisy structural measurements," *Journal of Applied Mechanics*, Vol. 80, 2013, DOI: 10.1115/1.4007794.

[122] Alioli, M., Masarati, P., Morandini, M., Carpenter, T., and Albertani, R., "Nonlinear Membrane Direct and Inverse FEM Analysis," *ASME 2014 International Design Engineering Technical Conferences and Computers and Information in Engineering Conference*, American Society of Mechanical Engineers, 2014, DOI: 10.2514/6.2015-2051 .

[123] Schlichting, H. and Gersten, K., *Boundary-layer theory*, Springer Science & Business Media, 2003, Chpt. 21.

[124] Moreau, D. J., Doolan, C., Alexander, W. N., Meyers, T. W., and Devenport, W. J., "Wall-Mounted Finite Airfoil Noise Production and Prediction," *21st AIAA/CEAS Aeroacoustics Conference (AIAA 2015-2831)*, 2015, DOI: 10.2514/1.J054493.

Appendix A

Derivation of Wall-Interference Corrections Based on Panel Method Flow Solution

Panel methods offer an approach to wall-interference corrections that are not restricted by the boundary conditions required by classical method of images analyses. In this appendix, the classical wall-interference correction of Allen and Vincenti[17] is put in more general terms appropriate for use with the panel method approach. The goal of this appendix is to determine the corrections to apply to measured coefficients and angles of attack based on flow velocities and their derivatives as queried from a panel method simulation.

A.1 Vorticity Induced by an Airfoil

According to Glauert's representation of vorticity around an airfoil, the induced velocity field of a two-dimensional airfoil in free-flight is given by Equation A.1

$$\frac{v}{V} = \sqrt{1 - M^2}[-A_0 + \sum_{n=1}^{\infty} A_n cos(n\theta)] \tag{A.1}$$

where v is the vertical velocity induced by the airfoil, V is the freestream velocity of the airfoil, and the coefficients A_0 and A_n are equal to

$$A_0 = \frac{1}{\sqrt{1 - M^2}}[\alpha - \int_0^{\pi} \frac{dy_c}{dx} d\theta] \tag{A.2}$$

$$A_n = \frac{1}{\sqrt{1-M^2}} \frac{2}{\pi} \int_0^\pi \frac{dy_c}{dx} cos(n\theta) d\theta \tag{A.3}$$

and θ is related to the chordwise location x according to the transformation

$$x = \frac{1}{2} c(1 - cos\theta). \tag{A.4}$$

Accounting for the restriction of the wind tunnel walls using the method of images, Allen and Vincenti show that Equation A.1 becomes Equation A.5

$$\frac{v'}{V} = \sqrt{1-M^2}[-A'_0 + \frac{\sigma}{1-M^2}(A'_0 + \frac{1}{2}A'_2) + [A'_1 - \frac{\sigma}{1-M^2}(2A'_0 + A'_1)]cos\theta + \sum_{n=2}^{\infty} A'_n cos(n\theta)]. \tag{A.5}$$

where the ($'$) symbol denotes values in the tunnel as opposed to free-flight. Equations A.1 and A.5 give the vertical velocities induced by the airfoil for the free-flight and in-tunnel cases, respectively. The velocity fields cannot be identical between the cases because of the constricting effect of the wind tunnel walls. A choice must be made as to how the coefficients relate between the free-flight and in-tunnel cases. Per Allen and Vincenti's approach, all coefficients are maintained constant between the free-flight and wind tunnel cases except that the A_1 coefficient is given as

$$A_1 = A'_1 - \frac{\sigma}{1-M^2}(2A'_0 + A'_1). \tag{A.6}$$

This approach represents the constriction of the walls as an effective change in the camber of the model. An alternative approach is to assume the camber is the same for the model between the free-flight and in-tunnel cases, and instead use the panel method to determine the effective change in upwash distribution imposed by the wind tunnel walls. Using $A_n = A'_n$ for all n, the difference between Equations A.5 and A.1 is Equation A.7

$$\frac{v'}{V} - \frac{v}{V} = \frac{v_{wall}}{V_\infty} = \frac{\sigma}{\sqrt{1-M^2}}(A'_0 + \frac{1}{2}A'_2) - \frac{\sigma}{\sqrt{1-M^2}}(2A'_0 + A'_1)cos\theta. \tag{A.7}$$

The term v_{wall}/V_∞ is found from the panel method solution by querying the slope of the velocity vector at the model location due to the influence of the walls only and not the model.

The first term on the right-hand side of Equation A.7 represents a wall-induced velocity that is constant over the chord of the airfoil; this is an effective angle of attack change induced by the walls. At the mid-chord of the model, the second term on the right-hand side of

Equation A.7 vanishes, so that the slope of the velocity vector gives the correction to the angle of attack as given by Equation A.8

$$\alpha = \alpha' + \frac{\sigma}{\sqrt{1-M^2}}(A'_0 + \frac{1}{2}A'_2) \tag{A.8}$$

where the small angle approximation has been applied.

The second term on the right-hand side of Equation A.7 represents a wall-induced velocity that varies depending on the location over the chord of the airfoil; this is a change to the upwash distribution as induced by the walls. Equation A.7 is first transformed to be in terms of x by way of Equation A.4, and the result is differentiated with respect to x to give

$$\frac{\partial(v_{wall}/V_\infty)}{\partial x} = \frac{2}{c}[\frac{\sigma}{\sqrt{1-M^2}}(2A'_0 + A'_1)] \tag{A.9}$$

$\partial(v_{wall}/V_\infty)/\partial x$ is found from the panel method solution by differentiating with respect to x the wall-induced velocity vector at the model location. Combining Equations A.6 and A.9 results in Equation A.10

$$A_1 = A'_1 - \frac{1}{\sqrt{1-M^2}}\frac{c}{2}\frac{\partial(v_{wall}/V_\infty)}{\partial x}) \tag{A.10}$$

A.2 Lift and Pitching Moment Correction

Integrating the pressure distribution from the Glauert representation of the airfoil, the lift and pitching moment coefficients in free-flight are given as

$$C_l = \pi(2A_0 + A_1) \tag{A.11}$$

$$C_m = -\frac{\pi}{4}(A_1 - A_2). \tag{A.12}$$

Substituting Equation A.10 into Equations A.11 and A.12 and again using the relations $A_0 = A'_0$ and $A_2 = A'_2$ results in Equations A.13 and A.14

$$C_l = \pi(2A'_0 + A'_1 - \frac{1}{\sqrt{1-M^2}}\frac{c}{2}\frac{\partial(v_{wall}/V_\infty)}{\partial x}) \tag{A.13}$$

$$C_m = -\frac{\pi}{4}(A'_1 - \frac{1}{\sqrt{1-M^2}}\frac{c}{2}\frac{\partial(v_{wall}/V_\infty)}{\partial x} - A'_2). \tag{A.14}$$

The corresponding in-tunnel versions of Equations A.11 and A.12 are given as

$$C_l' = \pi(1 + u_{wall}/V_\infty)^2(2A_0' + A_1') \tag{A.15}$$

$$C_m' = -\frac{\pi}{4}(1 + u_{wall}/V_\infty)^2(A_1' - A_2') \tag{A.16}$$

where u_{wall}/V_∞ is the blockage given by Equation 2.1. Combining Equations A.13 and A.15 and then A.14 and A.16 results in the corrected lift and pitching moment in the same form given in Equations 2.34 and 2.35, respectively,

$$C_{l,c} = C_l \frac{1}{(1 + u_{wall}/V_\infty)^2} - \frac{1}{\sqrt{1 - M^2}} \frac{\pi}{2} c \frac{\partial(v_{wall}/V_\infty)}{\partial x}$$

$$C_{m,c} = C_m \frac{1}{(1 + u_{wall}/V_\infty)^2} + \frac{1}{\sqrt{1 - M^2}} \frac{\pi}{8} c \frac{\partial(v_{wall}/V_\infty)}{\partial x}$$

where the *wall* subscript has been dropped. Note that u/V_∞ is found from the panel method solution by querying the streamwise velocity at the model location due to the influence of the walls only and not the model. Therefore, we now have equations to correct the lift and pitching moment coefficients that require only the measured coefficients, values queried from the panel method simulation at the model location, and the chord length of the model.

A.3 Angle of Attack Correction

Equation A.8 gives a correction to first-order to account for the streamline curvature induced by the tunnel walls. We can now derive this equation for a more general boundary condition such that the angle of attack change is given by the panel method solution. Solving Equation A.15 for A_0' and Equation A.16 for A_2' and inserting the results into Equation A.8 gives, after rearranging,

$$\alpha = \alpha' + \frac{\sigma}{2}(2A_0' + A_1') + 2\sigma(2A_0' + A_1')\frac{C_m'}{C_l'}. \tag{A.17}$$

Substituting Equation A.9 into Equation A.17 results in Equation 2.33

$$\alpha_c = \alpha_e + \sqrt{1 - M^2} c \left(\frac{1}{4} + \frac{C_m}{C_l}\right) \frac{\partial(v_{wall}/V_\infty)}{\partial x}.$$

Equation 2.33 is the correction to the angle of attack due to the streamline curvature induced by the walls. The panel method also affords the ability to predict any far-field change in angle of attack due to the flexible, porous boundary conditions. The far-field angle of attack, α_e, is found from the panel method simulation by querying the slope of the velocity vector at the model chordwise location where Equation A.7 sums to zero. Using a singularity representation of the model, an appropriate location for querying is at the singularities. The effective angle of attack, α_e, is different from the geometric angle of attack, α_g, according to Equation A.18

$$\alpha_e = \alpha_g + \frac{v}{V_\infty}\frac{180}{\pi} \quad (degrees) \tag{A.18}$$

as indicated by Equation 2.48.

A.4 Drag Correction

Allen and Vincenti give the relation between the measured and corrected drag coefficient as

$$C_d = C'_d \frac{1}{(1 + u_{wall}/V_\infty)^2}[1 - \frac{1 + 0.4(M)^2}{[1 - (M)^2]^{3/2}}\Lambda\sigma] \tag{A.19}$$

where σ is given in Equation 2.6 and Λ is calculated as described in Section 2.1.2.1. Drag measured from a wake rake, however, does include effect of the pressure gradient, so only the first term on the right-hand side of Equation A.19 is retained. Keeping only the first term on the right-hand side and dropping the *wall* subscript yields Equation 2.36

$$C_{d,c} = C_d \frac{1}{(1 + u/V_\infty)^2}$$

A.5 Airfoil Pressure Correction

Corrections to the airfoil pressure coefficients can also be made using the panel method approach. Allen and Vincenti give a seven step process for how to correct such data, and the appropriate modifications for the panel method approach occur in step five. Here the term $\sigma C'_l/1 - M^2$ must be replaced by a value that is queried from the panel method and thus not dependent on the boundary conditions assumed in the method of images analysis. With the help of Equations A.9 and A.15, it can be shown that

$$\frac{\sigma C_l'}{1-M^2} = \frac{1}{1-M^2}\pi\sigma\frac{c}{2}(1+\frac{u_{wall}}{V_\infty})^2(2A_0'+A_1') = \frac{1}{\sqrt{1-M^2}}\pi\frac{c}{2}(1+\frac{u_{wall}}{V_\infty})^2\frac{\partial(v_{wall}/V_\infty)}{\partial x}. \tag{A.20}$$

Appendix B

Development of Wall Boundary Layer Model for Panel Method Flow Solution

As a solution, the wall boundary layer is modeled using the *transpiration velocity* method[96]. Instead of changing the paneling of the wall to reflect the boundary layer growth, the transpiration velocity method adds mass to the test section to accelerate the flow in the same manner as the blocking effect of the displacement thickness of a growing wall boundary layer. The transpiration velocity method is preferred here not only because the coefficient matrix only has to be calculated once within the inner porosity iteration loop, but also because the boundary layer transpiration can be seamlessly integrated into the suction and blowing transpiration already occurring across the Kevlar. It follows that flow blown out of the test section will reduce the boundary layer influence, and flow sucked into the test section will exaggerate it. Equation B.1 gives the inwards transpiration velocity, v, normal to the test section walls as a function of distance along the test section

$$v(x) = \frac{\partial}{\partial x}(U_e \delta^*) \tag{B.1}$$

where U_e is the edge velocity at the boundary layer and δ^* is the displacement thickness. As a first-order approximation, a simple zero-pressure gradient boundary layer is employed which uses the assumption of a 1/7-power law velocity distribution and the approximation that $\delta^* = \frac{\delta}{8}$. According to the product rule and with the zero-pressure gradient assumption, U_e comes outside the partial derivative and is taken as the realized freestream velocity in the panel method. The displacement thickness δ^* and its derivative are given in Equations B.2 and B.3[123], respectively,

$$\delta^* = \frac{1}{8} 0.37x \left(\frac{U_\infty x}{\nu}\right)^{-1/5} \tag{B.2}$$

$$\frac{\partial \delta^*}{\partial x} = \frac{1}{10} 0.37 \left(\frac{U_\infty x}{\nu}\right)^{-1/5} \tag{B.3}$$

where x is the streamwise length along the test section. The streamwise origin of x was varied until the thickness at a location 0.23-m upstream of the quarter-chord location matched hotwire results to within 1-mm[124]. As such, the streamwise origin was calculated to be 5.2-m upstream of quarter-chord. Calculating the transpiration velocities at every control point downstream of the origin, the velocities are then doubled to account for the boundary layer growth on the floor and ceiling and added to the panel method residual vector along the control points of the port and starboard walls.

Pressure coefficients in the panel method are given relative to the realized freestream conditions at a location 10-m upstream of the model. However, the addition of the boundary layer 5.2-m upstream of the model causes acceleration of the freestream flow so that the original upstream reference point is no longer an appropriate reference. Since the reference point cannot be moved any closer when a model is being simulated in the test section, the solution is to apply a freestream correction based on simulation results in an empty test section. Following the same reasoning that led to Equation 3.1, the static pressure at quarter-chord is queried for different flow velocities through the empty test section. This quarter-chord pressure coefficient, relative to the reference point 10-m upstream, was found to be $C_{p,r\infty}$ as shown in Equation B.4. With a model added back into the simulation, the C_p relative to the conditions 10-m upstream is corrected to C_p' which is relative to the freestream conditions at quarter-chord according to Equation B.4

$$C_p' = \frac{C_p - C_{p,r\infty}}{1 - C_{p,r\infty}}, \quad C_{p,r\infty} = 0.0001365 U_\infty - 0.03992. \tag{B.4}$$

Correspondingly, the corrected freestream velocity at quarter-chord is $\sqrt{1 - C_{p,r\infty}}$ times the velocity at the upstream reference point. After convergence of the panel method simulation, the above freestream correction is applied to all panel method data in this study which use the boundary layer simulation.

The adequacy of the boundary layer model is first validated using a solid-wall configuration as shown in Figure B.1 for two different freestream velocities. The experimental data are static pressures measured on the floor of the Stability Wind Tunnel's solid-wall test section with no model in the tunnel. The simulated data are static pressures measured along the walls of an empty test section which includes the wall boundary layers. Note that without the freestream correction noted above, the simulated curves would fall well below the measured curves. As indicated by the more negative C_p' slope of the 35-m/s case, the growth of the boundary layer is faster for the slower velocity case which is expected from Equation B.3.

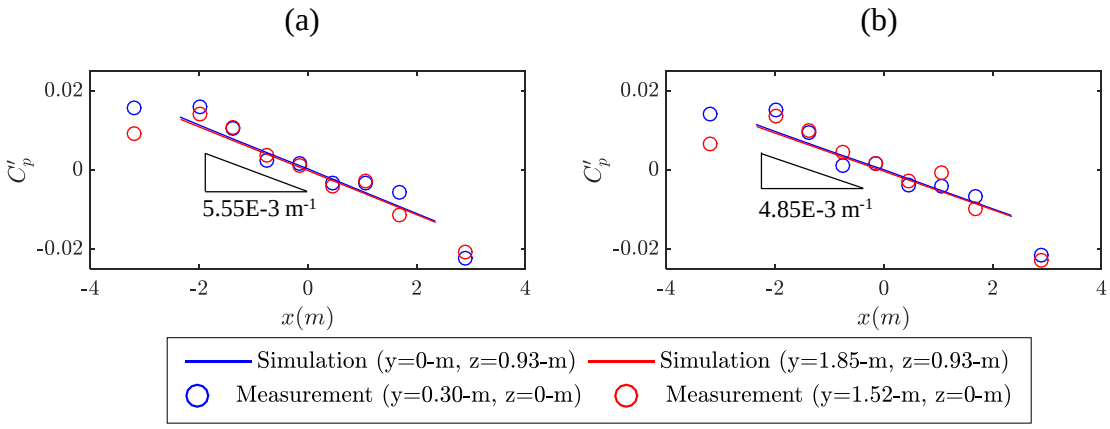

Figure B.1: Coefficient of pressure relative to the pressure at quarter-chord, C'_p, versus distance along the test section, x, for an empty test section at freestream velocities of (a) 35-m/s and (b) 70-m/s. Measurement locations are given according to the right-hand coordinate system of Figure 3.2.

Now considering the Kevlar-wall test section, it is noted that the boundary layer update in Kevlar configuration is incorporated into the wall porosity iteration loop which is nested within the wall deflection loop. After the transpiration velocities due to Kevlar porosity have been calculated, the inward transpiration of the boundary layer model is added to the flow and the flow solution is calculated. This process repeats until the convergence parameter has been met in the nested inner loop. Each time the code leaves the inner loop, the boundary layer thickness is re-scaled based on the reference freestream velocity. It is noted that the transpiration velocities due to the boundary layer growth are not accounted in the calculation of total mass flow through each Kevlar window. This detail ensures that the mass exchange between chambers as described in Section 2.2.2.2.1 is appropriately applied.

Appendix C

Baseline Data for NACA0012 Reference Cases

This appendix gives a systematic presentation of the baseline data corresponding to the runs cataloged in Table 3.3. First are given the global aerodynamic coefficients, followed by airfoil pressure distributions, wall pressure distributions, and wall deformations, if applicable.

Wherever applicable, corrections applied to the data below are performed with a two-dimensional panel method simulation using the singularity representation of the airfoil introduced in Section 2.1.2.2. For the Kevlar-wall cases, the panel method abides by that of Devenport *et al.* as introduced in Section 2.2.2.2.1 except that the singularity representation of the model is used rather than a full paneled airfoil. Devenport *et al.* did not report a porosity relation for Fabric B or the speckled version thereof that was used in Campaign 3, so the results of Section 4.3.3 were curve-fit to Equation 2.45 to yield $k_c = 0.01081\ m/(s\sqrt{Pa})$ assuming $k_p = 50\text{-}Pa$. Additionally, the values of pre-tension and leakage area for Campaign 3 are updated from the original values of Devenport *et al.* according to the new measurements as listed in Table 3.3. As not all the lift polars have corresponding drag data available, the source strength of Equation 2.37 for data from every campaign is calculated with the drag measured during Run 2-1.

C.1 Global Aerodynamic Coefficients

Corrections to the angle of attack and global aerodynamic coefficients are performed using Equations 2.33, 2.34, 2.35, and 2.36.

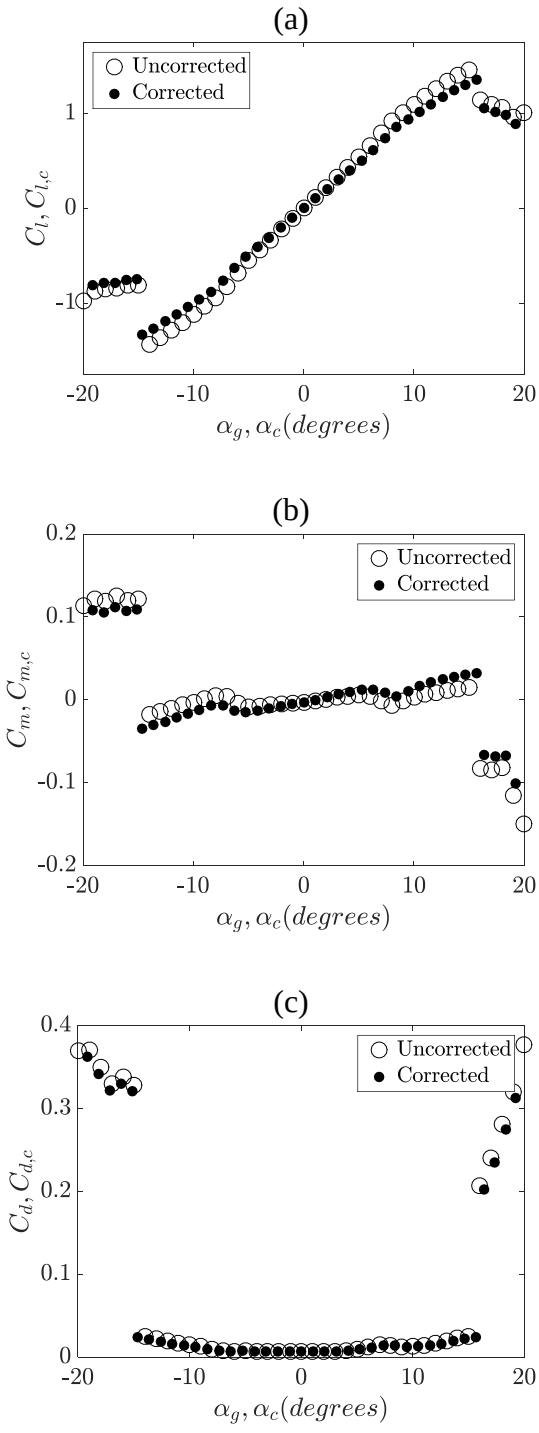

Figure C.1: Global aerodynamic coefficients for Run 1-1 of Table 3.3. Angles of attack have been offset by 0.05 degrees in the positive direction to align zero-lift with the origin.

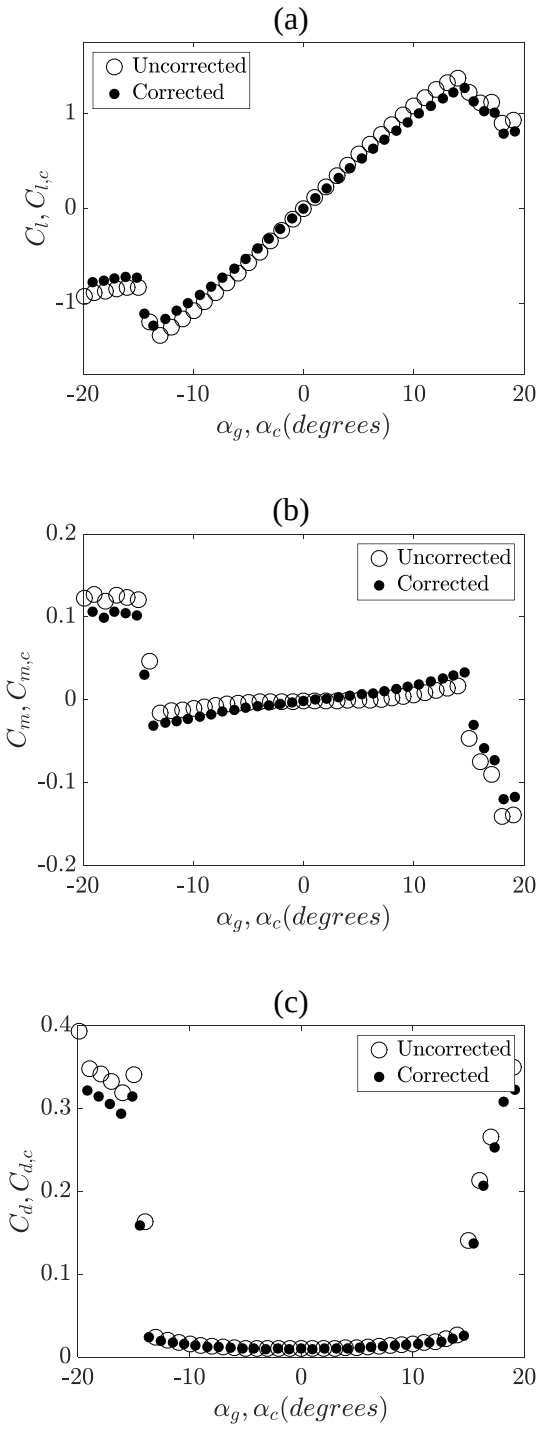

Figure C.2: Global aerodynamic coefficients for Run 1-2 of Table 3.3. Angles of attack have been offset by 0.04 degrees in the positive direction to align zero-lift with the origin.

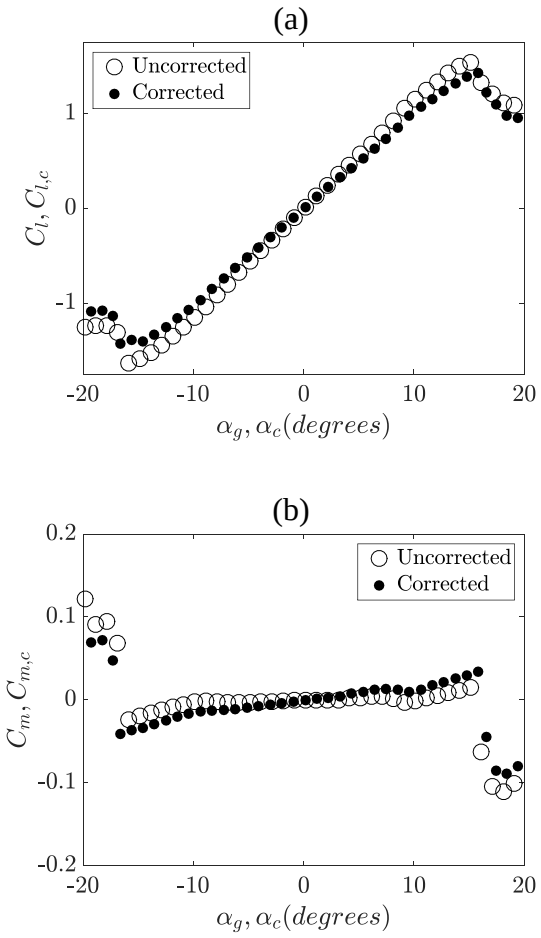

Figure C.3: Global aerodynamic coefficients for Run 1-3 of Table 3.3. Angles of attack have been offset by 0.16 degrees in the positive direction to align zero-lift with the origin.

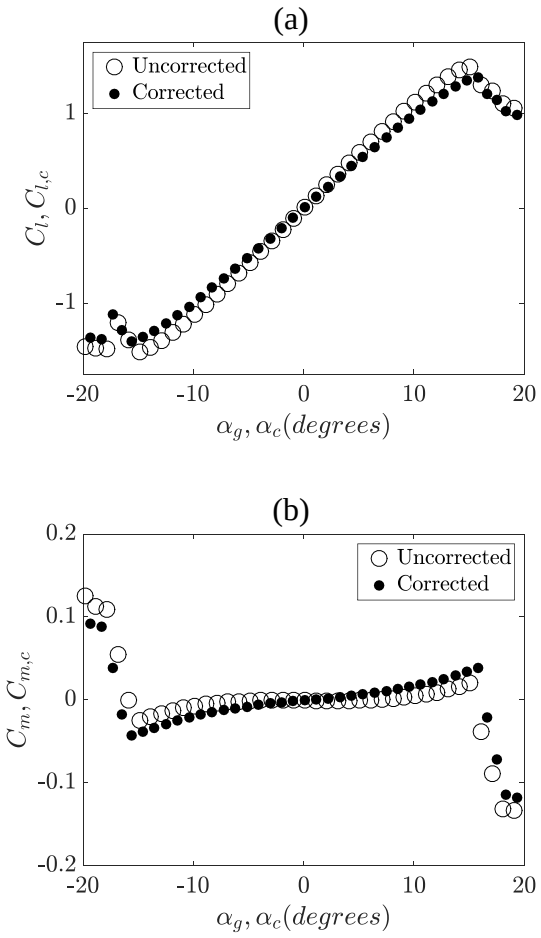

Figure C.4: Global aerodynamic coefficients for Run 1-4 of Table 3.3. Angles of attack have been offset by 0.14 degrees in the positive direction to align zero-lift with the origin.

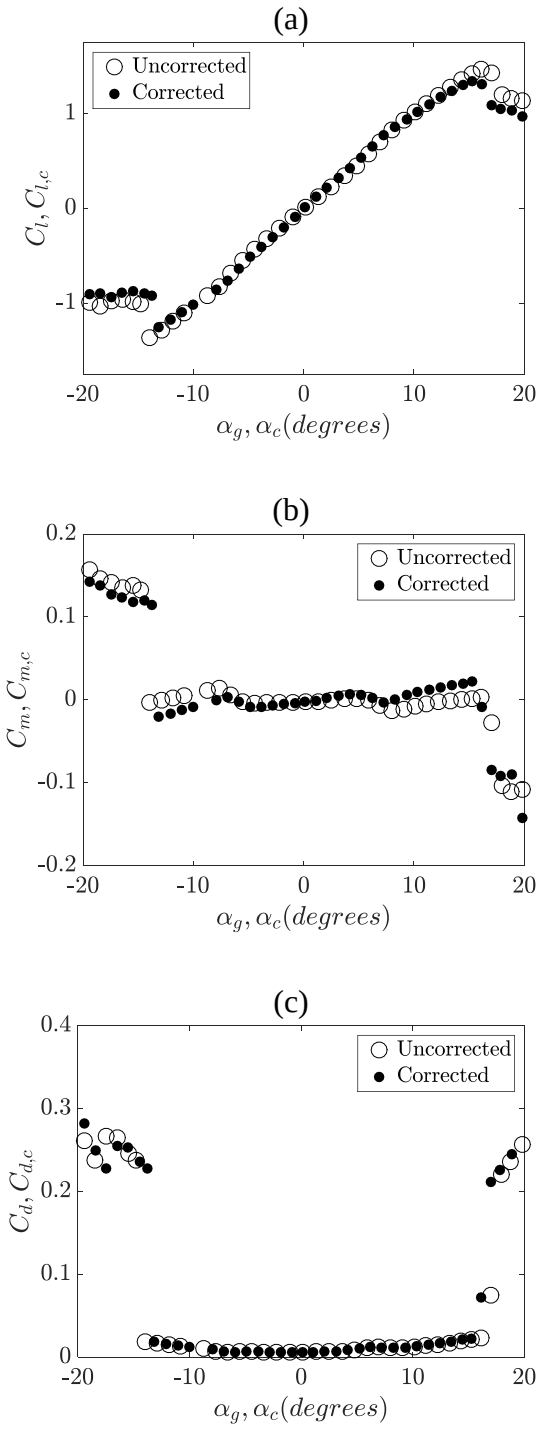

Figure C.5: Global aerodynamic coefficients for Run 2-1 of Table 3.3. Angles of attack have been offset by 0.24 degrees in the positive direction to align zero-lift with the origin.

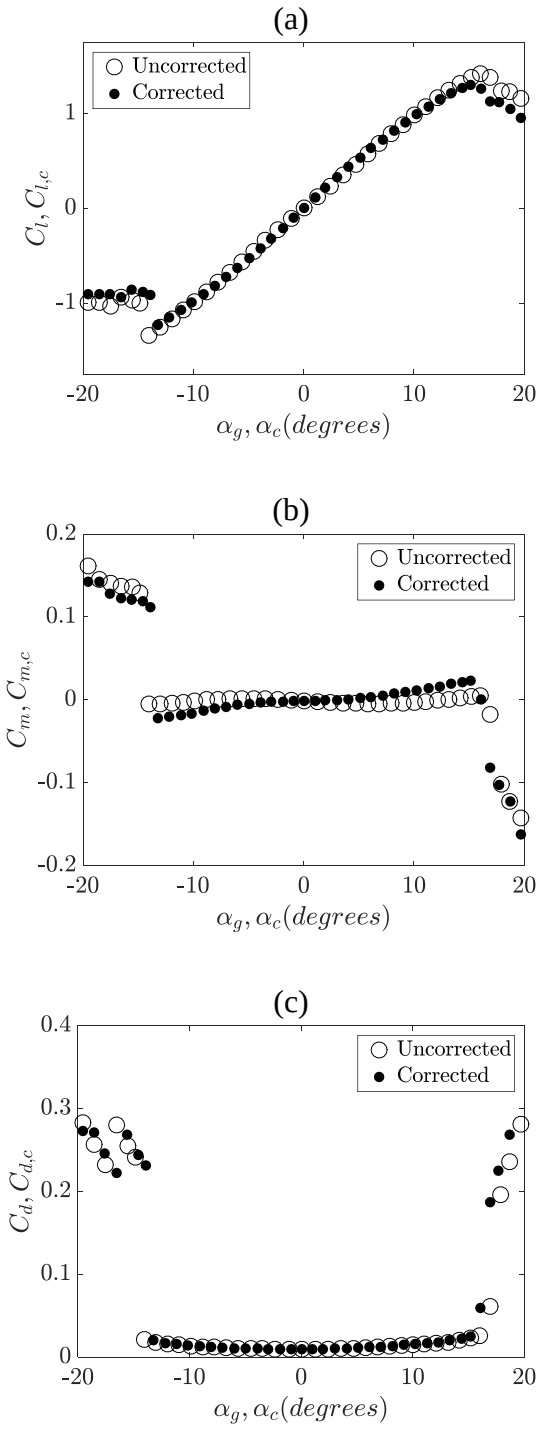

Figure C.6: Global aerodynamic coefficients for Run 2-2 of Table 3.3. Angles of attack have been offset by 0.14 degrees in the positive direction to align zero-lift with the origin.

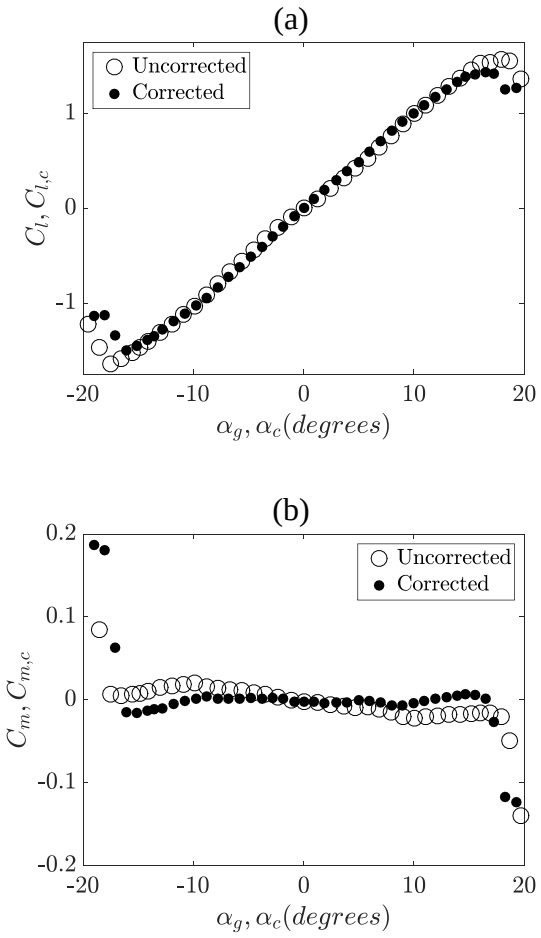

Figure C.7: Global aerodynamic coefficients for Run 2-3 of Table 3.3. Angles of attack have been offset by 0.15 degrees in the positive direction to align zero-lift with the origin.

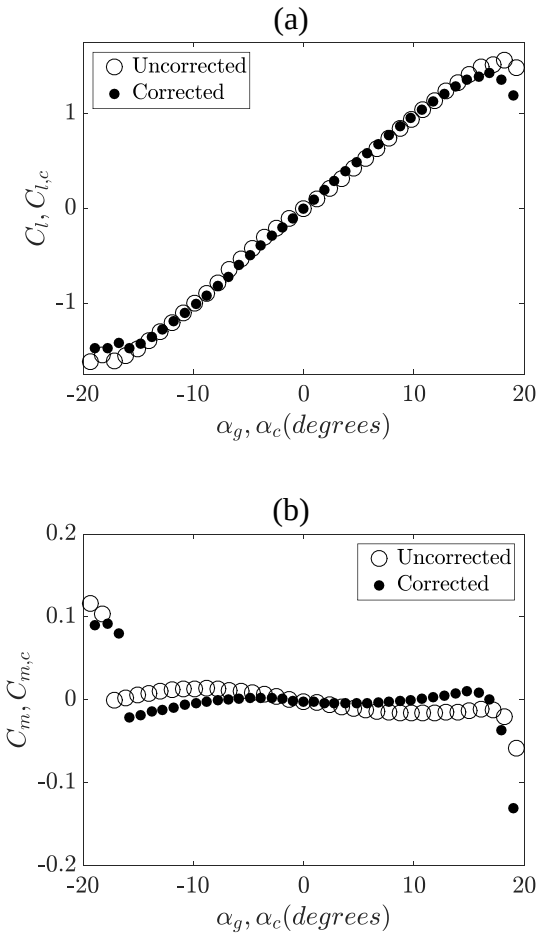

Figure C.8: Global aerodynamic coefficients for Run 2-4 of Table 3.3. Angles of attack have been offset by 0.03 degrees in the positive direction to align zero-lift with the origin.

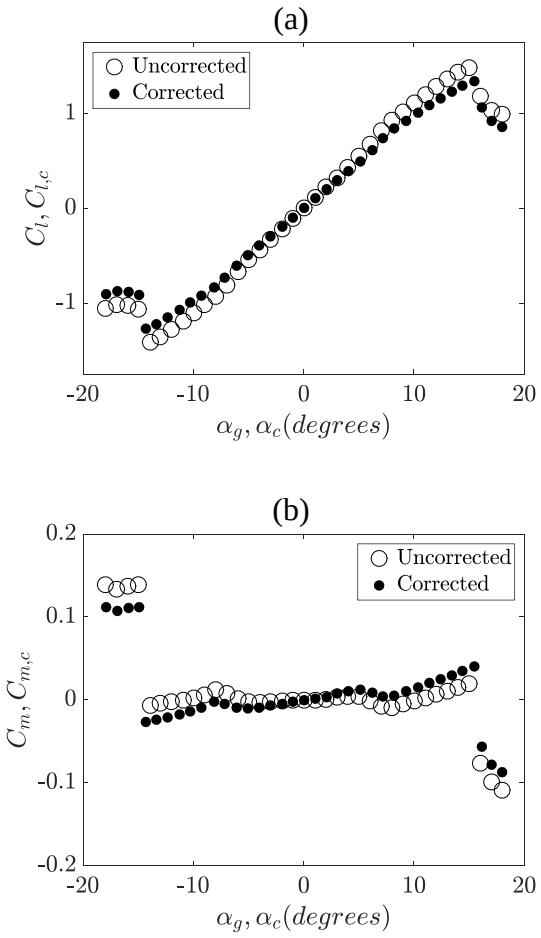

Figure C.9: Global aerodynamic coefficients for Run 3-1 of Table 3.3. Angles of attack have been offset by 0.01 degrees in the negative direction to align zero-lift with the origin.

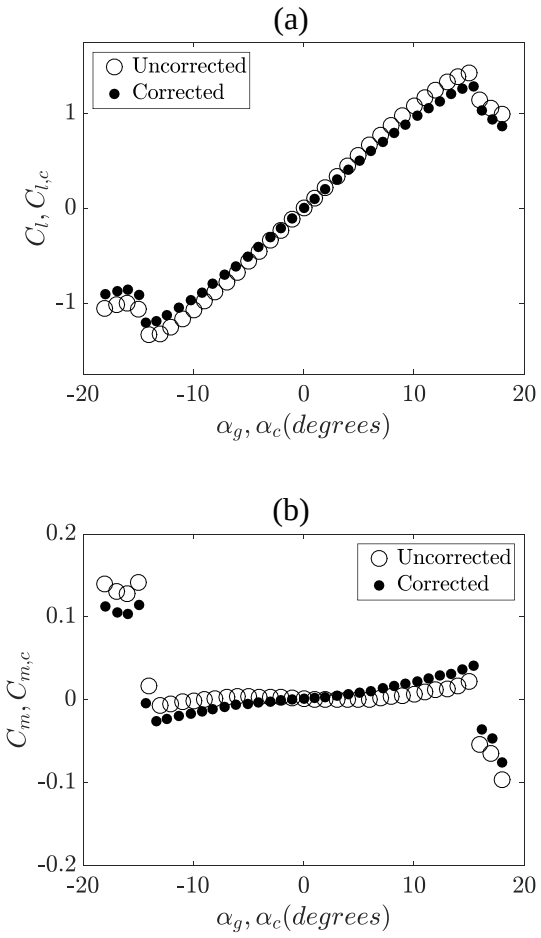

Figure C.10: Global aerodynamic coefficients for Run 3-2 of Table 3.3. Angles of attack have been offset by 0.05 degrees in the negative direction to align zero-lift with the origin.

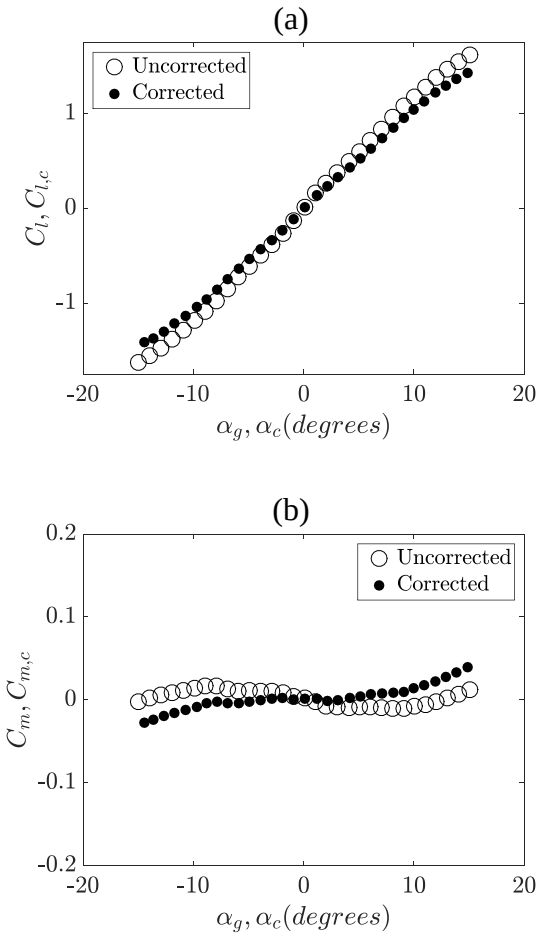

Figure C.11: Global aerodynamic coefficients for Run 3-3 of Table 3.3. Angles of attack have been offset by 0.05 degrees in the positive direction to align zero-lift with the origin.

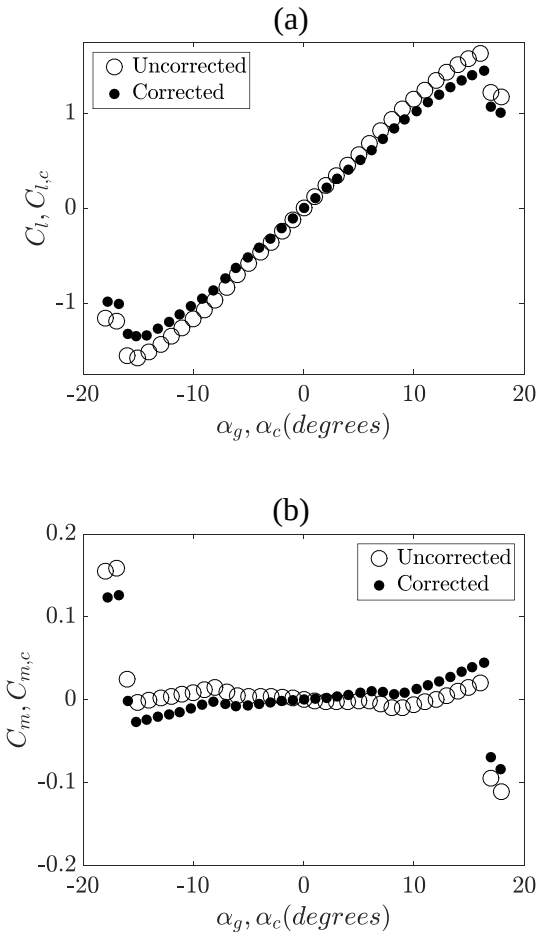

Figure C.12: Global aerodynamic coefficients for Run 3-5 of Table 3.3. Angles of attack have been offset by 0.04 degrees in the negative direction to align zero-lift with the origin.

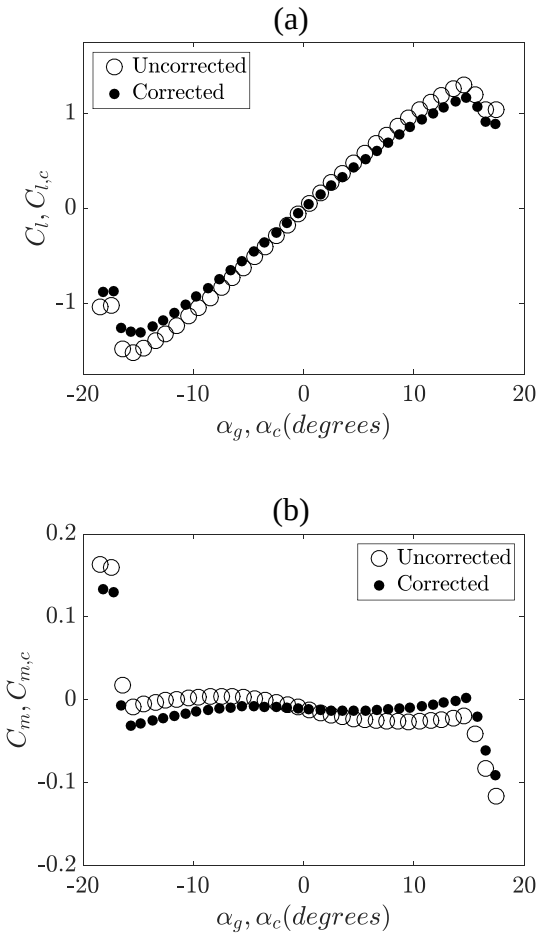

Figure C.13: Global aerodynamic coefficients for Run 3-6 of Table 3.3. Angles of attack have been offset by 0.52 degrees in the negative direction to align zero-lift with the origin.

C.2 Airfoil Pressure Coefficients

Corrections to the airfoil pressure coefficients are performed using the method of Allen and Vincenti[17] according to Appendix A.

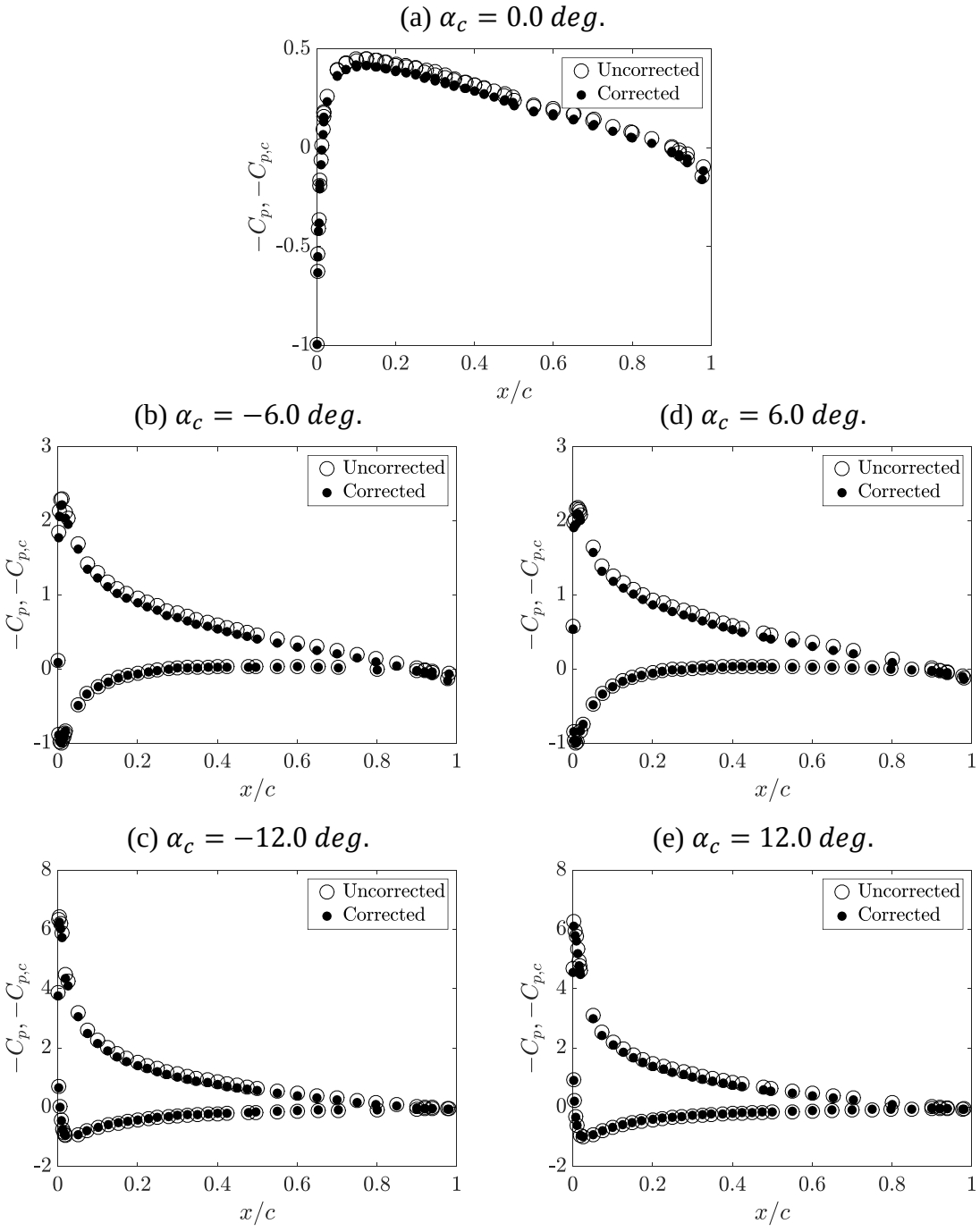

Figure C.14: Airfoil $-C_p$ vs. x/c for Run 1-1 of Table 3.3. Angles of attack have been offset by 0.05 degrees in the positive direction to align zero-lift with the origin. Data have been interpolated to the nominal angles reported.

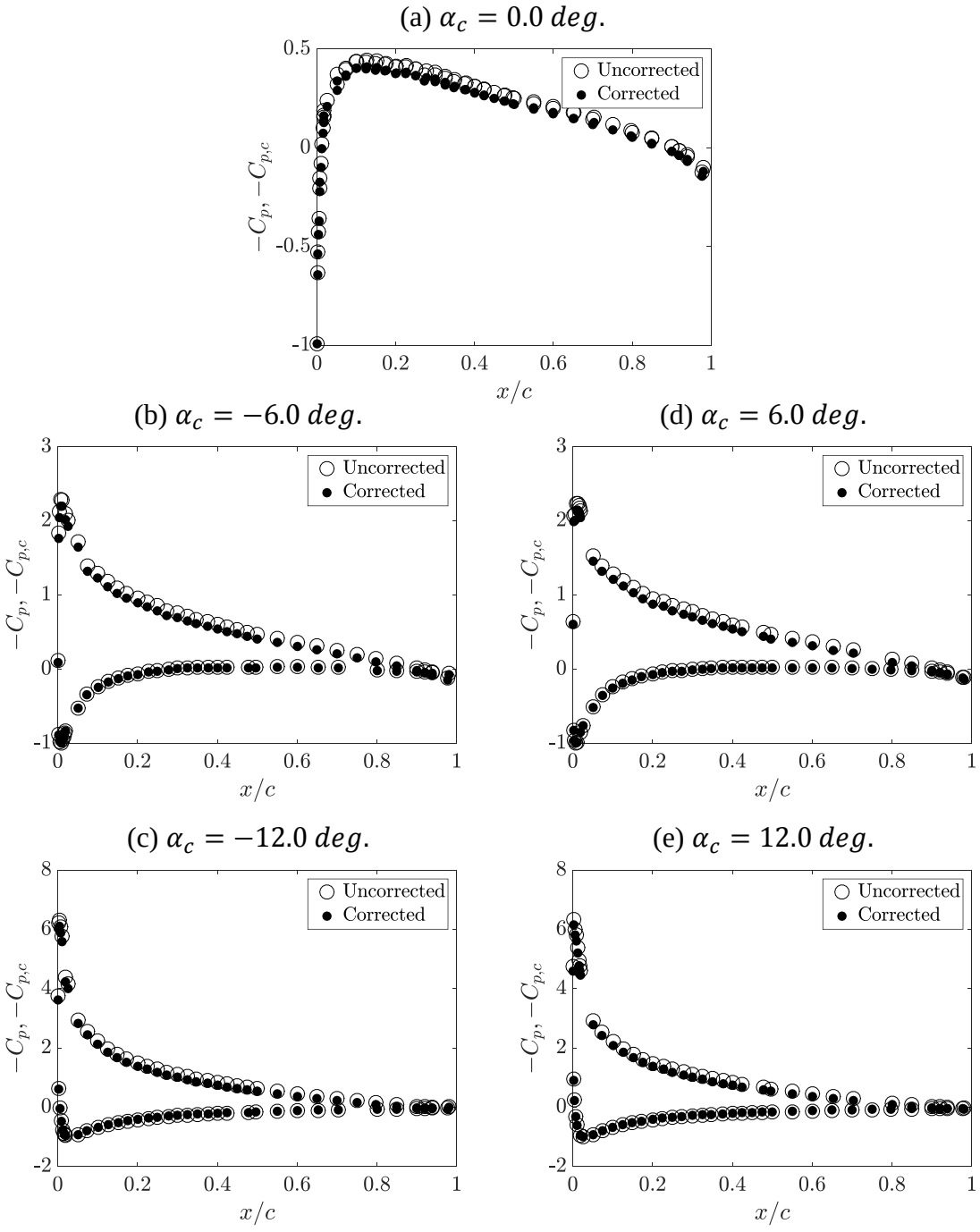

Figure C.15: Airfoil $-C_p$ vs. x/c for Run 1-2 of Table 3.3. Angles of attack have been offset by 0.04 degrees in the positive direction to align zero-lift with the origin. Data have been interpolated to the nominal angles reported.

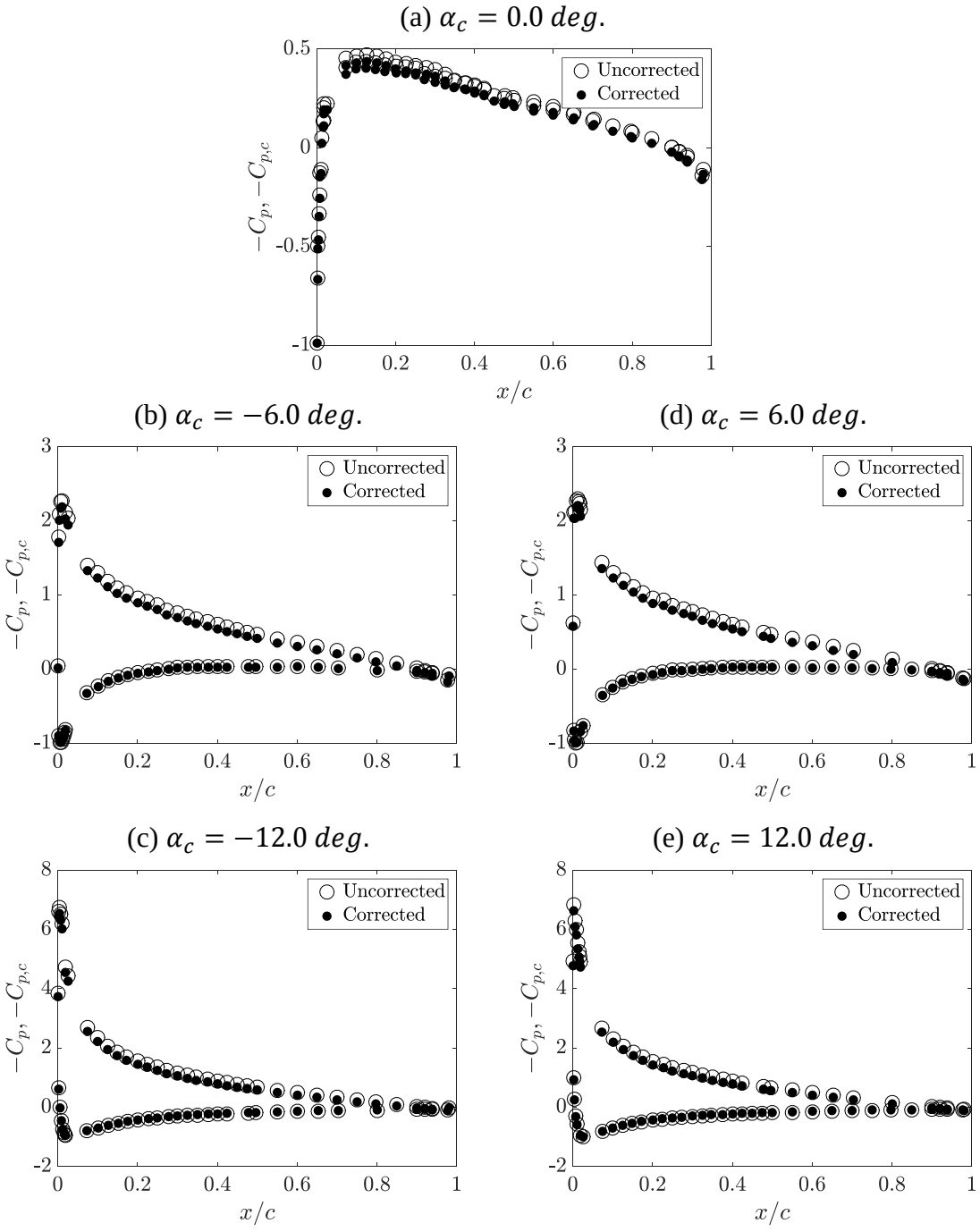

Figure C.16: Airfoil $-C_p$ vs. x/c for Run 1-3 of Table 3.3. Angles of attack have been offset by 0.16 degrees in the positive direction to align zero-lift with the origin. Data have been interpolated to the nominal angles reported.

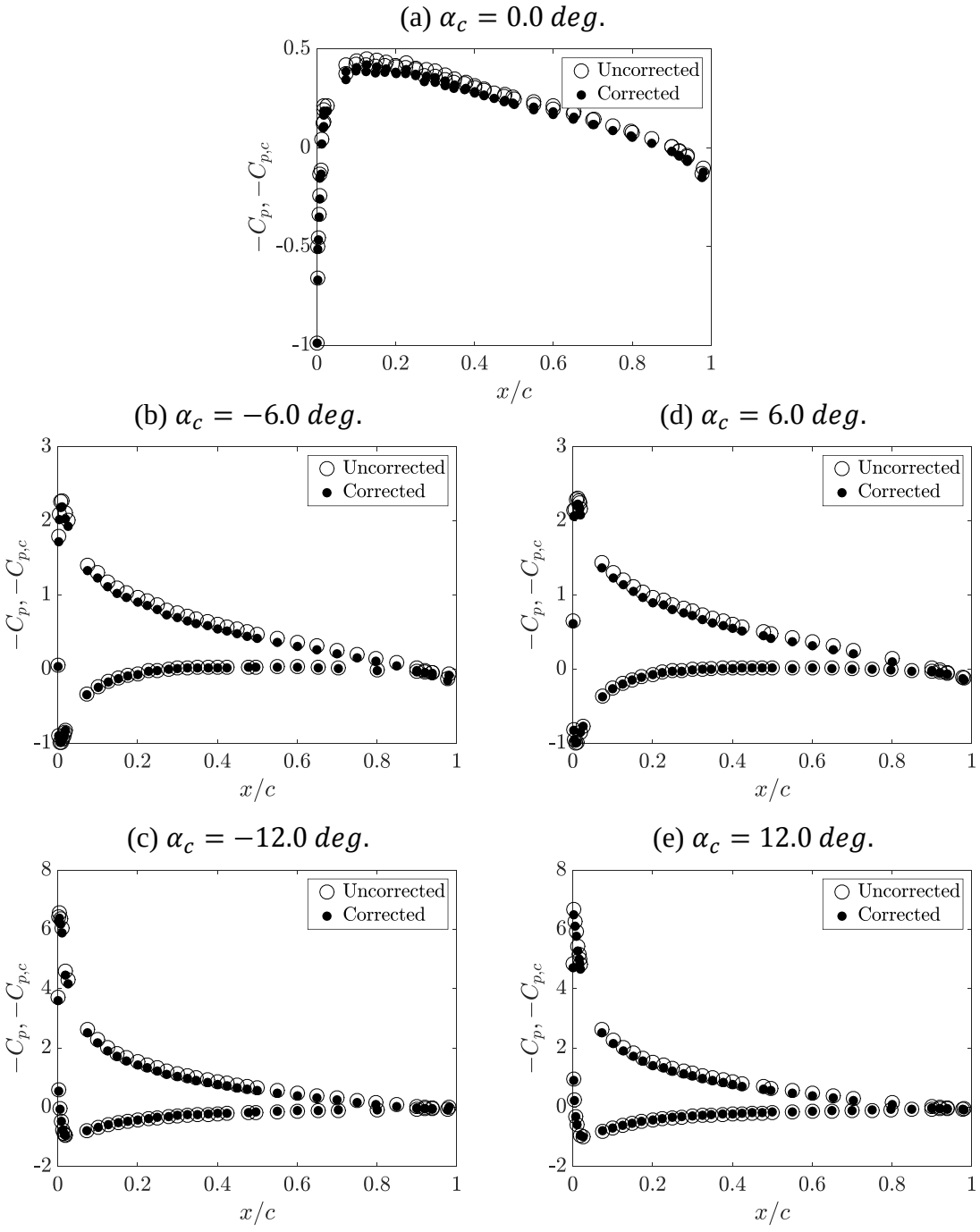

Figure C.17: Airfoil $-C_p$ vs. x/c for Run 1-4 of Table 3.3. Angles of attack have been offset by 0.14 degrees in the positive direction to align zero-lift with the origin. Data have been interpolated to the nominal angles reported.

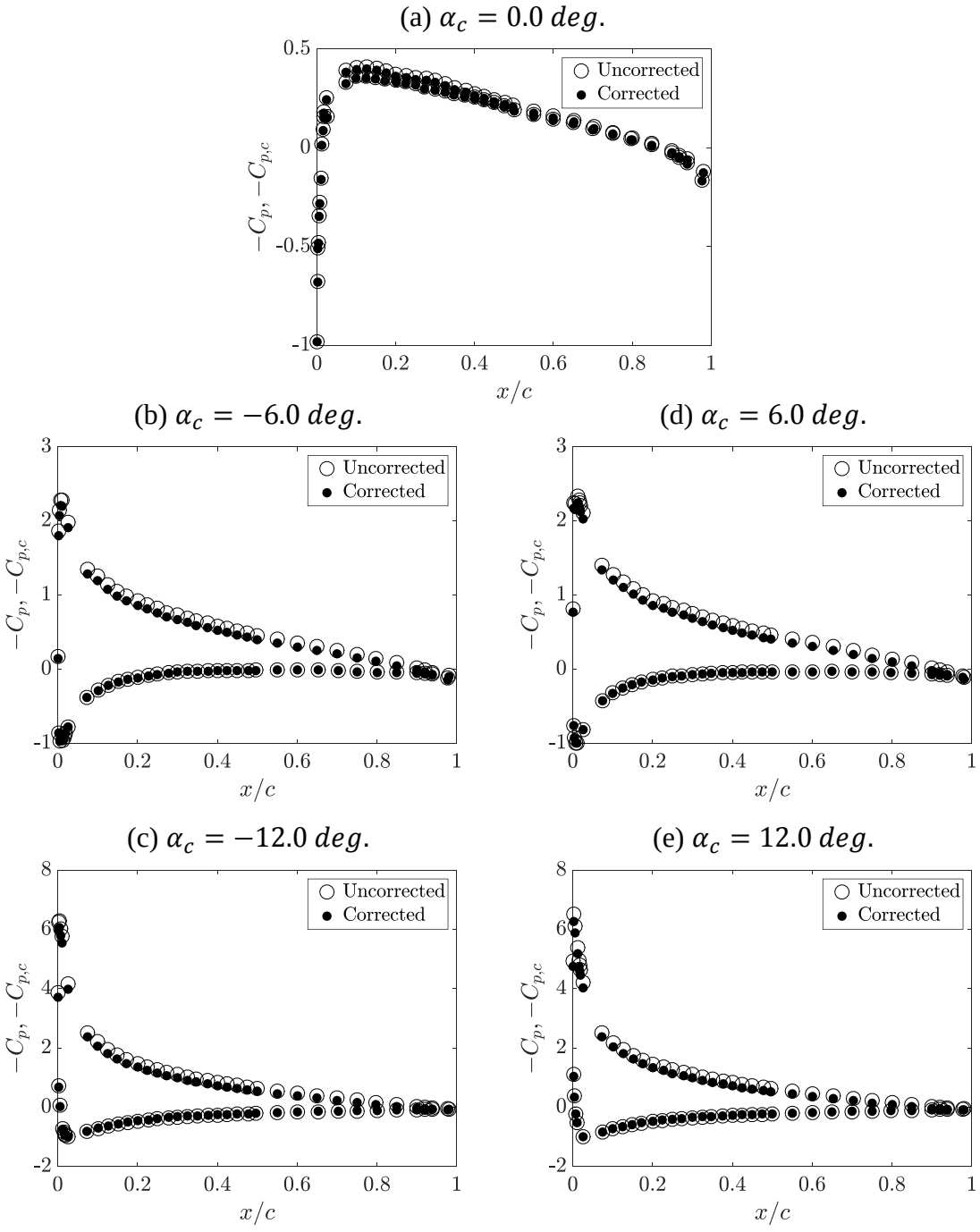

Figure C.18: Airfoil $-C_p$ vs. x/c for Run 2-1 of Table 3.3. Angles of attack have been offset by 0.24 degrees in the positive direction to align zero-lift with the origin. Data have been interpolated to the nominal angles reported.

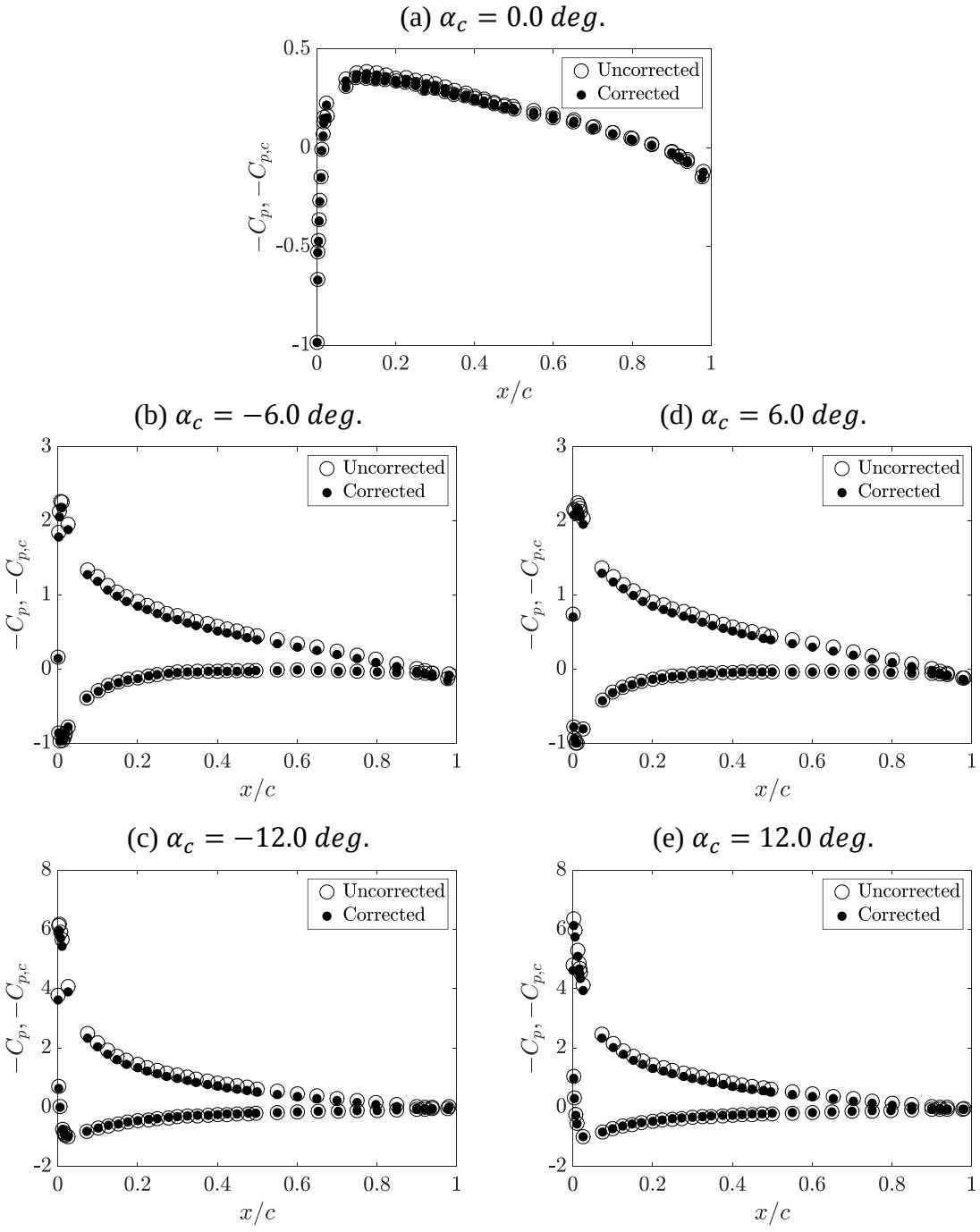

Figure C.19: Airfoil $-C_p$ vs. x/c for Run 2-2 of Table 3.3. Angles of attack have been offset by 0.14 degrees in the positive direction to align zero-lift with the origin. Data have been interpolated to the nominal angles reported.

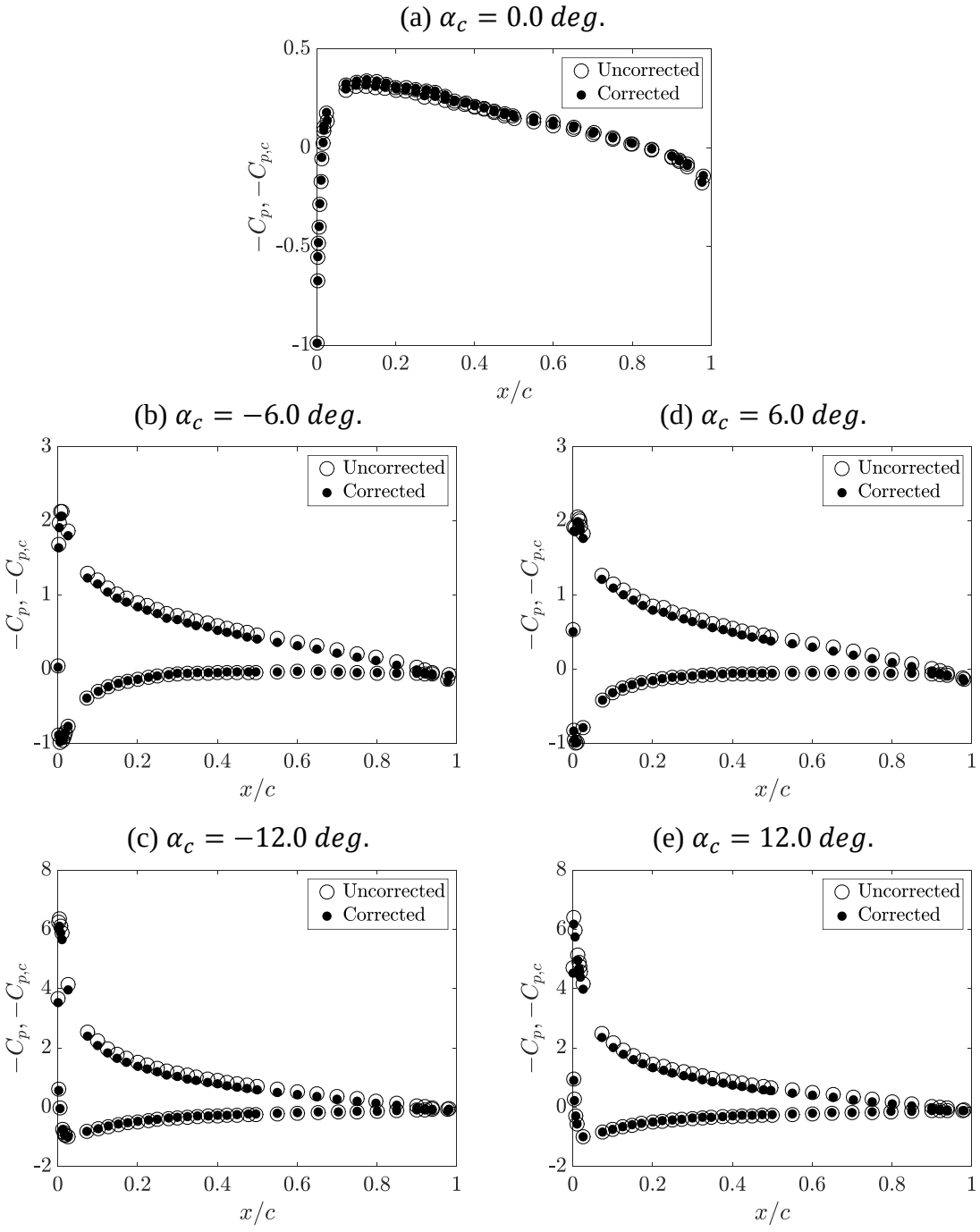

Figure C.20: Airfoil $-C_p$ vs. x/c for Run 2-3 of Table 3.3. Angles of attack have been offset by 0.15 degrees in the positive direction to align zero-lift with the origin. Data have been interpolated to the nominal angles reported.

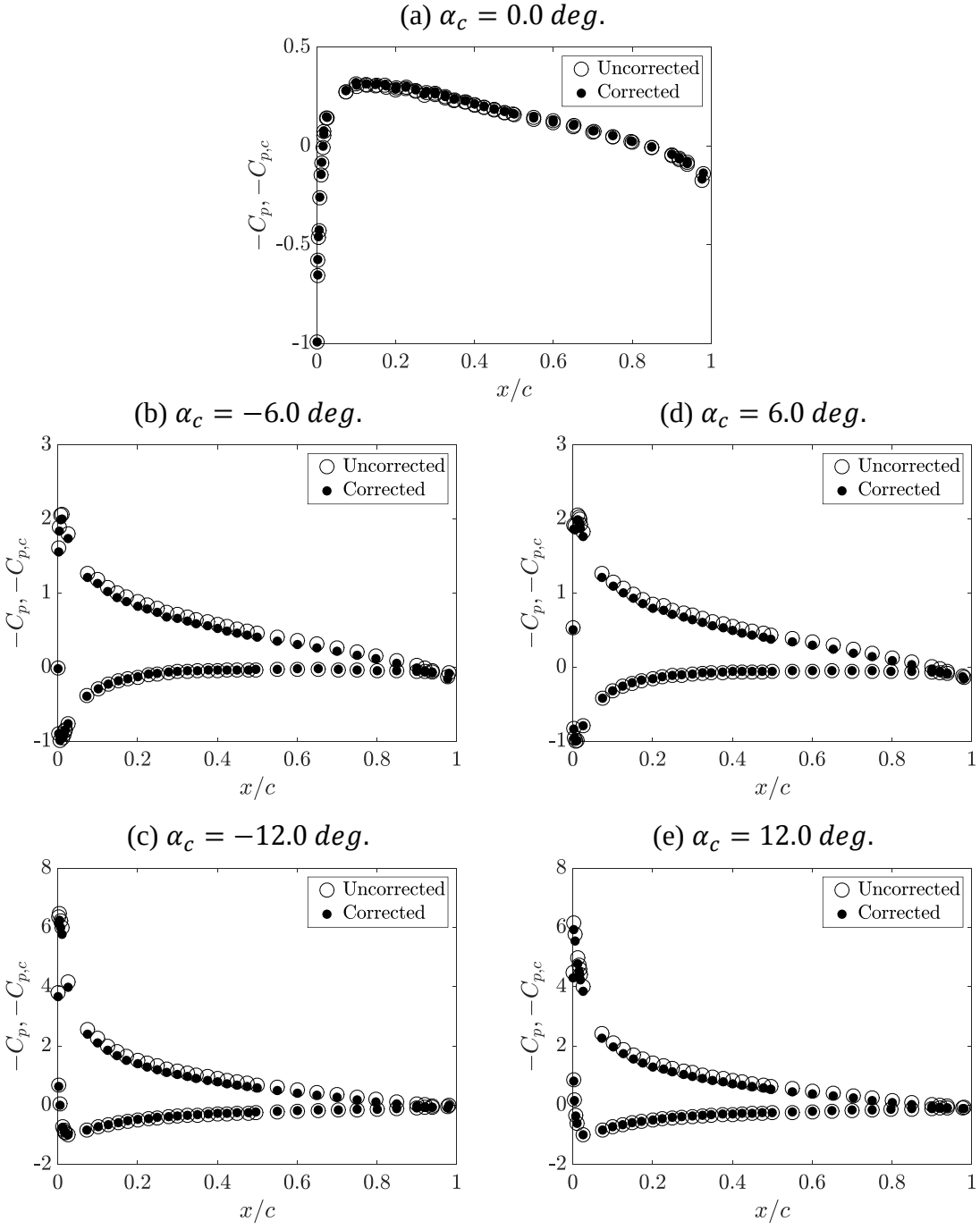

Figure C.21: Airfoil $-C_p$ vs. x/c for Run 2-4 of Table 3.3. Angles of attack have been offset by 0.03 degrees in the positive direction to align zero-lift with the origin. Data have been interpolated to the nominal angles reported.

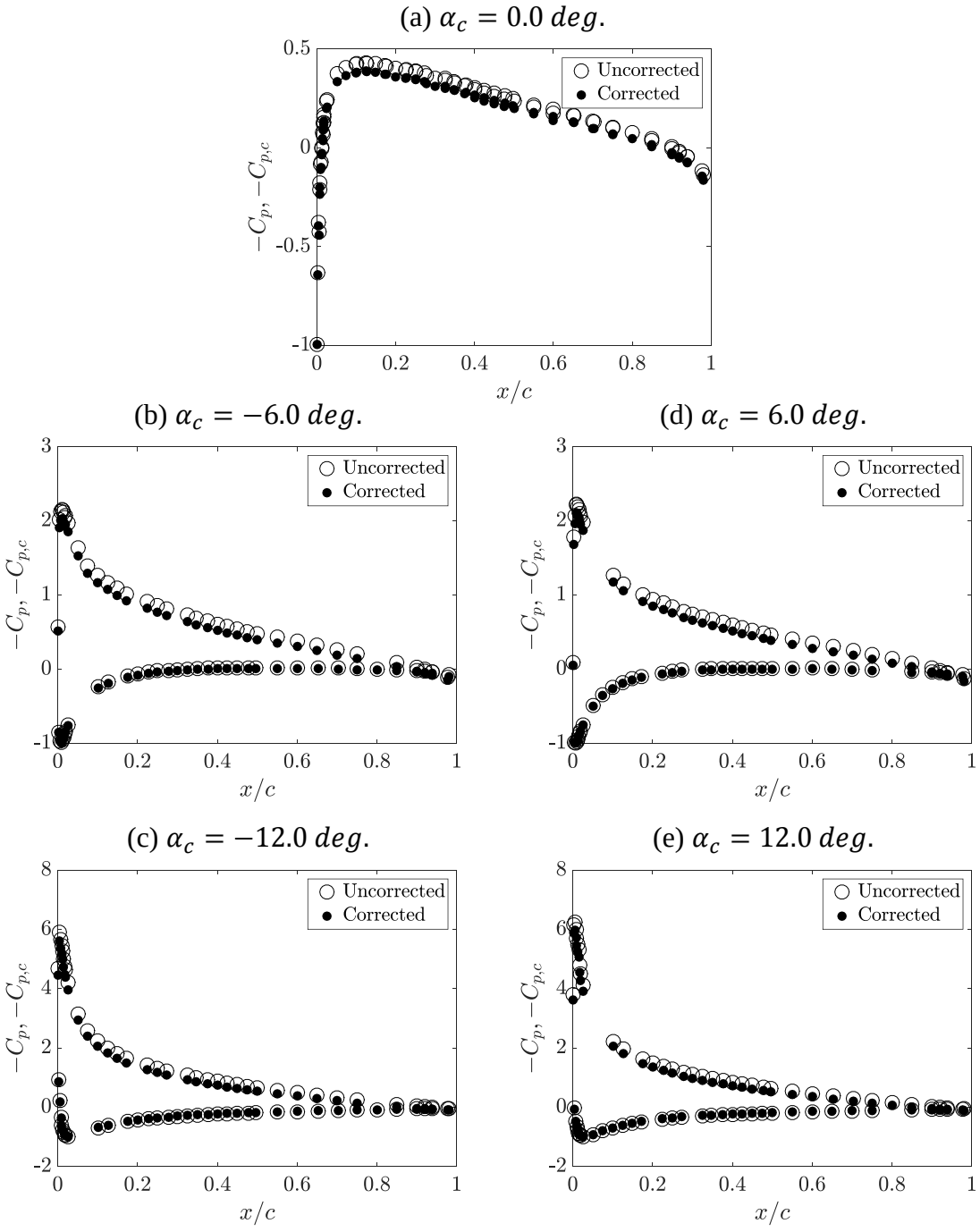

Figure C.22: Airfoil $-C_p$ vs. x/c for Run 3-1 of Table 3.3. Angles of attack have been offset by 0.01 degrees in the negative direction to align zero-lift with the origin. Data have been interpolated to the nominal angles reported.

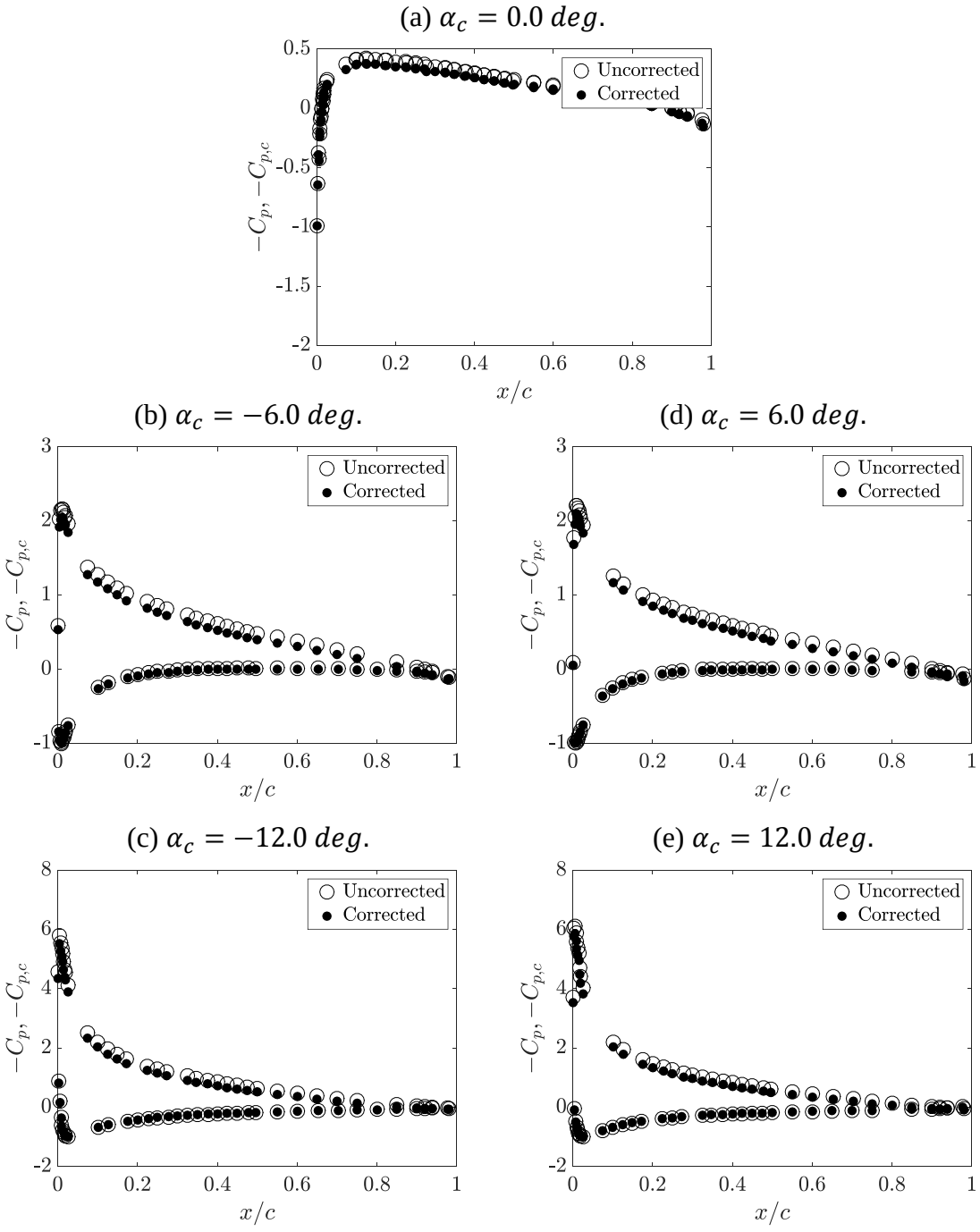

Figure C.23: Airfoil $-C_p$ vs. x/c for Run 3-2 of Table 3.3. Angles of attack have been offset by 0.05 degrees in the negative direction to align zero-lift with the origin. Data have been interpolated to the nominal angles reported.

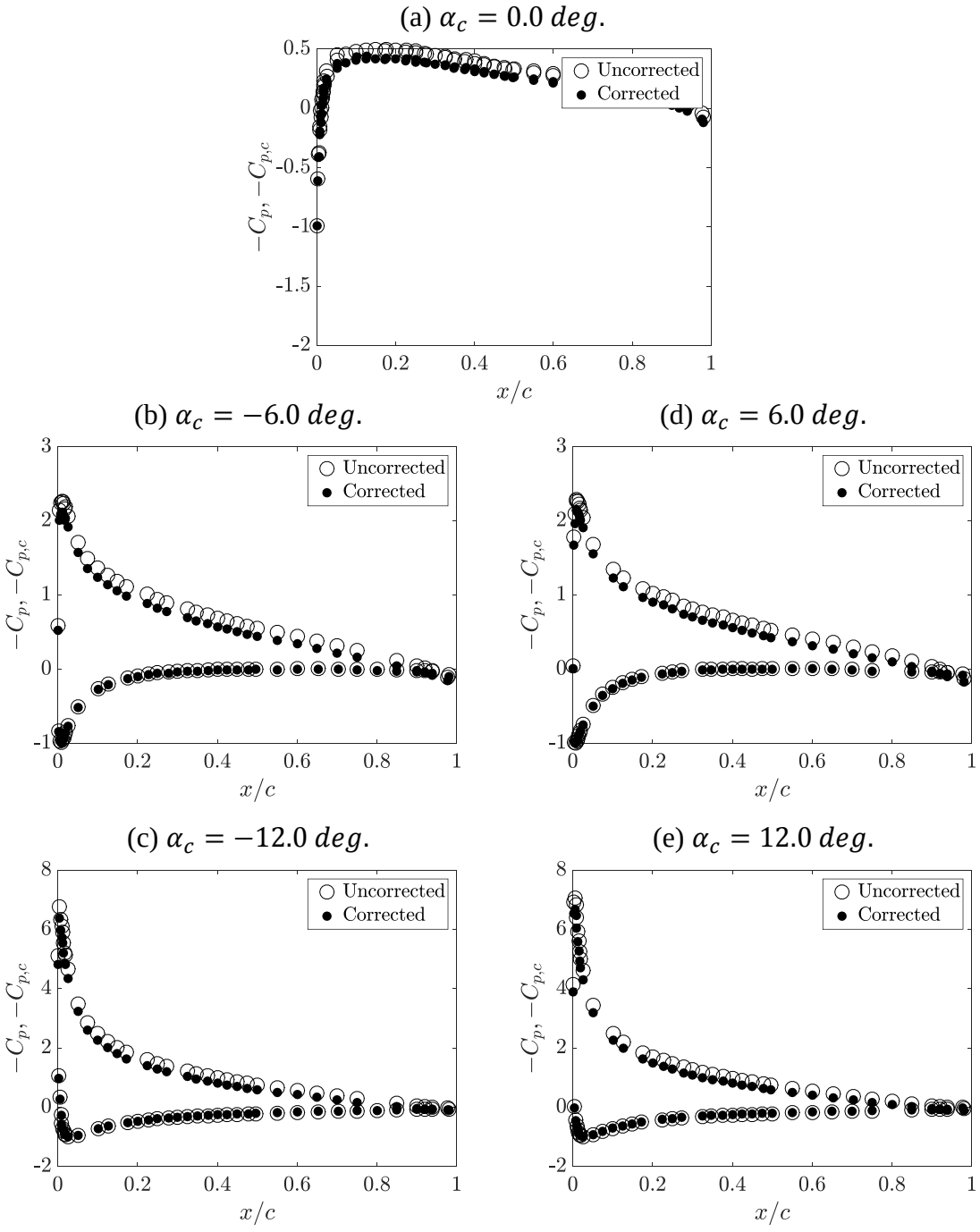

Figure C.24: Airfoil $-C_p$ vs. x/c for Run 3-3 of Table 3.3. Angles of attack have been offset by 0.05 degrees in the positive direction to align zero-lift with the origin. Data have been interpolated to the nominal angles reported.

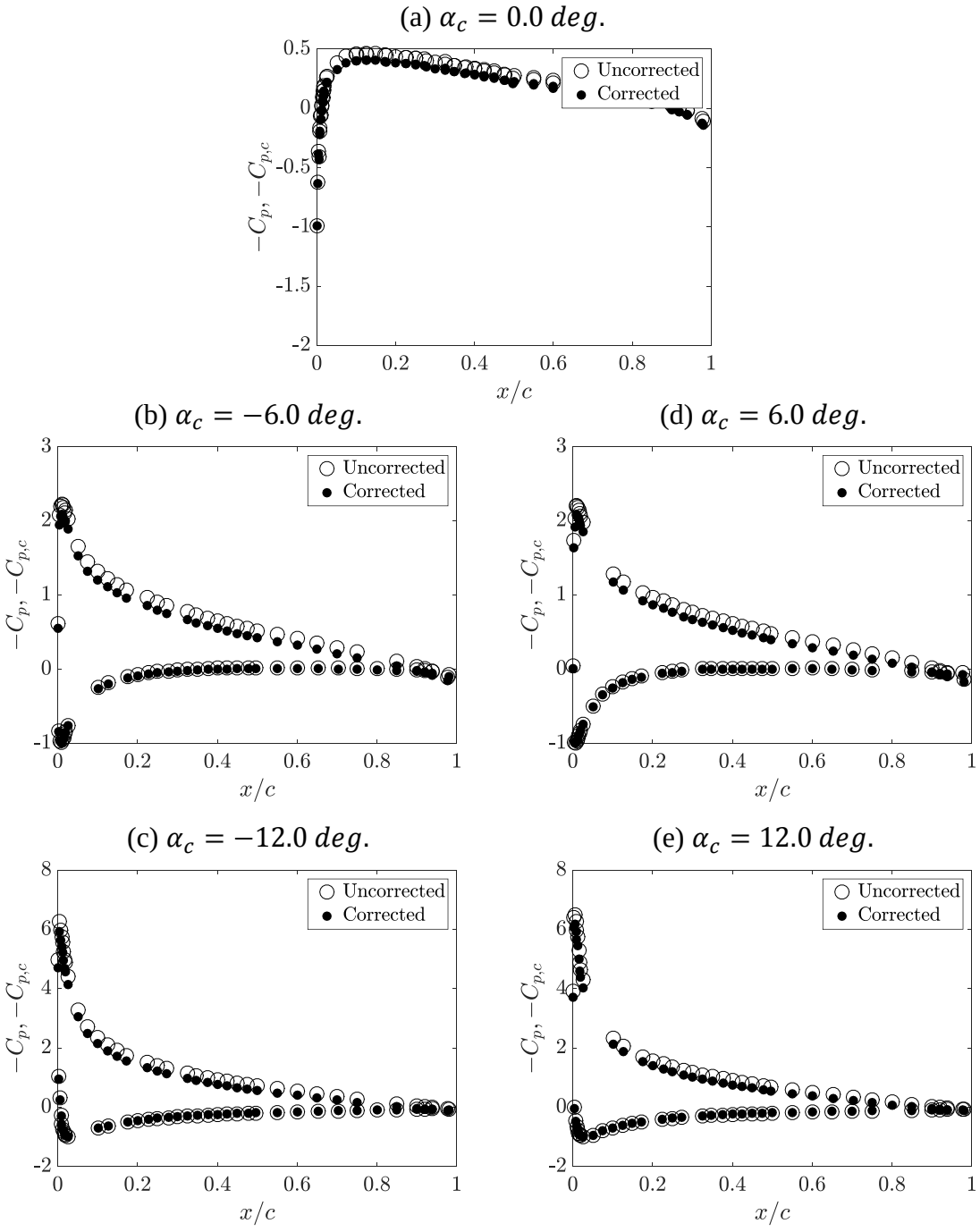

Figure C.25: Airfoil $-C_p$ vs. x/c for Run 3-5 of Table 3.3. Angles of attack have been offset by 0.04 degrees in the negative direction to align zero-lift with the origin. Data have been interpolated to the nominal angles reported.

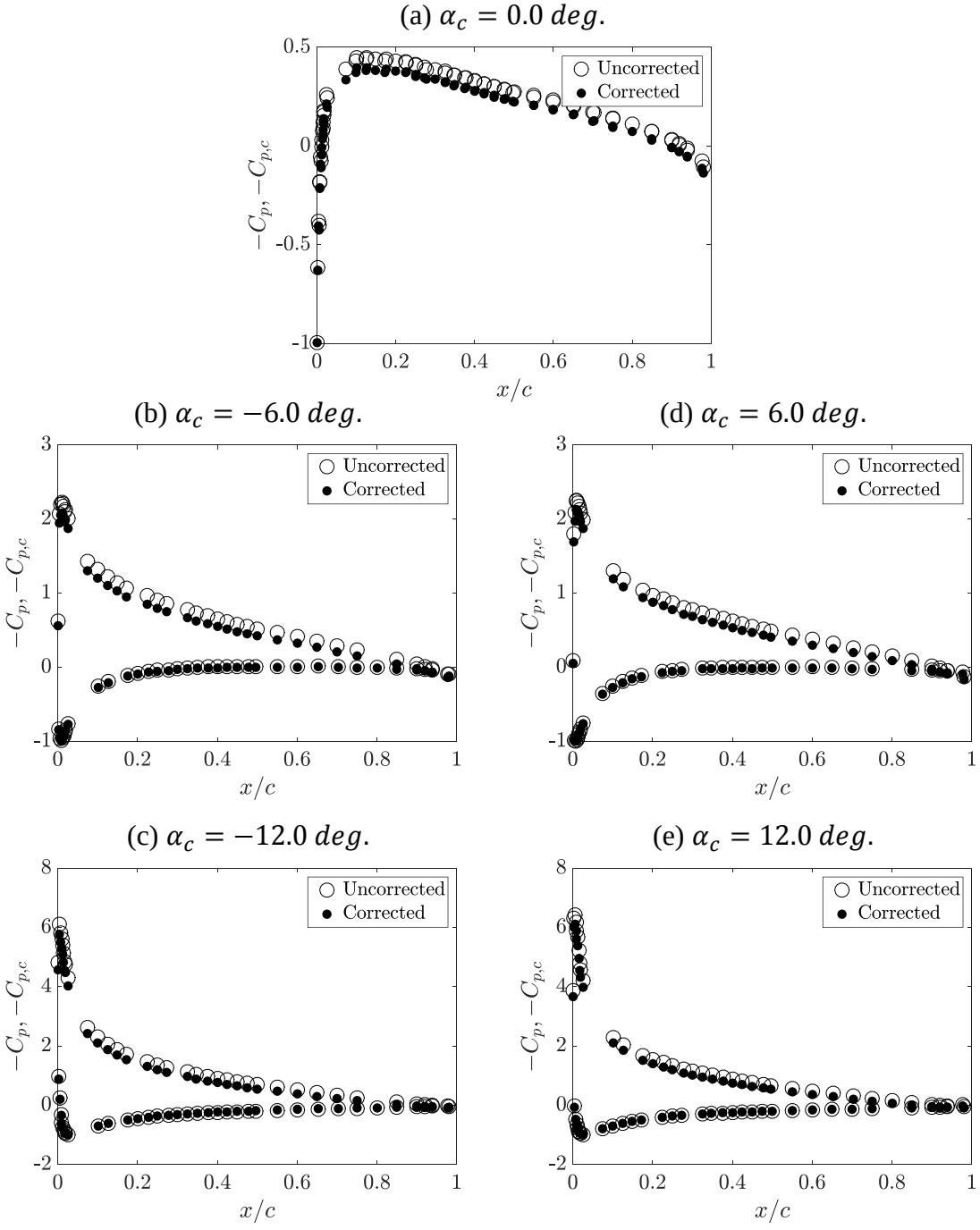

Figure C.26: Airfoil $-C_p$ vs. x/c for Run 3-6 of Table 3.3. Angles of attack have been offset by 0.52 degrees in the negative direction to align zero-lift with the origin. Data have been interpolated to the nominal angles reported.

C.3 Wall Pressure Coefficients

Wall pressure data measured by the physical wall taps described in Section 3.1.6 are given for all the runs in Campaigns 2 and 3. The pressure tap arrangements for the two campaigns are indicated in Figure 3.11. Only midspan data will be presented below. For each angle of attack sweep, the raw and empty-subtracted C_p's are plotted, the latter being equal to the raw C_p minus the C_p values measured in empty test section runs of the appropriate freestream velocity.

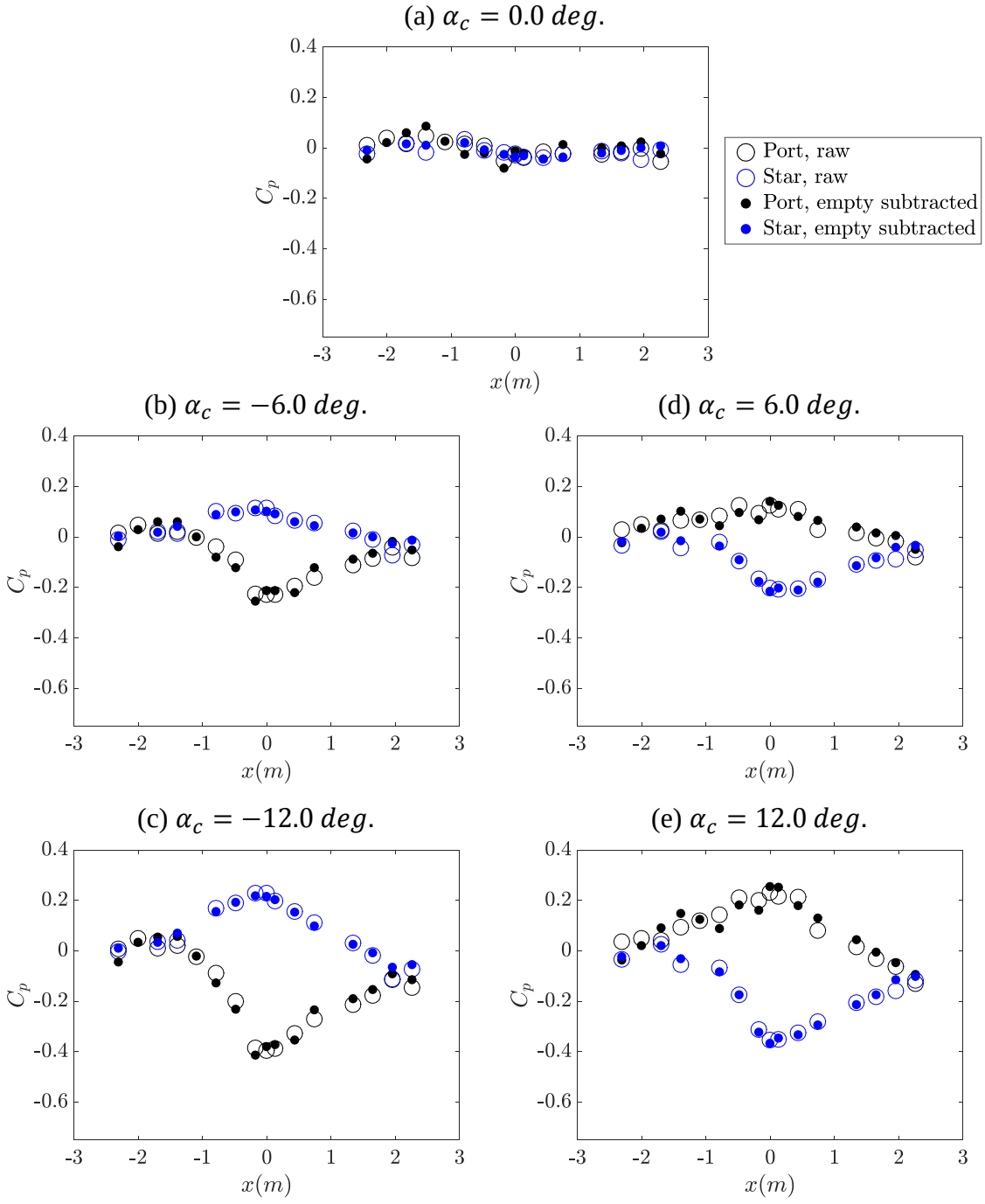

Figure C.27: Wall C_p at midspan vs. streamwise location, x, for Run 2-1 of Table 3.3. Angles of attack have been offset by 0.24 degrees in the positive direction to align zero-lift with the origin. Data have been interpolated to the nominal angles reported.

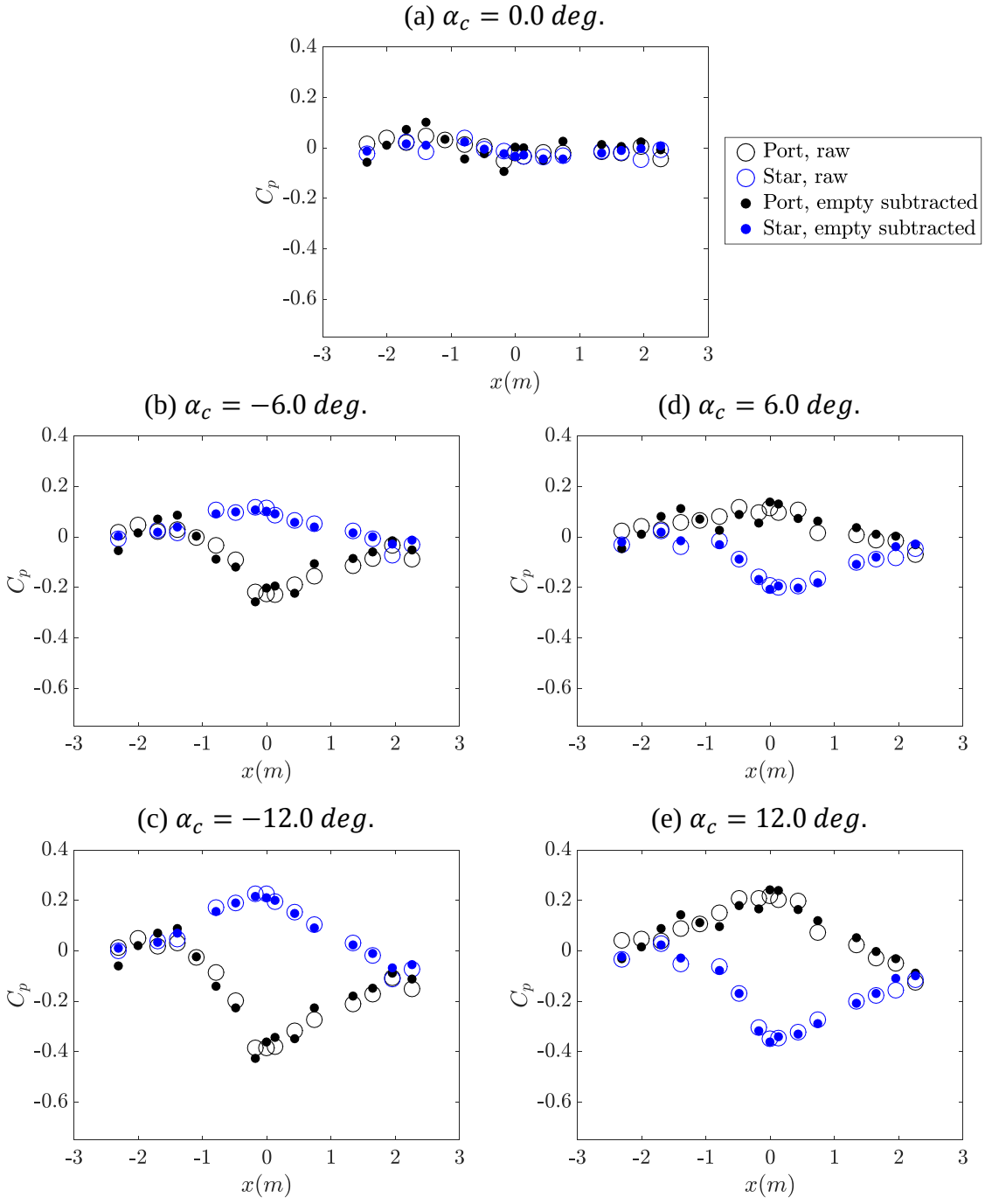

Figure C.28: Wall C_p at midspan vs. streamwise location, x, for Run 2-2 of Table 3.3. Angles of attack have been offset by 0.14 degrees in the positive direction to align zero-lift with the origin. Data have been interpolated to the nominal angles reported.

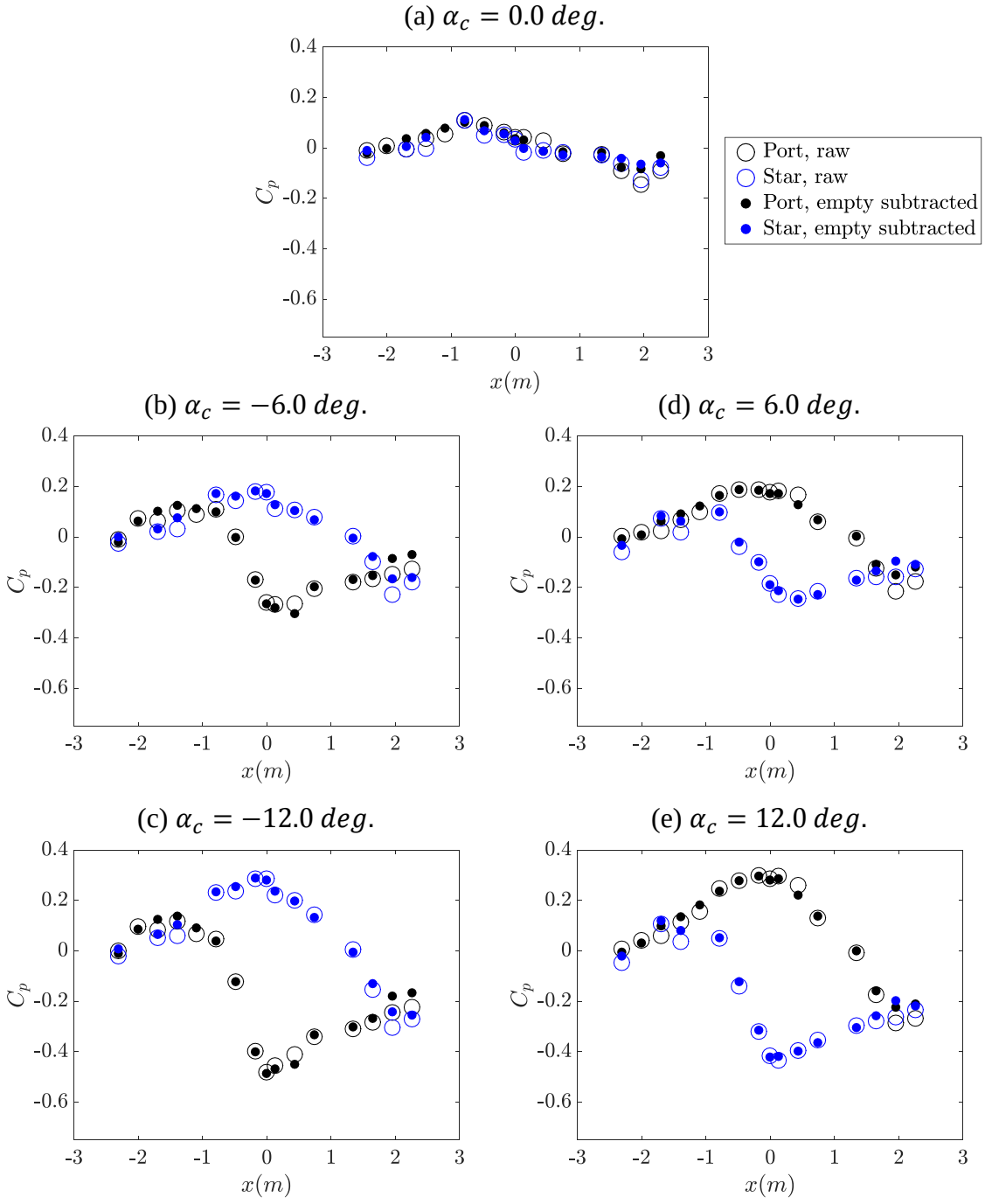

Figure C.29: Wall C_p at midspan vs. streamwise location, x, for Run 2-3 of Table 3.3. Angles of attack have been offset by 0.15 degrees in the positive direction to align zero-lift with the origin. Data have been interpolated to the nominal angles reported.

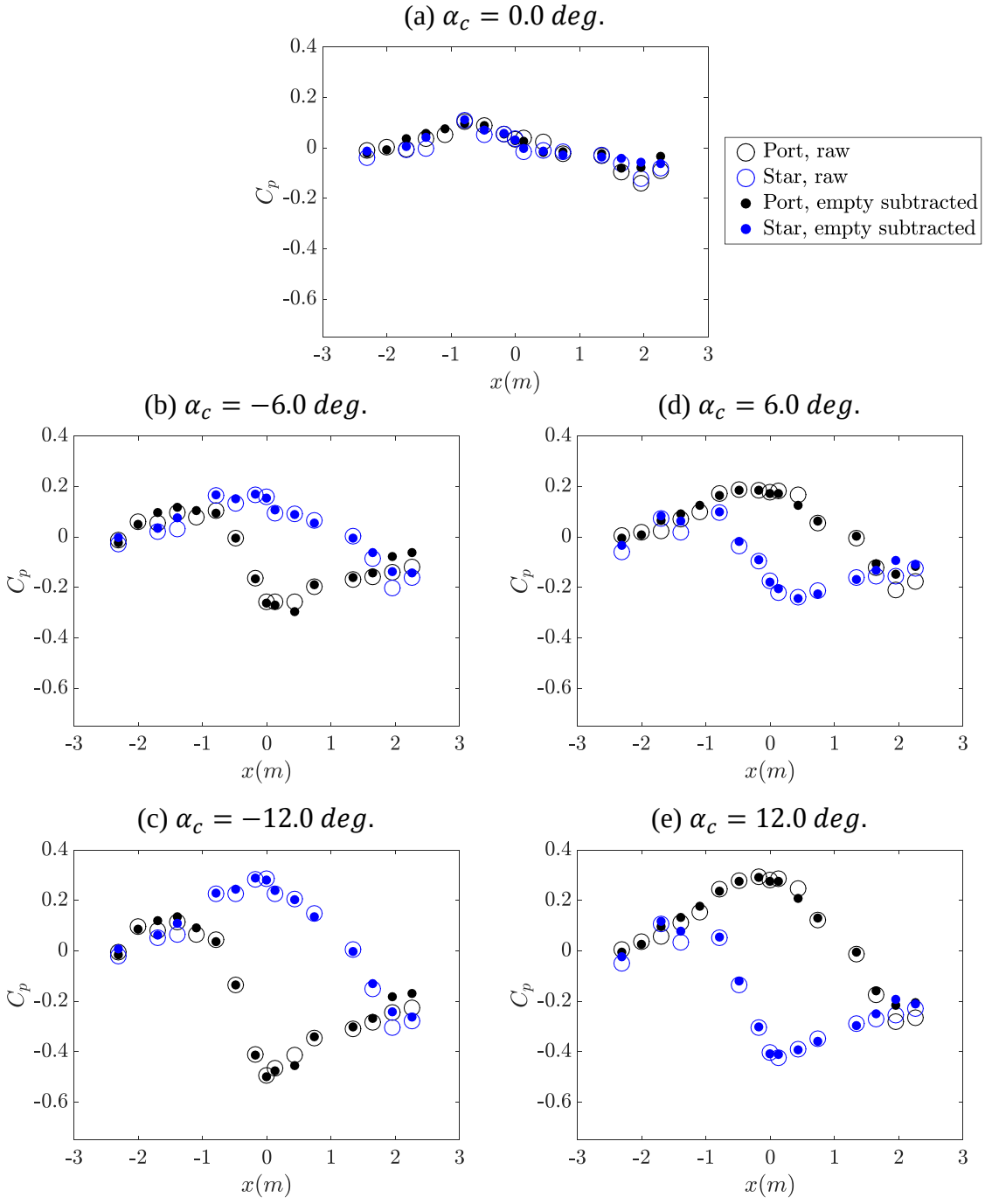

Figure C.30: Wall C_p at midspan vs. streamwise location, x, for Run 2-4 of Table 3.3. Angles of attack have been offset by 0.03 degrees in the positive direction to align zero-lift with the origin. Data have been interpolated to the nominal angles reported.

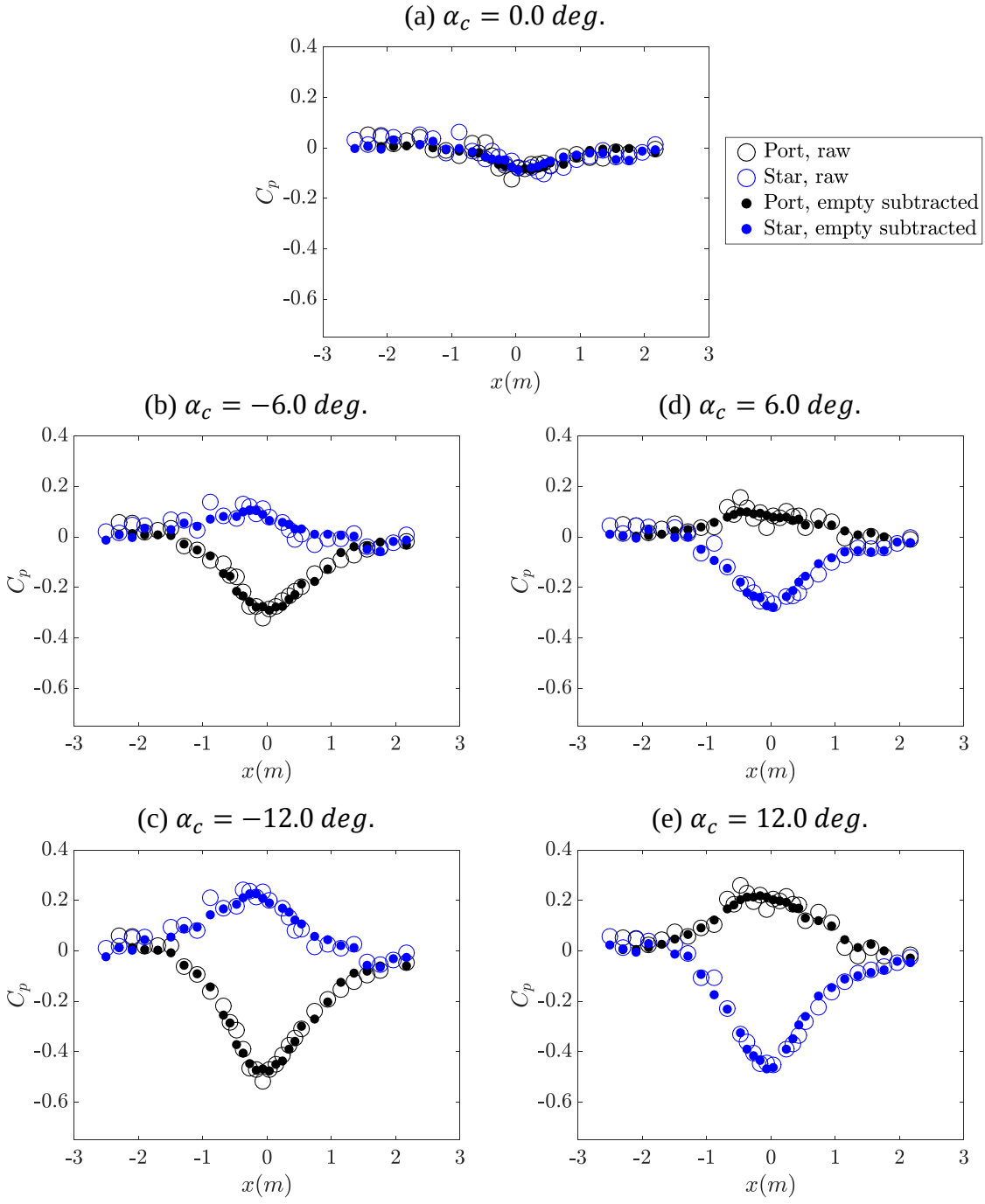

Figure C.31: Wall C_p at midspan vs. streamwise location, x, for Run 3-1 of Table 3.3. Angles of attack have been offset by 0.01 degrees in the negative direction to align zero-lift with the origin. Data have been interpolated to the nominal angles reported.

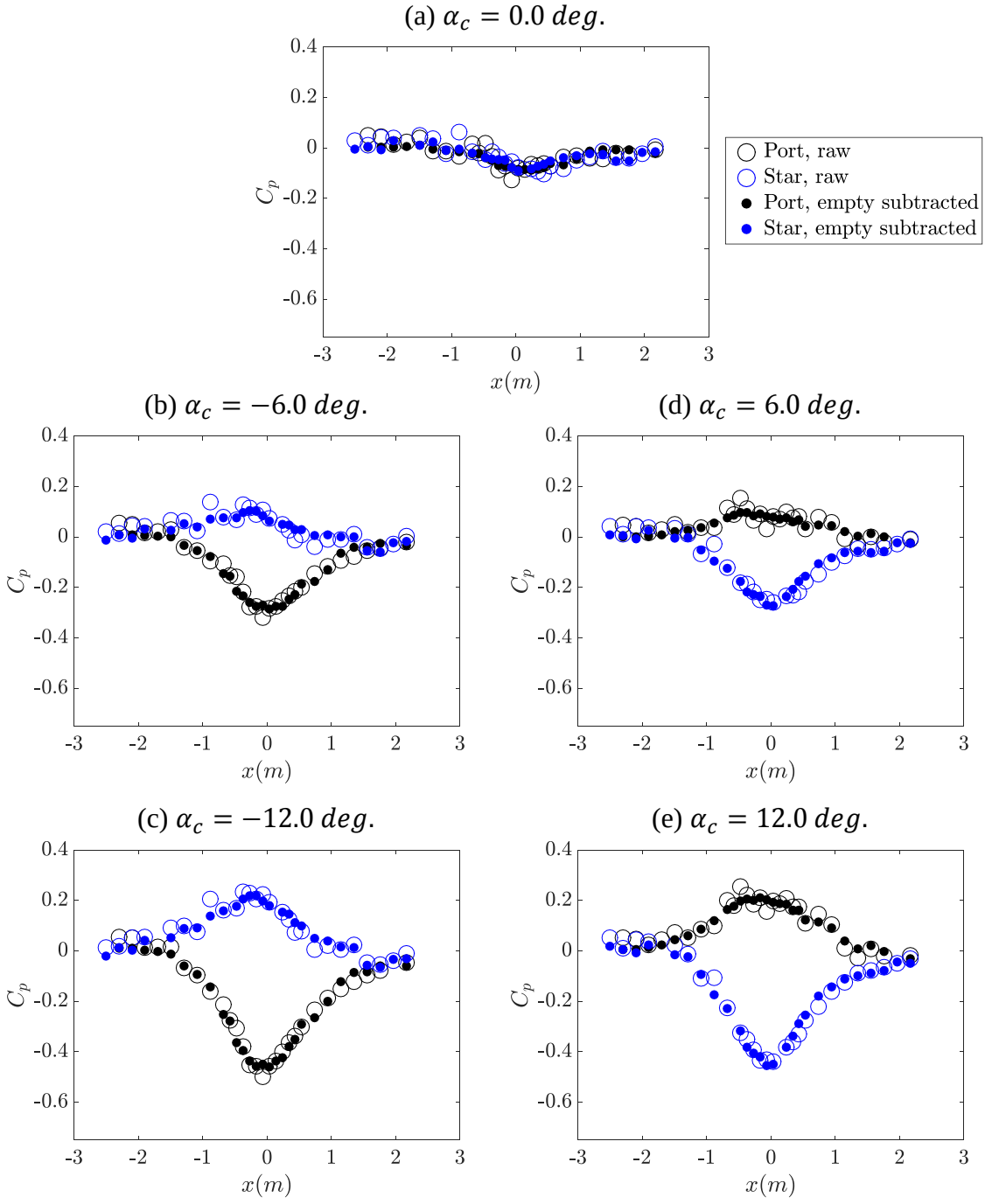

Figure C.32: Wall C_p at midspan vs. streamwise location, x, for Run 3-2 of Table 3.3. Angles of attack have been offset by 0.05 degrees in the negative direction to align zero-lift with the origin. Data have been interpolated to the nominal angles reported.

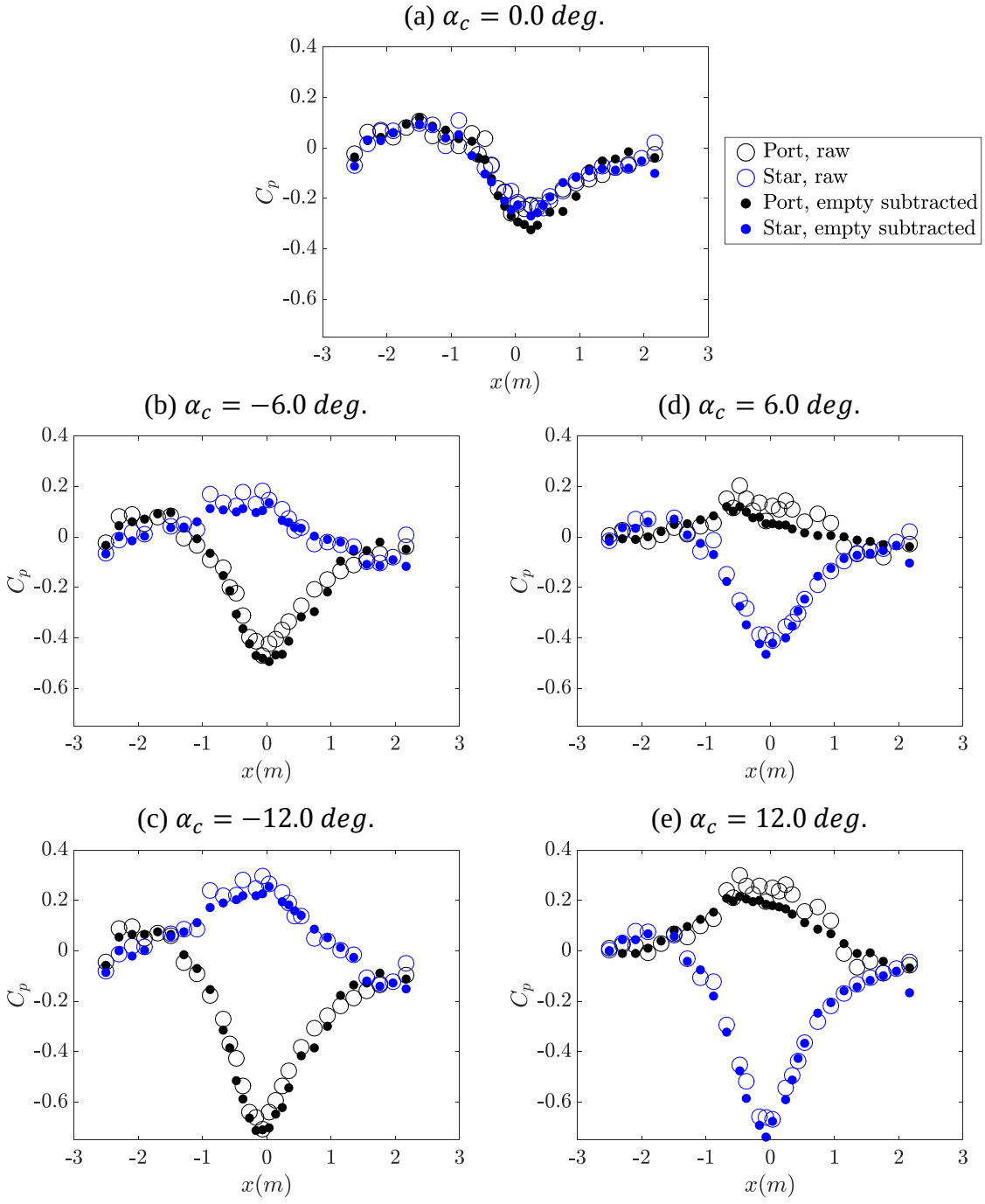

Figure C.33: Wall C_p at midspan vs. streamwise location, x, for Run 3-3 of Table 3.3. Angles of attack have been offset by 0.05 degrees in the positive direction to align zero-lift with the origin. Data have been interpolated to the nominal angles reported.

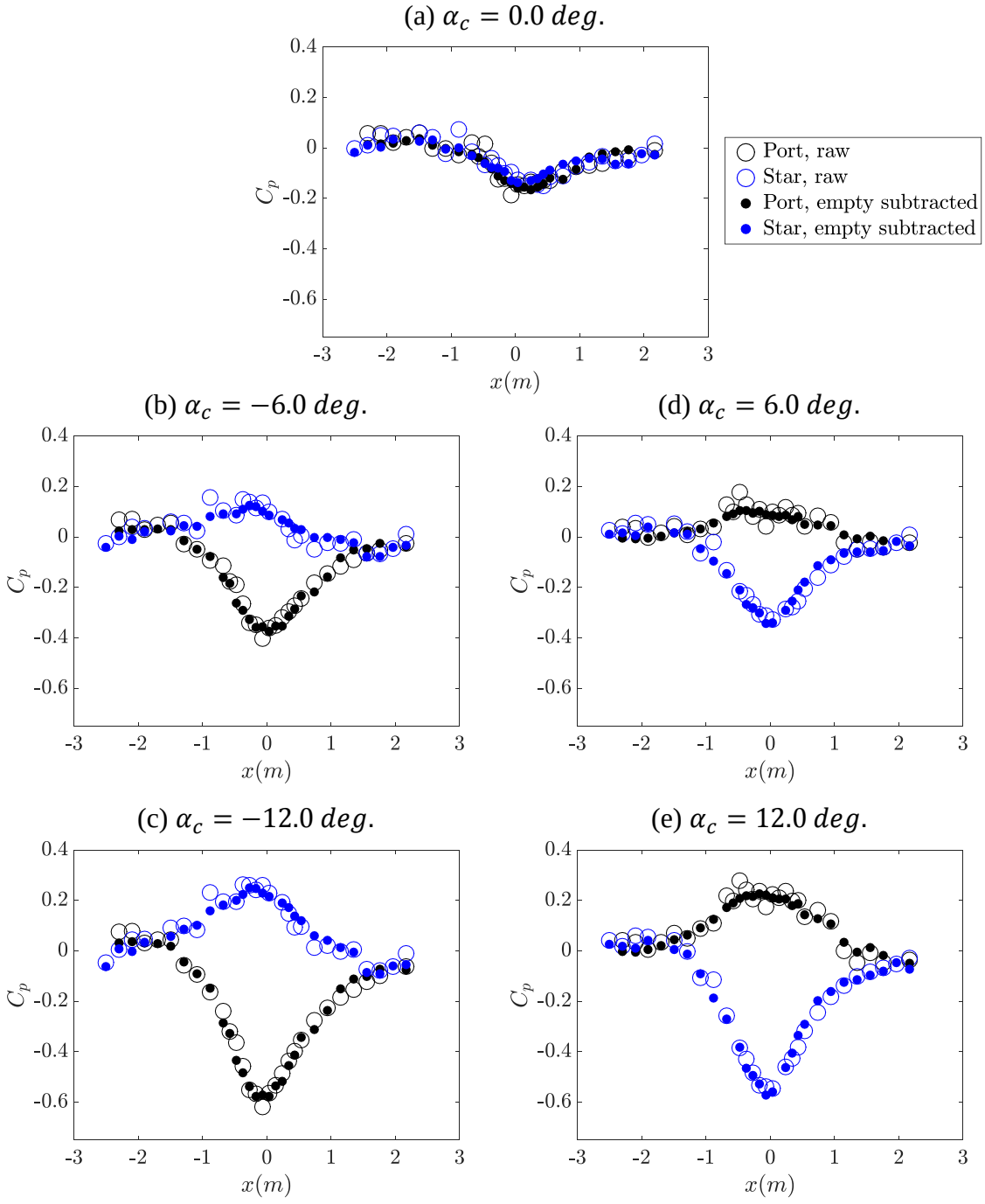

Figure C.34: Wall C_p at midspan vs. streamwise location, x, for Run 3-5 of Table 3.3. Angles of attack have been offset by 0.04 degrees in the negative direction to align zero-lift with the origin. Data have been interpolated to the nominal angles reported.

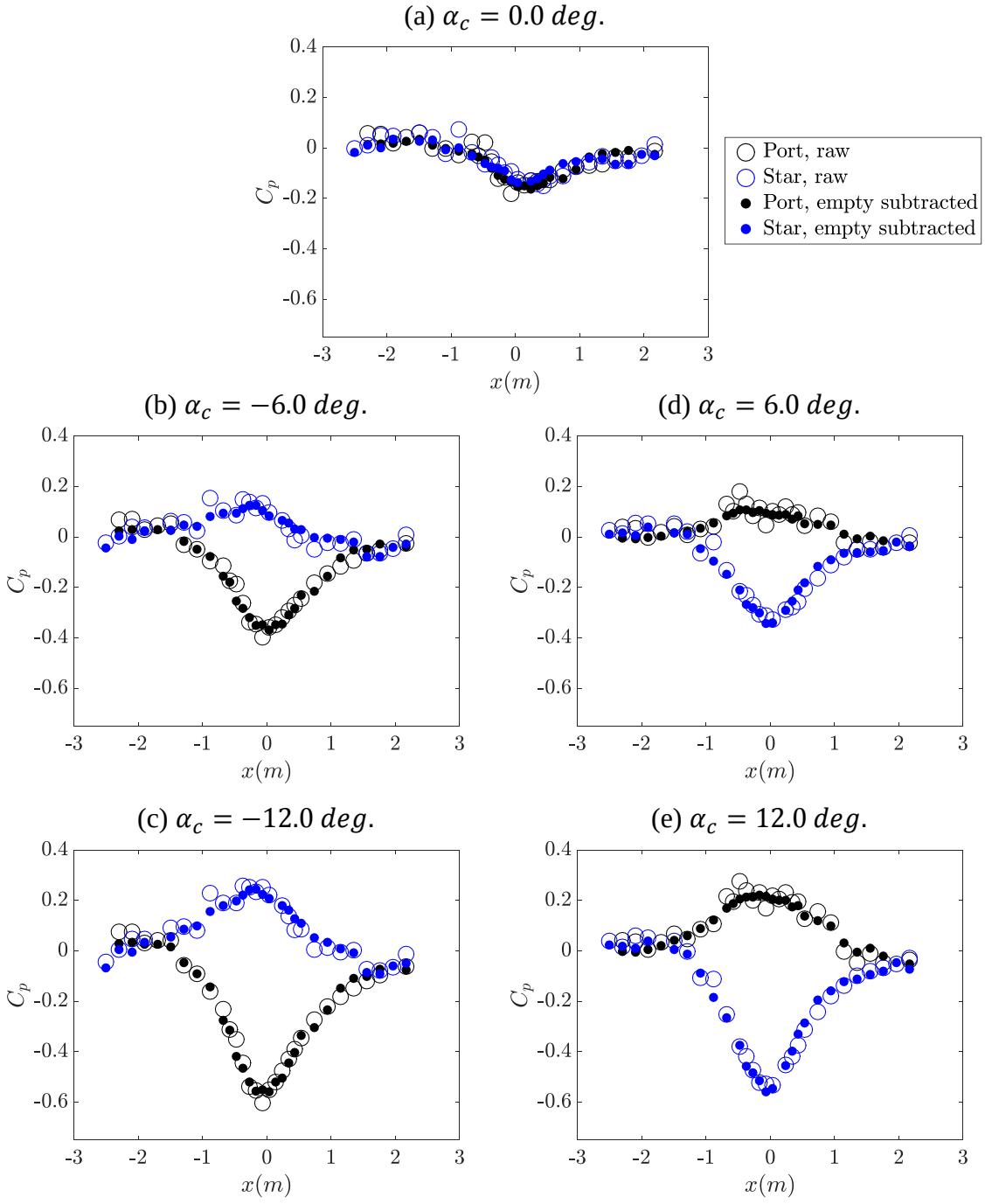

Figure C.35: Wall C_p at midspan vs. streamwise location, x, for Run 3-6 of Table 3.3. Angles of attack have been offset by 0.52 degrees in the negative direction to align zero-lift with the origin. Data have been interpolated to the nominal angles reported.

C.4 Wall Deformation

Below are given the raw out-of-of-plane deformations measured by the camera system described in Section 3.1.7. The midspan plane at $y = 0$ is an approximate plane of symmetry as expected for two-dimensional airfoil testing. Here is included only data from the Campaign 3 runs of Table 3.3; the preliminary results from Campaign 2 are not presented.

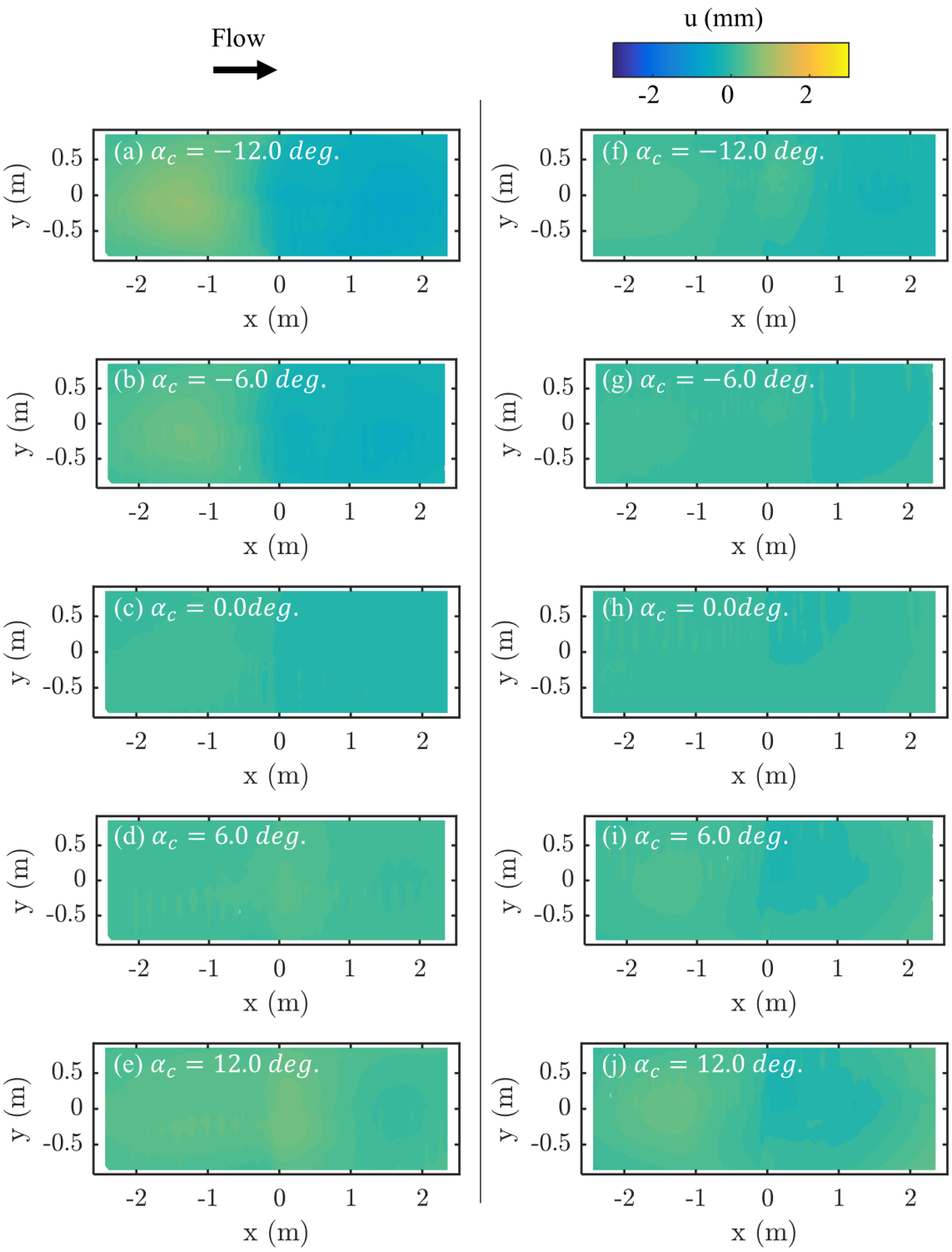

Figure C.36: Wall deformation in the u-component vs. location over the wall for Run 3-1 of Table 3.3. The port wall is shown in (a)-(e) and the starboard wall is shown in (f)-(j). Angles of attack have been offset by 0.01 degrees in the negative direction to align zero-lift with the origin. Data have been interpolated to the nominal angles reported.

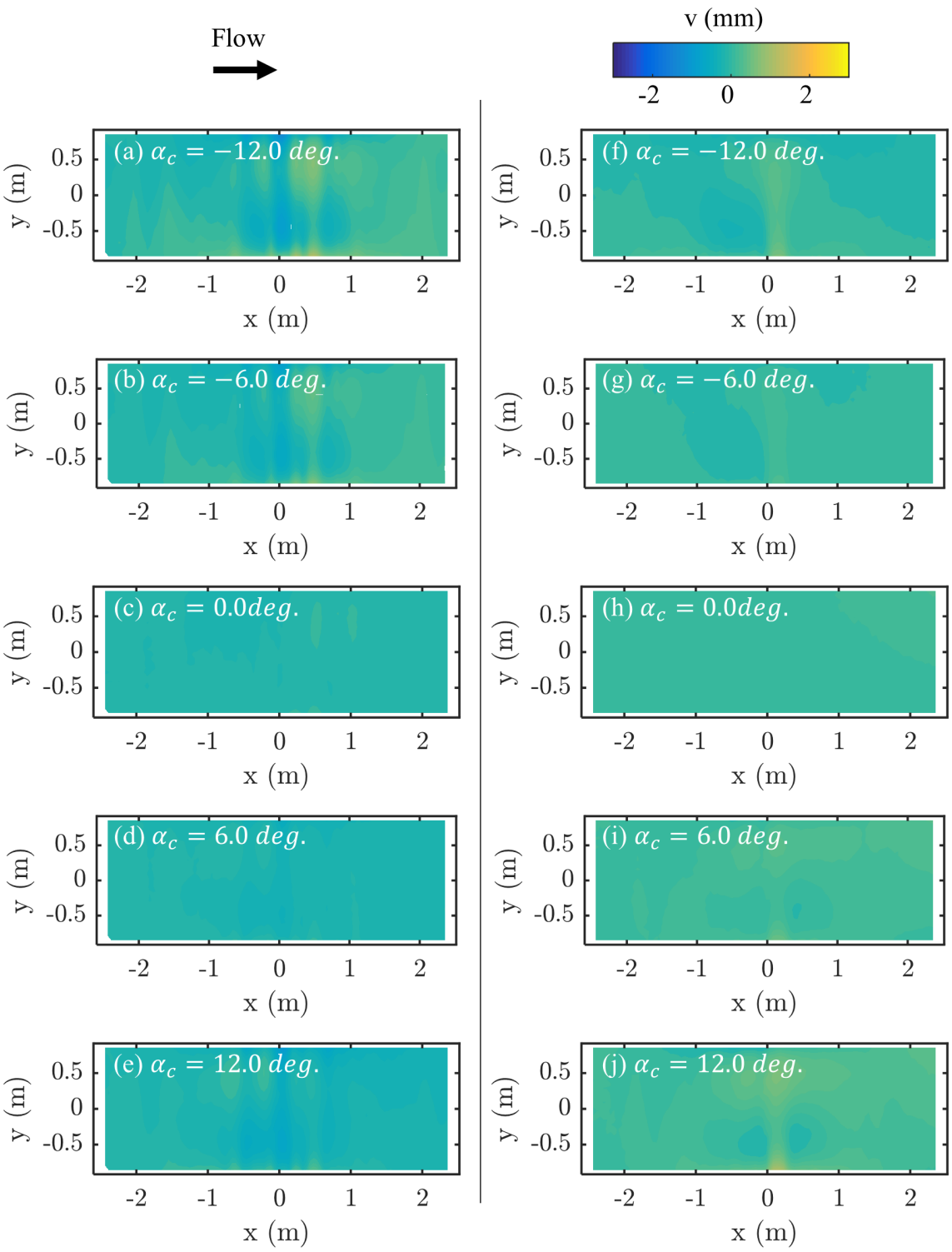

Figure C.37: Wall deformation in the v-component vs. location over the wall for Run 3-1 of Table 3.3. The port wall is shown in (a)-(e) and the starboard wall is shown in (f)-(j). Angles of attack have been offset by 0.01 degrees in the negative direction to align zero-lift with the origin. Data have been interpolated to the nominal angles reported.

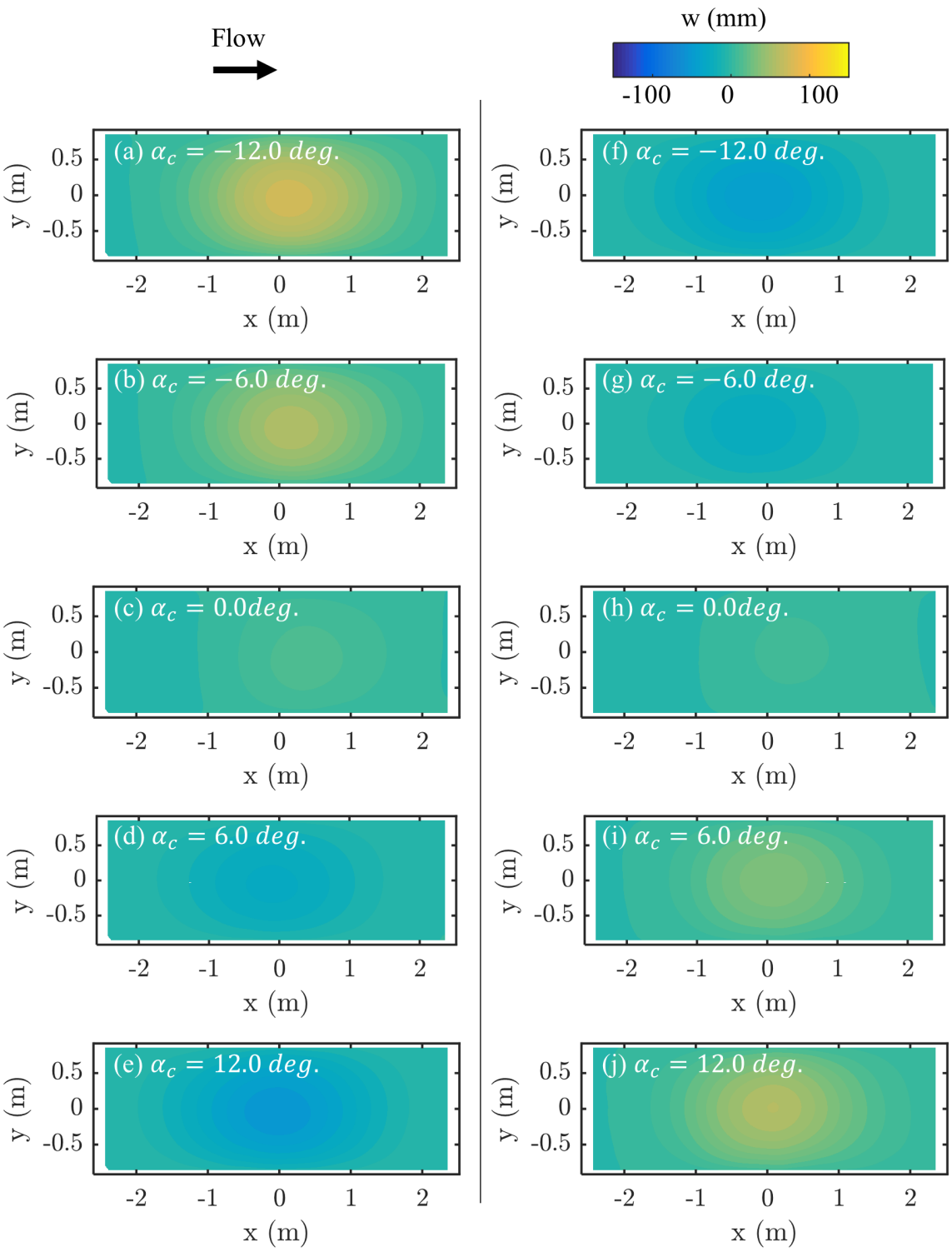

Figure C.38: Wall deformation in the w-component vs. location over the wall for Run 3-1 of Table 3.3. The port wall is shown in (a)-(e) and the starboard wall is shown in (f)-(j). Angles of attack have been offset by 0.01 degrees in the negative direction to align zero-lift with the origin. Data have been interpolated to the nominal angles reported.

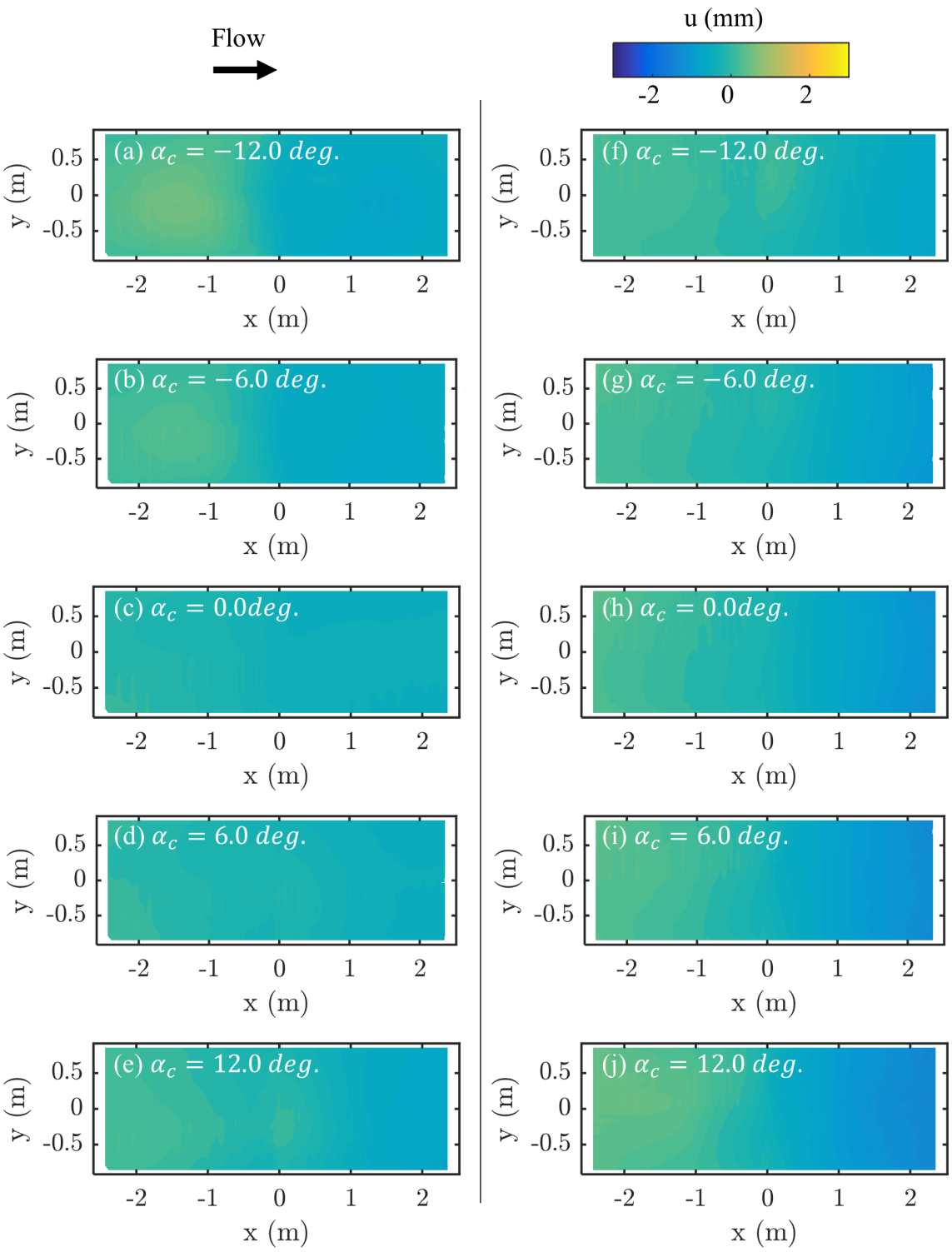

Figure C.39: Wall deformation in the u-component vs. location over the wall for Run 3-2 of Table 3.3. The port wall is shown in (a)-(e) and the starboard wall is shown in (f)-(j). Angles of attack have been offset by 0.05 degrees in the negative direction to align zero-lift with the origin. Data have been interpolated to the nominal angles reported.

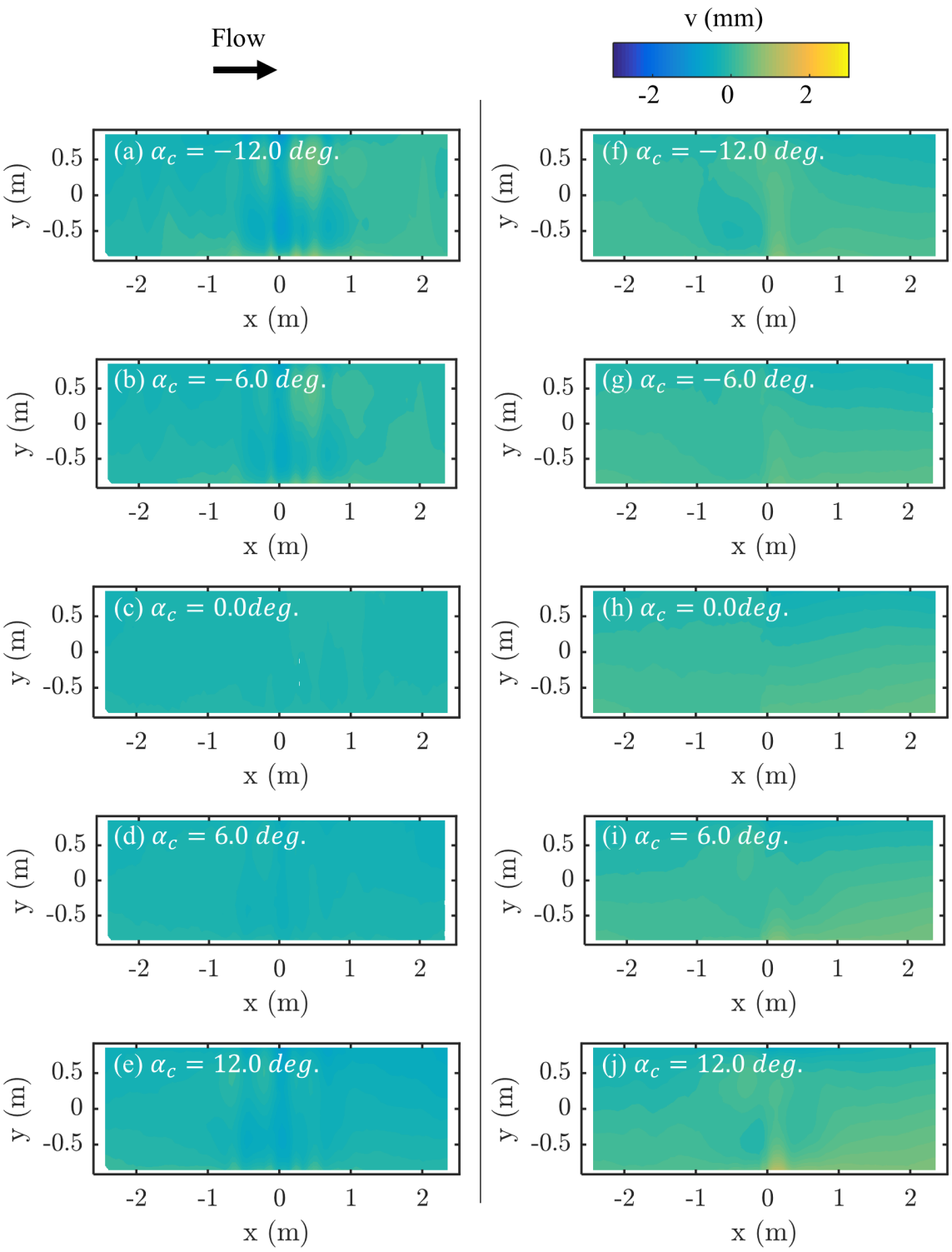

Figure C.40: Wall deformation in the v-component vs. location over the wall for Run 3-2 of Table 3.3. The port wall is shown in (a)-(e) and the starboard wall is shown in (f)-(j). Angles of attack have been offset by 0.05 degrees in the negative direction to align zero-lift with the origin. Data have been interpolated to the nominal angles reported.

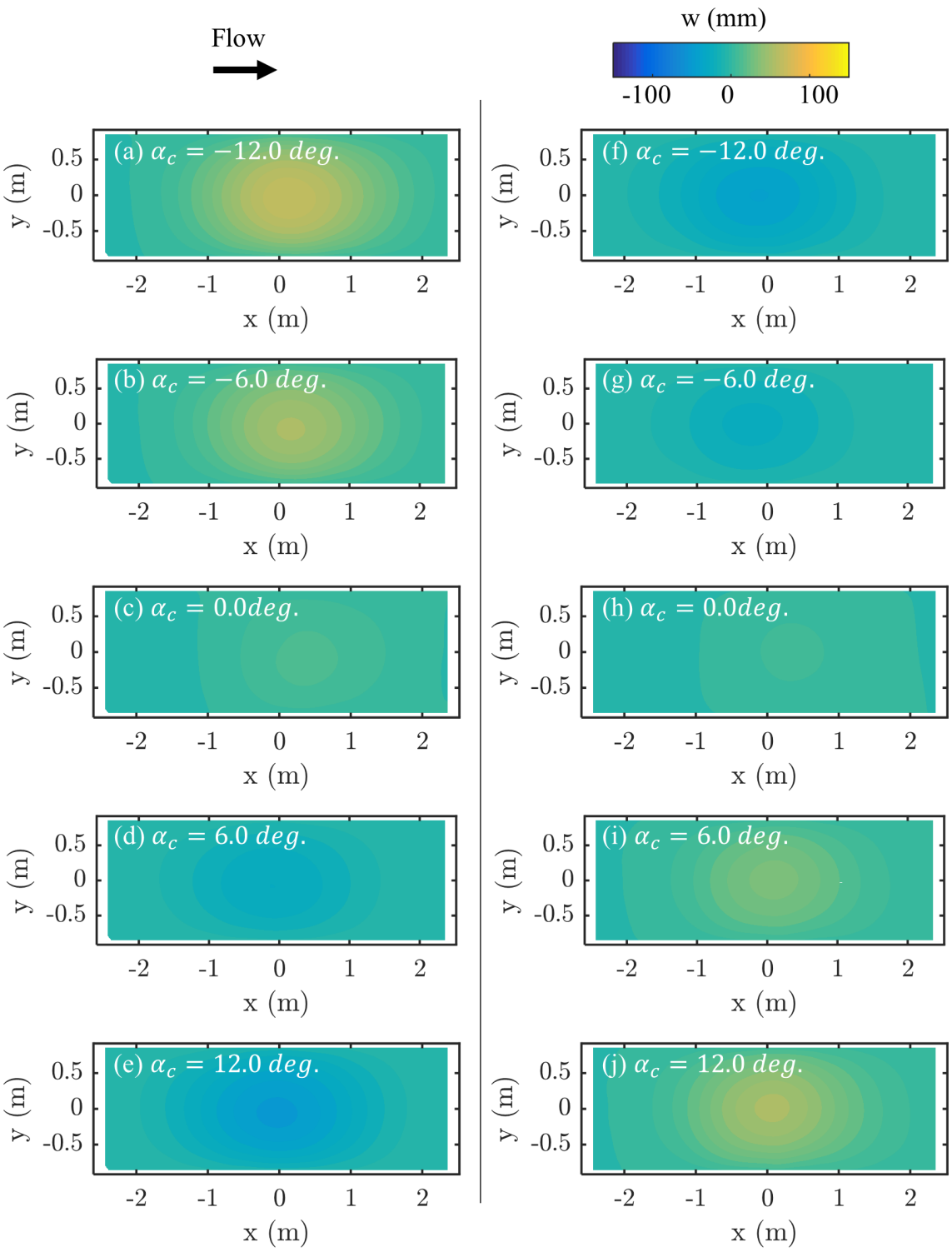

Figure C.41: Wall deformation in the w-component vs. location over the wall for Run 3-2 of Table 3.3. The port wall is shown in (a)-(e) and the starboard wall is shown in (f)-(j). Angles of attack have been offset by 0.05 degrees in the negative direction to align zero-lift with the origin. Data have been interpolated to the nominal angles reported.

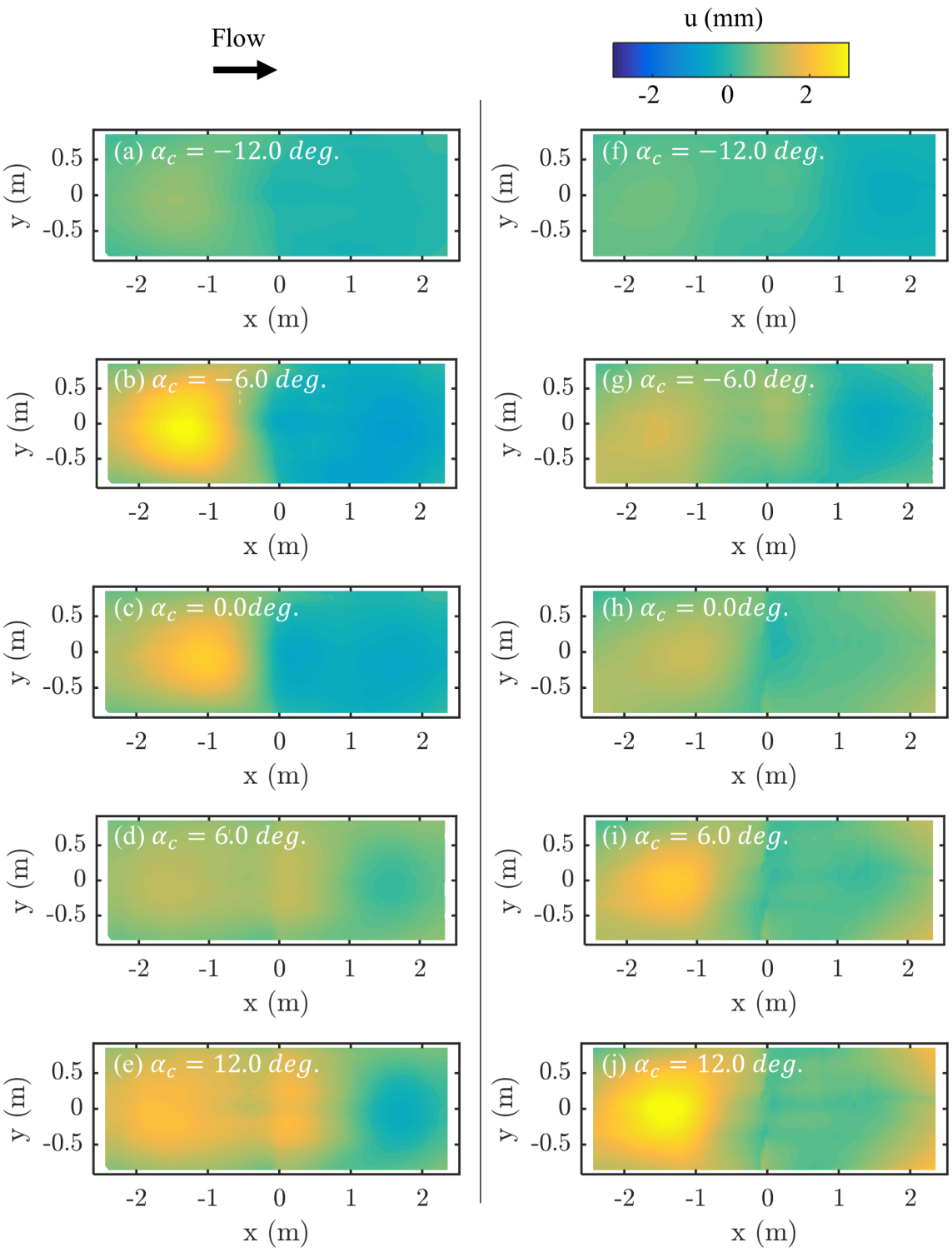

Figure C.42: Wall deformation in the u-component vs. location over the wall for Run 3-3 of Table 3.3. The port wall is shown in (a)-(e) and the starboard wall is shown in (f)-(j). Angles of attack have been offset by 0.05 degrees in the positive direction to align zero-lift with the origin. Data have been interpolated to the nominal angles reported.

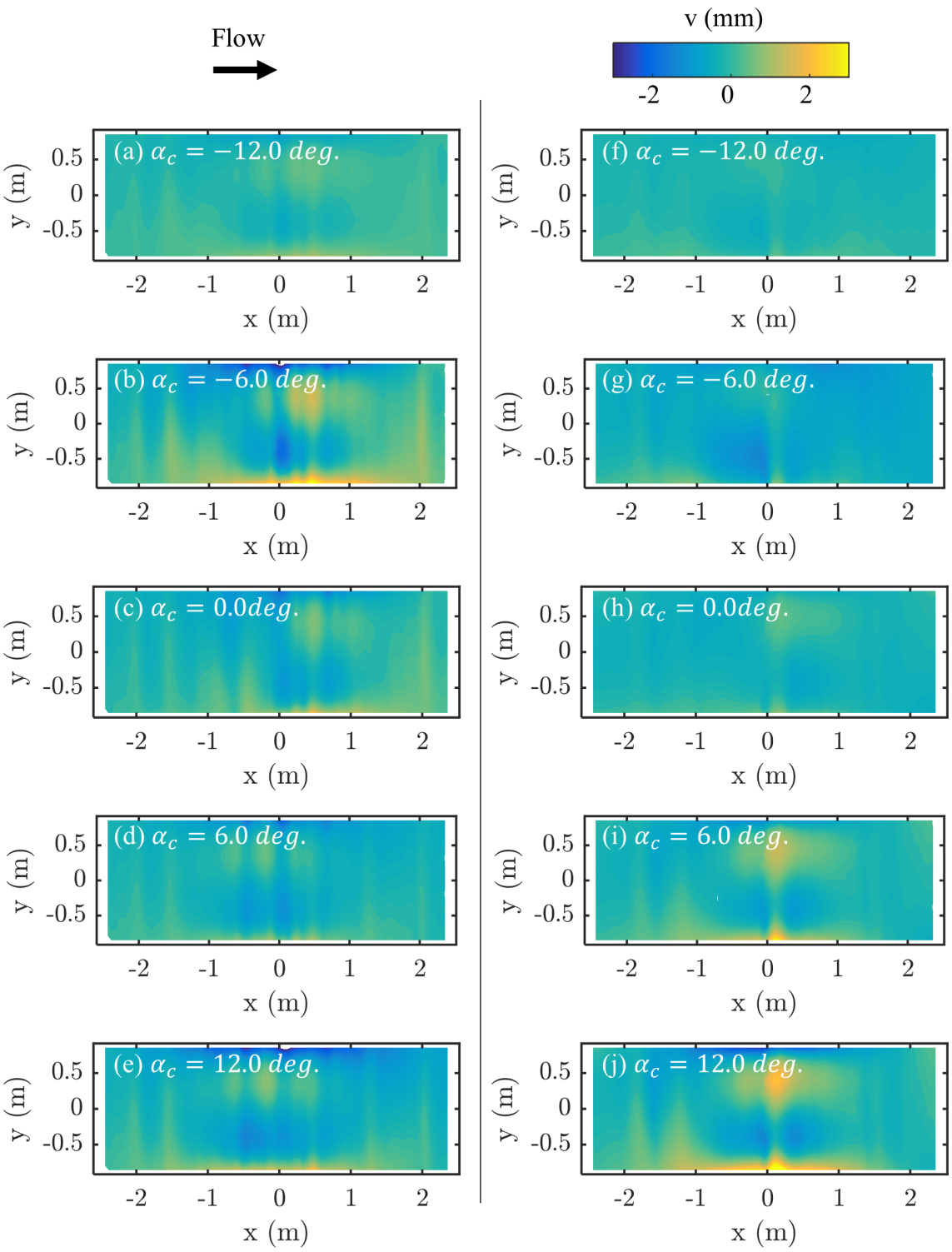

Figure C.43: Wall deformation in the v-component vs. location over the wall for Run 3-3 of Table 3.3. The port wall is shown in (a)-(e) and the starboard wall is shown in (f)-(j). Angles of attack have been offset by 0.05 degrees in the positive direction to align zero-lift with the origin. Data have been interpolated to the nominal angles reported.

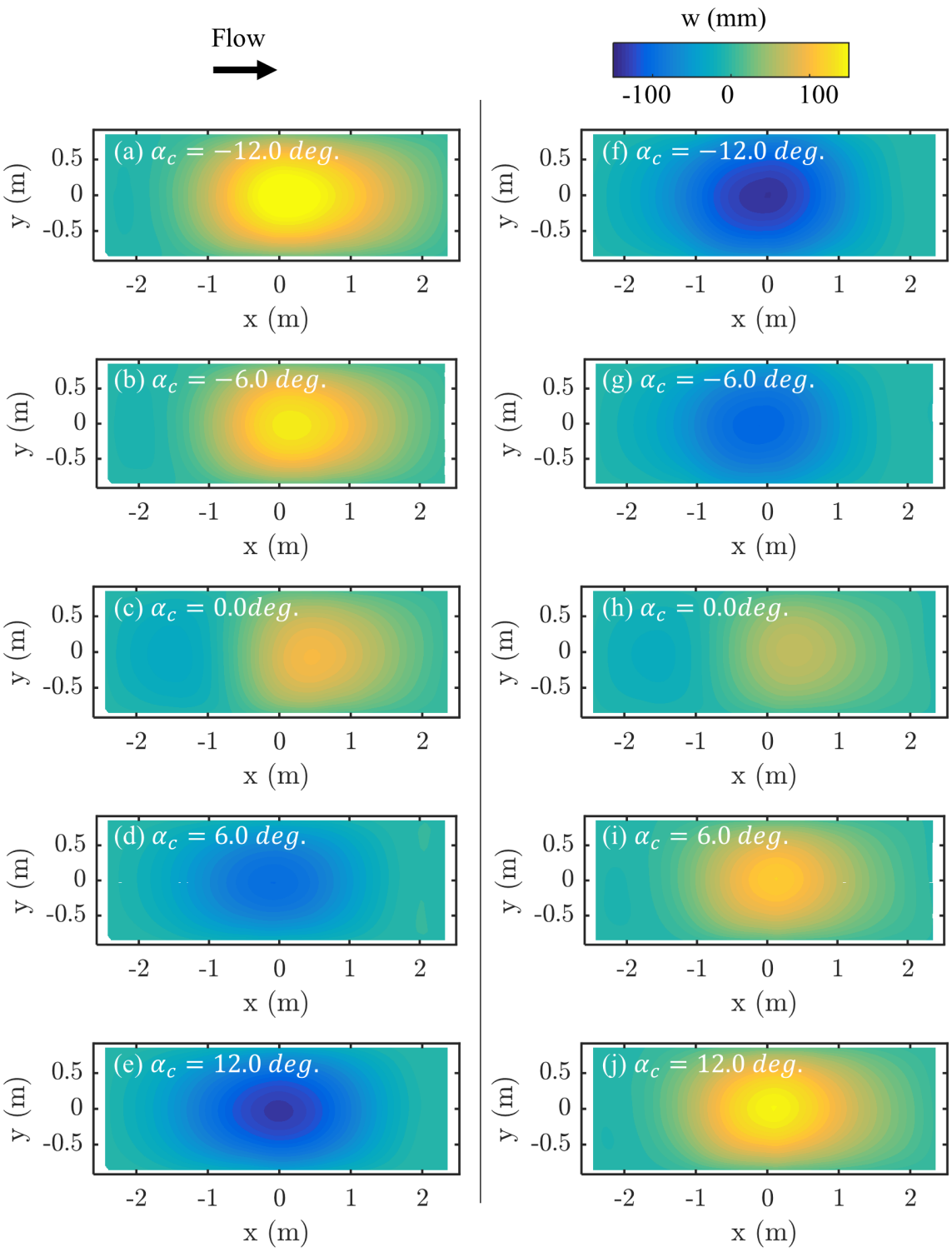

Figure C.44: Wall deformation in the w-component vs. location over the wall for Run 3-3 of Table 3.3. The port wall is shown in (a)-(e) and the starboard wall is shown in (f)-(j). Angles of attack have been offset by 0.05 degrees in the positive direction to align zero-lift with the origin. Data have been interpolated to the nominal angles reported.

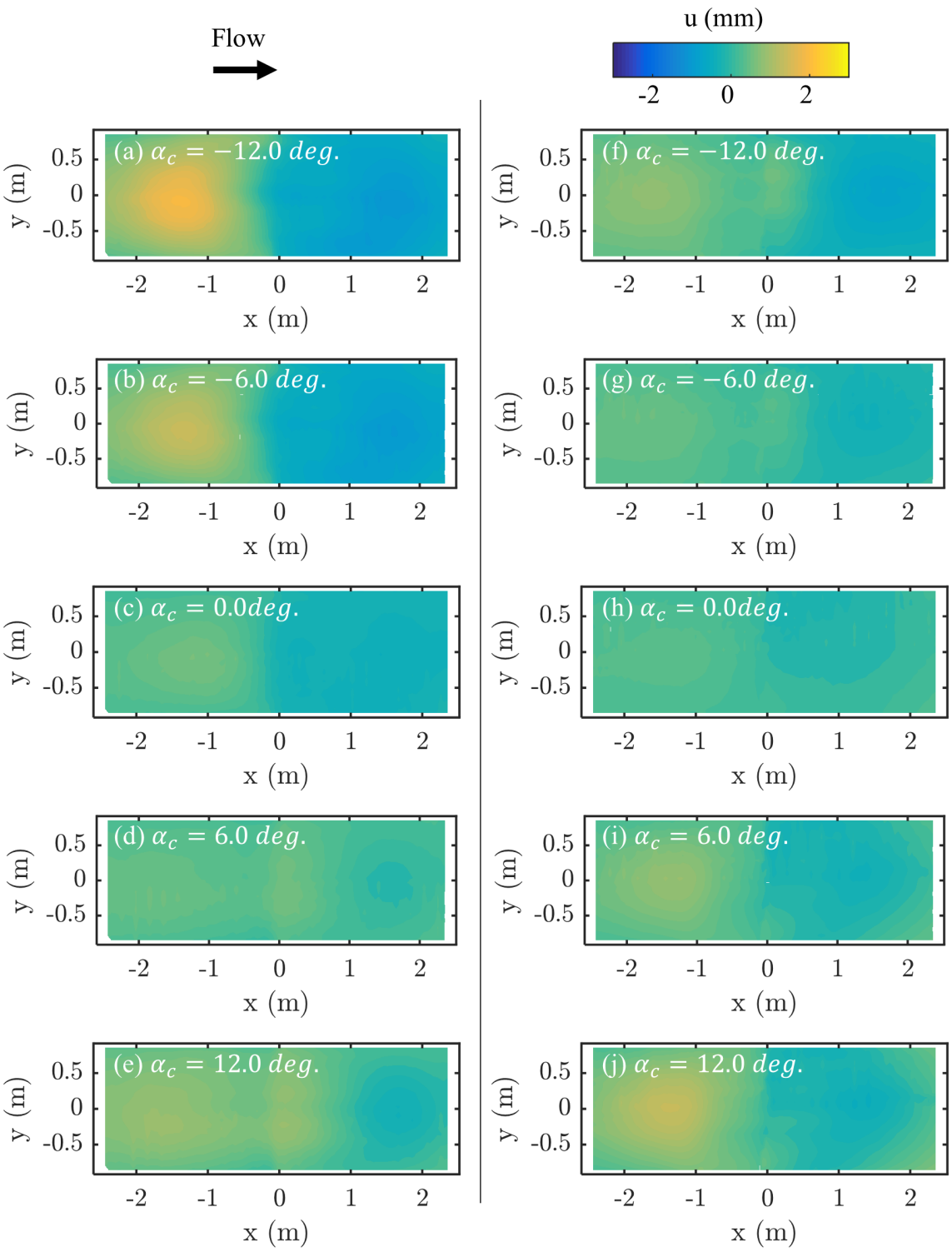

Figure C.45: Wall deformation in the u-component vs. location over the wall for Run 3-5 of Table 3.3. The port wall is shown in (a)-(e) and the starboard wall is shown in (f)-(j). Angles of attack have been offset by 0.04 degrees in the negative direction to align zero-lift with the origin. Data have been interpolated to the nominal angles reported.

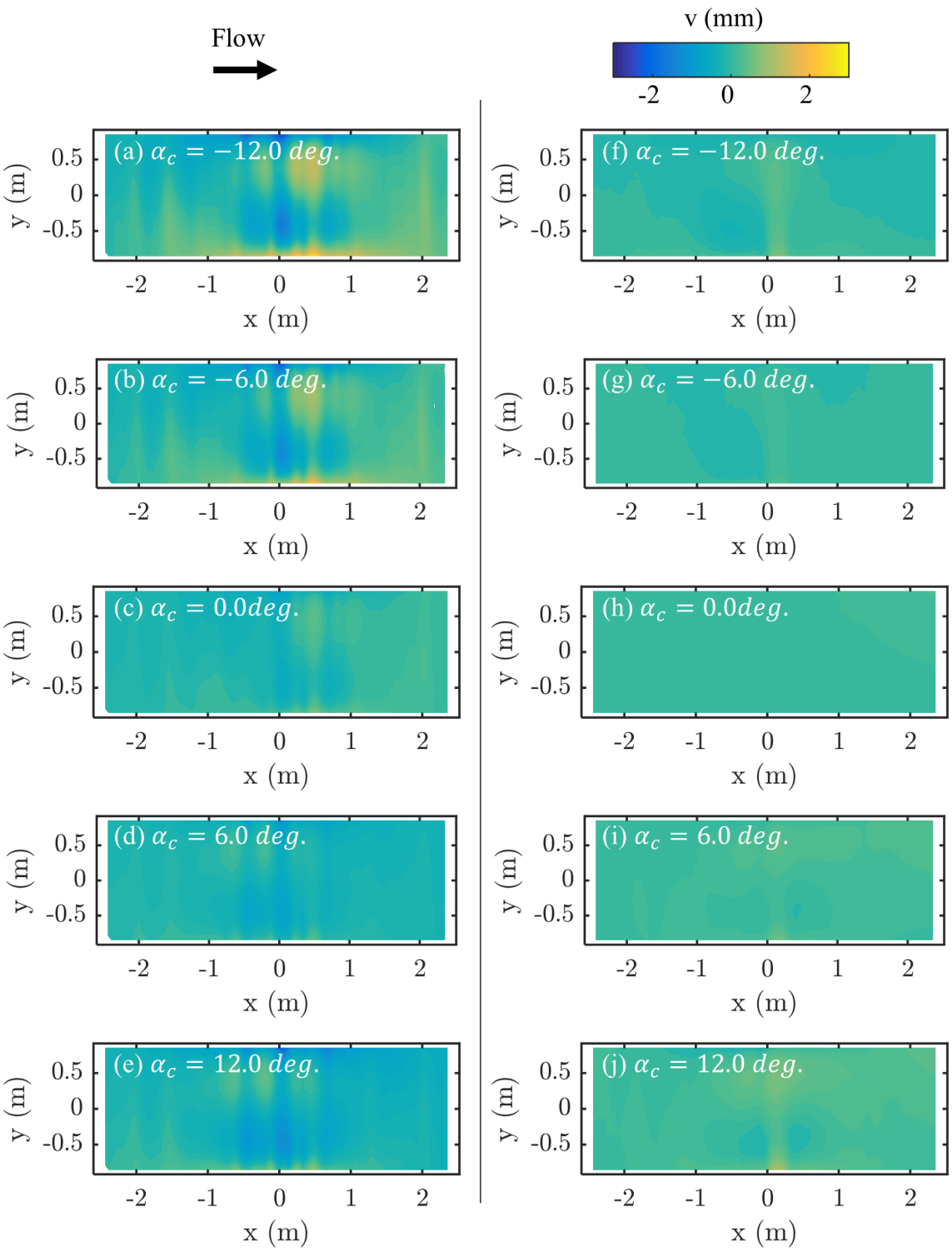

Figure C.46: Wall deformation in the v-component vs. location over the wall for Run 3-5 of Table 3.3. The port wall is shown in (a)-(e) and the starboard wall is shown in (f)-(j). Angles of attack have been offset by 0.04 degrees in the negative direction to align zero-lift with the origin. Data have been interpolated to the nominal angles reported.

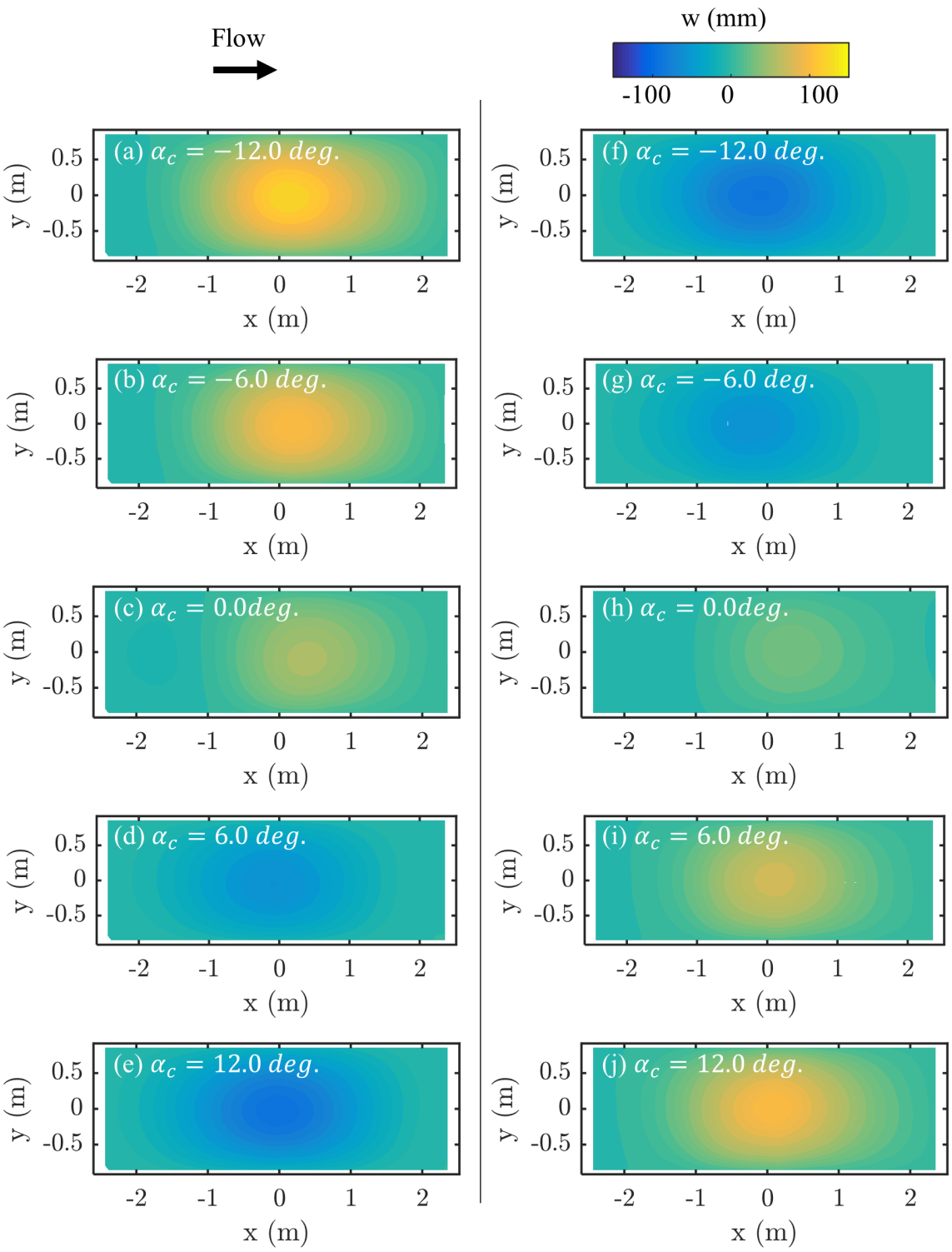

Figure C.47: Wall deformation in the w-component vs. location over the wall for Run 3-5 of Table 3.3. The port wall is shown in (a)-(e) and the starboard wall is shown in (f)-(j). Angles of attack have been offset by 0.04 degrees in the negative direction to align zero-lift with the origin. Data have been interpolated to the nominal angles reported.

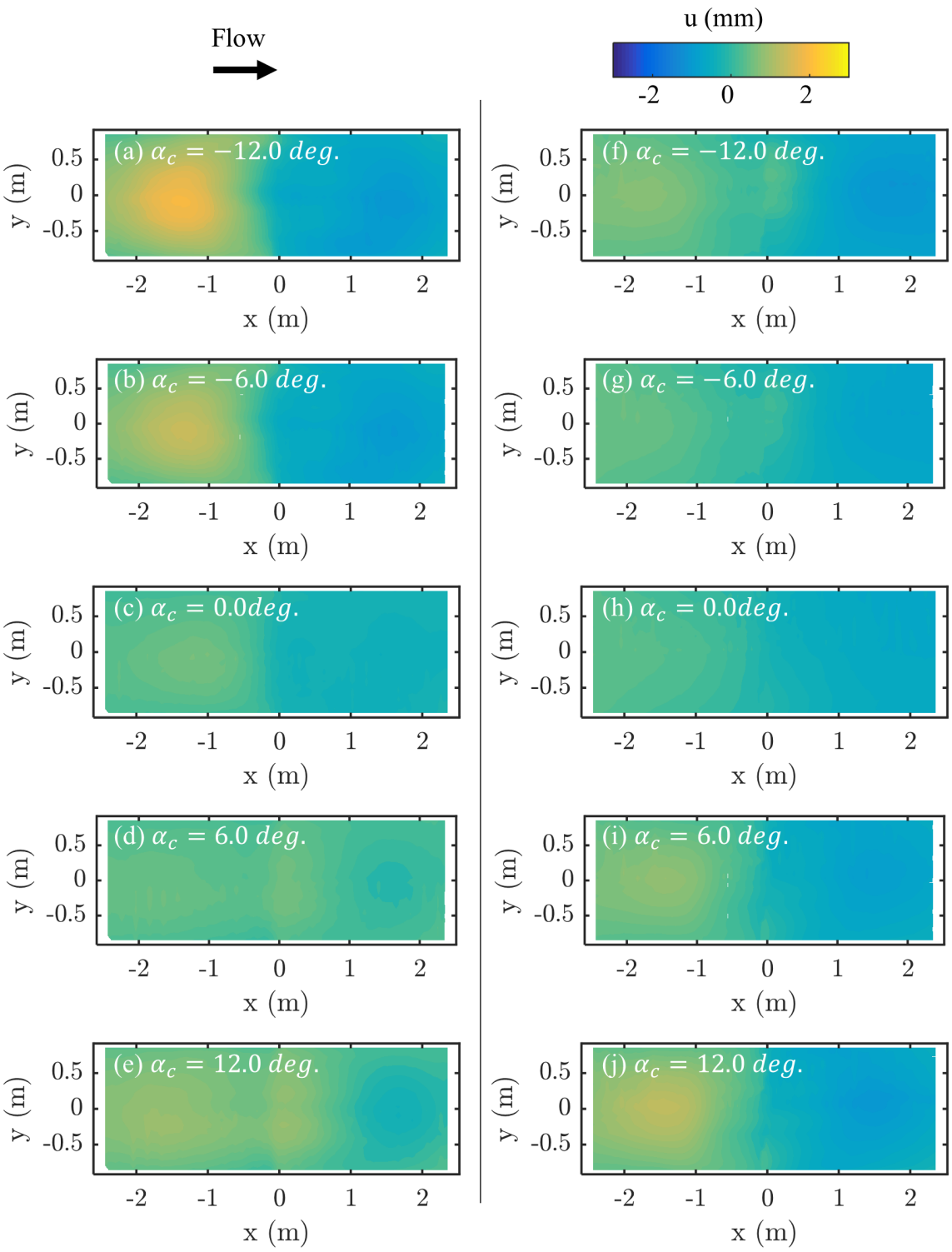

Figure C.48: Wall deformation in the u-component vs. location over the wall for Run 3-6 of Table 3.3. The port wall is shown in (a)-(e) and the starboard wall is shown in (f)-(j). Angles of attack have been offset by 0.52 degrees in the negative direction to align zero-lift with the origin. Data have been interpolated to the nominal angles reported.

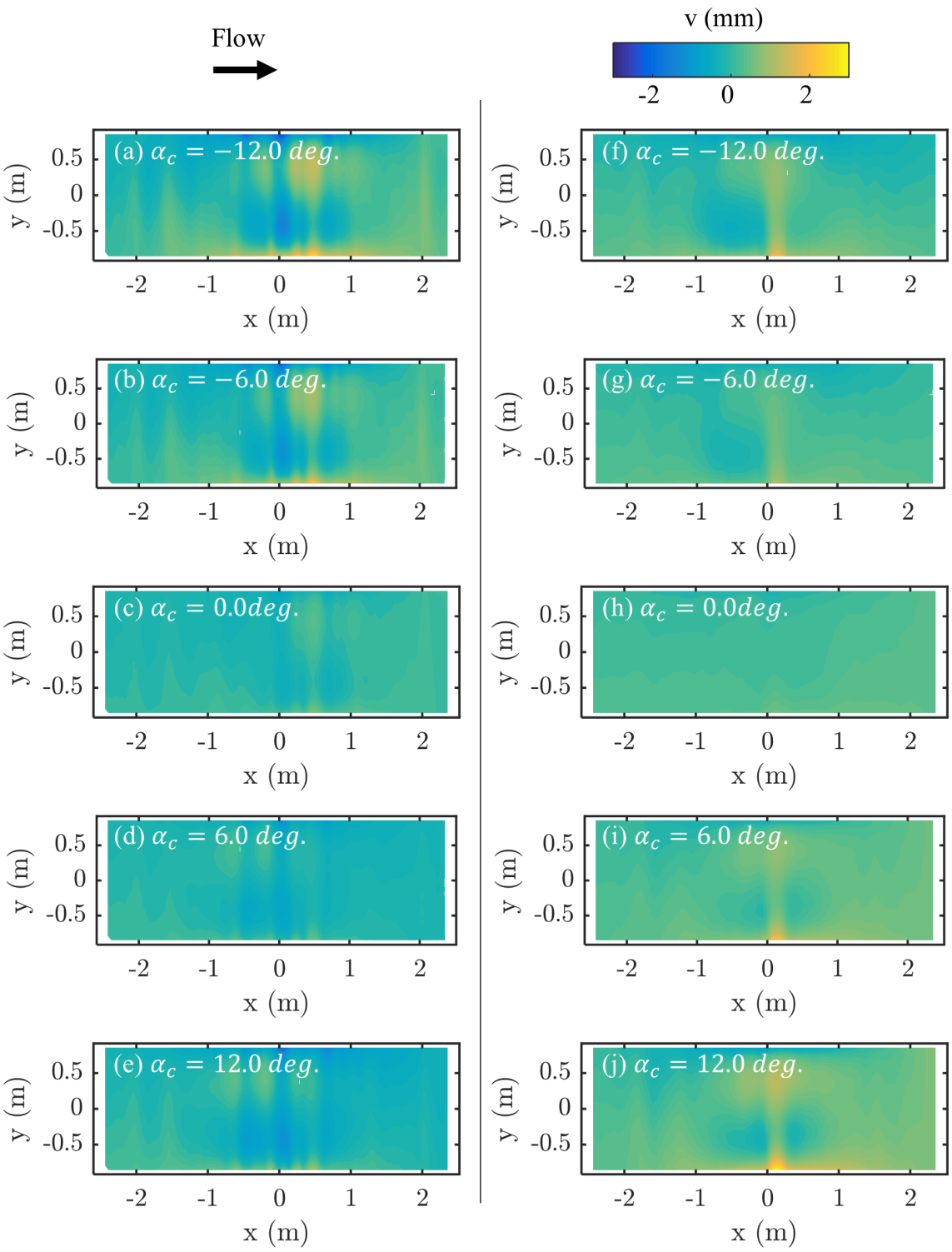

Figure C.49: Wall deformation in the v-component vs. location over the wall for Run 3-6 of Table 3.3. The port wall is shown in (a)-(e) and the starboard wall is shown in (f)-(j). Angles of attack have been offset by 0.52 degrees in the negative direction to align zero-lift with the origin. Data have been interpolated to the nominal angles reported.

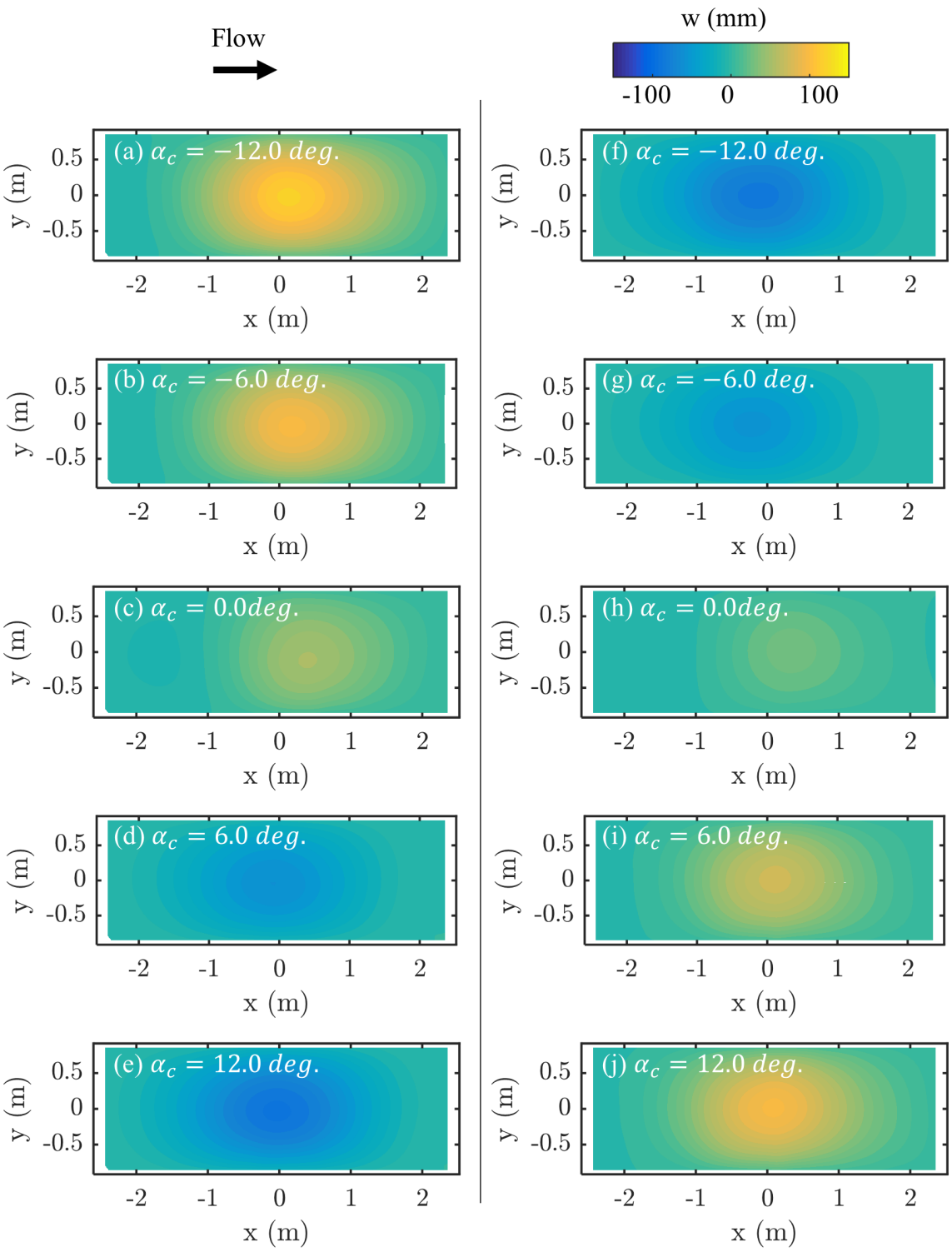

Figure C.50: Wall deformation in the w-component vs. location over the wall for Run 3-6 of Table 3.3. The port wall is shown in (a)-(e) and the starboard wall is shown in (f)-(j). Angles of attack have been offset by 0.52 degrees in the negative direction to align zero-lift with the origin. Data have been interpolated to the nominal angles reported.

C.5 Chamber Pressure

Below are given the measured chamber C_p's for all the runs in Campaigns 2 and 3. The chamber C_p's are measured at each angle of attack with a pressure line running to each anechoic chamber.

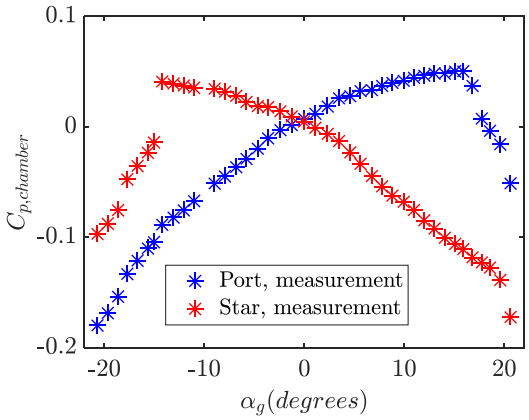

Figure C.51: Chamber C_p vs. geometric angle of attack, α_g, for Run 2-1 of Table 3.3.

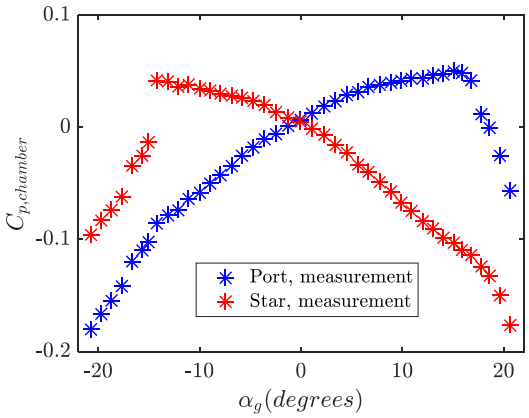

Figure C.52: Chamber C_p vs. geometric angle of attack, α_g, for Run 2-2 of Table 3.3.

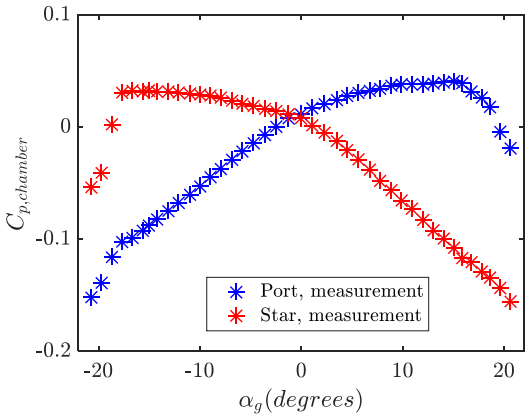

Figure C.53: Chamber C_p vs. geometric angle of attack, α_g, for Run 2-3 of Table 3.3.

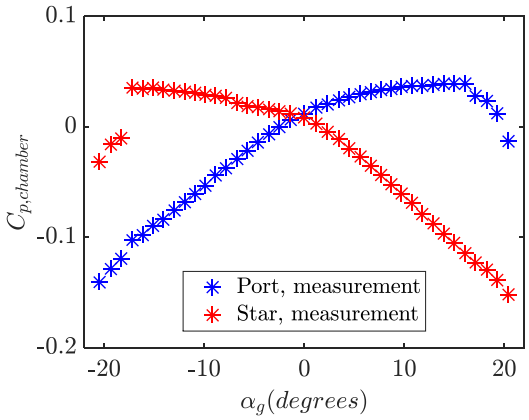

Figure C.54: Chamber C_p vs. geometric angle of attack, α_g, for Run 2-4 of Table 3.3.

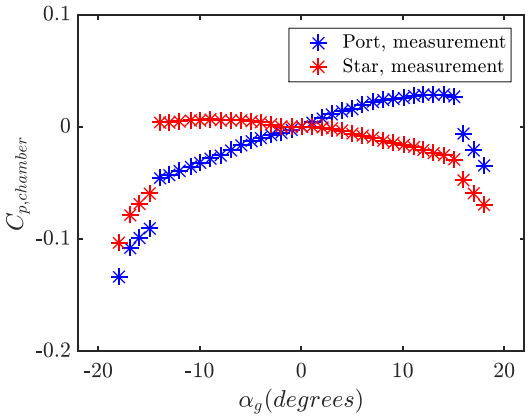

Figure C.55: Chamber C_p vs. geometric angle of attack, α_g, for Run 3-1 of Table 3.3.

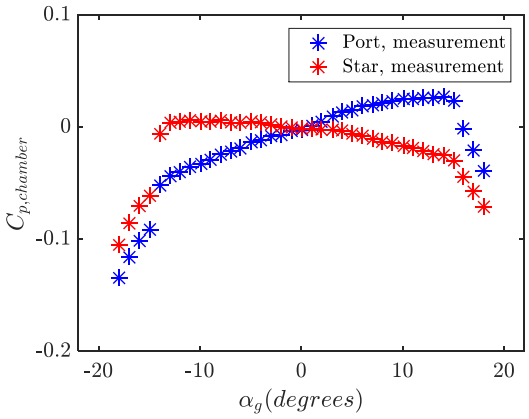

Figure C.56: Chamber C_p vs. geometric angle of attack, α_g, for Run 3-2 of Table 3.3.

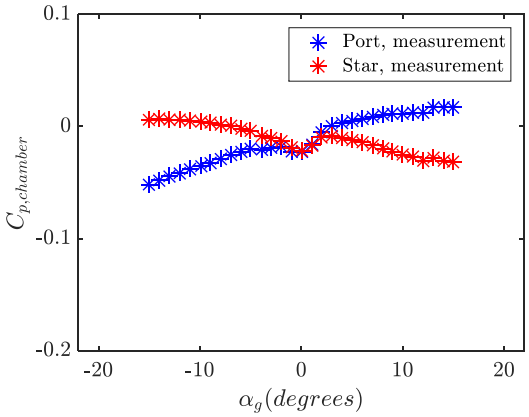

Figure C.57: Chamber C_p vs. geometric angle of attack, α_g, for Run 3-3 of Table 3.3.

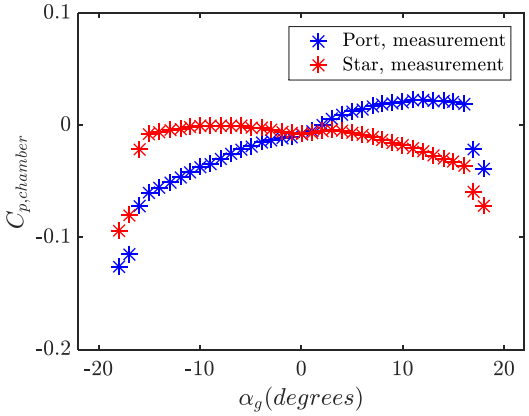

Figure C.58: Chamber C_p vs. geometric angle of attack, α_g, for Run 3-5 of Table 3.3.

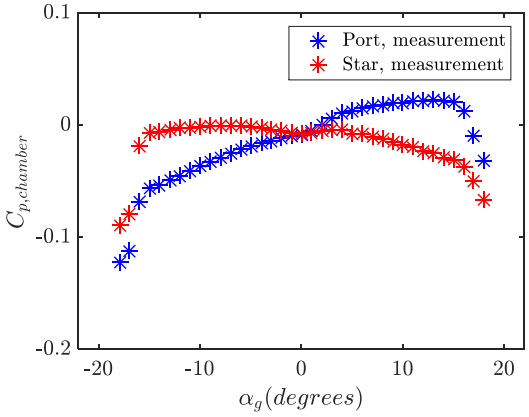

Figure C.59: Chamber C_p vs. geometric angle of attack, α_g, for Run 3-6 of Table 3.3.

Appendix D

Uncertainty Analysis for Airfoil Pressure Measurements

The uncertainties of some of the important calculated values in this study were calculated by propagating the error in the primary measurements to the final calculations. Given some final calculated quantity, f, the 20:1 odds uncertainty of the quantity, U_f, are given by

$$U_f = \sqrt{(\frac{\partial f}{\partial x})^2 U_x^2 + (\frac{\partial f}{\partial y})^2 U_y^2 + (\frac{\partial f}{\partial z})^2 U_z^2 + ...} \tag{D.1}$$

where U_x, U_y, and U_z are the 20:1 odds uncertainties of some primary measurements x, y, and z. Equation D.1 assumes that f is a linear function of each of the primary measurements within the range of uncertainties of the measurements, as well as that errors in the primary measurements are uncorrelated and follow a Gaussian distribution.

This appendix demonstrates a numerical approach to uncertainty propagation where the partial derivatives with respect to each primary measurement are never themselves calculated. Instead, the nominal value of each of the primary measurements are jittered one at a time and the resulting f calculated for each. The root-sum-square value of all the jittered calculations yields the overall uncertainty of the measurement.

Runs 3-1, 3-3, and 3-5 of Table 3.3 are shown as examples in this appendix. The uncertainty in the freestream properties for these runs are tabulated below in Tables D.1-D.3. The primary measurements are the measurements of the contraction pressure, settling chamber pressure, barometric pressure, and temperature. The nominal values of these measurements and their uncertainties are tabulated below for the selected tests.

Table D.1: Uncertainty analysis of the freestream properties of Run 3-1.

	Nominal Quantity	Uncertainty	Notes
Constants			
Cps	0.9871	-	
Cpc	0.4074	-	
R (J/K/kg)	287.058	-	
Primary measurements			
Barometer reading, p_{atm} (Pa)	9.357E+04	1.693E+02	
Thermometer reading, T_f (K)	2.980E+02	2.000E-01	
Contraction pressure, p_c (Pa)	4.044E+02	8.618E+00	
Settling chamber pressure, p_s (Pa)	8.395E+02	8.618E+00	
Derived Quantities			
Air density, ρ (kg/m^3)	1.094E+00	2.111E-03	$\rho = p_{atm}/T_f/R$
Freestream velocity, V (m/s)	3.705E+01	5.201E-01	$V = \sqrt{2(p_s - p_c)/(Cps - Cpc)/\rho}$
Freestream dynamic pressure, q (Pa)	7.507E+02	2.103E+01	$q = (p_s - p_c)/(Cps - Cpc)$
Freestream static pressure, p (Pa)	9.854E+01	1.588E+01	$p = (p_c Cps - p_s Cpc)/(Cps - Cpc)$

Table D.2: Uncertainty analysis of the freestream properties of 3-5.

	Nominal Quantity	Uncertainty	Notes
Constants			
Cps	0.9871	-	
Cpc	0.4074	-	
R (J/K/kg)	287.058	-	
Primary measurements			
Barometer reading, p_{atm} (Pa)	9.272E+04	1.693E+02	
Thermometer reading, T_f (K)	2.930E+02	2.000E-01	
Contraction pressure, p_c (Pa)	8.628E+02	8.618E+00	
Settling chamber pressure, p_s (Pa)	1.814E+03	8.618E+00	
Derived Quantities			
Air density, ρ (kg/m^3)	1.102E+00	2.149E-03	$\rho = p_{atm}/T_f/R$
Freestream velocity, V (m/s)	5.457E+01	3.535E-01	$V = \sqrt{2(p_s - p_c)/(Cps - Cpc)/\rho}$
Freestream dynamic pressure, q (Pa)	1.641E+03	2.103E+01	$q = (p_s - p_c)/(Cps - Cpc)$
Freestream static pressure, p (Pa)	1.941E+02	1.588E+01	$p = (p_c Cps - p_s Cpc)/(Cps - Cpc)$

Table D.3: Uncertainty analysis of the freestream properties of Run 3-3.

	Nominal Quantity	Uncertainty	Notes
Constants			
Cps	0.9871	-	
Cpc	0.4074	-	
R (J/K/kg)	287.058	-	
Primary measurements			
Barometer reading, p_{atm} (Pa)	9.126E+04	1.693E+02	
Thermometer reading, T_f (K)	3.090E+02	2.000E-01	
Contraction pressure, p_c (Pa)	1.324E+03	8.618E+00	
Settling chamber pressure, p_s (Pa)	3.092E+03	8.618E+00	
Derived Quantities			
Air density, ρ (kg/m^3)	1.029E+00	2.021E-03	$\rho = p_{atm}/T_f/R$
Freestream velocity, V (m/s)	7.700E+01	2.759E-01	$V = \sqrt{2(p_s - p_c)/(Cps - Cpc)/\rho}$
Freestream dynamic pressure, q (Pa)	3.050E+03	2.103E+01	$q = (p_s - p_c)/(Cps - Cpc)$
Freestream static pressure, p (Pa)	8.108E+01	1.588E+01	$p = (p_c Cps - p_s Cpc)/(Cps - Cpc)$

D.1 Airfoil Pressure Measurements

Uncertainties of the C_l values measured with the airfoil pressure taps on the NACA0012 in the Stability Wind Tunnel are calculated below. In addition to the primary measurements required to calculate the freestream dynamic pressure, this C_l calculation also requires model pressure readings, the model pressure tap locations, and model chord length. The nominal model pressures are found throughout Appendix C.2, and the uncertainty of these readings is 9-Pa according to the quoted accuracy of the Esterline 9816/98RK with $\pm$2.5-psi range. The nominal model pressure tap locations are found in Appendix H, and the uncertainty in these values is taken at 0.5-mm according to the achieved accuracy of the coordinate measurement machine used to digitize the model. The model chord length is 0.913-m which also has an uncertainty of 0.5-mm associated with it due to the coordinate measurement machine.

The final uncertainty in C_l is calculated by jittering the primary measurements according to Equation D.1 where f is taken as $C_l = \int_0^c (p_- p_{static}) dx_p / q_/ c$. The results for Runs 3-1, 3-5, and 3-3 are shown in Figure D.1. It is clear that the uncertainty in the C_l calculated via the airfoil pressure taps is dominated by the uncertainty in the freestream dynamic pressure. The 20:1 odds uncertainties at $C_{l,max}$ are 0.039, 0.020, and 0.011 for Figure D.1(a)-(c), respectively, which correspond to 2.4%, 1.3%, and 0.7% of the measurement.

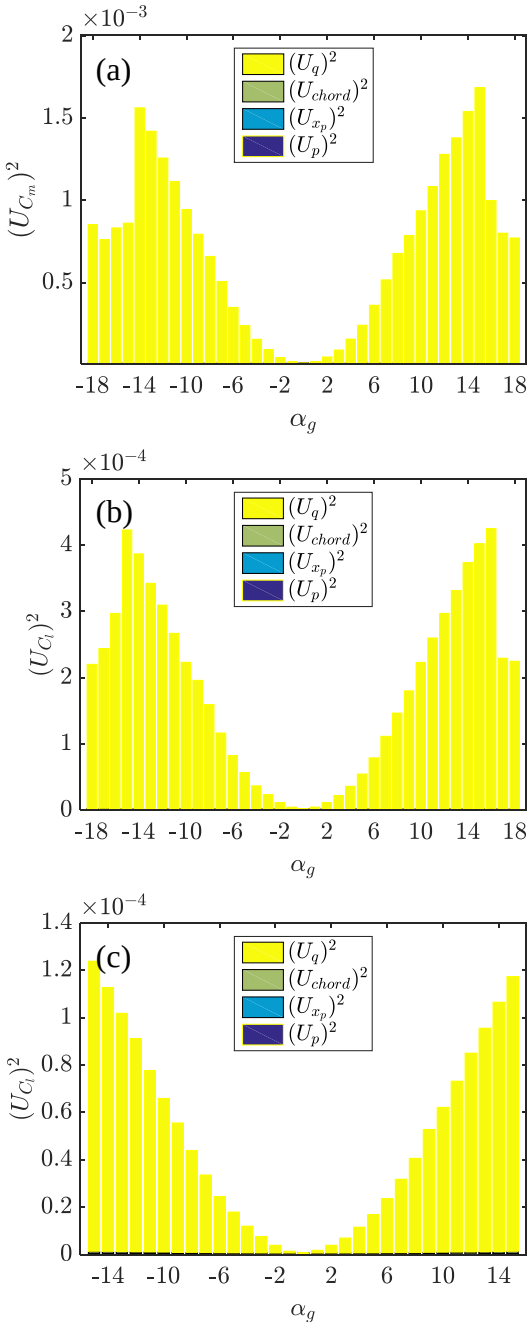

Figure D.1: Uncertainty of lift coefficient, $(U_{C_l})^2$, vs. angle of attack, α_g, for the measurement with airfoil pressure taps. The data shown are for (a) Run 3-1 (770-Pa dynamic pressure), (b) Run 3-5 (1770-Pa dynamic pressure), and (c) Run 3-3 (3300-Pa dynamic pressure).

D.2 Wall Pressure Measurement with Physical Taps

Uncertainties of the C_l values measured with the physical wall pressure taps for the NACA0012 in the Stability Wind Tunnel are calculated below. In addition to the primary measurements required to calculate the freestream dynamic pressure, this C_l calculation also requires wall pressure readings, the wall pressure tap locations, and model chord length. The nominal wall pressures are found throughout Appendix C.3, and the uncertainty of these readings is 1-Pa according to the quoted accuracy of the Esterline 9816/98RK with $\pm$10 inches of water range. The nominal wall pressure tap locations are found in the Campaign 3 values of Figure 3.11, and the uncertainty in these values is taken at 1-cm according to estimated accuracy of the tape measurements. The model chord length is 0.913-m which has an uncertainty of 0.5-mm associated with it due to the coordinate measurement machine.

The final uncertainty in C_l is calculated by jittering the primary measurements according to Equation D.1 where f is taken as the first term of Equation 7.24 and approximating $cos\theta cos\varphi = 1$. The results for Runs 3-1, 3-5, and 3-3 are shown in Figure D.2. As with the airfoil pressure measurements, the uncertainty in the C_l calculated via the wall pressure taps is dominated by the uncertainty in the freestream dynamic pressure. The 20:1 odds uncertainties at $C_{l,max}$ are 0.039, 0.020, and 0.012 for Figure D.1(a)-(c), respectively, which correspond to 2.4%, 1.3%, and 0.8% of the measurement.

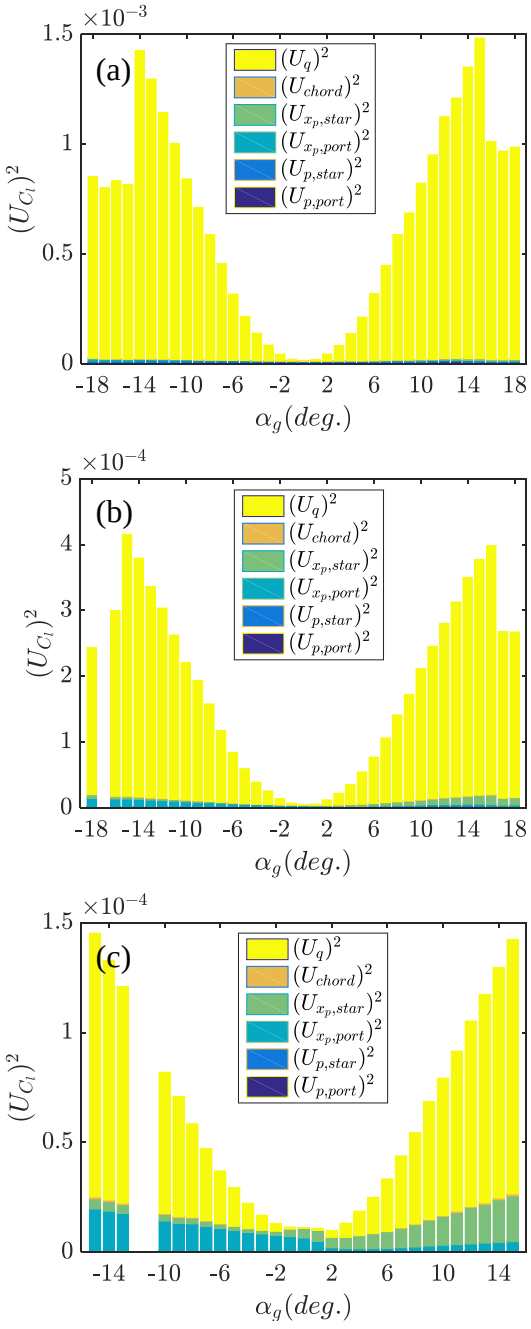

Figure D.2: Uncertainty of lift coefficient, $(U_{C_l})^2$, vs. angle of attack, α_g, for the measurement with physical wall pressure taps. The data shown are for (a) Run 3-1 (770-Pa dynamic pressure), (b) Run 3-5 (1770-Pa dynamic pressure), and (c) Run 3-3 (3300-Pa dynamic pressure).

D.3 Wall Pressure Measurement with Optical System

Uncertainties of the C_l values measured with the optical wall pressure system for the NACA0012 in the Stability Wind Tunnel are calculated below. In addition to the primary measurements required to calculate the freestream dynamic pressure, this C_l calculation also requires wall pressure values, the locations of the wall pressure values, and model chord length. The nominal wall pressures at selected angles of attack are found in Figures 7.11-7.16, and the uncertainty of these readings varies based on the location of the measurement and the dynamic pressure in the wind tunnel as is discussed in the following paragraph. The uncertainty of the nominal wall pressure locations is taken to be negligible since the accuracy of the camera calibration model described in Section 3.1.7 is on the order of millimeters or less. The model chord length is 0.913-m which has an uncertainty of 0.5-mm associated with it due to the coordinate measurement machine.

As seen in Equation 7.21, the optically calculated wall pressures require knowledge of the first and second derivatives of the deflection components of the Kevlar, the material properties of the Kevlar, the pre-tension distribution in the Kevlar, and the pressures in the anechoic chambers. For the deflection terms in Equation 7.21, data at selected angles of attack are found in Appendix C.4, however, no uncertainty estimates have been made for the derivatives of these values. Rather, it is assumed that these uncertainties are negligible which will be true in the limit of ideal regularization of the measured deflection contours. For the material properties terms in Equation 7.21, the values used derive from the measurements reported in Section 4.2.3 ($E_x = 1.33\text{E}10\text{-}Pa$, $E_y = 3.12\text{E}10\text{-}Pa$, and $\nu_{xy} = 0.40$ with $h = 0.021\text{-}mm$). Considering the high degree of non-linearity observed in the material properties of woven Kevlar fabric in Section 2.3.3, the uncertainties in the elastic moduli are taken to be 50% of their nominal values. The uncertainties of the Poisson's ratios are taken to be 0.2. These estimates are roughly based on Figure 2.3 from consideration of the spread of the material properties over the range of strains experienced by the Kevlar in the wind tunnel. For the pre-tension terms in Equation 7.21 including $T_{x,0}$ and $T_{y,0}$, the 20:1 uncertainty is given as $\sim$140-N/m in Appendix G. For the chamber pressure term in Equation 7.21, the nominal readings are given in Appendix C.5, and the uncertainty of these readings is 1-Pa according to the quoted accuracy of the Esterline 9816/98RK with $\pm$10 inches of water range.

The final uncertainty in C_l is calculated by jittering the primary measurements according to Equation D.1 where f is taken as the first term of Equation 7.24, $cos\theta cos\varphi = 1$, and C_p is calculated via Equation 7.21. The results for Runs 3-1, 3-5, and 3-3 are shown in Figure D.3. The uncertainty in the C_l calculated via the optical wall pressures has significant contributions both from the uncertainty in the freestream dynamic pressure and the uncertainty of the wall pressures. The breakdown of uncertainty within the wall pressure measurement reveals that the pre-tension measurements dominate the pressure uncertainty at the low dynamic pressure cases as in Figure D.3 (a) whereas the material properties estimates dominate the pressure uncertainty at the high dynamic pressure cases as in Fig-

ure D.3 (c). The uncertainty increases as the frestream dynamic pressure increases because of greater stretching of the Kevlar. As the geometric non-linearity of the membrane deflection increases, the uncertainty in the material properties estimates contribute more strongly to the overall uncertainty. The 20:1 odds uncertainties at $C_{l,max}$ are 0.049, 0.071, and 0.012 for Figure D.1(a)-(c), respectively, which correspond to 3.1%, 3.7%, and 4.4% of the measurement.

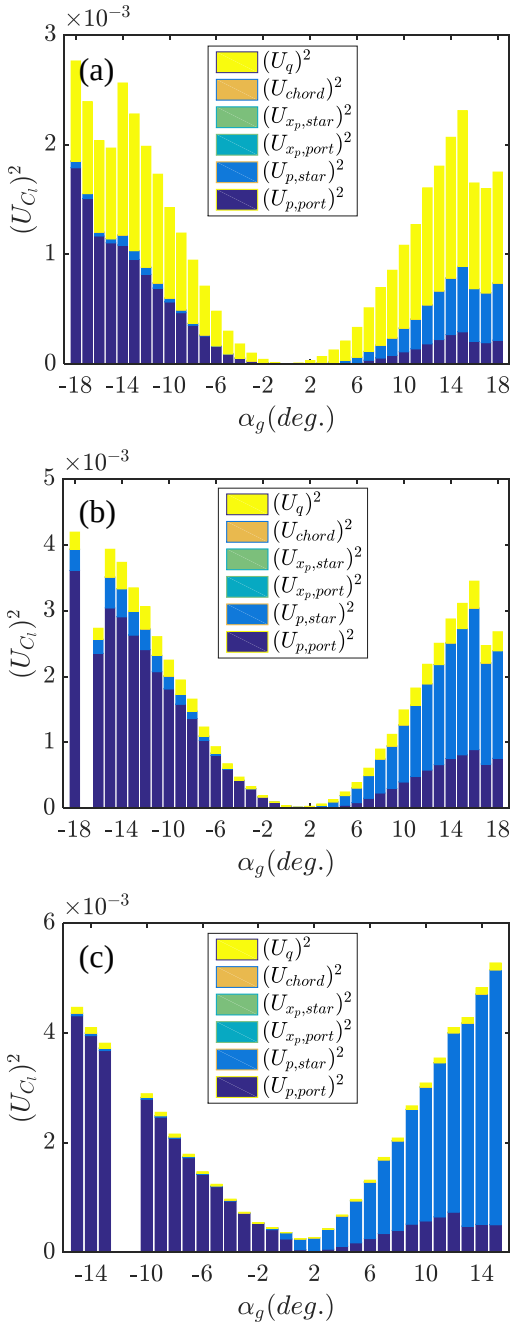

Figure D.3: Uncertainty of lift coefficient, $(U_{C_l})^2$, vs. angle of attack, α_g, for the measurement with optical system. The data shown are for (a) Run 3-1 (770-Pa dynamic pressure), (b) Run 3-5 (1770-Pa dynamic pressure), and (c) Run 3-3 (3300-Pa dynamic pressure).

Appendix E

Introduction and Verification of Finite Element Simulation

Finite element simulations are used in Chapter 4 to support experimental data. Below is described the setup of the finite element simulation and verification versus previous solutions.

The finite element simulations are performed in MSC-NASTRAN with four-noded shell elements (CQUAD4) and geometric nonlinear analysis which includes both element coordinate update and follower forces. The elements are materially linear but are capable of supporting orthotropic behavior (MAT8). A rectangular membrane with the same 2.43- by 1.38-m outer dimensions of the reduced-scale Kevlar frame is fixed in all 6 degrees of freedom at the boundaries. The pre-tension is developed with thermal loading of elements whose coefficient of thermal expansion can be specified in both orthogonal directions, and uniform pressure loading is applied to replicate the uniform pressure field of the physical bulge test.

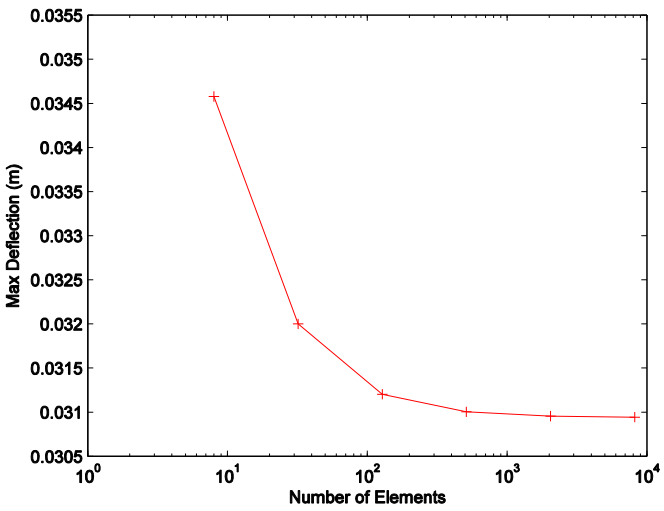

Figure E.1: Convergence of the finite element simulation with increasing number of elements.

Convergence of the finite element simulation with increasing number of elements is first verified. For the convergence sweep, the pressure difference is 957.54-Pa, the elastic modulus is 3.30E10-Pa, shear modulus is 0.5000E6-Pa, Poisson's ratio is 0.6, the pre-tension is

1,200-N/m, and the effective thickness is 0.0210E-3-m. An element aspect ratio of 1.14 is maintained throughout the convergence sweep, as well as for all the studies in this section. The results of the convergence sweep are shown in Figure E.1. The maximum deflection at the membrane centerpoint converges to a value of 0.03094-m for the maximum number of elements studied which corresponds to a grid of 128 by 64 elements. As the change in maximum deflection is only 0.06% between the 64 by 32 case to 128 by 64 case, the latter is deemed a converged result with sufficient element density for simulations moving forward.

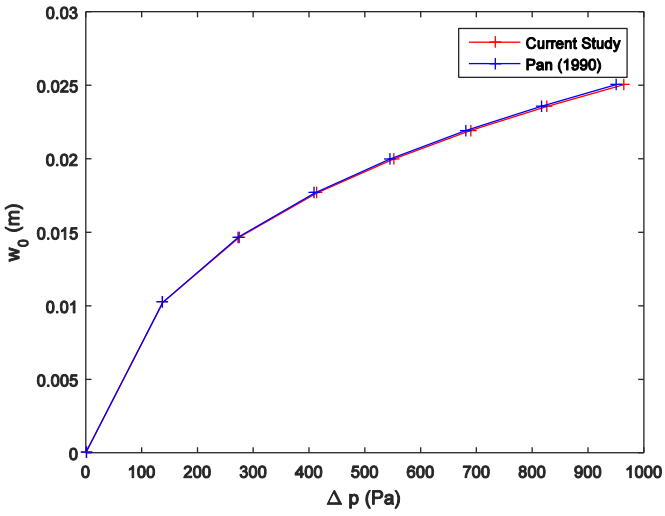

Figure E.2: Comparison of the maximum deflection of geometrically nonlinear membranes from the finite element simulations of the present study and the formula of Pan, 1990.

The accuracy of the solution can be assessed by comparison with other studies in literature. Pan (1990) uses geometrically nonlinear finite element simulations of square membranes and plots the maximum deflection versus pressure. The comparison of Pan's formula to the finite element simulation of the present study is shown in Figure E.2. For the finite element simulation, the inputs are the same as given previously except that the 2.43-m sides are shortened to 1.38-m to yield a square membrane and the shear modulus is brought to 1.03E10-Pa which is representative of an isotropic membrane. The largest percent error between the two sets of data is 1.5% which occurs at the highest pressure difference case.

Appendix F

Study of Inverse Problem with Finite Element Simulation

Several studies mentioned in Section 7.1.2 demonstrate a useful technique for refining the inverse calculation methodology which is the use of a reference finite element model in the place of experimental data. The reference model, usually of finer mesh than the inverse model to promote independence of the reference and inverse solutions, may be used without noise added [107][109][110][118], or may be used with artificial noise added to the output to simulate experimental uncertainty [112][113][114][116][117][119][120][121]. Therefore, as a prequel to the experiments performed in Chapter 7, several numerical studies were performed to aid in the experimental design and offer predictions for the selection of the number of basis functions for the experimental data.

Unless otherwise noted, the finite element simulations included in this section are performed in the same manner as described in Appendix E. The simulations use the same 5.14-m by 1.85-m Kevlar region as the Stability Wind Tunnel walls and have a uniform pressure difference of 470-Pa enforced across the Kevlar with a uniform pretension of 1,500-N/m in both x- and y-directions. The elastic moduli are 3.65E10-Pa in the x-direction and 4.68E10-Pa in the y-direction with a shear modulus of 1.20E6-Pa and an apparent Poisson's ratio of 0.6. The mesh consists of 400 by 150 shell elements in the x- and y-directions, respectively.

The inverse method is applied to wall deflections to calculate wall pressure as outlined in Section 7.4, except that this time the deflections originate from the finite element simulation rather than from the experiment. Specifically, the polynomial basis functions of Equation 7.22 are fit to the simulated deflections from which p in Equation 7.21 is calculated at selected locations around the Kevlar. The inversely-calculated p can then be compared to the actual simulated pressure.

In the presence of measurement noise, the number of terms in the basis functions must be selected with care so as to balance the attenuation of noise propagation with the loss

of information due to under-fitting as discussed in Section 7.1.1.1. The procedure in this appendix is to perform the inverse calculation with increasing numbers of polynomial basis functions to find the optimal number of basis functions to use in both the x- and y-directions. In other words, it is desired to know the optimal values of a, b, c, d, e, and f in Equation 7.22. The x-direction parameters in this appendix are set equal to each other so that $a = c = e$. Similarly, $b = d = f$ for the y-direction parameters. The optimal values for these parameters is here defined as that which produces the lowest RMS pressure difference between the inversely-calculated pressure and specified pressure across all the measurement points in the domain. With such a methodology, the sensitivity of the inverse solution and basis function selection to experimental setup parameters including measurement sampling density and noise level of deflection measurements will be studied.

To provide a starting point, a reference case is first introduced with no noise added to the simulated deflection data. This reference case uses a measurement density of 30 $samples/m^2$ which equates to 286 deflection measurements across the Kevlar. The RMS pressure difference for a sweep of polynomial basis functions is plotted in Figure F.1(a)(i). As expected for this no-noise case, the location of minimum RMS difference comes as the number of polynomial terms is maximized. The difference between the inversely-calculated pressure and the specified pressure, as well as the measurement locations, across the Kevlar are shown in Figure F.1(a)(ii). The differences become exaggerated in the regions where there is no measurement data such as at $x < -2$ and $x > 2$. As these regions are difficult to measure in the Stability Wind Tunnel, the results in Figure F.1(b) suggest that inverse pressure calculations outside the range of $-2 < x < 2$ will be erroneous. There are slight asymmetries in the pressure solution because of the propagation of error as found in all finite element simulations.

As an example of the result when noise is added, Figure F.1(b) shows the corresponding plots to those of Figure F.1(a) except with measurement noise included. The noise is Gaussian with a standard deviation of 60-μm in the in-plane directions and 120-μm in the out-of-plane direction. The optimal number of basis functions drops from 8-by-6 with no noise to 5-by-4 with noise for the x- and y-directions, respectively. The RMS error at these optimum parameters correspondingly increases from 3.0-Pa to 15.7-Pa.

Figure F.2 shows the same data as Figure F.1 except for a pressure difference of 2350-Pa across the Kevlar rather than 470-Pa. The results are qualitatively the same except for two main differences. First, in Figure F.2(a)(i), the minimum RMS pressure difference does not occur when the maximum six y-direction basis functions are employed but rather when only five y-terms are used. This puzzling result may be related to the small angle assumption being violated near the boundaries of the Kevlar, specifically at extreme y-values. With the pressure difference across the Kevlar set to a relatively high 2350-Pa, the deflection angle of the Kevlar is around 10 degrees at extreme y-values. It is speculated that increasing the number of polynomial basis functions, while decreasing the residual of the deflection fit, actually increases the RMS pressure error due to the inconsistency in the formulation of Equation 7.21 with large angle deflections. The second difference is apparent between

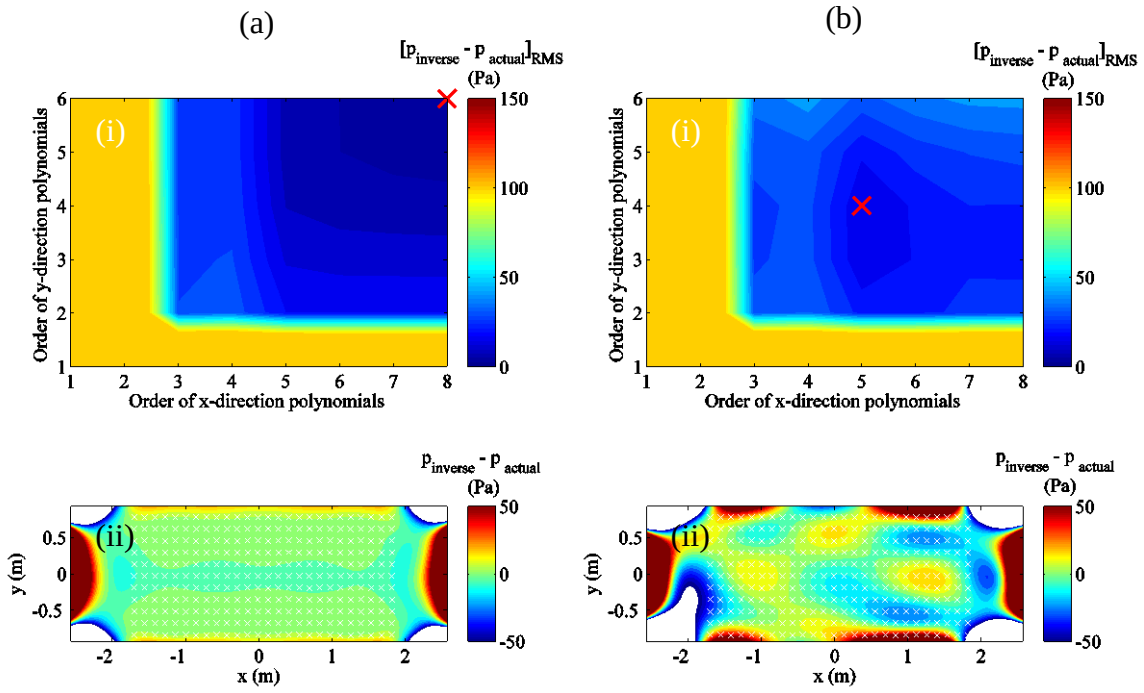

Figure F.1: Results of inverse pressure calculations for a 470-Pa uniform pressure difference on (a) a reference case with no added noise and (b) an example case with added Gaussian noise of standard deviation 60-μm in the in-plane directions and 120-μm in the out-of-plane direction. Subplots (i) show the RMS error in the inverse-calculated pressure for varying orders of polynomial basis functions. The x-axis shows the value of $a = c = e$ and the y-axis shows the value of $b = d = f$ in Equation 7.22. Subplots (b) show the error in the inverse calculated pressure over the full simulation space corresponding to the case marked by the red 'x' in (a) which is the location of lowest RMS difference. The white 'x' markers in (ii) indicate the points where deflections are sampled.

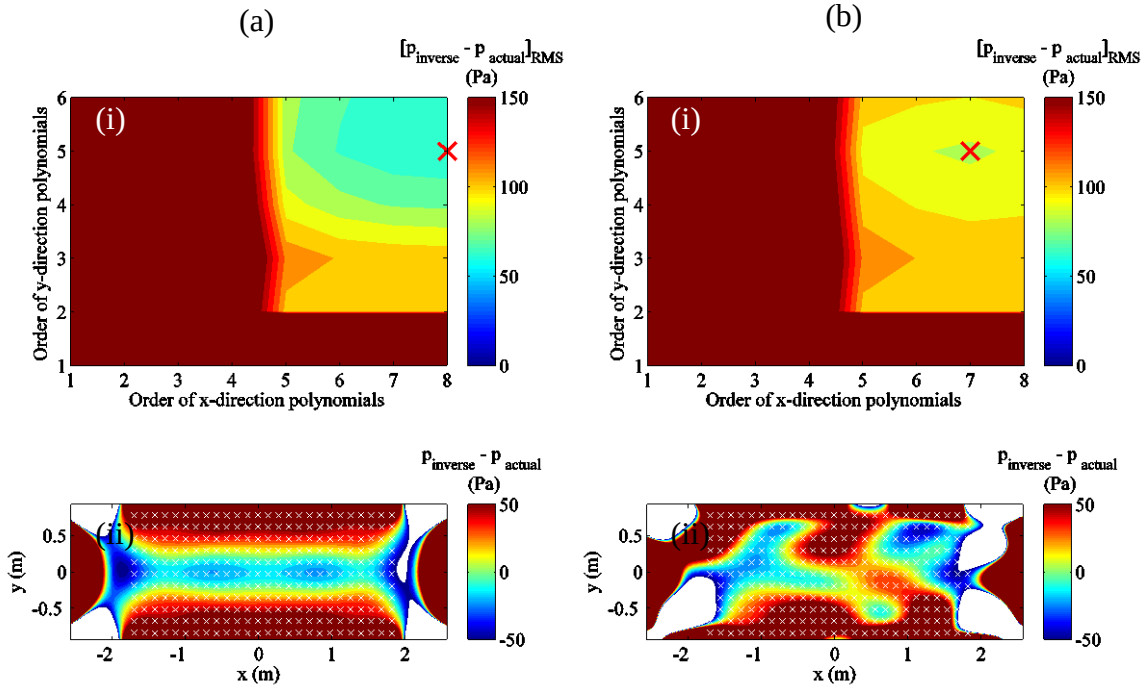

Figure F.2: Results of inverse pressure calculations for a 2350-Pa uniform pressure difference on (a) a reference case with no added noise and (b) an example case with added Gaussian noise of standard deviation 60-μm in the in-plane directions and 120-μm in the out-of-plane direction. Subplots (i) show the RMS error in the inverse-calculated pressure for varying orders of polynomial basis functions. The x-axis shows the value of $a = c = e$ and the y-axis shows the value of $b = d = f$ in Equation 7.22. Subplots (b) show the error in the inverse calculated pressure over the full simulation space corresponding to the case marked by the red 'x' in (a) which is the location of lowest RMS difference. The white 'x' markers in (ii) indicate the points where deflections are sampled.

Figure F.1(b) and Figure F.2(b). In the latter, the inverse calculation with added noise finds the optimal number of polynomial basis functions to be 7-by-5 rather than 5-by-4 as in the former. The reason is that the case with the larger pressure difference exhibits greater deflection magnitudes but is still subject to the same noise levels. Thus, the signal-to-noise ratio of the larger pressure case is greater which allows for a higher fidelity polynomial representation.

Figure F.3 shows the results of two sensitivity studies. Figure F.3(a) indicates the increase in the order of the optimal polynomial basis functions and corresponding decrease in RMS error as the level of measurement noise falls. Figure F.3(b) shows a similar comparison except with the independent variable being the density of deflection measurement locations. In other words, as the measurement density increases, the fitting problem becomes more over-determined, and the basis functions are more capable of accurately smoothing noisy data. The trends revealed in Figure F.3 confirm the understanding presented in Section 7.1.1.1 regarding the sensibility of using more basis function terms as both the measurement accuracy and over-determinedness of the fitting problem increase.

It is noted that as measurement accuracy and over-determinedness increase, the RMS error of the inverse-calculated pressure will approach the accuracy of a high fidelity pressure scanner. For instance, the Esterline 9816/98RK with ±10 inches of water range as described in Section 3.1.4 has ±1-Pa uncertainty. Such an uncertainty appears attainable given the curves in Figure F.3. However, it should be borne in mind that in the actual experimental implementation of the inverse method, there will be present additional uncertainties in the material properties estimates and pre-tension measurements which were not present in the work in this appendix.

In this appendix, both even and odd orders of polynomial terms have been included even though the deflection profiles are consistently symmetric. The small non-zero values of the best-fit coefficients of the odd terms are apparently a result of small error in the underlying finite element solution. The best-fit coefficients of the even terms are generally several orders of magnitude greater than those of the odd terms.

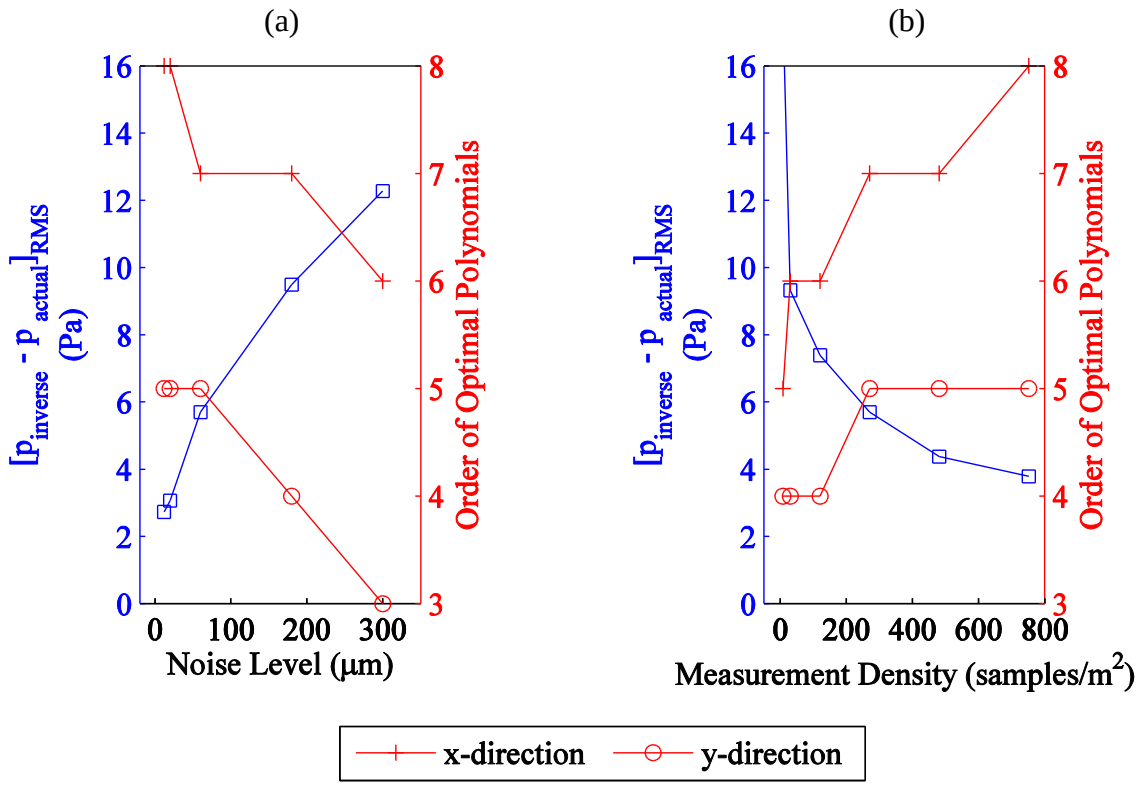

Figure F.3: The effect of (a) measurement noise level and (b) measurement density on the inverse pressure calculation. The left axes of both plots indicate the minimum obtainable RMS pressure difference between the inversely-calculated pressures and actual simulated pressure. The minimum obtainable RMS difference occurs with the number of polynomial terms in either direction as indicated by the right axes. For the calculations in (a), a measurement density of 271 samples/m^2 is assumed while for those in (b), a noise level of 60-μm is used. The noise levels quoted are for the out-of-plane direction while the in-plane noise is assumed to be half the out-of-plane noise.

Appendix G

Development of Handheld Tension Meter

A reliable means to measure the Kevlar tension was desired for the testing throughout this study. There exist a number of commercially available tension meters for screen tensioning applications that operate on the principle of measuring the sag in a fabric under a known force. The mathematical basis for the measurement is seen in the simplified out-of-plane equilibrium equation

$$T_x \frac{\partial^2 w}{\partial x^2} + T_y \frac{\partial^2 w}{\partial y^2} = -p \tag{G.1}$$

where the T's are the fabric tensions in their respective directions in force per length, x and y are the in-plane directions, w is the out-of-plane displacement, and p is the applied out-of-plane pressure. Here, the shear term has been neglected which is generally appropriate for fabrics as discussed previously. To calculate T values, tension meters may either enforce a known p and measure w, enforce a known w and measure p, or do a combination of both.

Good practice is to design the tension meter to have high sensitivity to the tension in only one in-plane direction at a time so that the meter can measure anisotropic tension fields. Such design is accomplished by applying the pressure loading along a line rather than through a point. The common design is two reference bars flanking a central indentor bar which extends further than the reference bars towards the tensioned surface. Pressing the bars up against the surface, as long as all three bars are touching the surface, the slope and change in slope of the fabric are specified by the relative arrangement of the three bars. In an idealized representation, the deformed surface forms a prism with $\partial w/\partial x$ equal to $2h/c$ where h is the extension of the indentor bar past the reference bars and c is the separation between the two reference bars. Then, $\partial^2 w/\partial x^2$ is calculated as $4h/c$ when evaluated at the tip of the prism where the slope discontinuously jumps from $2h/c$ to $-2h/c$.

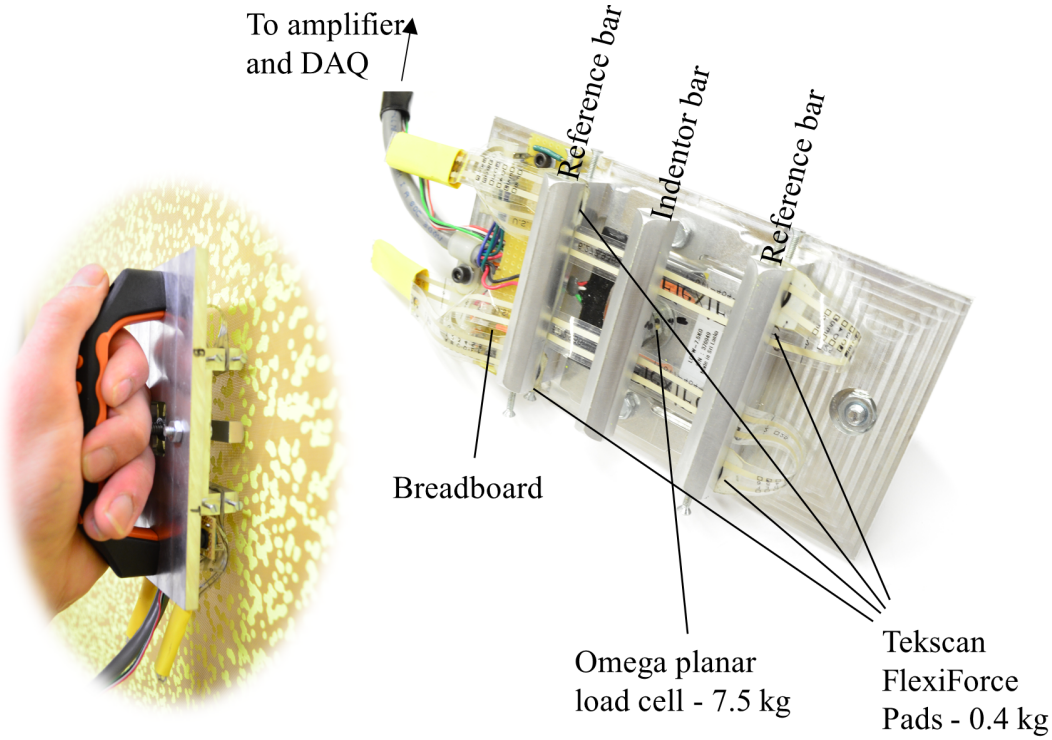

Figure G.1: Operation and construction of the in-house tension meter.

In the configuration described above, the major contribution to p comes from the tension acting along the axis perpendicular to the indentor bar although there are some end-effects due to the finite length of the bars. Neglecting these end effects as insignificant allows the left-hand side of Equation G.1 to reduce to a single term, and the calculation for the tension in any one direction can be made given the force, F, on the indentor bar as

$$T = F\frac{c}{4h} \tag{G.2}$$

Tension meters may be either gravity-driven or spring-driven, meaning either gravity or a spring-loaded gear provide the known force, F. The challenge with the present measurements is that the tension meter must be used to measure vertically-oriented rather than horizontally-oriented fabric. A gravity-driven device thus appears unsuitable, and without the availability of a spring-driven tension meter on-hand, an in-house tension meter was developed. The in-house meter operates on the spring-driven principle except that the spring stiffness is enforced to be quite high so that the geometry of the three bars is essentially fixed. The indentor bar is pressed into the fabric until the fabric just touches the two reference bars, and the load is measured by the force on the central indentor bar. The slope and change in slope of the fabric in the measurement direction are specified by the relative geometry of

the three bars which are taken to be fixed. Note that with such a high spring stiffness, the extension h must be kept as small as possibly to avoid inducing significant amounts of added tension in the fabric during the measurement.

The operation and construction of such a tension meter are shown in Figure G.1. All components are mounted on an aluminum plate of thickness 6.4-mm (0.25-in.). The height of the indentor bar is 1-mm above that of the side reference bars, the length of the bars is each 6.4-cm (2.5-in.), and the separation of the reference bars is 6.0-cm (2.35-in.).

The load on the indentor bar is measured with an Omega planar beam load cell, LCPW-7.5. The load cell has a capacity of 7.5-kg, and the uncertainty due to linearity and hysteresis are each ±0.02% full scale. Signal conditioning and amplification are accomplished by a 2310 Signal Conditioning Amplifier from the Measurements Group (now Vishay Precision Group) which supplies a 5-VDC excitation voltage to the bridge. The output signal is low-pass filtered to 10-Hz cutoff frequency and has 1000x amplification. The bridge is typically balanced before measurements. The output from the amplifier is sent to a National Instruments DAQ, model USB 6211, which has 16-bit resolution.

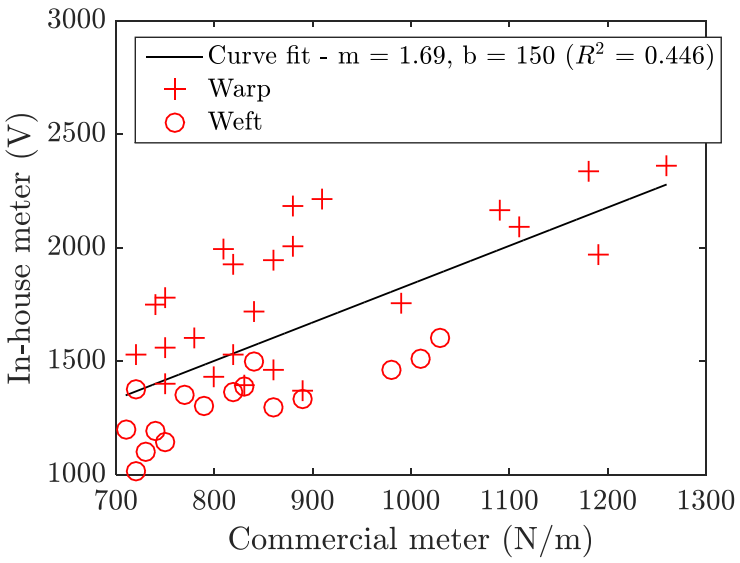

Figure G.2: Calibration of in-house tension meter versus commercial tension meter.

In order to enforce the condition that the reference edges are resting on the fabric without applying significant loading, four FlexiForce A201 contact pads with 4.4-N capacity from Tekscan were mounted on the reference bars. The signal from each of these contact pads is measured through the National Instruments DAQ. Contact is assumed to have been made when each contact pad reaches 25% of its rated capacity.

Taking measurements with the in-house meter, it was found inaccurate to calculate tension analytically with Equation G.2, perhaps because of inaccurate definition of h or error introduced by assuming infinitely long bars. The in-house tension meter was thus calibrated versus a commercially-available tension meter from Stretch Devices, Inc., the Newman ST Meter 1E. This meter has a quoted uncertainty of ±1% of the reading, however, the repeatability of the actual meter used for this study has been found to be roughly ±100-N/m based on accumulated experience of the author. Calibration was performed by taking back-to-back

measurements with each meter on a horizontally-oriented piece of tensioned Kevlar. Data were taken in both the warp and weft direction of the fabric. It should be noted that the maximum tension measured over the Kevlar in the wind tunnel is greater than the maximum calibration value by more than a factor or two. The calibration is shown in Figure G.2 including the raw data and a best-fit line. Given the segregation of the data between the warp and weft directions, it is apparent that either the commercial or the in-house meter has some degree of contamination from the off-axis component of tension. The in-house meter generally reads higher tensions for the warp direction than the weft direction, while the same is not generally true for the commercial meter. It may be that the commercial meter, which has a relatively short indentor bar compared to the in-house meter, provides a weighted average of the tension over the warp and weft directions while the in-house meter measures primarily the tension in only one direction. While this difference between the meters and apparently other error sources lead to a relatively low R^2 value of 0.446 for the best-fit line, the accuracy of the tension data rendered from the in-house meter are sufficient for the purposes of this study. Analysis of the residuals indicates that the 20:1 odds uncertainty of the in-house device is $\sim$140-N/m.

Appendix H

NACA0012 Airfoil Pressure Tap Coordinates

This appendix catalogs the pressure tap locations of the 0.91-m chord NACA0012 described by Section 3.1.3.

Table H.1: Pressure tap locations for NACA0012 airfoil. The z-coordinate indicates the height of the pressure tap above the span-end of the model which sits at the wind tunnel floor.

Suction Side			**Pressure Side**		
x/c	y/c	z/c	x/c	y/c	z/c
9.84E-05	1.55E-03	-9.31E-01	2.82E-03	-9.07E-03	-1.06E+00
3.16E-03	1.03E-02	-9.35E-01	4.08E-03	-1.08E-02	-1.06E+00
6.37E-03	1.44E-02	-9.33E-01	8.39E-03	-1.60E-02	-1.06E+00
8.51E-03	1.65E-02	-9.36E-01	1.09E-02	-1.78E-02	-1.06E+00
9.89E-03	1.75E-02	-9.35E-01	1.31E-02	-1.92E-02	-1.05E+00
1.29E-02	1.99E-02	-9.37E-01	1.42E-02	-2.00E-02	-1.06E+00
1.56E-02	2.21E-02	-9.37E-01	1.70E-02	-2.22E-02	-1.05E+00
1.73E-02	2.31E-02	-9.36E-01	1.86E-02	-2.32E-02	-1.05E+00
1.86E-02	2.39E-02	-9.37E-01	2.68E-02	-2.71E-02	-1.05E+00
2.53E-02	2.74E-02	-9.39E-01	5.15E-02	-3.66E-02	-1.05E+00
5.14E-02	3.73E-02	-9.44E-01	7.48E-02	-4.27E-02	-1.04E+00
7.40E-02	4.30E-02	-9.50E-01	9.99E-02	-4.75E-02	-1.04E+00
1.02E-01	4.84E-02	-9.56E-01	1.25E-01	-5.14E-02	-1.03E+00
1.28E-01	5.20E-02	-9.61E-01	1.48E-01	-5.41E-02	-1.02E+00
1.52E-01	5.47E-02	-9.67E-01	1.73E-01	-5.64E-02	-1.02E+00
1.76E-01	5.68E-02	-9.74E-01	2.02E-01	-5.83E-02	-1.01E+00
2.01E-01	5.85E-02	-9.79E-01	2.25E-01	-5.95E-02	-1.01E+00
2.27E-01	5.98E-02	-9.84E-01	2.50E-01	-6.04E-02	-1.00E+00
2.78E-01	6.12E-02	-9.96E-01	2.74E-01	-6.07E-02	-9.95E-01
3.01E-01	6.13E-02	-1.00E+00	3.00E-01	-6.09E-02	-9.91E-01
3.26E-01	6.11E-02	-1.01E+00	3.26E-01	-6.07E-02	-9.85E-01
3.51E-01	6.06E-02	-1.01E+00	3.49E-01	-6.05E-02	-9.77E-01
3.78E-01	5.99E-02	-1.02E+00	3.75E-01	-5.99E-02	-9.73E-01
4.01E-01	5.91E-02	-1.03E+00	4.00E-01	-5.92E-02	-9.64E-01
4.26E-01	5.80E-02	-1.03E+00	4.27E-01	-5.81E-02	-9.61E-01
4.52E-01	5.66E-02	-1.04E+00	4.50E-01	-5.70E-02	-9.54E-01
4.78E-01	5.53E-02	-1.04E+00	4.75E-01	-5.57E-02	-9.48E-01
4.99E-01	5.41E-02	-1.05E+00	5.00E-01	-5.43E-02	-9.44E-01
5.51E-01	5.07E-02	-1.06E+00	5.50E-01	-5.10E-02	-9.30E-01
6.01E-01	4.70E-02	-1.05E+00	6.01E-01	-4.72E-02	-9.43E-01
6.53E-01	4.25E-02	-1.04E+00	6.51E-01	-4.29E-02	-9.56E-01
7.03E-01	3.76E-02	-1.02E+00	7.01E-01	-3.83E-02	-9.65E-01
7.51E-01	3.26E-02	-1.01E+00	7.50E-01	-3.34E-02	-9.78E-01
8.01E-01	2.71E-02	-1.00E+00	7.99E-01	-2.81E-02	-9.90E-01
8.51E-01	2.15E-02	-9.89E-01	8.51E-01	-2.22E-02	-9.99E-01
9.02E-01	1.56E-02	-9.77E-01	9.00E-01	-1.60E-02	-1.01E+00
9.22E-01	1.31E-02	-9.73E-01	9.21E-01	-1.33E-02	-1.02E+00
9.40E-01	1.07E-02	-9.68E-01	9.39E-01	-1.08E-02	-1.02E+00
9.61E-01	7.79E-03	-9.63E-01	9.61E-01	-7.63E-03	-1.03E+00
9.82E-01	4.22E-03	-9.59E-01	9.81E-01	-4.61E-03	-1.03E+00